

# INSIGHTS IN TECHNICAL ADVANCES IN PLANT SCIENCE: 2021

EDITED BY: Roger Deal

PUBLISHED IN: Frontiers in Plant Science







# frontiers

## Frontiers eBook Copyright Statement

The copyright in the text of individual articles in this eBook is the property of their respective authors or their respective institutions or funders. The copyright in graphics and images within each article may be subject to copyright of other parties. In both cases this is subject to a license granted to Frontiers.

The compilation of articles constituting this eBook is the property of Frontiers.

Each article within this eBook, and the eBook itself, are published under the most recent version of the Creative Commons CC-BY licence.

The version current at the date of publication of this eBook is CC-BY 4.0. If the CC-BY licence is updated, the licence granted by Frontiers is automatically updated to the new version.

When exercising any right under the CC-BY licence, Frontiers must be attributed as the original publisher of the article or eBook, as applicable.

Authors have the responsibility of ensuring that any graphics or other materials which are the property of others may be included in the CC-BY licence, but this should be checked before relying on the CC-BY licence to reproduce those materials. Any copyright notices relating to those materials must be complied with.

Copyright and source acknowledgement notices may not be removed and must be displayed in any copy, derivative work or partial copy which includes the elements in question.

All copyright, and all rights therein, are protected by national and international copyright laws. The above represents a summary only. For further information please read Frontiers' Conditions for Website Use and Copyright Statement, and the applicable CC-BY licence.

ISSN 1664-8714

ISBN 978-2-83250-272-3

DOI 10.3389/978-2-83250-272-3

## About Frontiers

Frontiers is more than just an open-access publisher of scholarly articles: it is a pioneering approach to the world of academia, radically improving the way scholarly research is managed. The grand vision of Frontiers is a world where all people have an equal opportunity to seek, share and generate knowledge. Frontiers provides immediate and permanent online open access to all its publications, but this alone is not enough to realize our grand goals.

## Frontiers Journal Series

The Frontiers Journal Series is a multi-tier and interdisciplinary set of open-access, online journals, promising a paradigm shift from the current review, selection and dissemination processes in academic publishing. All Frontiers journals are driven by researchers for researchers; therefore, they constitute a service to the scholarly community. At the same time, the Frontiers Journal Series operates on a revolutionary invention, the tiered publishing system, initially addressing specific communities of scholars, and gradually climbing up to broader public understanding, thus serving the interests of the lay society, too.

## Dedication to Quality

Each Frontiers article is a landmark of the highest quality, thanks to genuinely collaborative interactions between authors and review editors, who include some of the world's best academicians. Research must be certified by peers before entering a stream of knowledge that may eventually reach the public - and shape society; therefore, Frontiers only applies the most rigorous and unbiased reviews.

Frontiers revolutionizes research publishing by freely delivering the most outstanding research, evaluated with no bias from both the academic and social point of view. By applying the most advanced information technologies, Frontiers is catapulting scholarly publishing into a new generation.

## What are Frontiers Research Topics?

Frontiers Research Topics are very popular trademarks of the Frontiers Journals Series: they are collections of at least ten articles, all centered on a particular subject. With their unique mix of varied contributions from Original Research to Review Articles, Frontiers Research Topics unify the most influential researchers, the latest key findings and historical advances in a hot research area! Find out more on how to host your own Frontiers Research Topic or contribute to one as an author by contacting the Frontiers Editorial Office: [frontiersin.org/about/contact](https://frontiersin.org/about/contact)



# INSIGHTS IN TECHNICAL ADVANCES IN PLANT SCIENCE: 2021

Topic Editor:

**Roger Deal**, Emory University, United States

**Citation:** Deal, R., ed. (2022). Insights in Technical Advances in Plant Science: 2021. Lausanne: Frontiers Media SA.  
doi: 10.3389/978-2-83250-272-3



# Table of Contents

- 05    *Tracing Mobile DNAs: From Molecular to Population Scales***  
Wenwen Fan, Ling Wang, Jie Chu, Hui Li, Eun Yu Kim and Jungnam Cho
- 13    *Effects of Stem Density on Crown Architecture of Scots Pine Trees***  
Ninni Saarinen, Ville Kankare, Saija Huuskonen, Jari Hynynen, Simone Bianchi, Tuomas Yrttimaa, Ville Luoma, Samuli Junntila, Markus Holopainen, Juha Hyypä and Mikko Vastaranta
- 27    *Loop-Mediated Isothermal Amplification for Detection of Plant Pathogens in Wheat (Triticum aestivum)***  
Sandra V. Gomez-Gutierrez and Stephen B. Goodwin
- 43    *Durability and Moisture Dynamics of Douglas-Fir Wood From Slovenia***  
Miha Humar, Viljem Vek, Primož Oven, Boštjan Lesar, Davor Kržišnik, Eli Keržič, Miha Hočevár and Robert Brus
- 58    *Relationships Between Wood-Anatomical Features and Resistance Drilling Density in Norway Spruce and European Beech***  
Domen Arnič, Luka Krajnc, Jožica Gričar and Peter Prisan
- 71    *Applications of a Hyperspectral Imaging System Used to Estimate Wheat Grain Protein: A Review***  
Junjie Ma, Bangyou Zheng and Yong He
- 81    *Real-Time Visualization of Scent Accumulation Reveals the Frequency of Floral Scent Emissions***  
Hyoungsoo Kim, Gilgu Lee, Junyong Song and Sang-Gyu Kim
- 90    *An Improved Agrobacterium-Mediated Transformation and Genome-Editing Method for Maize Inbred B104 Using a Ternary Vector System and Immature Embryos***  
Minjeong Kang, Keunsub Lee, Todd Finley, Hal Chappell, Veena Veena and Kan Wang
- 110    *Low-Input High-Molecular-Weight DNA Extraction for Long-Read Sequencing From Plants of Diverse Families***  
Alessia Russo, Baptiste Mayjonade, Daniel Frei, Giacomo Potente, Roman T. Kellenberger, Léa Frachon, Dario Copetti, Bruno Studer, Jürg E. Frey, Ueli Grossniklaus and Philipp M. Schlüter
- 122    *Assessing Grapevine Biophysical Parameters From Unmanned Aerial Vehicles Hyperspectral Imagery***  
Alessandro Matese, Salvatore Filippo Di Gennaro, Giorgia Orlandi, Matteo Gatti and Stefano Poni
- 136    *Exploration of Alternative Approaches to Phenotyping of Late Leaf Spot and Groundnut Rosette Virus Disease for Groundnut Breeding***  
Ivan Chapu, David Kalule Okello, Robert C. Ongom Okello, Thomas Lapaka Odong, Sayantan Sarkar and Maria Balota



**153    *A Substantial Role of Agro-Textiles in Agricultural Applications***

Neha Sharma, Ben Allardyce, Rangam Rajkhowa, Alok Adholeya and Ruchi Agrawal

**164    *Overexpression of TwSQS, TwSE, and TwOSC Regulates Celastrol Accumulation in Cambial Meristematic Cells and Dedifferentiated Cells***

Yadi Song, Jiawei Zhou, Yifeng Zhang, Yujun Zhao, Xiujuan Wang, Tianyuan Hu, Yuru Tong, Luqi Huang and Wei Gao





# Tracing Mobile DNAs: From Molecular to Population Scales

Wenwen Fan<sup>1,2†</sup>, Ling Wang<sup>1,2†</sup>, Jie Chu<sup>1,2†</sup>, Hui Li<sup>1,2†</sup>, Eun Yu Kim<sup>1\*</sup> and Jungnam Cho<sup>1,2,3\*</sup>

<sup>1</sup> National Key Laboratory of Plant Molecular Genetics, CAS Center for Excellence in Molecular Plant Sciences, Shanghai Institute of Plant Physiology and Ecology, Chinese Academy of Sciences, Shanghai, China, <sup>2</sup> University of Chinese Academy of Sciences, Beijing, China, <sup>3</sup> CAS-JIC Centre of Excellence for Plant and Microbial Science, Chinese Academy of Sciences, Shanghai, China

## OPEN ACCESS

### Edited by:

Roger Deal,  
Emory University, United States

### Reviewed by:

Stefan Grob,  
University of Zurich, Switzerland

### \*Correspondence:

Eun Yu Kim  
eunyukim@cemps.ac.cn  
Jungnam Cho  
jungnamcho@cemps.ac.cn

<sup>†</sup> These authors have contributed  
equally to this work

### Specialty section:

This article was submitted to  
Technical Advances in Plant Science,  
a section of the journal  
Frontiers in Plant Science

**Received:** 16 December 2021

**Accepted:** 11 January 2022

**Published:** 01 February 2022

### Citation:

Fan W, Wang L, Chu J, Li H,  
Kim EY and Cho J (2022) Tracing  
Mobile DNAs: From Molecular  
to Population Scales.  
*Front. Plant Sci.* 13:837378.  
doi: 10.3389/fpls.2022.837378

Transposable elements (TEs, transposons) are mobile DNAs that are prevalent in most eukaryotic genomes. In plants, their mobility has vastly contributed to genetic diversity which is essential for adaptive changes and evolution of a species. Such mobile nature of transposon has been also actively exploited in plant science research by generating genetic mutants in non-model plant systems. On the other hand, transposon mobilization can bring about detrimental effects to host genomes and they are therefore mostly silenced by the epigenetic mechanisms. TEs have been studied as major silencing targets and acted a main feature in the remarkable growth of the plant epigenetics field. Despite the importance of transposon in plant biology and biotechnology, their mobilization and the underlying mechanisms are largely left unanswered. This is mainly because of the sequence repetitiveness of transposons, which makes their detection and analyses difficult and complicated. Recently, some attempts have been made to develop new experimental methods detecting active transposons and their mobilization behavior. These techniques reveal TE mobility in various levels, including the molecular, cellular, organismal and population scales. In this review, we will highlight the novel technical approaches in the study of mobile genetic elements and discuss how these techniques impacted on the advancement of transposon research and broadened our understanding of plant genome plasticity.

**Keywords:** transposon, long terminal repeat (LTR) retrotransposon, retrotransposition, ALE-seq, mobilome-seq, long-read sequencing, droplet digital PCR (ddPCR)

## INTRODUCTION

Transposable elements (TEs or transposons) are stretches of DNA that move around the genomes and are ubiquitous in most eukaryotic genomes (Feschotte, 2008; Lisch, 2012; Chuong et al., 2017). Particularly, the genomes of major food crops such as barley, wheat and maize contain myriads of transposons making up more than 80% of their genomes (Tenaillon et al., 2010). Among the diverse types of transposons, the long terminal repeat (LTR) retrotransposon is the predominant type of TEs in most plant genomes (Casacuberta and Santiago, 2003; Grandbastien, 2015; Cho, 2018; Satheesh et al., 2021) and thus will be the main focus of this review. The mobilization of an LTR retrotransposon is mediated by the reverse transcription of TE mRNAs to cDNAs (also referred to as extrachromosomal DNA, ecDNA), which happens in virus-like particles (VLPs) and is followed by the insertion to new genomic positions by the integrase (Cho et al., 2019;



Satheesh et al., 2021). Due to the mobile nature of transposons and thereby potential danger of genomic instability, they are subject to the host genomes' epigenetic silencing pathways, including chromatin modification and DNA methylation (Slotkin and Martienssen, 2007; Matzke and Mosher, 2014). On the other hand, transposon is one of the major sources of genetic diversity, which is critical for evolution and adaptive changes of plants (Lisch, 2012; Dubin et al., 2018). Besides, TEs have been actively exploited in the plant science field as useful mutagenic reagents. For example, *Tos17* in rice is specifically activated by *in vitro* tissue culture and the resulting random insertional mutants tagged with *Tos17* are important genetic resources in the rice functional genomics (Hirochika et al., 1996; Hirochika, 2010). Similarly, *Tnt1* was used to generate genetic mutants in *Medicago truncatula*, *Brachypodium distachyon*, and *Glycine max* (D'Erfurth et al., 2003; Tadege et al., 2008; Revalska et al., 2011; Cui et al., 2012; Nandety et al., 2020), and the maize *Ac/Ds* DNA transposon system was used as a functional genomics tool in *Arabidopsis*, *Oryza sativa*, and *Glycine max* (Long et al., 1993; Mathieu et al., 2009; Wang et al., 2013). Despite the vast importance of transposons, little is known about the regulatory mechanisms of their mobilization, which is largely because of the lack of experimental methods that can detect the transposition events with sufficient sensitivity and precision.

It is well documented that transposons can be transcriptionally activated by the environmental challenges and at specific cell types and developmental stages (Martínez and Slotkin, 2012; Cho, 2018; Cho et al., 2019). However, the mobilization of activated transposons hardly happens likely because of complex regulation at the post-transcriptional steps (Hung and Slotkin, 2021; Kim et al., 2021b). Owing to the scarcity of transposition events and technical difficulty to detect it, it has been challenging to study transposon mobilization. In the past, transposon insertion was inferred by phenotypic abnormalities caused by deleterious mutations of a gene disrupted by TE integration. For example, some of the epigenetic recombinant inbred lines (epiRILs) generated from the *met1* mutant in *Arabidopsis* exhibited various abnormal phenotypes, which were associated with gene disruption caused by the transposition of *Evade* retroelement (Mirouze et al., 2009; Reinders et al., 2009; Reinders and Paszkowski, 2009). A PCR-based technique called transposon display (TD) and its derivative methods are usually the experimental approaches of choice to detect and locate new insertions of a transposon of interest (Kim et al., 2021a). Briefly, the adapter with known sequence is ligated to the restriction enzyme-digested DNA ends. PCR amplification by the specific sequences of the adapter and transposon ends yields amplicons containing the genomic regions flanking the transposon of interest. Although TD is an efficient and versatile method to study transposition events, it has certain fundamental limitations; for instance, transposon of high copy number is difficult to be amplified and hardly detected for new insertions. In addition, TD requires prior knowledge of TE sequences and thus relies on the quality of TE annotation. Most importantly, TD can only reveal the insertions that are meiotically inherited and fixed in the genomes, thus is not able to detect transpositions in real time and those

happened in somatic cells (Figure 1). Over the last several years, there have been significant efforts to unveil the landscape of transpositions in the plant genomes by developing novel experimental methods. These innovative approaches reveal the mobilomes at varying scales from molecular to population levels. In this review, we will introduce and discuss the up-to-date experimental techniques tracing mobile DNAs in the plant genomes.

## Molecular Level

The mobilization cycle of an LTR retrotransposon consists of transcription, reverse transcription, and integration to new genomic positions. Since the direct detection of transposon integration is relatively more challenging, the DNA intermediate which is the final product of reverse transcription reaction and the direct target of integration has been studied to infer the transposon mobility. In this section, the cutting edge methods detecting the DNA intermediates of LTR retrotransposons will be highlighted (Figures 2A,B).

### Detection of Linear ecDNA

The reverse transcription reaction of transposon gives rise to linear extrachromosomal DNAs (ecDNAs) and it is the linear form of ecDNAs that is capable of integrating to genomic DNA (Cho et al., 2019; Wang et al., 2021a,b). As an attempt to detect ecDNA, Griffiths et al. (2018) established a method named sequence-independent retrotransposon trapping (SIRT). SIRT employs the adapter ligation to the end of ecDNAs and specific amplification targeted to the conserved primer-binding site (PBS) sequence, which is located immediately after the upstream LTR. Using this method a novel family of LTR retrotransposon named *DODGER* was identified in the *Landsberg erecta* ecotype of *Arabidopsis* mutated with *MET1* (Griffiths et al., 2018). Unfortunately, SIRT exhibited limited robustness when tested in crop genomes, presumably because of the large size of the crop genomes and abundance of transposon-related sequences. An improved method was then developed named amplification of LTR extrachromosomal DNA followed by sequencing (ALE-seq), which is able to detect the LTRs of crop genomes with larger size (Cho et al., 2019). ALE-seq uses two primers specific to sequences of the adapter and PBS in two separate reactions: *in vitro* transcription and reverse transcription. Using this novel method, Cho et al. (2019) identified a new *Copia*-family LTR retrotransposon *Go-on* in the heat-stressed rice plants. Importantly, the ALE-seq method is particularly useful in non-reference crop species because the final amplicon product can reveal the full-length sequences of the LTR region. Such reference- and annotation-free approach was successfully tested in tomato pericarp samples and identified a novel *Gypsy*-family retroelement *Fruit-Induced RetroElement (FIRE)* (Cho et al., 2019). Although ALE-seq is sensitive enough to identify ecDNAs from crop genomes, it can only sequence the 5' LTR regions and it is desired to further improve this method to cover full range of a TE. Altogether, ALE-seq is a versatile, efficient and high-throughput method identifying active LTR retroelements in crop genomes.

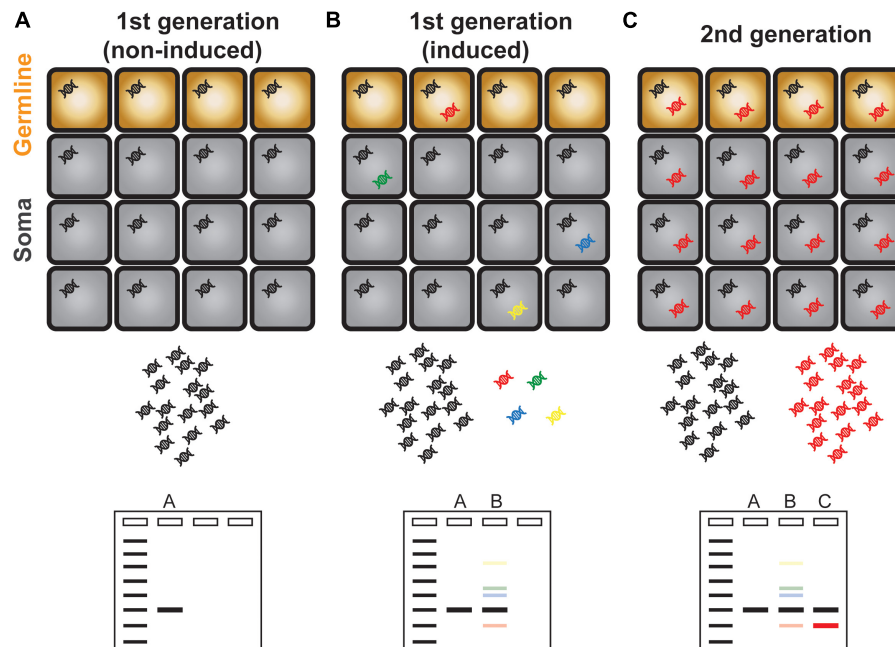


**FIGURE 1 |** Schematic illustration of transposon display. **(A)** A single copy TE is present evenly in all cells and is represented as a single band in a transposon display experiment. **(B)** Activation and mobilization of a TE gave rise to new and additional copies inserted in different genomic positions as represented in different colors. Because of the scarcity of newly copied DNA, transposon display method is unable to amplify these DNAs which are illustrated as faint bands. **(C)** The new TE copy that mobilized in germline cells is inherited to the next generation. The transgenerationally maintained new TE DNA can be amplified efficiently and is visible as a discrete band in a gel electrophoresis.

## Detection of Circular ecDNA

Two LTRs of ecDNAs are bound by the integrases and homodimerization of integrases place two ends of an ecDNA close next to each other, which is then recognized as a DNA double-strand break by the cellular DNA damage response pathways (Møller et al., 2015, 2016; Lanciano et al., 2017). The homologous recombination and non-homologous end joining pathways repair the LTR-LTR gap, resulting in single-LTR and double-LTR extrachromosomal circular DNAs (eccDNAs), respectively (Lanciano et al., 2017). As a by-product of an activated LTR retrotransposon (albeit incapable of integration) eccDNA is considered to represent active TE mobility. Lanciano et al. (2017) established an experimental method called mobilome-seq that specifically sequences circular DNAs including retrotransposon-derived eccDNAs. The mobilome-seq procedure first initiates with digestion of linear DNA (mostly derived from genomic DNA) and randomly amplifying the remaining circular DNA by the isothermal stand displacement amplification (i.e., rolling circle amplification, **Figure 2B**). Unlike ALE-seq, mobilome-seq has additional advantage that can sequence full-length retroelement; however, it is also important to note that it reads sequences derived from organellar circular DNAs requiring additional filtering steps to remove them, which compromises the sequencing efficiency (Lanciano et al., 2017; Sathesh et al., 2021). Nonetheless, mobilome-seq can be a useful approach to investigate active retroelements because it requires relatively low sequence coverage, which can be particularly useful to

studies using rare plant materials and samples with limited availability. For example, Lanciano et al. (2017) discovered a *PopRice* retrotransposon family that becomes active in the rice endosperm. In addition, Thieme et al. (2017) identified *Houba*, a *Copia*-like retrotransposon in rice, that was activated by the treatment of chemical inhibitors of RNA Polymerase II and DNA methylation. Moreover, Esposito et al. (2019) found that *nightshade*, a *Copia/Ale* retrotransposon in potatoes, produces large amount of eccDNAs in non-stressed plants, while under the cold stress condition is no longer active, presumably because of the hypermethylation induced by cold stress. More recently, mobilome-seq revealed that *Onsen*, a *Copia*-like retrotransposon specifically activated in the heat-stressed *Arabidopsis* plants, produces eccDNAs mostly from two copies, *AT1G11265* and *AT5G13205* (Roquis et al., 2021). In summary, mobilome-seq is a useful method detecting the retrotransposon mobility by sequencing eccDNAs.

## Long-Read Sequencing

One of the challenges in the study of transposon is that TE sequences are repetitive in genomes and thus cause serious ambiguity in their analysis. This is particularly more troublesome when analyzing short-read sequencing data. Recently, the long-read sequencing technologies advanced remarkably and greatly improved the accuracy of transposon sequence analysis. For example, in the recent work of Panda and Slotkin, Oxford Nanopore Technology (ONT) sequencing was tested in the DNA methylation-deficient mutants of *Arabidopsis*, which significantly



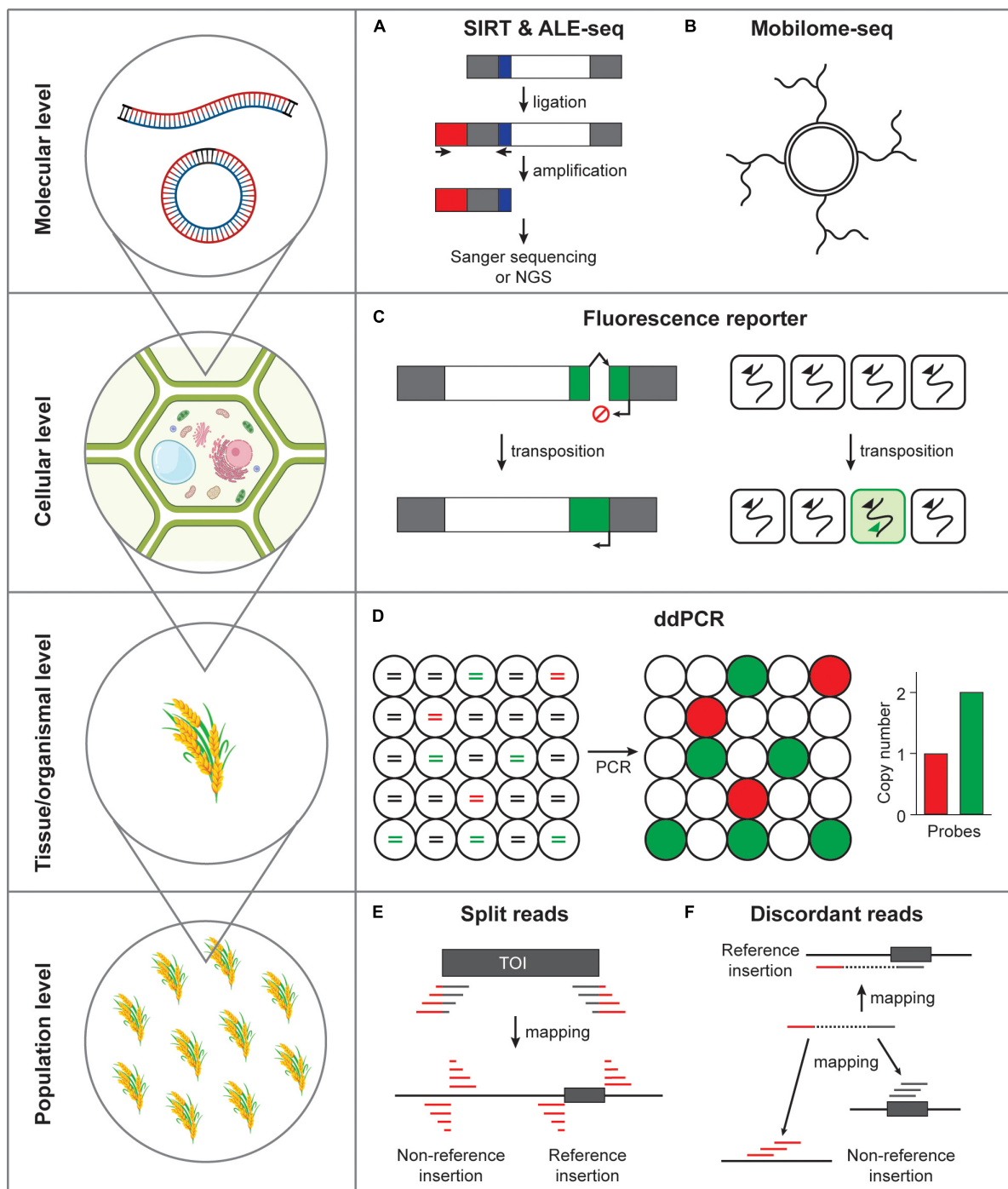


**FIGURE 2 |** Methods detecting transposon mobility at varying scales. **(A)** Activated retrotransposon gives rise to extrachromosomal DNAs in both linear and circular forms. SIRT and ALE-seq are the methods that can detect linear DNA intermediates of retroelements. Gray box, long terminal repeats; white box, open reading frame; red box, adapter; blue box, PBS. **(B)** Extrachromosomal circular DNAs can be amplified by the isothermal strand displacement DNA polymerization. **(C)** Fluorescence reporter retrotransposition system can specifically label the cells in which transposition occurred. Green box, fluorescence reporter gene; arrows, transcriptional start sites; broken arrow, intron. **(D)** Transposon mobilization at tissue or organismal level can be assessed by ddPCR. Fragmented DNAs are randomly distributed in separate droplets and independently amplified. Lines in circles represent fragmented genomic DNA colored for different PCR templates. Red, a single-copy reference gene; green, transposon of interest; black, non-templated DNA. **(E)** The split reads method uses the reads tagged with transposon sequences that map to the insertion positions. TOI, transposon of interest; gray box, transposon; gray line, transposon sequence; red line, flanking sequence of transposon. **(F)** The discordant reads method uses the paired-end reads, which map to transposon from one side and to a distant genomic site from the other side of a read pair.

improved the quality of TE annotation (Panda and Slotkin, 2020). In an independent work by Lee et al. (2020) the ONT method was tested in the VLP fraction collected from the epigenetic mutants of *Arabidopsis*. This allowed direct identification of active transposable elements in their full lengths and also revealed diverse forms of DNA intermediates (Lee et al., 2020). Overall, the long-read sequencing technology is apparently a game-changer in the field of transposon research and highly expected to unveil the hidden aspects of transposon mobilization which was previously unable to be studied.

## Cellular Level

In the previous section, we focused on the methods detecting the DNA intermediates produced from active LTR retrotransposons which could be used as a proxy of TE mobility. It is important to note that the presence of DNA intermediates can be a good indication of TE activation; however, it does not necessarily represent transposition events directly. While in plants there has not been any robust methods detecting transposition events at the cellular level so far, the transposition reporter system used in humans and yeast has served as a standard method assessing transposon mobility. In this section, the transposition reporter assay systems revealing transposon insertion at the cellular level will be introduced (Figure 2C).

Retrotransposition reporter system was first suggested in yeast using the *Ty* retroelement *TyH3* that includes an intron fragment (Boeke et al., 1985). Heidmann et al. (1988) had later developed an improved version using the *neo* (neomycin phosphotransferase) gene cassette (neoRT). In this system, the *neo* gene is disrupted by an artificial intron containing polyadenylation signals, thereby the functional *neo* proteins can be produced only from the transposed intron-free DNA (Heidmann et al., 1988). This method allows for determination of transposition efficiency when cells are grown in the selective G418-containing media (Heidmann et al., 1988). Similar methods have been developed to study mobilization of other types of TEs including the intracisternal A-type particles (IAPs) in mice and the long interspersed elements (LINEs) in *Drosophila* and human cells (Heidmann and Heidmann, 1991; Jensen and Heidmann, 1991; Tchenio et al., 1993; Maestre et al., 1995; Esnault et al., 2000). Further improvement of retrotransposition assay system was attempted by Moran et al. (1996) by developing the reporter cassette consisting of an antisense copy of *neo* gene incorporated in two human L1 elements (L1.2 and LRE2) in a cultured human cell line (Rangwala and Kazazian, 2009). In addition, other alternative methods have also been developed by employing blasticidin S deaminase, *his3* auxotrophic marker and a *lacZ* colorimetric indicator (Curcio and Garfinkel, 1991; Tchenio and Heidmann, 1992; Goodier et al., 2007). However, such intron-containing reporter systems had some drawbacks that retrotransposition assay is dependent on antibiotics resistance and assessed by counting colonies, which usually takes long time and has relatively low throughput. Recently, innovations to this classical method have been made by replacing the antibiotics resistance genes to visual fluorescence (Ostertag et al., 2000) and bioluminescence genes (Xie et al., 2011), which dramatically increases the sensitivity and throughput, enabling large-scale

screening experiments. In summary, the retrotransposition assay systems have been widely used to determine the transposition rate of a retroelement mostly in non-plant systems. Introducing such system to the plant systems will enable single-cell detection of transposition and greatly improve our understanding of transposon mobilization.

## Tissue/Organism Level Droplet Digital PCR

The retrotransposition reporter assay system described in the previous section can be potentially useful for cell- and tissue-level detection of transposition events. The synthetic artificial retrotransposon mobility assay is powerful because it enables direct visualization of transposition; however, such transgenic approach can be challenging in many non-reference plant species. Determination of copy number changes of an endogenous TE can be one of the easiest alternative methods to assess transpositional activity. It is worth noting, however, that the logarithmic quantitative real-time PCR analysis is difficult to measure subtle differences of copy number (Bubner and Baldwin, 2004; Bubner et al., 2004; Fan and Cho, 2021). Droplet digital PCR (ddPCR) is a far more accurate and sensitive technique that allows for digital measurement of DNA copy number (Hindson et al., 2013; Doi et al., 2015; Campomenosi et al., 2016; Głowacka et al., 2016; Fan and Cho, 2021). The ddPCR experiment performs DNA amplification in thousands of nanoliter-scale droplets that read-out positive or negative fluorescence signals (Figure 2D). The resulting digital data is then processed by a Poisson probability distribution to derive copy numbers. In fact, we previously showed that ddPCR can be a robust method that accurately detects the copy number of a retrotransposon (Fan and Cho, 2021). Importantly, the ddPCR technique only requires a trace amount of DNA and is therefore possible to be performed in DNAs extracted from small amount of tissues and rare samples.

## Population Level Next-Generation Sequencing-Based Transposable Element Mapping

*Arabidopsis* 1,001 genome project produced massive paired-end short-read whole-genome sequencing data from 1,135 accessions from a worldwide collection (Weigel and Mott, 2009; Cao et al., 2011; Alonso-Blanco et al., 2016). Similar attempt has been made in rice generating sequencing data from a total of more than 3,000 germplasm accessions (Li J.-Y. et al., 2014; Li Z. et al., 2014). Equipped with relatively well-assembled and annotated reference genomes available for both plant species, TE insertion polymorphisms have been intensively profiled at population level. Several softwares have been developed so far to systematically identify transposon insertions. These tools take advantage of diverse sequencing read information; for instance, split reads in Transposon Insertion Finder (TIF) (Nakagome et al., 2014), SPLITREADER (Baduel et al., 2021b), and RTRIP (Liu et al., 2020), discordant read pair alignment in TRACKPOSON (Carpentier et al., 2019), and combination of these two as demonstrated in TEPID (Stuart et al., 2016). Additionally, in a recent work of Baduel et al. (2021a) SPLITREADER and

TEPID pipelines were integrated, building an intensive map of TE landscape in *Arabidopsis*.

The split-reads method first searches for reads containing the end sequences of a TE and target site duplications (TSDs), which are identical sequences flanking a TE and created as a result of transposition (**Figure 2E**). In TIF, the read sequences tagged with transposon end sequences are mapped to the reference genome to identify the locations of *de novo* insertions (Nakagome et al., 2014). Similarly, SPLITREADER extracts reads that do not properly map to the reference genome and forcedly map to 5' and 3' TE sequence extremities (within a range of 300 bp) by soft clipping (Baduel et al., 2021b). Then, the bona fide insertions and their locations are identified by mapping the clipped reads to the reference genome. Recently, Liu et al. (2020) tested a similar method in rice and generated the RTRIP database, which contains the comprehensive profile of transposon insertion polymorphisms in the rice 3K genome project.

The discordant read pair method employs mapping of reads from one side to the target TE and the other side to a distant genomic region (**Figure 2F**). TRACKPOSON, for instance, first maps all reads of a given accession onto each TE family represented by a single consensus sequence, and then maps the unmapped paired reads to the rice reference genome to determine its location (Carpentier et al., 2019). The transposition landscape revealed by these methods uncovered that transposon proliferation is most strongly associated with the presence of a transposon at a specific location, which was somehow activated during the evolutionary process (Carpentier et al., 2019).

## CONCLUDING REMARKS AND FUTURE PERSPECTIVES

We reviewed the recent technical advances in transposon research by highlighting several new methods identifying active TEs and detecting transposition events (**Figure 2**). These novel experimental methods and improved transposon annotation aided by the long-read sequencing technologies and population-scale genome resequencing databases will open-up a new window to unveil a long-lasting mystery of jumping genes. Although the experimental techniques described above has greatly improved our ability to observe transposition events, there are still several issues left to be dealt with. Firstly, detection of transposition

events at single-cell level will be obviously the next task to be accomplished. To this end, a novel approach for the single-cell detection of transposon mobilization is highly desired. Secondly, the single-cell genomics will vastly benefit the transposon biology. The transposition reporter systems introduced above rely on the artificially engineered TE sequences. The investigation of the native TEs and their transposition at high resolution will only be possible when the single-cell genomics technologies become more available. Thirdly, the detection sensitivity of transposon research tools will have to be improved further. The new experimental tools to study transposon such as ALE-seq and mobilome-seq are mostly tested in the epigenetic mutants where transposons become unusually active in mobility. Although these methods were sensitive enough to discover novel active retroelements (*Go-on* and *PopRice*), the moderately active TEs were difficult to be identified (Lanciano et al., 2017; Cho et al., 2019). Considering the rarity of DNAs representing activated TE intermediates or derived from transposed copy, the improvement of detection sensitivity of these methods will help identify new transposons that are present in small niches of cells or activated only to a moderate level. Altogether, the technical advances of transposon research at varying scales have greatly contributed to our understanding of TE life cycle and will broaden the breadth of knowledge on mobile genetic elements and genome plasticity.

## AUTHOR CONTRIBUTIONS

WF, LW, JiC, HL, and EK drafted the manuscript. EK and JuC edited the manuscript. JuC revised the manuscript. All authors contributed to the article and approved the submitted version.

## FUNDING

The work was supported by the grants from the National Natural Science Foundation of China (31970518, 32150610473, and 32111540256), the Strategic Priority Research Program of the Chinese Academy of Sciences (XDB27030209), and the General Program of Natural Science Foundation of Shanghai (21ZR1470700). EK was the recipient of a President's International Fellowship Initiative (PIFI) young staff fellowship (2021FYB0001) from CAS.

## REFERENCES

- Alonso-Blanco, C., Andrade, J., Becker, C., Bemm, F., Bergelson, J., Borgwardt, K. M., et al. (2016). 1,135 genomes reveal the global pattern of polymorphism in *Arabidopsis thaliana*. *Cell* 166, 481–491. doi: 10.1016/j.cell.2016.05.063
- Baduel, P., Quadrana, L., and Colot, V. (2021b). Efficient detection of transposable element insertion polymorphisms between genomes using short-read sequencing data. *Methods Mol. Biol.* 2250, 157–169. doi: 10.1007/978-1-0716-1134-0\_15
- Baduel, P., Leduque, B., Ignace, A., Gy, I., Gil, J., Loudet, O., et al. (2021a). Genetic and environmental modulation of transposition shapes the evolutionary potential of *Arabidopsis thaliana*. *Genome Biol.* 22, 138. doi: 10.1186/s13059-021-02348-5
- Boeke, J. D., Garfinkel, D. J., Styles, C. A., and Fink, G. R. (1985). Ty elements transpose through an RNA intermediate. *Cell* 40, 491–500. doi: 10.1016/0092-8674(85)90197-7
- Bubner, B., and Baldwin, I. T. (2004). Use of real-time PCR for determining copy number and zygosity in transgenic plants. *Plant Cell Rep.* 23, 263–271. doi: 10.1007/s00299-004-0859-y
- Bubner, B., Gase, K., and Baldwin, I. T. (2004). Two-fold differences are the detection limit for determining transgene copy numbers in plants by real-time PCR. *BMC Biotechnol.* 4:14. doi: 10.1186/1472-6750-4-14
- Campomenosi, P., Gini, E., Noonan, D. M., Poli, A., D'Antona, P., Rotolo, N., et al. (2016). A comparison between quantitative PCR and droplet digital PCR technologies for circulating microRNA quantification in human lung cancer. *BMC Biotechnol.* 16:60. doi: 10.1186/s12896-016-0292-7



- Cao, J., Schneeberger, K., Ossowski, S., Günther, T., Bender, S., Fitz, J., et al. (2011). Whole-genome sequencing of multiple *Arabidopsis thaliana* populations. *Nat. Genet.* 43, 956–963. doi: 10.1038/ng.911
- Carpentier, M.-C., Manfroi, E., Wei, F.-J., Wu, H.-P., Lasserre, E., Llauro, C., et al. (2019). Retrotranspositional landscape of Asian rice revealed by 3000 genomes. *Nat. Commun.* 10:24. doi: 10.1038/s41467-018-07974-5
- Casacuberta, J. M., and Santiago, N. (2003). Plant LTR-retrotransposons and MITEs: control of transposition and impact on the evolution of plant genes and genomes. *Gene* 311, 1–11. doi: 10.1016/S0378-1119(03)00557-2
- Cho, J. (2018). Transposon-derived Non-coding RNAs and their function in plants. *Front. Plant Sci.* 9:600. doi: 10.3389/fpls.2018.00600
- Cho, J., Benoit, M., Catoni, M., Drost, H.-G., Brestovitsky, A., Oosterbeek, M., et al. (2019). Sensitive detection of pre-integration intermediates of long terminal repeat retrotransposons in crop plants. *Nat. Plants* 5, 26–33. doi: 10.1038/s41477-018-0320-9
- Chuong, E. B., Elde, N. C., and Feschotte, C. (2017). Regulatory activities of transposable elements: from conflicts to benefits. *Nat. Rev. Genet.* 18, 71–86. doi: 10.1038/nrg.2016.139
- Cui, Y., Barampuram, S., Stacey, M. G., Hancock, C. N., Findley, S., Mathieu, M., et al. (2012). Tnt1 retrotransposon mutagenesis: a tool for soybean functional genomics. *Plant Physiol.* 161, 36–47. doi: 10.1104/pp.112.205369
- Curcio, M. J., and Garfinkel, D. J. (1991). Single-step selection for Ty1 element retrotransposition. *Proc. Natl. Acad. Sci. U.S.A.* 88, 936–940. doi: 10.1073/pnas.88.3.936
- D'Erforth, I., Cosson, V., Eschstruth, A., Lucas, H., Kondorosi, A., and Ratet, P. (2003). Efficient transposition of the Tnt1 tobacco retrotransposon in the model legume *Medicago truncatula*. *Plant J.* 34, 95–106. doi: 10.1046/j.1365-313X.2003.01701.x
- Doi, H., Takahara, T., Minamoto, T., Matsushashi, S., Uchii, K., and Yamanaka, H. (2015). Droplet digital polymerase chain reaction (PCR) outperforms real-time PCR in the detection of environmental DNA from an invasive fish species. *Environ. Sci. Technol.* 49, 5601–5608. doi: 10.1021/acs.est.5b00253
- Dubin, M. J., Mittelsten Scheid, O., and Becker, C. (2018). Transposons: a blessing curse. *Curr. Opin. Plant Biol.* 42, 23–29. doi: 10.1016/j.pbi.2018.01.003
- Esnault, C., Maestre, J., and Heidmann, T. (2000). Human LINE retrotransposons generate processed pseudogenes. *Nat. Genet.* 24, 363–367. doi: 10.1038/74184
- Espósito, S., Barteri, F., Casacuberta, J., Mirouze, M., Carputo, D., and Aversano, R. (2019). LTR-TEs abundance, timing and mobility in *Solanum commersonii* and *S. tuberosum* genomes following cold-stress conditions. *Planta* 250, 1781–1787. doi: 10.1007/s00425-019-03283-3
- Fan, W., and Cho, J. (2021). “Quantitative measurement of transposon copy number using the droplet digital PCR,” in *Plant Transposable Elements. Methods in Molecular Biology*, Vol. 2250, ed. J. Cho (New York, NY: Humana), 171–176. doi: 10.1007/978-1-0716-1134-0\_16
- Feschotte, C. (2008). Transposable elements and the evolution of regulatory networks. *Nat. Rev. Genet.* 9, 397–405. doi: 10.1038/nrg2337
- Głowacka, K., Kromdijk, J., Leonelli, L., Niyogi, K. K., Clemente, T. E., and Long, S. P. (2016). An evaluation of new and established methods to determine T-DNA copy number and homozygosity in transgenic plants. *Plant Cell Environ.* 39, 908–917. doi: 10.1111/pce.12693
- Goodier, J. L., Zhang, L., Vetter, M. R., and Kazazian, H. H. (2007). LINE-1 ORF1 protein localizes in stress granules with other RNA-binding proteins, including components of RNA interference RNA-induced silencing complex. *Mol. Cell Biol.* 27, 6469–6483. doi: 10.1128/mcb.00332-07
- Grandbastien, M. A. (2015). LTR retrotransposons, handy hitchhikers of plant regulation and stress response. *Biochim. Biophys. Acta Gene Regul. Mech.* 1849, 403–416. doi: 10.1016/j.bbagrm.2014.07.017
- Griffiths, J., Catoni, M., Iwasaki, M., and Paszkowski, J. (2018). Sequence-independent identification of active LTR Retrotransposons in *Arabidopsis*. *Mol. Plant* 11, 508–511. doi: 10.1016/j.molp.2017.10.012
- Heidmann, T., Heidmann, O., and Nicolas, J. F. (1988). An indicator gene to demonstrate intracellular transposition of defective retroviruses. *Proc. Natl. Acad. Sci. U.S.A.* 85, 2219–2223. doi: 10.1073/pnas.85.7.2219
- Heldmann, O., and Heidmann, T. (1991). Retrotransposition of a mouse IAP sequence tagged with an indicator gene. *Cell* 64, 159–170. doi: 10.1016/0092-8674(91)90217-M
- Hindson, C. M., Chevillet, J. R., Briggs, H. A., Gallichotte, E. N., Ruf, I. K., Hindson, B. J., et al. (2013). Absolute quantification by droplet digital PCR versus analog real-time PCR. *Nat. Methods* 10, 1003–1005. doi: 10.1038/nmeth.2633
- Hirochika, H. (2010). Insertional mutagenesis with Tos17 for functional analysis of rice genes. *Breed. Sci.* 60, 486–492. doi: 10.1270/jsbbs.60.486
- Hirochika, H., Sugimoto, K., Otsuki, Y., Tsugawa, H., and Kanda, M. (1996). Retrotransposons of rice involved in mutations induced by tissue culture. *Proc. Natl. Acad. Sci. U.S.A.* 93, 7783–7788. doi: 10.1073/pnas.93.15.7783
- Hung, Y.-H., and Slotkin, R. K. (2021). The initiation of RNA interference (RNAi) in plants. *Curr. Opin. Plant Biol.* 61, 102014. doi: 10.1016/j.pbi.2021.102014
- Jensen, S. A., and Heidmann, T. (1991). An indicator gene for detection of germline retrotransposition in transgenic *Drosophila* demonstrates RNA-mediated transposition of the LINE I element. *EMBO J.* 10, 1927–1937. doi: 10.1002/j.1460-2075.1991.tb07719.x
- Kim, E. Y., Wang, L., Lei, Z., Li, H., Fan, W., and Cho, J. (2021b). Ribosome stalling and SGS3 phase separation prime the epigenetic silencing of transposons. *Nat. Plants* 7, 303–309. doi: 10.1038/s41477-021-00867-4
- Kim, E. Y., Fan, W., and Cho, J. (2021a). Determination of TE insertion positions using transposon display. *Methods Mol. Biol.* 2250, 115–121. doi: 10.1007/978-1-0716-1134-0\_11
- Lanciano, S., Carpentier, M.-C., Llauro, C., Jobet, E., Robakowska-Hyzorek, D., Lasserre, E., et al. (2017). Sequencing the extrachromosomal circular mobilome reveals retrotransposon activity in plants. *PLoS Genet.* 13:e1006630. doi: 10.1371/journal.pgen.1006630
- Lee, S. C., Ernst, E., Berube, B., Borges, F., Parent, J.-S., Ledon, P., et al. (2020). Arabidopsis retrotransposon virus-like particles and their regulation by epigenetically activated small RNA. *Genome Res.* 30, 576–588. doi: 10.1101/gr.259044.119
- Li, J.-Y., Wang, J., and Zeigler, R. S. (2014). The 3,000 rice genomes project: new opportunities and challenges for future rice research. *Gigascience* 3:8. doi: 10.1186/2047-217X-3-8
- Li, Z., Fu, B. Y., Gao, Y. M., Wang, W. S., Xu, J. L., Zhang, F., et al. (2014). The 3,000 rice genomes project. *Gigascience* 3:7. doi: 10.1186/2047-217X-3-7
- Lisch, D. (2012). How important are transposons for plant evolution? *Nat. Rev. Genet.* 14, 49–61. doi: 10.1038/nrg3374
- Liu, Z., Wang, T., Wang, L., Zhao, H., Yue, E., Yan, Y., et al. (2020). RTRIP: a comprehensive profile of transposon insertion polymorphisms in rice. *Plant Biotechnol. J.* 18, 2379–2381. doi: 10.1111/pbi.13425
- Long, D., Martin, M., Sundberg, E., Swinburne, J., Puangsomlee, P., and Coupland, G. (1993). The maize transposable element system Ac/Ds as a mutagen in *Arabidopsis*: identification of an albino mutation induced by Ds insertion. *Proc. Natl. Acad. Sci. U.S.A.* 90, 10370–10374. doi: 10.1073/pnas.90.21.10370
- Maestre, J., Tchénio, T., Dhellin, O., and Heidmann, T. (1995). mRNA retroposition in human cells: processed pseudogene formation. *EMBO J.* 14, 6333–6338. doi: 10.1002/j.1460-2075.1995.tb00324.x
- Martínez, G., and Slotkin, R. K. (2012). Developmental relaxation of transposable element silencing in plants: functional or byproduct? *Curr. Opin. Plant Biol.* 15, 496–502. doi: 10.1016/j.pbi.2012.09.001
- Mathieu, M., Winters, E. K., Kong, F., Wan, J., Wang, S., Eckert, H., et al. (2009). Establishment of a soybean (*Glycine max* Merr. L.) transposon-based mutagenesis repository. *Planta* 229, 279–289. doi: 10.1007/s00425-008-0827-9
- Matzke, M. A., and Mosher, R. A. (2014). RNA-directed DNA methylation: an epigenetic pathway of increasing complexity. *Nat. Rev. Genet.* 15, 394–408. doi: 10.1038/nrg3683
- Mirouze, M., Reinders, J., Bucher, E., Nishimura, T., Schneeberger, K., Ossowski, S., et al. (2009). Selective epigenetic control of retrotransposition in *Arabidopsis*. *Nature* 461, 427–430. doi: 10.1038/nature08328
- Møller, H. D., Larsen, C. E., Parsons, L., Hansen, A. J., Regenberg, B., and Mourier, T. (2016). Formation of extrachromosomal circular DNA from long terminal repeats of retrotransposons in *Saccharomyces cerevisiae*. *G3* 6, 453–462. doi: 10.1534/g3.115.025858
- Møller, H. D., Parsons, L., Jørgensen, T. S., Botstein, D., and Regenberg, B. (2015). Extrachromosomal circular DNA is common in yeast. *Proc. Natl. Acad. Sci. U.S.A.* 112, 3114–3122. doi: 10.1073/pnas.1508825112
- Moran, J. V., Holmes, S. E., Naas, T. P., Debernardinis, R. J., Boeke, J. D., and Kazazian, H. H. (1996). High frequency retrotransposition in cultured mammalian cells. *Cell* 87, 917–927.

- Nakagome, M., Solovieva, E., Takahashi, A., Yasue, H., Hirochika, H., and Miyao, A. (2014). Transposon insertion finder (TIF): a novel program for detection of de novo transpositions of transposable elements. *BMC Bioinformatics* 15:71. doi: 10.1186/1471-2105-15-71
- Nandety, R. S., Serrani-Yarce, J. C., Gill, U. S., Oh, S., Lee, H., Zhang, X., et al. (2020). Insertional mutagenesis of *Brachypodium distachyon* using the Tnt1 retrotransposable element. *Plant J.* 103, 1924–1936. doi: 10.1111/tpj.14813
- Ostertag, E. M., Luning Prak, E. T., DeBerardinis, R. J., Moran, J. V., and Kazazian, H. H. (2000). Determination of L1 retrotransposition kinetics in cultured cells. *Nucleic Acids Res.* 28, 1418–1423. doi: 10.1093/nar/28.6.1418
- Panda, K., and Slotkin, R. K. (2020). Long-Read cDNA sequencing enables a “Gene-Like” transcript annotation of transposable elements. *Plant Cell* 32, 2687–2698. doi: 10.1105/tpc.20.00115
- Rangwala, S. H., and Kazazian, H. H. (2009). The L1 retrotransposition assay: a retrospective and toolkit. *Methods* 49, 219–226. doi: 10.1016/j.ymeth.2009.04.012
- Reinders, J., and Paszkowski, J. (2009). Unlocking the *Arabidopsis* epigenome. *Epigenetics* 4, 557–563. doi: 10.4161/epi.4.8.10347
- Reinders, J., Wulff, B. B. H., Mirouze, M., Mari-Ordóñez, A., Dapp, M., Rozhon, W., et al. (2009). Compromised stability of DNA methylation and transposon immobilization in mosaic *Arabidopsis* epigenomes. *Genes Dev.* 23, 939–950. doi: 10.1101/gad.524609
- Revalska, M., Vassileva, V., Goormachtig, S., Van Hautegeem, T., Ratet, P., and Iantcheva, A. (2011). Recent progress in development of Tnt1 functional genomics platform for *Medicago truncatula* and *Lotus japonicus* in Bulgaria. *Curr. Genomics* 12, 147–152. doi: 10.2174/138920211795564313
- Roquis, D., Robertson, M., Yu, L., Thieme, M., Julkowska, M., and Bucher, E. (2021). Genomic impact of stress-induced transposable element mobility in *Arabidopsis*. *Nucleic Acids Res.* 49, 10431–10447. doi: 10.1093/nar/gkab828
- Satheesh, V., Fan, W., Chu, J., and Cho, J. (2021). Recent advancement of NGS technologies to detect active transposable elements in plants. *Genes Genomics* 43, 289–294. doi: 10.1007/s13258-021-01040-z
- Slotkin, R. K., and Martienssen, R. (2007). Transposable elements and the epigenetic regulation of the genome. *Nat. Rev. Genet.* 8, 272–285. doi: 10.1038/nrg2072
- Stuart, T., Eichten, S. R., Cahn, J., Karpievitch, Y. V., Borevitz, J. O., and Lister, R. (2016). Population scale mapping of transposable element diversity reveals links to gene regulation and epigenomic variation. *Elife* 5:e20777. doi: 10.7554/eLife.20777
- Tadege, M., Wen, J., He, J., Tu, H., Kwak, Y., Eschstruth, A., et al. (2008). Large-scale insertional mutagenesis using the Tnt1 retrotransposon in the model legume *Medicago truncatula*. *Plant J.* 54, 335–347. doi: 10.1111/j.1365-313X.2008.03418.x
- Tchenio, T., and Heidmann, T. (1992). High-frequency intracellular transposition of a defective mammalian provirus detected by an in situ colorimetric assay. *J. Virol.* 66, 1571–1578. doi: 10.1128/jvi.66.3.1571-1578.1992
- Tchenio, T., Segal-Bendirdjian, E., and Heidmann, T. (1993). Generation of processed pseudogenes in murine cells. *EMBO J.* 12, 1487–1497. doi: 10.1002/j.1460-2075.1993.tb05792.x
- Tenaillon, M. I., Hollister, J. D., and Gaut, B. S. (2010). A triptych of the evolution of plant transposable elements. *Trends Plant Sci.* 15, 471–478. doi: 10.1016/j.tplants.2010.05.003
- Thieme, M., Lanciano, S., Balzergue, S., Daccord, N., Mirouze, M., and Bucher, E. (2017). Inhibition of RNA polymerase II allows controlled mobilisation of retrotransposons for plant breeding. *Genome Biol.* 18, 134. doi: 10.1186/s13059-017-1265-4
- Wang, L., Cho, J., and Satheesh, V. (2021a). Bioinformatics analysis guides to LTR retrotransposon-derived extrachromosomal linear DNAs identified by ALE-seq. *Methods Mol. Biol.* 2250, 111–114. doi: 10.1007/978-1-0716-1134-0\_10
- Wang, L., Kim, E. Y., and Cho, J. (2021b). High-throughput profiling of extrachromosomal linear DNAs of long terminal repeat retrotransposons by ALE-seq. *Methods Mol. Biol.* 2250, 103–110. doi: 10.1007/978-1-0716-1134-0\_9
- Wang, N., Long, T., Yao, W., Xiong, L., Zhang, Q., and Wu, C. (2013). Mutant resources for the functional analysis of the rice genome. *Mol. Plant* 6, 596–604. doi: 10.1093/mp/sss142
- Weigel, D., and Mott, R. (2009). The 1001 genomes project for *Arabidopsis thaliana*. *Genome Biol.* 10:107. doi: 10.1186/gb-2009-10-5-107
- Xie, Y., Rosser, J. M., Thompson, T. L., Boeke, J. D., and An, W. (2011). Characterization of L1 retrotransposition with high-throughput dual-luciferase assays. *Nucleic Acids Res.* 39:e16. doi: 10.1093/nar/gkq1076

**Conflict of Interest:** The authors declare that the research was conducted in the absence of any commercial or financial relationships that could be construed as a potential conflict of interest.

**Publisher’s Note:** All claims expressed in this article are solely those of the authors and do not necessarily represent those of their affiliated organizations, or those of the publisher, the editors and the reviewers. Any product that may be evaluated in this article, or claim that may be made by its manufacturer, is not guaranteed or endorsed by the publisher.

Copyright © 2022 Fan, Wang, Chu, Li, Kim and Cho. This is an open-access article distributed under the terms of the Creative Commons Attribution License (CC BY). The use, distribution or reproduction in other forums is permitted, provided the original author(s) and the copyright owner(s) are credited and that the original publication in this journal is cited, in accordance with accepted academic practice. No use, distribution or reproduction is permitted which does not comply with these terms.



# Effects of Stem Density on Crown Architecture of Scots Pine Trees

Ninni Saarinen<sup>1\*</sup>, Ville Kankare<sup>1</sup>, Saija Huuskonen<sup>2</sup>, Jari Hynynen<sup>2</sup>, Simone Bianchi<sup>2</sup>, Tuomas Yrttimaa<sup>1</sup>, Ville Luoma<sup>3</sup>, Samuli Junttila<sup>1</sup>, Markus Holopainen<sup>3</sup>, Juha Hyyppä<sup>4</sup> and Mikko Vastaranta<sup>1</sup>

<sup>1</sup> School of Forest Sciences, University of Eastern Finland, Joensuu, Finland, <sup>2</sup> Natural Resources Institute Finland, Helsinki, Finland, <sup>3</sup> Department of Forest Sciences, University of Helsinki, Helsinki, Finland, <sup>4</sup> Department of Remote Sensing and Photogrammetry, Finnish Geospatial Research Institute, Masala, Finland

## OPEN ACCESS

### Edited by:

Roger Deal,  
Emory University, United States

### Reviewed by:

Miguel Montoro Girona,  
Université du Québec en  
Abitibi-Témiscamingue, Canada  
Jaroslav Klápšte,  
New Zealand Forest Research  
Institute Limited (Scion), New Zealand

### \*Correspondence:

Ninni Saarinen  
ninni.saarinen@uef.fi

### Specialty section:

This article was submitted to  
Technical Advances in Plant Science,  
a section of the journal  
Frontiers in Plant Science

**Received:** 18 November 2021

**Accepted:** 17 January 2022

**Published:** 09 March 2022

### Citation:

Saarinen N, Kankare V,  
Huuskonen S, Hynynen J, Bianchi S,  
Yrttimaa T, Luoma V, Junttila S,  
Holopainen M, Hyyppä J and  
Vastaranta M (2022) Effects of Stem  
Density on Crown Architecture  
of Scots Pine Trees.  
Front. Plant Sci. 13:817792.  
doi: 10.3389/fpls.2022.817792

Trees adapt to their growing conditions by regulating the sizes of their parts and their relationships. For example, removal or death of adjacent trees increases the growing space and the amount of light received by the remaining trees enabling their crowns to expand. Knowledge about the effects of silvicultural practices on crown size and shape and also about the quality of branches affecting the shape of a crown is, however, still limited. Thus, the aim was to study the crown structure of individual Scots pine trees in forest stands with varying stem densities due to past forest management practices. Furthermore, we wanted to understand how crown and stem attributes and also tree growth affect stem area at the height of maximum crown diameter (SAHMC), which could be used as a proxy for tree growth potential. We used terrestrial laser scanning (TLS) to generate attributes characterizing crown size and shape. The results showed that increasing stem density decreased Scots pine crown size. TLS provided more detailed attributes for crown characterization compared with traditional field measurements. Furthermore, decreasing stem density increased SAHMC, and strong relationships (Spearman's correlations > 0.5) were found between SAHMC and crown and stem size and also stem growth. Thus, this study provided quantitative and more comprehensive characterization of Scots pine crowns and their growth potential. The combination of a traditional growth and yield study design and 3D characterization of crown architecture and growth potential can open up new research possibilities.

**Keywords:** growth and yield, terrestrial laser scanning, ground-based LiDAR, pipe-model theory, silviculture, forest management, thinning

## INTRODUCTION

Trees are direct available resources to reproduction and growth and can regulate their size and the relationship between their parts. That way, trees adapt to changes in their growing conditions. The size of a tree correlates with the space a tree occupies and it defines tree growth that is linked to carbon sequestration (Vanninen and Mäkelä, 2000, 2005; Rayment et al., 2002; Pretzsch et al., 2015). Removal or death of trees enhances the light regime and photosynthesis for the remaining trees, which increases the crown size. This is particularly evident near the lowest limit of live crown where changes in the amount of light increase considerably more compared to the top of a tree



(Oker-Blom and Kellomäki, 1982; Messier and Nikinmaa, 2000; Ilomäki et al., 2003; Niinemets, 2010).

Trees of different species require differing amount of growing space; birch (*Betula* sp.) requires more space than Scots pine (*Pinus sylvestris* L.), which in turn is more demanding than Norway spruce [*Picea abies* (H. Karst) L.] (Aaltonen, 1925; Pretzsch et al., 2015). Tolerant species [e.g., sugi (*Cryptomeria japonica* D. Don), eastern white pine [*Pinus strobus* L.]], response to light condition and modify their crown architecture (Hashimoto, 1990; O'Connell and Kelty, 1994). Mitchell (1969) reported that growth of branches is similar on the free side of a white spruce [*Picea glauca* (Moech) Voss] to a completely free-growing white spruce. Additionally, crown architecture (e.g., crown width and live-crown length) varies between mixed stands compared to monocultures (Bauhus et al., 2004; Bayer et al., 2013; Dieler and Pretzsch, 2013; Pretzsch, 2014). There is a relationship between tree size and growing conditions that can be assessed through the light regime. In dense forests, lower branches die due to the limited amount of light (Heikinheimo, 1953; Flower-Ellis et al., 1976; Kellomäki, 1980) specifically for light-demanding species such as Scots pines and birches (Kellomäki and Tuimala, 1981) and also loblolly pine (*Pinus taeda* L.) (Zeide, 1998), and this decreases live-crown ratio (i.e., proportion of live crown from tree height). Raulier et al. (1996) discovered that stand structure did not affect crown adjustment of black spruce [*Picea mariana* (Mill.) BSP].

Forest management is mainly aimed at increasing size and quality of the trees left to grow by regulating stand density and thus improving their growing conditions. First commercial thinning is especially important for Scots pines, and later thinnings, even if intensive, do not offer recovery from reduced live-crown ratio as it has been shown to reduce up to 37% of tree height (Mäkinen and Isomäki, 2004). The crowns of young trees recover better compared to old trees because height growth of young trees increases the length of live crown (Hynynen, 1995). In mature and old trees, height growth is slower, and recovery of a crown is limited to increasing the width and the number of leaves or needles. However, knowledge about the effects of silvicultural practices on more sophisticated crown attributes such as volume and also crown diameter and its variation that affects the shape of a crown is still limited. In addition, crown attributes from standing trees have mainly been limited to crown-base height, crown length, and live-crown ratio as adequate measurement techniques have been lacking.

Laser scanning (or light detecting and ranging LiDAR) has provided new opportunities for characterizing trees in more detail in three-dimensional space. Specifically, terrestrial laser scanning (TLS) has increasingly been used in producing a variety of tree attributes (Seidel et al., 2011, 2015; Metz et al., 2013; Saarinen et al., 2017; Hess et al., 2018; Chianucci et al., 2020; Georgi et al., 2021; Owen et al., 2021; Rais et al., 2021; Zhu et al., 2021). One of the challenging stem-related attributes to be measured from standing trees has been taper curve (i.e., diameters at various heights of a stem), and TLS data have been shown to overcome that challenge (Liang et al., 2014; Yrttimaa et al., 2019, 2020). Additionally, versatile crown attributes such as volume (Fernández-Sarría et al., 2013), surface area

(Metz et al., 2013), asymmetry (Seidel et al., 2011), and height of the maximum crown projection area (Seidel et al., 2011) have been generated. Binkley et al. (2013) and Forrester (2014) have stated that crown projection area and crown volume, which can be obtained with TLS data, can be used as proxies for leaf area and leaf biomass. Furthermore, crown surface area has been used as a proxy for the photosynthetically active surface of the tree (Seidel et al., 2019a). TLS has also been used for studying competition between species (Martin-Ducup et al., 2016; Barbeito et al., 2017; Juchheim et al., 2019; Pretzsch, 2019; Hildebrand et al., 2021), the effects of management intensity on tree structure (Juchheim et al., 2017; Georgi et al., 2018; Bogdanovich et al., 2021), and also structural complexity of individual trees (Seidel, 2018; Seidel et al., 2019b; Saarinen et al., 2021). Thus, TLS provides a vast range of opportunities for understanding tree growth.

There is a long history of research where the relationship between crown and stem dimensions has been investigated (Krajicek et al., 1961; Larson, 1963; Grinrich, 1967; Curtin, 1970; Seymour and Smith, 1987; Pamerleau-Couture et al., 2015; Montoro Girona et al., 2016, 2017). Process-based models simulate tree growth as a function of leaf biomass, in other words of their photosynthetic elements (e.g., Valentine and Mäkelä, 2005). Shinozaki et al. (1964), on the other hand, proposed a conceptual framework for the relationship between the amount of stem tissue and corresponding supported leaves known as the pipe-model theory (PMT). The idea behind the PMT is that certain amount of leaves needs mechanical support and also enough water and nutrient supply to be sustained. One of the PMT's properties is a proportional relationship between conductive area of the stem at a certain height and the mass of foliage above. This is related to Pressler's law in which a cross-sectional area of an annual increment of a stem-ring is proportional to the quantity of foliage above that point (Pressler 186, cited in Larson, 1963). The PMT is part of a branch of science called allometry that has widely used for exploring plant growth and development (Niklas, 1994; Le Roux et al., 2001; Niklas and Enquist, 2002; Fourcaud et al., 2008; McDowell and Allen, 2015). The PMT has inspired investigations to understand relationships that are related to the amount of foliage. It has been shown that the total cross-sectional area of living branches is strongly correlated with foliage mass (Vanninen et al., 1996; Ilomäki et al., 2003; Kantola and Mäkelä, 2004). Longuetaud et al. (2006) reported that statistically significant indicators for tree vitality were the total cross-sectional area of branches, height-diameter at breast height (DBH) ratio (i.e., height/DBH), and the relative and absolute height of the crown base. More specifically, Lehtonen et al. (2020) and Hu et al. (2020) found leaf biomass of Scots pine to be proportional to the stem cross-sectional area at the crown base. However, in both cases, the relationship was influenced by other factors, such as age, site type, and temperature. There are indeed criticisms on the validity of the PMT, for which we direct the reader to the extensive review from Lehnebach et al. (2018). In any case, if traditional empirical models are using DBH as a proxy for growth potential, the question still remains if diameter at the crown base (DCB) could be a more accurate predictor.

The aim of this study is to investigate how crown structure of individual Scots pine trees varies when growing in different

conditions due to the intensity and type of past thinning treatments. It is hypothesized that crown size decreases with increasing stem density (H1) and increases when suppressed and codominant trees were removed (H2) due to decreasing and increasing growing space, respectively. Related to the PMT, the objective is to understand the relationship between stem area at the height of the maximum crown diameter (SAHMC) and crown and stem dimensions and also growth of the tree. This relates to the question of the usefulness of DCB as a proxy for growth potential as it is of renewed importance since new technology such as TLS can now estimate this parameter more easily.

## MATERIALS AND METHODS

### Study Area

The study area is located in southern boreal forest zone in Finland and consists of three study sites (Palomäki, Pollari, and Vesijako) (Figure 1) with relatively flat terrain (elevation above sea level  $\sim 137 \pm 17$  m) in mesic heath forest [i.e., Myrtillus forest site type according to Cajander (1909)] dominated by Scots pine. The study sites were established and are maintained by the Natural Resources Institute Finland (Luke). The Palomäki study site was established in 2005, whereas Pollari and Vesijako study sites were established in 2006. The temperature sum for Palomäki, Pollari, and Vesijako are 1,195, 1,130, and 1,256 degree days, respectively. At the time of the establishment, the stand age was 50, 45, and 59 years for Palomäki, Pollari, and Vesijako, respectively. The proportion of Norway spruce and deciduous trees (i.e., *Betula* sp and *Alnus* sp) from the total stem volume was 3.06 and 0.03%, respectively, in 2019.

### Sampling Protocol and Silvicultural Treatments

Nine rectangular sample plots (sized 1,000–1,200 m<sup>2</sup>) were placed on each study site, and first in situ measurements were carried out at the same time. The experimental study design included two levels of thinning intensity and three thinning types (Figure 2), which resulted in six different thinning treatments (i.e., moderate from below, moderate from above, moderate systematic, intensive from below, intensive from above, and intensive systematic) that were replicated from one to two times in each study site using a randomized block design. One plot at each study site was left as a control plot where no thinning has been carried out since the establishment of the sites. Finally, there were four plots with either moderate or intensive thinning from below, five plots with either moderate or intensive systematic thinning, three plots with moderate or intensive thinning from above and also three control plots.

Thinning intensity was defined as the remaining basal area whereas thinning type determined which trees (based on a crown class) were removed. The remaining relative stand basal area after moderate thinning was  $\sim 68\%$  of the stocking before thinning and intensive thinning reduced the stocking levels down to 34%. Suppressed and codominant trees were removed in thinning from below whereas dominant trees were mainly removed in thinning from above. Dominant trees were removed and small, suppressed

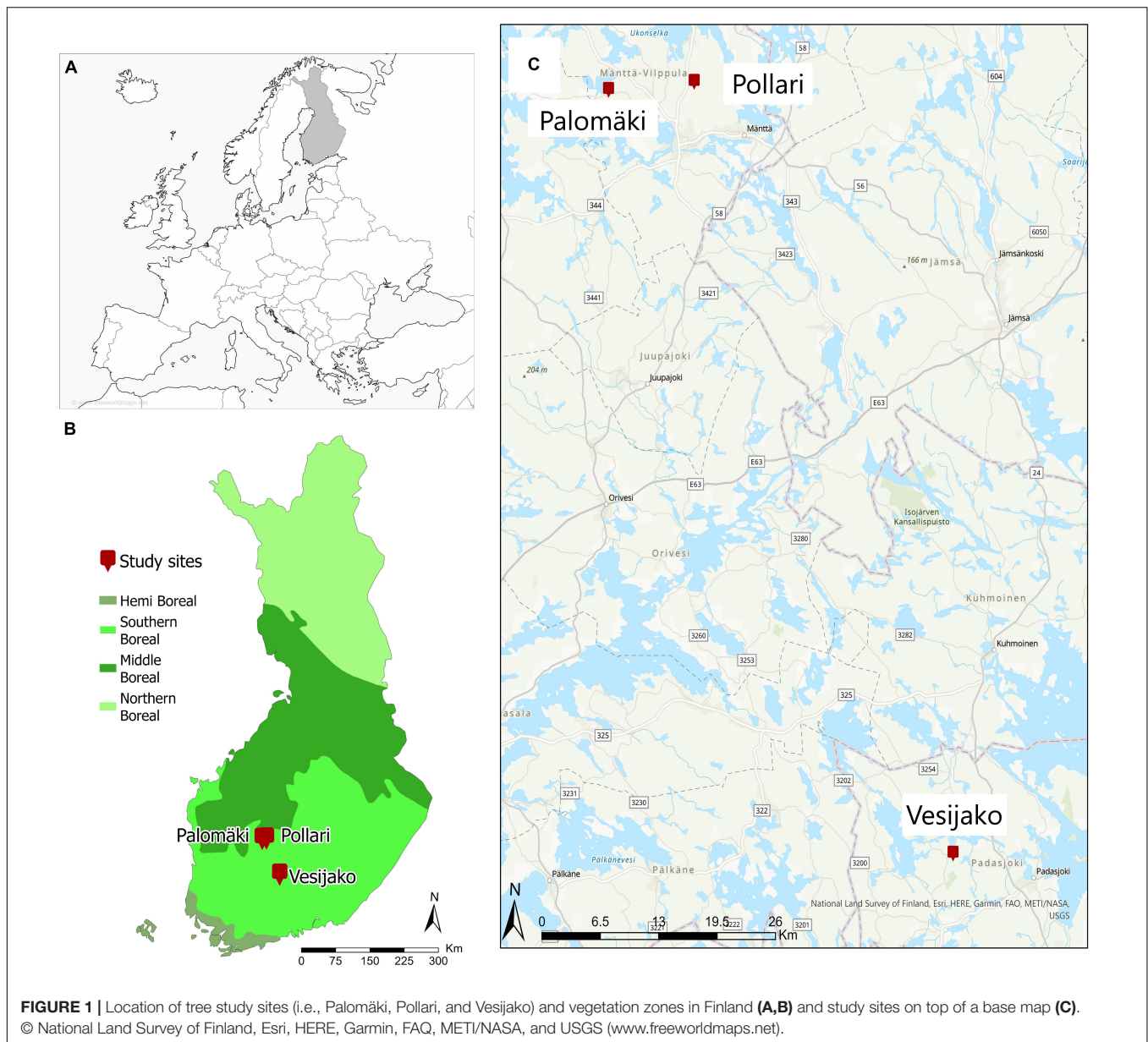
trees were left to grow in systematic thinning without considering regular spatial distribution of the remaining trees, which was considered in thinnings from below and above. Additionally, unsound and damaged trees (e.g., crooked and forked) were removed in thinnings from below and above.

Tree species, DBH from two perpendicular directions, crown layer, and health status were recorded for each tree within a plot during all in situ measurements (i.e., at the establishment, 10 years after the establishment, and between October 2018 and April 2019 for this study). Each sample plot also includes  $\sim 22$  sample trees from which also tree height, live-crown-base height, and height of the lowest dead branch were measured. Plot-level attributes before and after thinning treatments (i.e., at the establishment) and also based on the in situ measurements in 2018–2019 are presented in Table 1, and the development of tree-level attributes for each thinning treatment can be found in Table 2.

### Terrestrial Laser Scanning Data

Terrestrial laser scanning data acquisition was carried out with a Trimble TX5 3D phase-shift laser scanner (Trimble Navigation Limited, United States) operating at a 1,550 nm wavelength and measuring 9,76,000 points per second. This resulted in a hemispherical ( $300^\circ$  vertical  $\times$   $360^\circ$  horizontal) point cloud with a point distance approximately 6.3 mm at a 10-m distance. Eight scans were acquired from each sample plot between September and October 2018. Two scans were placed on two sides of the plot center, and six auxiliary scans were placed closer to the plot borders (Figure 3). Artificial targets (i.e., white spheres with a diameter of 198 mm) were placed around each sample plot to be used as reference objects for registering the eight scans into a single, aligned coordinate system with a FARO Scene software (version 2018). The automatic registration utilizing the reference targets resulted in a mean distance error of  $2.9 \pm 1.2$  mm, with mean horizontal and vertical error of  $1.3 \pm 0.4$  mm and  $2.3 \pm 1.2$  mm, respectively, provided by the FARO Scene software for each reference target. LAStools software (Isenburg 2019) was used to normalize the point heights to heights above ground by applying a point cloud normalization workflow presented by Ritter et al. (2017).

First, plot-level TLS point clouds were segmented to identify points from individual trees. Local maxima from canopy height models (CHMs) with a 20-cm resolution were identified using the Variable Window Filter approach (Popescu and Wynne, 2004), and the Marker-Controlled Watershed Segmentation (Meyer and Beucher, 1990) was applied to delineate crown segments. A point-in-polygon approach was applied for identifying all points belonging to each crown segment. To identify points that originated from stem and crown within each crown segment, a point cloud classification procedure by Yrttimaa (2021) was used. The classification of stem and non-stem points assumed that stem points have more planar, vertical, and cylindrical characteristics compared to non-stem points that represent branches and foliage (Liang et al., 2014; Yrttimaa et al., 2020). The method by Yrttimaa et al. (2019, 2020) is an iterative procedure beginning from the base of a tree and proceeding toward treetop. More detailed description of the point cloud classification workflow can be



found in Yrttimäa et al. (2019, 2020). The result of this step was 3D point clouds for each individual Scots pine tree ( $n = 2,174$ ) within the 27 sample plots.

## Data Analyses

We investigated several traits characterizing crown size and shape (Table 3). Points from TLS that were classified originating from branches and foliage (i.e., crown points) in the previous step were utilized. A 2D convex hull was fitted to envelope the crown points of each tree of which crown projection area was derived. Crown diameter, on the other hand, was defined as the distance between the two most outer points in xy-space of the 2D convex hull. To obtain crown volume and surface area, a 3D convex hull was fitted to the crown points. We also wanted to investigate crown shape and thus divided the crown points into

height percentiles (i.e., slices) of 10% starting from the lowest points. Then, 2D convex hull was fitted for each slice and its area and diameter were similarly obtained to the maximum crown diameter. Furthermore, mean, standard deviation, and range (i.e., crown taper) of these slice diameters were saved.

Height of the maximum crown diameter (HMC) from TLS was used to define crown length (i.e., live-crown-base height was deducted from tree height) and live-crown ratio (i.e., proportion of crown length from tree height). Finally, stem diameter at the HMC was obtained from the taper curve, and stem area at the SAHMC was calculated as  $\pi/4 \cdot d^2$ .

Traits characterizing stem included DBH, stem volume, height-DBH ratio (i.e., height/DBH), and cumulative volume. Tree height was obtained using the height of the highest TLS point of each tree (i.e., normalized above ground) whereas DBH



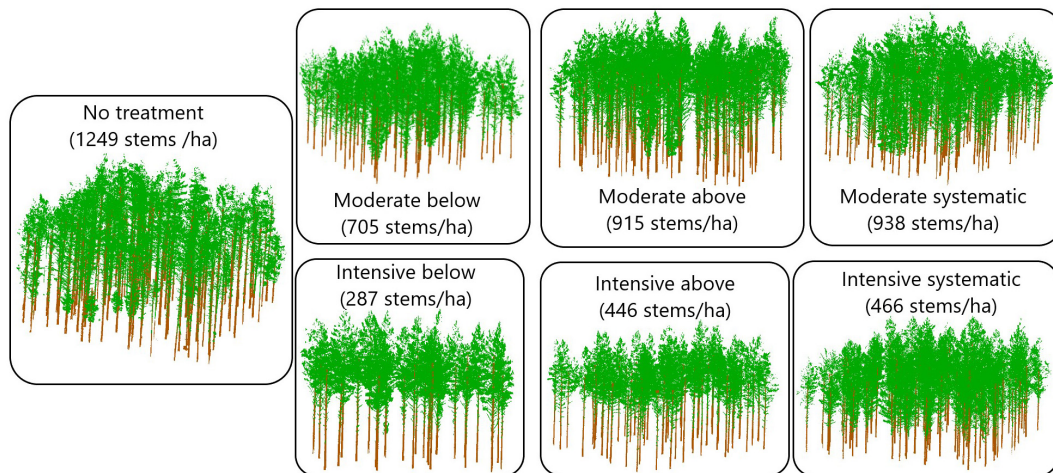


**FIGURE 2** | Schematic representation of the effects of silviculture treatments on stand density based on TLS data collected in October 2018.

**TABLE 1** | Mean and standard deviation (with  $\pm$ ) of stand characteristics by treatments before and after the thinning treatments (2005–2006) and also after the growth period (2018–2019).

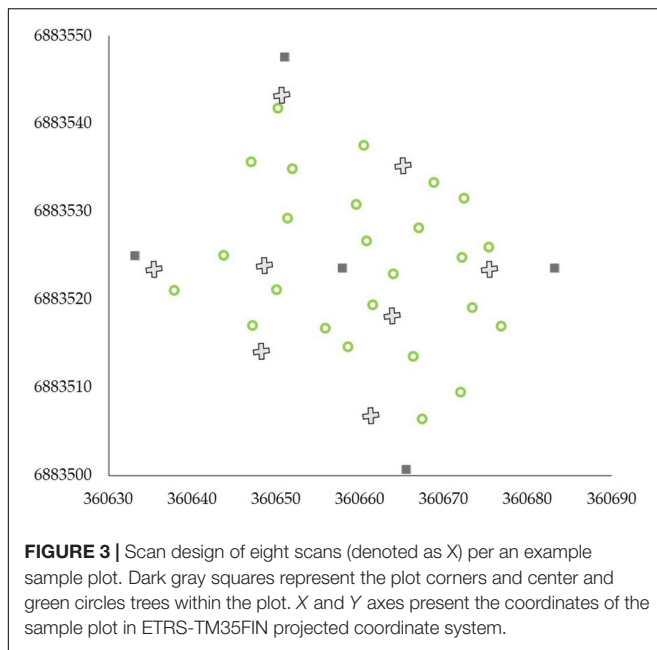
	No treatment	Moderate below	Moderate above	Moderate systematic	Intensive below	Intensive above	Intensive systematic
<b>Before thinning (2005–2006)</b>							
G (m <sup>2</sup> /ha)	27.6 $\pm$ 6.7	26.9 $\pm$ 6.9	27.8 $\pm$ 2.0	25.4 $\pm$ 2.6	26.9 $\pm$ 4.5	24.7 $\pm$ 2.6	20.6 $\pm$ 4.2
N/ha	1336 $\pm$ 97	1285 $\pm$ 270	1417 $\pm$ 419	1256 $\pm$ 129	1260 $\pm$ 158	1201 $\pm$ 78	1218 $\pm$ 333
V (m <sup>3</sup> /ha)	224.0 $\pm$ 93.4	215.4 $\pm$ 70.4	216.9 $\pm$ 18.7	199.7 $\pm$ 42.4	216.6 $\pm$ 55.4	191.0 $\pm$ 35.6	210.6 $\pm$ 62.3
D <sub>w</sub> (cm)	17.8 $\pm$ 3.4	17.5 $\pm$ 2.1	17.3 $\pm$ 1.7	17.5 $\pm$ 1.6	18.0 $\pm$ 2.1	17.6 $\pm$ 1.3	18.0 $\pm$ 3.6
H <sub>w</sub> (m)	16.1 $\pm$ 3.3	16.1 $\pm$ 1.8	15.9 $\pm$ 1.1	15.9 $\pm$ 2.1	16.3 $\pm$ 1.8	15.6 $\pm$ 1.6	16.2 $\pm$ 2.9
<b>After thinning (2005–2006)</b>							
G (m <sup>2</sup> /ha)	27.6 $\pm$ 6.7	18.3 $\pm$ 2.1	18.5 $\pm$ 1.1	18.2 $\pm$ 1.1	8.9 $\pm$ 0.8	9.1 $\pm$ 0.8	8.7 $\pm$ 0.7
N/ha	1336 $\pm$ 97	719 $\pm$ 130	955 $\pm$ 258	988 $\pm$ 129	292 $\pm$ 55	479 $\pm$ 113	522 $\pm$ 183
V (m <sup>3</sup> /ha)	224.0 $\pm$ 92.8	148.8 $\pm$ 30.2	144.0 $\pm$ 15.3	141.3 $\pm$ 23.6	72.9 $\pm$ 12.4	69.1 $\pm$ 11.3	67.3 $\pm$ 14.7
D <sub>w</sub> (cm)	17.8 $\pm$ 3.4	18.7 $\pm$ 2.4	16.9 $\pm$ 1.9	16.5 $\pm$ 1.6	20.4 $\pm$ 2.7	16.5 $\pm$ 2.5	15.7 $\pm$ 3.0
H <sub>w</sub> (m)	16.1 $\pm$ 3.3	16.5 $\pm$ 1.9	15.7 $\pm$ 1.2	15.6 $\pm$ 2.1	16.9 $\pm$ 1.8	15.3 $\pm$ 1.9	15.5 $\pm$ 2.7
<b>After growth period (2018–2019)</b>							
G (m <sup>2</sup> /ha)	37.1 $\pm$ 4.6	28.4 $\pm$ 2.5	28.3 $\pm$ 28.3	27.6 $\pm$ 1.8	15.9 $\pm$ 0.7	16.1 $\pm$ 1.2	15.9 $\pm$ 1.6
N/ha	1249 $\pm$ 159	705 $\pm$ 113	915 $\pm$ 214	938 $\pm$ 111	287 $\pm$ 65	446 $\pm$ 82	466 $\pm$ 172
V (m <sup>3</sup> /ha)	380.3 $\pm$ 93.9	291.8 $\pm$ 44.7	282.3 $\pm$ 6.1	267.9 $\pm$ 16.1	160.8 $\pm$ 9.1	150.5 $\pm$ 12.6	150.4 $\pm$ 9.9
D <sub>w</sub> (cm)	21.2 $\pm$ 3.0	23.5 $\pm$ 2.2	21.2 $\pm$ 1.9	20.7 $\pm$ 1.2	27.5 $\pm$ 3.1	22.3 $\pm$ 2.1	22.2 $\pm$ 3.0
H <sub>w</sub> (m)	21.3 $\pm$ 3.1	21.7 $\pm$ 2.0	21.0 $\pm$ 1.1	20.3 $\pm$ 1.4	21.6 $\pm$ 1.6	19.5 $\pm$ 1.2	20.0 $\pm$ 2.2

G, basal area; N, stem number per hectare; V, volume; D<sub>w</sub>, mean diameter weighted by basal area; H<sub>w</sub>, mean height weighted by basal area.

**TABLE 2** | Mean tree-level attributes with their standard deviation (with  $\pm$ ) for each treatment at the year of the establishment (2005–2006) and after the growth period (2018–2019).

	No treatment	Moderate below	Moderate above	Moderate systematic	Intensive below	Intensive above	Intensive systematic
<b>2005–2006</b>							
DBH (cm)	15.4 $\pm$ 4.6	17.6 $\pm$ 3.3	15.3 $\pm$ 3.3	14.8 $\pm$ 3.5	19.3 $\pm$ 3.4	15.1 $\pm$ 3.1	14.8 $\pm$ 4.1
Height (m)	14.7 $\pm$ 2.6	15.9 $\pm$ 1.9	15.3 $\pm$ 1.2	14.6 $\pm$ 1.9	16.5 $\pm$ 1.8	14.8 $\pm$ 1.8	14.7 $\pm$ 2.6
Volume (dm <sup>3</sup> )	160.5 $\pm$ 119.7	202.7 $\pm$ 89.3	149.6 $\pm$ 76.2	138.1 $\pm$ 77.8	249.2 $\pm$ 107.0	141.8 $\pm$ 73.4	145.6 $\pm$ 97.1
<b>2018–2019</b>							
DBH (cm)	18.7 $\pm$ 5.0	22.2 $\pm$ 3.7	19.3 $\pm$ 4.3	18.8 $\pm$ 4.2	26.4 $\pm$ 3.9	21.1 $\pm$ 3.5	20.8 $\pm$ 4.3
Height (m)	20.2 $\pm$ 3.0	21.2 $\pm$ 2.1	20.4 $\pm$ 1.6	19.4 $\pm$ 2.2	21.2 $\pm$ 1.7	19.1 $\pm$ 1.5	19.6 $\pm$ 2.8
Volume (dm <sup>3</sup> )	299.4 $\pm$ 190.8	408.3 $\pm$ 106.3	306.4 $\pm$ 145.6	282.5 $\pm$ 137.2	563.8 $\pm$ 202.5	335.2 $\pm$ 125.4	347.0 $\pm$ 173.3

DBH, diameter at breast height.



was defined from taper curve obtained with a combination of circle fitting to original stem points and fitting a cubic spline (see Yrttimaa et al., 2019; Saarinen et al., 2020). Stem volume, on the other hand, was defined by considering the stem as a sequence 10-cm vertical cylinders and summing up the volumes of the cylinders using the estimated taper curve. Finally, cumulative stem volume was calculated as the height at which 50% of stem volume was accumulated.

As TLS data were only available for one time point, in situ measurements were utilized for obtaining growth information of individual Scots pine trees. Growth of DBH, tree height, stem volume, and change in height/DBH were calculated using in situ measurements conducted in 2005–2006 (i.e., at the time of establishment of the study sites) and 2018–2019 (i.e., the latest in-situ measurements) for all live Scots pine trees that were identified from the sample plots during the latest field measurements.

Due to the data structure (i.e., several sample plots in each study site), a nested two-level linear mixed-effects model (Equation 1) was fitted using restricted maximum likelihood included in package “nlme” (Pinheiro et al., 2013) of the R software to assess the effects of thinning treatment on crown, stem, and growth traits and also on SAHMC.

$$y_{ij} = \beta_1 \text{Moderate below}_i + \beta_2 \text{Moderate above}_i + \beta_3 \text{Moderate systematic}_i + \beta_4 \text{Intensive below}_i + \beta_5 \text{Intensive above}_i + \beta_6 \text{Intensive systematic}_i + \beta_7 \text{No treatment}_i + a_j + c_{ij} + \epsilon_{ij}, \quad (1)$$

where,  $y_{ij}$  is each crown, stem, and growth trait and also SAHMC at a time,  $\beta_1, \dots, \beta_7$  are fixed parameters,  $i = 1, \dots, M$ , refers to study site,  $j = 1, \dots, n_i$ , to a plot,  $a_j$  and  $c_{ij}$  are normally distributed random effects for sample plot  $j$  and for sample plot  $j$

within study site  $i$ , respectively, with mean zero and unknown, unrestricted variance-covariance matrix, and  $\epsilon_{ij}$  is a residual error with a mean zero and unknown variance. The random effects are independent across study sites and sample plots and also residual errors are independent across trees. The effects of a study site and a sample plot within the study sites on crown, stem, and growth traits and also on SAHMC were assessed through their variances. Furthermore, we used Tukey’s honest significance test to reveal possible statistically significant differences in crown, stem, and growth traits and also in SAHMC between different thinning treatments.

Correlations between dependent and independent variables were investigated using Pearson’s correlation coefficient. Furthermore, the significance level of the correlation was investigated. The nested two-level linear mixed-effect model in Equation 1 was utilized in investigating the possible relationship between SAHMC and different crown, stem, and growth traits. Each crown (Table 2), stem (i.e., DBH, stem volume, and height/DBH), and growth ( $\Delta$ DBH,  $\Delta$ tree height,  $\Delta$ stem volume, and  $\Delta$ height/DBH) trait was separately used in Equation 1 as a single predictor variable.

## RESULTS

### The Effects of Stem Density on Crown Architecture

Difference in stem density/ha varied from 430 to 470 between moderate and intensive thinning and from 310 to 960 stem/ha between no treatment and thinned (i.e., all other) plots. When thinning intensity increased (i.e., stem density/ha decreased) from moderate to intensive thinning from below, crown volume, projection area, and maximum and mean diameter increased (Figure 4) statistically significantly ( $p < 0.05$ ). Similarly, live-crown ratio and also crown diameter at the bottom of a crown (i.e., 10–30 percentiles) (Figure 5) statistically significantly ( $p < 0.05$ ) increased when thinning intensity increased, but this was true for all thinning types. However, there was no statistically significant ( $p > 0.05$ ) difference in crown traits between of moderate thinnings and no treatment.

Thinning type (i.e., removal of suppressed and codominant or dominant trees) had a less clear effect on crown size and shape. Statistically significant ( $p < 0.05$ ) differences were only present in crown volume, surface and projection area, maximum and mean diameter, and also diameters at the top part of a crown when intensive thinning from below was compared with other intensive thinnings (difference in stem density/ha between 20 and 180). In other words, in intensive thinning crown attributes were significantly larger when suppressed and codominant trees had been removed (i.e., thinning from below) compared to when dominant trees were removed (i.e., thinning from above and systematic thinning). This is also visible for example trees from different thinning treatments (Figure 6).

**TABLE 3** | Crown traits and how they were defined and/or generated from TLS point clouds.

Trait	Definition/Calculation
Projection area	Area of the maximum crown diameter from 2D convex hull
Crown volume	Calculated using 3D convex hull
Surface area	Surface area of the 3D convex hull
Crown diameters	Crown points were divided in height percentiles (i.e., slices) of 10% starting from the lowest part and their diameter was calculated using 2D convex hull
Maximum crown diameter	Maximum diameter based on the 2D convex hull of the crown slices
Mean crown diameter	Mean diameter of the crown slices
Standard deviation of crown diameter	Standard deviation of the diameters of the crown slices
Height at the maximum crown diameter (HMC)	Defined from the crown slices
Crown length	Distance between the HMC and tree height
Crown tapering	Difference between maximum and minimum diameter of the crown slices
Live-crown ratio	Proportion of crown length from the tree height
Stem area at the height of the maximum crown diameter (SAHMC)	Stem diameter at the HMC was obtained from the taper curve and basal area was then calculated as $\pi/4 \cdot d^2$

## The Effects of Stem Density on Stem Area at the Height of Maximum Crown Diameter

Stem area at the height of maximum crown diameter ranged from 67.4 cm<sup>2</sup> to 170.2 cm<sup>2</sup> being the smallest with no treatment and the largest with intensive thinning from below (Figure 7). For moderate thinnings, SAHMC was 90.6 cm<sup>2</sup>, on average, whereas with intensive thinnings, it was 132.2 cm<sup>2</sup>. Lower stem densities increased SAHMC, and SAHMC was statistically significantly ( $p < 0.05$ ) greater when stem density increased from ~290 stems/ha (i.e., intensive below) to at least ~720 stems/ha (i.e., moderate below). In other words, SAHMC was statistically significantly different between intensive thinning from below and all other thinning treatments, which include no treatment, except between intensive thinning from above.

## Relationship Between Stem Area at the Height of Maximum Crown Diameter and Crown and Stem Attributes as Well as Tree Growth

There was high correlation ( $\geq 0.5$ ) between SAHMC and crown volume (Table 4). Specifically, traits characterizing stem size (i.e., DBH, stem volume, and height at which 50% of stem volume accumulated) and size growth (i.e., DBH growth and stem volume growth) showed high positive correlation ( $> 0.5$ ). Height/DBH ratio, on the other hand, showed negative correlation with SAHMC. Correlations between SAHMC and all crown, stem, and growth attributes were statistically significant.

Crown diameters at different heights also showed positive correlation ( $\geq 0.4$ ) with SAHMC. Furthermore, the results from the nested two-level linear mixed-effect model showed that increment in most of the crown, stem, and growth attribute, when independently included as a predictor variable, increased SAHMC. HMC and height/DBH were exceptions as their increment decreased SAHMC. Increasing live-crown ratio, relative stem volume, and change in height/DBH increased

SAHMC ten times more than other crown, stem, and growth attributes, whereas the effect of increasing height/DBH was of similar magnitude but to different directions, in other words, it decreased SAHMC. When each trait characterizing crown, stem, and growth was separately added as a predictor variable to estimate SAHMC, each of them was statistically significant ( $p < 0.001$ ) for the models (Table 4).

## DISCUSSION

The results showed how thinning treatments carried out >10 years ago affected crown shape and size of Scots pine trees. As stem density decreased, crown volume, surface area, and maximum diameter increased. Also, diameter of the lower part of a crown (<80th height percentile) increased with decreasing stem density. These results suggest that stem density affects crown shape and size of Scots pine trees in boreal forests. Lower stem densities (i.e.,  $\leq 700$  stems/ha) also increased SAHMC. Furthermore, when crown and stem size and also stem growth increased, SAHMC also grew.

One of the traditional parameters used for characterizing crown architecture is live-crown ratio, and the results here showed that it differed between stem densities, similar to the findings by Kellomäki and Tuimala (1981), Clark Baldwin et al. (2000), and Tahvanainen and Forss (2008). Mäkelä (1997) presented a model where lower stem densities led to larger live-crown ratio, whereas Vanninen (2004) developed a model for aboveground growth allocation and found that increasing crown ratio increased growth allocation to branches. Live-crown ratio has also been used as a measure for growth and tree vigor (Dyer and Burkhart, 1987; Zarnoch et al., 2004). Mäkelä and Vanninen (2001) reported that the maximum foliage density was lower in height for dominant Scots pine trees compared to suppressed, whereas in our study, lower part of a crown was similar in size for all social crown classes but upper part was significantly larger for Scots pines that were originally considered as dominant trees and were left to grow in the sparsest plots (i.e., intensive thinning carried out). We also found significant



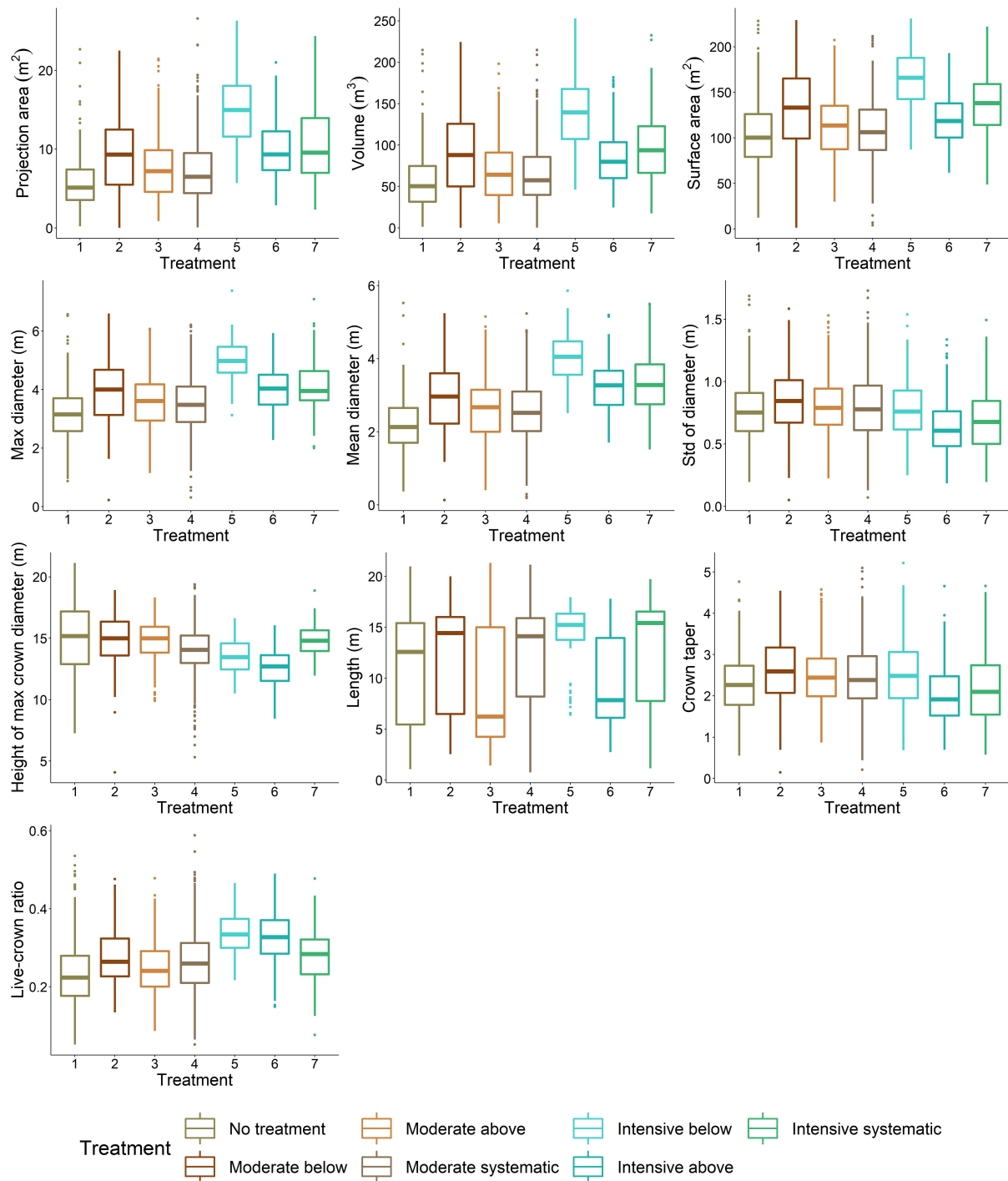


**FIGURE 4 |** Variation in crown attributes between thinning treatments. 1, no treatment (i.e., control); 2, moderate thinning from below; 3, moderate thinning from above; 4, moderate systematic thinning from above; 5, intensive thinning from below; 6, intensive thinning from above; and 7, intensive systematic thinning from above.

differences between advanced crown traits (namely crown surface area and volume) at least among the sparsest stem densities (i.e., intensive thinning). Finally, the study confirmed the results presented by Oker-Blom and Kellomäki (1982) as the lowest

part of a Scots pine tree crown was larger in low stem densities. Our study enabled assessing crown architecture for 2,174 live Scots pine trees; thus, the use of TLS for obtaining enhanced information on canopy structure and architecture can be justified.

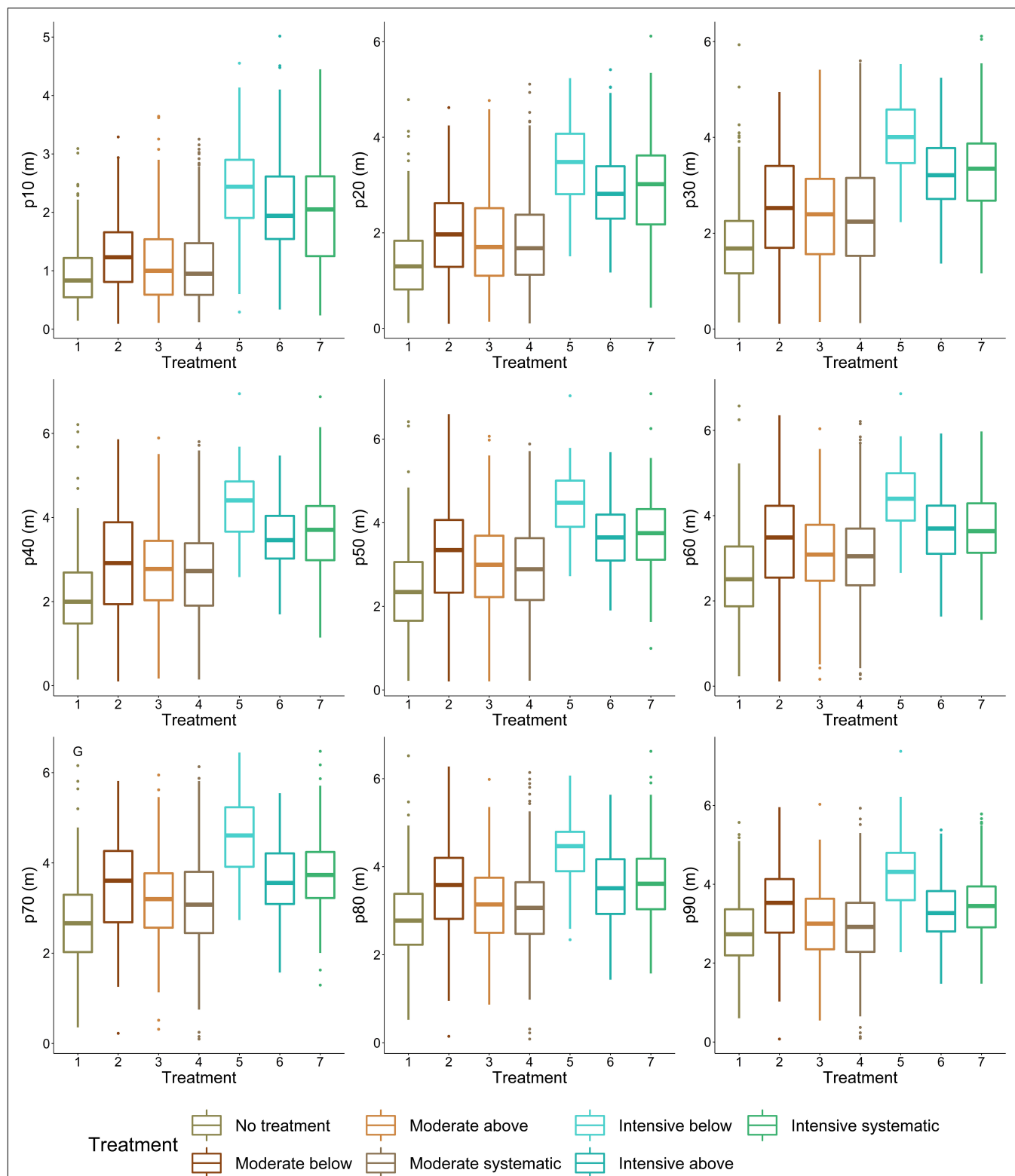
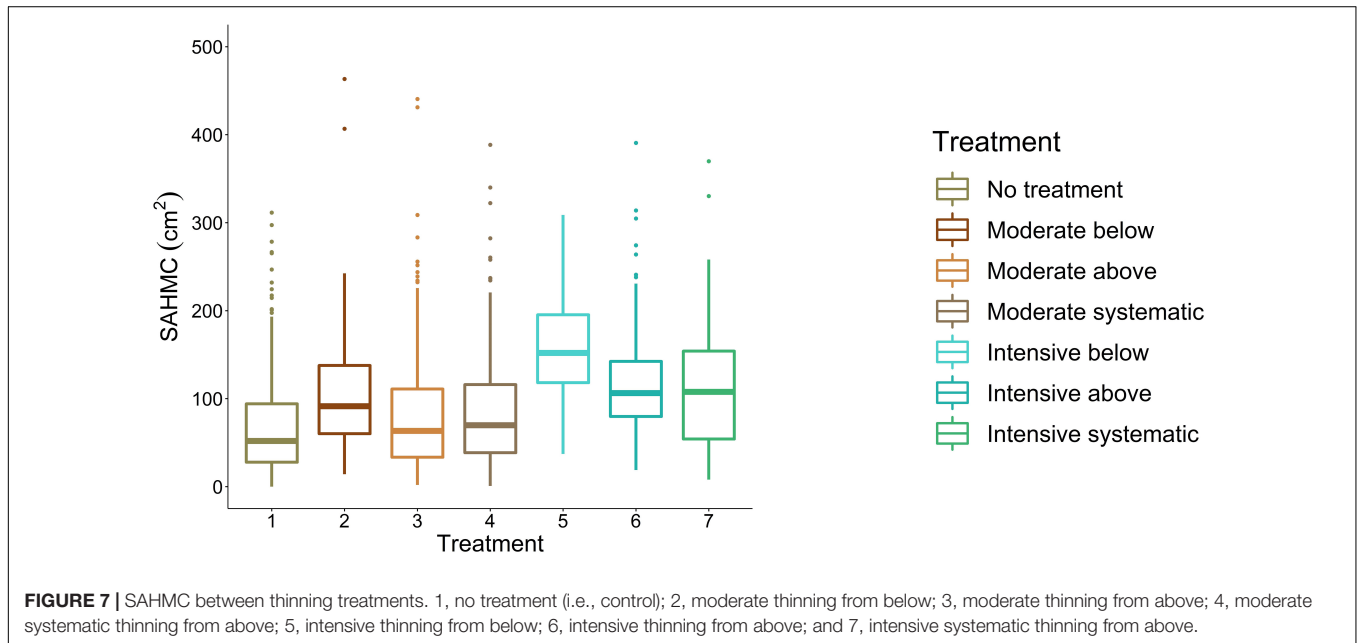
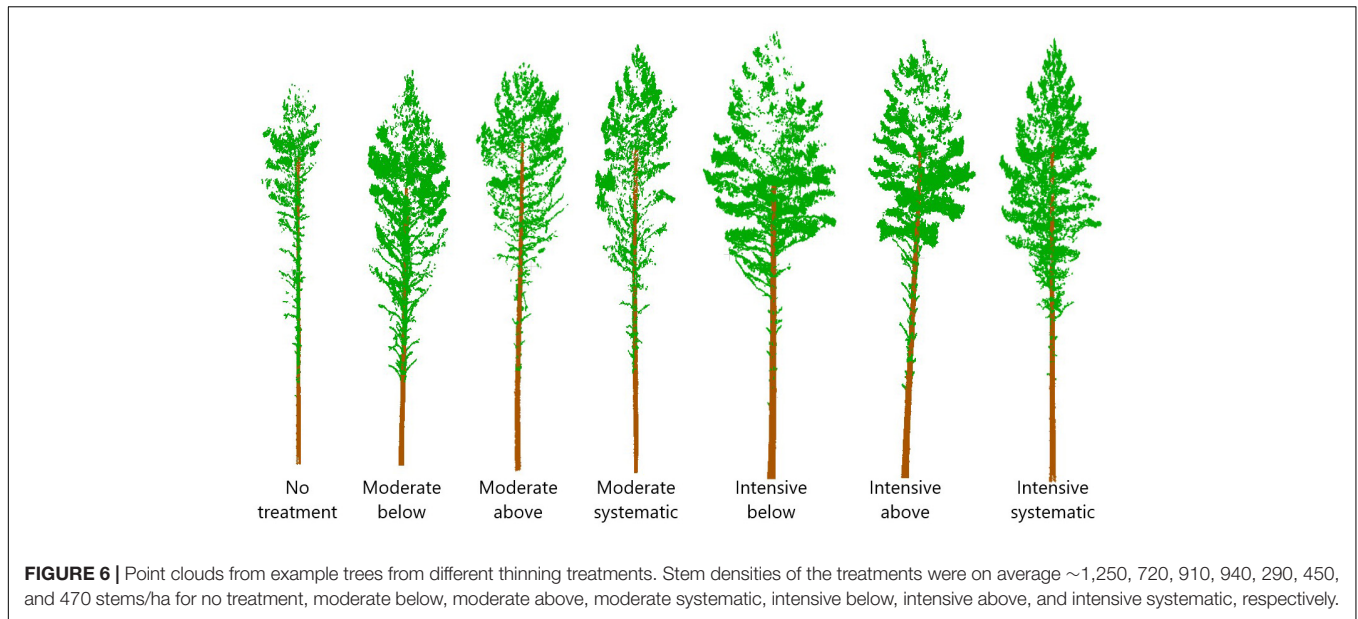


**FIGURE 5 |** Variation in crown diameter at height percentiles between thinning treatments. P10 indicates the lowest height percentile (i.e., the most bottom part of a crown), whereas p100 is the highest height percentile (i.e., the highest part of a crown). 1, no treatment (i.e., control); 2, moderate thinning from below; 3, moderate thinning from above; 4, moderate systematic thinning from above; 5, intensive thinning from below; 6, Intensive thinning from above; and 7, intensive systematic thinning from above.



There is uncertainty in the SAHMC as the HMC may not represent the height of crown-base height, which is traditionally used for crown length and live-crown ratio. Thus, also SAHMC may not represent the true DCB. However, it has not been traditionally feasible to measure DCB from standing trees, whereas measurements on stem diameters from TLS data offer this. Thus, our results show a way toward assessing the usefulness of DCB as a proxy for growth potential of individual trees. There was strong correlation ( $\geq 0.5$ ) between SAHMC and crown volume but also with DBH and stem volume, and their growth. This indicates that DCB or SAHMC could also be used when assessing growth potential, and TLS offers a means for obtaining this information.

Studies utilizing TLS in assessing tree development include European beech [*Fagus sylvatica* (L.)] (Juchheim et al., 2017; Georgi et al., 2018) and holm oak (*Quercus ilex* L.) (Bogdanovich et al., 2021). Juchheim et al. (2017) found that increasing thinning intensity increased crown surface area of European beech, which is in line with our results for Scots pine. Georgi et al. (2018) reported that crown size (i.e., crown volume, projection area, surface area, length, and live-crown ratio) of European beech trees growing in stands without forest management in  $\geq 50$  years was statistically significantly lower compared to European beech trees growing in managed stands or stands with  $\leq 20$  years without forest management. Our results showed that intensive thinning resulted in statistically

**TABLE 4 |** Pearson's correlation coefficients between SAHMC diameter and crown, stem, and growth attributes and also coefficient value from the nested two-level linear mixed-effect models where each trait was independently included as a single predictor variable against SAHMC.

	Trait	Pearson's correlation coefficient	Coefficient value
Crown attributes	Projection area	0.49*	6.32*
	Crown volume	<b>0.50*</b>	0.72*
	Surface area	0.47*	0.78*
	Maximum crown diameter	0.45*	24.61*
	Mean crown diameter	0.47*	28.68*
	Standard deviation of crown diameter	0.09*	29.89*
	Height at the maximum crown diameter	−0.36*	−14.34*
	Crown length	0.20*	13.52*
	Crown tapering	0.14*	12.46*
	Live-crown ratio	<b>0.66*</b>	521.22*
Stem attributes	DBH	<b>0.66*</b>	10.40*
	Stem volume	<b>0.70*</b>	0.32*
	Height/DBH	<b>−0.61*</b>	−167.17*
	Relative stem volume	0.38*	310.10*
	Height at which 50% of stem volume accumulated	<b>0.70*</b>	12.71*
Growth attributes	DBH growth	<b>0.59*</b>	21.85*
	Height growth	0.23*	21.24*
	Stem volume growth	<b>0.67*</b>	0.52*
	Change in height/DBH	0.35*	215.64*

DBH, diameter at breast height. \* denotes statistically significant correlation or importance in the model. Correlation  $\geq |0.5|$  are bolded.

significant difference in crown traits (e.g., crown volume, projection area, and maximum and mean diameter) when compared to moderate thinning and no treatment. However, moderate thinning had no effect on crown size when compared to no treatment. Our previous study utilizing the same dataset showed no statistically significant difference between traits characterizing stem size and shape between moderate thinning and no treatment (Saarinen et al., 2020). This, together with the results from this study, suggests that although moderate thinning increased the growing space of the remaining trees, the difference in stem density (i.e., ~310–540 stems/ha) did not lead to a statistically significant growth response of individual Scots pine trees. When the difference in stem density was almost the double (i.e., intensive thinning), there was, however, a statistically significant difference in the growth response of Scots pine crowns.

As height/DBH and absolute height of the crown base have been identified as indicators for tree vitality (Longuetaud et al., 2006), this study presented a means for obtaining those attributes. Height/DBH has been shown to increase as forest management intensity increased (Saarinen et al., 2020), whereas HMC did not differ significantly between tree densities in this study. However, this study provided DCB and stem cross-sectional area at the HMC, which enables studies on their suitability as proxies for growth potential. Competition between trees can be regulated through forest management, and although competition was not studied here, stem density provides an indication for pressure trees encounter around them (Pretzsch, 2014). Competition in young stands is more intense compared to more old-growth stands (Brassard and Chen, 2006) where especially in natural stands dominant trees start to die (Chen and Popadiouk 2002).

Trees with larger crowns have more foliage for photosynthesis, and they are thus larger in size (Zarnoch et al., 2004); results from this and our previous study (Saarinen et al., 2020) confirm this.

As TLS provides crown characteristics and also DCB and SAHMC, future studies could include them in growth models to understand their potential in predicting tree growth, and competition between trees could be studied through crown traits instead of stem dimensions (e.g., DBH), and are there differences in growth response of crown traits between tree species and geographical regions. This study only concentrated on Scots pine trees but the methodology can be applied to other tree species. This study was conducted in one study area, and the results may not apply to Scots pine trees growing in other vegetation zones or forest site types. Another limitation of this study is related to identify individual trees from TLS point clouds as there are uncertainties in the methodology, such as non-detection of trees and only a part of the points originating from a crown can correctly be identified (Yrttimaa et al., 2019, 2020). Nevertheless, as shown with other studies utilizing TLS data, it can be seen as a useful tool for providing crown traits from individual trees.

This study concentrated on investigating crown structure of individual Scots pine trees in different stem densities. Increasing stem density decreased crown size, confirming our hypothesis (H1). With low stem densities (i.e., intensive thinning), crown size also increased when suppressed and codominant trees were removed (i.e., thinning from below) partly confirming the H2 (i.e., no difference in moderate thinnings). Furthermore, a relationship between SAHMC and crown and stem attributes was found. Thus, this study showed how tree density affects crown shape and size of Scots pine trees and how they are adapted to the growing conditions of the trees. As stem density can be regulated



through forest operations such as thinning, the results of this study can be utilized when planning management actions.

## CONCLUSION

Stem densities affected crown size and shape of Scots pine trees growing in boreal forests. When growing in a denser forest, the crown size of Scots pine tree decreased, which indicates more competition on light between adjacent tree crowns. Although this has been known for decades as growth and yield studies have a long history, this study provided quantitative attributes assessing crown size (e.g., crown volume, projection area, surface area, and diameter) and shape (i.e., diameters at different heights of a crown, their mean and standard deviation) of Scots pine trees. Additionally, the study provided stem diameter and cross-sectional area at the height of maximum crown diameter (i.e., SAHMC) that can be assumed to present crown-base height. Increasing forest management intensity increased the SAHMC, and there was strong relationship between it and crown, stem, and growth attributes. Thus, this study provided more insight on the effects of forest management on crown architecture of Scots pine trees, and it can be concluded that this study expanded our knowledge on the crown response of Scots pine trees to the past forest management activities. This was enabled with detailed 3D TLS data that offered quantitative and more comprehensive characterization of Scots pine crowns and growth potential. The novelty of the study is to couple a traditional growth and yield study design (i.e., two thinning intensities and three thinning

types) with a 3D characterization of stem and crown of Scots pine trees with TLS. This type of combination can give answers to new questions related to forest and tree dynamics.

## DATA AVAILABILITY STATEMENT

The raw data supporting the conclusions of this article are openly available at Zenodo (<https://doi.org/10.5281/zenodo.5783404>).

## AUTHOR CONTRIBUTIONS

NS, VK, SH, JaH, and SB were involved in conceptualization. NS, TY, VK, and VL contributed in the data curation. NS performed formal analysis, investigated the study, contributed in project administration, visualized the study, and was involved in roles/writing – original draft. NS, SJ, MH, and JuH contributed in funding acquisition. NS and TY carried out methodology and validated the manuscript. SH, JaH, MH, and JuH provided the resources. TY provided the software. MV supervised the study. All authors participated in writing, reviewing, and editing.

## FUNDING

This study was funded by the Academy of Finland postdoctoral projects 315079, 345166, and 330422 and also Finnish Flagship Program of the Academy of Finland (Grant Numbers 337127, 337655, and 337656).

## REFERENCES

- Aaltonen, V. T. (1925). Metsikön itseharvenemisesta ja puiden kasvutilasta luonnonmetsissä. *Commun. Instit. Quaestionum Forest. Finlandiae* 9, 1–17.
- Barbeito, I., Dassot, M., Bayer, D., Collet, C., Drössler, L., Löf, M., et al. (2017). Terrestrial laser scanning reveals differences in crown structure of *Fagus sylvatica* in mixed vs. pure European forests. *For. Ecol. Manag.* 405, 381–390. doi: 10.1016/j.foreco.2017.09.043
- Bauhus, J., van Winden, A. P., and Nicotra, A. B. (2004). Aboveground interactions and productivity in mixed-species plantations of *Acacia mearnsii* and *Eucalyptus globulus*. *Can. J. For. Res.* 34, 686–694. doi: 10.1139/x03-243
- Bayer, D., Seifert, S., and Pretzsch, H. (2013). Structural crown properties of Norway spruce (*Picea abies* [L.] Karst.) and European beech (*Fagus sylvatica* [L.]) in mixed versus pure stands revealed by terrestrial laser scanning. *Trees* 27, 1035–1047. doi: 10.1007/s00468-013-0854-4
- Binkley, D., Camargo Campoe, O., Gspaltl, M., and Forrester, D. I. (2013). Light absorption and use efficiency in forests: why patterns differ for trees and stands. *For. Ecol. Manag.* 288, 5–13. doi: 10.1016/j.foreco.2011.11.002
- Bogdanovich, E., Perez-Priego, O., El-Madany, T. S., Guderle, M., Pacheco-Labrador, J., Levick, S. R., et al. (2021). Using terrestrial laser scanning for characterizing tree structural parameters and their changes under different management in a Mediterranean open woodland. *For. Ecol. Manag.* 486:118945. doi: 10.1016/j.foreco.2021.118945
- Brassard, B. W., and Chen, H. Y. H. (2006). Stand structural dynamics of North American boreal forests. *Crit. Rev. Plant Sci.* 25, 115–137. doi: 10.1080/07352680500348857
- Cajander, A. K. (1909). Ueber die aldtypen. *Acta For. Fenn.* 1, 1–175.
- Chen, H. Y. H., and Popadiouk, R. V. (2002). Dynamics of North American boreal mixedwoods. *Environ. Rev.* 10, 137–166. doi: 10.1139/a02-007
- Chianucci, F., Puletti, N., Grotti, M., Ferrara, C., Giorcelli, A., Coaloa, D., et al. (2020). Nondestructive tree stem and crown volume allometry in hybrid poplar plantations derived from terrestrial laser scanning. *For. Sci.* 66, 737–746. doi: 10.1093/forsci/fxaa021
- Clark Baldwin, V. Jr., Peterson, K. D., Clark, A. III, Ferguson, R. B., Strub, M. R., and Bower, D. R. (2000). The effects of spacing and thinning on stand and tree characteristics of 38-year-old loblolly pine. *For. Ecol. Manag.* 137, 91–102. doi: 10.1016/S0378-1127(99)00340-0
- Curtin, R. A. (1970). Dynamics of tree and crown structure in *Eucalytus obliqua*. *For. Sci.* 16, 321–328. doi: 10.1093/forestscience/16.3.321
- Dieler, J., and Pretzsch, H. (2013). Morphological plasticity of European beech (*Fagus sylvatica* L.) in pure and mixed-species stands. *For. Ecol. Manag.* 295, 97–108. doi: 10.1016/j.foreco.2012.12.049
- Dyer, M. E., and Burkhart, H. E. (1987). Compatible crown ratio and crown height models. *Can. J. For. Res.* 17, 572–574. doi: 10.1139/x87-096
- Fernández-Sarria, A., Velázquez-Marí, B., Sadjak, M., Martnez, L., and Estornell, J. (2013). Residual biomass calculation from individual tree architecture using terrestrial laser scanner and ground-level measurements. *Comput. Electron. Agric.* 93, 90–97. doi: 10.1016/j.compag.2013.01.012
- Flower-Ellis, J., Albrektsson, A., and Olsson, L. (1976). *Structure and Growth of Some Young Scots Pine Stands: (1) Dimensional and Numerical Relationships*. Swedish Conifer Project Technical Report 3. Uppsala: University of Uppsala, 1–98.
- Forrester, D. I. (2014). The spatial and temporal dynamics of species interactions in mixed-species forests: from pattern to process. *For. Ecol. Manag.* 312, 282–292.
- Fourcaud, T., Zhang, X., Stokes, A., Lambers, H., and Körner, C. (2008). Plant growth modeling and application: the increasing importance of plant architecture in growth models. *Ann. Bot.* 101, 1053–1063. doi: 10.1093/aob/mcn050

- Georgi, L., Kunz, M., Fichter, A., Härdtle, W., Reich, K. R., Strum, K., et al. (2018). Long-term abandonment of forest management has a strong impact on tree morphology and wood volume allocation pattern of European beech (*Fagus sylvatica* L.). *Forests* 9:704. doi: 10.3390/f9110704
- Georgi, L., Kz, M., Fichtner, A., Reich, K. F., Bienert, A., Maas, H.-G., et al. (2021). Effects of local neighbourhood diversity on crown structure and productivity of individual tree in mature mixed-species forests. *For. Ecosyst.* 8:26. doi: 10.1186/s40663-021-00306-y
- Grinrich, S. F. (1967). Measuring and evaluating stocking and stand density in upland hardwood forests in the central states. *For. Sci.* 13, 38–53. doi: 10.1093/forestscience/13.1.38
- Hashimoto, R. (1990). Analysis of the morphology and structure of crown in a young sugi (*Cryptomeria japonica*) stand. *Tree Physiol.* 6, 119–134. doi: 10.1093/treephys/6.2.119
- Heikinheimo, O. (1953). Puun rungon luontaisesta karsitumisesta. *Commun. Instit. Forest. Fenniae* 41, 1–39.
- Hess, C., Härdtle, W., Kunz, M., Fichtner, A., and von Oheimb, G. (2018). A high-resolution approach for the spatiotemporal analysis of forest canopy space using terrestrial laser scanning. *Ecol. Evol.* 8, 6800–6811. doi: 10.1002/ece3.4193
- Hildebrand, M., Perles-Garcia, M. D., Kunz, M., Härdtle, W., von Oheimb, G., and Fichter, A. (2021). Tree-tree interactions and crown complementarity: the role of functional diversity and branch traits for canopy packing. *Basic Appl. Ecol.* 50, 217–227. doi: 10.1016/j.baee.2020.12.003
- Hu, M., Lehtonen, A., Minunno, F., and Mäkelä, A. (2020). Age effect on tree structure and biomass allocation in Scots pine (*Pinus sylvestris* L.) and Norway spruce (*Picea abies* [L.] Karst.). *Ann. For. Sci.* 77:90. doi: 10.1007/s13595-020-00988-4
- Hynynen, J. (1995). Predicting tree crown ratio for unthinned and thinned Scots pine stands. *Can. J. For. Res.* 25, 57–62. doi: 10.1139/x95-007
- Ilomäki, S., Nikinmaa, E., and Mäkelä, A. (2003). Crown rise due to competition drives biomass allocation in silver birch. *Can. J. For. Res.* 33, 2395–2404. doi: 10.1139/x03-164
- Juchheim, J., Annighöfer, P., Ammer, C., Calders, K., Raunonen, P., and Seidel, D. (2017). How management intensity and neighborhood composition affect the structure of beech (*Fagus sylvatica* L.) trees. *Trees* 31, 1723–1735. doi: 10.1007/s00468-017-1581-z
- Juchheim, J., Ehbrecht, M., Schall, P., Ammer, C., and Seidel, D. (2019). Effect of species mixing on stand structural complexity. *Forestry* 93, 75–83. doi: 10.1093/forestry/cpz046
- Kantola, A., and Mäkelä, A. (2004). Crown development in Norway spruce [*Picea abies* (L.) Karst.]. *Trees* 18, 408–421. doi: 10.1007/s00468-004-0319-x
- Kellomäki, S. (1980). Growth dynamics of young Scots pine crowns. *Commun. Instit. Forest. Fenniae* 98, 1–50.
- Kellomäki, S., and Tuimala, A. (1981). Puuston tiheyden vaikutus puiden oksikkuuteen taimikko- ja riukuvaiheen männiköissä. *Folia Forestalia* 478, 1–27.
- Krajicek, J. E., Brinkman, K. A., and Gingrich, S. F. (1961). Crown competition—a measure of density. *For. Sci.* 7, 35–42. doi: 10.1093/forestscience/7.1.35
- Larson, P. R. (1963). Stem form development of forest trees. *For. Sci.* 9, 1–42. doi: 10.1093/forestscience/9.s2.a0001
- Le Roux, X., Lacoite, A., Escobar-Gutiérrez, A., and Le Dizés, S. (2001). Carbon-based models of individual tree growth: a critical appraisal. *Ann. For. Sci.* 58, 469–506. doi: 10.1051/forest:2001140
- Lehnebach, R., Beyer, R., Letort, V., and Heuret, P. (2018). The pipe model theory half a century on: a review. *Ann. Bot.* 121, 773–795. doi: 10.1093/aob/mcx194
- Lehtonen, A., Heikkinen, J., Petersson, H., Tūpek, B., Liski, E., and Mäkelä, A. (2020). Scots pine and Norway spruce foliage biomass in Finland and Sweden – testing traditional models vs. the pipe model theory. *Can. J. For. Res.* 50, 146–154. doi: 10.1139/cjfr-2019-0211
- Liang, X., Kankare, V., Yu, X., Hyypä, J., and Holopainen, M. (2014). Automated stem curve measurement using terrestrial laser scanning. *IEEE Trans. Geosci. Remote Sens.* 52, 1739–1748. doi: 10.1109/TGRS.2013.2253783
- Longuetaud, F., Mothe, F., Leban, J.-M., and Mäkelä, A. (2006). *Picea abies* sapwood width: variations within and between trees. *Scand. J. For. Res.* 21, 41–53. doi: 10.1080/02827580500518632
- Mäkelä, A. (1997). A carbon balance model of growth and self-pruning in trees based on structural relationships. *For. Sci.* 41, 7–24. doi: 10.1093/forestscience/43.1.7
- Mäkelä, A., and Vanninen, P. (2001). Vertical structure of Scots pine crowns in different age and size classes. *Trees* 15, 385–392. doi: 10.1007/s004680100118
- Mäkinen, H., and Isomäki, A. (2004). Thinning intensity and long-term changes in increment and stem form of Scots pine trees. *For. Ecol. Manag.* 201, 21–34. doi: 10.1016/j.foreco.2004.07.028
- Martin-Ducup, O., Schneider, R., and Fournier, R. A. (2016). Response of sugar maple (*Acer saccharum*, Marsh.) tree crown structure to competition in pure versus mixed stands. *For. Ecol. Manag.* 374, 20–32. doi: 10.1016/j.foreco.2016.04.047
- McDowell, N. G., and Allen, C. D. (2015). Darcy's law predicts widespread forest mortality under climate warming. *Nat. Clim. Change* 5, 669–672. doi: 10.1038/nclimate2641
- Messier, C., and Nikinmaa, E. (2000). Effects of light availability and sapling size on the growth, biomass allocation, and crown morphology of understory sugar maple, yellow birch, and beech. *Ecoscience* 7, 345–356. doi: 10.1080/11956860.2000.11682604
- Metz, J., Seidel, D., Schall, P., Scheffer, D., Schulze, E.-D., and Ammer, C. (2013). Crown modeling by terrestrial laser scanning as an approach to assess the effect of aboveground intra- and interspecific competition on tree growth. *For. Ecol. Manag.* 213, 275–288. doi: 10.1016/j.foreco.2013.08.014
- Meyer, F., and Beucher, S. (1990). Morphological segmentation. *J. Vis. Commun. Image Represent.* 1, 21–46. doi: 10.1016/1047-3203(90)90014-M
- Mitchell, K. J. (1969). *Simulation of the Growth Of Even-Aged Stands Of White Spruce*. New Haven: Yale University.
- Montoro Girona, M., Morin, H., Lussier, J.-M., and Walsh, D. (2016). Radial growth response of black spruce stands ten years after experimental shelterwoods and seed-trees cuttings in boreal forest. *Forests* 7:240. doi: 10.3390/f7100240
- Montoro Girona, M., Rossi, S., Lussier, J.-M., Walsh, D., and Morin, H. (2017). Understanding tree growth responses after partial cuttings: a new approach. *PLoS One* 12:e0172653. doi: 10.1371/journal.pone.0172653
- Niinemets, Ü. (2010). A review of light interception in plant stands from leaf to canopy in different plant functional types and in species with varying shade tolerance. *Ecol. Res.* 25, 693–714. doi: 10.1007/s11284-010-0712-4
- Niklas, K. J. (1994). *Plant Allometry The Scaling Of Form and Process*. Chicago, IL: The University of Chicago Press.
- Niklas, K. J., and Enquist, B. J. (2002). Canonical rules for plant organ biomass partitioning and annual allocation. *Am. J. Bot.* 89, 812–819. doi: 10.3732/ajb.89.5.812
- O'Connell, B. M., and Kelt, M. J. (1994). Crown architecture of understory and open-grown white pine (*Pinus strobus* L.) saplings. *Tree Physiol.* 14, 89–102. doi: 10.1093/treephys/14.1.89
- Oker-Blom, P., and Kellomäki, S. (1982). Metsikön tiheyden vaikutus puun latvukseen sisäiseen valoilmastoon ja oksien kuolemiseen – Teoreettinen tutkimus. *Folia Forestalia* 509, 1–14.
- Owen, H. J. F., Flynn, W. R. M., and Lines, E. R. (2021). Competitive drivers of interspecific deviations of crown morphology from theoretical predictions measured with terrestrial laser scanning. *J. Ecol.* 109, 2612–2628. doi: 10.1111/1365-2745.13670
- Pamerleau-Couture, É., Krause, C., Pothier, D., and Weiskittel, A. (2015). Effect of three partial cutting practices on stand structure and growth of residual black spruce trees in north-eastern Quebec. *Forestry* 88, 471–483. doi: 10.1093/forestry/cpv017
- Pinheiro, J., Bates, M. D., DebRoy, S. S., and Sarkar, D. (2013). *Nlme: Linear and Nonlinear Mixed Effects Models. R Package*.
- Popescu, S. C., and Wynne, R. H. (2004). Seeing the trees in the forest. *Photogramm. Eng. Remote Sens.* 70, 589–604. doi: 10.14358/PERS.70.5.589
- Pretzsch, H. (2014). Canopy space filling and tree crown morphology in mixed-species stands compared with monocultures. *For. Ecol. Manag.* 327, 251–264. doi: 10.1016/j.foreco.2014.04.027
- Pretzsch, H. (2019). The effect of tree crown allometry on community dynamics on mixed-species stands versus monocultures. A review and perspectives for modeling and silvicultural regulation. *Forests* 10:810. doi: 10.3390/f10090810
- Pretzsch, H., Biber, P., Uhl, E., Dahlhausen, J., Rötzer, T., Calderntey, J., et al. (2015). Crown size and growing space requirement of common tree species

- in urban centres, parks, and forests. *Urban For. Urban Green.* 14, 466–479. doi: 10.1016/j.ufug.2015.04.006
- Rais, A., Jacobs, M., van de Kuilen, J.-W. G., and Pretzsch, H. (2021). Crown structure of European beech (*Fagus sylvatica*): a noncausal proxy for mechanical-physical wood properties. *Can. J. For. Res.* 51, 834–841. doi: 10.1139/cjfr-2020-0382
- Raulier, F., Ung, C.-H., and Ouellet, D. (1996). Influence of social status on crown geometry and volume increment in regular and irregular black spruce stands. *Can. J. For. Res.* 26, 1742–1753. doi: 10.1139/x26-198
- Rayment, M. B., Loustau, D., and Jarvis, P. G. (2002). Photosynthesis and respiration of black spruce at three organizational scales: shoot, branch and canopy. *Tree Physiol.* 22, 219–229. doi: 10.1093/treephys/22.4.219
- Ritter, T., Schwarz, M., Tockner, A., Leisch, F., and Nothdurft, A. (2017). Automatic mapping of forest stands based on three-dimensional point clouds derived from terrestrial laser-scanning. *Forests* 8:265. doi: 10.3390/f8080265
- Saarinen, N., Calders, K., Kankare, V., Yrttimaa, T., Junttila, S., Luoma, V., et al. (2021). Understanding 3D structural complexity of individual Scots pine trees with different management history. *Ecol. Evol.* 11, 2561–2572. doi: 10.1002/ece3.7216
- Saarinen, N., Kankare, V., Vastaranta, M., Luoma, V., Pyörälä, J., Tanhuanpää, T., et al. (2017). Feasibility of terrestrial laser scanning for collecting stem volume information from single trees. *ISPRS J. Photogr. Remote Sens.* 123, 140–158. doi: 10.1016/j.isprsjprs.2016.11.012
- Saarinen, N., Kankare, V., Yrttimaa, T., Viljanen, N., Honkavaara, E., Holopainen, M., et al. (2020). Assessing the effects of thinning on stem growth allocation of individual Scots pine trees. *For. Ecol. Manag.* 474:118344. doi: 10.1016/j.foreco.2020.118344
- Seidel, D. (2018). A holistic approach to determine tree structural complexity based on laser scanning data and fractal analysis. *Ecol. Evol.* 8, 128–134. doi: 10.1002/ece3.3661
- Seidel, D., Annighöfer, P., Stiers, M., Zemp, C. D., Burkardt, K., Ehbrecht, M., et al. (2019a). How a measure of tree structural complexity relates to architectural benefit-to-cost ratio, light availability, and growth of trees. *Ecol. Evol.* 9, 7134–7142. doi: 10.1002/ece3.5281
- Seidel, D., Ehbrecht, M., Dorji, Y., Jambay, J., Ammer, C., and Annighöfer, P. (2019b). Identifying architectural characteristics that determine tree structural complexity. *Trees* 33, 911–949. doi: 10.1007/s00468-019-01827-4
- Seidel, D., Leuschner, C., Müller, A., and Krause, B. (2011). Crown plasticity in mixed forests—Quantifying asymmetry as a measure of competition using terrestrial laser scanning. *For. Ecol. Manag.* 261, 2123–2132. doi: 10.1016/j.foreco.2011.03.008
- Seidel, D., Scalll, P., Gille, M., and Ammer, C. (2015). Relationship between tree growth and physical dimensions of *Fagus sylvatica* crown assessed from terrestrial laser scanning. *iForest Biosci. For.* 8, 735–742. doi: 10.3832/for1566-008
- Seymour, R. S., and Smith, D. M. (1987). A new stocking guide formulation applied to eastern white pine. *For. Sci.* 33, 469–484. doi: 10.1093/forestscience/33.2.469
- Shinozaki, K., Yoda, K., Hozumi, K., and Kira, T. (1964). A quantitative analysis of plant form – the pipe model theory. I. Basic analyses. *Jpn. J. Ecol.* 14, 97–105. doi: 10.1093/aob/mcx194
- Tahvanainen, T., and Forss, E. (2008). Individual tree models for the crown biomass distribution of Scots pine, Norway spruce and birch in Finland. *For. Ecol. Manag.* 255, 455–467. doi: 10.1016/j.foreco.2007.09.035
- Valentine, H. T., and Mäkelä, A. (2005). Bridging process-based and empirical approaches to modeling tree growth. *Tree Physiol.* 25, 769–779. doi: 10.1093/treephys/25.7.769
- Vanninen, P. (2004). Allocation of above-ground growth in *Pinus sylvestris* – impacts of tree size and competition. *Silva Fennica* 38:425. doi: 10.14214/sf.425
- Vanninen, P., and Mäkelä, A. (2000). Needle and stem wood production in Scots pine (*Pinus sylvestris*) trees of different age, size, and competitive status. *Tree Physiol.* 20, 527–533. doi: 10.1093/treephys/20.8.527
- Vanninen, P., and Mäkelä, A. (2005). Carbon budget for Scots pine trees: effects of size, competition and site fertility on growth allocation and production. *Tree Physiol.* 25, 17–30. doi: 10.1093/treephys/25.1.17
- Vanninen, P., Ylitalo, H., Sievanen, R., and Makela, A. (1996). Effects of age and site quality on the distribution of biomass in Scots pine (*Pinus sylvestris* L.). *Trees* 10, 231–238. doi: 10.1007/BF02185674
- Yrttimaa, T. (2021). *Automatic Point Cloud Processing Tools to Characterize Trees (Point-Cloud-Tools: v1.0.1)*.
- Yrttimaa, T., Saarinen, N., Kankare, V., Hynynen, J., Huuskonen, S., Holopainen, M., et al. (2020). Performance of terrestrial laser scanning to characterize managed Scots pine (*Pinus sylvestris* L.) stands is dependent on forest structural variation. *ISPRS J. Photogr. Remote Sens.* 168, 277–287. doi: 10.1016/j.isprsjprs.2020.08.017
- Yrttimaa, T., Saarinen, N., Kankare, V., Liang, X., Hyypä, J., Holopainen, M., et al. (2019). Investigating the feasibility of multi-scan terrestrial laser scanning to characterize tree communities in southern boreal forests. *Remote Sens.* 11:1423. doi: 10.3390/rs11121423
- Zarnoch, S. J., Bechtold, W. A., and Stolte, K. W. (2004). Using crown condition variable as indicators of forest health. *Can. J. For. Res.* 34, 1057–1070. doi: 10.1139/x03-277
- Zeide, B. (1998). Fractal analysis of foliage distribution in loblolly pine crowns. *Can. J. For. Res.* 28, 106–114. doi: 10.1139/x97-202
- Zhu, Z., Kleinn, C., and Nöle, N. (2021). Assessing tree crown volume—A review. *Forestry* 94, 18–35. doi: 10.1093/forestry/cpaa037

**Conflict of Interest:** The authors declare that the research was conducted in the absence of any commercial or financial relationships that could be construed as a potential conflict of interest.

**Publisher's Note:** All claims expressed in this article are solely those of the authors and do not necessarily represent those of their affiliated organizations, or those of the publisher, the editors and the reviewers. Any product that may be evaluated in this article, or claim that may be made by its manufacturer, is not guaranteed or endorsed by the publisher.

Copyright © 2022 Saarinen, Kankare, Huuskonen, Hynynen, Bianchi, Yrttimaa, Luoma, Junttila, Holopainen, Hyypä and Vastaranta. This is an open-access article distributed under the terms of the Creative Commons Attribution License (CC BY). The use, distribution or reproduction in other forums is permitted, provided the original author(s) and the copyright owner(s) are credited and that the original publication in this journal is cited, in accordance with accepted academic practice. No use, distribution or reproduction is permitted which does not comply with these terms.



# Loop-Mediated Isothermal Amplification for Detection of Plant Pathogens in Wheat (*Triticum aestivum*)

Sandra V. Gomez-Gutierrez<sup>1</sup> and Stephen B. Goodwin<sup>2\*</sup>

<sup>1</sup>Department of Botany and Plant Pathology, Purdue University, West Lafayette, IN, United States, <sup>2</sup>USDA-Agricultural Research Service, West Lafayette, IN, United States

## OPEN ACCESS

### Edited by:

Ruslan Kalendar,  
University of Helsinki, Finland

### Reviewed by:

Luis Antonio Tortajada-Genaro,  
Universitat Politècnica de València,  
Spain

Melanie Kalischuk,

University of Guelph, Canada  
Amirudeen Abdul Kader Jallani,  
University of Florida, United States

### \*Correspondence:

Stephen B. Goodwin  
steve.goodwin@USDA.gov;  
sgoodwin@purdue.edu

### Specialty section:

This article was submitted to  
Technical Advances in Plant Science,  
a section of the journal  
Frontiers in Plant Science

**Received:** 18 January 2022

**Accepted:** 17 February 2022

**Published:** 15 March 2022

### Citation:

Gomez-Gutierrez SV and  
Goodwin SB (2022) Loop-Mediated  
Isothermal Amplification for Detection  
of Plant Pathogens in Wheat (*Triticum  
aestivum*).  
Front. Plant Sci. 13:857673.  
doi: 10.3389/fpls.2022.857673

Wheat plants can be infected by a variety of pathogen species, with some of them causing similar symptoms. For example, *Zymoseptoria tritici* and *Parastagonospora nodorum* often occur together and form the Septoria leaf blotch complex. Accurate detection of wheat pathogens is essential in applying the most appropriate disease management strategy. Loop-mediated isothermal amplification (LAMP) is a recent molecular technique that was rapidly adopted for detection of plant pathogens and can be implemented easily for detection in field conditions. The specificity, sensitivity, and facility to conduct the reaction at a constant temperature are the main advantages of LAMP over immunological and alternative nucleic acid-based methods. In plant pathogen detection studies, LAMP was able to differentiate related fungal species and non-target strains of virulent species with lower detection limits than those obtained with PCR. In this review, we explain the amplification process and elements of the LAMP reaction, and the variety of techniques for visualization of the amplified products, along with their advantages and disadvantages compared with alternative isothermal approaches. Then, a compilation of analyses that show the application of LAMP for detection of fungal pathogens and viruses in wheat is presented. We also describe the modifications included in real-time and multiplex LAMP that reduce common errors from post-amplification detection in traditional LAMP assays and allow discrimination of targets in multi-sample analyses. Finally, we discuss the utility of LAMP for detection of pathogens in wheat, its limitations, and current challenges of this technique. We provide prospects for application of real-time LAMP and multiplex LAMP in the field, using portable devices that measure fluorescence and turbidity, or facilitate colorimetric detection. New technologies for detection of plant pathogen are discussed that can be integrated with LAMP to obtain elevated analytical sensitivity of detection.

**Keywords:** loop-mediated isothermal amplification, wheat, diseases, diagnosis, detection, quantification



## INTRODUCTION

Wheat is one of the world's most important cereal crops, with global production estimated at 762.6 million tons for 2020 and a growing area of 222.28 million hectares (Manjunatha et al., 2018). Wheat plants can be infected by a variety of fungal pathogens, which cause losses totaling about 20% of global production (Kuzdraliński et al., 2017). The top 10 fungal diseases of wheat include rusts (caused by *Puccinia* spp.), the Septoria leaf blotch complex (*Zymoseptoria tritici* and *Parastagonospora nodorum*), powdery mildew (*Blumeria graminis*), wheat blast (*Pyricularia oryzae* Triticum lineage), and several afflictions incited by species of *Fusarium* (Serfling et al., 2017; Thierry et al., 2020). Regionally important fungal pathogens include *Pyrenophora tritici-repentis*, which causes tan spot, and *Bipolaris sorokiniana* (formerly known as *Cochliobolus sativus*), the causal agent of spot blotch disease (Serfling et al., 2017). The species of rust pathogens that affect wheat include *Puccinia striiformis* f. sp. *tritici*, which causes stripe rust, *P. graminis* f. sp. *tritici*, the cause of stem rust, and *P. triticea* (synonym: *P. recondita* f. sp. *tritici*), which causes leaf rust and is the most widely distributed (Figueroa et al., 2018).

The Septoria leaf blotch pathogens, *Zymoseptoria tritici* (cause of Septoria tritici blotch) and *Parastagonospora nodorum* (incitant of Stagonospora nodorum leaf and glume blotch), form a major disease complex of wheat that affects worldwide production and causes up to 25% yield losses in numerous countries, such as Germany (Tian et al., 2005). In the United Kingdom, Septoria tritici blotch (STB) causes 10%–20% average annual losses (Fones and Gurr, 2015). This disease can reduce yield in durum wheat by 40% in Tunisia (Bel Hadj Chedli et al., 2020), while in Morocco, Algeria, and other Mediterranean regions severe epidemics reduce yield in bread and durum wheat by 35%–50% (Siah et al., 2014; Bel Hadj Chedli et al., 2020). In the worst-affected areas of Ethiopia, STB causes 25%–82% losses (Mekonnen et al., 2020). Septoria nodorum blotch (SNB) causes up to 31% yield losses in European regions (Downie et al., 2018) and around 9% yield loss across the wheat belt of Western Australia (Shankar et al., 2021).

Wheat blast caused by *Pyricularia* (formerly *Magnaporthe*) *oryzae* Triticum lineage is also a major threat that can cause total crop losses. This disease has not been reported yet in the United States. However, the widespread dissemination of this pathogen to major wheat-producing areas of the world caused by global trade is a major concern because of the seedborne nature of the *P. oryzae* Triticum lineage (Goulart and Paiva, 1990).

Currently, detection of pathogens and assessment of resistance in wheat plants depend mostly on visual or microscopic examination of the symptoms. Because similar symptoms can be caused by *Z. tritici*, *P. nodorum*, and other leaf pathogens, such as *P. oryzae* or *Pyrenophora tritici-repentis*, accurate detection of these pathogens can be challenging, particularly when they occur together. Moreover, some symptoms are often non-specific and may be confused with lesions associated with biotic stress or normal development, such as natural senescence, with which the coalescing lesions caused by *P. nodorum* can be easily confused (Tian et al., 2005).

Fast and accurate detection of wheat pathogens is required to limit and prevent their spread into disease-free regions (Cruz and Valent, 2017). Accurate detection of pathogens in wheat is a crucial step in applying the most appropriate disease management strategy based on the biology of the causal agents. Morphological and microscopic approaches to identify plant pathogens in wheat require taxonomic knowledge and time to determine the causal agent of observed symptoms. Although these methodologies are an important part of disease diagnostics, they can give unreliable results due to the large number of pathogens and symptoms, and the need for trained experts (Aslam et al., 2017). In recent years, a variety of molecular tools has been developed for fungal detection and identification. These include immunological methods, also known as serological assays, and nucleic acid-based techniques, which are predominantly based on the PCR (Lazcka et al., 2007; Aslam et al., 2017).

PCR-based methods were the foundation to develop numerous DNA-based approaches for plant pathogen detection that give reliable results. Multiple modifications and improvements to PCR have been developed that increase efficiency of the technique. The development of real-time quantitative PCR allowed both detection and quantification of the pathogens, which is relevant to determine the severity of infections (Lau and Botella, 2017). However, PCR-based methods involve challenges for multiple plant pathogen detection and field applications. The equipment required along with reaction time and high-temperature requirements demand the application of other techniques that overcome these difficulties and are suitable for field application.

Many isothermal (constant temperature) amplification techniques have been developed that can be more easily applied in the field. One of the most promising of these is loop-mediated isothermal amplification (LAMP). This approach was first developed by Notomi et al. (2000) and was rapidly adopted for detection of plant pathogens due to its high specificity, sensitivity, efficiency, and isothermal conditions that can be conducted in the field (Iwamoto et al., 2003). In this review, we explain the LAMP principles and LAMP-based approaches. Then we focus on the application of LAMP for detection of fungal pathogens and viruses in wheat, including a compilation of studies that demonstrate its application. We discuss the advantages and disadvantages of LAMP for field applications, compare LAMP against other isothermal-based techniques and present different alternatives for LAMP to be applied as a field assay.

## CONVENTIONAL METHODS FOR PLANT PATHOGEN DETECTION

### Morphological Methods

Microscopic evaluation of characteristic morphological features of plant pathogens is a traditional detection method. This approach relies on initial pathogen isolation on selective culture media that supplies the nutritional requirements of the microorganism. Obligate pathogens must be grown on their host species, which

can be inconvenient and time-consuming (Buja et al., 2021). This is followed by observation of colony appearance and morphological attributes of structures, such as spores, mycelia, and fruiting bodies in fungal organisms through microscopy techniques (Mahlein, 2016). The interpretation of visual symptoms in the host is a tool to verify the causal agent, although multiple plant pathogens can co-exist and cause disease to the plants, which makes accurate detection a difficult task. Disadvantages of these approaches include the laboriousness of pathogen isolation and growth on culture media and the production of structures. For instance, colonies must experience specific conditions to produce spores, which may cause delays in laboratory work flow, and some fungal reproductive structures are not always produced on culture media (Buja et al., 2021). Nowadays, detailed guidelines and standards are available for visual identification. However, recognition of morphology in pathogen structures relies on the human eye and the training and taxonomical knowledge of the field expert, which can lead to misleading conclusions.

## Microbiological Methods

Microbiological approaches require culturing of the pathogen on various appropriate artificial and selective media under a variety of conditions, which is followed by microscopic techniques (Ward et al., 2004). Microscopic observation is accompanied by examination of structures by staining. For instance, the gram stain is one of the most useful tools to differentiate bacteria beyond the genus level. Biochemical and selective tests based on degradation of particular substrates and nutritional requirements can be applied to differentiate particular species (Lazcka et al., 2007). Production and characteristics of sporulating structures in fungi, as well as biochemical-based methods, are used for pathogen detection to yield better results (Ray et al., 2017). Conventional microbiology methods are still the simplest and least expensive. However, culturing of pathogenic species often requires days or weeks to complete. This is a major disadvantage when accurate and rapid diagnosis is required. Also, the results might not always be conclusive, as traditional methods are not highly sensitive and they are not always suitable for detection of pre-symptomatic infections (Ward et al., 2004).

## Serological Assays

The ELISA approach relies on interaction between antigens from pathogens and specific antibodies. This technique is fast and simple to implement and interpret its results, which makes it frequently used for high-throughput testing. Use of monoclonal and recombinant antibodies is an improvement of ELISA applications because it increases the sensitivity and specificity of the assays (Boonham et al., 2014). ELISA is the most widely used and cost-effective serological technique for diagnostics due to its high sensitivity (Khater et al., 2017). However, important limitations of ELISA are low availability of enzyme-conjugated antibodies and low specificity (Tomlinson and Boonham, 2008; Khater et al., 2017). Additionally, the production of monoclonal antibodies may be expensive (Baldi and La Porta, 2020).

ELISA requires high-quality antisera to achieve a sensitive and specific binding to viral antigens. Generation of such antisera requires purification of virions and other viral proteins as antigen. This requires high virology expertise (Boonham et al., 2014). Nevertheless, double-antibody sandwich (DAS)-ELISA, which involves enzyme attachment to the antibody probe has been reported for pathogen detection. Moreover, in the indirect method termed DASI-ELISA, the antibody probe remains unlabeled and, instead, the enzyme is attached to a second antibody specific to the probe antibody. DASI-ELISA has greater sensitivity and convenience compared to DAS-ELISA (Rowhani et al., 2005). Other modifications, such as triple-antibody sandwich (TAS)-ELISA and Dot-ELISA (where reagents are spotted onto a surface such as a nitrocellulose membrane), increased the efficiency of the technique and provide alternatives for detecting plant viruses. Antibodies against viral pathogens in plants are available and the techniques can be adapted for diagnosis of plant viruses that affect wheat (Gao and Wu, 2022).

## PCR Assays

DNA-based identification tools have provided researchers and farmers with plant pathogen detection techniques that are both precise and reliable (Aslam et al., 2017; Thierry et al., 2020). PCR is the most common DNA amplification technique for detection of plant pathogens (Lau and Botella, 2017). It is 100 times more sensitive than serological methods and can provide both qualitative and quantitative results, the latter when coupled with ability to detect DNA in real time (Ray et al., 2017). Real-time PCR follows the same procedures as the conventional approach but includes quantification in real time of amplified DNA products, using a fluorescent marker that binds to the DNA (Alemu, 2014). All PCR techniques employ high heat to obtain a single-stranded target DNA by denaturation of the double-stranded template, which requires expensive equipment (Wong et al., 2018). This is an obvious limitation of using PCR for detection of plant pathogens in the field (Khater et al., 2017).

## Isothermal Amplification Techniques

In contrast to PCR, which requires cycling between a high temperature for DNA denaturation and lower temperatures for primer annealing and DNA synthesis, many techniques are available in which DNA amplification can occur at a single, constant (isothermal) temperature, usually by employing enzymes to provide the denaturing function of higher temperatures. For example, recombinase polymerase amplification (RPA) is a recently developed isothermal amplification technique (Piepenburg et al., 2006) that uses recombinase activity for DNA denaturation and strand displacement synthesis to amplify DNA targets. RPA uses two primers; the reaction runs between 37°C and 42°C and the results can be obtained in 10–30 min. The cyclic repetition of the process leads to exponential amplification (Ereku et al., 2018).

Helicase-dependent amplification (HDA) uses *uvrD* helicase of *Escherichia coli* instead of thermal denaturation to produce single-stranded DNA for primer annealing, and then primer

extension occurs under isothermal conditions. The reaction occurs at 37°C and uses a reparation protein to activate uvrD helicase (Lau and Botella, 2017). Other techniques, such as nucleic acid sequence-based amplification (NASBA), can be used for amplification of either RNA or DNA sequences, although the technique is more used for RNA targets. NASBA is based on serial steps of transcription and reverse transcription processes. It uses a DNA oligonucleotide containing T7 promoter sequence at the 5' end that anneals with target RNA and a T7 DNA polymerase. The reaction is conducted at 65°C, and the products are detected by quantification of fluorescently labeled probes (Ivanov et al., 2021).

In another approach, rolling-circle amplification (RCA) uses rolling replication of short, circular, single-stranded DNA molecules. This technique uses circularizing oligonucleotide probes, which are single-stranded DNA molecules that have target recognition sequences of 20 nucleotides present at both 5' and 3' ends. These oligonucleotide probes are hybridized to target regions and then become circularized using ligase. RCA requires a DNA polymerase, the component nucleotides, unwinding proteins, and primers with dual functions as signal amplifier and complementary sequence to the target DNA (Aslam et al., 2017).

Among these isothermal techniques, loop-mediated isothermal amplification (LAMP) is the best developed and most commonly applied for plant pathogen detection. A high number of LAMP-based approaches have been applied for detection of plant pathogens and numerous modifications that include portable devices, visualization techniques and standardization for multiple detection have been developed to improve its efficiency for detection of pathogens in the field. This is supported by more than 250 research articles on LAMP assays for detection of plant pathogens that have been published in the first decade following the original publication by Notomi et al. (2000) and a year-over-year increase in published LAMP research articles for plant pathogen detection since 2010 (Le and Vu, 2017). The focus of this review will be LAMP for detection of plant pathogens in wheat.

## LAMP Principle

LAMP is an alternative technique to PCR because it is time-efficient, labor-saving and shows a similar or better sensitivity and specificity compared with other RNA/DNA amplification methods (Panno et al., 2020). LAMP typically uses a set of six primers that are complementary to 8 regions in the target DNA coupled with a *Bst* DNA polymerase enzyme with strand displacement activity (Notomi et al., 2000; Nagamine et al., 2002). A primary advantage of LAMP is that it can be performed at a constant temperature between 60°C and 65°C, using only a simple water bath, and can be used even on crude template DNA or directly on tissue samples (Nagamine et al., 2002).

LAMP generates DNA products with stem loop and cauliflower-like structures with multiple loops that result from auto-cycling, strand displacement DNA synthesis and the action of two inner primers, two outer primers and two optional loop primers (Iwamoto et al., 2003). The inner primers are used for priming the initial steps of the process (Figure 1,

Steps 2 and 5) and for self-priming during the later stages of amplification (Figure 1, Steps 9 and 11). The first compound primer is called the forward inner primer (FIP), constituted by joining from 5' to 3' sequences designated F1c and F2. The second is designated the backward inner primer (BIP), constituted by joining sequences B2 and B1c (Notomi et al., 2000). Two outer primers only play a role during the non-cyclic step of strand displacement (Figure 1, Steps 3 and 6), and are denominated as the forward (F3) and backward (B3) outer primers (Parida et al., 2008). There are two loop primers that bind to additional sequences in the DNA that are not targeted by the four internal primers (Figure 1, Steps 9 and 11; Nagamine et al., 2002). Those are called the forward (LF) and backward (LB) loop primers; their role is to improve the amplification and accelerate the reaction (Parida et al., 2008; Duan et al., 2014b).

The reaction initiates with the FIP. The target DNA is denatured by heating to 95°C (Figure 1, Step 1) and rapidly cooled on ice. This permits primer invasion and annealing of the FIP to the target sequence (Notomi et al., 2000). The F2 region of the FIP anneals to the F2c section in the target DNA and initiates the synthesis of a complementary strand (Figure 1, Step 2). Use of a strand displacement polymerase allows this to occur at a constant temperature of 65°C. The outer primer F3 hybridizes to its complementary F3c sequence and initiates strand displacement DNA synthesis (Figure 1, Step 3), releasing a FIP-linked complementary strand (Figure 1, Step 4), which forms a loop structure at one end when the F1c half of the primer anneals to its F1 complementary sequence in the strand DNA (Figure 1, Step 5). This single-stranded DNA acts as a template for DNA synthesis initiated by the B2 sequence at the 3' end of the BIP followed by B3-primed strand displacement DNA synthesis, which releases a BIP-linked complementary strand (Figure 1, Steps 5 to 7). This single-stranded DNA produces a dumb-bell structure, which is then converted to a stem-loop DNA by self-primed DNA synthesis (Figure 1, Step 8).

The stem-loop DNA produced during the non-cyclic part of the process provides the starting material for LAMP cycling, which is initiated by the FIP after annealing to the F2c sequence in the loop of the stem-loop DNA followed by primer strand displacement DNA synthesis (Figure 1, Steps 9 and 10). If added to the reaction, the LB primer binds to the loop between the B1 and B2 regions of the stem-loop DNA. This will generate additional stem-loop structures to which LB and LF primers can anneal to promote exponential amplification. At the same time, a strand displacement occurs from the 3' end of the F1 region (Figure 1, Step 9), which opens the 5' end loop (Figure 1, Step 10). Subsequently, a second strand displacement takes place from the 3' end loop of the B1 region, which produces two intermediate structures (Steps 11a and 13a). One is a complementary double stem-loop DNA to the original one (Figure 1, Steps 11a to 11) and a new stem-loop DNA with a stem that is twice as long (Figure 1, Step 13a). These products provide the template for a BIP-primed strand displacement reaction in subsequent cycles (Figure 1, Step 13), which are called elongation and recycling. For the complementary double stem-loop DNA

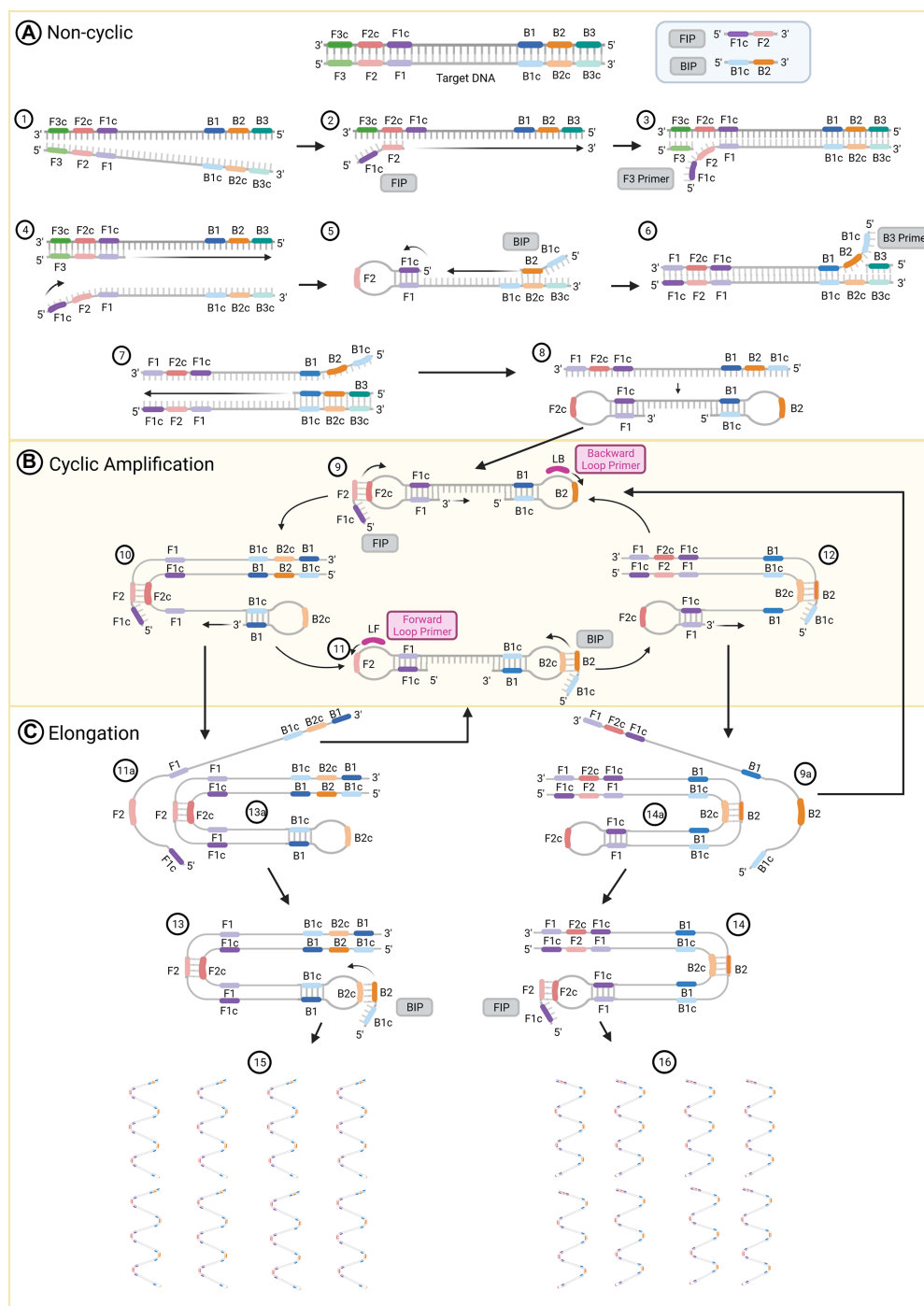


**FIGURE 1 |** The loop-mediated isothermal amplification (LAMP) technique amplification process. **(A)** Non-cyclic steps that produce a DNA strand with two loops at their 5' and 3' ends. **(B)** Cyclic amplification steps and **(C)** elongation. Figure was created with BioRender.com.

produced in steps 11a and 11, the subsequent DNA synthesis is initiated by the BIP through annealing to the loop in the stem-loop DNA and primer strand displacement DNA (Figure 1, Steps 11 and 12) in the same manner as for the original stem loop in step 9. If present, the LF primer binds to the loop between the F1 and F2 regions of this stem-loop

structure and performs in the same manner as the LB primer to further accelerate LAMP. Two intermediate structures (Steps 9a and 14a) are produced from the structure in step 12. These structures are a double stem-loop DNA, which is the original one that was the starting material for LAMP cycling (Figure 1, Steps 9a and 9) and a new stem-loop DNA with



a stem that is twice as long (Figure 1, Step 14a). These products will generate the template for a FIP-primed strand displacement reaction in the following cycles of elongation and recycling. Finally, more elongated structures (Figure 1, Steps 15 and 16) are produced. Through this process, the DNA target sequence is amplified 3-fold every half cycle (Notomi et al., 2000; Tomita et al., 2008; Bruce et al., 2015; Li and Macdonald, 2015).

Reverse transcription-LAMP (RT-LAMP) uses the Avian Myeloblastosis Virus (AMV) reverse transcriptase to amplify RNA target material which can perform the reaction in 60 min at a constant temperature in the same way as LAMP (Tomita et al., 2008).

## Visualization of Amplified Products

LAMP DNA amplicons can be visualized through gel electrophoresis or by adding post-amplification dyes to the solution. These methods require opening the tubes and involve a contamination risk due to the high amount of DNA that is produced during the reaction (Karthik et al., 2014; Fischbach et al., 2015). To fix that problem, a variety of visualization methods that are suitable for closed-tube amplification reactions can be used.

A closed-tube visual inspection uses DNA-intercalating dyes, such as SYBR Green, EvaGreen, ethidium bromide, propidium iodide, and Quanti-iT PicoGreen, or Hydroxynaphthol blue (HNB; Duan et al., 2014a), calcein (Zhou et al., 2014), or CuSO<sub>4</sub> (Tomita et al., 2008), which are metal ion indicators (Zhang et al., 2013; Panno et al., 2020).

SYBR Green has been shown to inhibit real-time LAMP reactions when it is present at concentrations of 1–5 µM or when 0.5 mM Mn<sup>2+</sup> is added to the pre-reaction solution (Goto et al., 2009; Abbasi et al., 2016). To fix this problem, SYBR Green has been replaced with SYTO-16 stain for real-time LAMP or with metal indicators (HNB and calcein) in common LAMP reactions. HNB shows a very good performance in product visualization. Its detection sensitivity is equivalent to SYBR green and it can be present during the reaction, which decreases cross-contamination (Goto et al., 2009). Calcein and HNB can identify amplified products by detecting the change of metal ion concentration in the solution during LAMP. In this process, pyrophosphate ions are produced in great amounts and form insoluble salts by binding with metal ions, such as manganese. As a result, the manganese concentration decreases and the manganese ions that were previously combined with calcein for the reaction to quench, make the solution appear orange. Once LAMP starts in the presence of DNA, calcein is deprived of manganese ions by the new pyrophosphate ion that is generated and calcein can combine with residual magnesium, producing fluorescence (Tomita et al., 2008).

Detection of LAMP products also can be conducted through visual observation of turbidity in the solution, or with a photometer for quantitative detection. The latter is a real-time process that monitors the increase in DNA amplicons by measuring Mg<sup>2+</sup> ion concentration in the solution (Parida et al., 2005; Goto et al., 2009; Zhang et al., 2013).

## Quantitative LAMP

Post-amplification methods to measure LAMP products in end-point analysis can lead to cross-contamination, false positives, or non-specific detection of amplicons. These methods include agarose gel electrophoresis, turbidity observation, detection using intercalating dyes and addition of metal ions as indicators (Gadkar et al., 2018). The development of quantitative or real-time LAMP reduces potential errors from post-amplification detection, enables quantitative detection of the amplified products and is more convenient for multi-sample analysis.

The most widely used real-time LAMP methods are based on measuring the turbidity of the solution or on measurement of fluorescence emission by intercalating dyes, such as ethidium bromide or SYBR Green I (Panno et al., 2020). More recently, the use of fluorescent assimilating probes has optimized real-time LAMP and is a solution to non-specific problems of dye-based detection systems (Villari et al., 2017; Gadkar et al., 2018). The real-time turbidity approach quantifies the amount of magnesium pyrophosphate produced as a byproduct of the LAMP reaction using a real-time turbidimeter. A commercial real-time turbidimeter device (Eiken Chemical, Co., Ltd., Japan) was developed by Mori et al. (2004) and is currently available for quantitative LAMP. The device can maintain the LAMP reaction at an optimum temperature (60°C–65°C) and measures the turbidity of multiple samples simultaneously (Mori et al., 2004; Panno et al., 2020). Regardless of the utility of the turbidity-based detection method, it is 10 times less sensitive than real-time LAMP using fluorescent probes (Quyen et al., 2019).

The fluorescence resonance energy transfer (FRET) approach uses a pair of labeled oligonucleotide probes to optimize LAMP for quantitative detection, in which a quenching strand is displaced from a partially complementary fluorescent strand during the DNA synthesis process. Several portable devices are commercially available to apply this technology, such as “Bioranger” (Diagenetix, Inc., Honolulu, HI, United States) and “Genie II and III” (Optigene Ltd., West Sussex, United Kingdom; Thiessen et al., 2018). Additionally, quantification of LAMP products using a fluorescent dye can be performed using a real-time PCR thermal cycler. A portable fluorescence reader called the ESE-Quant Tube Scanner is also used and offers a convenient alternative for rapid on-site detection (Cao et al., 2017). Recently, this method was used for detection of *Ustilago maydis* in infested soil samples and maize plants using the effector genes *Pep1*, *Pit2*, and *See1* as targets and the Bio-Rad CFX96 Real-Time PCR system to measure the fluorescence signal (Cao et al., 2017). For detection of pathogens in wheat, real-time LAMP has been used for quantification and identification of Wheat Dwarf Virus (Trzmiel and Hasiów-Jaroszewska, 2020; Hao et al., 2021), *Pyricularia oryzae* Triticum lineage (Yasuhara-Bell et al., 2018), *Tilletia* species (Pieczul et al., 2018), *F. graminearum* (Gupta et al., 2020) and trichothecene mycotoxins produced by *Fusarium* species (Denschlag et al., 2014) as will be described later. A quantitative, assimilating probe-based LAMP has been applied for airborne inoculum detection of *Magnaporthe oryzae*, the causal agent of gray leaf spot in turfgrass fields. They combined this approach with the

use of a spore trap system and tested its suitability for implementation in the field (Villari et al., 2017).

## Multiplex LAMP

Traditional techniques for detection of LAMP products are only useful for a single target sequence in the same reaction. Multiplex LAMP (mLAMP) can discriminate target-specific amplicons from a mixture of LAMP products. It is commonly performed by introducing an endonuclease recognition site into the LAMP primers which allows generation of endonuclease-digested amplicons with a length that is specific to the target species (Liang et al., 2012).

mLAMP can use sequence-based barcodes coupled with nicking endonuclease-mediated pyrosequencing (Liang et al., 2012). In this method, a short sequence in the middle of a FIP is used as a target-specific barcode. A recognition site for nicking endonuclease (NEase) is introduced into the FIP. After LAMP reaction, this recognition site allows the use of pyrosequencing, a sequence-by-synthesis method, to decode the barcodes. Because NEases only cleave one specific strand of a duplex DNA, the 3' end at the nick is extendable by *Bst* polymerase, which has strand displacement activity. NEase-digested LAMP products then can be pyrosequenced directly without the use of any primer annealing process (Liang et al., 2012).

Another technique, the multiple endonuclease restriction real-time (MERT)-LAMP assay, combines endonuclease restriction and real-time fluorescence detection with LAMP (Wang et al., 2015). The real-time mLAMP technique combines a standard real-time fluorimeter with the mLAMP assay and can detect 1–4 target sequences in a single reaction tube (Tanner et al., 2012). This technique uses LAMP primers with a quencher–fluorophore duplex region, which displays a fluorescent signal after strand separation (Panno et al., 2020).

mLAMP has been coupled with a variety of multiplex product detection methods to differentiate each amplicon in the products. This technique has been combined with dot-ELISA (Nkouawa et al., 2016), and a LAMP-PCR in combination with hybridization, digestion with restriction endonuclease and the colorimetric method of ELISA has also been applied in medical studies (Lee et al., 2010).

A mLAMP assay was applied to detect the *P. oryzae* Lolium and Triticum lineages in wheat. The mitochondrial NADH-dehydrogenase (*nad5*) gene was used as an internal control for plant DNA, and it was multiplexed with the Pot2 and MoT3 genes (Yasuhara-Bell et al., 2018). This assay was conducted to confirm results from a previous LAMP assay and to compare the sensitivity of mLAMP for rapid detection of *P. oryzae* pathotypes. The Nad5/Pot2 mLAMP assay was first applied to detect *P. oryzae* in the samples. Then, the Nad5/MoT3 assay was applied to confirm whether the identified *P. oryzae* strain corresponded to the *P. oryzae* Triticum lineage. The mLAMP assay results were measured using a CFX96 Real-Time System (Bio-Rad, Hercules, CA, United States) with fluorescence reading at 1-min intervals. The results obtained in the mLAMP assay were comparable to those of the individual analysis (Yasuhara-Bell et al., 2018). Multiplex LAMP techniques do not appear to have been developed for other pathogens of wheat.

## Other LAMP Approaches

LAMP assay can be combined with microfluidic technology to miniaturize the LAMP detection system and facilitate point-of-care pathogen detection. This was motivated by developments in microfluidics technology that allow the manipulation of small volumes of liquids in microfabricated channels or in microchannels to perform all analytical steps (Fang et al., 2010). LAMP is integrated on a microfluidic chip either for readout by eye or for measurement by an optic sensor, which allows detection of target nucleic acids and maintains the sensitivity, rapidity, and specificity of LAMP. This technique is called  $\mu$ LAMP and requires a small sample volume of 0.4  $\mu$ l. This integrated approach has great potential to make LAMP highly portable for on-site analyses (Panno et al., 2020).

Digital LAMP (dLAMP) is an approach that allows accurate quantification of DNA or RNA in a target sample. The total sample is distributed into small compartments such that each compartment contains approximately less than one template molecule (Gansen et al., 2012; Panno et al., 2020). DNA amplification is conducted in each compartment and the number of initial templates in the original sample is equivalent to the number of compartments that show amplification. A sample self-digitization (SD) chip was developed to provide a simple, inexpensive, and sample-conserving device with self-consistent nanoliter compartments and straightforward chip operation. This device is robust and can automatically digitize a sample into an array of nanoliter wells without losing any sample volume. This is called a self-digitization of the total sample. These nanoliter individual volumes will later be used in dLAMP (Gansen et al., 2012).

Electric LAMP (eLAMP) is conducted through an electronic simulation that performs putative tests of LAMP primers on target sequences to determine compatibility. eLAMP can be used to test previously available sets of primers to detect recently discovered sequence variants (Wong et al., 2018). In-disc LAMP (iD-LAMP) is based on the “lab-on-a-disc” concept, in which genomic assays are performed in centrifugal devices that integrate all the analytical steps by controlling the rotation rate. iD-LAMP integrates LAMP amplification and compact disc technology, using an integrated device composed of micro-reactors embedded onto CDs for real-time targeted DNA determination. The real-time curves are measured by cyclic scanning using the optics of a DVD drive and the measurement is taken with standard instruments, such as colorimeters or fluorescence microscopes (Santiago-Felipe et al., 2016).

LAMP can be coupled with a Lateral Flow Dipstick (LFD) device, which can detect biotin-labeled amplicons upon hybridization to a fluorescein-labeled DNA probe complexed with a gold-labeled anti-fluorescein antibody (Rigano et al., 2014; Ivanov et al., 2021). LAMP reaction is carried out for 30 min at 65°C, then a specific fluorescence-labeled probe is added to the reaction mixture and incubated for another 10 min. The LFD strip is inserted into the tube. The resulting complex moves by capillarity and is trapped by a biotin ligand at the test zone. The local gold concentration increases, and the positive reaction can be observed as a reddish-brown color line that develops on the test zone (Ivanov et al., 2021). This

has the potential to replace visualization methods that are not compatible with field applications, such as gel electrophoresis (Rigano et al., 2014).

Other approaches, such as lyophilized LAMP, aim to simplify the reaction process by providing a lyophilized LAMP mix that contains all the reagents (Le and Vu, 2017). The incubation is performed after adding water and sample or DNA–RNA template into the lyophilized mix. There are some lyophilized LAMP kits that are commercially available associated with portable thermal cyclers and other devices, which make it suitable under field conditions (Panno et al., 2020).

## LAMP FOR DETECTION OF WHEAT PATHOGENS

### *Fusarium* Species

*Fusarium graminearum*, the causal agent of Fusarium head blight (FHB), was detected using LAMP in an experiment that also tested DNA from 177 strains from 21 genera of filamentous fungi and two genera of yeast. The primers were designed from a 2042 bp fragment of the *gaoA* gene (galactose oxidase precursor) from *F. austroamericanum* isolate NRRL 2903, and the LAMP technique was applied directly to barley grains and wheat seeds. The *gaoA* gene was selected as a target because *F. graminearum* is the only species showing galactose oxidase activity in culture supernatants (Niessen and Vogel, 2010). Calcein fluorescence was observed with DNA from all *F. graminearum* isolates and in strains representing very similar lineages, such as those in section *Discolor*, which presumably possess sequences homologous to the *gaoA* gene. However, when they tested a species that is closely related to *F. graminearum*, only the target species gave fluorescence signals, which confirmed the specificity of these primers and the LAMP technique. Sensitivity was also confirmed by obtaining fluorescence and amplified products of a predicted size of 145 bp with DNA concentrations below 2 pg/reaction (Niessen and Vogel, 2010).

Traditional and real-time duplex LAMP reactions were conducted to detect deoxynivalenol (DON), nivalenol (NIV), and T2-Toxin, which are trichothecene mycotoxins produced by *Fusarium* species on cereals. Target genes for LAMP reactions were *tri6* (657-bp coding sequence of a regulatory protein) from *F. graminearum* and *tri5* (694-bp trichodiene synthase coding sequence) from *F. sporotrichioides*. The LAMP reaction was performed on 100 wheat samples and 127 fungal species that were used as controls to confirm the specificity of the technique to detect only the target trichothecene-producing *Fusarium* spp. A real-time turbidimeter was used for incubation and the optimum temperature to obtain DNA amplification was 64°C for both primer sets *Tri6* and *Tri5*. The LAMP assay produced DNA amplicons if DON concentration was greater than 162 ppb in the samples. When both sets of primers were used in the duplex assay, it was possible to detect *F. graminearum*, *F. culmorum*, *F. cerealis*, *F. sporotrichioides*, *F. langsethiae*, and *F. poae* in a group-specific manner. This means that the whole group of potentially trichothecene-producing *Fusarium* spp.

was detected with this assay. The LAMP assay was able to detect amplified products for the species between DNA concentrations of 0.004 ng for *F. graminearum* and 15.74 ng for *F. poae* (Denschlag et al., 2014).

### *Pyricularia oryzae*

Wheat blast caused by *P. oryzae* Triticum lineage shows symptoms similar to those seen with FHB. High specificity was achieved in identifying the *P. oryzae* Triticum lineage using LAMP on 158 strains of *P. oryzae* and 50 strains of *F. graminearum* (Yasuhara-Bell et al., 2018). The primers used for this experiment were designed to target the PoT2 locus (Harmon et al., 2003), which differentiates *P. oryzae* from other genera of fungi, and the MoT3 locus to differentiate between pathotypes. Identification of *P. oryzae* was achieved with a minimum amount of 5 pg/μl of DNA per reaction, which indicates high detection sensitivity. The detection was performed using a portable and robust instrument for isothermal amplification called the Genie II system (Yasuhara-Bell et al., 2018).

LAMP, along with PCR and qPCR were used to develop a toolkit of detection tests that can improve current wheat blast detection. The ability of these tests to detect the *P. oryzae* Triticum lineage on contaminated wheat grains was evaluated. Five groups of primers were designed for LAMP and were applied on three wheat-derived isolates and four non-wheat-derived isolates (Thierry et al., 2020). The primers targeted polymorphisms located in genomic regions to find a detection method with improved specificity for the Triticum lineage of *P. oryzae*. One group of primers amplified DNA from every wheat-derived isolate in a very short time, although full specificity was not achieved. However, high sensitivity was obtained with these primers when used on dilutions of down to 5 pg of genomic DNA of three isolates. LAMP failed to amplify DNA of *P. oryzae* from contaminated seed lots when no incubation of the seeds in potato dextrose broth was conducted. However, when this incubation step was included, the detection improved in all tests and LAMP primers were able to detect the pathogen for all replicates in less than 5 min. PCR did not amplify *P. oryzae* isolated from other species in the Poaceae which demonstrated a higher level of specificity. LAMP was suggested as a quick pre-screening test that can provide results within 8 min; a posterior confirmation of positive results should be done by PCR or qPCR (Thierry et al., 2020).

### *Puccinia* Species

*Puccinia striiformis* f. sp. *tritici* is the causal agent of wheat stripe (or yellow) rust. The specificity of LAMP was tested to identify DNA from *P. striiformis* using four isolates of this pathogen and DNA samples from the related rust fungi *P. graminis* f. sp. *tritici* (the cause of stem rust) and *P. recondita* f. sp. *tritici* (synonym *P. tritricina*, leaf rust), plus the unrelated wheat pathogens *Alternaria tritricina* (leaf blight), *Blumeria graminis* f. sp. *tritici* (powdery mildew), *Bipolaris sorokiniana* (*Cochliobolus sativus*, spot blotch, foot, and root rot), *Fusarium graminearum* (FHB), and *Rhizoctonia cerealis* (sharp eyespot). LAMP primers were designed from  $\beta$ -tubulin gene sequence.



*P. striiformis* was detected using SYBR Green I and the amplified product showed bands of the expected size, while no bands were observed for any other fungal pathogens including close relatives. Sensitivity was confirmed with DNA samples from spores, which were amplified from a concentration of 2 pg/μl. Even higher sensitivity was obtained with DNA from inoculated wheat leaves (Huang et al., 2011).

The accuracy and specificity of LAMP for detection of *P. striiformis* f. sp. *tritici* was confirmed with DNA from urediniospores and wheat seedlings with latent infections. The wheat pathogens *Bipolaris sorokiniana*, *Blumeria graminis*, *Fusarium graminearum*, and *Tilletia indica* (Karnal bunt), plus the additional fungi *Aspergillus niger*, *Bipolaris oryzae*, and *Rhizoctonia solani* were used as negative controls to confirm specific detection of *P. striiformis* f. sp. *tritici*. Primers were designed from a qPCR-based marker developed from the ketopantoate reductase coding sequence present in the genome. This gene has been used to analyze the evolutionary relationships among *P. striiformis* f. sp. *tritici* pathotypes (Aggarwal et al., 2018). DNA fragments were detected through the use of HNB dye and ethidium bromide reagent, and ladder-like DNA fragments were amplified with up to 1 pg/μl of DNA concentration, being 10-fold more sensitive than conventional PCR. LAMP also produced an accurate detection with field samples under optimized conditions. Together, these results showed that LAMP has very high sensitivity for detection of *P. striiformis* f. sp. *tritici* and can be applied directly to field samples (Aggarwal et al., 2017).

## Smut Pathogens

LAMP was used to detect three species of smut fungi that cause common bunt and dwarf bunt, which are important seedborne diseases in wheat. DNA samples from wheat grains infected with teliospores from *Tilletia caries* (common bunt), *T. controversa* (dwarf bunt), and *T. laevis* (common bunt, smooth-spored wheat bunt, stinking smut) were used in a LAMP reaction to test for accurate detection of these pathogens. Other common fungal species in wheat grain (*Alternaria alternata*, *Cladosporium cladosporioides*, *Fusarium avenaceum*, *F. culmorum*, *F. graminearum*, *F. poae*, *Helminthosporium* sp., and *Penicillium* sp.) were also subjected to the assay to determine LAMP specificity. Negative results were obtained for all the tested isolates of the non-smut fungal species plus a control that contained water with the reagents but no DNA. Amplification was obtained for *T. caries* and *T. laevis*, with a detection limit in wheat grain of 20 μg of teliospores per 100 g of grain, while *T. controversa* had a detection limit of 20 mg of teliospores per 100 g of grain. The minimum DNA concentration that LAMP was able to detect for the three smut species was around 0.001 ng/μl (Piecuzul et al., 2018).

*Ustilago tritici*, causal agent of loose smut of wheat, also was detected using LAMP. The amplification technique showed a detection limit of 100 fg/μl of DNA, which was 100 times lower than that obtained with qPCR (10 pg/μl). Primers for LAMP were designed to target the large ribosomal subunit gene and the ITS region. DNA samples from the wheat pathogens *Bipolaris sorokiniana*, *Blumeria graminis*, *F. graminearum*,

*P. striiformis*, and *R. cerealis*, plus the potato and tomato pathogen *Alternaria solani* were used as negative controls to test LAMP specificity for detection of *U. tritici* by confirming the non-amplification of DNA from samples of these pathogens. These pathogens were used as controls because there are previous reports on the detection of some of them by qPCR analysis and the detection of Fusarium head blight and wheat stripe rust by LAMP assays. No amplification was obtained with the designed primers on the negative controls. This result was confirmed through fluorescence detection using SYBR Green I. The optimum reaction temperature for detection of *U. tritici* was 63°C (Yan et al., 2019).

## Viruses

Wheat yellow mosaic virus (WYMV) was detected using reverse transcription, loop-mediated isothermal amplification (RT-LAMP). Four primer sets, designed to target the coat protein of the virus, were used to perform the reaction. The specificity of the reaction was tested with two wheat viruses [Chinese Wheat Mosaic Virus (CWMV) and Barley Stripe Mosaic Virus (BSMV)], and the negative control was RNA collected from healthy wheat. Total RNA from wheat leaves infected with each virus was extracted and used for the reaction. They found that 65°C for 80 min were the optimal temperature and time to obtain DNA amplicons, although they could detect the virus after 30 or 45 min. DNA amplicons were visualized through observation of turbidity in the solution and agarose gel electrophoresis. Amplification was obtained only for WYMV, and no DNA amplicons were observed for CWMV or BSMV. The RT-LAMP technique was 100 times more sensitive than RT-PCR and detected RNA that was diluted up to 10<sup>-5</sup> (Zhang et al., 2011).

## Other Pathogens of Wheat

Despite the importance of wheat leaf blotch-pathogenic fungi, such as *Z. tritici*, *Parastagonospora nodorum*, *Pyrenophora tritici-repentis*, and *B. sorokiniana*, no LAMP assay has yet been reported for detection of these pathogens in the field. However, a LAMP assay was reported for specific detection of fungicide resistance in *Z. tritici*, using two promoter inserts in the *MgCYP51* and *MgMFS1* genes as a target, which are associated with gene overexpression and increased fungicide efflux in this fungus (King et al., 2016). This LAMP assay was validated through its application on a variety of *Z. tritici* isolates, in which PCR was also applied for confirmation. They concluded that the LAMP assay can be used to detect geographical spread of these promoter inserts in *Z. tritici* strains and can be a useful tool for Septoria tritici blotch management and to minimize fungicide resistance (King et al., 2016). The leaf blotch diseases caused by all of these fungi can co-occur and often are difficult to diagnose, so a LAMP assay to identify and detect these pathogens should be a high priority for future research. A summary of research on the detection of wheat pathogens using LAMP is provided in Table 1 and a summary of research on the detection of wheat pathogens using other isothermal-based techniques is provided in Table 2.



**TABLE 1 |** LAMP-based detection of various pathogens in wheat.

Pathogen	Disease	Target gene	Visualization technique	References
<i>Wheat dwarf virus</i> (WDV)	Wheat dwarf	Coat protein	Gel electrophoresis, real-time monitoring of amplification curves, SYBRGreen I dye	Trzmiel and Hasiów-Jaroszewska, 2020
<i>Wheat streak mosaic virus</i> (WSMV)	Wheat streak mosaic	Poly-protein coding gene	Electrophoresis in agarose gel	Lee et al., 2015
<i>Wheat yellow mosaic virus</i> (WYMV)	Wheat yellow mosaic	Coat protein	Turbidity observation and electrophoresis	Zhang et al., 2011
<i>Pyricularia oryzae</i> Triticum lineage	Wheat blast	PoT2 and MoT3 loci	Real-time fluorescence and Genie II system	Yasuhara-Bell et al., 2018
<i>Puccinia triticina</i> (synonym: <i>P. recondita</i> f. sp. <i>tritici</i> )	Leaf rust	<i>PtRA</i> <sub>68</sub> specific marker	Hydroxy naphthol Blue (HNB) visualizing indicator; electrophoresis in agarose gel	Manjunatha et al., 2018
<i>Puccinia striiformis</i> f. sp. <i>tritici</i>	Wheat stripe (or yellow) rust	$\beta$ -tubulin gene	SYBR Green I and electrophoresis in agarose gel	Huang et al., 2011
<i>Tilletia caries</i> , <i>T. controversa</i> , and <i>T. laevis</i>	Common bunt, dwarf bunt and smooth-spored wheat bunt	Ketopantoate reductase coding sequence	HNB dye and ethidium bromide, electrophoresis	Aggarwal et al., 2017
<i>Tilletia caries</i> , <i>T. controversa</i> , and <i>T. laevis</i>	Common bunt, dwarf bunt and smooth-spored wheat bunt	IGS 2 rDNA	Real-time monitoring with melting curves, electrophoresis, and direct fluorescence	Pieczul et al., 2018
<i>Ustilago tritici</i>	Loose smut of wheat	Large ribosomal unit and ITS region	SYBR Green I	Yan et al., 2019
<i>Fusarium asiaticum</i>	Fusarium head blight	<i>CYP51C</i> gene	Hydroxy naphthol Blue (HNB) visualizing indicator	Xu et al., 2017
<i>Fusarium graminearum</i>	Fusarium head blight	218-bp region from a partial sequence of <i>F. graminearum</i> chromosome 1	Hydroxy naphthol Blue (HNB) visualizing indicator; electrophoresis in agarose gel	Gupta et al., 2020
<i>Fusarium</i> species	Deoxynivalenol (DON), nivalenol (NIV) and T2-Toxin	<i>gaoA</i> gene (galactose oxidase precursor)	Real-time calcein fluorescence; electrophoresis in agarose gel	Niessen and Vogel, 2010
<i>Fusarium</i> species	Deoxynivalenol (DON), nivalenol (NIV) and T2-Toxin	<i>tri5</i> gene (trichodiene synthase) and <i>tri6</i> (biosynthesis of trichothecenes)	Real-time turbidimeter amplification curves	Denschlag et al., 2014
<i>Zymoseptoria tritici</i> (fungicide resistance)	Septoria tritici blotch	<i>MgCYP51</i> and <i>MgMFS1</i> genes	Gel electrophoresis	King et al., 2016

**TABLE 2 |** Isothermal-based detection of various pathogens in wheat.

Isothermal-based technique	Pathogen	Disease	Target gene	References
RPA	<i>Bipolaris sorokiniana</i>	Root rot and spot blotch	Calmodulin ( <i>cal</i> )	Zhao et al., 2021
RPA	<i>Wheat dwarf virus</i> (WDV)	Wheat dwarf	Polymorphic 12 nucleotides motif (nt 1,433–1,444)	Glaes and Jacquot, 2015
RT-RPA	<i>Barley yellow dwarf virus</i> (BYDV)	Yellow dwarf of wheat	Coat protein (CP) gene	Kim et al., 2020
RCA	<i>Fusarium graminearum</i> species complex (FGSC)	Fusarium Head Blight (FHB)	Elongation factor 1- $\alpha$ (EF-1 $\alpha$ )	Davari et al., 2012
RT-HDA	<i>High plains virus</i> (HPV)	High plains of wheat	Nucleoprotein gene	Arif et al., 2014

RPA, recombinase polymerase amplification; RT-RPA, reverse transcription RPA; RCA, rolling-circle amplification; and RT-HDA, reverse transcription helicase-dependent amplification.

## DISCUSSION

The most significant features of LAMP are the constant temperature conditions, that avoid the use of a thermal cycler, and the rapidity of the reaction, which can be completed in about an hour, or in less than 30 min if loop primers are used. LAMP shows high specificity and sensitivity due to the use of six primers that can target eight regions in the DNA. The technique can be applied either on purified DNA samples or directly in infected wheat tissues, which reduces the detection time and the equipment required.

LAMP is a versatile molecular technique due to the variety of visualization methods and to modifications of the original LAMP procedure, which have given rise to RT-LAMP (Reverse transcriptase—Loop-Mediated Isothermal Amplification), real-time LAMP, and multiplex LAMP. These methods have shown specificity and sensitivity levels similar to or better than those of PCR techniques. The efficiency of RT-LAMP is due to the rapid amplification provided by the loop structure and strand displacement polymerase, plus the robustness of the enzymes used for this methodology, which minimizes inhibitor problems.

**TABLE 3** | Recent LAMP-based approaches for detection of pathogens in other plants.

LAMP-based approach	Pathogen	Disease	Target sequence	References
Multiplex RT-LAMP	Banana bunchy top virus (BBTV), banana streak viruses (BSVs), cucumber mosaic virus (CMV)	Banana bunchy top, banana streak, cucumber mosaic	Conserved regions of coat protein sequence	Zhang et al., 2018
Portable LAMP. Genie II instrument	<i>Neofabraea perennans</i>	Bull's eye rot (BER) in apple and pear	$\beta$ -tubulin gene	Enicks et al., 2020
LAMP-Coupled CRISPR-Cas12a module	Tomato yellow leaf curl virus (TYLCV) and Tomato leaf curl New Delhi virus (ToLCNDV)	Tomato yellow leaf curl and Tomato leaf curl New Delhi	Coat protein gene (CP)	Mahas et al., 2021
Real-time colorimetric LAMP	<i>Xanthomonas gardneri</i>	Bacterial spot (BS) of tomato and pepper	<i>hrpB</i> gene	Stehlíková et al., 2020
Probe-based real-time LAMP	<i>L. acicola</i> , <i>D. pini</i> and <i>D. septosporum</i>	Spot needle blight (BSNB) and <i>Dothistroma</i> needle blight (DNB)	Elongation factor ( <i>EF1-<math>\alpha</math></i> ) and beta-tubulin ( $\beta$ -tub2)	Aglietti et al., 2021
FRET-based probe qLAMP LAMP-based Turn-on Fluorescent Paper (ToFP)	<i>Erysiphe necator</i> <i>Rosellinia necatrix</i>	Grape powdery mildew White root rot (WRR)	ITS region Template candidates from regions in strain W97, scaffold, contig 1 sequence	Thiessen et al., 2018 Lee et al., 2020
Microneedle-smartphone-based LAMP and RT-LAMP	<i>Phytophthora infestans</i> and Tomato spotted wilt virus (TSWV)	Late blight on potato and tomato, and tomato spotted wilt	ITS sequence in <i>P. infestans</i> and N gene of TSWV.	Paul et al., 2021
Cas12a PAM-free LAMP (Cas-PfLAMP)	<i>Xanthomonas oryzae</i> pv. <i>Oryzae</i> , rice stripe virus (RSV), and rice black-streaked dwarf virus (RBSDV)	Rice bacterial leaf blight, rice stripe, rice black-streaked dwarf	<i>PilV</i> gene from <i>X. oryzae</i> pv. <i>Oryzae</i> , RSV SD-JN2 <i>RNA4</i> segment, RBSDV N89 <i>P1</i> gene.	Zhu et al., 2022

Real-time LAMP assays have been applied for portable detection of plant pathogens in other crops and can be an alternative for applications in wheat. These assays have applied real-time LAMP using the portable instrument Genie<sup>®</sup> II (Aglietti et al., 2019). This opens a new perspective for use of portable devices that apply the LAMP technique in the field. Genie II and Genie III are small, low-maintenance, and portable devices. These instruments are capable of temperature control up to 100°C and simultaneous fluorescence detection *via* the FAM channel. Genie II contains two blocks with eight samples in each block, while Genie III includes a single block that accommodates eight samples (Domesle et al., 2020). A LAMP assay with a portable fluorometer (Genalyzer III) using a toothpick method has also been used for detection of plant pathogens (Wilisiani et al., 2019).

Recently, a LAMP-based foldable microdevice platform based on fuchsin colorimetric detection was developed to detect *P. oryzae* and *Sarocladium oryzae* in rice seeds, but this approach will require standardization before its application to other pathogen species (Prasannakumar et al., 2021). Other examples of portable devices for detecting LAMP products include the ESE-Quant tube scanner (Qiagen, Netherlands) and the Bio-Rad CFX96 Real-Time PCR system that were used for portable real-time LAMP and fluorescence measurement for detection of *Ustilago maydis* (Cao et al., 2017). A POCKET (point-of-care kit for the entire test) platform was developed that can be coupled with isothermal amplification techniques (Xu et al., 2020). This device is ultraportable and uses a smartphone as a heater to maintain an isothermal incubation, and as a signal detector and result readout. Additionally, a commercial membrane instead of a chip to conduct dLAMP was developed to be applied for point-of-care detection (Lin et al., 2019). The membrane

is made of track-etched polycarbonate and each pore within the membrane functions as an individual nanoreactor for single DNA amplification. The new method is portable and possibly the most inexpensive way to perform dLAMP (Lin et al., 2019). A summary of recent LAMP-based approaches for detection of pathogens in plants other than wheat is provided in **Table 3**.

Limitations of the LAMP technique include a high risk of cross-contamination and subsequent false-positive results in controls, because of its high efficiency in DNA amplification. Additional caution is required for open-tube visualization to avoid cross-contamination (Le and Vu, 2017). Use of multiple primers also increases the chances of dimer formation and primer–primer hybridizations, which can give unreliable results (Wong et al., 2018). Designing the primers used in LAMP can be a complicated and non-intuitive process, which makes it difficult for those who are not experts (Lau and Botella, 2017). However, a LAMP primer tool exists (Primer Explorer V5) and is available online, which includes tutorials and a step-by-step guide for primer design (Notomi et al., 2015). Also, the design and use of six primers in LAMP, although more challenging, provides very high specificity and sensitivity.

Compared to PCR, LAMP may not be as cost-effective for reagents because it requires the use of multiple primer sets and *Bst* polymerase. However, LAMP only needs a water bath or a block heater, which shows its applicability in a resource-limited context and is cheaper than a dedicated PCR machine. Also, LAMP saves time and labor because the reaction is rapid and can be performed by non-specialized personnel (Panno et al., 2020). For LAMP applications in the field, the temperature required (60°C–65°C) can be a limitation. A common block heater or water bath can be used, but these tools require

electricity which may not be available in the field. This can be overcome with an electricity-free heater based on exothermic chemical reactions and engineered phase change materials that is suitable for any kind of isothermal amplification technique (LaBarre et al., 2011; Panno et al., 2020). In addition, a device, such as POCKET that uses smartphone technology as a heater for isothermal reactions, is a great alternative to convert LAMP into an efficient and convenient field assay (Xu et al., 2020).

Simultaneous detection of multiple plant pathogens in wheat is required to achieve early discrimination of the causal agent and rapid application of management techniques. Parallelized LAMP and mLAMP are two alternatives that can be applied for this purpose. The first one can be performed using microfluidic diagnostic or lab-on-a-chip devices (Zhao et al., 2019). Microfluidic devices integrate a network of microchannels, in which individual samples and different sets of LAMP primers can be added for specific detection of target pathogens (Natsuhara et al., 2020). Parallel LAMP using this technology requires lower consumption of reagents than mLAMP and can increase the portability of the technique, allowing on-site detection without expert knowledge and skills (Zhao et al., 2019). A drawback is the cost of some lab-on-a-chip devices, which require the use of unique and sophisticated equipment for their manufacture or signal interpretation. To date, most existing microfluidic systems are complex and expensive to integrate into a functional system (Zhao et al., 2019; Ivanov et al., 2021).

Different techniques have been developed and tested to improve mLAMP for pathogen detection, such as portable fluorescence devices, multiple endonuclease restriction real-time (MERT)-LAMP, and mLAMP coupled with dot-ELISA (Wang et al., 2015; Nkouawa et al., 2016). These showed promising results in detection of pathogens and can be alternatives for applications in plant pathogen detection, although they can be time-consuming and require expensive sequencing equipment and reagents (Wang et al., 2015). mLAMP assays applied to detect numerous species also need to be designed carefully to avoid interference or non-desired interactions between primers. In contrast, microfluidic technology for parallelized LAMP allows for detection of up to 1,200 samples simultaneously while maintaining sensitivity (Oliveira et al., 2021). Some mLAMP techniques have shown great potential to be applied for detection of wheat pathogens (Yasuhara-Bell et al., 2018; Kang et al., 2020), while parallelized LAMP using microfluidics is starting to become popular for plant pathogen detection with some examples involving plant viruses (Natsuhara et al., 2020).

Application of LAMP-based approaches to detect pathogens in wheat will require some modifications and factors that must be taken into consideration. First, the design of primer sets must allow for specific detection of each species in the pathogen complex that affect this crop. The uniqueness of the selected target sequences in each species must be validated to ensure no similarity with other pathogen species of wheat is found (Manjunatha et al., 2018). This is highly relevant for the wheat pathogen complex, in which some species are closely related and produce very similar symptoms.

Special attention should be given to diseases, such as wheat blast, which is caused by different isolates belonging to the

*Triticum* lineage. In this case, the LAMP technique must be able to discriminate lineages responsible for wheat blast epidemics from those belonging to the other host-specific lineages of the species, which do not incite blast but may be capable of causing opportunistic infections on wheat plants (Thierry et al., 2020). For this purpose, primers have been designed that target new genomic regions to identify polymorphisms fully specific to the *Triticum* lineage (Thierry et al., 2020).

Co-occurrence of pathogen species in wheat is common and is thought to have important implications for pathogen ecology and evolution, as well as for management techniques (Abdullah et al., 2018). Co-infections in wheat are caused by pathogens from different lifestyles and modes of nutrition, which may impact the selection of management techniques. Detection and quantification of the predominant causal agent provides useful information to direct early strategies for control. Accurate detection of the dominant causal agent in wheat can be achieved by applying qLAMP coupled with mLAMP. For this purpose, the MERT-LAMP assay (Wang et al., 2015) is a promising technique for application in wheat that is able to detect and quantify multiple target sequences in a short time. To our knowledge, this technique has not yet been applied to detect plant pathogens.

Portable real-time fluorometers for pathogen detection in the field with limited infrastructure have been developed and applied to different crop systems. In wheat, a LAMP-based foldable microdevice is a promising alternative for detection of pathogens, and its performance was evaluated for detection of *P. oryzae* in rice seeds (Prasannakumar et al., 2021). This approach can be combined with the toothpick DNA extraction method, which saves time and cost for DNA extractions (Wilisiani et al., 2019).

The convenience of LAMP for detection of plant pathogens in wheat should be compared with other isothermal amplification methods. For instance, RPA does not require an initial heating step for DNA denaturation (Baldi and La Porta, 2020). One of the main advantages of RPA is the lower temperature required to conduct the reaction, which is an improvement for field applications where access to electricity may be limited (Panno et al., 2020). Additionally, the use of only two primers in RPA reactions compared to six for LAMP simplifies primer design, and use of the recombinase polymerase lowers detection time. However, the lower reaction temperatures (between 30°C and 55°C) make RPA more prone to non-specific primer binding compared to other isothermal amplification techniques, which can cause amplification of non-target templates (Oliveira et al., 2021). Other limitations of RPA include amplification of only small DNA fragments of less than 1,500 bp with long primers (30–50 nt), which can yield non-specific amplification and a highly variable sensitivity (Ivanov et al., 2021).

RPA has also shown promise for field detection of wheat pathogens. RPA was applied recently for detection of *B. sorokiniana* using the calmodulin gene as a target. The technique showed high specificity when tested against 20 wheat-pathogenic fungal strains. The sensitivity was high with a lower detection limit of 10 pg for pure fungal DNA. RPA was able to detect *B. sorokiniana* directly from field wheat samples (Zhao et al., 2021). Compared to RPA, numerous studies that have successfully conducted LAMP-based approaches to detect pathogen species

that affect wheat and other crops are available (Liu et al., 2014; Yasuhara-Bell et al., 2018; Zhang et al., 2018), which support the standardization of LAMP to detect other wheat pathogens. The first multiplex RPA assay coupled with a lateral flow device was recently reported for plant–pathogen detection of bacteria in the genus *Clavibacter* (Larrea-Sarmiento et al., 2021), which opens new possibilities for standardization of this isothermal technique for detection of wheat pathogens.

Rolling-circle amplification (RCA) provides a sensitive method suitable for detection of plant pathogen species. It has been successfully implemented to detect species in the *Fusarium graminearum* complex (Davari et al., 2012). Because RCA does not require expensive instrumentation, it can be suitable for local, point-of-care measurements. A major advantage of RCA over LAMP is the avoidance of carry-over contamination because there is no new 3′-end single-stranded DNA product generated throughout the RCA process (Lau and Botella, 2017). Helicase-dependent amplification (HDA) does not require an initial heat denaturation step and uses uvrD helicase and a reparation protein to activate uvrD. The main disadvantage compared to LAMP, is that HDA demands complex optimization to ensure a coordinated enzyme activity between the helicase and DNA polymerase (Lau and Botella, 2017).

New techniques for detection of plant pathogens in wheat and other crops are currently emerging. The clustered regularly interspaced short palindromic repeats (CRISPR) are an immune system from bacteria and archaea that has been adapted for gene editing in recent years (Wang et al., 2020). CRISPR-related Cas proteins (Cas12 and Cas13) that can recognize and cleave targets complementary to guide sequences (Chen et al., 2018; Gootenberg et al., 2018) give new possibilities for portable and rapid detection. Cas12 and Cas13 proteins have collateral cleavage activities that can detect nucleic acids and return an amplified signal by activating nuclease activity. This technology can be integrated with PCR or LAMP to produce elevated analytical sensitivity for detection (Wang et al., 2020).

A technique for nucleic acid detection named the Specific High-Sensitivity Enzymatic Reporter UnLOCKing (SHERLOCK) system that uses a Cas13a-based molecular detection platform was developed to detect the target sequence by isothermal amplification with RPA/Reverse Transcriptase (RT)-RPA or Loop-mediated Isothermal Amplification (LAMP)/RT-LAMP (Gootenberg et al., 2017). The CRISPR-Cas system for detection involves pre-amplification of the target molecule by isothermal amplification methods, such as LAMP, or RT-LAMP depending on the type of target pathogen genome. Then, the target amplicons

are subjected to *in vitro* transcription, followed by the detection of RNA or DNA molecules by a Cas-guided reporter system. A fluorometer or lateral flow device can be used to detect the final products (Gootenberg et al., 2018).

Cas12a ssDNase activation was combined with isothermal amplification to create a method termed DNA endonuclease-targeted CRISPR trans reporter (DETECTR), which achieved attomolar ( $10^{-18}$  molecules/ml) sensitivity for DNA detection (Chen et al., 2018). This technique was the foundation for a recently applied method for detection of the *P. oryzae* Triticum lineage using genome-specific primers and Cas12a-mediated technology. Two target markers (*MoT-6098* and *MoT-6099*) were used and its efficiency for detection was evaluated using the LAMP technique. Cas12a along with RPA and nucleic acid lateral flow immunoassay (NALFIA) detected *MoT*-specific DNA sequences in infected wheat plants with accurate, sensitive, and cost-effective results (Kang et al., 2020). CRISPR-Cas technology is an emerging alternative for rapid diagnosis of wheat diseases that can be integrated with LAMP for application in the field (Kang et al., 2020).

LAMP provides many advantages over other detection methods, but much still needs to be done for detection of diseases in wheat. One need is for LAMP protocols for the many leaf blotch diseases that can co-occur and are difficult to diagnose. Coupled with this would be quantitative and multiplex LAMP that could allow plant pathologists to identify not only the correct species causing disease but also to estimate their relative abundances. Combining the advantages of CRISPR with LAMP approaches for detection of wheat pathogens is another high priority. With the rapid developments of the past few years and availability of these approaches individually the path for future advances is promising.

## AUTHOR CONTRIBUTIONS

SG-G and SG wrote the manuscript. SG provided significant comments on the article and language editing support. Both authors contributed to the article and approved the submitted version.

## FUNDING

This work was supported by USDA-ARS research project 5020-21220-019-00D.

## REFERENCES

- Abbasi, I., Kirstein, O. D., Hailu, A., and Warburg, A. (2016). Optimization of loop-mediated isothermal amplification (LAMP) assays for the detection of *Leishmania* DNA in human blood samples. *Acta Trop.* 162, 20–26. doi: 10.1016/j.actatropica.2016.06.009
- Abdullah, A. S., Turo, C., Moffat, C. S., Lopez-Ruiz, F. J., Gibberd, M. R., Hamblin, J., et al. (2018). Real-time PCR for diagnosing and quantifying co-infection by two globally distributed fungal pathogens of wheat. *Front. Plant Sci.* 9:1086. doi: 10.3389/fpls.2018.01086
- Aggarwal, R., Kulshreshtha, D., Sharma, S., Singh, V. K., Manjunatha, C., Bhardwaj, S. C., et al. (2018). Molecular characterization of Indian pathotypes of *Puccinia striiformis* f. sp. *tritici* and multigene phylogenetic analysis to establish inter- and intraspecific relationships. *Genet. Mol. Biol.* 41, 834–842. doi: 10.1590/1678-4685-gmb-2017-0171
- Aggarwal, R., Sharma, S., Manjunatha, C., Gupta, S., and Singh, V. K. (2017). Development and validation of loop mediated isothermal amplification based detection assay for *Puccinia striiformis* f. sp. *tritici* causing stripe rust of wheat. *Australas. Plant Pathol.* 46, 577–583. doi: 10.1007/s13313-017-0524-x



- Aglietti, C., Luchi, N., Pepori, A. L., Bartolini, P., Pecori, F., Raio, A., et al. (2019). Real-time loop-mediated isothermal amplification: an early-warning tool for quarantine plant pathogen detection. *AMB Express* 9:50. doi: 10.1186/s13568-019-0774-9
- Aglietti, C., Meinecke, C. D., Ghelardini, L., Barnes, I., van der Nest, A., and Villari, C. (2021). Rapid detection of pine pathogens *Lecanosticta acicola*, *Dothistroma pini* and *D. septosporum* on needles by probe-based LAMP assays. *Forests* 12:479. doi: 10.3390/f12040479
- Alemu, K. (2014). "Real-time PCR and its application in plant disease diagnostics," in *Advances in Life Sciences and Technology*. Vol. 27, 39–49.
- Arif, M., Aguilar-Moreno, G. S., Wayadande, A., Fletcher, J., and Ochoa-Corona, F. M. (2014). Primer modification improves rapid and sensitive in vitro and field-deployable assays for detection of high plains virus variants. *Appl. Environ. Microbiol.* 80, 320–327. doi: 10.1128/AEM.02340-13
- Aslam, S., Tahir, A., Aslam, M. F., Alam, M. W., Shedayi, A. A., and Sadia, S. (2017). Recent advances in molecular techniques for the identification of phytopathogenic fungi: a mini review. *J. Plant Interact.* 12, 493–504. doi: 10.1080/17429145.2017.1397205
- Baldi, P., and La Porta, N. (2020). Molecular approaches for low-cost point-of-care pathogen detection in agriculture and forestry. *Front. Plant Sci.* 11:570862. doi: 10.3389/fpls.2020.570862
- Bel Hadj Chedli, R., Ben M'Barek, S., Souissi, A., Yahyaoui, A., Rezgui, S., and Chaabane, H. (2020). Screening for resistance of Tunisian, Moroccan and Algerian wheat cultivars to *Zymoseptoria tritici* in northern Tunisia. *J. Plant Pathol.* 102, 1085–1095. doi: 10.1007/s42161-020-00563-w
- Boonham, N., Kreuze, J., Winter, S., van der Vlugt, R., Bergervoet, J., Tomlinson, J., et al. (2014). Methods in virus diagnostics: from ELISA to next generation sequencing. *Virus Res.* 186, 20–31. doi: 10.1016/j.virusres.2013.12.007
- Bruce, K. L., Leterme, S. C., Ellis, A. V., and Lenehan, C. E. (2015). Approaches for the detection of harmful algal blooms using oligonucleotide interactions. *Anal. Bioanal. Chem.* 407, 95–116. doi: 10.1007/s00216-014-8193-x
- Buja, I., Sabella, E., Monteduro, A. G., Chiriaco, M. S., De Bellis, L., Luvisi, A., et al. (2021). Advances in plant disease detection and monitoring: from traditional assays to in-field diagnostics. *Sensors* 21, 1–22. doi: 10.3390/s21062129
- Cao, Y., Wang, L., Duan, L., Li, J., Ma, J., Xie, S., et al. (2017). Development of a real-time fluorescence loop-mediated isothermal amplification assay for rapid and quantitative detection of *Ustilago maydis*. *Sci. Rep.* 7, 13394–13312. doi: 10.1038/s41598-017-13881-4
- Chen, J. S., Ma, E., Harrington, L. B., Da Costa, M., Tian, X., Palefsky, J. M., et al. (2018). CRISPR-Cas12a target binding unleashes indiscriminate single-stranded DNase activity. *Science* 360, 436–439. doi: 10.1126/science.aar6245
- Cruz, C. D., and Valent, B. (2017). "Wheat blast disease: danger on the move," in *Tropical Plant Pathology*. Vol. 42, 210–222.
- Davari, M., van Diepeningen, A. D., Babai-Ahari, A., Arzanlou, M., Najafzadeh, M. J., van der Lee, T. A. J., et al. (2012). Rapid identification of *Fusarium graminearum* species complex using rolling circle amplification (RCA). *J. Microbiol. Methods* 89, 63–70. doi: 10.1016/j.mimet.2012.01.017
- Denschlag, C., Rieder, J., Vogel, R. F., and Niessen, L. (2014). Real-time loop-mediated isothermal amplification (LAMP) assay for group specific detection of important trichothecene producing *Fusarium* species in wheat. *Int. J. Food Microbiol.* 177, 117–127. doi: 10.1016/j.ijfoodmicro.2014.02.010
- Domesle, K. J., Young, S. R., Yang, Q., and Ge, B. (2020). Loop-mediated isothermal amplification for screening *Salmonella* in animal food and confirming *Salmonella* from culture isolation. *J. Vis. Exp.* 159:e61239. doi: 10.3791/61239
- Downie, R. C., Bouvet, L., Furuki, E., Gosman, N., Gardner, K. A., Mackay, I. J., et al. (2018). Assessing European wheat sensitivities to *Parastagonospora nodorum* necrotrophic effectors and fine-mapping the *Snn3-B1* locus conferring sensitivity to the effector SnTox3. *Front. Plant Sci.* 9:881. doi: 10.3389/fpls.2018.00881
- Duan, Y.-B., Ge, C.-Y., Zhang, X.-K., Wang, J.-X., and Zhou, M.-G. (2014a). Development and evaluation of a novel and rapid detection assay for *Botrytis cinerea* based on loop-mediated isothermal amplification. *PLoS One* 9:e111094. doi: 10.1371/journal.pone.0111094
- Duan, Y., Zhang, X., Ge, C., Wang, Y., Cao, J., Jia, X., et al. (2014b). Development and application of loop-mediated isothermal amplification for detection of the F167Y mutation of carbendazim-resistant isolates in *Fusarium graminearum*. *Sci. Rep.* 4, 1–8. doi: 10.1038/srep07094
- Enicks, D. A., Bomberger, R. A., and Amiri, A. (2020). Development of a portable LAMP assay for detection of *Neofabraea perennans* in commercial apple fruit. *Plant Dis.* 104, 2346–2353. doi: 10.1094/PDIS-09-19-2036-RE
- Ereku, L. T., Mackay, R. E., Craw, P., Naveenathayalan, A., Stead, T., Branavan, M., et al. (2018). RPA using a multiplexed cartridge for low cost point of care diagnostics in the field. *Anal. Biochem.* 547, 84–88. doi: 10.1016/j.ab.2018.02.010
- Fang, X., Liu, Y., Kong, J., and Jiang, X. (2010). Loop-mediated isothermal amplification integrated on microfluidic chips for point-of-care quantitative detection of pathogens. *Anal. Chem.* 82, 3002–3006. doi: 10.1021/ac1000652
- Figueroa, M., Hammond-Kosack, K. E., and Solomon, P. S. (2018). A review of wheat diseases: a field perspective. *Mol. Plant Pathol.* 19, 1523–1536. doi: 10.1111/mpp.12618
- Fischbach, J., Xander, N. C., Frohme, M., and Glöckler, J. F. (2015). Shining a light on LAMP assays: a comparison of LAMP visualization methods including the novel use of berberine. *BioTechniques* 58, 189–194. doi: 10.2144/000114275
- Fones, H., and Gurr, S. (2015). The impact of *Septoria tritici* blotch disease on wheat: an EU perspective. *Fungal Genet. Biol.* 79, 3–7. doi: 10.1016/j.fgb.2015.04.004
- Gadkar, V. J., Goldfarb, D. M., Gantt, S., and Tilley, P. A. G. (2018). Real-time detection and monitoring of loop mediated amplification (LAMP) reaction using self-quenching and de-quenching fluorogenic probes. *Sci. Rep.* 8, 1–10. doi: 10.1038/s41598-018-23930-1
- Gansen, A., Herrick, A. M., Dimov, I. K., Lee, L. P., and Chiu, D. T. (2012). Digital LAMP in a sample self-digitization (SD) chip. *Lab Chip* 12, 2247–2254. doi: 10.1039/c2lc21247a
- Gao, S., and Wu, J. (2022). Detection of tomato spotted wilt virus (TSWV) infection in plants using DAS-ELISA and dot-ELISA. *Methods Mol. Biol.* 2400, 253–261. doi: 10.1007/978-1-0716-1835-6\_24
- Glais, L., and Jacquot, E. (2015). Detection and characterization of viral species/subspecies using isothermal recombinase polymerase amplification (RPA) assays. *Methods Mol. Biol.* 1302, 207–225. doi: 10.1007/978-1-4939-2620-6\_16
- Gootenberg, J. S., Abudayyeh, O. O., Kellner, M. J., Joung, J., Collins, J. J., and Zhang, F. (2018). Multiplexed and portable nucleic acid detection platform with Cas13, Cas12a and Csm6. *Science* 360, 439–444. doi: 10.1126/science.aag0179
- Gootenberg, J. S., Abudayyeh, O. O., Lee, J. W., Essletzbichler, P., Dy, A. J., Joung, J., et al. (2017). Nucleic acid detection with CRISPR-Cas13a/C2c2. *Science* 356, 438–442. doi: 10.1126/science.aam9321
- Goto, M., Honda, E., Ogura, A., Nomoto, A., and Hanaki, K. I. (2009). Colorimetric detection of loop-mediated isothermal amplification reaction by using hydroxy naphthol blue. *BioTechniques* 46, 167–172. doi: 10.2144/000113072
- Goulart, A. C. P., and Paiva, F. A. (1990). Transmission of *Pycarilaria oryzae* by wheat *Triticum aestivum* seeds. *Fitopatol. Bras.* 26, 1983–1988.
- Gupta, S., Saharan, M. S., Gurjar, M. S., Singh, J., Bashyal, B. M., and Aggarwal, R. (2020). Molecular detection of *Fusarium graminearum* causing head blight of wheat by loop mediated isothermal amplification (LAMP) assay. *Indian Phytopathol.* 73, 667–672. doi: 10.1007/s42360-020-00261-8
- Hao, X., Wang, L., Zhang, X., Zhong, Q., Hajano, J.-U.-D., Xu, L., et al. (2021). A real-time loop-mediated isothermal amplification for detection of the wheat dwarf virus in wheat and the insect vector *Psammotettix alienus*. *Plant Dis.* 105, 4113–4120. doi: 10.1094/pdis-10-20-2279-re
- Harmon, P. F., Dunkle, L. D., and Latin, R. (2003). A rapid PCR-based method for the detection of *Magnaporthe oryzae* from infected perennial ryegrass. *Plant Dis.* 87, 1072–1076. doi: 10.1094/PDIS.2003.87.9.1072
- Huang, C., Sun, Z., Yan, J., Luo, Y., Wang, H., and Ma, Z. (2011). Rapid and precise detection of latent infections of wheat stripe rust in wheat leaves using loop-mediated isothermal amplification. *J. Phytopathol.* 159, 582–584. doi: 10.1111/j.1439-0434.2011.01806.x
- Ivanov, A. V., Safenkova, I. V., Zherdev, A. V., and Dzantiev, B. B. (2021). The potential use of isothermal amplification assays for in-field diagnostics of plant pathogens. *Plan. Theory* 10:2424. doi: 10.3390/plants10112424
- Iwamoto, T., Sonobe, T., and Hayashi, K. (2003). Loop-mediated isothermal amplification for direct detection of *Mycobacterium tuberculosis* complex, *M. avium*, and *M. intracellulare* in sputum samples. *J. Clin. Microbiol.* 41, 2616–2622. doi: 10.1128/JCM.41.6.2616-2622.2003
- Kang, H., Peng, Y., Hua, K., Deng, Y., Bellizzi, M., Gupta, D. R., et al. (2020). Rapid detection of wheat blast pathogen *Magnaporthe oryzae* Triticum pathotype using genome-specific primers and Cas12a-mediated technology. *Engineering* 7, 1326–1335. doi: 10.1016/j.eng.2020.07.016

- Karthik, K., Rathore, R., Thomas, P., Arun, T. R., Viswas, K. N., Dhama, K., et al. (2014). New closed tube loop mediated isothermal amplification assay for prevention of product cross-contamination. *MethodsX* 1, e137–e143. doi: 10.1016/j.mex.2014.08.009
- Khater, M., de la Escosura-Muñoz, A., and Merkoçi, A. (2017). Biosensors for plant pathogen detection. *Biosens. Bioelectron.* 93, 72–86. doi: 10.1016/j.bios.2016.09.091
- Kim, N. K., Kim, S. M., and Jeong, R. D. (2020). Reverse transcription recombinase polymerase amplification assay for rapid and sensitive detection of barley yellow dwarf virus in oat. *Plant Pathol. J.* 36, 497–502. doi: 10.5423/PPJ.NT.08.2020.0148
- King, K., Kirikyali, N., West, J., and Fraaije, B. (2016). “Rapid LAMP assays to detect MgCYP51 and/or MgMFS1 overexpressing strains of *Zymoseptoria tritici* in leaf samples,” in *Modern Fungicides and Antifungal Compounds*. Vol. 8, 67–72.
- Kuzdraliński, A., Kot, A., Szczerba, H., Nowak, M., and Muszyńska, M. (2017). A review of conventional PCR assays for the detection of selected phytopathogens of wheat. *J. Mol. Microbiol. Biotechnol.* 27, 175–189. doi: 10.1159/000477544
- LaBarre, P., Hawkins, K. R., Gerlach, J., Wilmoth, J., Beddoe, A., Singleton, J., et al. (2011). A simple, inexpensive device for nucleic acid amplification without electricity-toward instrument-free molecular diagnostics in low-resource settings. *PLoS One* 6:e19738. doi: 10.1371/journal.pone.0019738
- Larrea-Sarmiento, A., Stack, J. P., Alvarez, A. M., and Arif, M. (2021). Multiplex recombinase polymerase amplification assay developed using unique genomic regions for rapid on-site detection of genus *Clavibacter* and *C. nebraskensis*. *Sci. Rep.* 11:12017. doi: 10.1038/s41598-021-91336-7
- Lau, H. Y., and Botella, J. R. (2017). Advanced DNA-based point-of-care diagnostic methods for plant diseases detection. *Front. Plant Sci.* 8:2016. doi: 10.3389/fpls.2017.02016
- Lazcka, O., del Campo, F. J., and Muñoz, F. X. (2007). Pathogen detection: a perspective of traditional methods and biosensors. *Biosens. Bioelectron.* 22, 1205–1217. doi: 10.1016/j.bios.2006.06.036
- Le, D. T., and Vu, N. T. (2017). Progress of loop-mediated isothermal amplification technique in molecular diagnosis of plant diseases. *Appl. Biol. Chem.* 60, 169–180. doi: 10.1007/s13765-017-0267-y
- Lee, M. F., Chen, Y. H., Hsu, H. J., and Peng, C. F. (2010). One-tube loop-mediated isothermal amplification combined with restriction endonuclease digestion and ELISA for colorimetric detection of resistance to isoniazid, ethambutol and streptomycin in *Mycobacterium tuberculosis* isolates. *J. Microbiol. Methods* 83, 53–58. doi: 10.1016/j.mimet.2010.07.018
- Lee, S., Kim, J. H., Choi, J. Y., and Jang, W. C. (2015). Loop-mediated isothermal amplification assay to rapidly detect wheat streak mosaic virus in quarantined plants. *Plant Pathol. J.* 31, 438–440. doi: 10.5423/PPJ.NT.06.2015.0110
- Lee, S. H., Lee, S., Won, K., Kim, M., Ryu, H., Kim, H., et al. (2020). Loop-mediated isothermal amplification (LAMP)-based turn on fluorescence paper (ToFP) device for detecting *Rosellinia necatrix*. *J. Biomed. Nanotechnol.* 16, 166–178. doi: 10.1166/jbn.2020.2889
- Li, J., and Macdonald, J. (2015). Advances in isothermal amplification: novel strategies inspired by biological processes. *Biosens. Bioelectron.* 64, 196–211. doi: 10.1016/j.bios.2014.08.069
- Liang, C., Chu, Y., Cheng, S., Wu, H., Kajiyama, T., Kambara, H., et al. (2012). Multiplex loop-mediated isothermal amplification detection by sequence-based barcodes coupled with nicking endonuclease-mediated pyrosequencing. *Anal. Chem.* 84, 3758–3763. doi: 10.1021/ac3003825
- Lin, X., Huang, X., Urmann, K., Xie, X., and Hoffmann, M. R. (2019). Digital loop-mediated isothermal amplification on a commercial membrane. *ACS Sens.* 4, 242–249. doi: 10.1021/acssensors.8b01419
- Liu, X., Zhao, X. T., Muhammad, I., Ge, B. B., and Hong, B. (2014). Multiplex reverse transcription loop-mediated isothermal amplification for the simultaneous detection of CVB and CSVd in chrysanthemum. *J. Virol. Methods* 210, 26–31. doi: 10.1016/j.jviromet.2014.09.008
- Mahas, A., Hassan, N., Aman, R., Marsic, T., Wang, Q., Ali, Z., et al. (2021). LAMP-coupled CRISPR-Cas12a module for rapid and sensitive detection of plant dna viruses. *Viruses* 13:466. doi: 10.3390/v13030466
- Mahlein, A.-K. (2016). Plant disease detection by imaging sensors: parallels and specific demands for precision agriculture and plant phenotyping. *Plant Dis.* 100, 241–251. doi: 10.1094/PDIS-03-15-0340-FE
- Manjunatha, C., Sharma, S., Kulshreshtha, D., Gupta, S., Singh, K., Bhardwaj, S. C., et al. (2018). Rapid detection of *Puccinia triticina* causing leaf rust of wheat by PCR and loop mediated isothermal amplification. *PLoS One* 13:e0196409. doi: 10.1371/journal.pone.0196409
- Mekonnen, T., Haileselassie, T., Goodwin, S. B., and Tesfaye, K. (2020). Genetic diversity and population structure of *Zymoseptoria tritici* in Ethiopia as revealed by microsatellite markers. *Fungal Genet. Biol.* 141:103413. doi: 10.1016/j.fgb.2020.103413
- Mori, Y., Kitao, M., Tomita, N., and Notomi, T. (2004). Real-time turbidimetry of LAMP reaction for quantifying template DNA. *J. Biochem. Biophys. Methods* 59, 145–157. doi: 10.1016/j.jbbm.2003.12.005
- Nagamine, K., Hase, T., and Notomi, T. (2002). Accelerated reaction by loop-mediated isothermal amplification using loop primers. *Mol. Cell. Probes* 16, 223–229. doi: 10.1006/mcpr.2002.0415
- Natsuhara, D., Takishita, K., Tanaka, K., Kage, A., Suzuki, R., Mizukami, Y., et al. (2020). A microfluidic diagnostic device capable of autonomous sample mixing and dispensing for the simultaneous genetic detection of multiple plant viruses. *Micromachines* 11:540. doi: 10.3390/mi11060540
- Niessen, L., and Vogel, R. F. (2010). Detection of *Fusarium graminearum* DNA using a loop-mediated isothermal amplification (LAMP) assay. *Int. J. Food Microbiol.* 140, 183–191. doi: 10.1016/j.jfoodmicro.2010.03.036
- Nkouawa, A., Sako, Y., Okamoto, M., and Ito, A. (2016). Simple identification of human *Taenia* species by multiplex loop-mediated isothermal amplification in combination with dot enzyme-linked immunosorbent assay. *Am. J. Trop. Med. Hyg.* 94, 1318–1323. doi: 10.4269/ajtmh.15-0829
- Notomi, T., Mori, Y., Tomita, N., and Kanda, H. (2015). Loop-mediated isothermal amplification (LAMP): principle, features, and future prospects. *J. Microbiol.* 53, 1–5. doi: 10.1007/s12275-015-4656-9
- Notomi, T., Okayama, H., Masubuchi, H., Yonekawa, T., Watanabe, K., Amino, N., et al. (2000). Loop-mediated isothermal amplification of DNA. *Nucleic Acids Res.* 28:e63. doi: 10.1093/nar/28.12.e63
- Oliveira, B. B., Veigas, B., and Baptista, P. V. (2021). Isothermal amplification of nucleic acids: the race for the next “gold standard”. *Front. Sens.* 2:752600. doi: 10.3389/fsens.2021.752600
- Panno, S., Matic, S., Tiberini, A., Caruso, A. G., Bella, P., Torta, L., et al. (2020). Loop mediated isothermal amplification: principles and applications in plant virology. *Plan. Theory* 9:461. doi: 10.3390/plants9040461
- Parida, M., Horioke, K., Ishida, H., Dash, P. K., Saxena, P., Jana, A. M., et al. (2005). Rapid detection and differentiation of dengue virus serotypes by a real-time reverse transcription-loop-mediated isothermal amplification assay. *J. Clin. Microbiol.* 43, 2895–2903. doi: 10.1128/JCM.43.6.2895-2903.2005
- Parida, M., Sannarangaiah, S., Dash, P. K., Rao, P. V. L., and Morita, K. (2008). Loop mediated isothermal amplification (LAMP): a new generation of innovative gene amplification technique; perspectives in clinical diagnosis of infectious diseases. *Rev. Med. Virol.* 18, 407–421. doi: 10.1002/rmv.593
- Paul, R., Ostermann, E., Chen, Y., Saville, A. C., Yang, Y., Gu, Z., et al. (2021). Integrated microneedle-smartphone nucleic acid amplification platform for in-field diagnosis of plant diseases. *Biosens. Bioelectron.* 187:113312. doi: 10.1016/j.bios.2021.113312
- Pieczul, K., Perek, A., and Kubiak, K. (2018). Detection of *Tilletia caries*, *Tilletia laevis* and *Tilletia controversa* wheat grain contamination using loop-mediated isothermal DNA amplification (LAMP). *J. Microbiol. Methods* 154, 141–146. doi: 10.1016/j.mimet.2018.10.018
- Piepenburg, O., Williams, C. H., Stemple, D. L., and Armes, N. A. (2006). DNA detection using recombination proteins. *PLoS Biol.* 4:e204. doi: 10.1371/journal.pbio.0040204
- Prasannakumar, M. K., Parivallal, P. B., Pramesh, D., Mahesh, H. B., and Raj, E. (2021). LAMP-based foldable microdevice platform for the rapid detection of *Magnaporthe oryzae* and *Sarocladium oryzae* in rice seed. *Sci. Rep.* 11:178. doi: 10.1038/s41598-020-80644-z
- Quyen, T. L., Ngo, T. A., Bang, D. D., Madsen, M., and Wolff, A. (2019). Classification of multiple DNA dyes based on inhibition effects on real-time loop-mediated isothermal amplification (LAMP): prospect for point of care setting. *Front. Microbiol.* 10:2234. doi: 10.3389/fmicb.2019.02234
- Ray, M., Ray, A., Dash, S., Mishra, A., Achary, K. G., Nayak, S., et al. (2017). Fungal disease detection in plants: traditional assays, novel diagnostic techniques and biosensors. *Biosens. Bioelectron.* 87, 708–723. doi: 10.1016/j.bios.2016.09.032
- Rigano, L. A., Malamud, F., Orce, I. G., Filippone, M. P., Marano, M. R., Do Amaral, A. M., et al. (2014). Rapid and sensitive detection of *Candidatus Liberibacter asiaticus* by loop mediated isothermal amplification combined

- with a lateral flow dipstick. *BMC Microbiol.* 14:86. doi: 10.1186/1471-2180-14-86
- Rowhani, A., Uyemoto, J. K., Golino, D. A., and Martelli, G. P. (2005). Pathogen testing and certification of *Vitis* and *Prunus* species. *Annu. Rev. Phytopathol.* 43, 261–278. doi: 10.1146/annurev.phyto.43.040204.135919
- Santiago-Felipe, S., Tortajada-Genaro, L. A., Carrascosa, J., Puchades, R., and Maquieira, Á. (2016). Real-time loop-mediated isothermal DNA amplification in compact disc micro-reactors. *Biosens. Bioelectron.* 79, 300–306. doi: 10.1016/j.bios.2015.12.045
- Serfling, A., Kopahnke, D., Habekuss, A., Novakazi, F., and Ordon, F. (2017). “Wheat diseases: an overview,” in *Achieving Sustainable Cultivation of Wheat*. ed. P. Langridge (London: Burleigh Dodds Science Publishing), 263–294.
- Shankar, M., Reeves, K., Bradley, J., Varischetti, R., and Loughman, R. (2021). Effect of varietal resistance on the yield loss function of wheat to nodorum blotch. *Plant Pathol.* 70, 745–759. doi: 10.1111/ppa.13317
- Siah, A., Elbekali, A. Y., Ramdani, A., Torriani, S. F. F., Brunner, P. C., and Halama, P. (2014). QoI resistance and mitochondrial genetic structure of *Zymoseptoria tritici* in Morocco. *Plant Dis.* 98, 1138–1144. doi: 10.1094/PDIS-10-13-1057-RE
- Stehlíková, D., Beran, P., Cohen, S. P., and Curn, V. (2020). Development of real-time and colorimetric loop mediated isothermal amplification assay for detection of *Xanthomonas gardneri*. *Microorganisms* 8:1301. doi: 10.3390/microorganisms8091301
- Tanner, N. A., Zhang, Y., and Evans, T. C. (2012). Simultaneous multiple target detection in real-time loop-mediated isothermal amplification. *BioTechniques* 53, 81–89. doi: 10.2144/0000113902
- Thierry, M., Chatet, A., Fournier, E., Tharreau, D., and Ioos, R. (2020). A PCR, qPCR, and LAMP toolkit for the detection of the wheat blast pathogen in seeds. *Plan. Theory* 9:277. doi: 10.3390/plants9020277
- Thiessen, L. D., Neill, T. M., and Mahaffee, W. F. (2018). Development of a quantitative loop-mediated isothermal amplification assay for the field detection of *Erysiphe necator*. *PeerJ* 6:e4639. doi: 10.7717/peerj.4639
- Tian, S., Wolf, G. A., and Weinert, J. (2005). Accurate assessment of wheat and triticale cultivar resistance to *Septoria tritici* and *Stagonospora nodorum* infection by biotin/avidin ELISA. *Plant Dis.* 89, 1229–1234. doi: 10.1094/PD-89-1229
- Tomita, N., Mori, Y., Kanda, H., and Notomi, T. (2008). Loop-mediated isothermal amplification (LAMP) of gene sequences and simple visual detection of products. *Nat. Protoc.* 3, 877–882. doi: 10.1038/nprot.2008.57
- Tomlinson, J., and Boonham, N. (2008). Potential of LAMP for detection of plant pathogens. *CAB Rev.: Perspect. Agric. Vet. Sci. Nutr. Nat. Resour.* 3:66. doi: 10.1079/PAVSNNR20083066
- Trzmiel, K., and Hasiów-Jaroszewska, B. (2020). Development of loop-mediated isothermal amplification assay for rapid detection of genetically different wheat dwarf virus isolates. *Mol. Biol. Rep.* 47, 8325–8329. doi: 10.1007/s11033-020-05846-0
- Villari, C., Mahaffee, W. F., Mitchell, T. K., Pedley, K. F., Pieck, M. L., and Hand, F. P. (2017). Early detection of airborne inoculum of *Magnaporthe oryzae* in turfgrass fields using a quantitative LAMP assay. *Plant Dis.* 101, 170–177. doi: 10.1094/PDIS-06-16-0834-RE
- Wang, Y., Wang, Y., Lan, R., Xu, H., Ma, A., Li, D., et al. (2015). Multiple endonuclease restriction real-time loop-mediated isothermal amplification: a novel analytically rapid, sensitive, multiplex loop-mediated isothermal amplification detection technique. *J. Mol. Diagn.* 17, 392–401. doi: 10.1016/j.jmoldx.2015.03.002
- Wang, M., Zhang, R., and Li, J. (2020). CRISPR/cas systems redefine nucleic acid detection: principles and methods. *Biosens. Bioelectron.* 165:112430. doi: 10.1016/j.bios.2020.112430
- Ward, E., Foster, S. J., Fraaije, B. A., and McCartney, H. A. (2004). Plant pathogen diagnostics: immunological and nucleic acid-based approaches. *Ann. Appl. Biol.* 145, 1–16. doi: 10.1111/j.1744-7348.2004.tb00354.x
- Wilisiani, F., Tomiyama, A., Katoh, H., Hartono, S., Neriya, Y., Nishigawa, H., et al. (2019). Development of a LAMP assay with a portable device for real-time detection of begomoviruses under field conditions. *J. Virol. Methods* 265, 71–76. doi: 10.1016/j.jviromet.2018.10.005
- Wong, Y. P., Othman, S., Lau, Y. L., Radu, S., and Chee, H. Y. (2018). Loop-mediated isothermal amplification (LAMP): a versatile technique for detection of micro-organisms. *J. Appl. Microbiol.* 124, 626–643. doi: 10.1111/jam.13647
- Xu, H., Xia, A., Wang, D., Zhang, Y., Deng, S., Lu, W., et al. (2020). An ultraportable and versatile point-of-care DNA testing platform. *Sci. Adv.* 6:eaa7445. doi: 10.1126/sciadv.aaz7445
- Xu, M., Ye, W., Zeng, D., Wang, Y., and Zheng, X. (2017). Rapid diagnosis of wheat head blight caused by *Fusarium asiaticum* using a loop-mediated isothermal amplification assay. *Australas. Plant Pathol.* 46, 261–266. doi: 10.1007/s13313-017-0487-y
- Yan, H., Zhang, J., Ma, D., and Yin, J. (2019). QPCR and loop mediated isothermal amplification for rapid detection of *Ustilago tritici*. *PeerJ* 7:e7766. doi: 10.7717/peerj.7766
- Yasuhara-Bell, J., Valent, B., and Stack, J. P. (2018). Specific detection of the wheat blast pathogen (*Magnaporthe oryzae* *Triticum*) by loop-mediated isothermal amplification. *Plant Dis.* 102, 2550–2559. doi: 10.1094/PDIS-03-18-0512-RE
- Zhang, J., Borth, W., Lin, B., Melzer, M., Shen, H., Pu, X., et al. (2018). Multiplex detection of three banana viruses by reverse transcription loop-mediated isothermal amplification (RT-LAMP). *Trop. Plant Pathol.* 43, 543–551. doi: 10.1007/s40858-018-0257-6
- Zhang, Z. Y., Liu, X. J., Li, D. W., Yu, J. L., and Han, C. G. (2011). Rapid detection of wheat yellow mosaic virus by reverse transcription loop-mediated isothermal amplification. *Virol. J.* 8:550. doi: 10.1186/1743-422X-8-550
- Zhang, X., Zhang, H., Pu, J., Qi, Y., Yu, Q., Xie, Y., et al. (2013). Development of a real-time fluorescence loop-mediated isothermal amplification assay for rapid and quantitative detection of *Fusarium oxysporum* f. sp. *cubense* tropical race 4 in soil. *PLoS One* 8:e82841. doi: 10.1371/journal.pone.0082841
- Zhao, W., Chi, Y.-K., Ye, M.-D., Wang, T., Xu, A.-M., and Qi, R.-D. (2021). Development and application of Recombinase polymerase amplification assay for detection of *Bipolaris sorokiniana*. *Crop Prot.* 145:105619. doi: 10.1016/j.cropro.2021.105619
- Zhao, X., Li, M., and Liu, Y. (2019). Microfluidic-based approaches for foodborne pathogen detection. *Microorganisms* 7:381. doi: 10.3390/microorganisms7100381
- Zhou, D., Guo, J., Xu, L., Gao, S., Lin, Q., Wu, Q., et al. (2014). Establishment and application of a loop-mediated isothermal amplification (LAMP) system for detection of cry1Ac transgenic sugarcane. *Sci. Rep.* 4, 1–8. doi: 10.1038/srep04912
- Zhu, Z., Li, R., Zhang, H., Wang, J., Lu, Y., Zhang, D., et al. (2022). PAM-free loop-mediated isothermal amplification coupled with CRISPR/Cas12a cleavage (Cas-PfLAMP) for rapid detection of rice pathogens. *Biosens. Bioelectron.* 204:114076. doi: 10.1016/j.bios.2022.114076

**Conflict of Interest:** The authors declare that the research was conducted in the absence of any commercial or financial relationships that could be construed as a potential conflict of interest.

**Publisher’s Note:** All claims expressed in this article are solely those of the authors and do not necessarily represent those of their affiliated organizations, or those of the publisher, the editors and the reviewers. Any product that may be evaluated in this article, or claim that may be made by its manufacturer, is not guaranteed or endorsed by the publisher.

Copyright © 2022 Gomez-Gutierrez and Goodwin. This is an open-access article distributed under the terms of the Creative Commons Attribution License (CC BY). The use, distribution or reproduction in other forums is permitted, provided the original author(s) and the copyright owner(s) are credited and that the original publication in this journal is cited, in accordance with accepted academic practice. No use, distribution or reproduction is permitted which does not comply with these terms.



# Durability and Moisture Dynamics of Douglas-Fir Wood From Slovenia

Miha Humar\*, Viljem Vek, Primož Oven, Boštjan Lesar, Davor Kržišnik, Eli Keržič, Miha Hočevár and Robert Brus

Biotechnical Faculty, University of Ljubljana, Ljubljana, Slovenia

## OPEN ACCESS

### Edited by:

Roger Deal,  
Emory University, United States

### Reviewed by:

Anna Sandak,  
InnoRenew CoE, Slovenia  
Magdalena Broda,  
Poznan University of Life Sciences,  
Poland

### \*Correspondence:

Miha Humar  
miha.humar@bf.uni-lj.si

### Specialty section:

This article was submitted to  
Technical Advances in Plant Science,  
a section of the journal  
Frontiers in Plant Science

**Received:** 23 January 2022

**Accepted:** 10 March 2022

**Published:** 29 March 2022

### Citation:

Humar M, Vek V, Oven P, Lesar B, Kržišnik D, Keržič E, Hočevár M and Brus R (2022) Durability and Moisture Dynamics of Douglas-Fir Wood From Slovenia.  
Front. Plant Sci. 13:860734.  
doi: 10.3389/fpls.2022.860734

Wood in outdoor applications is subject to various decomposition factors. Wood degradation can be prevented by construction details, biocide protection of wood, wood modification or selection of naturally durable species. Unfortunately, most species in Europe do not have naturally durable wood. Imported tree species represent a new pool from which we can draw wood species with better natural durability and better resilience towards climate change. The performance of wood when used outdoors depends on the biologically active compounds (extractives) and the water exclusion efficacy. Considering decay, presence of biologically active compounds and water exclusion efficacy, we can estimate the density, modulus of elasticity, extractive content and resistance dose, which reflects the material properties of wood. Recently, the most commonly used model for this purpose is Meyer-Veltrup. Literature data indicate that the durability of the wood from native and new sites is not always comparable, so it is necessary to determine the resistance of non-native wood species from new sites. This paper presents original data on the wood's overall durability from American Douglas fir (*Pseudotsuga menziesii*) grown in Slovenia. Experimental data show that the mature heartwood of Douglas fir is more durable than the wood of European larch (*Larix decidua*). Durability can be attributed to good water exclusion efficacy and inherent durability. Inherent durability is primarily the result of the high content of extractives. Based on the results, it can be concluded that American Douglas fir grown in Central Europe has a high potential for outdoor use.

**Keywords:** wood, natural durability, wood decay, water exclusion efficacy, extractives

## INTRODUCTION

The climate is changing. Measurements show a trend towards rising air temperatures. Finally, the last ten years are among the warmest years in terms of weather observation in Slovenia and other central European countries. Moreover, we are experiencing increasingly intense extreme weather events (hail, storms and others; Oblak et al., 2021). We can likely expect even stronger and more pronounced climate change in the future (Bevacqua et al., 2021).

Climate change is already affecting the forest species composition and wood quality (Gričar et al., 2015). Increasingly higher temperatures and a changing precipitation regime are expected to affect tree species' distribution in these forests significantly. Assuming limited migration, most European species would significantly decline suitable habitat areas. Most biome shifts focus on ecological issues, as changes in dominant tree species will also lead to changes in



entire ecosystems and dependent organisms (Dyderski et al., 2018). Generally accepted models suggest that depending on the climate scenario, only the Mediterranean type of low-value oak forest will thrive on 21–60% (average 34%) of European forest area by 2,100. This will result in lower yields for forest owners and a shortage of raw material for the timber industry (Hanewinkel et al., 2013). In addition, it must be considered that CO<sub>2</sub> sequestration in such modified forests will also be reduced (Birdsey and Pan, 2015). Models showed that *Abies alba*, *Fagus sylvatica*, *Fraxinus excelsior*, *Quercus robur*, *Quercus petraea* and the non-native species *Pseudotsuga menziesii*, *Quercus rubra* and *Robinia pseudoacacia* could be considered climate winners (Dyderski et al., 2018).

Based on the data presented, one viable solution to improving the economic perspective of forest owners and related wood processing industries is the controlled introduction of non-native tree species such as Douglas fir (Eberhard et al., 2021) in Central Europe. The future use of these tree species must also be of long-term interest to the forest owner. The economic impact is primarily based on the relevant properties and the associated price of the forest assortments on the market. Most of the Slovenian wood processing industry is based on softwoods. Softwoods are of crucial importance for timber construction (roofs, skeletal structures, glue-laminated beams and cross-laminated timber) and the composite industry (particleboard and shuttering panels; Ansell, 2015). Today, the wood used for these purposes in Slovenia are mainly Norway spruce (*Picea abies*) and silver fir (*Abies alba*). However, their share in Slovenian forests decreases (Klopčič et al., 2017). Therefore, it is crucial to identify the relevant properties of a suitable wood species that could partially replace Norway spruce in the applications mentioned above. Douglas fir (*Pseudotsuga menziesii*) was defined as a potential candidate among different wood species. Douglas fir is already present in Europe and covers about 830,000 ha of forest area in Europe alone (Pötzelsberger et al., 2020; Eberhard et al., 2021). These tree species offer high productivity rates and thus ensure sustainable income for forest owners (Eilmann and Rigling, 2012).

The first documented introduction of a considerable number of non-native tree species on the territory of present-day Slovenia occurred in the late 18th and early 19th centuries. Initially, the species were planted in specialised plant collections, and the frequency of their planting was low. At the end of the 19th century, the planting frequency of some species increased, and several species were also introduced into forests (Brus and Gajšek, 2014). Most Douglas-fir plantations in Slovenia were established in the periods 1880–1940 and 1960–1990 in various parts of the country (Veselič et al., 2016). Douglas fir is currently the third most common non-native tree species, accounting for 0.05% (171,000 m<sup>3</sup>) of the total growing stock in Slovenian forests. It has clearly shown good adaptability under challenging conditions, e.g., resistance to ice storms, drought and bark beetle infestation in areas where Norway spruce was severely affected, as well as good growth performance. For this reason, Douglas fir has currently considered the most promising non-native tree species in Slovenian forests (Smolnikar et al., 2021).

The European standard EN 350 (CEN, 2016) clearly distinguishes the durability of Douglas fir from North America from Douglas fir growing in Europe. The durability of Douglas fir from North America is 3 (moderately durable), while the durability of Douglas fir grown in Europe has a higher variation of 3–4 (slightly to moderately durable). Douglas-fir wood is generally characterised as the species with one of the best ratios between growth rates and quality (Perić et al., 2011). The wood properties are determined by numerous factors: site conditions, provenance, forest management and location in the tree (Pollet et al., 2017; Balanzategui et al., 2021; Golob et al., 2021). Therefore, the properties of Douglas fir from North America are not comparable to those of Douglas fir from Europe (Blohm et al., 2014). The excellent reputation of Douglas-fir wood is due to the exceptional quality of wood from old-growth forests in north-western North America, which are characterised by slow growth rates (Gartner et al., 1999). However, the characteristics of wood from more dynamically growing second-growth forests in Europe may be different. European forest owners frequently bring smaller logs to market with a higher proportion of juvenile wood (Vikram et al., 2011). The higher proportion of juvenile wood could be problematic, as this wood has less favourable mechanical properties than mature wood (Pollet et al., 2017). On the other hand, faster growth might also result in different durability, as the growth reflects in the anatomy-related water performance and presence of biologically active secondary metabolites.

Wood is the biochemical product of living trees, which consists of basic building elements, i.e., cellulose, hemicelluloses and lignin, representing approx. 95% of the wood (Holmbom et al., 2008). Wood also contains smaller amounts of non-structural compounds, known also as extractives (Vek et al., 2020). Extractives include a large variety of compounds that can be removed from the wood tissue by relatively simple extraction methods. Although the amount of extractives in most of the wood species is relatively low, these non-structural components are reported to possess antifungal, antimicrobial and antioxidant properties (Lu et al., 2016; Belt et al., 2017; Valette et al., 2017). Phenolic extractives that increase the wood durability are biosynthesised *de novo* at the boundary between sapwood and heartwood (Magel et al., 1994; Dellus et al., 1997; Kebbi-Benkeder et al., 2017). Taxifolin and dihydrokaempferol are reported as such compounds for wood of Douglas fir (Dellus et al., 1997). It is known that the amounts of extractives in the wood of all trees, as well of Douglas fir vary (Adamopoulos et al., 2005; Vek et al., 2020). Specific woody tissues contain more extractives than others, e.g., the wood of dead branches embedded in a stem (wood of knots) is one of the richest sources of polyphenols in nature (Willför et al., 2004). The literature reviews on the chemical composition of extractives of Douglas fir shows that sapwood, heartwood, knotwood and bark have already been investigated (Willför et al., 2003; Miranda et al., 2021). Flavonoids, lignans and oligomeric polyphenols were the main phenolic compounds in wood extracts of Douglas fir (Lindberg et al., 2004; Brennan et al., 2021). Oleson and Schwartz (2016) have categorised proanthocyanidins, phlobaphenes, flavonoids, waxes, terpenoids, phytosterols and

lignans as the most abundant non-carbohydrate extractives in the wood and bark of Douglas fir. This review also shows that heartwood contains higher amounts of proanthocyanidins and flavonoids than sapwood. On the other hand, Douglas-fir sapwood and heartwood were reported to contain comparable amounts of waxes, terpenoids and phytosterols (Dellus et al., 1997; Oleson and Schwartz, 2016). In comparison with heartwood, extraction of sapwood with a mixture of acetone and water yield higher amounts of flavonoid glycosides and procyanidins (Dellus et al., 1997). The two goals of our chemical analysis were first to complement the existing literature data and to investigate the chemical composition of phenolic extractives in Douglas-fir heartwood samples of different ages, and then to study the possible correlation between the results of chemical analysis and the results of fungal testing.

The purpose of the respective document is to present information about material resistance and moisture dynamics of Douglas fir from Slovenian forests. This information is of great importance for assessing the suitability of the selected wood species in outdoor applications.

## MATERIALS AND METHODS

### Materials

In the area of Planina (45.818785 and 14.240381) and Celje (46.193462 and 15.269257), we cut three specimens per location (six trees in total) of Douglas fir (PsMe; *Pseudotsuga menziesii*). In both locations, coastal Douglas-fir (*P. menziesii* var. *menziesii*) provenances from Washington and Oregon were planted. Exact origin of seeds is not known. Recent genetic survey (Kraigher et al., 2021) revealed slightly lower genetic variation in these populations when compared to genetic variation in species' native range but no significant differences between Planina and Celje. The trees in the respective locations were selected randomly. The trees were of comparable size, dimension and age on the location. They were representative ones of the assessed population. The breast diameter of the trees used ranged from 40 to 45 cm, and all trees were about 70 years old. Locations Planina and Celje were selected as they are among largest and most typical areas of high-quality Douglas-fir stands in the country. In addition, Douglas-fir stands in Planina have shown good resistance to ice storms, drought and bark beetle infestation in comparison with Norway spruce, and stands in Celje have shown excellent growth performance. The trees in Planina grew in a mixed Norway spruce-Douglas-fir plantation established on a beech-fir site on the limestone at an elevation of 560 m. In contrast, the trees near Celje grew in a mixed conifer forest composed of Norway spruce (60%), Douglas-fir (23%), silver fir (6%) and common beech (3%) on the limestone at an elevation of 620 m. There is no difference in silviculture measures as group shelterwood silvicultural system is used in both forests.

We used the lower part (4 m height) of the logs and sawed them on a horizontal sawing machine into prisms suitable for further analysis. The following part of the log was considered for the analysis: sapwood (SW), mature heartwood (MW) and

juvenile heartwood (JW) of the Douglas-fir samples. Samples have full traceability. Each tree was analysed separately. However, as there were no considerable differences between the trees the data were merged on the location level. For comparison, we analysed the wood of Norway spruce (PiAb; *Picea abies*), Scots pine (PiSy; *Pinus sylvestris*) and European larch (LaDe; *Larix decidua*) from the same part of Slovenia as well. The wood originates from multiple trees as well.

### The Density and Modulus of Elasticity

The density of samples conditioned at standard laboratory climate [20°C; 65% RH (Relative Humidity)] was determined from the mass and dimensions of the samples measured with a digital calliper. The experiment was performed in 10 parallels. The modulus of elasticity (MoE) was determined according to the EN 310 (CEN, 1993) procedure with a static three-point bending test on a Zwick Z005 universal testing machine (Zwick-Roell). Samples (ten parallel samples for each tissue/tree) with dimensions  $65_A \text{ mm} \times 25_T \text{ mm} \times 5_R \text{ mm}$  were prepared and conditioned in a standard climate. Only MoE was determined, as the samples were consequently used to evaluate the terrestrial microcosms durability.

### Dynamic Vapour Sorption Analysis

The sorption isotherms of sapwood (SW), mature (HW) and juvenile heartwood (JW) of Douglas-fir samples were performed using a gravimetric dynamic sorption analyser (DVS Intrinsic, Surface Measurement Systems Ltd., London, United Kingdom). The milled samples were conditioned at  $20 \pm 0.2^\circ\text{C}$  and  $1 \pm 1\%$  RH for at least 24 h before the experiment. For analysis, a small amount (approximately 400 mg) of the sample was placed on the sample holder and suspended in a microbalance within a sealed, thermostatically controlled chamber in which a constant flow of dry compressed air was passed over the sample at a flow rate of  $200 \text{ cm}^3/\text{s}$  and a temperature of  $25 \pm 0.1^\circ\text{C}$  throughout the RH range. The DVS method was set to 20 steps of 5% between 0 and 95% RH for the sorption and desorption steps. Two total isothermal runs were performed to capture the sorption behaviour of the material fully; however, only one cycle is presented in the respective study. The instrument held the target RH constant until the rate of change in sample moisture content ( $\text{dm}/\text{dt}$ ) was less than 0.002% per minute for 10 min. The run time, target RH, actual RH and sample weight was recorded every 20 s throughout the isothermal run. Adsorption and desorption isotherms were constructed by plotting the change in equilibrium moisture content (EMC) against relative humidity (RH).

### SEM Microscopy

Scanning electron microscopy (SEM) was performed to reveal detailed anatomical features of the three-dimensional structure of the wood. Samples were cut into  $1 \text{ cm}^3$  cube, ensuring that they were oriented in all three anatomical planes. The surfaces were planed using a sliding microtome equipped with a new disposable blade. Samples were dried above silica gel and in a vacuum and coated with gold (Q150R ES Coating System

Quorum technologies, Laughton, United Kingdom) for 30 s at 20 mA intensity. SEM micrographs were then taken at high vacuum and low voltage (between 5 and 12.5 kV). A large field detector (LFD) and a concentric backscatter detector (CBS) were used in an FEI Quanta 250 SEM microscope (Hillsboro, Oregon, United States). Observations were made at a working distance between 8 and 11 mm.

## Analysis of Extractives

Wood extractives of Douglas fir were chemically investigated according to the methodology as already described (Singleton et al., 1965; Willför et al., 2004; Vek et al., 2019). Briefly, samples for chemical analysis were obtained from the same part of the wood as for the durability experiments. More sample discs were taken from each harvested tree of Douglas fir. One sample of sapwood and two heartwood samples, i.e., mature and juvenile heartwood, were pulled out from the stem discs using a band saw and chisel. The samples were then oven-dried (60°C, 24 h) and ground on a cutting mill Retsch SM2000 using a 1 mm sieve. Obtained wood fractions were then freeze-dried and extracted in Thermo Scientific ASE 350 system for speed extraction. Samples were extracted successively with cyclohexane and 95% acetone (v/v, aq) at 90°C and 100°C, respectively, and 10.34 MPa with two 5 min static cycles. Acetone has been demonstrated as a strong and 'cheap' solvent for extracting low-molecular-weight phenolic compounds from the wood of trees (Willför et al., 2006). The content of lipophilic and hydrophilic extractives was measured gravimetrically by oven drying 10 ml of an extract to constant mass. Total phenolic compounds in extracts were measured colourimetrically with Perkin Elmer Lambda UV-Vis spectrophotometer (Singleton et al., 1965; Vek et al., 2019). The Folin-Ciocalteu phenol reagent and sodium carbonate water solution were added to Douglas fir's wood extracts. After incubation, the absorbance was measured at 765 nm. Solutions of gallic acid were used for calibration. The method for semi-quantitative analysis of total phenols in the extracts was linear for a selected concentration range ( $R^2 > 0.99$ ). A Thermo Scientific Accela HPLC system equipped with a PDA detector performed identifying and quantifying individual phenolic compounds in the wood extracts. Phenolic compounds were separated on the Thermo Accucore ODS column, and methanol and water with 0.1% formic acid were used as a mobile phase. Phenolic extractives were eluted out of the column, applying a linear gradient from 5 to 95% of methanol in 20 min. The eluted compounds were detected at 280 nm, and spectra were recorded from 200 to 400 nm. Identification of phenolic extractives was made utilising external analytical standards. The HPLC method for quantitative evaluation was linear ( $R^2 > 0.99$ ). The analytical standards, i.e., catechin, epicatechin, homovanillic acid, coumaric acid, taxifolin, secoisolariciresinol, pinoresinol and matairesinol, were of an HPLC purity, and they were all purchased from Sigma Aldrich. Each sample was injected into the column three times. All the results were expressed as milligrams of extractives per gram of dry material (mg/g, dw). The results were analysed with basic statistical analysis using Statgraphics software.

ANOVA and Fisher's least significant difference (LSD) procedure at a 95.0% confidence level were performed.

## Performance Against Blue Staining and Moulding

Samples of sapwood (SW) and mature heartwood (HW) of Douglas fir were exposed to blue-stain fungi according to EN 152 (CEN, 2012b) and fungi in condensing environments AWPA E24-12 (AWPA, 2015). Juvenile wood was not exposed due to a lack of material. The laboratory blue-stain test was conducted with the blue-stain fungi *Aureobasidium pullulans* (de Bary and Löwenthal) G. Arnaud strain ZIM L060 and *Sydowia polyspora* (Bref. and Tavel) E. Müll. strain ZIM L070. Both strains were obtained from the Collection of wood decay fungi from the Department of Wood Science and Technology (Biotechnical Faculty, Ljubljana, Slovenia; Raspor et al., 1995). Before inoculation, wood samples were sterilised in an autoclave with hot steam at 121°C and 150 kPa for 15 min. Later, the sterilised samples were immersed in a spore suspension and placed horizontally in a Kolle flask inoculated with 15 ml of spore suspension. The flasks were then stored in an incubation chamber at 25°C and 85% RH for 6 weeks. After this time, the samples were visually evaluated and ranked from 0 to 3 according to the ranking system prescribed in EN 152 (rank 0 = not blue-stained; 1 = small spots less than 2 mm; 2 = blue-stained up to one-third of the surface; and 3 = intensely blue-stained). Only the uppermost side was evaluated for the colour measurements.

The parallel samples were exposed to the condensing environment in the chamber. The main objective of this standard was to evaluate the resistance of the surface of wood samples to mould growth. The samples were exposed above water in the climatic chamber, which contained soil and a shelf for the test samples, with an inclined roof preventing condensation deposition on the samples. The growth of fungi on the wood samples was evaluated weekly. To allow comparison, the assessment followed the recommendations of the modified Johansson protocol (Johansson et al., 2012). Surface mould was evaluated using a 0 to 4 rating scale as follows:

- 0 = not blue-stained;
- 1 = weakly blue-stained: few spots of blue stain on the surface;
- 2 = slightly blue-stained: up to 1.5 mm wide and 4 mm long;
- 3 = moderately blue-stained: up to one-third of the surface; and
- 4 = severely blue-stained.

## Determination of Factors Describing Inherent Durability ( $k_{inh}$ )

Agar block tests with pure fungal cultures were used to evaluate inherent durability. A decay test was performed according to a modified CEN/TS 15083-1 procedure (CEN, 2005a). Samples ( $1.5 \times 2.5 \times 5.0$  cm<sup>3</sup>) were conditioned in a standard laboratory climate ( $T = 25 \pm 1^\circ\text{C}$ ;  $RH = 65 \pm 2\%$ ) and steam-sterilised in an autoclave before incubation with decay fungi. A 350 ml experimental jars with aluminium lids and cotton wool with 50 ml potato dextrose agar (DIFCO, Fisher Scientific, Franklin Lakes, NJ, United States) were prepared and inoculated with



the white-rot fungus *Trametes versicolor* (L.) Lloyd (ZIM L057) and two brown-rot fungi, *Gloeophyllum trabeum* (Pers.) Murrill (ZIM L018) and *Fibroporia vaillantii* (DC.) Parmasto (ZIM L037). The fungal isolates came from the fungal Collection of the Biotechnical Faculty of the University of Ljubljana and are available on request for research institutions (Raspor et al., 1995). One week after inoculation, two random samples per jar were positioned on high-density polyethylene (HDPE) plastic mesh to avoid direct contact between the samples and the medium. The assembled test jars were then incubated at 25°C and 85% relative humidity (RH) for 16 weeks as required by the standard. After incubation, samples were cleaned of adhering fungal mycelium, weighed to the nearest 0.0001 g, oven-dried at 103 ± 2°C and weighed again to the nearest 0.0001 g to determine mass loss due to wood-destroying basidiomycetes. Five replicate samples for each of the selected materials/wood species were used for this test.

In addition to agar block tests, resistance to soft-rot micro-fungi and bacteria was determined according to CEN/TS 15083–2 (CEN, 2005b). Ten replicate samples (5 mm × 10 mm × 100 mm) from each wood tissue and additional reference samples from Norway spruce were exposed to terrestrial microcosms. Samples were buried to 4/5 of their length in containers filled with non-sterile compost soil (origin: Ribnica, Slovenia) and stored at 27 ± 2°C and 70 ± 5% RH. The soil was used at 95% of its water holding capacity. The samples were exposed for 32 weeks. After exposure, samples were cleaned of adherent soil particles and mycelium, weighed to the nearest 0.0001 g, oven-dried at 103 ± 2°C for 24 h and weighed to the nearest 0.0001 g to calculate the mass loss. Afterwards, the samples' modulus of elasticity (MoE) was determined using a three-point bending test according to EN 310 (CEN, 1993) before and after exposure to non-sterile soil. The MoE loss of the samples was calculated as a percentage of their initial values.

## Determination of Factors Describing Wettability ( $k_{wa}$ )

A series of laboratory tests were performed to evaluate wettability. Tests were performed on five replicate samples (1.5 × 2.5 × 5.0 cm<sup>3</sup>) of each material. One set of samples was used for sorption tests and the other for various immersion tests. The average relative values of the different tests were combined to calculate the wettability factor as described by Meyer-Veltrup et al. (2017).

Short-term capillary water uptake was carried out at 20°C and 50 ± 5% RH, on a K100MK2 Tensiometer device (Krüss, Hamburg, Germany) according to a modified EN 1609 (CEN, 2013) standard after samples were conditioned to constant mass at 20°C and 65% RH. The axial surfaces of the samples were positioned so that they were in contact with the test liquid (distilled water), and their masses were then measured continuously every 2 s for up to 200 s. Other parameters used were as: speed before contact with the water 6 mm/min, the sensitivity of the contact 0.005 g and the immersion depth 1 mm. The water uptake was calculated in g/cm<sup>2</sup> based on the final mass change of the immersed sample and the surface in contact with water.

Long-term water uptake was based on the leaching method ENV 1250–2 (CEN, 2004). Before testing, samples were oven-dried to constant mass at 60 ± 2°C and weighed to determine oven-dried mass. The dry wood blocks were placed in a jar and weighed to prevent floating. Then, 100 g of distilled water was added per sample. The mass of the samples was determined after 24 h, and the MC of five replicate samples was calculated. MC was determined gravimetrically as the ratio between the retained water and the oven-dried mass of the samples.

To determine the sorption properties of the samples, a water vapour uptake test was performed in a water-saturated atmosphere with a drying process over freshly activated silica gel. The samples were oven-dried at 60 ± 2°C to constant mass and weighed. The samples were stacked in a glass climate chamber with a fan over distilled water. The samples were positioned on mesh above the water with thin spacers (Meyer-Veltrup et al., 2017). After 24 h of exposure, they were weighed again, and the MC was calculated. The samples were then left in the same chamber for an additional 3 weeks until a constant mass was reached. In addition to wetting, outdoor performance is also influenced by drying. After the 3 weeks of conditioning, moist samples were positioned in a closed container over freshly activated silica gel for 24 h. The MC of the samples was calculated according to the procedure described by Meyer-Veltrup et al. (2017). Five replicate samples were used for this analysis.

## Factor Approach for Quantifying the Resistance Dose $D_{Rd}$

A modelling approach based on Isaksson et al. (2014) and Meyer-Veltrup et al. (2017) was applied to predict the field performance of the examined materials. The model describes the climatic exposure and the resistance of the material. The acceptability of the chosen design and material is expressed as follows:

$$\text{Exposure} \leq \text{Resistance} \quad (1)$$

The exposure can be expressed as exposure dose ( $D_{Ed}$ ), determined by daily temperatures and MC. Material property is expressed as resistance dose ( $D_{Rd}$ ) in days (d), with optimal wood MC and wood temperature conditions for fungal decay (Isaksson et al., 2013):

$$D_{Ed} \leq D_{Rd} \quad (2)$$

Where  $D_{Ed}$  is the exposure dose (d), and  $D_{Rd}$  is the resistance dose (d).

The exposure dose  $D_{Ed}$  depends on the annual dose at a given geographic location. Several factors describe the effect of driving rain, local climate, sheltering, distance from the ground and detailed design. Isaksson et al. (2014) describe the development of the corresponding exposure model in detail. The present study focused on the counterpart of the exposure dose, namely, the resistance, expressed as the resistance dose  $D_{Rd}$ , which is considered the product of the critical dose  $D_{crit}$  and two factors expressing the wettability of the wood ( $k_{wa}$ )



and its inherent durability ( $k_{inh}$ ). The approach is given by Equation (3) according to Isaksson et al. (2014; **Table 1**):

$$D_{Rd} = D_{crit} \times k_{wa} \times k_{inh} \quad (3)$$

Where  $D_{crit}$  is the critical dose corresponding to decay rating 1 (slight decay), according to EN 252 (CEN, 2012a),  $k_{wa}$  is a factor that considers the wettability of the tested materials [–], relative to the reference Norway spruce and  $k_{inh}$  is a factor that considers the inherent protective properties of the tested materials against decay [–], relative to the reference Norway spruce. Namely, the wettability and inherent durability of the Norway spruce were set to 1. Materials for which one of these values is better than that determined for Norway spruce have higher values overall but are limited to a value of 5.

Based on the results of the various moisture tests presented in this paper, the factor  $k_{wa}$  for wettability was calculated. The methodology for calculating  $k_{wa}$  followed that of the Meyer-Veltrup et al. (2017), except that the size of the samples differed. The original model prescribed samples (5 mm × 10 mm × 100 mm) that had a different shape than those used in the present study (15 mm × 25 mm × 50 mm). Since the methodology is based on relative values, the sample size has a minor influence on the results. The results of the durability tests were used to evaluate the inherent resistance factor  $k_{inh}$ , and both factors were used to determine the resistance dose  $D_{Rd}$  of the wood materials investigated in this study.

## RESULTS AND DISCUSSION

The anatomy of Douglas-fir wood is typical of conifers, with a sharp transition from early- to latewood. Resin canals with thick-walled epithelial cells are present (Wagenfuhr, 2007; Balanzategui et al., 2021; **Figure 1**). Annual ring widths varied from 1 cm in the juvenile wood to 1 mm in mature heartwood and in sapwood (**Figure 2**). Growth in the early years was fast compared to other softwoods growing in the region but comparable to growth rates of Douglas fir from other regions of Europe. In Belgium, for example the mean annual ring width varied from 3 mm to 8 mm (Pollet et al., 2017).

Significant differences in growth rates are also reflected in density. Densities of Douglas fir from Celje were lower than

densities from Planina. The lowest density was measured in juvenile wood, which is consistent with the distribution of annual rings. The lowest density was determined by Celje's Douglas-fir tree (342 kg/m<sup>3</sup>) with the broadest annual rings. The average density of Douglas-fir juvenile wood from Celje was 384 kg/m<sup>3</sup>, while the density of juvenile wood from Planina was slightly higher (527 kg/m<sup>3</sup>). The densities of juvenile wood are consistent with the literature data (Pollet et al., 2017). On the other hand, the density of mature wood was slightly higher, varying between 516 kg/m<sup>3</sup> (Celje) and 568 kg/m<sup>3</sup> (Planina). These values are also consistent with reference data for Douglas-fir wood (Wagenfuhr, 2007; Poletti et al., 2019). The density of Douglas fir is slightly higher than the average density of Norway spruce from Slovenia (457 kg/m<sup>3</sup>) and comparable to the density of Scots pine (578 kg/m<sup>3</sup>; **Figure 3**). The density and annual ring width are reflected in the MoE. Juvenile wood from Celje had the lowest MoE (6,766 MPa). In contrast, much higher values were obtained for mature wood and sapwood. The highest values were obtained for sapwood from Planina (14,724 MPa). The MoEs of mature heartwood from Planina (12,577 MPa) and Celje (11,882 MPa) are comparable to that measured on Norway spruce (12,024 MPa). The modulus of elasticity of mature Douglas-fir wood from Slovenia is comparable to the mechanical properties of Douglas-fir wood from Netherlands (Polman and Militz, 1996).

The amounts of extractives in the wood samples were measured to be 2.05% (SD=0.42) for sapwood (SW), 3.49% (SD=0.56) for mature heartwood (MW), and 2.48% (SD=1.63) for juvenile heartwood (JW). Statistical analysis revealed that MW samples' extraction gave significantly larger extractives than SW samples (LSD test). The content of measured lipophilic extractives was low, and the differences among the samples were not statistically different (ANOVA,  $p > 0.05$ ; **Figure 4**). It was found that MW samples contain significantly larger amounts of hydrophilic extractives and total phenolic extractives than SW samples (LSD test; **Figure 4**). Even though the numbers were higher for the MW samples, significant differences in the content of hydrophilic extractives between MW and JW samples were not statistically confirmed (LSD test; **Figure 4**). The content of phenolic extractives in SW, MW and JW samples was measured to be 0.53% (SD=0.09), 1.62% (SD=0.43) and 1.03% (SD=0.54). The differences in the contents of total phenols among SW, MW and JW samples were statistically significant (ANOVA,  $p < 0.01$ ). These results correspond to the estimates for amounts of flavonoids present in sapwood and heartwood of Douglas fir, i.e., 0.5 and 2% of the oven-dried mass, respectively (Oleson and Schwartz, 2016). The HPLC analysis confirmed presence of catechin ( $t_r=6.5$  min), epicatechin ( $t_r=8.0$  min), homovanillic acid ( $t_r=8.2$  min), coumaric acid ( $t_r=9.5$  min), taxifolin ( $t_r=9.6$  min), ferulic acid ( $t_r=10.0$  min), secoisolariciresinol ( $t_r=11.7$  min), pinoresinol ( $t_r=12.5$  min) and matairesinol ( $t_r=13.0$  min; **Figure 5**). These compounds have already been reported to be present in stem wood and knotwood of Douglas fir (Willför et al., 2003; Lindberg et al., 2004; Oleson and Schwartz, 2016). Isolariciresinol, lariciresinol and nortrachelogenin have also been reported to be present in smaller amounts in wood extracts of Douglas fir (Willför et al., 2003; Brennan et al., 2021).

**TABLE 1** | Description of key terms addressed in respective article.

Term	Description
$k_{wa}$	Factor describing the wetting ability of wood-based materials. The factor is expressed in relative values relative to the wetting ability of the spruce
$k_{inh}$	Factor describing the inherent durability of wood-based materials. The factor is expressed in relative values relative to the inherent durability of the spruce
$D_{Rd}$	Resistance dose reflects the material property and is expressed in days (d), with optimum wood MC and wood temperature conditions for fungal decay, before the first evidence of decay
Rel. $D_{Rd}$	Relative resistance dose. Usually, spruce is used as the normalisation factor

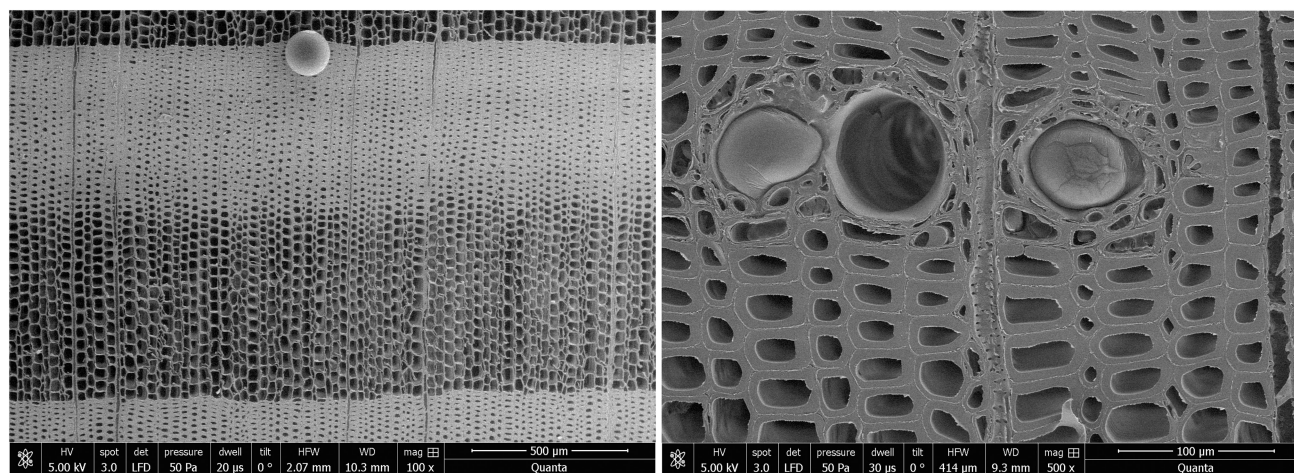


**FIGURE 1** | Annual ring of Douglas-fir mature heartwood (left) and resin canal in sapwood (right).

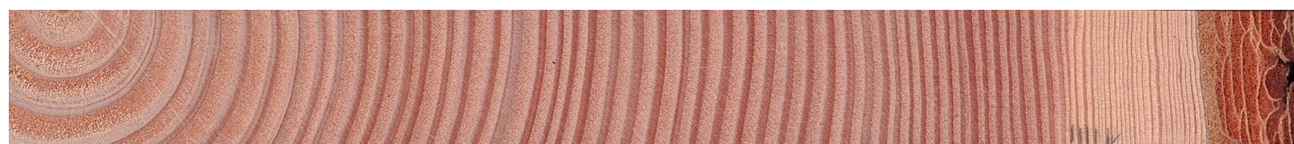
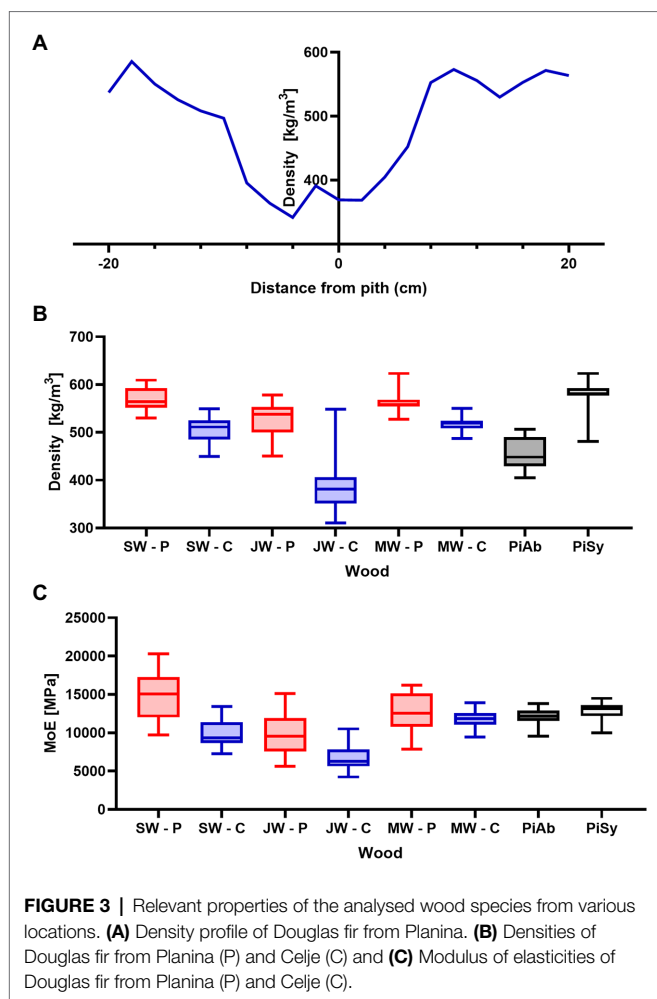


**FIGURE 2** | Cross-section of Douglas fir from Planina.

The chemical composition of extractives presents in bark and knotwood of Douglas fir have already been comprehensively investigated (Miranda et al., 2021). However, there is hard to find exact information on individual phenolic compounds present separately in sapwood and heartwood (Dellus et al., 1997). Literature data on differences in the composition of extractives between mature and juvenile heartwood are completely missing. The measured quantities of the identified compounds are presented in **Table 2**. Taxifolin was found and confirmed as the most abundant compound present in the wood extracts of Douglas fir (**Figure 5**). The differences in the content of taxifolin among the sapwood and heartwood samples were statistically significant (ANOVA,  $p < 0.05$ ; **Table 3**). The highest amounts of taxifolin gave the extraction of MW. The lowest amounts were measured in SW samples (LSD test) (**Figure 5**). The coumaric acid and especially ferulic acid were found to be characteristic for sapwood samples. These two simple phenolic acids were reported to be characteristic also for the resin of Douglas fir (Holmbom et al., 2008; **Figure 5**). Extraction of sapwood and heartwood samples gained somehow comparable amounts of lignans secoisolariciresinol and pinoresinol with no significant differences in the contents among the samples (ANOVA,  $p > 0.05$ , LSD test). Matairesinol was measured in the wood extracts in traces (**Table 2**). As well, catechin, epicatechin and homovanillic acid were present in the wood extracts of Douglas fir in traces (**Table 3**). Wood and bark extracts of Douglas fir are known to have antimicrobial properties

(Lindberg et al., 2004; Välimaa et al., 2007). Acetone extractives of Douglas-fir knotwood were also demonstrated to possess a high antioxidative potency and radical scavenging capacity (Willför et al., 2003). In the frames of the study, taxifolin was found as a phenolic compound with high antioxidative potency and radical scavenging capacity (Willför et al., 2003). Taxifolin is also reported as a *de novo* synthesised compound of Douglas-fir heartwood that increases wood durability (Dellus et al., 1997). Higher resistance of the mature heartwood of Douglas fir to the fungal decay (**Table 4**) could be therefore explained by higher amounts of phenolic extractives and taxifolin in these tissues.

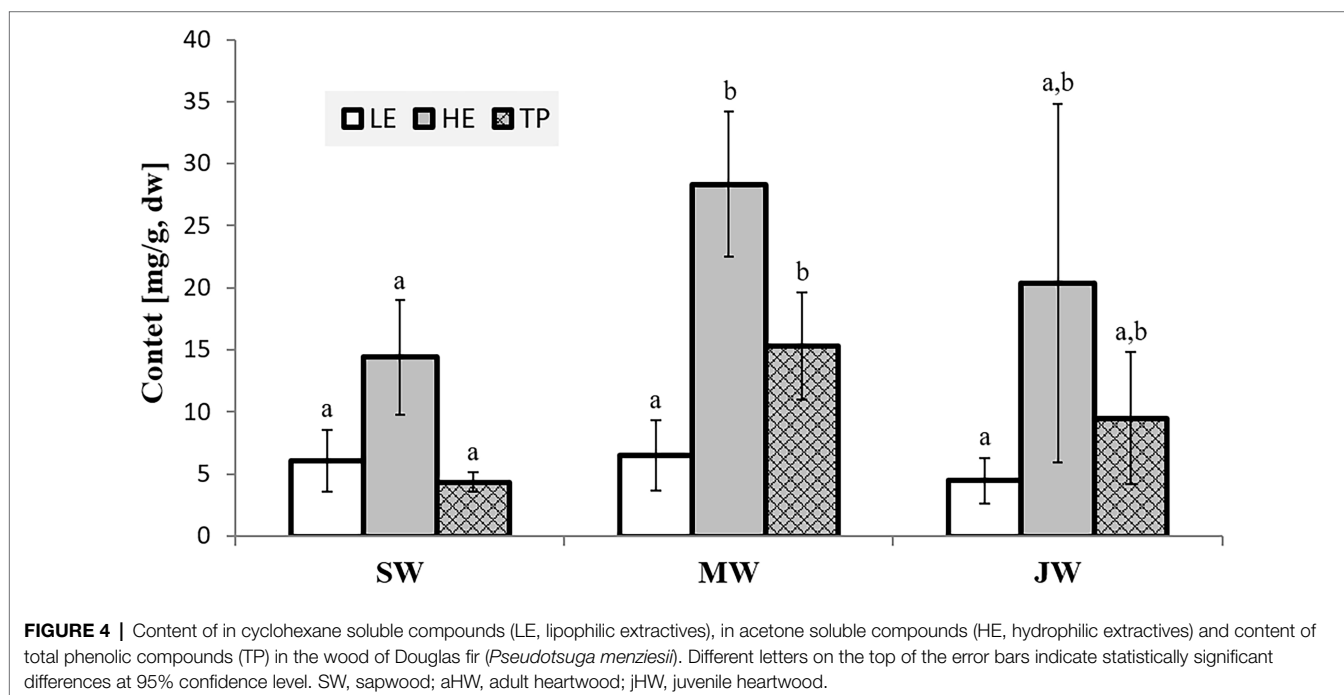
The relative humidity is an important factor affecting the properties and performance of wood. When RH is high, wood absorbs water vapour from the air. The importance of air humidity increases when the air temperature is below or near the dew point. The relationship between wood MC and RH is shown in **Figure 6**. Wood MC increases with increasing RH. Since there was no significant difference between the Douglas-fir from Celje and Planina, only the results from Planina are shown. The surfaces of the tested wood samples are more polar than water molecules and therefore show increased water absorption at low relative humidities (0–10%). Once a single (mono-)layer of water is formed, the additional adsorption increasingly resembles the condensation of water. At high humidities, i.e., above 70%, adsorption is enhanced by tiny surface pores (mesopores with pore diameter 2 nm–50 nm). These attract water molecules on more than one



side, i.e., capillary condensation. This leads to hysteresis in this humidity region caused by the reluctant release of adsorbed water (Mangel, 2000). There is no significant difference between juvenile and mature heartwood's sorption and desorption curves. On the other hand, the moisture content of sapwood is higher. For example, the MC of heartwood at 95% RH ranged from 19.36 (juvenile heartwood) to 19.83 (mature heartwood). The moisture content of the sapwood was significantly higher (21.93%; **Figure 6**). This is consistent with the data in the literature (Jankowska et al., 2016). Chemical analysis shows that sapwood contains significantly fewer extractives than heartwood (**Figure 4**). Generally, wood species with higher extractives content have lower equilibrium moisture content (Hernández, 2007).

We determined the MC of wood exposed above the saturated water atmosphere for modelling purposes after 24 h of conditioning. The RH above saturated water ranges between 98 and 100%. This value reflects the ability of the wood to absorb water from the air. The reference Norway spruce wood absorbs 16.8% of the oven-dry mass in 24 h. On the other hand, a difference was found between the wood from Celje and Planina. On average, the MC of wood exposed above the water for 24 h from Planina is significantly lower than the MC of wood from Celje. For example, the MC of mature heartwood from Planina was 12.5%. In contrast, the MC of mature heartwood from Celje was comparable to the MC of spruce (17.2%; **Table 4**). These differences can be partially attributed to the different densities. Due to the higher porosity of wood from Celje, water vapour diffusion occurs more rapidly than in denser wood with lower porosity (Sjökqvist et al., 2019).

In addition to water vapour, outdoor wood is frequently exposed to capillary water (Rice and Phillips, 2001;





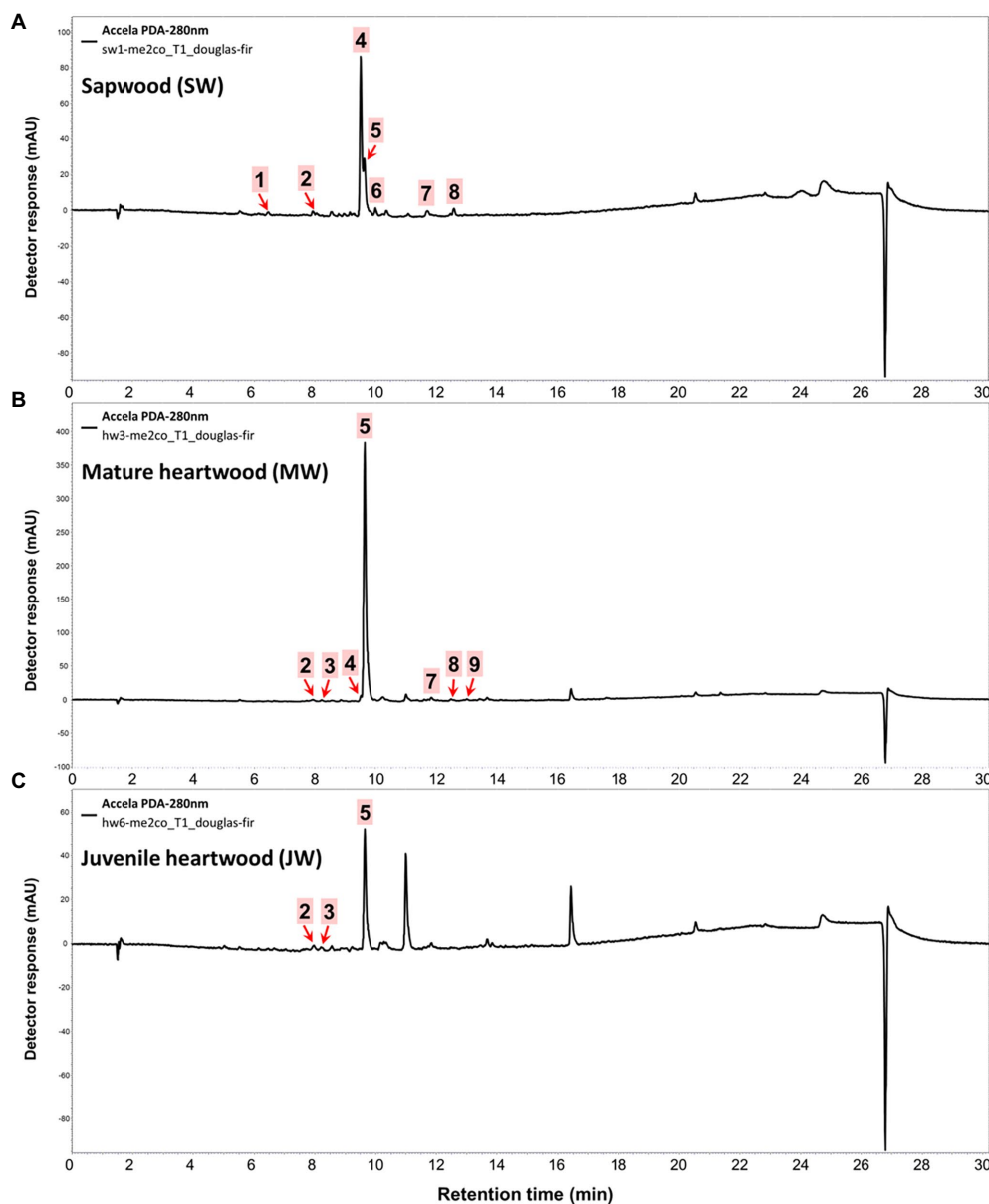


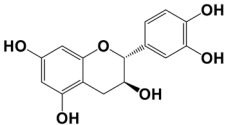
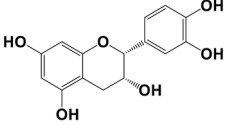
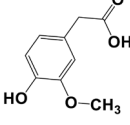
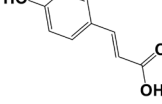
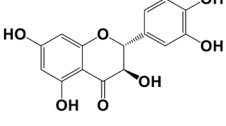
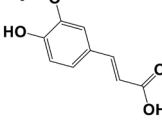
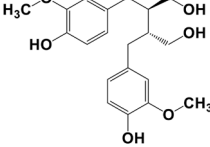
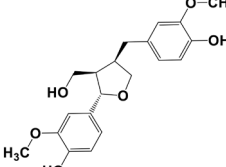
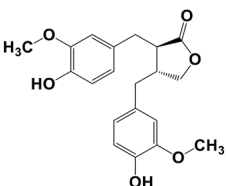
**FIGURE 5 |** HPLC chromatograms of acetone extracts from (A) sapwood, (B) adult heartwood and (C) juvenile Douglas fir (*Pseudotsuga menziesii*). For peak assignment, see **Table 2**.

Žlahtič-Zupanc et al., 2018). Therefore, special attention was paid to assessing this part of water performance. Namely, two types of tests were performed, short-term water uptake, determined in axial planes and long-term water uptake, determined by long-term immersion of the samples, with water penetrating the samples in all directions. Special attention is paid to penetration in axial planes, as these surfaces are usually the weakest point for both water penetration and fungal attack (Žlahtič Zupanc et al., 2019). Short-term water uptake into sapwood (Celje 0.0981 g/cm<sup>2</sup>; Planina 0.1185 g/cm<sup>2</sup>) was comparable to that determined on Norway spruce wood samples (0.1234 g/cm<sup>2</sup>). On the other hand, the water uptake

to Douglas-fir heartwood was much lower. Namely, water uptake of 0.0210 g/cm<sup>2</sup> was determined for mature heartwood from Celje (**Table 4**). The main reason for the low uptake can be attributed to aspirated pits and the presence of extractives (Bolton and Petty, 1977). The same phenomenon can be observed in other conifers as well (Reinprecht, 2016). A similar effect was observed in samples immersed in water for 1 h. Water uptake in the Douglas-fir sapwood samples is in the same range as in spruce wood, while lower values were obtained in heartwood samples. The results of short- and long-term capillary water take also showed that water uptake was lower on samples from Planina than on samples



**TABLE 2** | Chemical composition of phenolic extractives in sapwood and heartwood of Douglas fir (*Pseudotsuga menziesii*).

Compound	Chemical structure	Peak no.	SW		aHW		jHW	
			Avg	SD	Avg	SD	Avg	SD
Catechin		1	NQ<0.2		NQ<0.2		NQ<0.2	
Epicatechin		2	NQ<0.2		NQ<0.2		NQ<0.2	
Homovanillic acid		3	NQ<0.2		NQ<0.2		NQ<0.2	
<i>p</i> -Coumaric acid		4	1.26	0.49 <sup>a</sup>	0.78	0.31 <sup>a</sup>		
Taxifolin		5	0.48	0.25 <sup>a</sup>	6.45	5.19 <sup>b</sup>	3.61	2.70 <sup>a,b</sup>
Ferulic acid		6	0.47	0.09				
Secoisolariciresinol		7	0.60	0.38 <sup>a</sup>	0.43	0.34 <sup>a</sup>	0.89	
Pinoresinol		8	0.17	0.04 <sup>a</sup>	0.27	0.13 <sup>a</sup>	0.49	0.42 <sup>a</sup>
Matairesinol		9	NQ<0.2		NQ<0.2			

Results are expressed by the mean value of measurements (Avg) and the standard deviation (SD). Different letters within the same row indicate statistically significant differences at a 95.0% confidence level. NQ<0.2; identified in the extracts present in traces. The contents measured below 0.20mg/g (dw); SW, sapwood; aHW, adult heartwood; jHW, juvenile heartwood.

from Celje (Table 4). The lower water uptake can be ascribed to the Planina samples' higher density and lower porosity (Figure 3).

One of the main objectives of the manuscript was to determine the durability of the Douglas fir from Slovenia to wood-decaying fungi. The wood decay fungi used caused considerable mass

**TABLE 3** | Factors that determine the service life of the wood.

Wood species	Tissue	Growth location	$k_{wa}$	$k_{inh}$	$D_{Rd}$ (d)	$D_{Rd\ rel}$
PIAb	Heartwood	Slovenija	1.0	1.0	325	1.0
PISy	Sapwood	Slovenija	0.7	1.0	245	0.8
	Sapwood	Celje	1.0	1.3	436	1.3
	Sapwood	Planina	1.1	1.3	481	1.5
PsMe	Mature heartwood	Celje	2.2	2.9	2007	6.2
	Mature heartwood	Planina	1.8	2.6	1,500	4.6
	Juvenile heartwood	Celje	2.1	2.3	1,589	4.9
	Juvenile heartwood	Planina	2.0	2.6	1,652	5.1

The factors are the mean values of the individual factors calculated according to the methodology described in detail in Meyer-Veltrup et al. (2017) and Table 1.

**TABLE 4** | Moisture and decay indicators used to calculate factors that determine the service life of the wood.

Indicator	PIAb	PISy	PsMe					
			Sapwood		Heartwood			
			SW	SW	MW	MW	JW	JW
			Celje	Planina	Celje	Planina	Celje	Planina
RH100 24 h (%)	16.8 <sup>a</sup>	15.7 <sup>a</sup>	15.8 <sup>a</sup>	13.6 <sup>b</sup>	13.7 <sup>b</sup>	12.4 <sup>c</sup>	17.2 <sup>a</sup>	12.5 <sup>c</sup>
RH100 (%)	28.7 <sup>a</sup>	27.7 <sup>a</sup>	27.1 <sup>a</sup>	28.1 <sup>a</sup>	25.2 <sup>a</sup>	26.5 <sup>a</sup>	27.2 <sup>a</sup>	27.1 <sup>a</sup>
Release (%)	8.6 <sup>a</sup>	8.9 <sup>a</sup>	7.3 <sup>a</sup>	7.4 <sup>a</sup>	6.4 <sup>b</sup>	6.6 <sup>b</sup>	8.3 <sup>a</sup>	7.2 <sup>a</sup>
STWU (g/cm <sup>2</sup> )	0.1234 <sup>b</sup>	0.9528 <sup>a</sup>	0.0981 <sup>b</sup>	0.1185 <sup>b</sup>	0.0210 <sup>c</sup>	0.0428 <sup>c</sup>	0.0189 <sup>c</sup>	0.0331 <sup>c</sup>
MC 1 h (%)	25.8 <sup>b</sup>	52.7 <sup>a</sup>	27.5 <sup>b</sup>	18.1 <sup>c</sup>	10.0 <sup>d</sup>	8.5 <sup>d</sup>	11.6 <sup>d</sup>	8.0 <sup>d</sup>
MC 24 h (%)	51.7 <sup>a</sup>	67.4 <sup>a</sup>	53.2 <sup>a</sup>	40.5 <sup>b</sup>	30.6 <sup>c</sup>	25.9 <sup>c</sup>	35.9 <sup>bc</sup>	27.0 <sup>c</sup>
Mass loss – GT (%)	35 <sup>a</sup>	35 <sup>a</sup>	27 <sup>b</sup>	26 <sup>b</sup>	14 <sup>c</sup>	16 <sup>c</sup>	22 <sup>bc</sup>	16 <sup>c</sup>
Mass loss – FV (%)	21 <sup>a</sup>	23 <sup>a</sup>	19 <sup>a</sup>	20 <sup>a</sup>	15 <sup>b</sup>	14 <sup>b</sup>	18 <sup>ab</sup>	15 <sup>b</sup>
Mass loss – TV (%)	20 <sup>a</sup>	16 <sup>ab</sup>	13 <sup>c</sup>	12 <sup>c</sup>	2 <sup>d</sup>	4 <sup>d</sup>	3 <sup>d</sup>	2 <sup>d</sup>
DC	5	5	4	4	4	4	4	4
Mass loss – TMC (%)	23 <sup>a</sup>	26 <sup>a</sup>	18 <sup>b</sup>	17 <sup>b</sup>	9 <sup>c</sup>	10 <sup>c</sup>	14 <sup>bc</sup>	12 <sup>c</sup>
MoE loss (%)	34.2 <sup>b</sup>	48.4 <sup>a</sup>	28.3 <sup>b</sup>	32.6 <sup>b</sup>	–2.9 <sup>a</sup>	–2.7 <sup>a</sup>	–1.6 <sup>a</sup>	2.0 <sup>a</sup>

RH100 24 h—water vapour uptake after 24 h, RH100—water vapour uptake after 3 weeks, release—water release after drying over silica gel, STWU—short-term water uptake determined with a tensiometer, MC 1 h—moisture content after 1 h of immersion and MC 24 h—moisture content after 24 h of immersion, mass loss after exposure to the respective fungi and terrestrial microcosm (TMC) and MoE loss after exposure to terrestrial microcosm. DC is a durability classification into durability classes according to CEN/TS 15083–1. Different letters indicate a statistically significant difference ( $p > 0.05$ ) between different materials tested.

loss of 35% (*Gloeophyllum trabeum*) and 20% (*Trametes versicolor*) in the reference Norway spruce samples (Table 4). This indicates that the fungi were vital and that the wood was susceptible to fungal decay. Less decay of the Norway spruce samples exposed to the white-rot fungus *T. versicolor* is expected, as conifers are less susceptible to white-rot than brown-rot decay (Schmidt, 2006). The mass loss of the Douglas-fir sapwood after 16 weeks of exposure was slightly lower than the mass loss of the reference Norway spruce. Spruce wood exposed to *G. trabeum* lost 35%, while Douglas-fir sapwood samples lost between 27% (Celje) and 26% (Planina). A lower mass loss was observed in heartwood samples. Mature wood samples exposed to *G. trabeum* lost between 14% (Celje) and 16% (Planina). The *T. versicolor* showed a lower ability to degrade mature Douglas-fir heartwood, while the decay activity of *Fibroporia vaillantii* on heartwood was comparable to that of *G. trabeum* (Table 4). Better durability of the Douglas-fir wood can be ascribed to the higher concentration of biologically active extractives (Table 2).

Mass loss is a basis for the classification of durability according to the standard CEN/TS 15083–1 (CEN, 2005a). Based on the criteria of the respective standard, both sapwood and heartwood can be classified in durability class (DC) 4. Durability is on the borderline between DC 3 and DC 4, which is consistent with the standard EN 350 (CEN, 2016). Besides basidiomycetes, wood is frequently exposed to decay caused by terrestrial microorganisms, soft-rot fungi, and bacteria (Blanchette, 2000). Therefore, the parallel specimens were placed in the compost soil. The sapwood samples lost approximately 18% of the mass and 28% MoE. On the other hand, heartwood samples showed mass loss ranging from 9% (mature heartwood, Celje) to 14% (juvenile heartwood, Celje). However, the exposure did not result in significant losses of MoE. One of the possible explanations for this could be that the microorganisms eroded and abraded the surface, resulting in mass loss, but not loss of MoE.

Besides the decay fungi, the wood is also exposed to blue stain and sapstain fungi. All samples were completely covered

with blue stains after laboratory exposure and rated with grade 3 according to EN 152 standard. On the other hand, exposure in the condensation chamber showed more significant differences (Table 5). The sapwood of Scots pine was covered entirely with sap stain after 5 weeks of exposure. On the other hand, fungal degradation progressed most slowly in Norway spruce wood. Spruce wood samples were rated 1 after 9 weeks of exposure. The disfigurement of Douglas-fir wood proceeded more rapidly. The sapwood reached an average value of 3.2 and the heartwood 2.2. The difference between the sites was not noticeable.

Factors describing wettability and inherent durability were calculated based on experimental analyses. The wettability of wood materials is a factor that indicates how the wood will behave during rain events. Wood that wets less and dries faster is less susceptible to fungal decay than wood absorbs more water during rain events and dries slowly. Sorption properties, permeability, possible tyloses formation, pit aspiration and other

anatomically determined properties contribute to water penetration (Humar et al., 2020). As shown in Table 3, the moisture performance of Douglas-fir sapwood is comparable to that of Norway spruce. On the other hand, the  $k_{wa}$  factor of Douglas-fir heartwood is higher and is about 2 for both juvenile and mature heartwood, comparable to the moisture performance of European larch (Humar et al., 2019). It is known that the moisture resistance of heartwood is better than that of sapwood. In conifers, this is primarily due to pits aspiration and the process associated with heartwood formation (Bolton and Petty, 1977).

In addition to moisture performance, the  $k_{inh}$  factor, which characterises resistance to microbiological degradation, also plays a significant role in the performance of wood in outdoor environments. This durability primarily reflects the presence of biologically active extractives and biocides. Like the  $k_{wa}$  factor, the  $k_{inh}$  factor is also limited to 5. The durability of Douglas-fir mature heartwood varies between 2.9 (Celje) and 2.6 (Planina), which is slightly better than the value determined for European larch wood (1.8; Humar et al., 2019).

Based on the procedure proposed by Meyer-Veltrup et al. (2017), the material resistance dose ( $D_{rd}$ ) was calculated assuming a critical dose independent of wood species ( $D_{crit}=325$  d). This number corresponds to the number of days with optimal conditions for fungal decay before the first signs of deterioration appear. The resistance dose of Douglas-fir sapwood (436 days—Celje; 481 days—Planina) was higher than that of the reference Norway spruce. A much higher resistance dose was determined in the heartwood. The corresponding value ranged from 2007 days (mature heartwood from Celje) to 1,500 days (mature heartwood from Planina; Table 3). The difference between juvenile and mature heartwood was not significant. These values indicate that Douglas-fir heartwood will perform much better outdoors than the reference Norway spruce wood. The analysis indicated that the main reasons for the observed difference are the better water performance and inherent durability of Douglas fir. In contrast to the traditional durability classification, the dosimeter-based resistance model applied here showed the excellent performance of Douglas-fir heartwood, indicating that this material can be used for outdoor applications.

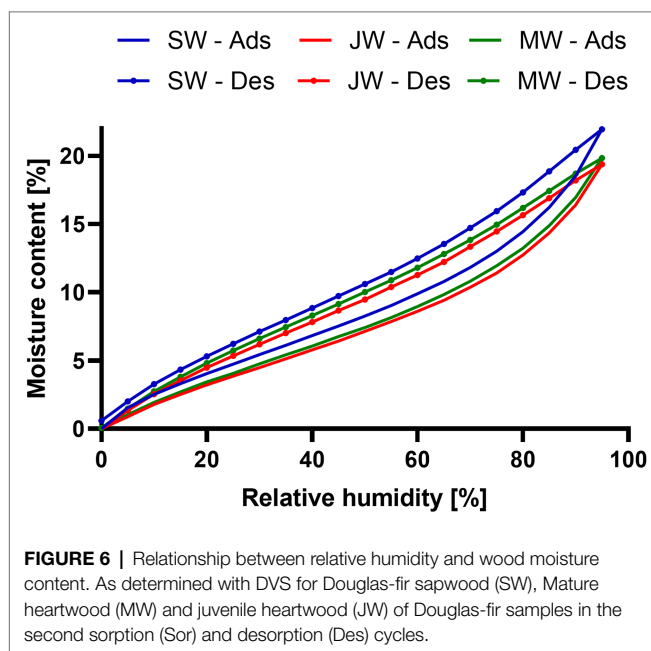


**TABLE 5 |** Sapstain development in the condensing chamber in the 2 months between 19 May 2020 and 21 July 2020.

Wood species/date	PsMe				PiAb	PiSy
	Sapwood		Heartwood		Sapwood	
	Planina	Celje	Planina	Celje	Slovenia	Slovenia
26 May 2020	0.2	0	0	0	0	0
2 June 2020	1.6	2.2	0.4	0.6	0	1.2
9 June 2020	2	2.4	1	0.8	0.2	1.8
16 June 2020	2.2	2.6	1.2	0.8	0.4	3.2
23 June 2020	2.2	2.6	1.2	0.8	0.4	4
1 July 2020	2.6	3.2	1.4	1.2	0.6	4
7 July 2020	2.8	3.2	1.4	1.8	0.6	4
14 July 2020	2.8	3.2	2.2	2.2	1	4
21 July 2020	3.2	3.2	2.2	2.2	1	4

## CONCLUSION

The average density of Douglas fir from two Slovenian sites was 489 kg/m<sup>3</sup> (sapwood), 507 kg/m<sup>3</sup> (mature heartwood) and 380 kg/m<sup>3</sup> (juvenile heartwood). The low density of the juvenile heartwood can be attributed to the fast growth in the first decade.

The chemical analysis revealed the highest amounts of hydrophilic extractives and phenolic compounds in younger heartwood parts, i.e., mature heartwood. These tissues also contain the highest amounts of taxifolin. Higher resistance of mature heartwood against wood-decaying fungi can be therefore explained with the higher content of phenolic extractives and taxifolin.

The durability of Douglas-fir wood heartwood was like the durability of European larch and can be classified in the group of less durable wood species (DC 4). On the other hand, Douglas-fir heartwood exhibits good water exclusion efficacy, which contributes to a high resistance dose that can be attributed to pit aspiration. Based on durability and moisture performance tests, factors affecting inherent durability and wetting ability were calculated for Douglas fir. Douglas-fir sapwood exhibited a higher resistance dose ( $D_{Rd}=459$ ) than Norway spruce ( $D_{Rd}=325$ ). An even higher resistance dose was noted in Douglas-fir heartwood. There was a minor difference between juvenile ( $D_{Rd}=1,621$ ) and mature ( $D_{Rd}=1754$ ) heartwood. This indicates that Douglas fir has potential for outdoor use, where it can at least partially replace European larch and Norway spruce. As the population of Douglas fir in Slovenia is one of the southernmost populations in Europe, it can be expected that the performance of the Douglas fir from locations north of Slovenia will become more and more comparable to the values presented in the respective article because of the climate changes. Data presented herein can be used as an input factor

for the prognosis of the future properties of Douglas fir from northern and central Europe.

## DATA AVAILABILITY STATEMENT

The raw data supporting the conclusions of this article will be made available by the authors, without undue reservation.

## AUTHOR CONTRIBUTIONS

MHu and VV designed the study and wrote the manuscript. BL, DK, VV, EK, and MHo carried out the experiments. RB found suitable trees and organised the harvesting of the trees. MHu and RB were responsible for project management. All authors contributed critically to the drafts and gave final approval for publication.

## FUNDING

The study was supported by Slovenian Research Agency (ARRS) within research program P4-0015 (Wood and lignocellulosic composites) and the infrastructural centre (IC LES PST 0481–09). Part of the published research was also supported by the Ministry of Agriculture, Forestry and Food in the frame of the project V4-1818.

## ACKNOWLEDGMENTS

The authors acknowledge the technical support of Drago Vidic, Andreja Žagar, Angela Balzano, and Samo Grbec.

## REFERENCES

- Adamopoulos, S., Voulgaridis, E., and Passialis, C. (2005). Variation of certain chemical properties within the stemwood of black locust (*Robinia pseudoacacia* L.). *Holz als Roh- und Werkstoff* 63, 327–333. doi: 10.1007/s00107-005-0018-3
- Ansell, M. P. (ed.) (2015). Wood composites. 1st Edn. Cambridge, UK: Woodhead Publishing.
- AWPA (2015). *Awpa Book of Standards*. Birmingham: Amer Wood Protection Assn.
- Balanategui, D., Nordhauf, H., Heinrich, I., Biondi, F., Miley, N., Hurley, A. G., et al. (2021). Wood anatomy of Douglas-fir in eastern Arizona and its relationship With Pacific Basin climate. *Front. Plant Sci.* 12:702442. doi: 10.3389/fpls.2021.702442
- Belt, T., Hänninen, T., and Rautkari, L. (2017). Antioxidant activity of scots pine heartwood and knot extractives and implications for resistance to brown rot. *Holzforschung* 71, 527–534. doi: 10.1515/hf-2016-0232
- Bevacqua, E., Shepherd, T. G., Watson, P. A. G., Sparrow, S., Wallom, D., and Mitchell, D. (2021). Larger spatial footprint of wintertime Total precipitation extremes in a warmer climate. *Geophys. Res. Lett.* 48, 1–12. doi: 10.1029/2020GL091990
- Birdsey, R., and Pan, Y. (2015). Trends in management of the world's forests and impacts on carbon stocks. *For. Ecol. Manag.* 355, 83–90. doi: 10.1016/j.foreco.2015.04.031
- Blanchette, R. A. (2000). A review of microbial deterioration found in archaeological wood from different environments. *Int. Bio.* 46, 189–204. doi: 10.1016/S0964-8305(00)00077-9
- Blohm, J. H., Melcher, E., Lenz, M. T., Koch, G., and Schmitt, U. (2014). Natural durability of Douglas fir (*Pseudotsuga menziesii* [Mirb.] Franco) heartwood grown in southern Germany. *Wood Mat. Sci. Eng.* 9, 186–191. doi: 10.1080/17480272.2014.903296
- Bolton, A. J., and Petty, J. A. (1977). Variation of susceptibility to aspiration of bordered pits in conifer wood. *J. Exp. Bot.* 28, 935–941. doi: 10.1093/jxb/28.4.935
- Brennan, M., Hentges, D., Cosgun, S., Dumarcay, S., Colin, F., Gérardin, C., et al. (2021). Intraspecific variability of quantity and chemical composition of ethanolic knotwood extracts along the stems of three industrially important softwood species: *Abies alba*, *Picea abies* and *Pseudotsuga menziesii*. *Holzforschung* 75, 168–179. doi: 10.1515/hf-2020-0108
- Brus, R., and Gajšek, D. (2014). “The introduction of non-native tree species to present-day Slovenia,” in *Man, Nature and Environment Between the Northern Adriatic and the Eastern Alps in Premodern Times*. eds. P. Štih and Ž. Zwitter (Ljubljana: Historical Association of Slovenia), 380–392.
- CEN (1993). *European Standard EN 310 – Wood Based Panels - Determination of Modulus of Elasticity in Bending and of Bending Strength*. Brussels, Belgium: European Committee for Standardisation; 8.
- CEN (2004). *European Standard TS ENV 1250-2 – Wood preservatives – Methods for measuring losses of active ingredients and other preservative ingredients from treated timber – Part 2: Laboratory method for obtaining samples for analysis to measure losses by leaching*. Brussels, Belgium: European Committee for Standardisation; 16.



- CEN (2005a). European Standard CEN/TS 15083-1 – durability of wood and wood-based products. Determination of the Natural Durability of Solid Wood against Food-Destroying Fungi, Test Methods. Basidiomycetes. Brussels, Belgium: European Committee for Standardisation; 20.
- CEN (2005b). European Standard CEN/TS 15083-2 – Durability of Wood and Wood-Based Products - Determination of the Natural Durability of Solid Wood against Wood-Destroying Fungi, Test Methods – Part 2: Soft Rotting Micro-Fungi. Brussels, Belgium: European Committee for Standardisation; 25.
- CEN (2012a). European Standard EN 252 – Field test method for determining protective effectiveness of a wood preservative in ground contact. Brussels, Belgium: European Committee for Standardisation; 24.
- CEN (2012b). European Standard EN 152 – Wood Preservatives - Determination of the Protective Effectiveness of a Preservative Treatment against Blue Stain in Wood in Service – Laboratory Method. Brussels, Belgium: European Committee for Standardisation; 45.
- CEN (2013). European Standard EN 1609 – Thermal insulating products for building applications – Determination of short term water absorption by partial immersion. Brussels, Belgium: European Committee for Standardisation; 10.
- CEN (2016). European Standard EN 350 – Durability of Wood and Wood-Based Products. Testing and classification of the durability to biological agents of wood and wood-based materials. Brussels, Belgium: European Committee for Standardisation; 67.
- Dellus, V., Mila, I., Scalbert, A., Menard, C., Michon, V., and Du Penhoat, H. C. L. M. (1997). Douglas-fir polyphenols and heartwood formation. *Phytochemistry* 45, 1573–1578. doi: 10.1016/S0031-9422(97)00245-8
- Dyderski, M. K., Paž, S., Frelich, L. E., and Jagodziński, A. M. (2018). How much does climate change threaten European forest tree species distributions? *Glob. Chang. Biol.* 24, 1150–1163. doi: 10.1111/gcb.13925
- Eberhard, B. R., Eckhart, T., and Hasenauer, H. (2021). Evaluating strategies for the management of Douglas-fir in central Europe. *Forests* 12, 1–17. doi: 10.3390/f12081040
- Eilmann, B., and Rigling, A. (2012). Tree-growth analyses to estimate tree species' drought tolerance. *Tree Physiol.* 32, 178–187. doi: 10.1093/treephys/tps004
- Gartner, B. L., Morrell, J. J., Freitag, C. M., and Spicer, R. (1999). Heartwood decay resistance by vertical and radial position in Douglas-fir trees from a young stand. *Can. J. For. Res.* 29, 1993–1996. doi: 10.1139/x99-166
- Golob, J., Levanič, T., and Hladnik, D. (2021). Growth of Norway spruce (*Picea abies* (L.) karst.) and European larch (*Larix decidua* mill.) on former slash and burn farming areas in Koprivna in the Karavanke mountains. *Acta Silvae et Ligni* 126, 23–39. doi: 10.20315/ASL.126.3
- Gričar, J., Prislán, P., De Luis, M., Gryc, V., Hacurová, J., Vavřík, H., et al. (2015). Plasticity in variation of xylem and phloem cell characteristics of Norway spruce under different local conditions. *Front. Plant Sci.* 6:730. doi: 10.3389/fpls.2015.00730
- Hanewinkel, M., Cullmann, D. A., Schelhaas, M. J., Nabuurs, G. J., and Zimmermann, N. E. (2013). Climate change may cause severe loss in the economic value of European forest land. *Nat. Clim. Chang.* 3, 203–207. doi: 10.1038/nclimate1687
- Hernández, R. E. (2007). Moisture sorption properties of hardwoods as affected by their extraneous substances, wood density, and interlocked grain. *Wood Fiber Sci.* 39, 132–145.
- Holmbom, T., Reunanen, M., and Fardim, P. (2008). Composition of callus resin of Norway spruce, scots pine, European larch and Douglas fir. *Holzforschung* 62, 417–422. doi: 10.1515/HF.2008.070
- Humar, M., Kržišnik, D., Lesar, B., and Brischke, C. (2019). The performance of wood decking after five years of exposure: verification of the combined effect of wetting ability and durability. *Forests* 10:903. doi: 10.3390/f10100903
- Humar, M., Lesar, B., and Kržišnik, D. (2020). Moisture performance of Façade elements made of thermally modified Norway spruce wood. *Forests* 11:348. doi: 10.3390/f11030348
- Isaksson, T., Brischke, C., and Thelandersson, S. (2013). Development of decay performance models for outdoor timber structures. *Mat. Struc. Mat. Construct.* 46, 1209–1225. doi: 10.1617/s11527-012-9965-4
- Isaksson, T., Thelandersson, S., Jermer, J., and Brischke, C. (2014). *Beständighet för utomhusträ ovan mark in guide för utformning och materialval (Rapport TVBK-3066)*. Lund, Sweden: Lunds Tekniska Högskola.
- Jankowska, A., Drożdżek, M., Sarnowski, P., and Horodeński, J. (2016). Effect of extractives on the equilibrium moisture content and shrinkage of selected tropical wood species. *Bioresources* 12, 597–607. doi: 10.15376/biores.12.1.597-607
- Johansson, P., Ekstrand-Tobin, A., Svensson, T., and Bok, G. (2012). Laboratory study to determine the critical moisture level for mould growth on building materials. *Int. Biodeterior. Biodegrad.* 73, 23–32. doi: 10.1016/j.ibiod.2012.05.014
- Kebbi-Benkeder, Z., Manso, R., Gérardin, P., Dumarçay, S., Chopard, B., and Colin, F. (2017). Knot extractives: a model for analysing the eco-physiological factors that control the within and between-tree variability. *Trees Struct. Fun.* 31, 1619–1633. doi: 10.1007/s00468-017-1573-z
- Klopčič, M., Mina, M., Bugmann, H., and Bončina, A. (2017). The prospects of silver fir (*Abies alba* mill.) and Norway spruce (*Picea abies* (L.) karst) in mixed mountain forests under various management strategies, climate change and high browsing pressure. *Eur. J. For. Res.* 136, 1071–1090. doi: 10.1007/s10342-017-1052-5
- Kraigher, H., Bajc, M., Božic, G., Breznikar, A., Dovc, N., Minic, M., et al. (2021). “Non-native tree species in domestic seed husbandry and nursery legislation and praxis,” in *Non-native Tree Species in Slovenian Forests*. ed. K. Jarni (Ljubljana: University of Ljubljana), 78–87.
- Lindberg, L. E., Willför, S. M., and Holmbom, B. R. (2004). Antibacterial effects of knotwood extractives on paper mill bacteria. *J. Ind. Microbiol. Biotechnol.* 31, 137–147. doi: 10.1007/s10295-004-0132-y
- Lu, J., Venäläinen, M., Julkunen-Tiitto, R., and Harju, A. M. (2016). Stilbene impregnation retards brown-rot decay of scots pine sapwood. *Holzforschung* 70, 261–266. doi: 10.1515/hf-2014-0251
- Magel, E., Jay-Allemand, C., and Ziegler, H. (1994). Formation of heartwood substances in the stemwood of *Robinia pseudoacacia* L. II. Distribution of nonstructural carbohydrates and wood extractives across the trunk. *Trees* 8, 165–171. doi: 10.1007/BF00196843
- Mangel, A. (2000). Identifying physical and chemical phenomena with gravimetric water sorption analysis. *J. Therm. Anal. Calorim.* 62, 529–537. doi: 10.1023/A:1010183407622
- Meyer-Veltrup, L., Brischke, C., Alfredeisen, G., Humar, M., Flæte, P. O., Isaksson, T., et al. (2017). The combined effect of wetting ability and durability on outdoor performance of wood: development and verification of a new prediction approach. *Wood Sci. Technol.* 51, 615–637. doi: 10.1007/s00226-017-0893-x
- Miranda, I., Ferreira, J., Cardoso, S., and Pereira, H. (2021). Composition and antioxidant properties of extracts from Douglas fir bark. *Holzforschung* 75, 677–687. doi: 10.1515/hf-2020-0097
- Oblak, J., Kobold, M., and Šraj, M. (2021). The influence of climate change on discharge fluctuations in Slovenian rivers. *Acta Geogr. Slov.* 61, 155–169. doi: 10.3986/ags.9942
- Oleson, K. R., and Schwartz, D. T. (2016). Extractives in Douglas-fir forestry residue and considerations for biofuel production. *Phytochem. Rev.* 15, 985–1008. doi: 10.1007/s11101-015-9444-y
- Perić, S., Tijardović, M., and Jazbec, A. (2011). Results of research on Douglas fir provenances in ecologically different continental parts of Croatia. *J. Forestry Soc. Croatia* 135, 190–199.
- Poletti, E., Vasconcelos, G., Branco, J. M., and Isopescu, B. (2019). Effects of extreme environmental exposure conditions on the mechanical behaviour of traditional carpentry joints. *Constr. Build. Mater.* 213, 61–78. doi: 10.1016/j.conbuildmat.2019.04.030
- Pollet, C., Henin, J. M., Hébert, J., and Jourez, B. (2017). Effect of growth rate on the physical and mechanical properties of Douglas-fir in western Europe. *Can. J. For. Res.* 47, 1056–1065. doi: 10.1139/cjfr-2016-0290
- Polman, J. E., and Militz, H. (1996). Wood quality of Douglas fir (*Pseudotsuga menziesii* (Mirb) Franco) from three stands in the Netherlands. *Annal. Sci. Forestieries* 53, 1127–1136. doi: 10.1051/forest:19960607
- Pötzelsberger, E., Spiecker, H., Neophytou, C., Mohren, F., Gazda, A., and Hasenauer, H. (2020). Growing non-native trees in European forests brings benefits and opportunities but also has its risks and limits. *Cur. Forestry Rep.* 6, 339–353. doi: 10.1007/s40725-020-00129-0
- Raspor, P., Smole Mozina, S., Podjavorek, J., Pohleven, F., Gogala, N., Nekrep, F. V., et al. (1995). *ZIM: Culture Collection of Industrial Microorganisms (ZIM) Ljubljana*. Ljubljana: University of Ljubljana.
- Reinprecht, L. (2016). *Wood Deterioration, Protection and Maintenance*. Oxford: John Wiley & Sons Ltd.
- Rice, R. W., and Phillips, D. P. (2001). Estimating the moisture excluding effectiveness of surface coatings on southern yellow pine using acoustic

- emission technology. *Wood Sci. Technol.* 34, 533–542. doi: 10.1007/s002260000057
- Schmidt, O. (2006). *Wood and Tree Fungi: Biology, Damage, Protection, and Use*. Berlin: Springer-Verlag Berlin Heidelberg.
- Singleton, V. L., Rossi, J. A., and Jr, J. (1965). Colorimetry of total phenolics with acid reagents. *Am. J. Enol. Vitic.* 16, 144–158.
- Sjökvist, T., Blom, A., and Wälinder, M. E. P. (2019). The influence of heartwood, sapwood and density on moisture fluctuations and crack formations of coated Norway spruce in outdoor exposure. *J. Wood Sci.* 65, 1–9. doi: 10.1186/s10086-019-1825-1
- Smolnikar, P., Brus, R., and Jarni, K. (2021). Differences in growth and log quality of Douglas-fir (*Pseudotsuga menziesii* (mirb.) Franco) provenances. *Forests* 12, 1–12. doi: 10.3390/f12030287
- Valette, N., Perrot, T., Sormani, R., Gelhaye, E., and Morel-Rouhier, M. (2017). Antifungal activities of wood extractives. *Fungal Biol. Rev.* 31, 113–123. doi: 10.1016/j.fbr.2017.01.002
- Välimaa, A. L., Honkalampi-Hämäläinen, U., Pietarinen, S., Willför, S., Holmbom, B., and von Wright, A. (2007). Antimicrobial and cytotoxic knotwood extracts and related pure compounds and their effects on food-associated microorganisms. *Int. J. Food Microbiol.* 115, 235–243. doi: 10.1016/j.ijfoodmicro.2006.10.031
- Vek, V., Poljanšek, I., and Oven, P. (2019). Efficiency of three conventional methods for extraction of dihydrorobinetin and robinetin from wood of black locust. *Eur. J. Wood. Prod.* 77, 891–901. doi: 10.1007/s00107-019-01430-x
- Vek, V., Poljanšek, I., and Oven, P. (2020). Variability in content of hydrophilic extractives and individual phenolic compounds in black locust stem. *Eur. J. Wood. Prod.* 78, 501–511. doi: 10.1007/s00107-020-01523-y
- Veselič, Ž., Grecs, Z., and Matijašič, D. (2016). “Predlog uporabe nekaterih tujerodnih vrst pri obnavljanju gozdov v Sloveniji – Proposal for the use of some alien tree species for forest restoration in Slovenia,” in *Invazivne Tujerodne Vrste v Gozdovih ter Njihov Vpliv na Trajnostno Rabo Gozdnih Virov*. ed. M. Jurc (Ljubljana: Biotehniška fakulteta, Oddelek za gozdarstvo in obnovljive gozdne vire), 149–158.
- Vikram, V., Cherry, M. L., Briggs, D., Cress, D. W., Evans, R., and Howe, G. T. (2011). Stiffness of Douglas-fir lumber: effects of wood properties and genetics. *Can. J. For. Res.* 41, 1160–1173. doi: 10.1139/x11-039
- Wagenfuhr, R. (2007). *Holzatlas*. Leipzig: Fachbuchverlag.
- Willför, S. M., Ahotupa, M. O., Hemming, J. E., Reunanen, M. H. T., Eklund, P. C., Sjöholm, R. E., et al. (2003). Antioxidant activity of Knotwood extractives and phenolic compounds of selected tree species. *J. Agric. Food Chem.* 51, 7600–7606. doi: 10.1021/jf030445h
- Willför, S., Nisula, L., Hemming, J., Reunanen, M., and Holmbom, B. (2004). Bioactive phenolic substances in industrially important tree species. Part 2: knots and stemwood of fir species. *Holzforschung* 58, 650–659. doi: 10.1515/HE.2004.119
- Willför, S. M., Smeds, A. I., and Holmbom, B. R. (2006). Chromatographic analysis of lignans. *J. Chromatogr. A* 1112, 64–77. doi: 10.1016/j.chroma.2005.11.054
- Žlahtič Zupanc, M., Mikac, U., Serša, I., Merela, M., and Humar, M. (2019). Water distribution in wood after short term wetting. *Cellulose* 26, 703–721. doi: 10.1007/s10570-018-2102-y
- Žlahtič-Zupanc, M., Lesar, B., and Humar, M. (2018). Changes in moisture performance of wood after weathering. *Constr. Build. Mater.* 193, 529–538. doi: 10.1016/j.conbuildmat.2018.10.196

**Conflict of Interest:** The authors declare that the research was conducted in the absence of any commercial or financial relationships that could be construed as a potential conflict of interest.

**Publisher's Note:** All claims expressed in this article are solely those of the authors and do not necessarily represent those of their affiliated organizations, or those of the publisher, the editors and the reviewers. Any product that may be evaluated in this article, or claim that may be made by its manufacturer, is not guaranteed or endorsed by the publisher.

Copyright © 2022 Humar, Vek, Oven, Lesar, Kržišnik, Keržič, Hočevar and Brus. This is an open-access article distributed under the terms of the Creative Commons Attribution License (CC BY). The use, distribution or reproduction in other forums is permitted, provided the original author(s) and the copyright owner(s) are credited and that the original publication in this journal is cited, in accordance with accepted academic practice. No use, distribution or reproduction is permitted which does not comply with these terms.



# Relationships Between Wood-Anatomical Features and Resistance Drilling Density in Norway Spruce and European Beech

Domen Arnič<sup>1,2\*</sup>, Luka Krajnc<sup>3</sup>, Jožica Gričar<sup>4</sup> and Peter Prislan<sup>1</sup>

<sup>1</sup>Department for Forest Technique and Economics, Slovenian Forestry Institute, Ljubljana, Slovenia, <sup>2</sup>Biotechnical Faculty, University of Ljubljana, Ljubljana, Slovenia, <sup>3</sup>Department of Forest Yield and Silviculture, Slovenian Forestry Institute, Ljubljana, Slovenia, <sup>4</sup>Department of Forest Physiology and Genetics, Slovenian Forestry Institute, Ljubljana, Slovenia

## OPEN ACCESS

### Edited by:

Lisbeth Garbrecht Thygesen,  
University of Copenhagen,  
Denmark

### Reviewed by:

Albin Lobo,  
University of Copenhagen,  
Denmark  
Marcin Klisz,  
Forest Research Institute (IBL),  
Poland

### \*Correspondence:

Domen Arnič  
domen.arnic@gozdis.si

### Specialty section:

This article was submitted to  
Technical Advances in Plant Science,  
a section of the journal  
Frontiers in Plant Science

**Received:** 10 February 2022

**Accepted:** 22 March 2022

**Published:** 08 April 2022

### Citation:

Arnič D, Krajnc L, Gričar J and  
Prislan P (2022) Relationships  
Between Wood-Anatomical Features  
and Resistance Drilling Density in  
Norway Spruce and European  
Beech.  
Front. Plant Sci. 13:872950.  
doi: 10.3389/fpls.2022.872950

Environmental conditions affect tree-ring width (TRW), wood structure, and, consequently, wood density, which is one of the main wood quality indicators. Although studies on inter- and intra-annual variability in tree-ring features or density exist, studies demonstrating a clear link between wood structure on a cellular level and its effect on wood density on a macroscopic level are rare. Norway spruce with its simple coniferous structure and European beech, a diffuse-porous angiosperm species were selected to analyze these relationships. Increment cores were collected from both species at four sites in Slovenia. In total, 24 European beech and 17 Norway spruce trees were sampled. In addition, resistance drilling measurements were performed just a few centimeters above the increment core sampling. TRW and quantitative wood anatomy measurements were performed on the collected cores. Resistance drilling density values, tree-ring (TRW, earlywood width–EWW, transition–TWW, and latewood width–LWW) and wood-anatomical features (vessel/tracheid area and diameter, cell density, relative conductive area, and cell wall thickness) were then averaged for the first 7 cm of measurements. We observed significant relationships between tree-ring and wood-anatomical features in both spruce and beech. In spruce, the highest correlation values were found between TRW and LWW. In beech, the highest correlations were observed between TRW and cell density. There were no significant relationships between wood-anatomical features and resistance drilling density in beech. However, in spruce, a significant negative correlation was found between resistance drilling density and tangential tracheid diameter, and a positive correlation between resistance drilling density and both TWW+LWW and LWW. Our findings suggest that resistance drilling measurements can be used to evaluate differences in density within and between species, but they should be improved in resolution to be able to detect changes in wood anatomy.

**Keywords:** wood structure, *Fagus sylvatica*, *Picea abies*, quantitative wood anatomy, xylem anatomy, wood density, increment borer

## INTRODUCTION

European beech (*Fagus sylvatica* L.) and Norway spruce (*Picea abies* (L.) H. Karst.) are ecologically and economically important species of European forests. Beech is considered to be a plastic species that can adapt to different environmental conditions (Lindner et al., 2010; Vitasse et al., 2010; Martínez del Castillo et al., 2018). Similarly, Norway spruce is a species with high adaptive potential (Gričar et al., 2015), but it is shown to be particularly vulnerable to anticipated climate change (Bošel'a et al., 2014). Due to their economic importance, climate-growth relationships at inter- and intra-annual levels have been extensively studied in both species (Čermák et al., 2019; Muffler et al., 2020; Arnič et al., 2021; Jevšenak et al., 2021).

Previous studies have shown that, in addition to tree-ring width (TRW), wood structure is related to environmental conditions (Hajek et al., 2016; Diaconu et al., 2016b; Castagneri et al., 2017). In coniferous spruce, tracheids make up most of the xylem tissue. Earlywood is formed in spring and is characterized by tracheids with large lumen and thin cell walls, while in latewood, they have small lumen and thick cell walls (Björklund et al., 2017). Extreme weather events, such as droughts, can trigger the formation of intra-annual density fluctuations (IADFs), i.e., when latewood-like cells are formed in earlywood or vice versa (e.g., Battipaglia et al., 2016; Klisz et al., 2019). In general, beech is a diffuse-porous angiosperm species with vessels of similar size evenly distributed across a tree ring (Bosshard, 1982). However, extreme events, for example, can affect tree-ring porosity, i.e., the distribution and size of vessels within a tree ring. Thus, it can change from diffuse-porous in normal years to nearly semi-ring porous in years with extremely dry summers (Arnič et al., 2021). In coniferous spruce, wood structural changes mainly refer to tracheid features (wall thickness and lumen size; e.g., Gao et al., 2021; Stangler et al., 2021), the ratio of earlywood to latewood (Samusevich et al., 2020), and the occurrence of IADFs (Mayer et al., 2020). In beech, the changes refer to the ratio between different cell types (i.e., vessels, fibers, and parenchyma; Zheng et al., 2019) and vessel features (i.e., size, distribution, and grouping; Diaconu et al., 2016a).

In general, any changes in wood structure have been shown to influence wood properties (Chave et al., 2009; Eder et al., 2009). Wood density is considered to be one of the most important predictors of wood quality due to its correlation with the calorific value and with mechanical properties, such as hardness, stiffness, and strength (Preston et al., 2006; Chave et al., 2009; Nabais et al., 2018). In addition, the density and porosity of wood have a significant influence on adsorption and impregnability and thermal conductivity (Lesar and Humar, 2011; Plötze and Niemz, 2011). Several studies have been already conducted to evaluate how density is affected by changes in wood structure and anatomy (Peters et al., 2020). In conifers, wood density is related to tracheid/lumen size and the amount of cell wall material (Björklund et al., 2017). It is known that, due to the fixed latewood width (LWW) in spruce, wood density decreases with increasing TRW (Bouriaud et al., 2015). In diffuse-porous beech, the relationship

between TRW and wood density is not significant (Bouriaud et al., 2004; Skomarkova et al., 2006; van der Maaten et al., 2012). As shown by Peters et al. (2020), wood density in beech is related to lumen area and the cell wall thickness of vessels, fibers, and axial and ray parenchyma cells. Most of these studies were conducted at a tree-ring level, evaluating variation in wood anatomy and wood density within and between tree-ring increments. However, little is known how such changes affect properties (i.e., density) of wood as an engineering material (Ross, 2010).

Wood density can vary considerably within a tree stem (Rathgeber, 2017), i.e., between earlywood and latewood in coniferous and ring-porous species (Björklund et al., 2017), between heartwood and sapwood (Fromm et al., 2001), and along tree height (Swenson and Enquist, 2008). Fast and reliable determination of wood density on standing trees is crucial for spatial- and large-scale analyses/estimates of carbon storage (Baker et al., 2004) and wood quality (Gao et al., 2017). Bulk wood density is traditionally determined volumetrically on large wood samples from felled trees, which is destructive and time consuming (Björklund et al., 2021). Similar as quantitative wood anatomy intra- and inter-annual variability in density can also be evaluated on increment cores, collected from standing trees (Bergsten et al., 2001; Chave et al., 2006, 2009; Klisz et al., 2016). An alternative way of measuring wood density in standing trees is the use of resistance drilling, whereby a handheld device is used to measure resistance to drilling with a specially shaped needle. This technology is more frequently applied in arboriculture, where it is used for assessing the presence of decay in trees. It creates less damage to the tree stem than extracting increment cores, since needle heads are usually around three millimeters wide (Fundova et al., 2018). With the use of special drilling needles that have been calibrated for assessing absolute wood density, such devices can also be used for an accurate estimation of wood density in the radial direction (Gao et al., 2017; Fundova et al., 2018). The use of such devices has the advantages of being quicker than other methods, which makes it easier to measure a larger number of trees and to capture more potential variation in wood density between trees. The main disadvantage of this method is that it nevertheless only provides an estimation of wood density. While accurate in general, it is also influenced by various factors, which need to be accounted for in the analysis. For example, drilling in larger trees increases the amount of friction compared to smaller trees and because of friction there is a linear trend in the measurements (Fundova et al., 2018). Moisture content also influences the measurements to some degree (Sharapov et al., 2020), although this trend is stronger at lower moisture contents and is probably negligible in living trees that have a moisture content above the fiber saturation point.

Although there have been studies on inter- and intra-annual variability in TRW and wood-anatomical features or density, analyses investigating relationships between wood structure on a cellular level and its effect on wood density at a macroscopic level are rare. The results can help to understand the effects of variable wood structure/anatomy on the suitability of wood



as a raw or engineering material. The aim of this study was thus (i) to investigate the relationships between the selected wood-anatomical features (TRW and features of conducting cells) and resistance drilling density in the youngest seven centimeters of the stem increment in Norway spruce and European beech and (ii) to evaluate the potential of resistance drilling measurements for studies on the effect of variations in wood anatomy on wood density. We hypothesized that (i) the relationships between TRW and features of conducting cells exist in both species at a tree ring as well as macroscopic level; (ii) the relationships between the selected anatomical features and resistance drilling density differ between coniferous spruce and diffuse-porous beech wood.

## MATERIALS AND METHODS

### Site, Species, Tree Selection, and Sampling

Sampling and measurements of European beech (*Fagus sylvatica* L.) and Norway spruce (*Picea abies* Karst.) were carried out at four sites in Slovenia to evaluate the relationship between wood-anatomical features and resistance drilling density. The sampling sites are representing Slovenian mountain forest with average altitude  $1,155 \pm 160$  m above sea level, mean temperature of  $7.2 \pm 1.5^\circ\text{C}$ , and  $1,410 \pm 150$  mm of annual sum of precipitations in last 70 years (**Supplementary Table 1; Supplementary Figure 1; Cornes et al., 2018**). On those sites, a total of 24 European beech and 17 Norway spruce old grown trees (DBH > 45 cm, tree height > 29 m) were sampled and measured in a natural stand between autumn 2019 and spring 2020. Two cores bark-to-pith were extracted at breast height from different sides of each individual tree using a 5-mm increment borer (Haglöf Sweden, Långsele, Sweden). Resistance drilling density measurements were taken 3–4 cm above the increment borer sampling point using a Resistograph R650-SC (Rinntech, Heidelberg, Germany) resistance borer (**Figure 1A**). Based on the diameter at breast height (DBH) of the tree, drilling was done to the approximate pith of each tree (i.e., half of the DBH, similarly to increment cores).

### Measurements of Tree-Ring Widths and Wood-Anatomical Features

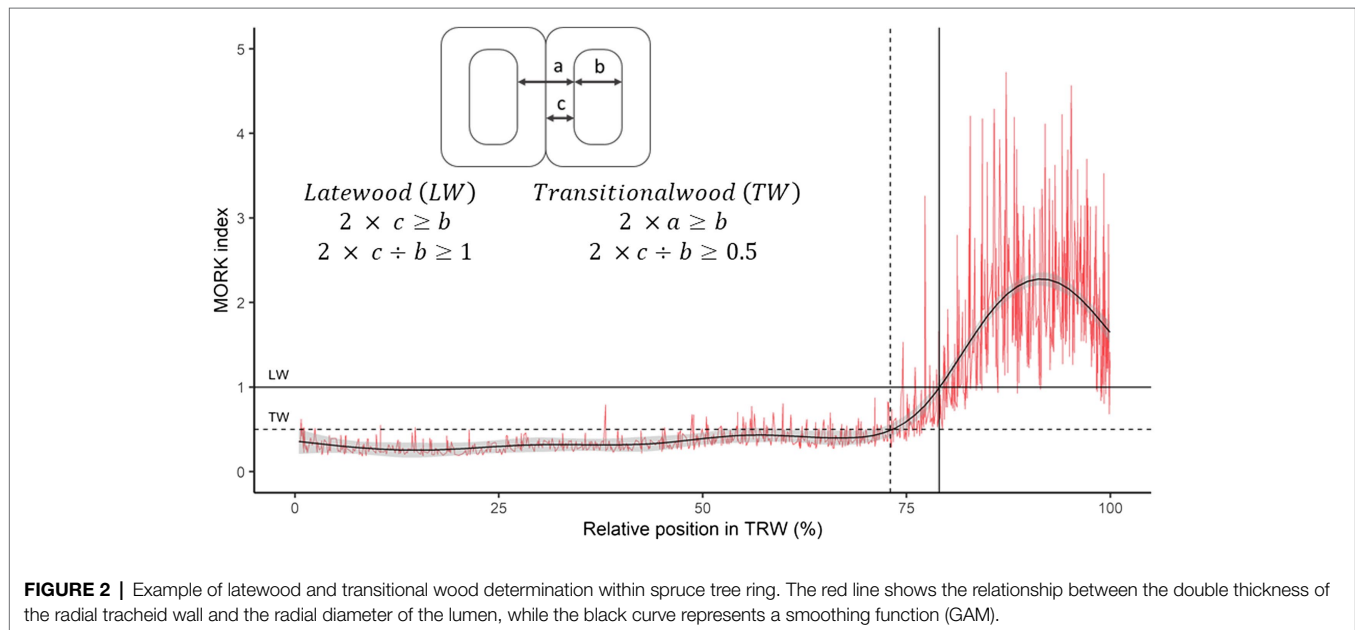
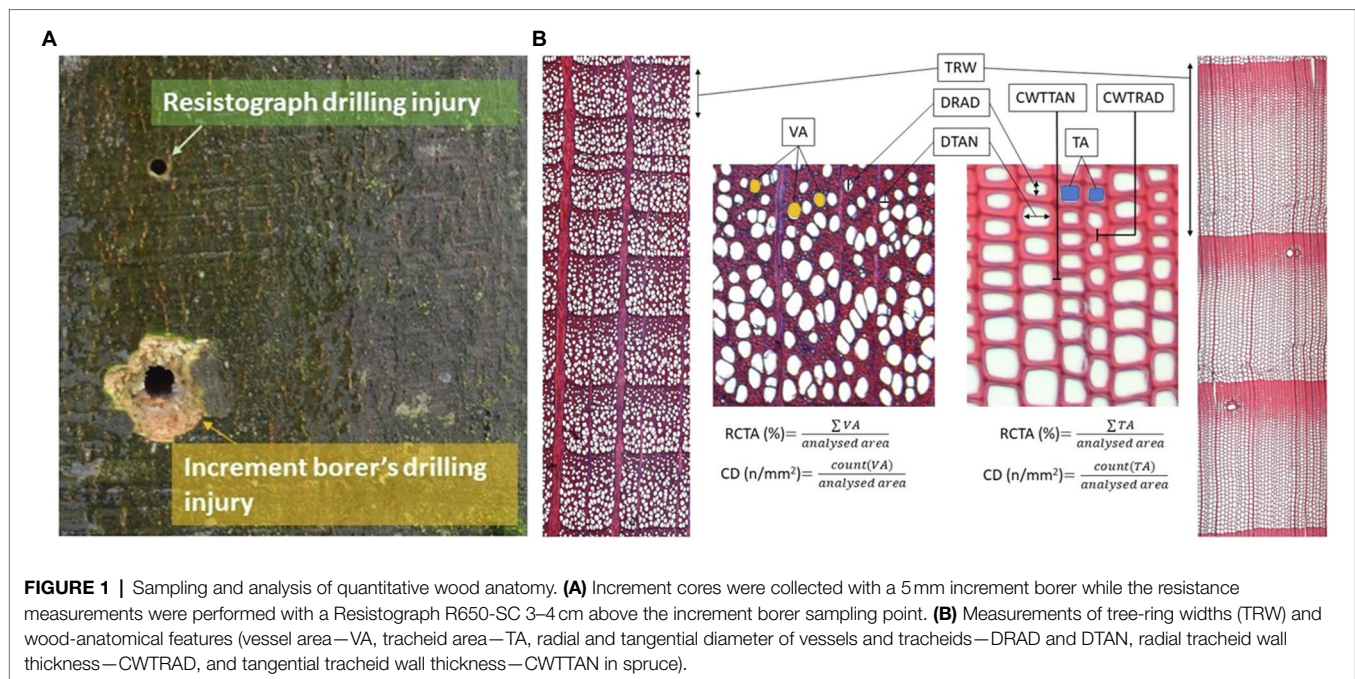
Measurements of wood-anatomical features and tree-ring width (TRW) were performed on 24 selected cores for beech and 17 cores for spruce. Each wooden core was split into segments of length from 3 to 4 cm. In the case of beech, a  $20\text{ }\mu\text{m}$  thick transverse section was cut from each segment with a WSL sledge microtome using OLFA-80  $\times 9$  mm spare blades (Gärtner et al., 2015). The Norway spruce segments were dehydrated in a graded series of ethanol and infiltrated with UltraClear (Avantor Performance Materials, Deventer, Netherlands) and paraffin (Paraplast plus, Leica Biosystems, Richmond, United States). After the infiltration of wood tissue, samples were embedded in paraffin blocks to stabilize the samples for further processing (Prislan et al., 2013).

Transverse sections of  $20\text{ }\mu\text{m}$  thickness were cut with a Leica RM 2245 rotary microtome (Leica Microsystems, Wetzlar, Germany) using Leica 819 Low Profile Microtome blades (Leica Biosystems, Nussloch, Germany). The sections were transferred to object glasses and the paraffin was then washed out with UltraClear and ethanol. The beech sections were treated with bleaching solution (5–15% chlorine content) to improve the staining intensity. The sections of both species were stained with a water mixture of safranin and Astra-blue and finally, the permanent slides were prepared using Euparal mounting medium (Arnič et al., 2021; Prislan et al., 2022).

To obtain macro-images of samples, the permanent slides were firstly scanned with a  $4800 \times 4800$  dpi Color Image scanner (Epson Perfection V19, Seiko Epson Corporation, Japan). The captured figures served for the measurements of TRW using CooRecorder & CDendro software (Cybis, Saltsjöbaden, Sweden). The final cross-dating was done using PAST-5 (SCIEM, Brunn, Austria) software. TRW measurements of individual trees served as control for accurate tree-ring dating in subsequent wood anatomy analyses.

To perform quantitative wood-anatomical measurements, high-resolution images (beech:  $0.514\text{ pixel}/\mu\text{m}$ , spruce:  $2.056\text{ pixel}/\mu\text{m}$ ) of the sections were prepared using a Leica DM 4000 B light microscope (Leica Microsystems, Wetzlar, Germany) at  $50\times$  (for beech) and  $100\times$  (for spruce) magnification with a Leica DFC 280 digital camera (Leica Microsystems, Wetzlar, Germany) and LAS image analysis software (Leica Application Suite, Leica Microsystems, Wetzlar, Germany). Image-sequences of the xylem rings were captured with at least 25% of the overlapping area and then merged using PTGui v11.16 Pro (New House Internet Services B.V., Rotterdam, Netherlands). Panoramic figures of both species were then processed with the image analysis software Image-Pro Plus 7.1 (Media cybernetics, Rockville, United States) and ROXAS (v3.0.437) to obtain the wood-anatomical features (von Arx and Carrer, 2014; von Arx et al., 2016).

Wood-anatomical measurements were performed for both species for tree rings formed between 1960 and 2019. In each ring, the following wood-anatomical features were measured (1) mean vessel lumen area (MVA) in beech and tracheid lumen area (MTA) in spruce, (2) cell density (CD) as the number of conduit cells per square mm, (3) relative conductive area (RCTA) representing the percentage of cumulative conductive area within the measured area, (4) mean radial cell diameter (DRAD) measured in a bark-to-pith direction, and (5) mean tangential cell diameter (DTAN; measured tangentially to pith). Radial (CWTRAD), tangential (CWTTAN), and mean cell wall thickness (CWTALL) were additionally measured in spruce (**Figure 1B**). Based on radial tracheid cell wall thickness and radial lumen diameter, we evaluated the distance of the latewood and transitional wood by the first and second Mork's interpretations (Denne, 1989; **Figure 2**). In further analyses, latewood width (LWW) and sum of latewood and transitional wood width (TWW + LWW), as well as their shares in TRW (share of latewood—LWS, the sum of shares of latewood and transitional wood—TWS + LWS), were used.



## Resistance Drilling Density Data Analysis

The resistance drilling measurements were imported into the R statistical environment using the R (R Core Team, 2021) package *densitr*, which enables further manipulation of the measurements in R (Krajnc et al., 2021). Wood density profiles of each tree were first trimmed to exclude the bark and determine the point of approximate cambium. Since the wood anatomy analyses were performed for the period between 1960 and 2019 and because some trees had been growing slowly during this period, we decided to standardize the analyses for

each tree to the first 7 cm of wood (in the direction from cambium to pith). The wood density profiles were thus secondarily trimmed at a distance of 7 cm from the approximate cambium location and detrended by removing the linear trend due to friction using the functions from the *densitr* R package (Figure 3).

## Wood-Anatomical Features and Wood Density Relationship Analyses

Wood-anatomical and density analyses were performed in open-source statistical environment R. Since low annual wood

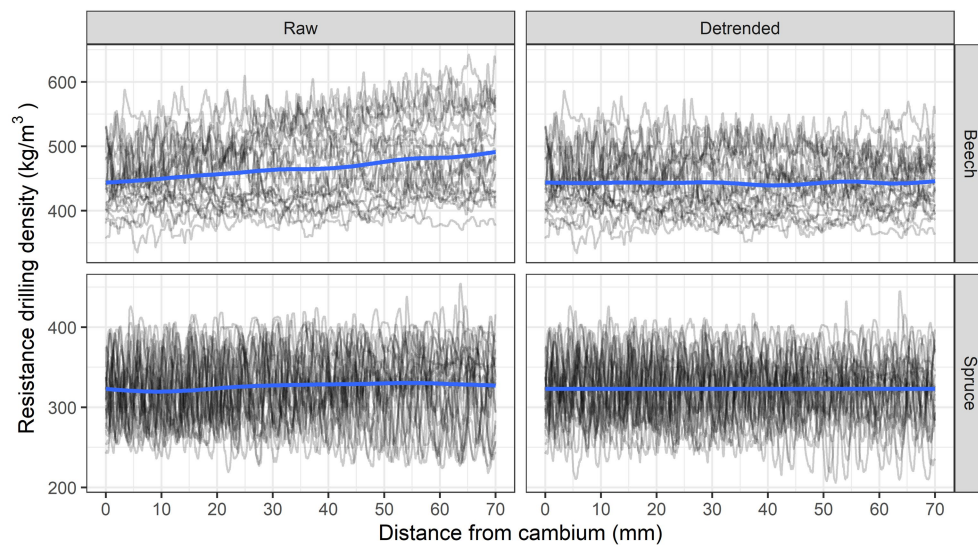


**FIGURE 3** | Unadjusted (raw) and detrended debarked resistance drilling density profiles for beech and spruce.

density variability and narrow TRW were found within the majority of trees, it was not possible to determine TRW within resistance drilling density profiles. We were thus unable to perform the analyses on an annual scale and therefore decided to calculate mean values of each wood-anatomical feature and resistance drilling density for the whole 7 cm for each analyzed tree (**Supplementary Figure 2**).

Since the Roxas output data for wood-anatomical variables (MVA and MTA, DRAD, DTAN, and RCTA) are given on annual scale, all wood-anatomical features were weighted by TRW to calculate weighted mean anatomical variables for the whole 7 cm of wood samples. Additionally, for a better insight into resistance drilling density and into wood-anatomical variability within species, we calculated the 5th-, 10th-, 25th-, 75th-, 90th-, and 95th-quantiles of resistance drilling density and selected wood-anatomical features for both species (TA and CWTALL for spruce, and VA for beech).

To determine the most pronounced relationships, Pearson correlation coefficients were calculated between wood-anatomical features and wood density quantiles. Furthermore, simple linear regression models were performed between selected resistance drilling density quantiles (mean resistance drilling density for both species and additionally 90th quantile of resistance drilling density for spruce) and selected wood-anatomical features (mean size of conduit cells—MVA and MTA, DRAD, DTAN, RCTA, and TRW for both species, and additional CWTALL, LWW, and LWW + TWW for spruce). Detailed information about used linear regression models are listed in **Supplementary Tables 4–6**.

## RESULTS

### Wood-Anatomical Features in Spruce and Beech

In spruce, TRW was  $1.78 \pm 0.6$  mm (mean  $\pm$  standard deviation), earlywood width (EWW)  $1.5 \pm 0.5$  mm, and latewood (LWW)

$0.27 \pm 0.17$  mm. The total width of transition wood and latewood (TWW + LWW) was  $0.68 \pm 0.37$  mm. Minimum (5th quantile) and maximum (95th quantile) tracheid lumen area was  $30.5 \pm 14.1 \mu\text{m}^2$  and  $1,316 \pm 170 \mu\text{m}^2$ , respectively, with mean values of  $552 \pm 86 \mu\text{m}^2$  (**Figure 4A**). Tangential and radial lumen diameters of tracheids were  $23.7 \pm 1.7 \mu\text{m}$  and  $25.4 \pm 2.9 \mu\text{m}$ , respectively. Relative conductive area was  $48.1 \pm 5.3\%$ . Mean tracheid wall thickness was  $5.3 \pm 0.6 \mu\text{m}$  (**Figure 4C**).

In spruce, a high positive correlation was found between TRW and LWW ( $\rho = 0.84$ ), and between the width of TWW + LWW and LWW ( $\rho = 0.96$ ; **Supplementary Table 2**). Furthermore, LWW and TWW + LWW showed a negative correlation with the relative conductive area (LWW:  $\rho = -0.59$ , TWW + LWW:  $\rho = -0.63$ ). Relative conductive area showed a positive correlation with mean tracheid lumen area ( $\rho = 0.85$ ) and radial ( $\rho = 0.88$ ) and tangential ( $\rho = 0.69$ ) tracheid diameters, whereas the correlation with mean-, radial-, and tangential cell wall thickness was negative ( $\rho = -0.94$ ,  $\rho = -0.93$ ,  $\rho = -0.94$ ). In contrast, cell density showed a negative correlation with mean tracheid lumen area ( $\rho = -0.74$ ) and radial ( $\rho = 0.67$ ) and tangential ( $\rho = 0.75$ ) lumen diameters, while there was no correlation with wall thickness in any direction (**Supplementary Table 2**).

In beech, TRW was  $1.82 \pm 0.4$  mm. Vessel lumen area varied from  $210 \pm 37 \mu\text{m}^2$  in the 5th quantile to  $3,534 \pm 458 \mu\text{m}^2$  in the 95th quantile (**Figure 4**). Tangential and radial vessel lumen diameters were  $49.9 \pm 2.3 \mu\text{m}$  and  $40.5 \pm 2.4 \mu\text{m}$ , respectively. The mean vessel area was  $1750 \pm 183 \mu\text{m}^2$ , whereas the relative conductive area was  $20.2 \pm 3.2\%$ . Cell density showed the highest negative correlations with TRW ( $\rho = -0.55$ ). In addition, high positive correlations were found between mean vessel area and tangential and radial vessel diameters ( $\rho = 0.96$  and  $\rho = 0.84$ , respectively), as well as between mean vessel area and relative conductive area ( $\rho = 0.74$ ; **Supplementary Table 3**).



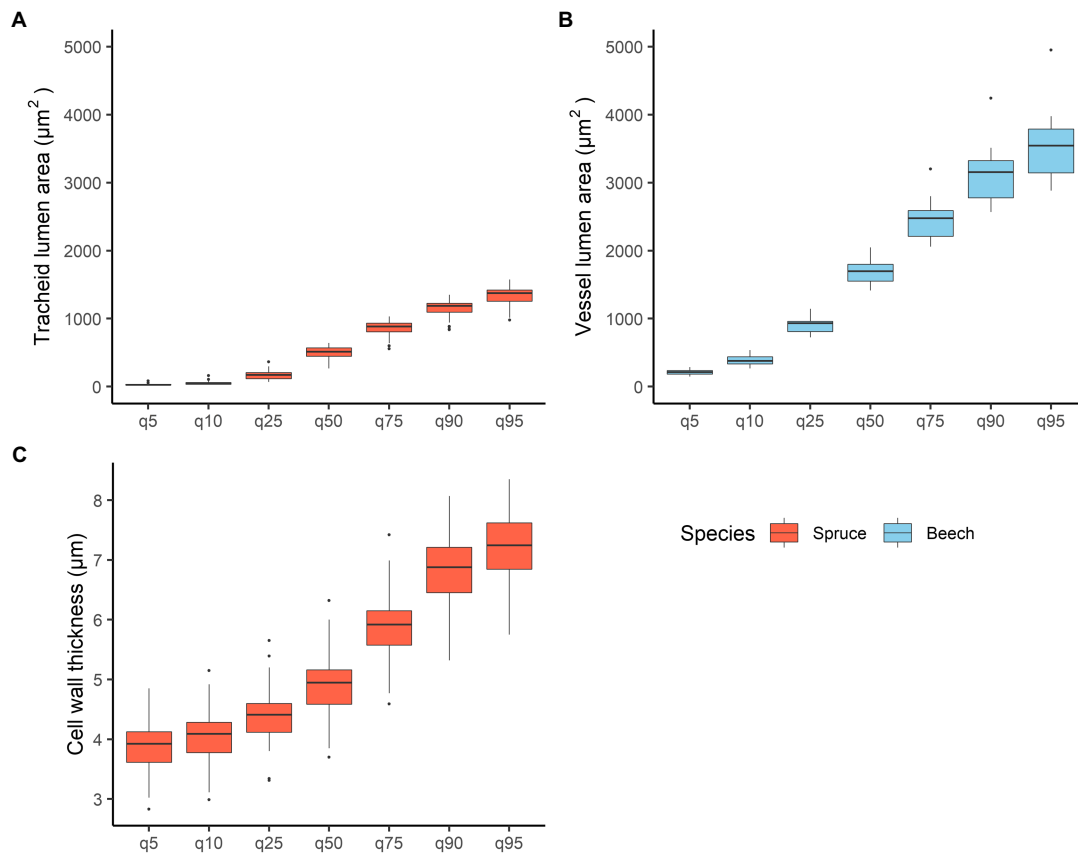


**FIGURE 4 |** Variation in (A) mean spruce tracheid lumen area, (B) mean beech vessel lumen area, and (C) mean tracheid cell wall thickness within the 5th, 10th, 25th, 75th, 90th, and 95th quantiles. Quantiles were calculated on 7 cm wood samples for both species.

## Variability in Resistance Drilling Density in Spruce and Beech

For spruce, the resistance drilling density ranged from  $277 \pm 31$  to  $365 \pm 27 \text{ kg/m}^3$  (mean  $\pm$  standard deviation). The lowest and highest measured values ranged from 219 to 341 and 304 to  $403 \text{ kg/m}^3$ , respectively. The mean resistance drilling density of spruce was  $320 \text{ kg/m}^3$  (Figure 5). In beech, resistance drilling density ranged from  $414 \pm 34$  to  $475 \pm 48 \text{ kg/m}^3$ . The lowest and highest measured values ranged from 354 to 493 and 396 to  $555 \text{ kg/m}^3$ , respectively. The mean resistance drilling density of beech was  $441 \text{ kg/m}^3$ .

## Relationships Between Resistance Drilling Density and Wood-Anatomical Features

In spruce, mean resistance drilling density increased with increasing TRW, but this relationship was not significant. In addition, a non-significant positive relationship was found between drilling density and LWW. Most of the analyzed wood-anatomical features showed no significant relationship with drilling density. A weak negative relationship ( $p < 0.1$ ) was found between drilling density and mean tracheid lumen area. While a significant negative relationship was found between drilling density and the tangential lumen diameter of tracheids, i.e., when tangential

lumen diameter or area of tracheid's increased, measured resistance drilling density decreased (Figure 6; Supplementary Table 4).

When evaluating the relationships with the nearly maximum resistance drilling density values (90th quantile), the correlations with LWW and TWW + LWW were positive and significant, while correlations with tracheid DTAN were significantly negative (Supplementary Table 2). Furthermore, weak ( $p < 0.1$ ) and significantly negative relationships were found for mean tracheid area and relative conductive area, i.e., resistance drilling density decreased with increasing mean tracheid lumen area and relative conductive area (Figure 7; Supplementary Tables 2, 5).

In beech, there was no clear relationship between resistance drilling density and TRW. Furthermore, no relationships were found between resistance drilling density and wood-anatomical features over the examined length (Figure 8; Supplementary Table 6). The results were similar whether maximum or minimum resistance drilling density values were evaluated.

## DISCUSSION

We confirmed our first hypothesis on the significant relationships between tree ring (i.e., TRW and ratio of EWW to LWW)



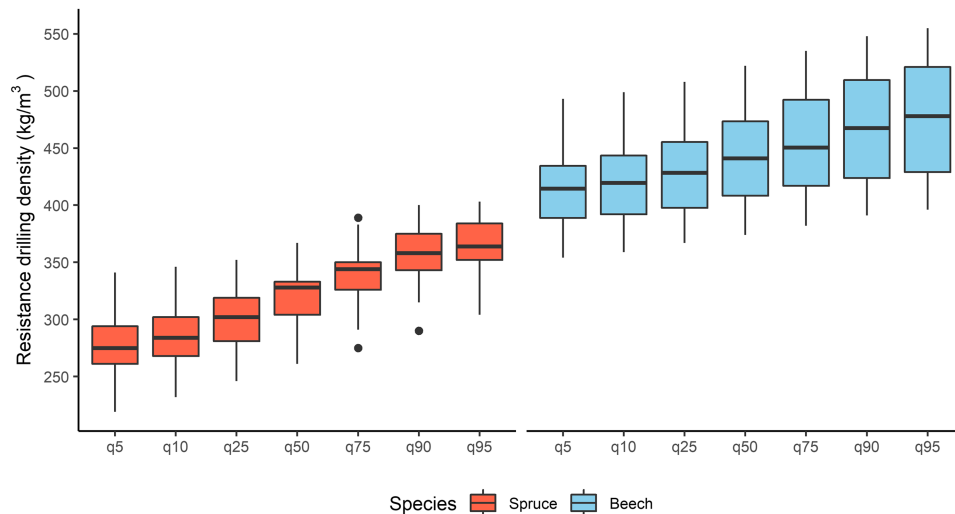


**FIGURE 5 |** Variation in mean resistance drilling density values for spruce and beech and variation within the 5th, 10th, 25th, 75th, 90th, and 95th quantiles.

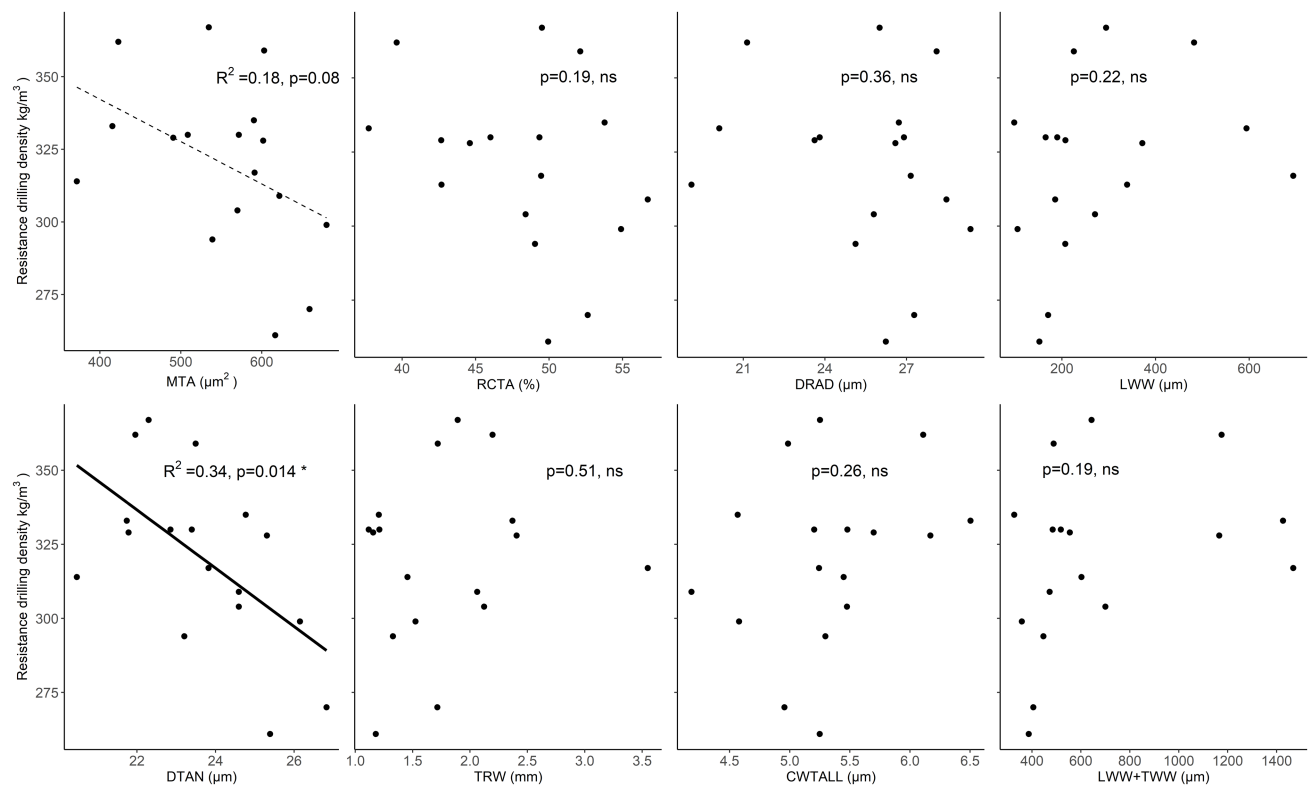


**FIGURE 6 |** Relationships between resistance drilling density values and wood-anatomical features (MTA—mean lumen area, RCTA—relative conducting area, DRAD—radial lumen diameter, LWW—latewood width, DTAN—tangential lumen diameter, TRW—tree-ring width, CWTALL—mean tracheid wall thickness, and TWW+LWW—the total width of transition wood and latewood) in spruce. Weak relationships ( $p < 0.1$ ) between wood-anatomical features and resistance drilling density are marked with a dotted line, while significant relationships ( $p < 0.05$ ) are shown by a full line. Further statistical information for the presented linear models is given in **Supplementary Table 4**.

and analyzed conduit features in both spruce and beech. In spruce, the highest correlation values were found between TRW and LWW. Among the analyzed anatomical features, radial

cell wall thickness showed the highest correlation with TRW. Surprisingly, there was no significant relationship between tracheid lumen area and TRW. In beech, vessel density was

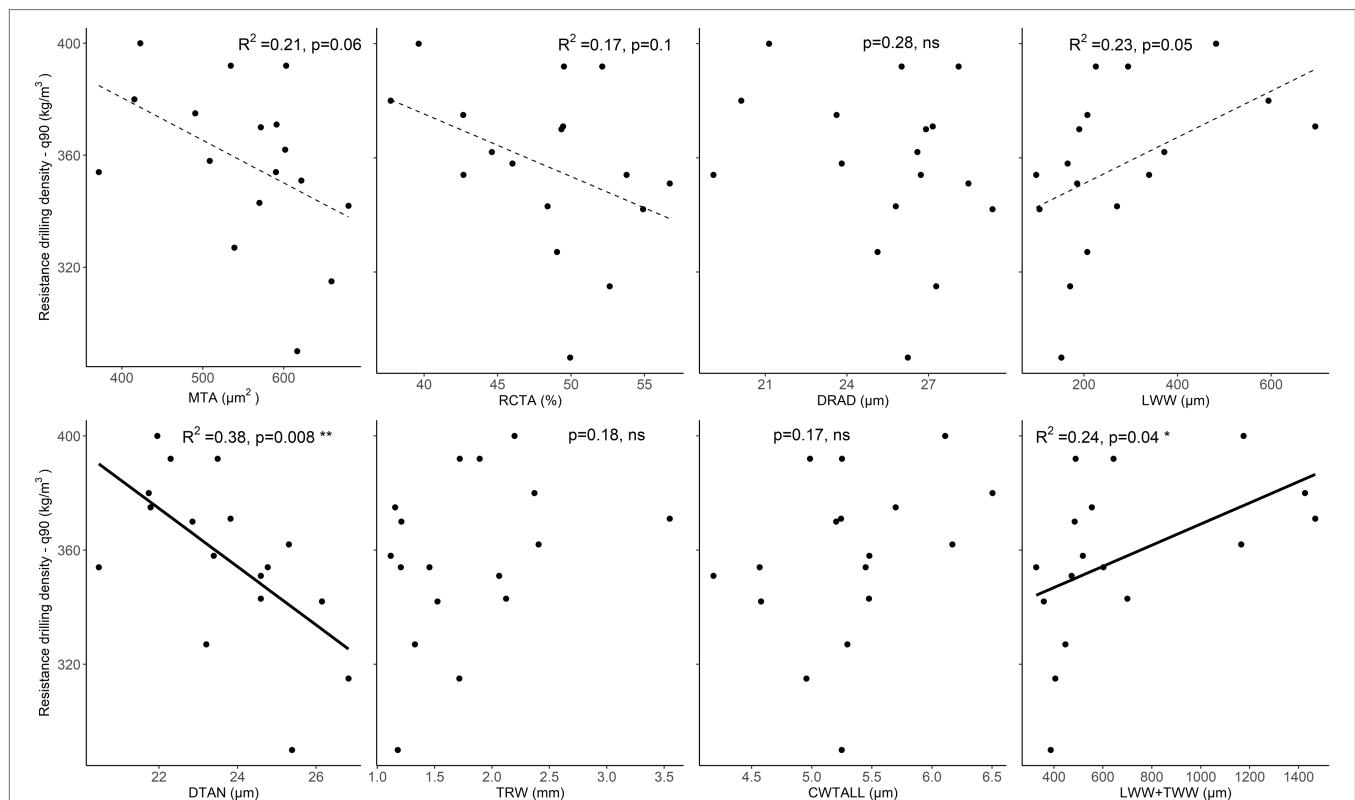


**FIGURE 7 |** Relationships between maximum resistance drilling density (90th quantile) values and wood-anatomical features (MLA—mean lumen area, RCTA—relative conducting area, DRAD—radial lumen diameter, LWW—latewood width, DTAN—tangential lumen diameter, TRW—tree-ring width, CWTALL—cell wall thickness, and TWW + LWW—the total width of transition wood and latewood) in spruce. The weak relationship ( $p > 0.1$ ) between wood-anatomical features and resistance drilling density is marked by a dotted line, while significant relationships ( $p < 0.05$ ) are shown by a full line. Further statistical information for the presented linear models is given in **Supplementary Table 5**.

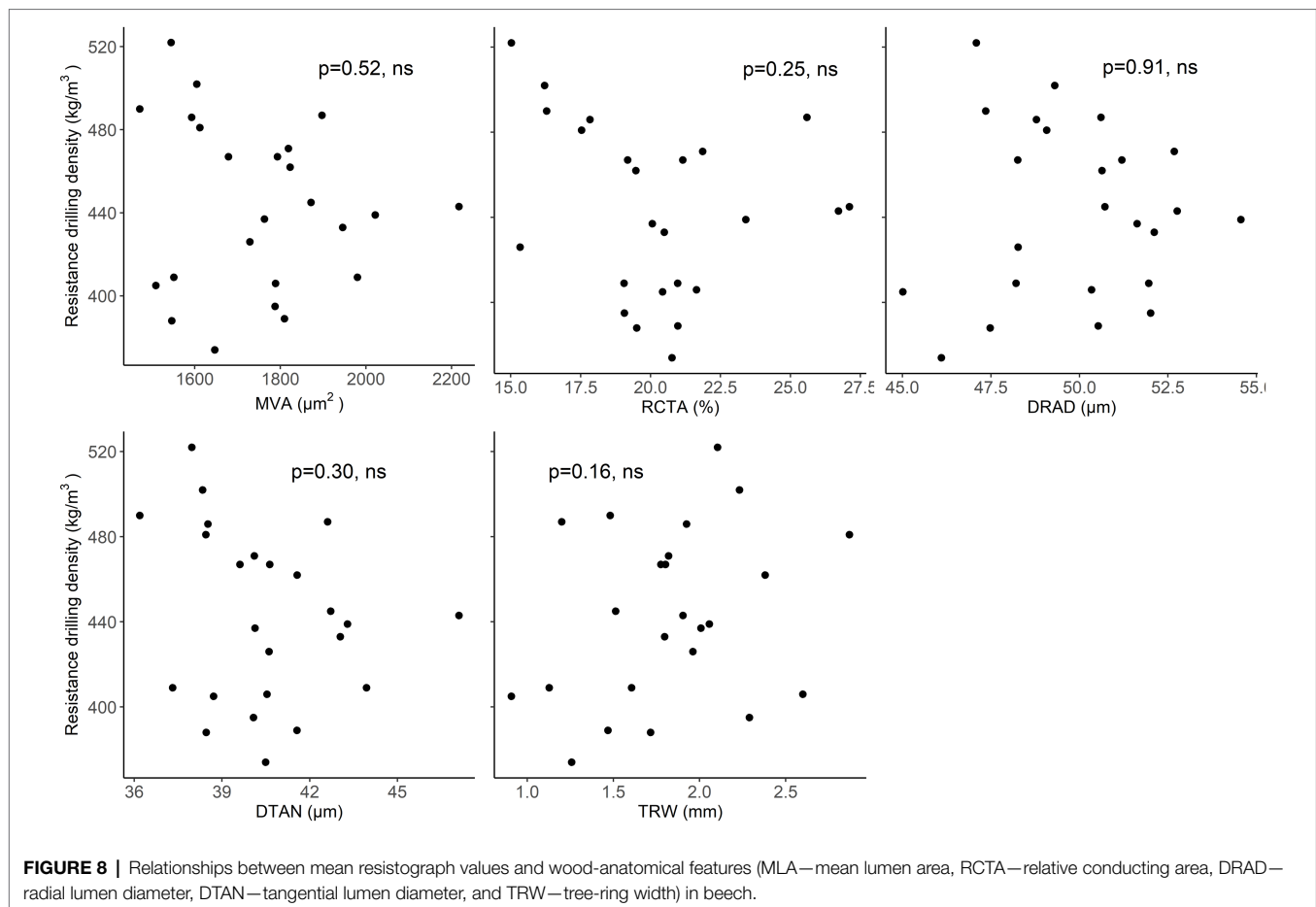
shown to have the highest influence on TRW. Our second hypothesis was confirmed only partly because there were no significant relationships between wood-anatomical features and resistance drilling density in beech. However, for spruce, a significant negative relationship was found between resistance drilling density and tangential tracheid diameter and a positive correlation with TWW + LWW and LWW.

## Relationship Between Tree Ring, Wood-Anatomical Features, and Resistance Drilling Density

When comparing the tree-ring and wood-anatomical features in beech, significant negative relationships were found between TRW and vessel density, meaning that in wider tree rings, the number of vessels is smaller. A smaller number of vessels within a growth ring is further related to a smaller relative conductive area. These relationships were also confirmed by previous studies on beech (i.e., Oladi et al., 2014; Diaconu et al., 2016b; Arnič et al., 2021). The relationship between wood anatomy and density depends on wood porosity. This would suggest that, in wider growth rings, the share of thick-walled fibers is higher, which positively affects wood density. Peters et al. (2020) found that the density of wider tree rings

in beech is higher by 0.0313 g/cm<sup>3</sup> per mm. In addition, they found that vessel density and vessel area are the main features affecting the density of tree rings. However, several studies have suggested that in diffuse-porous beech, the relationship between TRW and wood density is not significant (Bouriaud et al., 2004; Diaconu et al., 2016b), while others suggest that density decreases with increasing TRW (Pretzsch et al., 2018). The differences in results between studies can be explained by different methodological approaches; Peters et al. (2020), for example, calculated wood density based on quantitative wood anatomy data (measuring vessels and fibers but excluding parenchyma tissue) to estimate inter-annual variability in density, while Bouriaud et al. (2004) and Diaconu et al. (2016b) used X-ray densitometry. Furthermore, the differences may also be related to the high plasticity of beech, which is able to adjust vessel size and distribution (e.g., Hajek et al., 2016; Arnič et al., 2021) and cell wall thickness (e.g., Skomarkova et al., 2006; van der Maaten-Theunissen et al., 2012) depending on inter-annual variation in environmental conditions, which is reflected in the change of porosity from diffuse-porous to semi-porous (e.g., Arnič et al., 2021).

In conifers, the relationships between TRW and wood anatomy are less ambiguous, since they are mainly composed of tracheids. Increasing TRW leads to a higher proportion of



earlywood with low density, which in turn leads to lower wood density. However, these relationships can change because of the frequent presence of E type of IADFs (i.e., latewood-like cells in earlywood; Krajnc et al., 2021), whose formation is under environmental (De Micco et al., 2016) as well as genetic control (Klisz et al., 2016, 2019). In case of L type IADFs (i.e., earlywood-like cells in latewood), the density may decrease even more (e.g., Battipaglia et al., 2016). Piermattei et al. (2020) analyzed several tree-ring and wood-anatomical features in spruce; they found a strong positive relationship between TRW and earlywood width but also with the radial and tangential cell wall thickness ratio. In our study, the strongest correlation was found between TRW and transitional as well as latewood width. Our results also show that relative conductive area increases with radial and tangential tracheid diameter and decreases with radial and tangential cell wall thickness. Luostarinen et al. (2017) showed that the above-mentioned parameters affect wood density in different spruce clones.

The relationships between wood structure/anatomy and density are influenced by many other factors, such as genetics and environment, which are not yet fully understood. Consequently, the relationship between earlywood and latewood is not linear with TRW and the structure of earlywood and latewood (i.e., tracheid features) is also not homogeneous and

may change in response to various internal and external factors (Rao et al., 1997). Overall, all these changes affect the density and properties of the wood.

In our study, a significant negative correlation was found only between resistance drilling density and tangential tracheid diameter, as well as a positive correlation with TWW + LWW and LWW. In contrast, no correlation was found between wood-anatomical features and resistance drilling density in beech. The relationship between tangential tracheid diameter and resistance drilling density in spruce is probably a consequence of the drilling needle orientation when drilling in the radial direction. The major cutting surface of the needle cuts through the tracheids in the tangential direction, which is why a relationship was identified between those two factors. Such a relationship cannot be expected in diffuse-porous wood of beech due to the more variable wood structure, which varies in a smaller space than the minimum spatial resolution of the resistance drilling device to detect such changes.

### Differences Between Beech and Spruce in Resistance Drilling Density/ Wood-Anatomical Features Correlations

The above-mentioned differences in the findings between beech and spruce can thus be explained by: (i) the differences in

porosity between spruce and beech; (ii) the species-specific growth and structural response to local site conditions; and (iii) the different methodological approach.

A different methodological approach was used in this study to analyze the wood structure of spruce and beech. We focused only on analyses of the conductive cell features, i.e., the tracheids in spruce and the vessels in beech. While tracheids make up most of the wood tissue in spruce (about 95%), vessels make up 25–50% of the wood in beech (Wagenführ, 2007). Other axially oriented cells, such as fibers and axial parenchyma, account for 25–60% and 3.5–7% of wood in beech, respectively. In addition, there is also a difference between the two species in the proportion of rays, which were not included in the analyses and account for 4.4–5.5% and 11–21% of the tissue in spruce and beech, respectively (Wagenführ, 2007). These numbers show that, in the case of spruce, significantly more cells were included in the analysis (practically all of them), whereas in the case of beech, this proportion was always less than 50%, since it contained only conducting cells (i.e., vessels). The methodological approach influenced the results. We measured the relative conductive area as 50% for spruce, but 20% for beech. Because only conductive cells were included in our analyses, the values are lower than wood porosity, which is calculated from the proportions of the density of absolutely dry wood and the apparent density of cell walls ( $1.5\text{ g/cm}^3$ ; Plötze and Niemz, 2011). The calculated porosity, which includes all cell types in the wood, is 71.4% for spruce and 54.7% for beech. The low proportion of cells in beech included in the analysis undoubtedly affected the relationship between wood-anatomical features and resistance drilling density. Whether this relationship would improve in diffuse-porous beech if more cells (i.e., thick-walled fibers) were included in the analyses remains an open question for future studies.

## Potential of Resistance Drilling Measurements to Evaluate Wood Anatomy-Related Variations in Wood Density

The current study examined the possibilities of linking resistance drilling density to wood anatomy over a relatively short length of seven centimeters. Very few links were found and most of them were not very pronounced. Better relationships could perhaps be obtained if the data were examined over a fixed number of tree rings. However, this was not possible due to big differences in TRW between trees; a fixed length was therefore chosen instead. Poor relationships between wood-anatomical features and resistance drilling density are most likely related to the resolution of the resistance drilling device. Although the device used in the current study records a measurement of resistance drilling density every 1/100 of a millimeter, this measurement is an amalgamation of the measurements of two cutting surfaces of the drilling needle. The needle cuts wood along two different axes, being shaped like a triangle, with the leading spike in the middle. The practical spatial resolution of the device is therefore partly dictated by the height of the spike above the flat cutting

surface (in our case, around 0.5 mm), any features smaller than that will probably not be detected accurately. This also explains why some relationships were found in spruce and none in beech, since spruce wood is more homogenous and does not vary considerably within the practical resolution size of the device. The relationships would probably improve if a different needle shape, with only one cutting surface, was used, as examined by Sharapov et al. (2020) and as mentioned by evaluating these relationships by including measurements of fiber features. The typical needle shape (triangular with a leading spike) used by default in most resistance drilling devices nowadays makes them less appropriate for directly linking their measurements to wood anatomy. New and upgraded needle head shapes should first be explored in conifers, since their wood structure, in terms of different cell types, is less complex than that of broadleaves due to being evolutionarily older and the interpretation of potential relationships is therefore simpler.

Since wood density in conifers mainly depends on the average size and amount of wall material fixed in the tracheids (Björklund et al., 2017), the relationships between resistance drilling density and wood-anatomical features in conifers should be relatively straightforward (i.e., if the frequency of IADSs is minimal)—assuming that the shape of the needle head is adjusted to minimize interferences from the drilling process and to maximize measurement sensitivity. Different lengths over which resistance drilling density and anatomical features are being linked should also be explored in future research, to reduce the impact of localized changes in TRW and, consequently, the amount of wall material fixed in tracheids, on these relationships. In addition, TRW of analyzed trees should be comparable or at least accounted for in future studies.

## CONCLUSION

In our study, the relationships between tree-ring width, wood anatomy, and resistance drilling density were demonstrated by using material-centered approach. The increment width and wood anatomy data were presented only for the first 7 cm of the collected cores because it was not possible to synchronize wood anatomy data and resistance drilling density at annual levels. In general, the relationships between increment widths and wood-anatomical features show similar results when compared to studies conducted at the annual level. Resistance drilling densities showed weak correlations with anatomical features in spruce and no correlations in beech. Resistance drilling density measurements have been shown to be a rapid and reliable means of assessing differences in wood density between species or even within species (Krajnc et al., 2022). We propose to improve resistance drilling density measurements to increase resolution and accuracy so that we can assess variation at the intra-annual level. In addition, the methodology should be compared with other established methods, such as x-ray density measurements. If possible, different x-ray devices should be used to also assess potential differences in density



measurements between devices. Furthermore, the quantitative wood anatomy measurements and analysis should also be synchronized; namely, in the case of beech, only conducting cells were analyzed, while in the case of spruce, all tracheids were considered in the analysis. Such studies would improve our understanding of how environmental conditions affect tree ring and wood-anatomical features, as well as density as the main wood quality indicator.

## DATA AVAILABILITY STATEMENT

The raw data supporting the conclusions of this article will be made available by the authors, without undue reservation.

## AUTHOR CONTRIBUTIONS

PP, JG, LK, and DA planned and designed the research and wrote the manuscript. DA, PP, and LK performed the sampling. DA contributed to the sample preparation and capturing of high-resolution images with light microscope and analysis with Roxas and Image-Pro Plus. DA and LK performed and analyzed

the resistograph drilling measurements. All authors contributed to the article and approved the submitted version.

## FUNDING

This work was supported by the Slovenian Research Agency, young researchers' program (DA), program P4-0107 and P4-0430, and projects Z4-7318 and J4-2541.

## ACKNOWLEDGMENTS

The authors thank Neža Špenko and Gregor Skoberne for their help in the laboratory. We also to thank companies Slovenski državni gozdovi d.o.o. and Metropolitana d.o.o. for their support in the field.

## SUPPLEMENTARY MATERIAL

The Supplementary Material for this article can be found online at: <https://www.frontiersin.org/articles/10.3389/fpls.2022.872950/full#supplementary-material>

## REFERENCES

- Arnič, D., Gričar, J., Jevšenak, J., Božič, G., von Arx, G., and Prislan, P. (2021). Different wood anatomical and growth responses in European beech (*Fagus sylvatica* L.) at three Forest sites in Slovenia. *Front. Plant Sci.* 12:229. doi: 10.3389/fpls.2021.669229
- Baker, T. R., Phillips, O. L., Malhi, Y., Almeida, S., Arroyo, L., Di Fiore, A., et al. (2004). Variation in wood density determines spatial patterns in Amazonian forest biomass. *Glob. Chang. Biol.* 10, 545–562. doi: 10.1111/j.1365-2486.2004.00751.x
- Battipaglia, G., Campelo, F., Vieira, J., Grabner, M., De Micco, V., Nabais, C., et al. (2016). Structure and function of intra-annual density fluctuations: mind the gaps. *Front. Plant Sci.* 7:595. doi: 10.3389/fpls.2016.00595
- Bergsten, U., Lindeberg, J., Rindby, A., and Evans, R. (2001). Batch measurements of wood density on intact or prepared drill cores using x-ray microdensitometry. *Wood Sci. Technol.* 35, 435–452. doi: 10.1007/s002260100106
- Björklund, J., Seftigen, K., Schweingruber, F., Fonti, P., von Arx, G., Bryukhanova, M. V., et al. (2017). Cell size and wall dimensions drive distinct variability of earlywood and latewood density in northern hemisphere conifers. *New Phytol.* 216, 728–740. doi: 10.1111/nph.14639
- Björklund, J., von Arx, G., Fonti, P., Stridbeck, P., De Mil, T., Neycken, A., et al. (2021). The utility of bulk wood density for tree-ring research. *Dendrochronologia* 69:125880. doi: 10.1016/j.dendro.2021.125880
- Bošela, M., Sedmák, R., Sedmáková, D., Marušák, R., and Kulla, L. (2014). Temporal shifts of climate-growth relationships of Norway spruce as an indicator of health decline in the Beskids, Slovakia. *For. Ecol. Manag.* 325, 108–117. doi: 10.1016/j.foreco.2014.03.055
- Bosshard, H. (1982). *Holzkunde. Band 1: Mikroskopie und Makroskopie des Holzes*. Basel: Birkhauser Verlag.
- Bouriaud, O., Bréda, N., Le Moguédec, G., and Nepveu, G. (2004). Modelling variability of wood density in beech as affected by ring age, radial growth and climate. *Trees* 18, 264–276. doi: 10.1007/s00468-003-0303-x
- Bouriaud, O., Teodosiu, M., Kiryanov, A. V., and Wirth, C. (2015). Influence of wood density in tree-ring-based annual productivity assessments and its errors in Norway spruce. *Biogeosciences* 12, 6205–6217. doi: 10.5194/bg-12-6205-2015
- Castagneri, D., Fonti, P., von Arx, G., and Carrer, M. (2017). How does climate influence xylem morphogenesis over the growing season? Insights from long-term intra-ring anatomy in *Picea abies*. *Ann. Bot.* 119, 1011–1020. doi: 10.1093/aob/mcw274
- Čermák, P., Rybníček, M., Žid, T., Steffenrem, A., and Kolář, T. (2019). Site and age-dependent responses of *Picea abies* growth to climate variability. *Eur. J. For. Res.* 138, 445–460. doi: 10.1007/s10342-019-01182-6
- Chave, J., Coomes, D., Jansen, S., Lewis, S. L., Swenson, N. G., and Zanne, A. E. (2009). Towards a worldwide wood economics spectrum. *Ecol. Lett.* 12, 351–366. doi: 10.1111/j.1461-0248.2009.01285.x
- Chave, J., Muller-Landau, H. C., Baker, T. R., Easdale, T. A., Steege, H. T., and Webb, C. O. (2006). Regional and phylogenetic variation of wood density across 2456 neotropical tree species. *Ecol. Appl.* 16, 2356–2367. doi: 10.1890/1051-0761(2006)016[2356:RAPVOW]2.0.CO;2
- Cornes, R. C., van der Schrier, G., van den Besselaar, E. J. M., and Jones, P. D. (2018). An ensemble version of the E-OBS temperature and precipitation data sets. *J. Geophys. Res. Atmos.* 123, 9391–9409. doi: 10.1029/2017jd028200
- De Micco, V., Campelo, F., De Luis, M., Bräuning, A., Grabner, M., Battipaglia, G., et al. (2016). Intra-annual density fluctuations in tree rings: how, when, where, and why? *IAWA J.* 37, 232–259. doi: 10.1163/22941932-20160132
- Denne, M. P. (1989). Definition of latewood according to Mork (1928). *IAWA J.* 10, 59–62. doi: 10.1163/22941932-90001112
- Diaconu, D., Stangler, D. F., Kahle, H.-P., and Spiecker, H. (2016a). Vessel plasticity of European beech in response to thinning and aspect. *Tree Physiol.* 36, 1260–1271. doi: 10.1093/treephys/tpw053
- Diaconu, D., Wassenberg, M., and Spiecker, H. (2016b). Variability of European beech wood density as influenced by interactions between tree-ring growth and aspect. *Forest Ecosys.* 3:6. doi: 10.1186/s40663-016-0065-8
- Eder, M., Jungnickl, K., and Burgert, I. (2009). A close-up view of wood structure and properties across a growth ring of Norway spruce (*Picea abies* [L.] karst.). *Trees* 23, 79–84. doi: 10.1007/s00468-008-0256-1
- Fromm, J. R. H., Sautter, I., Matthies, D., Kremer, J., Schumacher, P., and Ganter, C. (2001). Xylem water content and wood density in spruce and oak trees detected by high-resolution computed tomography. *Plant Physiol.* 127, 416–425. doi: 10.1104/pp.010194
- Fundova, I., Funda, T., and Wu, H. X. (2018). Non-destructive wood density assessment of scots pine (*Pinus sylvestris* L.) using Resistograph and Pilodyn. *PLoS One* 13:e0204518. doi: 10.1371/journal.pone.0204518
- Gao, S., Wang, X., Wiemann, M. C., Brashaw, B. K., Ross, R. J., and Wang, L. (2017). A critical analysis of methods for rapid and nondestructive

- determination of wood density in standing trees. *Ann. For. Sci.* 74:27. doi: 10.1007/s13595-017-0623-4
- Gao, J., Yang, B., Peng, X., and Rossi, S. (2021). Tracheid development under a drought event producing intra-annual density fluctuations in the semi-arid China. *Agric. For. Meteorol.* 308–309:108572. doi: 10.1016/j.agrformet.2021.108572
- Gärtner, H., Lucchinetti, S., and Schweingruber, F. H. (2015). A new sledge microtome to combine wood anatomy and tree-ring ecology. *IAWA J.* 36, 452–459. doi: 10.1163/22941932-20150114
- Gričar, J., Prislan, P., De Luis, M., Gryc, V., Hacurowa, J., Vavřík, H., et al. (2015). Plasticity in variation of xylem and phloem cell characteristics of Norway spruce under different local conditions. *Front. Plant Sci.* 6:730. doi: 10.3389/fpls.2015.00730
- Hajek, P., Kurjak, D., von Wühlisch, G., Delzon, S., and Schuldt, B. (2016). Intraspecific variation in wood anatomical, hydraulic, and foliar traits in ten European beech provenances differing in growth yield. *Frontiers. Plant Sci.* 7:791. doi: 10.3389/fpls.2016.00791
- Jevšenak, J., Tychkov, I., Gričar, J., Levanič, T., Tumajer, J., Prislan, P., et al. (2021). Growth-limiting factors and climate response variability in Norway spruce (*Picea abies* L.) along an elevation and precipitation gradients in Slovenia. *Int. J. Biometeorol.* 65, 311–324. doi: 10.1007/s00484-020-02033-5
- Klisz, M., Koprowski, M., Ukalska, J., and Nabais, C. (2016). Does the genotype have a significant effect on the formation of intra-annual density fluctuations? A case study using larch decidua from Northern Poland. *Front. Plant Sci.* 7:691. doi: 10.3389/fpls.2016.00691
- Klisz, M., Ukalska, J., Koprowski, M., Tereba, A., Puchalka, R., Przybylski, P., et al. (2019). Effect of provenance and climate on intra-annual density fluctuations of Norway spruce *Picea abies* (L.) karst. In Poland. *Agric. For. Meteorol.* 269, 145–156. doi: 10.1016/j.agrformet.2019.02.013
- Krajnc, L., Hafner, P., and Gričar, J. (2021). The effect of bedrock and species mixture on wood density and radial wood increment in pubescent oak and black pine. *For. Ecol. Manag.* 481:118753. doi: 10.1016/j.foreco.2020.118753
- Krajnc, L., Prislan, P., Božič, G., Westergren, M., Arnič, D., Matyas, C., et al. (2022). A comparison of radial increment and wood density from beech provenance trials in Slovenia and Hungary. *Euro. J. For. Res.* (in press).
- Lesar, B., and Humar, M. (2011). Use of wax emulsions for improvement of wood durability and sorption properties. *Europ. J. Wood Prod.* 69, 231–238. doi: 10.1007/s00107-010-0425-y
- Lindner, M., Maroschek, M., Netherer, S., Kremer, A., Barbati, A., Garcia-Gonzalo, J., et al. (2010). Climate change impacts, adaptive capacity, and vulnerability of European forest ecosystems. *For. Ecol. Manag.* 259, 698–709. doi: 10.1016/j.foreco.2009.09.023
- Luostarinen, K., Pikkariainen, L., Ikonen, V.-P., Gerendiain, A. Z., Pulkkinen, P., and Peltola, H. (2017). Relationships of wood anatomy with growth and wood density in three Norway spruce clones of Finnish origin. *Can. J. For. Res.* 47, 1184–1192. doi: 10.1139/cjfr-2017-0025
- Martinez del Castillo, E., Prislan, P., Gričar, J., Gryc, V., Merela, M., Giaghi, K., et al. (2018). Challenges for growth of beech and co-occurring conifers in a changing climate context. *Dendrochronologia* 52, 1–10. doi: 10.1016/j.dendro.2018.09.001
- Mayer, K., Grabner, M., Rosner, S., Felhofer, M., and Gierlinger, N. (2020). A synoptic view on intra-annual density fluctuations in *Abies alba*. *Dendrochronologia* 64:125781. doi: 10.1016/j.dendro.2020.125781
- Muffler, L., Weigel, R., Hackett-Pain, A. J., Klisz, M., van der Maaten, E., Wilmking, M., et al. (2020). Lowest drought sensitivity and decreasing growth synchrony towards the dry distribution margin of European beech. *J. Biogeogr.* 47, 1910–1921. doi: 10.1111/jbi.13884
- Nabais, C., Hansen, J. K., David-Schwartz, R., Klisz, M., López, R., and Rozenberg, P. (2018). The effect of climate on wood density: what provenance trials tell us? *For. Ecol. Manag.* 408, 148–156. doi: 10.1016/j.foreco.2017.10.040
- Oladi, R., Bräuning, A., and Pourtahmasi, K. (2014). “Plastic” and “static” behavior of vessel-anatomical features in oriental beech (*Fagus orientalis* Lipsky) in view of xylem hydraulic conductivity. *Trees* 28, 493–502. doi: 10.1007/s00468-013-0966-x
- Peters, R. L., von Arx, G., Nievergelt, D., Ibrom, A., Stillhard, J., Trotsiuk, V., et al. (2020). Axial changes in wood functional traits have limited net effects on stem biomass increment in European beech (*Fagus sylvatica*). *Tree Physiol.* 40, 498–510. doi: 10.1093/treephys/tpaa002
- Piermattei, A., von Arx, G., Avanzi, C., Fonti, P., Gärtner, H., Piotti, A., et al. (2020). Functional relationships of wood anatomical traits in Norway spruce. *Front. Plant Sci.* 11:683. doi: 10.3389/fpls.2020.00683
- Plötze, M., and Niemz, P. (2011). Porosity and pore size distribution of different wood types as determined by mercury intrusion porosimetry. *Europ. J. Wood Prod.* 69, 649–657. doi: 10.1007/s00107-010-0504-0
- Preston, K. A., Cornwell, W. K., and DeNoyer, J. L. (2006). Wood density and vessel traits as distinct correlates of ecological strategy in 51 California coast range angiosperms. *New Phytol.* 170, 807–818. doi: 10.1111/j.1469-8137.2006.01712.x
- Pretzsch, H., Biber, P., Schütze, G., Kemmerer, J., and Uhl, E. (2018). Wood density reduced while wood volume growth accelerated in central European forests since 1870. *For. Ecol. Manag.* 429, 589–616. doi: 10.1016/j.foreco.2018.07.045
- Prislan, P., Gričar, J., de Luis, M., Smith, K. T., and Čufar, K. (2013). Phenological variation in xylem and phloem formation in *Fagus sylvatica* from two contrasting sites. *Agric. For. Meteorol.* 180, 142–151. doi: 10.1016/j.agrformet.2013.06.001
- Prislan, P., Martinez Del Castillo, E., Skoberne, G., Špenko, N., and Gričar, J. (2022). Dendrochronologia's tutoring recipes: sample preparation protocol for wood and phloem formation analyses. *Dendrochronologia* in press.
- R Core Team (2021). “A Language and Environment for Statistical Computing”. (Vienna, Austria: R Foundation for Statistical Computing).
- Rao, R. V., Aebischer, D. P., and Denne, M. P. (1997). Latewood density in relation to wood fibre diameter, wall thickness, and fibre and vessel percentages in *Quercus robur* L. *IAWA J.* 18, 127–138. doi: 10.1163/22941932-90001474
- Rathgeber, C. B. K. (2017). Conifer tree-ring density inter-annual variability – anatomical, physiological and environmental determinants. *New Phytol.* 216, 621–625. doi: 10.1111/nph.14763
- Ross, R. J. (2010). Wood handbook: wood as an engineering material. Centennial ed. general technical report FPL-GTR-190. Madison, U.S. Department of Agriculture, Forest Service, Forest Products Laboratory: 508.
- Samusevich, A., Lexa, M., Vejstková, M., Altman, J., and Zeidler, A. (2020). Comparison of methods for the demarcation between earlywood and latewood in tree rings of Norway spruce. *Dendrochronologia* 60:125686. doi: 10.1016/j.dendro.2020.125686
- Sharapov, E., Brischke, C., Militz, H., and Smirnova, E. (2020). Combined effect of wood moisture content, drill bit rotational speed and feed rate on drilling resistance measurements in Norway spruce (*Picea abies* (L.) karst.). *Wood Mat. Sci. Eng.* 15, 198–204. doi: 10.1080/17480272.2018.1557249
- Skomarkova, M. V., Vaganov, E. A., Mund, M., Knohl, A., Linke, P., Boerner, A., et al. (2006). Inter-annual and seasonal variability of radial growth, wood density and carbon isotope ratios in tree rings of beech (*Fagus sylvatica*) growing in Germany and Italy. *Trees-Struct. Func.* 20, 571–586. doi: 10.1007/s00468-006-0072-4
- Stangler, D. F., Kahle, H.-P., Raden, M., Larysch, E., Seifert, T., and Spiecker, H. (2021). Effects of intra-seasonal drought on kinetics of tracheid differentiation and seasonal growth dynamics of Norway spruce along an elevational gradient. *Forests* 12:274. doi: 10.3390/f12030274
- Swenson, N. G., and Enquist, B. J. (2008). The relationship between stem and branch wood specific gravity and the ability of each measure to predict leaf area. *Am. J. Bot.* 95, 516–519. doi: 10.3732/ajb.95.4.516
- van der Maaten, E., van der Maaten-Theunissen, M., and Spiecker, H. (2012). Temporally resolved intra-annual wood density variations in European beech (*Fagus sylvatica* L.) as affected by climate and aspect. *Ann. For. Res.* 55, 113–124.
- van der Maaten-Theunissen, M., Boden, S., and van der Maaten, E. (2012). Wood density variations of Norway spruce (*Picea abies* (L.) karst.) under contrasting climate conditions in southwestern Germany. *Ann. For. Res.* 56, 91–103.
- Vitasse, Y., Bresson, C. C., Kremer, A., Michalet, R., and Delzon, S. (2010). Quantifying phenological plasticity to temperature in two temperate tree species. *Funct. Ecol.* 24, 1211–1218. doi: 10.1111/j.1365-2435.2010.01748.x
- von Arx, G., and Carrer, M. (2014). ROXAS – A new tool to build centuries-long tracheid-lumen chronologies in conifers. *Dendrochronologia* 32, 290–293. doi: 10.1016/j.dendro.2013.12.001
- von Arx, G., Crivellaro, A., Prendin, A. L., Cufar, K., and Carrer, M. (2016). Quantitative wood anatomy - practical guidelines. *Front. Plant Sci.* 7:781. doi: 10.3389/fpls.2016.00781

Wagenführ, R. (2007). *Holzatlas*. Leipzig: Fachbuchverlag Leipzig.

Zheng, J., Zhao, X., Morris, H., and Jansen, S. (2019). Phylogeny best explains latitudinal patterns of xylem tissue fractions for woody angiosperm species across China. *Front. Plant Sci.* 10:556. doi: 10.3389/fpls.2019.00556

**Conflict of Interest:** The authors declare that the research was conducted in the absence of any commercial or financial relationships that could be construed as a potential conflict of interest.

**Publisher's Note:** All claims expressed in this article are solely those of the authors and do not necessarily represent those of their affiliated organizations,

or those of the publisher, the editors and the reviewers. Any product that may be evaluated in this article, or claim that may be made by its manufacturer, is not guaranteed or endorsed by the publisher.

Copyright © 2022 Arnič, Krajnc, Gričar and Prislan. This is an open-access article distributed under the terms of the Creative Commons Attribution License (CC BY). The use, distribution or reproduction in other forums is permitted, provided the original author(s) and the copyright owner(s) are credited and that the original publication in this journal is cited, in accordance with accepted academic practice. No use, distribution or reproduction is permitted which does not comply with these terms.



# Applications of a Hyperspectral Imaging System Used to Estimate Wheat Grain Protein: A Review

Junjie Ma<sup>1</sup>, Bangyou Zheng<sup>2</sup> and Yong He<sup>1\*</sup>

<sup>1</sup> Institute of Environment and Sustainable Development in Agriculture, Chinese Academy of Agricultural Sciences, Beijing, China, <sup>2</sup> CSIRO Agriculture and Food, Queensland Bioscience Precinct, St. Lucia, QLD, Australia

## OPEN ACCESS

### Edited by:

Roger Deal,  
Emory University, United States

### Reviewed by:

Monica Moroni,  
DICEA-Sapienza University of Rome,  
Italy  
Davide Cammarano,  
Aarhus University, Denmark

### \*Correspondence:

Yong He  
heyong01@caas.cn

### Specialty section:

This article was submitted to  
Technical Advances in Plant Science,  
a section of the journal  
Frontiers in Plant Science

**Received:** 16 December 2021

**Accepted:** 10 March 2022

**Published:** 08 April 2022

### Citation:

Ma J, Zheng B and He Y (2022)  
Applications of a Hyperspectral  
Imaging System Used to Estimate  
Wheat Grain Protein: A Review.  
Front. Plant Sci. 13:837200.  
doi: 10.3389/fpls.2022.837200

Recent research advances in wheat have focused not only on increasing grain yields, but also on establishing higher grain quality. Wheat quality is primarily determined by the grain protein content (GPC) and composition, and both of these are affected by nitrogen (N) levels in the plant as it develops during the growing season. Hyperspectral remote sensing is gradually becoming recognized as an economical alternative to traditional destructive field sampling methods and laboratory testing as a means of determining the N status within wheat. Currently, hyperspectral vegetation indices (VIs) and linear nonparametric regression are the primary tools for monitoring the N status of wheat. Machine learning algorithms have been increasingly applied to model the nonlinear relationship between spectral data and wheat N status. This study is a comprehensive review of available N-related hyperspectral VIs and aims to inform the selection of VIs under field conditions. The combination of feature mining and machine learning algorithms is discussed as an application of hyperspectral imaging systems. We discuss the major challenges and future directions for evaluating and assessing wheat N status. Finally, we suggest that the underlying mechanism of protein formation in wheat grains as determined by using hyperspectral imaging systems needs to be further investigated. This overview provides theoretical and technical support to promote applications of hyperspectral imaging systems in wheat N status assessments; in addition, it can be applied to help monitor and evaluate food and nutrition security.

**Keywords:** hyperspectral imaging, wheat, grain protein, vegetation index, machine learning

## INTRODUCTION

Wheat accounts for 21% of global food crops, with a production of 766 million tons in 2019 (FAO, 2020), and it is one of the most important foods for human survival. The viscoelastic properties of dough made with wheat allow it to be formed into a variety of baked goods, which require the highest possible flour quality. Grain protein concentration (GPC) is the main descriptor for indicating flour quality; it affects the formation of gluten in bread production and the technological properties in baked products and determines the monetary value of wheat grain (Asseng et al., 2019). However, GPC alone may not be a suitable parameter for evaluating flour quality, which is a complex parameter and needs to be determined by combining GPC and composition characteristics (Chaudhary et al., 2016).



Grain proteins are polymorphic and based on their solubility properties, can be divided into various components: albumins, globulins, gliadins, and glutenins. Albumin and globulin have high nutritional value as well as structural and metabolic functions (Shewry et al., 1995). Gliadins and glutenins are gluten proteins, and their composition is decisive for flour quality, accounting for roughly 80% of the protein in wheat flour (Shewry and Halford, 2002). Specifically, the viscosity and ductility of dough are highly influenced by gliadins, while the strength and elasticity of the dough are mainly influenced by glutenins (Wieser, 2007). Increasing the nitrogen (N) content and changing the N distribution would increase the GPC and improve the composition by changing N partitioning in the grain proteins, thus enhancing flour quality and helping to ensure food and nutrition security (Zörb et al., 2010; Xue et al., 2016).

N is absorbed throughout the growing season as an essential nutrient as illustrated in **Figure 1** (Hawkesford, 2017). It is absorbed by seedling roots to supply the seed, as the seed's reserves are rapidly exhausted. It continues to be absorbed during growth, driving the establishment of the canopy before anthesis. N uptake is highest around jointing and does not continue to rise after heading. Changes in N uptake, accumulation, and further partitioning within the plant lead to variations in the final GPC and its components (Hirel et al., 2007; Gaju et al., 2011). Differences in N uptake between the pre- and post-anthesis periods may affect N partitioning in wheat plants (Bogard et al., 2010) and the N content in the grains, as this mainly comes from two different sources: N stored in vegetative organs during the pre-flowering stage and N absorbed from the soil after flowering. Grain N is mainly remobilized from senescing canopy tissues and from the soil through the roots. Furthermore, N uptake efficiency is mainly related to the ability of the plant to maintain root activity and/or the plant's ability to regulate N uptake during the grain-filling period (Foulkes et al., 2009; Hawkesford, 2014). The process of post-anthesis N remobilization to the grain affects the final GPC and composition during grain filling (Barraclough et al., 2010; Gaju et al., 2014), with the leaves and stems being the most valuable sources of N to the grain (Gaju et al., 2014). Canopy reflectance has been widely reported to be a good indicator of the N status in wheat plants because it is related to chlorophyll (Chl) *a* and *b* content (Wang et al., 2004; Zhao et al., 2005; Reyniers and Vrindts, 2006). Therefore, studying the eco-physiological characteristics of wheat canopy N during the growth period can provide a way to obtain field information in real time for agricultural production and can inform the breeding of high-yielding and good-quality wheat.

Numerous studies have already shown the potential of hyperspectral imaging techniques to estimate the quality of wheat grain (**Figure 1**). Traditional methods of assessing wheat N status requires destruction of the plant for chemical analysis. Although this method is more accurate, it is also time-consuming and laborious. To monitor the N status in wheat plants in real time and non-invasively, hyperspectral remote sensing has gradually been applied in recent years. This new method also reflects the spatial and temporal variation of N during the growing season using appropriate algorithms, which allows for recommendations before mid-season fertilization

(Feng et al., 2008; Saberioon et al., 2014; Moharana and Dutta, 2016; Raya-Sereno et al., 2022). It is helpful for the early diagnosis of N stress, to inform remedial measures to ameliorate the stress. Moreover, it is of great significance to study the effect of environmental conditions on wheat grain quality.

Spectral data obtained from hyperspectral remote sensing instruments have a non-linear relationship with N in wheat plants. Hyperspectral vegetation indices (VIs) and machine learning are gradually being applied for the assessment of N status in wheat plants (Ranjan et al., 2012; Camps-Valls et al., 2018). The objectives of this study were (1) to investigate the existing wheat N-related hyperspectral VIs, which were inferred by hyperspectral inversion, with the aim of providing a reference method for selecting VIs in agricultural fields; (2) to summarize machine learning algorithms that can analyze field-derived hyperspectral data for wheat N status assessments; and (3) to explore the main challenges and future directions for the continued development of predicting wheat GPC and composition.

## **HYPERSPECTRAL TECHNIQUES AND CANOPY SPECTRAL VEGETATION INDICES OF NITROGEN STATUS IN WHEAT PLANTS**

Hyperspectral analysis can be used as a high-throughput phenotyping tool for assessing the N status in wheat plants during the growing season (**Figure 1**). Optical remote sensing techniques can measure eco-physiological traits in a high-throughput manner in field trials. Remote sensing of vegetation is mainly achieved by passive sensors that acquire electromagnetic wave reflection information from the canopy. It has been established that the reflectance of a wheat canopy in terms of its electromagnetic spectrum (spectral reflectance or emission characteristics of the canopy) is determined by the morphological and chemical characteristics of the leaf surface (Zhang and Kovacs, 2012). This data typically ranges from 350 to 2,500 nm, with unique reflectance value profiles in the visible (400–700 nm), near-infrared (700–1,200 nm), and short-wave infrared regions (1,200–2,500 nm), which are generally used to infer wheat plant growth characteristics (Serbin et al., 2015; Heckmann et al., 2017; Yendrek et al., 2017). Remotely-sensed data that indicate the growth, vigor, and N dynamics of a wheat canopy can provide necessary information for estimating grain quality and beneficial insights for agricultural production (Xue and Su, 2017).

In recent years, progress has been made in studying canopy spectral reflectance VIs in wheat plants with respect to N. When sunlight hits a wheat plant, most of the irradiance is consumed by water transpiration, and a small portion is used for CO<sub>2</sub> assimilation. Part of the light energy is absorbed by the canopy and a part is reflected to space. The reflected light in the visible region of the electromagnetic spectrum is influenced by the chlorophyll pigment content in the wheat canopy, which in turn is related to the concentration of leaf N (Thomas and Gausman, 1977; Wessman, 1990). Blue (450 nm) and red

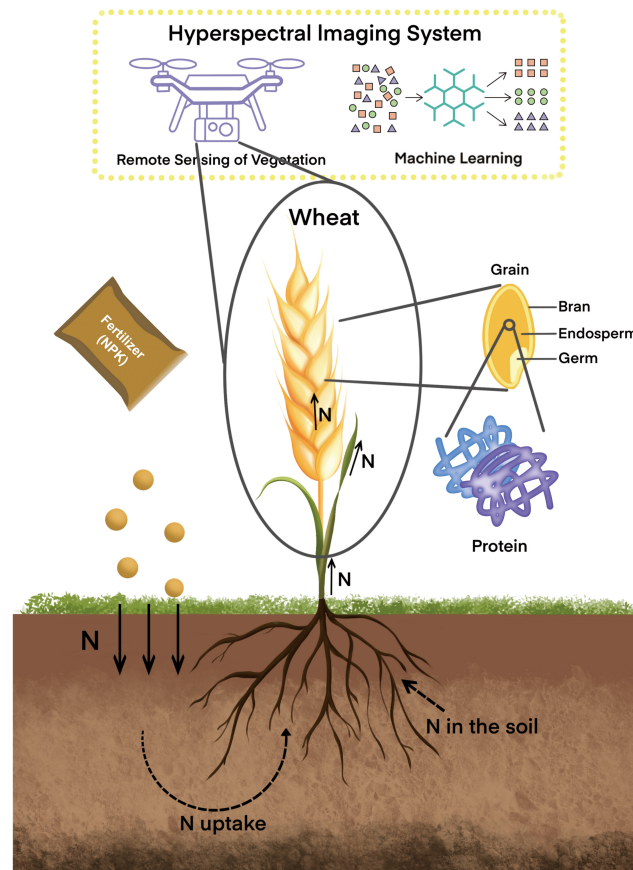


**FIGURE 1 |** It is a review of hyperspectral imaging systems for evaluating wheat grain protein. Hyperspectral imaging systems, a combination of hyperspectral remote sensing and machine learning, have significant advantages in evaluating wheat grain proteins. Hyperspectral remote sensing can capture information reflecting nitrogen (N) status in wheat plants in real-time and non-destructively. Meanwhile, machine learning can effectively simulate the non-linear relationship between nitrogen and spectral data of wheat. Hyperspectral imaging systems are now widely used to predict wheat grain protein content (GPC), and crop models can complement the analysis of eco-physiological mechanisms in the prediction process.

(670 nm) wavelengths are two major absorption bands, due to the uptake of Chl *a* and *b*, the two main leaf pigments in wheat, which account for approximately 65% of the total pigment concentration in wheat plants. Therefore, it is possible to rapidly estimate the N status of wheat plants by remotely sensing the canopy Chl content.

The VIs, which are derived from wheat canopy hyperspectral reflectance, are used to describe vegetation characteristics that depend on the environment. The list of indices in **Table 1** summarizes 20 VIs that quickly provide information on the N status of the entire wheat plant under field conditions (Gamon et al., 1997; le Maire et al., 2004; Herrmann et al., 2010). VIs for predicting Chl contents are usually based on (i) reflectance values far from the pigment absorption maxima and (ii) the selection of wavelengths close to the absorption bands. Another exciting region of the spectral area is the region between the strong red light absorption by Chl (680 nm) and the highly reflective near-infrared wavelengths (780 nm), a region of the spectrum known as the “red edge;” several red edge indices have been described (Vogelmann et al., 1993;

Filella and Penuelas, 1994; Barnes et al., 2000). In wheat plants, Chl reduction caused by N deficiency leads to increased reflectance in the visible range (400–700 nm), changing the spectral signature, which reduces symptom-specific spectral characteristics (Osborne et al., 2002). Conducting experiments under diverse ecological conditions is helpful for validating other known VIs and for developing more broadly applicable monitoring models to indirectly assess the eco-physiological traits associated with N stress (El-Hendawy S. E. et al., 2019). Rodriguez et al. (2006) tested several developed VIs for estimating the level of canopy N nutrition in wheat plants under different environmental conditions and they derived a simple canopy reflectance index entirely independent of environmental factors. A N stress-free VI was developed that adjusts shoot %N according to the plant's biomass and area; thus, it considers the environmental conditions affecting wheat growth.

Two-band VIs are increasingly used for N estimation (**Table 1**). VIs are calculated from canopy reflectance values for specific visible and near-infrared wavelengths (Frels et al., 2018). These indices can estimate changes in canopy Chl content and

**TABLE 1** | The 27 selected vegetation indices (VIs) that have been applied to wheat under field conditions were reviewed in the study, together with their number of spectral bands, band-specific formulations, and associated principal reference, including 17 two-band VIs and 10 three-band VIs.

Number of Bands	Vegetation Indices	Full Name	Formulation	References
Two-bands	CI <sub>rededge</sub>	Red Edge Model	$(R_{800}/R_{700}) - 1$	Jin et al., 2013
	EVI <sub>800,660</sub>	Enhanced Vegetation Index	$2.56 (R_{800} - R_{660}) / (1 + R_{800} + 2.4R_{660})$	Jin et al., 2013
	GI	Green Index	$R_{554}/R_{677}$	Duan et al., 2019
	NDSI <sub>860,720</sub>	Normalized Difference Spectral Indices based on the original spectrum	$(R_{860} - R_{720}) / (R_{860} + R_{720})$	Yao et al., 2010
	NDSI <sub>FD860,FD720</sub>	Normalized Difference Spectral Indices based on the First Derivative spectrum	$(FD_{860} - FD_{720}) / (FD_{860} + FD_{720})$	Yao et al., 2010
	NDVI	Normalized Differenced Vegetation Index	$(R_{790} - R_{660}) / (R_{790} + R_{660})$	Hansen and Schjoerring, 2003; Hassan et al., 2019
	NDWI	Normalized Difference Water Index	$(R_{860} - R_{1240}) / (R_{860} + R_{1240})$	Tuvdendorj et al., 2019
	NWI <sub>970,990</sub>	Normalized Water Index (R <sub>970</sub> , R <sub>990</sub> )	$(R_{970} - R_{990}) / (R_{970} + R_{990})$	Babar et al., 2006
	NWI <sub>970,850</sub>	Normalized Water Index (R <sub>970</sub> , R <sub>850</sub> )	$(R_{970} - R_{850}) / (R_{970} + R_{850})$	Babar et al., 2006
	NPCI	Normalized Pigments Chlorophyll Ratio Index	$(R_{680} - R_{430}) / (R_{680} + R_{430})$	Tan C.-W. et al., 2018
	ONLI	Optimized Non-Linear Index	$1.5(0.6R_{798}^2 - R_{728}) / (0.6R_{798}^2 + R_{728} + 0.05)$	Feng et al., 2019
	OSAVI	Optimized Soil-Adjusted Vegetation Index	$1.16 (R_{800} - R_{670}) / (R_{800} + R_{670} + 0.16)$	Jin et al., 2013
	PRI	Photochemical Reflectance Index	$(R_{531} - R_{570}) / (R_{531} + R_{570})$	Robles-Zazueta et al., 2021
	RSI <sub>990,720</sub>	Ratio Spectral Indices based on the original spectrum	$R_{990}/R_{720}$	Yao et al., 2010
	RSI <sub>FD725,FD516</sub>	Ratio Spectral Indices based on the First Derivative spectrum	$FD_{990}/FD_{720}$	Yao et al., 2010
Three-band	RVI <sub>870,660</sub>	Ratio Vegetation Index	$R_{870}/R_{660}$	Zhu et al., 2008
	RVI <sub>810,660</sub>	Ratio Vegetation Index	$R_{810}/R_{660}$	Zhu et al., 2008
	EVI	Enhanced Vegetation Index	$2.5 [(R_{900} - R_{680}) / (R_{900} + 6R_{680} - 7.5R_{475} + 1)]$	Wang et al., 2012; Robles-Zazueta et al., 2021
	MCARI <sub>705,750</sub>	Modified Chlorophyll Absorption Ratio Index calculated with reflectance from 705 to 750 nm	$[(R_{750} - R_{705}) - 0.2 (R_{750} - R_{550})] (R_{750}/R_{705})$	Wu et al., 2008
	MCARI2	Modified Chlorophyll Absorption Ratio Index Improved	$1.5[2.5(R_{803} - R_{671}) - 1.3(R_{803} - R_{549})] / \sqrt{(2R_{803} + 1)2 - (6R_{803}) - 5\sqrt{R_{671}}} - 0.5$	Haboudane et al., 2004
	mNDVI	Modified Normalized Differenced Vegetation Index	$(R_{924} - R_{703} + 2R_{423}) / (R_{924} - R_{703} - 2R_{423})$	Wang et al., 2012
	MTVI2	Modified Triangular Vegetation Index Improved	$1.5[1.2(R_{800} - R_{550}) - 2.5(R_{670} - R_{550})] / \sqrt{(2R_{800} + 1)2 - (6R_{800}) - 5\sqrt{R_{670}}} - 0.5$	Li et al., 2019
	MTCI	Medium Terrestrial Chlorophyll Index	$(R_{750} - R_{710}) / (R_{710} + R_{680})$	Tan C.-W. et al., 2018
	SIPI-1	Structure Insensitive Pigment Index-1	$(R_{800} - R_{445}) / (R_{800} - R_{680})$	Robles-Zazueta et al., 2021
	SIPI-2	Structure Insensitive Pigment Index-2	$(R_{800} - R_{435}) / (R_{415} - R_{435})$	Robles-Zazueta et al., 2021
	TCARI <sub>670,700</sub>	Transformed Chlorophyll Absorption Reflectance Index	$3 [(R_{700} - R_{670}) - 0.2 (R_{700} - R_{550}) (R_{700}/R_{670})]$	Wang et al., 2012; Wu et al., 2021
	TCARI <sub>705,750</sub>	Transformed Chlorophyll Absorption Reflectance Index calculated with reflectance from 705 to 750 nm	$3 [(R_{750} - R_{705}) - 0.2 (R_{750} - R_{550}) (R_{750}/R_{705})]$	Wu et al., 2008

$R_{\lambda}$  is the spectral reflectance of random wavelengths ( $\lambda$ );  $FD_{\lambda}$  is the corresponding derivative spectrum.

thus indicate the N status of wheat plants (Gutierrez et al., 2004). Hansen and Schjoerring (2003) used two-band combinations of the normalized vegetation index  $(\lambda_1 - \lambda_2)/(\lambda_1 + \lambda_2)$  to predict N-related crop variables at different growth stages during the winter wheat growing season in a field experiment. Zhu et al. (2008) identified common spectral bands and VIs to characterize the N status of wheat leaves and analyze the quantitative relationship between leaf N status and canopy reflectance. In their study, ratio VIs (RVIs) ( $R_{870}$ ,  $R_{660}$ ) and RVIs ( $R_{810}$ ,  $R_{660}$ ) showed the highest correlation with leaf N status compared to other specific RVIs, differential VIs (DVI), and normalized VIs (NDVIs) in the 16 bands from the MSR16 radiometer. Yao et al. (2010) conducted real-time monitoring of wheat canopy hyperspectral reflectance and leaf N status under different treatments in a field experiment. They found that the sensitive spectral bands of the leaf N status concentrated in the visible and near-infrared regions, and that NDSIs ( $R_{860}$ ,  $R_{720}$ ), RSIs ( $R_{990}$ ,  $R_{720}$ ), NDSIs ( $FD_{736}$ ,  $FD_{526}$ ), and RSIs ( $FD_{725}$ ,  $FD_{516}$ ) were the best VIs for estimating the N status in wheat plants. However, the values of VIs calculated by combining two bands were found to be closely related to the number of leaves in the canopy. A dense canopy can quickly saturate the two bands, making it less sensitive to the plant's high eco-physiological content (Gitelson, 2004). Therefore, three-band VIs were developed to solve the problem of canopy saturation that can occur in two-band VIs (Wang et al., 2012).

Selecting the optimal central bands for three-band VIs requires a comprehensive analysis of two-band VIs based on hyperspectral information (Hansen and Schjoerring, 2003; Zhu et al., 2008; Yao et al., 2010). Selecting the central band of the three-band VIs is a bandwidth issue, and is controversial in wheat plant growth monitoring. Broge and Mortensen (2002) predicted eco-physiological traits in wheat at three newton levels in the field by comparing the predictive power of broadband-based VIs with narrowband-based VIs. They concluded that narrowband-based VIs were more sensitive to changes in wheat plants during growth and more effective at minimizing noise and saturation in eco-physiological trait estimation. In contrast, Wang et al. (2012) conducted field experiments with different N levels, moisture conditions, and wheat varieties, and concluded that broadband-based VIs are more realistic. Therefore, they constructed a new three-band VI by combining narrowband-based VIs and broadband-based VIs to reduce the saturation of broadband-based two-band VIs on the basis of reality (Table 1). Based on this, a reliable and stable linear monitoring model for leaf N concentration was established, which provides a good index and an accurate estimation model for monitoring the N status in wheat plants using a three-band VI (Wang et al., 2012).

There is little agreement in previous studies on which VIs are most suitable for determining the N status in wheat plants. Main et al. (2011) investigated 73 VIs and ranked them according to their relationship with total Chl content, which is related to N. They found that indices using the red-edge region (680–730 nm) were better predictors of the N status of wheat canopy (via canopy Chl content), with a better linear relationship and lower saturation than other VIs. Frels et al. (2018) used 299 wheat genotypes in a 2-year trial near Ithaca,

NE, United States, to compare the correlation between 28 VIs inferred from canopy spectral reflectance during the grain filling stage and N-related traits in wheat plants. They concluded that it is more accurate to use VIs to estimate N traits in wheat plants during the early grain filling stage, as more traits were associated with the Maccioni index. This index captures many components of the N use efficiency. Incorporating it into the existing selection programs could yield more N-related indicators (Frels et al., 2018).

## DISSECTION OF HYPERSPECTRAL REFLECTANCE TO ESTIMATE NITROGEN STATUS IN WHEAT PLANTS BASED ON MACHINE LEARNING ALGORITHMS

Machine learning is an effective method for solving complex problems such as multicollinearity and overfitting in multiple linear models (MLMs) to estimate the N status in wheat plants (Figure 1). With the development of hyperspectral imaging systems, the amount of computation required has gradually increased. Moreover, the massive data features tend to cause overfitting and affect estimations produced by MLM. Selecting a suitable estimation method can reduce the dimensionality of the raw data, screen out necessary information from the data, significantly improve the validity of the data, and is an important aspect of improving the accuracy of N status estimation in wheat plants (Li D. et al., 2020). Most studies have used MLM to quantitatively assess the relationship between spectral indices and N status (Babar et al., 2006; Pavuluri et al., 2015). However, when many characteristic dimensions are used, the correlations between VIs and leaf N status are generally low, and the models are prone to multicollinearity and overfitting, which reduces the accuracy of the estimated N status (El-Hendawy S. et al., 2019). To address these issues, machine learning methods can reduce the wide range of co-linear variables and non-correlated factors, and reduce the impact of background effects on model precision (Singh et al., 2021).

Machine learning techniques are advantageous for estimating agricultural indices from hyperspectral remote sensing data (Zhang et al., 2021). Wheat canopy reflectance is a function of the wheat leaf's optical properties, wheat canopy structure, soil background, atmospheric conditions, observation geometry, and solar zenith angle (Boegh et al., 2002; Baret et al., 2007; Homolová et al., 2013). The relationship between canopy reflectance and wheat N status is controlled by many influencing factors. Thus, finding the response mechanism of canopy hyperspectral reflectance to the wheat N status is often complicated and nonlinear in character (Fu et al., 2021). Most machine learning algorithms are often considered "black boxes" because they provide no information about how they work. Therefore, machine learning can be used to explore the complex nonlinear relationships between spectral features and the N status in wheat plants without a clear understanding of the original data



distribution (Singh et al., 2021). This not only provides a multi-faceted and flexible direction for data analysis, but also a wider scope for experts to apply their theoretical knowledge to explain the principles in conjunction with algorithms. Previous spectral indices have depended on a few available spectral bands and, therefore, do not use all the information conveyed by the spectral trace. In contrast, machine learning techniques not only use inverse VIs but also all the spectral information, demonstrating the potential to analyze hyperspectral reflectance data with a large number of bands and to evaluate additional features. This provides more information for high-precision prediction modeling of the N status in wheat plants (Chlingaryan et al., 2018). Recently, the advantages of machine learning over VI-based approaches have been highlighted. Specifically, machine learning has excelled in modeling the complex mechanisms of canopy-scale spectral features in response to the N status in wheat plants, without the need to know the underlying data distribution (Thorpe et al., 2017; Miphokasap and Wannasiri, 2018; Tan K. et al., 2018). With the proliferation of spaceborne, airborne, and unmanned aerial vehicle (UAV) imaging spectrometers, many types of hyperspectral data are now available and has ushered in the era of “big data” in the field of remote sensing. This requires machine learning algorithms to mine available information to more effectively monitor the N status in wheat plants in real time and to predict their GPC and composition (Fu et al., 2021).

Machine learning involves various types of learning techniques. Partial least squares regression (PLSR) is a commonly used technique for estimating eco-physiological traits in wheat from hyperspectral data (Fu et al., 2014). Hansen and Schjoerring (2003) calculated NDVIs for all possible combinations of wavelengths in the range of 438–884 nm. They found that linear regression and PLSR can be used to estimate Chl and N concentrations in wheat plants. Pimstein et al. (2007) also used PLSR to estimate the N content of wheat leaves from spectral (350–2,500 nm) data collected in the field. The authors concluded that the appropriate wavelength and application of derivatives to the raw spectra could improve the predictive quality of the estimated model. Li et al. (2014) also estimated canopy N content in wheat plants using optimized hyperspectral VIs combined with PLSR. Mahesh et al. (2015) used PLSR to predict wheat GPC based on hyperspectral reflectance. In conclusion, PLSR has been applied as a method capable of analyzing a large amount of noise-laden co-linear data to monitor N content in wheat plants and predict wheat GPC in agricultural fields. Its accuracy improves with an increase in the number of relevant variables and observations (Berger et al., 2020).

In addition to PLSR, kernel-based regression methods are becoming more popular in wheat N status assessment using hyperspectral data. Machine learning algorithms require a few statistical assumptions to be applied to the data to develop linear and nonlinear models. Among them, kernel-based regression methods [e.g., support vector regression (SVR) and Gaussian process regression (GPR)] use structural risk minimization. Therefore, with a limited training set, these methods are considered to have a better generalization ability than artificial neural networks (ANNs) (Fu et al., 2020). Li et al. (2016) compared four chemometric techniques used to estimate N

status in winter wheat plants using spectral features. In their study, the predictive power and the impact of sample size were assessed. They proposed that SVR is more suitable than back-propagation neural networks (BPNN) for estimating winter wheat N concentrations when the sample size is insufficient. Different kernel functions differ in their ability to embed geometric structures in the training samples. To combine the advantages of different kernel functions, Wang et al. (2017) constructed a multiple-kernel SVR (MK-SVR) consisting of a radial basis function (RBF) kernel and polynomial kernel for N status estimation in wheat plants. They found that the MK-SVR outperformed multiple linear regression (MLR), partial least squares (PLS), ANNs, and single kernel SVR (SK-SVR) models, introducing a new method for non-destructive and rapid monitoring of the N status in wheat plants based on hyperspectral data.

Physical and hybrid methods have also been applied to wheat N-inversion. Their application is based on the high degree of correlation between leaf Chl and the N status in wheat plants, and their effectiveness depends on the radiative transfer models (RTM) used, the inversion technique applied, and the quality of the data measured (Danner et al., 2021). PROSAIL is a widely used radiative transfer model for estimating the N status in wheat because it provides a good compromise between model realism and inversion possibilities. Yang et al. (2015) developed an N-PROSPECT model to estimate the N status of the winter wheat canopy by replacing the Chl uptake coefficient with the N uptake coefficient in the original PROSPECT model. Coupling of the N-PROSPECT model and the SAIL model (N-PROSAIL) has been used to estimate canopy N density in wheat plants, and the model has been shown to have a high potential for establishing the N status in wheat plants (Li et al., 2018b, 2019). However, the ability of PROSAIL and N-PROSAIL models to characterize a non-homogenous canopy structure before complete canopy closure is poor, resulting in less accurate estimates of the N status in wheat plants (Botha et al., 2010).

## DEFICIENCIES AND PROSPECTS OF THE HYPERSPECTRAL IMAGING SYSTEM FOR ESTIMATING THE NITROGEN STATUS IN WHEAT PLANTS

The use of the hyperspectral imaging system often allows for immediate and punctuated estimates of the wheat N status over wide regions. However, there are intrinsic inevitable shortcomings in the empirical methods. Hyperspectral VIs are widely used in crop N estimation due to its simple, timely and efficient computation. Further, machine learning techniques are expected to be more suitable for simulating wheat N status from such data due to their ability to deal with nonlinear problems. Many combinations of hyperspectral VIs and machine learning algorithms have yielded improved N status estimates for wheat plants, and there have been studies modeling the relationship between VIs and GPC based on machine learning algorithms. For example, Tan et al. (2020) analyzed 14 VIs by

using PLSR and found that 12 of them were closely related to wheat GPC (model prediction accuracy > 90%). Nevertheless, PLSR was not compared with other machine learning methods in the study. Although PLSR is superior to linear regression and principal component analysis model, decision tree, random forest, artificial neural networks and other methods may have better simulation results for wheat GPC. Furthermore, the hyperspectral imaging system still needs improvement. First, the results of models calibrated with hyperspectral data are significantly influenced by seasonal characteristics, cropping environments and experimental design, which is characterized by poor spatio-temporal heterogeneity. Therefore, applying a model from one specific environment or growing season to any other environment or growing seasons may result in poor prediction results of wheat grain nutrition (Colaço and Bramley, 2018, 2019). Second, the spectral features identified by the available feature mining techniques involve statistical models and largely depend on a dataset without any inherent relationships between GPC, the environment, and management, with unclear physical meaning and poor explanation of mechanism (Li Z. et al., 2020; **Figure 1**). Some researchers have argued that as (i) wheat growth is a dynamic process and (ii) wheat canopy N status changes dynamically; a better understanding of the physical processes underlying the hyperspectral response to wheat canopy N status is required. This would enable the development of robust assessment models with causal relationships that complement the eco-physiologically hyperspectral imaging systems (Li et al., 2018a; Fu et al., 2021).

The combination of crop models and remote sensing data is emerging as a promising approach for monitoring wheat growth and grain protein accumulation. Crop models can simulate the dynamic biological processes of wheat growth based on the quantitative relationships between wheat growth and environmental conditions, including weather, soil conditions, wheat genotype information, and field management (Jin et al., 2018). Crop models combined with hyperspectral data can provide time continuity for wheat quality prediction systems. This can enable the effective development of crops based on the environment and stress conditions (water or N), improve the temporal and spatial expansion ability of wheat quality prediction, enhance the agronomic and mechanical rationality of prediction, and can be used for scenario testing and strategic (long-term) decisions (Li Z. et al., 2020). In previous studies, the transfer of N to the grain has been simulated at various levels of complexity. Both simpler harvest indexing approaches [e.g., SIRIUS (Jamieson et al., 1998) and STATISTICS (Brisson et al., 1998)] and more sophisticated source-aggregation models [e.g., SIRIUS (Jamieson and Semenov, 2000)] illustrate this evolution. The CERES-Wheat grain filling program applied independent controls for dry matter and N accumulation in the grain, dividing the grain filling process into stages. However, variation in N accumulation due to genetic variance was not considered in this procedure (Ritchie et al., 1998). APSIM-Nwheat used the same grain protein program as CERES-Wheat and applied the model to study the effect of seasonal temperature and rainfall interactions on grain N concentrations (Asseng and Milroy, 2006). Meanwhile, other

studies have proposed a framework to model the mechanisms of N uptake and partitioning in wheat plants, thus advancing toward more accurate modeling of N dynamics (Jamieson and Semenov, 2000). In recent years, crop models have been used to assess the impact of climate change on wheat GPC, however, uncertainty varies with location (Asseng et al., 2019).

In addition, the SiriusQuality model has been developed to consider the assignment of structural and storage proteins in wheat grain. Within the routine, the model divides N into structural/metabolic proteins and major storage proteins, and it provides predictions of the protein compositions, which are the alcoholic and glutenin fractions (Martre et al., 2003, 2006). The SiriusQuality model also assumes that the partitioning of N between the storage protein compositions, alcoholic, and gluten remains constant during the grain filling stage. It also assumes that the interactions between the genotype and environment alters the total grain N through source limitation rather than through partitioning of N between different protein compositions (Martre et al., 2006). This provides proof of concept that crop models can be extended to explain protein composition. In general, existing crop models can correctly simulate GPC in the absence of stress treatments; however, the performance of models under extreme temperature conditions still needs to be improved (Osman et al., 2020). In addition, some important model input parameters are difficult or impossible to obtain, and the information provided to crop models on wheat growth is limited to scattered points (Fu et al., 2021).

## CONCLUSION

An accurate assessment of the in-plant N status of wheat is essential for predicting GPC and composition, in addition to ensuring food and nutritional safety. We are at the beginning of a promising path toward using hyperspectral imaging systems to predict GPC and composition in wheat plants. On the one hand, as a high-throughput phenotypic tool, hyperspectral remote sensing has the potential to complement or even replace types of field measurements for some wheat N-related traits in the growing season. On the other hand, the combination of hyperspectral VIs and machine learning algorithms is a powerful tool for estimating agricultural indices from hyperspectral remote sensing data. However, VIs and the spectral features identified by machine learning algorithms in hyperspectral imaging systems depend heavily on the input dataset without any intrinsic relationship between GPC, the environment, and field management. Based on our review, we suggest that these issues can be understood in conjunction with crop models. Crop models consider the environmental effects of wheat growth. These methods strive to uncover the underlying mechanisms of wheat growth when using hyperspectral data to predict wheat GPC and composition. Insight into the limitations of these methods will help us select the appropriate method for monitoring the N status in wheat plants and contribute to further developing methods for wheat grain quality studies.

## AUTHOR CONTRIBUTIONS

YH: conceptualization, funding acquisition, and writing-review and editing. JM and YH: formal analysis. JM, BZ, and YH: writing the manuscript, read, and agreed to the submitted version.

## FUNDING

This research was funded by the National Natural Science Foundation of China (41975148), the Chinese Academy of

Agricultural Sciences Elite Youth Program, and the Chinese Academy of Agricultural Sciences Central Public-interest Scientific Institution Basal Research Fund (BSRF202202 and BSRF202005).

## ACKNOWLEDGMENTS

The authors are grateful to reviewers for their valuable comments and suggestions.

## REFERENCES

- Asseng, S., Martre, P., Maiorano, A., Rotter, R. P., O'Leary, G., Fitzgerald, G. J., et al. (2019). Climate change impact and adaptation for wheat protein. *Glob. Change Biol.* 25, 155–173. doi: 10.1111/gcb.14481
- Asseng, S., and Milroy, S. P. (2006). Simulation of environmental and genetic effects on grain protein concentration in wheat. *Eur. J. Agron.* 25, 119–128. doi: 10.1016/j.eja.2006.04.005
- Babar, M. A., Reynolds, M. P., van Ginkel, M., Klatt, A. R., Raun, W. R., and Stone, M. L. (2006). Spectral reflectance to estimate genetic variation for in-season biomass, leaf chlorophyll, and canopy temperature in wheat. *Crop Sci.* 46, 1046–1057. doi: 10.2135/cropsci2005.0211
- Baret, F., Houllès, V., and Guérif, M. (2007). Quantification of plant stress using remote sensing observations and crop models: the case of nitrogen management. *J. Exp. Bot.* 58, 869–880. doi: 10.1093/jxb/erl231
- Barnes, E., Clarke, T. R., Richards, S. E., Colaizzi, P., Haberland, J., Kostrzewski, M., et al. (2000). "Coincident detection of crop water stress, nitrogen status and canopy density using ground-based multispectral data," in *Proceedings of the 2000 5th International Conference on Precision Agriculture*, Bloomington, MN, 1–15. doi: 10.1094/cm-2009-1211-01-rs
- Barracough, P. B., Howarth, J. R., Jones, J., Lopez-Bellido, R., Parmar, S., Shepherd, C. E., et al. (2010). Nitrogen efficiency of wheat: genotypic and environmental variation and prospects for improvement. *Eur. J. Agron.* 33, 1–11. doi: 10.1016/j.eja.2010.01.005
- Berger, K., Verrelst, J., Féret, J.-B., Wang, Z., Woche, M., Strathmann, M., et al. (2020). Crop nitrogen monitoring: recent progress and principal developments in the context of imaging spectroscopy missions. *Remote Sens. Environ.* 242:111758. doi: 10.1016/j.rse.2020.111758
- Boegh, E., Soegaard, H., Broge, N., Hasager, C. B., Jensen, N. O., Schelde, K., et al. (2002). Airborne multispectral data for quantifying leaf area index, nitrogen concentration, and photosynthetic efficiency in agriculture. *Remote Sens. Environ.* 81, 179–193. doi: 10.1016/S0034-4257(01)00342-X
- Bogard, M., Allard, V., Brancourt-Hulmel, M., Heumez, E., Machet, J.-M., Jeuffroy, M.-H., et al. (2010). Deviation from the grain protein concentration–grain yield negative relationship is highly correlated to post-anthesis N uptake in winter wheat. *J. Exp. Bot.* 61, 4303–4312. doi: 10.1093/jxb/erq238
- Botha, E. J., Leblon, B., Zebbarth, B. J., and Watmough, J. (2010). Non-destructive estimation of wheat leaf chlorophyll content from hyperspectral measurements through analytical model inversion. *Int. J. Remote Sens.* 31, 1679–1697. doi: 10.1080/01431160902926574
- Brisson, N., Mary, B., Ripoche, D., Jeuffroy, M.-H., Ruget, F., Nicoulaud, B. B., et al. (1998). STICS: a generic model for the simulation of crops and their water and nitrogen balances. I. Theory and parameterization applied to wheat and corn. *Agronomie* 18, 311–346. doi: 10.1051/agro:19980501
- Broge, N. H., and Mortensen, J. V. (2002). Deriving green crop area index and canopy chlorophyll density of winter wheat from spectral reflectance data. *Remote Sens. Environ.* 81, 45–57. doi: 10.1016/S0034-4257(01)00332-7
- Camps-Valls, G., Martino, L., Svendsen, D. H., Campos-Taberner, M., Muñoz-Mari, J., Laparra, V., et al. (2018). Physics-aware Gaussian processes in remote sensing. *Appl. Soft Comput.* 68, 69–82. doi: 10.1016/j.asoc.2018.03.021
- Chaudhary, N., Dangi, P., and Khatkar, B. S. (2016). Relationship of molecular weight distribution profile of unreduced gluten protein extracts with quality characteristics of bread. *Food Chem.* 210, 325–331. doi: 10.1016/j.foodchem.2016.04.043
- Chlingaryan, A., Sukkari, S., and Whelan, B. (2018). Machine learning approaches for crop yield prediction and nitrogen status estimation in precision agriculture review. *Comput. Electron. Agric.* 151, 61–69. doi: 10.1016/j.compag.2018.05.012
- Colaco, A. F., and Bramley, R. G. V. (2018). Do crop sensors promote improved nitrogen management in grain crops? *Field Crops Res.* 218, 126–140. doi: 10.1016/j.fcr.2018.01.007
- Colaco, A. F., and Bramley, R. G. V. (2019). Site-Year Characteristics Have a Critical Impact on Crop Sensor Calibrations for Nitrogen Recommendations. *Agron. J.* 111, 2047–2059. doi: 10.2134/agronj2018.11.0726
- Danner, M., Berger, K., Woche, M., Mauser, W., and Hank, T. (2021). Efficient RTM-based training of machine learning regression algorithms to quantify biophysical & biochemical traits of agricultural crops. *ISPRS J. Photogramm. Remote Sens.* 173, 278–296. doi: 10.1016/j.isprsjprs.2021.01.017
- Duan, D.-D., Zhao, C.-J., Li, Z.-H., Yang, G.-J., and Yang, W.-D. (2019). Estimating total leaf nitrogen concentration in winter wheat by canopy hyperspectral data and nitrogen vertical distribution. *J. Integr. Agric.* 18, 1562–1570. doi: 10.1016/S2095-3119(19)62686-9
- El-Hendawy, S., Al-Suhaibani, N., Alotaibi, M., Hassan, W., Elsayed, S., Tahir, M. U., et al. (2019). Estimating growth and photosynthetic properties of wheat grown in simulated saline field conditions using hyperspectral reflectance sensing and multivariate analysis. *Sci. Rep.* 9:16473. doi: 10.1038/s41598-019-52802-5
- El-Hendawy, S. E., Al-Suhaibani, N. A., Hassan, W. M., Dewir, Y. H., Elsayed, S., Al-Ashkar, I., et al. (2019). Evaluation of wavelengths and spectral reflectance indices for high-throughput assessment of growth, water relations and ion contents of wheat irrigated with saline water. *Agric. Water Manage.* 212, 358–377. doi: 10.1016/j.agwat.2018.09.009
- FAO (2020). *Food and Agriculture Organization of the United Nations*. Available online at: from <http://www.fao.org/faostat/en/#data/QC> (accessed July 12, 2020).
- Feng, W., Wu, Y., He, L., Ren, X., Wang, Y., Hou, G., et al. (2019). An optimized non-linear vegetation index for estimating leaf area index in winter wheat. *Precis. Agric.* 20, 1157–1176. doi: 10.1007/s11119-019-09648-8
- Feng, W., Yao, X., Zhu, Y., Tian, Y. C., and Cao, W. X. (2008). Monitoring leaf nitrogen status with hyperspectral reflectance in wheat. *Eur. J. Agron.* 28, 394–404. doi: 10.1016/j.eja.2007.11.005
- Filella, I., and Penuelas, J. (1994). The red edge position and shape as indicators of plant chlorophyll content, biomass and hydric status. *Int. J. Remote Sens.* 15, 1459–1470. doi: 10.1080/01431169408954177
- Foulkes, M. J., Hawkesford, M. J., Barracough, P. B., Holdsworth, M. J., Kerr, S., Kightley, S., et al. (2009). Identifying traits to improve the nitrogen economy of wheat: recent advances and future prospects. *Field Crops Res.* 114, 329–342. doi: 10.1016/j.fcr.2009.09.005
- Frels, K., Guttieri, M., Joyce, B., Leavitt, B., and Baenziger, P. S. (2018). Evaluating canopy spectral reflectance vegetation indices to estimate nitrogen use traits in hard winter wheat. *Field Crops Res.* 217, 82–92. doi: 10.1016/j.fcr.2017.12.004
- Fu, Y., Yang, G., Li, Z., Li, H., Li, Z., Xu, X., et al. (2020). Progress of hyperspectral data processing and modelling for cereal crop nitrogen monitoring. *Comput. Electron. Agric.* 172:105321. doi: 10.1016/j.compag.2020.105321



- Fu, Y., Yang, G., Pu, R., Li, Z., Li, H., Xu, X., et al. (2021). An overview of crop nitrogen status assessment using hyperspectral remote sensing: current status and perspectives. *Eur. J. Agron.* 124:126241. doi: 10.1016/j.eja.2021.126241
- Fu, Y., Yang, G., Wang, J., Song, X., and Feng, H. (2014). Winter wheat biomass estimation based on spectral indices, band depth analysis and partial least squares regression using hyperspectral measurements. *Comput. Electron. Agric.* 100, 51–59. doi: 10.1016/j.compag.2013.10.010
- Gaju, O., Allard, V., Martre, P., Gouis, J. L., Moreau, D., Bogard, M., et al. (2014). Nitrogen partitioning and remobilization in relation to leaf senescence, grain yield and grain nitrogen concentration in wheat cultivars. *Field Crops Res.* 155, 213–223. doi: 10.1016/j.fcr.2013.09.003
- Gaju, O., Allard, V., Martre, P., Snape, J. W., Heumez, E., LeGouis, J., et al. (2011). Identification of traits to improve the nitrogen-use efficiency of wheat genotypes. *Field Crops Res.* 123, 139–152. doi: 10.1016/j.fcr.2011.05.010
- Gamon, J. A., Serrano, L., and Surfus, J. S. (1997). The photochemical reflectance index: an optical indicator of photosynthetic radiation use efficiency across species, functional types, and nutrient levels. *Oecologia* 112, 492–501. doi: 10.1007/s004420050337
- Gitelson, A. A. (2004). Wide Dynamic Range Vegetation Index for remote quantification of biophysical characteristics of vegetation. *J. Plant Physiol.* 161, 165–173. doi: 10.1078/0176-1617-01176
- Gutierrez, M., Reynolds, M., Escalante Estrada, J. A., and Rodríguez-González, M. (2004). Association between canopy reflectance indices and yield and physiological traits in bread wheat under drought and well-irrigated conditions. *Aust. J. Agric. Res.* 55, 1139–1147. doi: 10.1071/AR04214
- Haboudane, D., Miller, J. R., Pattey, E., Zarco-Tejada, P. J., and Strachan, I. B. (2004). Hyperspectral vegetation indices and novel algorithms for predicting green LAI of crop canopies: modeling and validation in the context of precision agriculture. *Remote Sens. Environ.* 90, 337–352. doi: 10.1016/j.rse.2003.12.013
- Hansen, P. M., and Schjoerring, J. K. (2003). Reflectance measurement of canopy biomass and nitrogen status in wheat crops using normalized difference vegetation indices and partial least squares regression. *Remote Sens. Environ.* 86, 542–553. doi: 10.1016/s0034-4257(03)00131-7
- Hassan, M. A., Yang, M., Rasheed, A., Yang, G., Reynolds, M., Xia, X., et al. (2019). A rapid monitoring of NDVI across the wheat growth cycle for grain yield prediction using a multi-spectral UAV platform. *Plant Sci.* 282, 95–103. doi: 10.1016/j.plantsci.2018.10.022
- Hawkesford, M. J. (2014). Reducing the reliance on nitrogen fertilizer for wheat production. *J. Cereal Sci.* 59, 276–283. doi: 10.1016/j.jcs.2013.12.001
- Hawkesford, M. J. (2017). Genetic variation in traits for nitrogen use efficiency in wheat. *J. Exp. Bot.* 68, 2627–2632. doi: 10.1093/jxb/erx079
- Heckmann, D., Schlüter, U., and Weber, A. P. M. (2017). Machine learning techniques for predicting crop photosynthetic capacity from leaf reflectance spectra. *Mol. Plant* 10, 878–890. doi: 10.1016/j.molp.2017.04.009
- Herrmann, I., Karnieli, A., Bonfil, D. J., Cohen, Y., and Alchanatis, V. (2010). SWIR-based spectral indices for assessing nitrogen content in potato fields. *Int. J. Remote Sens.* 31, 5127–5143. doi: 10.1080/01431160903283892
- Hirel, B., Le Gouis, J., Ney, B., and Gallais, A. (2007). The challenge of improving nitrogen use efficiency in crop plants: towards a more central role for genetic variability and quantitative genetics within integrated approaches. *J. Exp. Bot.* 58, 2369–2387. doi: 10.1093/jxb/erm097
- Homolová, L., Malenovsky, Z., Clevers, J. G. P. W., García-Santos, G., and Schaepman, M. E. (2013). Review of optical-based remote sensing for plant trait mapping. *Ecol. Complex.* 15, 1–16. doi: 10.1016/j.ecocom.2013.06.003
- Jamieson, P. D., Semenov, M., Brooking, I., and Francis, G. (1998). Sirius: a mechanistic model of wheat response to environmental variation. *Eur. J. Agron.* 8, 161–179. doi: 10.1016/s1161-0301(98)00020-3
- Jamieson, P. D., and Semenov, M. A. (2000). Modelling nitrogen uptake and redistribution in wheat. *Field Crops Res.* 68, 21–29. doi: 10.1016/s0378-4290(00)00103-9
- Jin, X., Kumar, L., Li, Z., Feng, H., Xu, X., Yang, G., et al. (2018). A review of data assimilation of remote sensing and crop models. *Eur. J. Agron.* 92, 141–152. doi: 10.1016/j.eja.2017.11.002
- Jin, X. L., Diao, W. Y., Xiao, C. H., Wang, F. Y., Chen, B., Wang, K. R., et al. (2013). Estimation of wheat agronomic parameters using new spectral indices. *PLoS One* 8:e72736. doi: 10.1371/journal.pone.0072736
- le Maire, G., François, C., and Dufrene, E. (2004). Towards universal broad leaf chlorophyll indices using PROSPECT simulated database and hyperspectral reflectance measurements. *Remote Sens. Environ.* 89, 1–28. doi: 10.1016/j.rse.2003.09.004
- Li, D., Zhang, P., Chen, T., and Qin, W. (2020). Recent development and challenges in spectroscopy and machine vision technologies for crop nitrogen diagnosis: a review. *Remote Sens.* 12:2578. doi: 10.3390/rs12162578
- Li, F., Miste, B., Hu, Y., Chen, X., and Schmidhalter, U. (2014). Reflectance estimation of canopy nitrogen content in winter wheat using optimised hyperspectral spectral indices and partial least squares regression. *Eur. J. Agron.* 52, 198–209. doi: 10.1016/j.eja.2013.09.006
- Li, Z., Jin, X., Yang, G., Drummond, J., Yang, H., Clark, B., et al. (2018b). Remote sensing of leaf and canopy nitrogen status in winter wheat (*Triticum aestivum* L.) based on N-PROSAIL model. *Remote Sens.* 10:1463. doi: 10.3390/rs10091463
- Li, Z., He, J., Xu, X., Jin, X., Huang, W., Clark, B., et al. (2018a). Estimating genetic parameters of DSSAT-CERES model with the GLUE method for winter wheat (*Triticum aestivum* L.) production. *Comput. Electron. Agric.* 154, 213–221. doi: 10.1016/j.compag.2018.09.009
- Li, Z., Li, Z., Fairbairn, D., Li, N., Xu, B., Feng, H., et al. (2019). Multi-LUTs method for canopy nitrogen density estimation in winter wheat by field and UAV hyperspectral. *Comput. Electron. Agric.* 162, 174–182. doi: 10.1016/j.compag.2019.04.005
- Li, Z., Nie, C., Wei, C., Xu, X., Song, X., and Wang, J. (2016). Comparison of four chemometric techniques for estimating leaf nitrogen concentrations in winter wheat (*Triticum aestivum*) Based on Hyperspectral Features. *J. Appl. Spectrosc.* 83, 240–247. doi: 10.1007/s10812-016-0276-3
- Li, Z., Taylor, J., Yang, H., Casa, R., Jin, X., Li, Z., et al. (2020). A hierarchical interannual wheat yield and grain protein prediction model using spectral vegetative indices and meteorological data. *Field Crops Res.* 248:107711. doi: 10.1016/j.fcr.2019.107711
- Mahesh, S., Jayas, D. S., Paliwal, J., and White, N. D. G. (2015). Comparison of Partial Least Squares Regression (PLSR) and Principal Components Regression (PCR) Methods for Protein and Hardness Predictions using the Near-Infrared (NIR) Hyperspectral Images of Bulk Samples of Canadian Wheat. *Food Bioproc. Technol.* 8, 31–40. doi: 10.1007/s11947-014-1381-z
- Main, R., Cho, M. A., Mathieu, R., O'Kennedy, M. M., Ramoelo, A., and Koch, S. (2011). An investigation into robust spectral indices for leaf chlorophyll estimation. *ISPRS J. Photogramm. Remote Sens.* 66, 751–761. doi: 10.1016/j.isprsjprs.2011.08.001
- Martre, P., Jamieson, P. D., Semenov, M. A., Zyskowski, R., Porter, J. R., and Triboi, E. (2006). Modelling protein content and composition in relation to crop nitrogen dynamics for wheat. *Eur. J. Agron.* 25, 138–154. doi: 10.1016/j.eja.2006.04.007
- Martre, P., Porter, J. R., Jamieson, P. D., and Triboi, E. N. (2003). Modeling grain nitrogen accumulation and protein composition to understand the sink/source regulations of nitrogen remobilization for wheat. *Plant Physiol.* 133, 1959–1967. doi: 10.1104/pp.103.030585
- Miphokasap, P., and Wannasiri, W. (2018). Estimations of nitrogen concentration in sugarcane using hyperspectral imagery. *Sustainability* 10:1266. doi: 10.3390/su10041266
- Moharana, S., and Dutta, S. (2016). Spatial variability of chlorophyll and nitrogen content of rice from hyperspectral imagery. *ISPRS J. Photogramm. Remote Sens.* 122, 17–29. doi: 10.1016/j.isprsjprs.2016.09.002
- Osborne, S. L., Schepers, J. S., Francis, D. D., and Schlemmer, M. R. (2002). Detection of phosphorus and nitrogen deficiencies in corn using spectral radiance measurements. *Agron. J.* 94, 1215–1221. doi: 10.2134/agronj2002.1215
- Osman, R., Zhu, Y., Ma, W., Zhang, D., Ding, Z., Liu, L., et al. (2020). Comparison of wheat simulation models for impacts of extreme temperature stress on grain quality. *Agric. For. Meteorol.* 288–289:107995. doi: 10.1016/j.agrformet.2020.107995
- Pavuluri, K., Chim, B. K., Griffey, C. A., Reiter, M. S., Balota, M., and Thomason, W. E. (2015). Canopy spectral reflectance can predict grain nitrogen use efficiency in soft red winter wheat. *Precis. Agric.* 16, 405–424. doi: 10.1007/s11119-014-9385-2
- Pimstein, A., Karnieli, A., and Bonfil, D. (2007). Wheat and maize monitoring based on ground spectral measurements and multivariate data analysis. *J. Appl. Remote Sens.* 1:013530. doi: 10.1117/1.2784799
- Ranjan, R., Chopra, U. K., Sahoo, R. N., Singh, A. K., and Pradhan, S. (2012). Assessment of plant nitrogen stress in wheat (*Triticum aestivum* L.) through



- hyperspectral indices. *Int. J. Remote Sens.* 33, 6342–6360. doi: 10.1080/01431161.2012.687473
- Raya-Serenio, M. D., Alonso-Ayuso, M., Pancorbo, J. L., Gabriel, J. L., Camino, C., Zarco-Tejada, P. J., et al. (2022). Residual Effect and N Fertilizer Rate Detection by High-Resolution VNIR-SWIR Hyperspectral Imagery and Solar-Induced Chlorophyll Fluorescence in Wheat. *IEEE Trans. Geosci. Remote Sens.* 60, 1–17. doi: 10.1109/TGRS.2021.3099624
- Reyniers, M., and Vrindts, E. (2006). Measuring wheat nitrogen status from space and ground-based platform. *Int. J. Remote Sens.* 27, 549–567. doi: 10.1080/01431160500117907
- Ritchie, J. T., Singh, U., Godwin, D. C., and Bowen, W. T. (1998). “Cereal growth, development and yield,” in *Understanding Options for Agricultural Production*, eds G. Y. Tsuji, G. Hoogenboom, P. K. Thornton (Dordrecht: Kluwer Academic Publishers), 79–98. doi: 10.1007/978-94-017-3624-4\_5
- Robles-Zazueta, C. A., Molero, G., Pinto, F., Foulkes, M. J., Reynolds, M. P., and Murchie, E. H. (2021). Field-based remote sensing models predict radiation use efficiency in wheat. *J. Exp. Bot.* 72, 3756–3773. doi: 10.1093/jxb/erab115
- Rodriguez, D., Fitzgerald, G., Belford, R., and Christensen, L. (2006). Detection of nitrogen deficiency in wheat from spectral reflectance indices and basic crop eco-physiological concepts. *Aust. J. Agric. Res.* 57, 781–789. doi: 10.1071/AR05361
- Saberioon, M., Amin, M., Gholizadeh, A., and Ezrin, M. (2014). A Review of Optical Methods for Assessing Nitrogen Contents During Rice Growth. *Appl. Eng. Agric.* 30, 657–669. doi: 10.13031/aea.30.10478
- Serbin, S. P., Singh, A., Desai, A. R., Dubois, S. G., Jablonski, A. D., Kingdon, C. C., et al. (2015). Remotely estimating photosynthetic capacity, and its response to temperature, in vegetation canopies using imaging spectroscopy. *Remote Sens. Environ.* 167, 78–87. doi: 10.1016/j.rse.2015.05.024
- Shewry, P. R., and Halford, N. G. (2002). Cereal seed storage proteins: structures, properties and role in grain utilization. *J. Exp. Bot.* 53, 947–958. doi: 10.1093/jxb/53.370.947
- Shewry, P. R., Tatham, A. S., Barro, F., Barcelo, P., and Lazzeri, P. (1995). Biotechnology of Breadmaking: unraveling and manipulating the multi-protein gluten complex. *Biotechnology* 13, 1185–1190. doi: 10.1038/nbt1195-1185
- Singh, H., Roy, A., Setia, R. K., and Pateriya, B. (2021). Estimation of nitrogen content in wheat from proximal hyperspectral data using machine learning and explainable artificial intelligence (XAI) approach. *Model. Earth Syst. Environ.* doi: 10.1007/s40808-021-01243-z
- Tan, C., Zhou, X., Zhang, P., Wang, Z., Wang, D., Guo, W., et al. (2020). Predicting grain protein content of field-grown winter wheat with satellite images and partial least square algorithm. *PLoS One* 15:e0228500. doi: 10.1371/journal.pone.0228500
- Tan, C.-W., Wang, D.-L., Zhou, J., Du, Y., Luo, M., Zhang, Y.-J., et al. (2018). Assessment of Fv/Fm absorbed by wheat canopies employing in-situ hyperspectral vegetation indexes. *Sci. Rep.* 8:9525. doi: 10.1038/s41598-018-27902-3
- Tan, K., Wang, S., Song, Y., Liu, Y., and Gong, Z. (2018). Estimating nitrogen status of rice canopy using hyperspectral reflectance combined with BPSO-SVR in cold region. *Chemometr. Intell. Lab. Syst.* 172, 68–79. doi: 10.1016/j.chemolab.2017.11.014
- Thomas, J. R., and Gausman, H. W. (1977). Leaf Reflectance vs. Leaf Chlorophyll and Carotenoid Concentrations for Eight Crops. *Agro. J.* 69, 799–802. doi: 10.2134/agronj1977.00021962006900050017x
- Thorp, K. R., Wang, G., Bronson, K. F., Badaruddin, M., and Mon, J. (2017). Hyperspectral data mining to identify relevant canopy spectral features for estimating durum wheat growth, nitrogen status, and grain yield. *Comput. Electron. Agric.* 136, 1–12. doi: 10.1016/j.compag.2017.02.024
- Tuvdendorj, B., Wu, B., Zeng, H., Batdelger, G., and Nanzad, L. (2019). Determination of appropriate remote sensing indices for spring wheat yield estimation in Mongolia. *Remote Sens.* 11:2568. doi: 10.3390/rs11212568
- Vogelmann, J. E., Rock, B. N., and Moss, D. M. (1993). Red edge spectral measurements from sugar maple leaves. *Int. J. Remote Sens.* 14, 1563–1575. doi: 10.1080/01431169308953986
- Wang, L., Zhou, X., Zhu, X., and Guo, W. (2017). Estimation of leaf nitrogen concentration in wheat using the MK-SVR algorithm and satellite remote sensing data. *Comput. Electron. Agric.* 140, 327–337. doi: 10.1016/j.compag.2017.05.023
- Wang, W., Yao, X., Yao, X., Tian, Y., Liu, X., Ni, J., et al. (2012). Estimating leaf nitrogen concentration with three-band vegetation indices in rice and wheat. *Field Crops Res.* 129, 90–98. doi: 10.1016/j.fcr.2012.01.014
- Wang, Z. J., Wang, J. H., Liu, L. Y., Huang, W. J., Zhao, C. J., and Wang, C. Z. (2004). Prediction of grain protein content in winter wheat (*Triticum aestivum* L.) using plant pigment ratio (PPR). *Field Crops Res.* 90, 311–321. doi: 10.1016/j.fcr.2004.04.004
- Wessman, C. A. (1990). “Evaluation of canopy biochemistry,” in *Remote Sensing of Biosphere Functioning*, eds R. J. Hobbs and H. A. Mooney (New York, NY: Springer).
- Wieser, H. (2007). Chemistry of gluten proteins. *Food Microbiol.* 24, 115–119. doi: 10.1016/j.fm.2006.07.004
- Wu, B., Huang, W., Ye, H., Luo, P., Ren, Y., and Kong, W. (2021). Using multi-angular hyperspectral data to estimate the vertical distribution of leaf chlorophyll content in wheat. *Remote Sens.* 13:1501. doi: 10.3390/rs13081501
- Wu, C., Niu, Z., Tang, Q., and Huang, W. (2008). Estimating chlorophyll content from hyperspectral vegetation indices: modeling and validation. *Agric. For. Meteorol.* 148, 1230–1241. doi: 10.1016/j.agrformet.2008.03.005
- Xue, C., Auf'm Erley, G. S., Rossmann, A., Schuster, R., Koehler, P., and Mühling, K.-H. (2016). Split nitrogen application improves wheat baking quality by influencing protein composition rather than concentration. *Front. Plant Sci.* 7:738. doi: 10.3389/fpls.2016.00738
- Xue, J., and Su, B. (2017). Significant remote sensing vegetation indices: a review of developments and applications. *J. Sens.* 2017:1353691. doi: 10.1155/2017/1353691
- Yang, G., Zhao, C., Pu, R., Feng, H., Li, Z., Li, H., et al. (2015). Leaf nitrogen spectral reflectance model of winter wheat (*Triticum aestivum*) based on PROSPECT: simulation and inversion. *J. Appl. Remote Sens.* 9:095976. doi: 10.1117/1.Jrs.9.095976
- Yao, X., Zhu, Y., Tian, Y., Feng, W., and Cao, W. (2010). Exploring hyperspectral bands and estimation indices for leaf nitrogen accumulation in wheat. *Int. J. Appl. Earth Obs. Geoinf.* 12, 89–100. doi: 10.1016/j.jag.2009.11.008
- Yendrek, C. R., Tomaz, T., Montes, C. M., Cao, Y., Morse, A. M., Brown, P. J., et al. (2017). High-Throughput Phenotyping of Maize Leaf Physiological and Biochemical Traits Using Hyperspectral Reflectance. *Plant Physiol.* 173, 614–626. doi: 10.1104/pp.16.01447
- Zhang, C., and Kovacs, J. M. (2012). The application of small unmanned aerial systems for precision agriculture: a review. *Precis. Agric.* 13, 693–712. doi: 10.1093/jeet/toz268
- Zhang, Y., Hui, J., Qin, Q., Sun, Y., Zhang, T., Sun, H., et al. (2021). Transfer-learning-based approach for leaf chlorophyll content estimation of winter wheat from hyperspectral data. *Remote Sens. Environ.* 267:112724. doi: 10.1016/j.rse.2021.112724
- Zhao, C. J., Liu, L. Y., Wang, J. H., Huang, W. J., Song, X. Y., and Li, C. J. (2005). Predicting grain protein content of winter wheat using remote sensing data based on nitrogen status and water stress. *Int. J. Appl. Earth Obs. Geoinf.* 7, 1–9. doi: 10.1016/j.jag.2004.10.002
- Zhu, Y., Yao, X., Tian, Y., Liu, X., and Cao, W. (2008). Analysis of common canopy vegetation indices for indicating leaf nitrogen accumulations in wheat and rice. *Int. J. Appl. Earth Obs. Geoinf.* 10, 1–10. doi: 10.1016/j.jag.2007.02.006
- Zörb, C., Grover, C., Steinfurth, D., and Hermann Mühling, K. (2010). Quantitative proteome analysis of wheat gluten as influenced by N and S nutrition. *Plant Soil* 327, 225–234. doi: 10.1007/s11104-009-0049-3

**Conflict of Interest:** The authors declare that the research was conducted in the absence of any commercial or financial relationships that could be construed as a potential conflict of interest.

**Publisher's Note:** All claims expressed in this article are solely those of the authors and do not necessarily represent those of their affiliated organizations, or those of the publisher, the editors and the reviewers. Any product that may be evaluated in this article, or claim that may be made by its manufacturer, is not guaranteed or endorsed by the publisher.

Copyright © 2022 Ma, Zheng and He. This is an open-access article distributed under the terms of the Creative Commons Attribution License (CC BY). The use, distribution or reproduction in other forums is permitted, provided the original author(s) and the copyright owner(s) are credited and that the original publication in this journal is cited, in accordance with accepted academic practice. No use, distribution or reproduction is permitted which does not comply with these terms.



# Real-Time Visualization of Scent Accumulation Reveals the Frequency of Floral Scent Emissions

Hyoungsoo Kim<sup>1\*</sup>, Gilgu Lee<sup>1</sup>, Junyong Song<sup>2</sup> and Sang-Gyu Kim<sup>2\*</sup>

<sup>1</sup> Department of Mechanical Engineering, Korea Advanced Institute of Science and Technology, Daejeon, South Korea,

<sup>2</sup> Department of Biological Sciences, Korea Advanced Institute of Science and Technology, Daejeon, South Korea

## OPEN ACCESS

### Edited by:

Roger Deal,  
Emory University, United States

### Reviewed by:

Ted C.J. Turlings,  
Université de Neuchâtel, Switzerland  
Eric R. Scott,  
University of Florida, United States

### \*Correspondence:

Hyoungsoo Kim  
hshk@kaist.ac.kr  
Sang-Gyu Kim  
sgkim1@kaist.ac.kr

### Specialty section:

This article was submitted to  
Technical Advances in Plant Science,  
a section of the journal  
Frontiers in Plant Science

Received: 14 December 2021

Accepted: 24 February 2022

Published: 18 April 2022

### Citation:

Kim H, Lee G, Song J and Kim S-G  
(2022) Real-Time Visualization of  
Scent Accumulation Reveals the  
Frequency of Floral Scent Emissions.  
Front. Plant Sci. 13:835305.  
doi: 10.3389/fpls.2022.835305

Flowers emit a bouquet of volatiles to attract pollinators or to protect flowers from pathogen and herbivore attacks. Most floral volatiles are synthesized in the cytoplasm of petals and released into the headspace at a specific time of day. Various floral scent sampling methods coupled with gas chromatography-mass spectrometry have been used to measure the quality and quantity of floral volatiles. However, little is known about the emission patterns of floral scents. In most cases, it is still unclear whether floral scents emit continuously or discontinuously. Here we measured the frequency with which lily flowers emit scents using optical interferometry. By analyzing the refractive index difference between volatile organic compounds and ambient air, we were able to visualize the accumulation of the volatile vapors. The frequency of volatile emission was calculated from the unique footprint of temporal power spectrum maps. Based on these real-time measurements, we found that lily flowers emit the volatile compounds discontinuously, with pulses observed around every 10–50 min.

**Keywords:** floral scent, direct optical measurement, irregular release, floral scent sedimentation, volatile organic component (VOC)

## 1. INTRODUCTION

To understand the ecological evolution of plants, the interactions between flowers, pollinators, and enemies—in particular, the frequency of pollinator visitors per flower and per unit time—has been widely explored. Because the fragrance of flowers may affect these interactions (Schiestl, 2010; Farina et al., 2020; Arnold et al., 2021), analyzing and understanding floral scents is crucial.

The term “floral scents” refers to a complex blend of volatile organic compounds [VOCs, Knudsen et al. (2006)]. Most floral scents function to mediate various interactions between plants and animals; some floral scents attract pollen-dispersing mutualists to produce seeds with high genetic diversity (Raguso, 2008), and some scents act as a repellent that functions against particular herbivores (Junker et al., 2011). In addition, a single-scent chemical can act as an attractant and also a repellent in the same plant (Kessler et al., 2019). Floral scents help bees locate other flowers of the same species, which increase the success rate of pollination (Farina et al., 2020; Arnold et al., 2021). To date, about 1,700 floral volatile compounds have been discovered (Knudsen et al., 2006); these compounds are largely classified as terpenoids, phenylpropanoids, and fatty acid-derivatives according to their biosynthetic pathways (Knudsen et al., 2006; Knudsen and Gershenzon, 2020). The timing of floral scent emission is also important for pollination success. Many flowering plants are able to synchronize their scent emission rhythms with times when pollinators are active for pollination. For instance, flowers in *Petunia axillaris* (Oyama-Okubo et al., 2005) and the wild

tobacco, *Nicotiana attenuata* (Kessler et al., 2008; Yon et al., 2016) emit volatile compounds at night to attract a night-active pollinator (Fenske et al., 2015; Yon et al., 2016). By characterizing floral scents and emission patterns, we can shed light on the ecological interactions between flowers and pollinators.

To measure floral scent emissions, adsorbent media is exposed to the headspace above flowers for a certain period of time. Headspace solid-phase extraction coupled to gas chromatography mass spectrometry (GC-MS) has been used to identify the scent compounds and to measure the quantity of each compound (Tholl et al., 2006; Burkle and Runyon, 2017). However, because the headspace volatiles are normally collected by time unit (hourly), whether floral scents are emitted continuously or discontinuously has been ignored. Recently, several analytical systems have been developed to monitor volatile emissions with high temporal resolution. A portable GC, e.g., zNose<sup>TM</sup> and Torion T-9, separates and analyzes volatile compounds within several minutes after a short sampling period (Tholl et al., 2006). The proton transfer reaction-mass spectrometry (PTR-MS) can perform real-time measurements of flower volatiles by directly injecting volatiles into a PTR-MS (Powers et al., 2020). A laser-based gas detection system monitors light intensity or frequency absorbed by volatile compounds with continuous airflow (Harren and Cristescu, 2013). Furthermore, a smartphone-based VOC-detection system using chemo-responsive dyes has been introduced (Li et al., 2019). Although these instruments allow researchers to monitor the emission of floral volatiles in real-time or near-real-time, access to the instruments is limited due to their price and complexity. Furthermore, these instruments have been used to monitor real-time volatile emissions from plants exposed to abiotic and abiotic stress. As a result, their ability to measure the emission frequency of floral VOCs in an ambient environment, which is crucial to understand the emission mechanism of floral scents, is limited. To solve this issue, we suggest using an optical measurement technique to detect VOCs in the air, as summarized in **Table 1**. If we can detect the refractive index

difference depending on the concentration of the gas media (i.e., VOCs), we should be able to measure temporal and spatial signals from flowers. Here, we develop and use the Mach-Zehnder interferometry system to monitor floral volatile emission in the lily. Using this instrument, we ask whether lily flowers emit scent compounds continuously or discontinuously.

## 2. RESULTS AND DISCUSSION

Using a laser interferometer, we investigated how often a flower emits a fragrance. The interferometer is able to detect the release of volatile organic components by measuring the relative refractive index ( $\Delta n$ ) between VOCs and air in time and space. We believe that our method can be used to explore dynamic interactions between plants and insects.

### 2.1. Real-Time Measurement of the Emission of Floral Scents

To directly see the signal of the floral scent from the lily flower, we set up the Mach-Zehnder interferometry with a closed hood box for lily, as shown in **Figure 1**. Using GC-MS to measure the components of VOCs from the lily, we had already found that linalool is one of the main components (see **Figure 2**). In this case,  $n_{\text{linalool}} = 1.463$  and  $n_{\text{air}} = 1.000293$  (Linstorm, 1998). The molar mass of linalool ( $\text{C}_{10}\text{H}_{18}\text{O}$ ) is 154.253 g/mol, which is much heavier than that of an ambient gas, typically 28.97 g/mol at room temperature ( $T = 295\text{ K}$ ). So, we presumed that if linalool is released from the lily, the molecules will sediment to the downward due to gravity. See more details about the sedimentation of linalool's vapors in the Methods. Based on this, we hung the lily upside down and designed the measurement container in **Figure 1B**. The lily's VOCs of lily—here mostly linalool—settle along a narrow channel and accumulate at the bottom, where they are captured by the Mach-Zehnder interferometry.

We recorded the interference signal of the lily's VOCs at the measurement area (i.e., the greenish box in **Figure 1**. As

**TABLE 1 |** Current gas sensing measurement techniques (○: Good, △: Fair, ×: Bad).

	Sensing mechanism	Sensitivity	Real time measurement	Spatial measurement
Electrochemical sensor (Tierney and Kim, 1993; Bhoga and Singh, 2007; Dossi et al., 2012)	Electromotive force	○	○	×
Catalytic combustion sensor (Han et al., 2007; Kim and Lee, 2014)	Electrical conductivity	×	○	×
Semiconductor sensor (Dey, 2018)	Electrical conductivity	×	○	×
Laser-based gas sensor (Richter et al., 2000; Werle et al., 2002)	Wavelength absorption rate	△	○	×
Gas chromatography-mass spectrometer (Karasek and Clement, 2012)	Chemical affinity and mass	○	×	×
Proton transfer reaction-mass spectrometer (Hansel et al., 1995; de Gouw and Warneke, 2007)	Proton affinity and mass	○	×	×
Chromatography (McNair et al., 2019)	Chemical affinity	○	×	×
Optical interferometry (Toker and Stricker, 1996; Dehaeck et al., 2014)	Refractive index	△	○	○

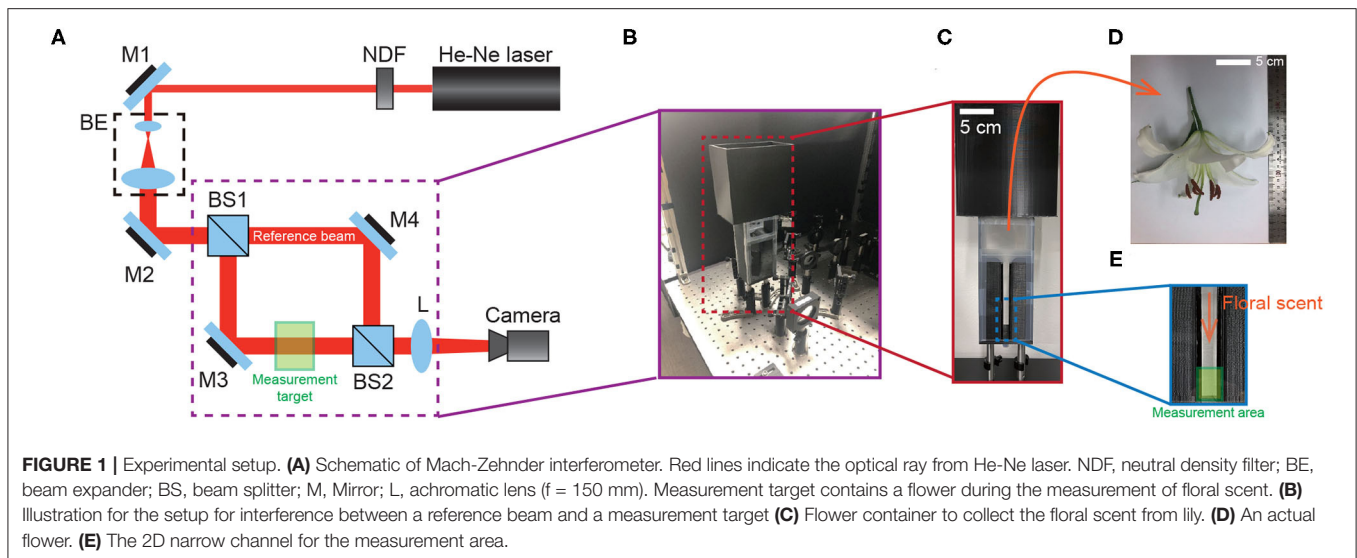


**FIGURE 1 |** Experimental setup. **(A)** Schematic of Mach-Zehnder interferometer. Red lines indicate the optical ray from He-Ne laser. NDF, neutral density filter; BE, beam expander; BS, beam splitter; M, Mirror; L, achromatic lens ( $f = 150$  mm). Measurement target contains a flower during the measurement of floral scent. **(B)** Illustration for the setup for interference between a reference beam and a measurement target **(C)** Flower container to collect the floral scent from lily. **(D)** An actual flower. **(E)** The 2D narrow channel for the measurement area.

long as the fragrance molecules accumulate at the bottom of the 2D channel (see **Figures 1C,E**), the phase of the fringe pattern will be shifted to one side, which is due to the refractive index change by the VOCs in the box. While the VOCs invaded and replaced the ambient gas, we measured the images every 10 min, the maximum recording time for the DSLR camera (Nikon 5,000, Japan). After each experiment, we cleaned up the flower container and reset the experiments for 20 min. Based on the Mach-Zehnder experiments, we measured the time-dependent phase shift in 2D,  $\phi(x, y, t)$ . Here,  $\phi(x, y, t)$  is related to the vapor concentration from the lily. Because the principle of the measurement technique is to detect and compare the refractive index change by the concentration of vapors, the mole fraction of VOCs of lily is proportional to the magnitude of the gradient of  $\phi(x, y)$ .

**Figure 3A** shows that the spatially-averaged phase signal changes over time,  $\bar{\phi}_{x,y}(t) = \frac{1}{wh} \int_0^h \int_0^w \phi(x, y, t) dx dy$  where  $w = 8$  mm and  $h = 5$  mm are the horizontal and vertical lengths of the field of view, respectively. From this result, we can confirm that the vapor molecules are released from the flower and those accumulated from the bottom. Furthermore, to examine the local accumulation of the floral scent along the vertical direction, we averaged the phase signal along the  $x$ -direction and plotted the results in **Figure 3B**. Then, we observed that the refractive index changed over time, which shows the non-uniform vapor distribution in the box along the  $y$ -direction. Also, the flux of the floral scent is not constant because  $[\bar{\phi}_x(4, t) - \bar{\phi}_x(0, t)]$  varies over time (see **Figure 3B**).

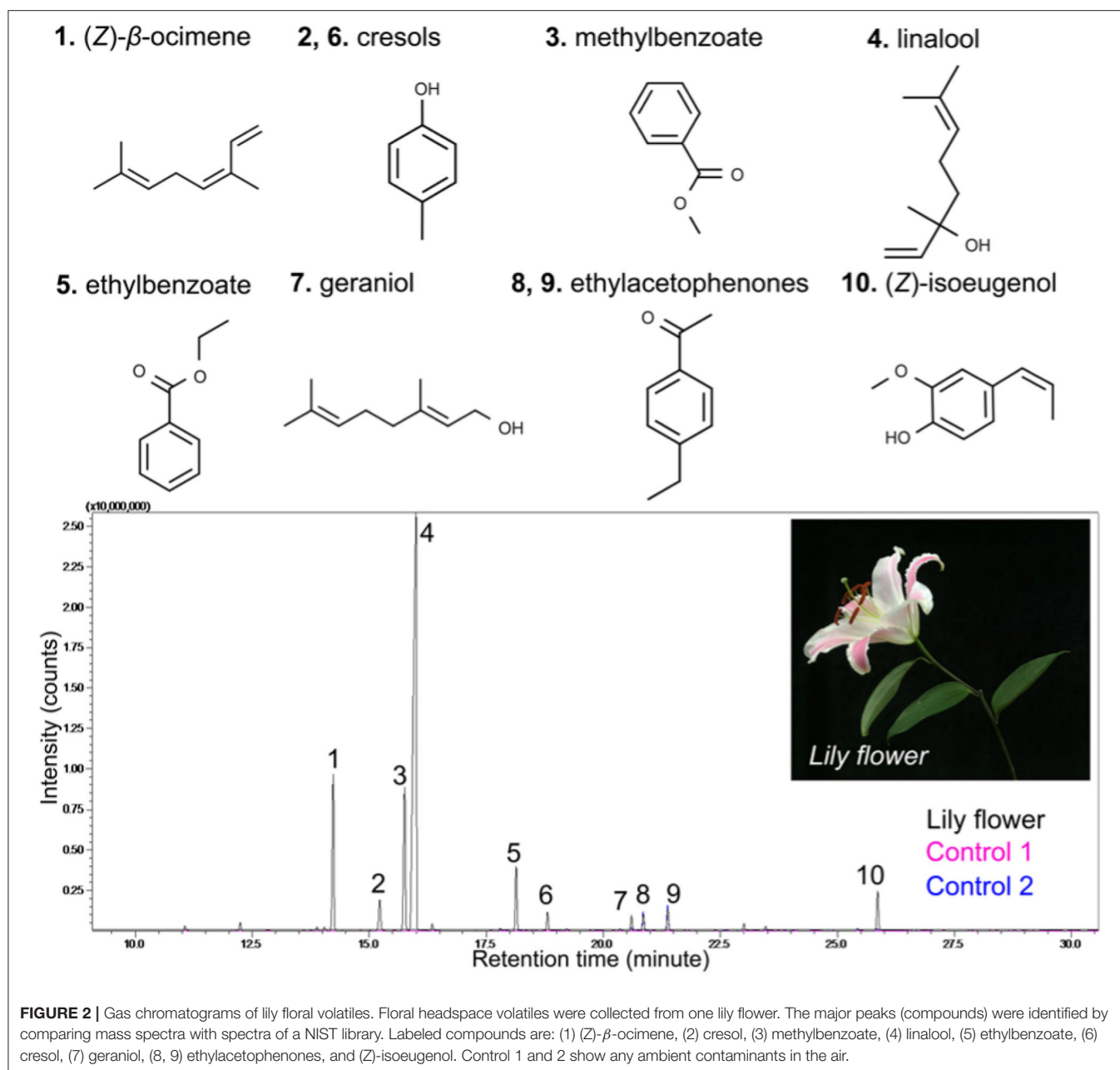
For the continuous and long-duration experiments, we used a USB camera (Ximea) that can record for over 1 h (see Methods). Because it has a relatively low spatial resolution compared to the DSLR camera, we mainly investigated a spatially-averaged phase signal for the whole measurement area ( $h \times w$ ). Finally, we performed long-duration experiments for several flowers, as shown in **Figure 4**. We randomly selected 5 different lilies (see **Figure 4A**) and executed the experiments on a different date but during the same time slot. We conducted experiments for 90 min

beginning at noon under the same experimental conditions (see detailed conditions in Methods). We observed that the spatially-averaged phase signals increased over time for all cases (see **Figure 4B**). The pastel colors indicate the real-time measurement results and the dark color of each pastel color represents the mean profile that is obtained from a moving average filter. We observed that the profiles do not have a constant slope. However,  $\bar{\phi}_{x,y}(t)$  monotonically increased with different fluctuations.

To examine the flux of the lily's scent, we calculated  $\frac{d}{dt} \bar{\phi}_{x,y}(t)$ . Using these data, we performed a fast Fourier transform (FFT) to measure the frequency of the lily's scent flux, as shown in **Figures 4C–G**. The insets are raw profiles of  $\frac{d}{dt} \bar{\phi}_{x,y}(t)$  for each lily. Although the signal contains some noise, we could see a rhythmical trend from 5 randomly chosen lilies. The frequencies of the flux of the floral scent are presented in **Figures 4C–G**. The first sample showed a 0.81 mHz lasting about 21 min. The second, third, fourth, and fifth samples presented 8, 8, 14, and 51 min, respectively. With the current measurement technique, we measured the emission rate of the lily's floral scent. Although various reports in literature have suggested that the visiting frequency of insects could be correlated with VOCs emission rates, it is still far from complete to confirm the relation between the unsteady visiting trend of insects and the floral scent emission rates. However, we believe that the current direct measurement results could be a key result to bare out this assumption.

Additionally, based on the Mach-Zehnder interferometer results, we can also obtain temporal power spectrum results where the contours represent a magnitude ( $F$ ) of the power spectrum. **Figure 5** showed the unsteadiness of the temporal power spectrum signals. The results indicate that over a short time period, the lily irregularly releases floral scents in both low- and high-frequency domains. First, the VOCs' emission signals that are highlighted in the white dashed-box (**Figure 5**) temporally disappear, suggesting that the lily either stops or slows down their release. Second, each flower might have a specific footprint of temporal power spectra. There are somewhat similar signals that are marked as a black rectangular box. The structure



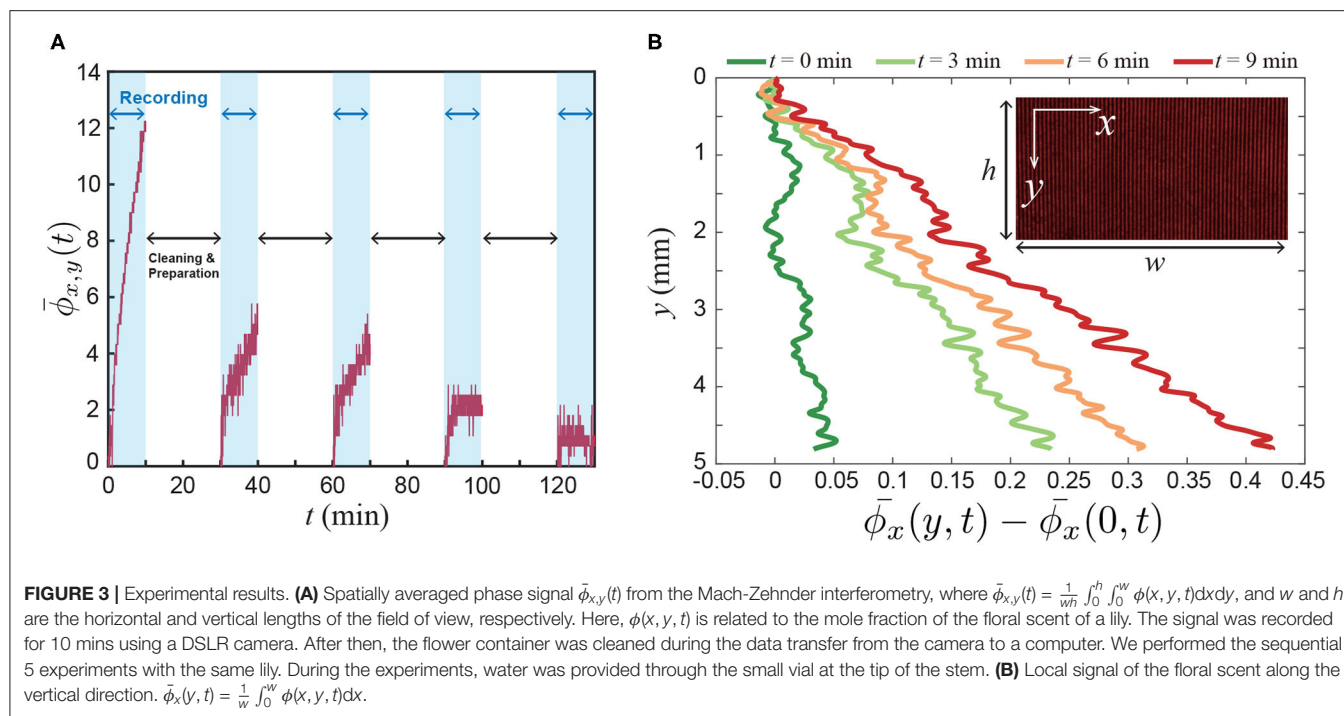


of the footprint images are not identical when the flower is different. We think that the individual emission patterns could be related to various factors including genotypes and horticultural environments. To be honest, at this moment, it is difficult to say what could be the reason. However, at least, we showed for the first time the pulsed emission of volatile organic components.

### 3. CONCLUSIONS AND OUTLOOK

In this study, we observed that a lily discontinuously releases fragrances over time. The emission of VOCs was visualized

by detecting the relative refractive index of linalool emitted by a lily. The temporal power spectrum indicates that each lily has its own profile of floral scents. The emission frequency of each flower might differ according to genotypes and/or growth conditions. However, the rate of emission is less than 1 h in all the lilies. Despite the ecological importance of floral volatiles, how flowers emit scent compounds remains unknown. Recently, Natalia Dudareva and colleagues demonstrated that floral volatiles in *Petunia hybrids* are actively transported across a plasma membrane from cytosol to cell wall by an adenosine triphosphate-binding cassette (ABC) transporter (Adebesin et al., 2017). Protein synthesis, localization, and the activity of the



ABC transporter would affect discontinuous release of lily's floral scents. The floral scents passing through the ABC transporter likely move through the cell wall and lipophilic cuticle layer (Liao et al., 2021). While the transport mechanism of the cuticle remains unknown, Liao et al. (2021) found that the 50% of internal floral scents were detected in the cuticle layer of petunia flowers. Scent compounds might pass through the cuticle layer when a certain level of chemicals accumulates, explaining the discontinuous rhythm of their emission. To unpuzzle the reason of the irregular floral scent emission, we think it needs to connect to biology much more strongly. Although we could not verify this point at this moment, we believe that the current measurement results can provide a new insight to understand and to further explore the biosynthesis and emission mechanism of floral volatiles.

## 4. METHODS

### 4.1. Plant Materials and Volatile Analysis

Lily flowers (*Lilium* Oriental Hybrid "Siberia") were used in this study. Cut flowers were obtained from local growers and transferred to our growth room (16 h light/8 h dark conditions at 26°C with  $\pm 2^\circ\text{C}$  variation). To collect floral volatiles, one fully opened flowers were put in a 7 L glass chamber. Headspace volatiles were trapped in silicone tubing (polydimethylsiloxane, PDMS) and analyzed as previously described in Kallenbach et al. (2014). Briefly, a clean PDMS tube (1 cm in length) was placed directly over the lily flower for 1 h, and GCMS-QP2020 (Shimadzu, Kyoto, Japan) coupled with a thermal desorption unit (TD-30, Shimadzu) containing the PDMS tube was used for volatile analysis. Volatiles were separated on an Rtx-5MS

capillary column (30 m  $\times$  0.25 mm; 0.25  $\mu\text{m}$ ; Shimadzu) using helium as a carrier gas. The GC-MS program was operated in split mode at a 1/20 ratio (250°C), with the oven temperature starting at 40°C for 5 min, increasing by 5°C min<sup>-1</sup> to 185°C, and by 30°C min<sup>-1</sup> to 280°C and holding for 0.83 min. See the results in Figure 2. Volatile compounds were identified by comparison of spectra against a library (NIST database), and, where possible, by comparison to standards. Chemical standard compounds (Ocimene, W353901; linalool, W263516) used in this study were purchased from Sigma-Aldrich (USA).

### 4.2. Experimental Condition and Setup for Optical Interferometry

During the experiment, water was provided through the small vial at the tip of the stem of the lily. We kept the experimental conditions that the temperature was  $295 \pm 1$  K and the relative humidity was  $45 \pm 6$  %. The CO<sub>2</sub> concentration was kept as 588  $\pm$  140 ppm in the lab all the time.

To measure the signal of the volatile organic compounds released from lilies, we used the Mach-Zehnder interferometry experimental setup (see illustration in Figure 1). The 632 nm He-Ne laser diode (10 mW, Melles Griot 25-LHP-991) was used as the light source. The intensity of the laser was adjusted using the metallic neutral density filter (NDF, Thorlabs Inc. NDL-25S-4) and the beam size of the light is expanded through the beam expander (BE) to observe the accumulation of the organic vapors in the chamber. The single laser source is precisely split into 50:50 % at the first beam splitter (BS1), and then the sample beam and the reference beam were interfered each other at the second beam splitter (BS2). The detailed experimental technique is summarized in

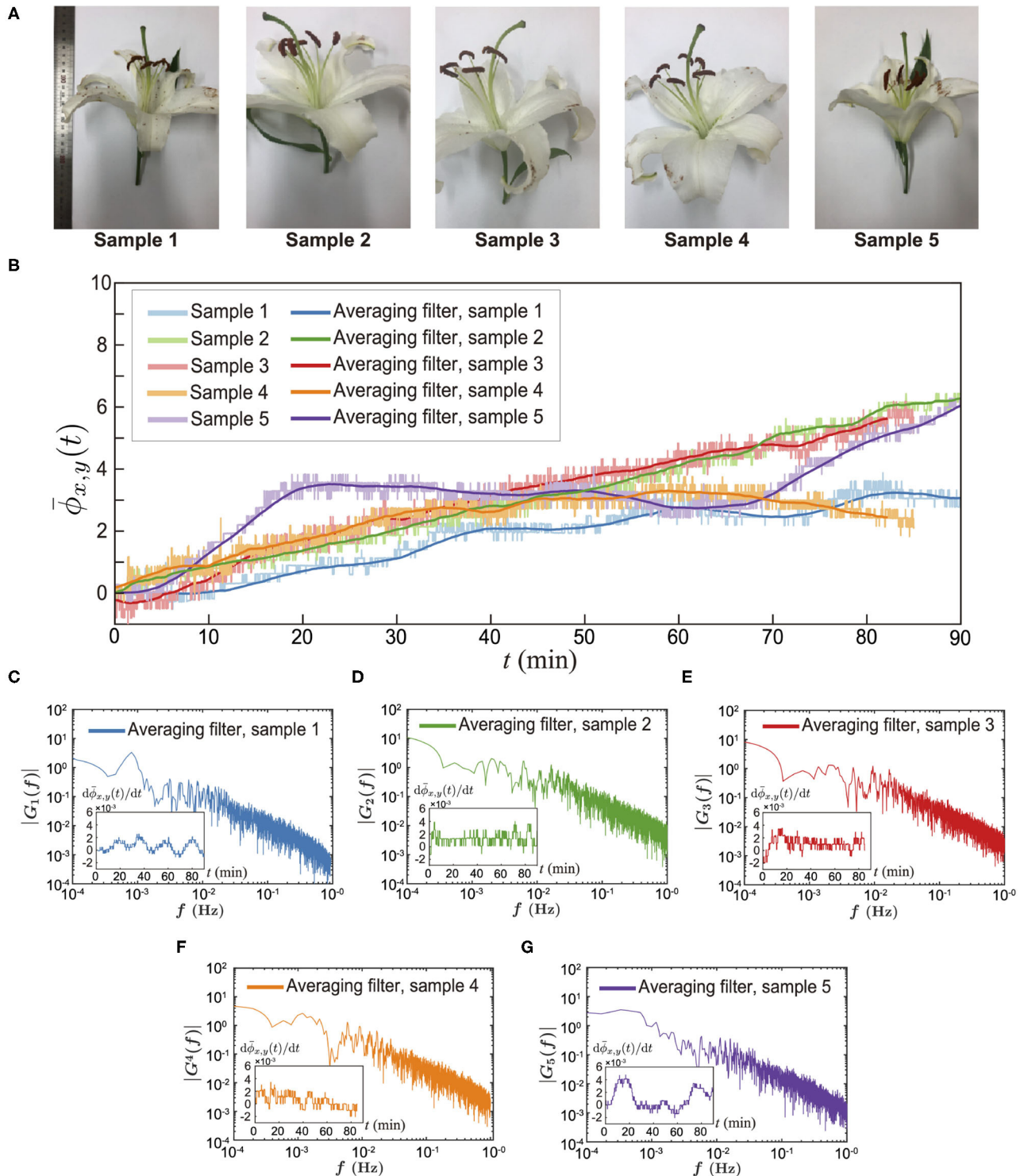


**FIGURE 4 |** Direct measurement of floral scents from alive lily. **(A)** Sample pictures. **(B)** Spatially averaged phase signal for 90 mins. The pastel colors are  $\bar{\phi}_{x,y}(t)$  for different samples. The dark colors represent the averaged data using a spatial filter. **(C–G)** Amplitude spectrum results of the time-dependent net flux of the floral scent emission [ $d\bar{\phi}_{x,y}(t)/dt$ ], which were obtained from Fast Fourier Transforms (MATLAB subroutine FFT). The inset of each figure is a raw data of the time-dependent floral scent emission rate,  $d\bar{\phi}_{x,y}(t)/dt$ .



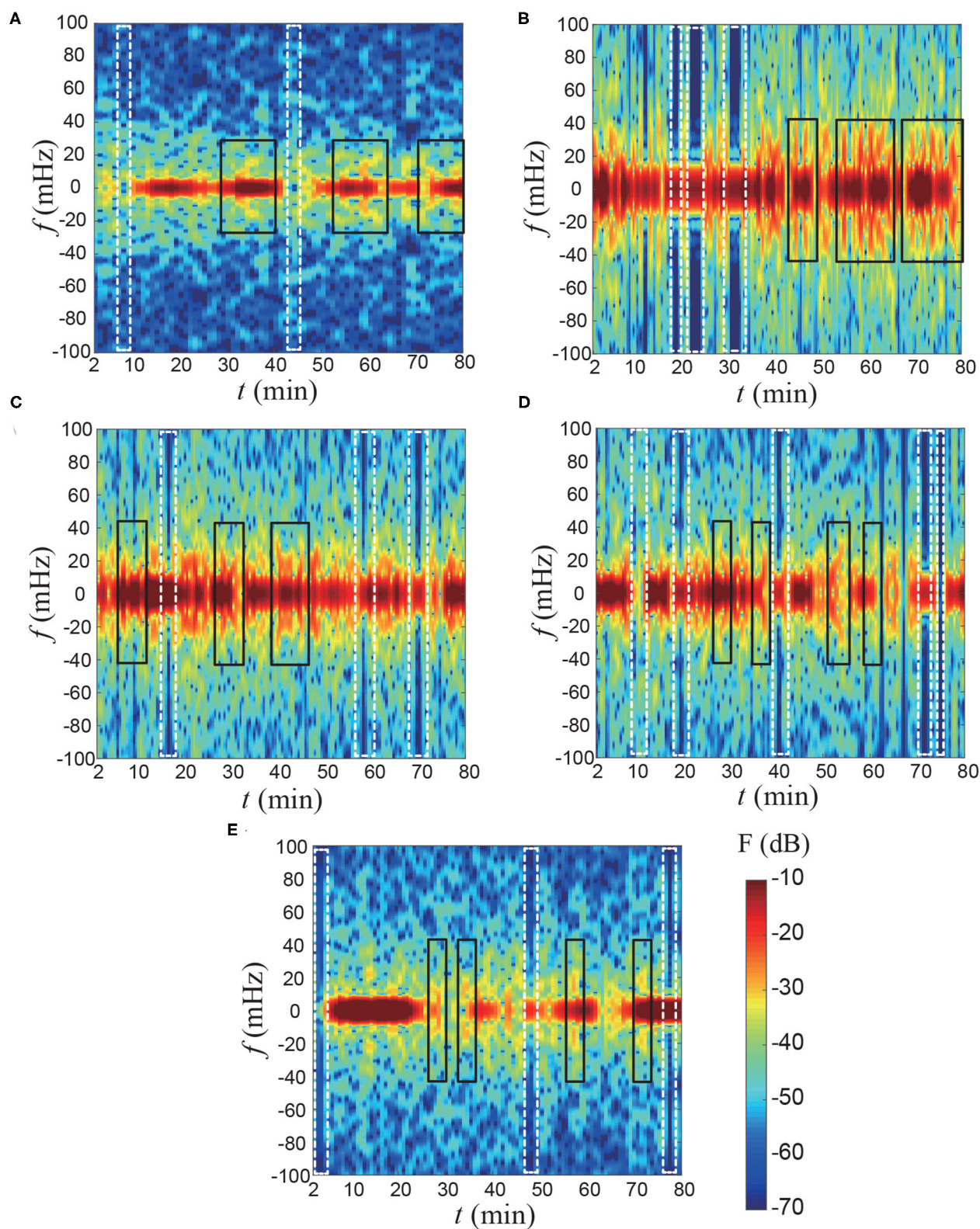


**FIGURE 5 |** Temporal power spectrum results of the flux of floral scents. The results are reconstructed based on **Figure 4B** using a moving average filter for every 5 min. **(A)** Sample 1, **(B)** Sample 2, **(C)** Sample 3, **(D)** Sample 4, and **(E)** Sample 5. The contours represent a magnitude **(F)** of the power spectrum. The white dashed-box indicates that the fragrance is temporally stopped emitting. The black rectangular box highlights the similar temporal power spectrum signal for each flower.



the preceding study (Lee and Kim, 2018). The interference patterns were captured by cameras (Nikon D6500 having  $1920 \times 1080$  pixel and Ximea camera having  $1280 \times 1024$  pixel) whose the nominal sizes of the image sensors are  $23.5 \times 15.7$  and  $6.2 \times 5$  mm, respectively. The recording frame rate is 60 frames per second for DSLR and 30 frames per second for Ximea. The spatial frequency of the resulting interference pattern in measurements were set to about  $11\text{--}14\text{ mm}^{-1}$ . The DSLR camera has a spatial resolution  $5.3\text{ }\mu\text{m/pixel}$  and the Ximea camera has  $4.9\text{ }\mu\text{m/pixel}$ . In this study, we reported 5 representative results for the emission rate of VOCs of lily among several experiments.

### 4.3. Post-processing for Fringe Pattern Results

The interference fringe pattern obtained from the Mach-Zehnder interferometer was described as

$$g(x, y) = a(x, y) + b(x, y)\cos[2\pi f_{x,c}x + \phi(x, y)], \quad (1)$$

where  $a(x, y)$  is a background,  $b(x, y)$  is a fringe modulation, and  $f_{x,c}$  is a spatial frequency.  $\phi(x, y)$  is represented as volatile component concentration from lily (see the inset of Figure 3B).

To extract  $\phi(x, y)$  from Equation (1), we used 2D Fourier transform profilometry method (Takeda and Mutoh, 1983; Lin and Su, 1995). Using Euler's formula, the complex form of Equation (1) is

$$g(x, y) = a(x, y) + c(x, y)e^{j2\pi f_{x,c}x} + c^*(x, y)e^{-j2\pi f_{x,c}x}, \quad (2)$$

where  $c(x, y) = \frac{1}{2}e^{j\phi(x, y)}$  and  $c^*(x, y) = \frac{1}{2}e^{-j\phi(x, y)}$  are complex conjugate. Equation (2) is 2D Fourier transformed with respect to  $x$  and  $y$  as

$$G(f_x, f_y) = A(f_x, f_y) + C(f_x - f_{x,c}, f_y) + C^*(f_x + f_{x,c}, f_y), \quad (3)$$

where  $G(f_x, f_y) = \mathcal{F}[g(x, y)]$ ,  $A(f_x, f_y) = \mathcal{F}[a(x, y)]$ ,  $C(f_x - f_{x,c}, f_y) = \mathcal{F}[c(x, y)e^{j2\pi f_{x,c}x}]$ ,  $C(f_x + f_{x,c}, f_y) = \mathcal{F}[c(x, y)^*e^{-j2\pi f_{x,c}x}]$ , respectively.  $\mathcal{F}$  is a Fourier operator. The spatial carrier frequency  $f_{x,c}$  was obtained from the reference fringe pattern without the droplet. By using this information,  $C(f_x - f_{x,c}, f_y)$  can be shifted to  $C(f_x, f_y)$ , which is 2D inverse Fourier transformed as  $c(x, y)$ . Finally, the phase difference  $\phi(x, y)$  can be obtained by the relation  $\phi(x, y) = \text{Im}[\ln[c(x, y)]]$ . The measured phase results  $\phi_s(x, y)$  reconstructed using fast cosine transforms and least-squares method. Then, to make the distribution of phase continuous, we used the phase unwrapping algorithm by Ghiglia and Romero (1994).

## REFERENCES

Adebesin, F., Widhalm, J. R., Boachon, B., Lefèvre, F., Pierman, B., Lynch, J. H., et al. (2017). Emission of volatile organic compounds from petunia flowers is facilitated by an abc transporter. *Science* 356, 1386–1388. doi: 10.1126/science.aan0826

To obtain the temporal power spectrum, we used the function stft (Short-Time Fourier Transform) of MATLAB 2020a with a Kaiser window of length 512 data points and shape parameter 5. The scale of the temporal window is approximately 2–5 min with an overlap ratio 78%. All the data set were segmented for about 30–66 s.

### 4.4. Sedimentation of Volatile Organic Components

Here, the relative atomic mass of evaporated vapors in air, so  $\Delta u = (M_u \text{ of linalool} - M_u \text{ of air})/N_A > 0$ , where  $N_A$  is the Avogadro's number,  $6.0221415 \times 10^{23}\text{ mol}^{-1}$ . To further estimate the gravitational effect, a dimensionless parameter, Rayleigh number (Ra), can be considered, which is the ratio between gravitational effect and viscous and diffusion effects (Dietrich et al., 2003). Ra number can be defined as  $\Delta\rho g w^3/\mu D$ , where  $g$  (gravitational acceleration) =  $10\text{ m/s}^2$ ,  $w$  (channel width) =  $8\text{ mm}$ ,  $\mu$  (viscosity of air) =  $10^{-5}\text{ Pa}\cdot\text{s}$ ,  $D$  is the diffusion coefficient of linalool in air. Here,  $\Delta\rho (= \rho_{\text{linalool}} - \rho_{\text{air}}) = 4.3\text{ g/cm}^3$  (Linstorm, 1998). In general, the diffusion coefficient of the alcohol component ranges from  $O(10^{-6}\text{ m}^2/\text{s})$  and  $O(10^{-5}\text{ m}^2/\text{s})$ . Then, we can estimate  $Ra \gg 1$ , so that the emitted linalool vapors can be sedimented along the channel.

## 5. DATA AVAILABILITY STATEMENT

The original contributions presented in the study are included in the article/supplementary material, further inquiries can be directed to the corresponding authors.

## AUTHOR CONTRIBUTIONS

HK and S-GK initiated and conceived the project and planned the experiments and wrote the first draft of the manuscript. HK and GL carried out the experiments. GL conducted data processing. JS and S-GK performed the biological experiments. HK, GL, JS, and S-GK analyzed the data. HK and GL contributed equally to this work. All authors discussed and edited the manuscript.

## FUNDING

This work was based on research which has been conducted as the KAIST-funded Global Singularity Research PREP-Program. HK was partially supported by Basic Science Research Program through the National Research Foundation (NRF) of Korea funded by the Ministry of Science (NRF- 2021R1A2C2007835). S-GK was partially supported from the Rural Development Administration (PJ016403) in South Korea.

Arnold, S. E., Dudenhöffer, J.-H., Fountain, M. T., James, K. L., Hall, D. R., Farman, D. I., et al. (2021). Bumble bees show an induced preference for flowers when primed with caffeinated nectar and a target floral odor. *Curr. Biol.* 31, 4127–4131. doi: 10.1016/j.cub.2021.06.068

Bhoga, S., and Singh, K. (2007). Electrochemical solid state gas sensors: an overview. *Ionics* 13, 417–427. doi: 10.1007/S11581-007-0150-7

- Burkle, L. A., and Runyon, J. B. (2017). The smell of environmental change: using floral scent to explain shifts in pollinator attraction. *Appl. Plant Sci.* 5, 1600123. doi: 10.3732/apps.1600123
- de Gouw, J., and Warneke, C. (2007). Measurements of volatile organic compounds in the earth's atmosphere using proton-transfer-reaction mass spectrometry. *Mass Spectrometry Rev.* 26, 223–257. doi: 10.1002/mas.20119
- Dehaeck, S., Rednikov, A., and Colinet, P. (2014). Vapor-based interferometric measurement of local evaporation rate and interfacial temperature of evaporating droplets. *Langmuir* 30, 2002–2008. doi: 10.1021/la404999z
- Dey, A. (2018). Semiconductor metal oxide gas sensors: a review. *Mater. Sci. Eng. B* 229, 206–217. doi: 10.1016/j.mseb.2017.12.036
- Dietrich, E., Wildeman, S., Visser, C. W., Hofhuis, K., Kooij, E. S., Zandvliet, H. J., et al. (2003). Role of natural convection in the dissolution of sessile droplets. *J. Exp. Botany* 54, 1801–1812. doi: 10.1017/jfm.2016.158
- Dossi, N., Toniolo, R., Pizzariello, A., Carrilho, E., Piccin, E., Battiston, S., et al. (2012). An electrochemical gas sensor based on paper supported room temperature ionic liquids. *Lab Chip* 12, 153–158. doi: 10.1039/c1lc20663j
- Farina, W. M., Arenas, A., Díaz, P. C., Martin, C. S., and Barcala, M. C. E. (2020). Learning of a mimic odor within beehives improves pollination service efficiency in a commercial crop. *Curr. Biol.* 30, 4284–4290. doi: 10.1016/j.cub.2020.08.018
- Fenske, M. P., Hazelton, K. D. H., Hempton, A. K., Shim, J. S., Yamamoto, B. M., Riffell, J. A., et al. (2015). Circadian clock gene late elongated hypocotyl directly regulates the timing of floral scent emission in petunia. *Proc. Natl. Acad. Sci. U.S.A.* 112, 9775–9780. doi: 10.1073/pnas.1422875112
- Ghiglia, D. C., and Romero, L. A. (1994). Robust two-dimensional weighted and unweighted phase unwrapping that uses fast transforms and iterative methods. *J. Opt. Soc. America* 11, 107–117.
- Han, C.-H., Hong, D.-W., Han, S.-D., Gwak, J., and Singh, K. C. (2007). Catalytic combustion type hydrogen gas sensor using tio<sub>2</sub> and uv-led. *Sens. Actuat. B Chem.* 125, 224–228. doi: 10.1016/j.snb.2007.02.017
- Hansel, A., Jordan, A., Holzinger, R., Prazeller, P., Vogel, W., and Lindinger, W. (1995). Proton transfer reaction mass spectrometry: on-line trace gas analysis at the ppb level. *In: J. Mass Spectrometry Ion Processes* 149, 609–619.
- Harren, F. J., and Cristescu, S. M. (2013). Online, real-time detection of volatile emissions from plant tissue. *AOB Plants* 5, plt003. doi: 10.1093/aobpla/plt003
- Junker, R. R., Gershenzon, J., and Unsicker, S. B. (2011). Floral odor bouquet loses its ant repellent properties after inhibition of terpene biosynthesis. *J. Chem. Ecol.* 37, 1323–1331. doi: 10.1007/s10886-011-0043-0
- Kallenbach, M., Oh, Y., Eilers, E. J., Veit, D., Baldwin, I. T., and Schuman, M. C. (2014). A robust, simple, high-throughput technique for time-resolved plant volatile analysis in field experiments. *Plant J.* 78, 1060–1072. doi: 10.1111/tpj.12523
- Karasek, F. W., and Clement, R. E. (2012). *Basic Gas Chromatography-Mass Spectrometry: Principles and Techniques*. Amsterdam: Elsevier.
- Kessler, D., Bing, J., Haverkamp, A., and Baldwin, I. T. (2019). The defensive function of a pollinator-attracting floral volatile. *Funct. Ecol.* 33, 1223–1232. doi: 10.1111/1365-2435.13332
- Kessler, D., Gase, K., and Baldwin, I. T. (2008). Field experiments with transformed plants reveal the sense of floral scents. *Science* 321, 1200–1202. doi: 10.1126/science.1160072
- Kim, H.-J., and Lee, J.-H. (2014). Highly sensitive and selective gas sensors using p-type oxide semiconductors: overview. *Sens. Actuat. B Chem.* 192, 607–627. doi: 10.1016/j.snb.2013.11.005
- Knudsen, J. T., Eriksson, R., Gershenzon, J., and Ståhl, B. (2006). Diversity and distribution of floral scent. *Botanical Rev.* 72, 1–120. doi: 10.1663/0006-8101(2006)72[1:DADOFS]2.0.CO;2
- Knudsen, J. T., and Gershenzon, J. (2020). *Biology of Plant Volatiles*. CRC press.
- Lee, G., and Kim, H. (2018). Direct optical measurement of evaporative flux of volatile liquid droplets. *Bull. Am. Phys. Soc.* 63.
- Li, Z., Paul, R., Tis, T. B., Saville, A. C., Hansel, J. C., Yu, T., et al. (2019). Non-invasive plant disease diagnostics enabled by smartphone-based fingerprinting of leaf volatiles. *Nat. Plants* 5, 856–866. doi: 10.1038/s41477-019-0476-y
- Liao, P., Ray, S., Boachon, B., Lynch, J. H., Deshpande, A., McAdam, S., et al. (2021). Cuticle thickness affects dynamics of volatile emission from petunia flowers. *Nat. Chem. Biol.* 17, 138–145. doi: 10.1038/s41589-020-00670-w
- Lin, J.-F., and Su, X. (1995). Two-dimensional Fourier transform profilometry for the automatic measurement of three-dimensional object shapes. *Opt. Eng.* 34, 3297–3303.
- Linstorm, P. (1998). NIST chemistry webbook, NIST standard reference database number 69. *J. Phys. Chem. Reference Data Monograph* 9, 1–1951.
- McNair, H. M., Miller, J. M., and Snow, N. H. (2019). *Basic Gas Chromatography*. John Wiley & Sons.
- Oyama-Okubo, N., Ando, T., Watanabe, N., Marchesi, E., Uchida, K., and Nakayama, M. (2005). Emission mechanism of floral scent in petunia axillaris. *Biosci. Biotechnol. Biochem.* 69, 773–777. doi: 10.1271/bbb.69.773
- Powers, J. M., Seco, R., Faiola, C. L., Sakai, A. K., Weller, S. G., Campbell, D. R., et al. (2020). Floral scent composition and fine-scale timing in two moth-pollinated hawaiian schiedea (caryophyllaceae). *Front. Plant Sci.* 11, 1116. doi: 10.3389/fpls.2020.01116
- Raguso, R. A. (2008). Wake up and smell the roses: the ecology and evolution of floral scent. *Ann. Rev. Ecol. Evol. Systematics* 39, 549–569. doi: 10.1146/annurev.ecolsys.38.091206.095601
- Richter, D., Lancaster, D. G., and Tittel, F. K. (2000). Development of an automated diode-laser-based multicomponent gas sensor. *Appl. Opt.* 39, 4444–4450. doi: 10.1364/AO.39.004444
- Schiestl, F. P. (2010). The evolution of floral scent and insect chemical communication. *Ecol. Lett.* 13, 643–656. doi: 10.1111/j.1461-0248.2010.01451.x
- Takeda, M., and Mutoh, K. (1983). Fourier transform profilometry for the automatic measurement of 3-d object shapes. *Appl. Opt.* 22, 3977–3982. doi: 10.1364/AO.22.003977
- Tholl, D., Boland, W., Hansel, A., Loreto, F., Röse, U. S., and Schnitzler, J.-P. (2006). Practical approaches to plant volatile analysis. *Plant J.* 45, 540–560. doi: 10.1111/j.1365-3113X.2005.02612.x
- Tierney, M. J., and Kim, H. O. L. (1993). Electrochemical gas sensor with extremely fast response times. *Anal. Chem.* 65, 3435–3440. doi: 10.1021/ac00071a017
- Toker, G., and Stricker, J. (1996). Holographic study of suspended vaporizing volatile liquid droplets in still air. *Int. J. Heat Mass Transf.* 39, 3475–3482. doi: 10.1016/0017-9310(96)00018-X
- Werle, P., Slemr, F., Maurer, K., Kormann, R., Mücke, R., and Jänker, B. (2002). Near-and mid-infrared laser-optical sensors for gas analysis. *Opt. Lasers Eng.* 37, 101–114. doi: 10.1016/S0143-8166(01)00092-6
- Yon, F., Joo, Y., Cortés Llorca, L., Rothe, E., Baldwin, I. T., and Kim, S.-G. (2016). Silencing nicotiana attenuata lhy and ztl alters circadian rhythms in flowers. *New Phytol.* 209, 1058–1066. doi: 10.1111/nph.13681

**Conflict of Interest:** The authors declare that the research was conducted in the absence of any commercial or financial relationships that could be construed as a potential conflict of interest.

**Publisher's Note:** All claims expressed in this article are solely those of the authors and do not necessarily represent those of their affiliated organizations, or those of the publisher, the editors and the reviewers. Any product that may be evaluated in this article, or claim that may be made by its manufacturer, is not guaranteed or endorsed by the publisher.

Copyright © 2022 Kim, Lee, Song and Kim. This is an open-access article distributed under the terms of the Creative Commons Attribution License (CC BY). The use, distribution or reproduction in other forums is permitted, provided the original author(s) and the copyright owner(s) are credited and that the original publication in this journal is cited, in accordance with accepted academic practice. No use, distribution or reproduction is permitted which does not comply with these terms.



# An Improved *Agrobacterium*-Mediated Transformation and Genome-Editing Method for Maize Inbred B104 Using a Ternary Vector System and Immature Embryos

## OPEN ACCESS

### Edited by:

Marcos Egea-Cortines,  
Universidad Politécnica de Cartagena,  
Spain

### Reviewed by:

Nian Wang,  
University of Florida, United States  
Anshu Alok,  
University of Minnesota Twin Cities,  
United States  
Hiroshi Ezura,  
University of Tsukuba, Japan

### \*Correspondence:

Kan Wang  
kanwang@iastate.edu  
Veena Veena  
vveena@danforthcenter.org

### Specialty section:

This article was submitted to  
Technical Advances in Plant Science,  
a section of the journal  
Frontiers in Plant Science

**Received:** 24 January 2022

**Accepted:** 07 March 2022

**Published:** 04 May 2022

### Citation:

Kang M, Lee K, Finley T,  
Chappell H, Veena V and Wang K  
(2022) An Improved  
*Agrobacterium*-Mediated  
Transformation and Genome-Editing  
Method for Maize Inbred B104 Using  
a Ternary Vector System  
and Immature Embryos.  
Front. Plant Sci. 13:860971.  
doi: 10.3389/fpls.2022.860971

Minjeong Kang<sup>1,2,3</sup>, Keunsub Lee<sup>1,2</sup>, Todd Finley<sup>4</sup>, Hal Chappell<sup>4</sup>, Veena Veena<sup>4\*</sup> and Kan Wang<sup>1,2\*</sup>

<sup>1</sup> Department of Agronomy, Iowa State University, Ames, IA, United States, <sup>2</sup> Crop Bioengineering Center, Iowa State University, Ames, IA, United States, <sup>3</sup> Interdepartmental Plant Biology Major, Iowa State University, Ames, IA, United States,

<sup>4</sup> Plant Transformation Facility, Donald Danforth Plant Science Center, St. Louis, MO, United States

For maize genome-editing and bioengineering, genetic transformation of inbred genotypes is most desired due to the uniformity of genetic background in their progenies. However, most maize inbred lines are recalcitrant to tissue culture and transformation. A public, transformable maize inbred B104 has been widely used for genome editing in recent years. This is primarily due to its high degree of genetic similarity shared with B73, an inbred of the reference genome and parent of many breeding populations. Conventional B104 maize transformation protocol requires 16–22 weeks to produce rooted transgenic plants with an average of 4% transformation frequency (number of T0 plants per 100 infected embryos). In this Method paper, we describe an advanced B104 transformation protocol that requires only 7–10 weeks to generate transgenic plants with an average of 6.4% transformation frequency. Over 66% of transgenic plants carried CRISPR/Cas9-induced indel mutations on the target gene, demonstrating that this protocol can be used for genome editing applications. Following the detailed and stepwise procedure described here, this quick and simplified method using the *Agrobacterium* ternary vector system consisting of a T-DNA binary vector and a compatible helper plasmid can be readily transferable to interested researchers.

**Keywords:** bialaphos, CRISPR-Cas9, helper plasmid, tissue culture, *Zea mays*

## INTRODUCTION

Maize is the most produced grain crop for humans and livestock throughout the world. It is grown in more countries than any other crop and serves as an important model plant system for fundamental studies (Freeling and Walbot, 1994). Recent advances in genomics and molecular biology tools have enabled rapid identification and isolation of plant genes on a large scale. Especially, the RNA-guided endonucleases adopted from the prokaryotic immune system,

i.e., Clustered Regularly Interspaced Short Palindromic Repeat (CRISPR) and CRISPR-associated protein (Cas) systems, have been widely used for precise gene editing in plants and agricultural research (Zhu et al., 2020). CRISPR-Cas9 represents one of the most efficient gene editing tools and has a great potential for gene functional analysis (Zhu et al., 2020). However, determining the functions of thousands of genes and applying that knowledge to crop improvement is now one of the major challenges facing plant biologists. Plant genetic transformation is a key technology for functional analysis of genes *via* strategies including complementation, overexpression, gene silencing, or genome editing, therefore, it is critical to improve the plant genetic transformation protocols to take full advantage of the revolutionary genome engineering tools.

Maize transformation can be achieved by either biolistic- or *Agrobacterium*-mediated methods (Kausch et al., 2021). While private laboratories are now routinely operating high throughput transformation pipelines, many public research groups face challenges in obtaining transgenic and genome-edited maize plants efficiently, especially when conducting transformation using maize inbred genotypes.

Like many other plant transformation processes, maize transformation is genotype-dependent (Que et al., 2014). The early maize transformation successes used specific hybrid maize genotypes such as A188 × B73 (Gordon-Kamm et al., 1990) and Hi Type II (Hi II, Frame et al., 2002) and a few old inbreds such as A188 (Ishida et al., 1996). To properly understand gene functions and compare changes made on the genes, a transgenic analysis should be performed in an inbred background. Frame et al. (2006) conducted experiments on ten maize inbred lines in an attempt to identify inbreds that can be transformed. Three inbred genotypes, B104, B114, and Ky21, were found to be transformable using the *Agrobacterium*-mediated infection of immature embryos (Frame et al., 2006). Among the three inbreds, B104 is particularly of interest because it was derived from the same populations as inbred B73 (Hallauer et al., 1997). B73 is a public inbred that currently serves as the reference genome (Schnable et al., 2009). B104 shares the same genetic background as B73; both were derived from the Iowa Stiff Stalk Synthetic lines10 (Hallauer et al., 1997). They share 93% similarity as calculated by the TYPsimSelector tool available at MaizeGDB (Romay et al., 2013; Manchanda et al., 2016).

Transformation of B104 uses Murashige and Skoog (MS) basal salts for callus initiation and regeneration. Interestingly, the same media regime and treatments did not work for B73 transformation (Frame et al., 2006). Because of the difficulty in B73 transformation, B104 has been used widely in the maize research community as an alternative inbred for functional gene analysis in recent years (Char et al., 2017; Sun et al., 2017; Lee et al., 2019). B104 can be transformed using both *Agrobacterium* and biolistic methods (Raji et al., 2018) with varied frequencies. Here, transformation frequency is defined as the number of herbicide (bialaphos) resistant events per 100 infected immature embryos. The average frequency of the *Agrobacterium*-mediated method was 4%, while the frequency of the biolistic approach was 6–13% (Raji et al., 2018).

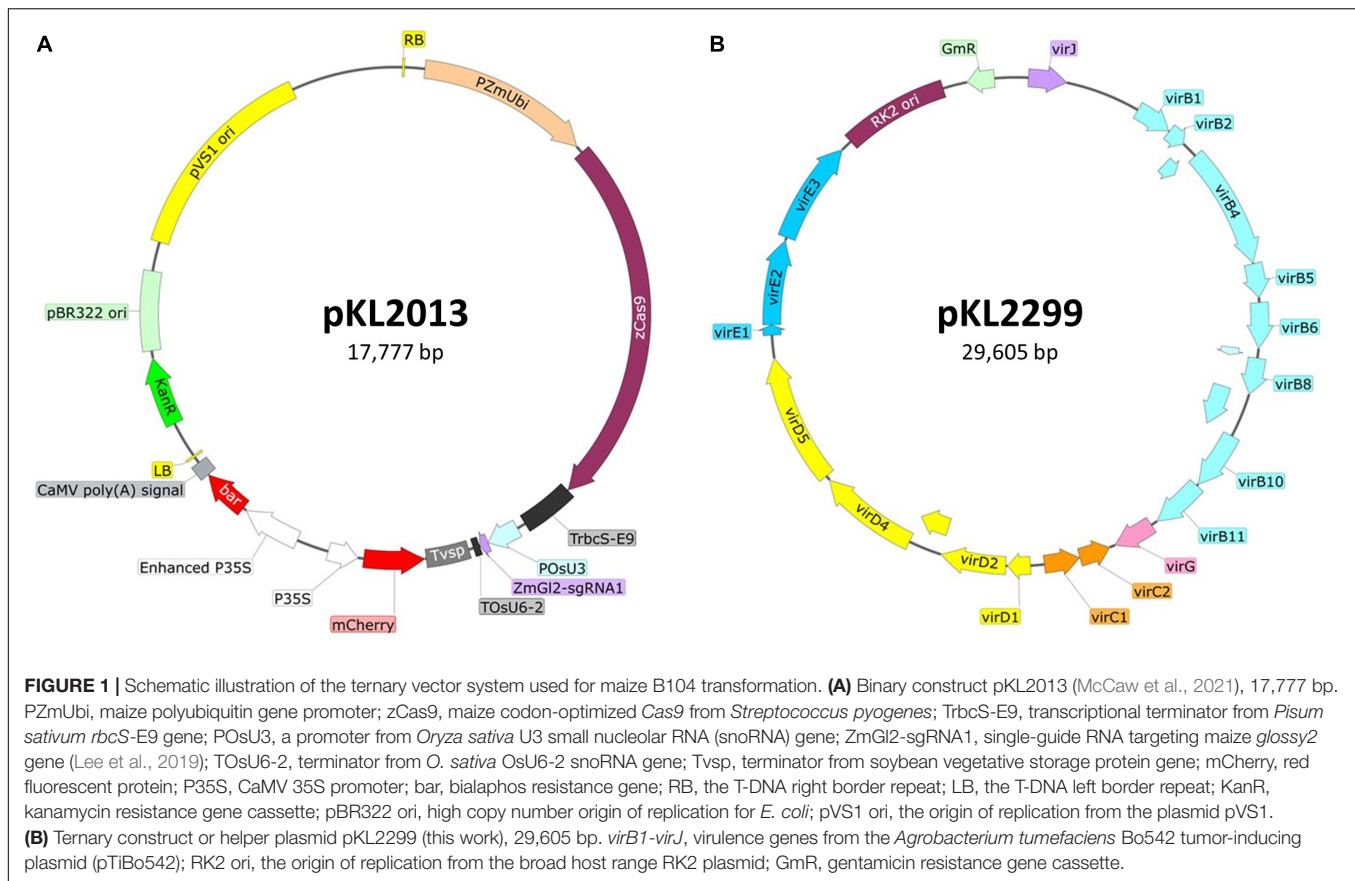
In general, the process of B104 transformation takes longer than that of Hi II transformation. Counting from the day of infection/bombardment to the day of moving regenerated plants to the soil, B104 transformation takes about 160 days (Frame et al., 2006; Raji et al., 2018), whereas Hi II transformation takes about 110 days (Frame et al., 2015). Because B104 produces type I callus from immature embryos, it can be challenging in managing effective regeneration of transformed cells, especially for less experienced researchers.

To overcome the genotype dependency in monocots transformation, researchers have been exploring plant genes that can promote somatic embryogenesis (Lardon and Geelen, 2020). Lowe et al. (2016) showed that when they introduced morphogenic genes *Baby boom* (*Bbm*) and *Wuschel2* (*Wus2*) into the cells of transformation-recalcitrant grass species, they could produce transgenic plants in these genotypes that were normally not amenable for genetic transformation. Subsequently, it was also shown that maize B73 inbred could also be transformed using the vectors containing the morphogenic genes (Mookkan et al., 2017; Masters et al., 2020). Importantly, the protocol developed by Lowe et al. (2016) allowed a significant reduction of time required for transformation. This morphogenic genes-enabled protocol was termed as “QuickCorn” method (Masters et al., 2020).

While the morphogenic genes can stimulate embryogenesis, they also regulate and impact other genes and their expressions in plant cells (Ikeuchi et al., 2019). The persistent presence of extra morphogenic genes in plant cells can negatively affect plant development and maturity (Boutillier et al., 2002; Zuo et al., 2002). To overcome this issue, all transformation vectors carrying the morphogenic genes also contain a *cre-loxP* recombinase system that can remove the morphogenic genes from the transgene after the initial transformation stage (Lowe et al., 2016). However, the presence of both morphogenic gene cassettes (~7 kb) and the *cre-loxP* system (~3.5 kb) substantially increases the T-DNA size on the transformation vectors (Lowe et al., 2016) and makes it difficult for further sequence modifications in the vectors. Moreover, larger T-DNA size on a transformation vector often leads to lower transformation frequencies (Park et al., 2000).

Here, we describe an improved protocol for B104 transformation using the *Agrobacterium*-mediated method. Like the original B104 transformation protocol (Frame et al., 2006), this protocol uses maize immature embryos harvested 10–12 days post-pollination. We use an *Agrobacterium* strain harboring a ternary vector system: a conventional T-DNA binary vector and a compatible helper plasmid that carries additional copies of *Agrobacterium* virulent (*vir*) genes. Extra copies of *vir* genes have been shown to greatly enhance maize transformation frequencies (Ishida et al., 1996; Anand et al., 2018). One major difference in this protocol is the adoption of the media regime from the QuickCorn method (Hoerster et al., 2020; Masters et al., 2020). These changes improve tissue responsiveness and overall regenerability. Most importantly, it greatly reduces the duration of the transformation process from 160 to 60 days, counting from the day of infection to the day of moving regenerated plants to soil. By delivering a CRISPR/Cas9 system *via* the T-DNA, we





demonstrate that this improved B104 transformation protocol can be used for efficient genome editing applications.

## MATERIALS AND EQUIPMENT

### Plant Material, Constructs, and *Agrobacterium* Strain

- Maize inbred B104: Seed can be obtained from the USDA Agricultural Research Service seed repository.<sup>1</sup>
- Plant material: Greenhouse-grown B104 embryo donor ears are harvested 10–12 days after pollination (depending upon the weather and day length) when immature zygotic embryos are 1.6–2.0 mm long. After harvest, maize ears (in their husks and inside their pollination bag) can be stored in a laboratory refrigerator (4°C) for 1–3 days prior to use.
- Binary vector pKL2013 (McCaw et al., 2021; **Figure 1A**): The T-DNA carries (1) 2X CaMV 35S promoter (P35S) driving the bialaphos resistant (*bar*) gene as a selectable marker, (2) a single P35S driving mCherry gene as a visual marker; (3) maize ubiquitin promoter driving a maize-codon-optimized *Cas9*, and (4) rice U3 promoter driving a guide RNA (gRNA) targeting maize *glossy2* (*Gl2*) gene (McCaw et al., 2021).

- Ternary helper plasmid pKL2299 (this work; **Figure 1B**): It carries the majority suite of *Agrobacterium* virulence genes from Ti plasmid pTiBo542 (Komari et al., 1986). The additional copies of *vir* genes have been shown to markedly enhance maize transformation frequencies when using *Agrobacterium* strain LBA4404 (Anand et al., 2018). To ensure vector compatibility, pKL2299 has the RK2 origin of replication. Therefore, this plasmid can be used as a ternary vector pairing with any binary vector plasmid that has a pVS1 origin of replication.
- *Agrobacterium tumefaciens* strain LBA4404Thy<sup>-</sup>: This is an auxotrophic version of LBA4404 with the thymidylate synthase gene (*thyA*) deleted from the chromosome (Ranch et al., 2012; Anand et al., 2018).
- *Agrobacterium* strain carrying the constructs: LBA4404Thy<sup>-</sup> harboring both pKL2013 and pKL2299 is called KL2013vir/thy and used in this study.

### Plant Growth Supplies

- Metromix 360 (Sungro, Agawam, MA, United States).
- Pro-Mix BRK20 (Pro-Mix, Quakertown, PA, United States).
- 1801 deep inserts (T.O. Plastic, Clearwater, MN, United States).
- Standard Flat with drain holes, STF-1020-OPEN (T.O. Plastic, Clearwater, MN, United States).

<sup>1</sup><https://www.ars-grin.gov/>

- Standard 2.5-gallon (9.4 L) nursery pots (Nursery Supplies Inc., Chambersburg, PA, United States).
- Humi-dome (Hummert International, Earth City, MO, United States).
- Tomato maker 4-2-6 (Organic labs, Fort Pierce, FL, United States).
- Osmocote 15-9-12 (Everris, Geldermalsen, Netherlands).
- Sprint 330 Iron chelate (BASF, Ludwigshafen, Germany).
- Pollination apron.
- Scissors.
- 70% Ethanol to sterilize scissors.
- Shoot bags (Lawson Pollinating Bags, Northfield, IL, United States).
- Tassel bags (Lawson Pollinating Bags, Northfield, IL, United States).
- Permanent marker–Chisel tip for broad strokes, black, standard (NOT ethanol resistant) recommended to avoid fading in the sun.
- Stapler and staples–(e.g., Ace Clipper Model no. 702).
- Non-skid paperclips.
- Greenhouse with tables and lighting–28°C, 16 h day/25°C, 8 h night.

## Transformation Supplies

- Stirring hot plate and stir bars.
- Beakers.
- Glass flasks and sterile pouring beaker or 1 L lidded bottles for autoclaving media.
- Water bath, 55°C.
- Autoclave.
- Petri dishes–100 mm × 15 mm and 100 mm × 25 mm, sterile.
- Large, sterile Petri plate (e.g., 120 mm × 120 mm × 15 mm square plate or 150 mm × 15 mm round plate).
- 0.22 µm syringe filter.
- 0.22 µm Stericup® vacuum filtration system.
- pH meter.
- Laminar flow hood.
- Sterile culture loops.
- Genesys 10S UV-VIS spectrophotometer (Thermo scientific, Waltham, MA, United States).
- Semi-micro cuvettes (Cat # 14955127, Fisher scientific, Pittsburgh, PA, United States).
- Bleach (8.25% sodium hypochlorite, e.g., Clorox).
- 70% ethanol in a spray bottle for disinfecting.
- Bead sterilizer.
- Forceps.
- Scalpel and blades.
- Handles for ears–recommend cheap, stamped sheet metal forks with all but one tine broken off.
- Embryo dissection tool (e.g., Fisher brand Handi-Hold Microspatula or Hu-Friedy plastic filling instrument #8A).
- Parafilm.
- Micropore tape.
- Plastic culture box to hold multiple plates, e.g., square plastic container with lid (31 cm × 23 cm × 10 cm, 12-5/16" × 9-1/16" × 4", W × L × H, Cat # 295C),

or square hinged plastic container with snap closure (33.3 cm × 9.2 cm × 5 cm, 13-1/8" × 9-3/16" × 2", W × L × H, Cat # 700C) (Pioneer plastic, Dixon, KY, United States).

- 26–28°C plant tissue culture incubator (dark).
- 26–28°C plant tissue culture incubator (lighted 16 h day/8 h night, 120–150 µmol/m<sup>2</sup>/s).

## Molecular Analysis Supplies

- DNA extraction buffer (200 mM Tris-Cl, 250 mM NaCl, 25 mM EDTA, 0.5% sodium dodecyl sulfate).
- RNase A (DNase and protease-free).
- Chloroform.
- Isopropanol.
- 80% ethanol.
- DNase-free water.
- ExoSAP-IT™ (Applied Biosystems, Waltham, MA, United States).
- 1.5 mL centrifuge tubes.
- Scalpel and blades.
- Forceps.

## Stock Solutions

See Table 1.

## Media

See Table 2.

## METHODS

### Growing B104 Plants to Produce Immature Embryos for Transformation

1. Maize B104 plants are grown in a greenhouse equipped with artificial lighting and reverse osmosis (RO) water systems in the Donald Danforth Plant Science Center (St. Louis, MO, United States). The greenhouse conditions are as follows: photoperiod, 14/10 h (day/night); temperatures, 28/22°C (day/night); relative humidity, 40/50% (day/night); Supplemental light intensity, 150 µmol/m<sup>2</sup>/s at 1.5 m (5 ft) above ground. Lighting is a mixture of 50% of 1000 W Metal Halide and 50% of 1000 W High-Pressure Sodium Fixtures mounted 4 m (13 ft) above ground.
2. Maize seeds are usually sown in small containers filled with commercial potting mix. Plastic inserts (1801 deep inserts) are filled with Metromix 360 potting mix and placed onto STF-1020-OPEN flat with drain holes (**Figure 2A**). Before sowing, the potting mix must be wetted thoroughly but not excessively.
3. B104 seeds (one per cell) are placed in the potting mix approximately 2.5 cm (1 inch) deep from the surface. The tray is covered with a plastic humi-dome (**Figure 2B**) and placed on a bench in the greenhouse with the conditions described above. In the case of needing year-long donor plant production, seeds can be sown every 3–4 days, depending on growth space availability.

**TABLE 1** | Stock solutions and preparations.\*

Item	Stock	Stock solution concentration	Quantity	Dissolve in	Preparation note	Storage temp (°C)	Storage days
1	2,4-Dichlorophenoxyacetic acid (2,4-D)	0.5 mg/mL	50 mg	10 mL 1 N NaOH + 90 mL H <sub>2</sub> O	Dissolve 2,4-D in 10 mL 1 M NaOH, then bring the volume to 100 mL with ddH <sub>2</sub> O.	4	60
2	6-Benzylaminopurine (BAP)	1 mg/mL	100 mg	10 mL 1 N NaOH + 90 mL H <sub>2</sub> O	Dissolve BAP in 10 mL 1 M NaOH, then bring the volume to 100 mL with ddH <sub>2</sub> O.	4	60
3	AB buffer (20X)	20X	See Note	dH <sub>2</sub> O, 1 L	60 g/L K <sub>2</sub> HPO <sub>4</sub> , 20 g/L NaH <sub>2</sub> PO <sub>4</sub>	4	60
4	AB salts (20X)	20X	See Note	dH <sub>2</sub> O, 1 L	20 g/L NH <sub>4</sub> Cl, 6 g/L MgSO <sub>4</sub> ·7H <sub>2</sub> O, 3 g/L KCl, 0.228 g/L CaCl <sub>2</sub> ·2H <sub>2</sub> O	4	60
5	Absciscic acid (ABA)	0.1 mg/mL	1 mg	1 mL 1 N NaOH + 9 mL H <sub>2</sub> O		−20	90
6	Acetosyringone (AS)	100 mM	196.2 mg	DMSO, 10 mL	Make 10 mL stock and aliquote for single use	−20	90
7	B5H minor salts	1000X	See Note	dH <sub>2</sub> O, 1 L	3 g/L H <sub>3</sub> BO <sub>3</sub> , 10 g/L MnSO <sub>4</sub> ·H <sub>2</sub> O, 0.25 g/L Na <sub>2</sub> MoO <sub>4</sub> ·2H <sub>2</sub> O, 0.75 g/L KI	Room temp	60
8	Bialaphos	2 mg/mL	20 mg	dH <sub>2</sub> O, 10 mL		−20	60
9	Carbenicilline	100 mg/mL	1 g	dH <sub>2</sub> O, 10 mL		−20	90
10	Cupric sulfate	1 mg/mL	100 mg	dH <sub>2</sub> O, 100 mL	Make 100 mL stock	4	1000
11	Dicamba	1 mg/mL	10 mg	0.5 mL EtOH + 9.5 mL ddH <sub>2</sub> O	Dissolve Dicamba in 5 mL 100% EtOH, then bring the volume to 10 mL with ddH <sub>2</sub> O. Media containing Dicamba should store in dark.	4	120
12	Eriksson's vitamins	1000X	See Note	dH <sub>2</sub> O, 100 mL	2 g/L glycine, 0.5 g/L nicotinic acid, 0.5 g/L pyridoxine-HCL, 0.5 g/L thiamine-HCL (or Phytotech E330)	4	90
13	FeSO <sub>4</sub> ·7H <sub>2</sub> O	1.25 mg/mL	125 mg	dH <sub>2</sub> O, 100 mL		25	90
14	Gentamicin	50 mg/mL	5 g	dH <sub>2</sub> O, 100 mL		−20	90
15	Kanamycin	50 mg/mL	5 g	dH <sub>2</sub> O, 100 mL		−20	90
16	N6 Macronutrient stock (10X)	(for 60 mL/L)	See Note	dH <sub>2</sub> O, 1 L	1.66 g/L CaCl <sub>2</sub> ·2H <sub>2</sub> O, 4.62 g/L (NH <sub>4</sub> ) <sub>2</sub> SO <sub>4</sub> , 4 g/L KH <sub>2</sub> PO <sub>4</sub> , 1.85 g/L MgSO <sub>4</sub> ·7H <sub>2</sub> O, 28.3 g/L KNO <sub>3</sub>	4	90
17	NaFe EDTA for B5H (100X)	(for 6 mL/L)	See Note	dH <sub>2</sub> O, 100 mL	3.7 g/L EDTA-Na <sub>2</sub> ·H <sub>2</sub> O, 2.79 g/L FeSO <sub>4</sub> ·7H <sub>2</sub> O	4	60
18	Nicotinic acid	1 mg/mL	100 mg	dH <sub>2</sub> O, 100 mL		4	120
19	Pyridoxine-HCl	1 mg/mL	100 mg	dH <sub>2</sub> O, 100 mL		4	120
20	Schenk and Hildebrandt Vitamin	100X	See Note	dH <sub>2</sub> O, 100 mL	100 g/L myo-inositol, 0.5 g/L nicotinic acid, 0.05 g/L pyridoxine-HCl, 0.5 g/L thiamine-HCl (or Phytotech, S826)	4	90
21	Silver Nitrate	2 mg/mL	200 mg	100 mL	Store in dark. Media containing silver nitrate should be stored in dark.	4	90
22	Spectinomycin	50 mg/mL	5 g	dH <sub>2</sub> O, 100 mL	If the stock is crystalized, rethaw and redissolve at 37°C before use.	−20	90

(Continued)

**TABLE 1 |** (Continued)

Item	Stock	Stock solution concentration	Quantity	Dissolve in	Preparation note	Storage temp (°C)	Storage days
23	Thiamine-HCl	1 mg/mL	100 mg	100 mL	Cover with aluminum foil and keep in dark.	4	60
24	Thidiazuron (TDZ)	0.1 mg/mL	1 mg	1 mL 1 N NaOH + 9 mL H <sub>2</sub> O		4	90
25	Thymidine	25 mg/mL	250 mg	dH <sub>2</sub> O, 10 mL	If the stock is crystalized, rethaw and redissolve at 37°C before use.	4	90
26	Zeatin, trans	0.5 mg/mL	50 mg	5 mL 1 N NaOH + 95 ml ddH <sub>2</sub> O	Dissolve <i>trans</i> -zeatin in 5 mL 1 N NaOH, then bring volume to 100 mL with ddH <sub>2</sub> O.	4	60

\*All stock solutions should be filter sterilized using 0.22 µm syringe filter or Stericup filtration system, except for item 6. Items 3 and 4 can also be sterilized by autoclave.

4. Soil moisture is monitored on daily basis. Sprouting seeds can be expected about 4 days after the sowing. Keep the humi-dome on the flat until the sixth day after the planting. Seedlings are watered only if the potting mix appears to be dry.
5. Seedlings with ~4–5 leaves can be transplanted into large pots approximately 2 weeks after the sowing (**Figure 2C**).
6. Potting mix Pro-Mix BRK20 is used to fill 2.5 gallons (9.4 L) nursery pots. Each pot is top-dressed with 2/3 tsp tomato maker, 2/3 tsp Osmocote, and 1/2 tsp Sprint Iron chelate. Then RO water is used to water the pot until the potting mix becomes saturated.
7. Seedling, with soil adhering to the roots, is carefully transplanted from a small plastic insert into the large pot with properly prepared and wetted potting mix (**Figure 2D**) and placed on a 1 m tall bench (about 2.7 m or 9 ft below the lights) for about 2 weeks (**Figure 2E**). Plants can be moved to the floor 2–3 weeks after the transplanting (**Figure 2F**) and spaced at least 12.5–15 cm (5–6 inches) apart between pots.
8. Plants are watered as needed. Overwatering of maize plants will result in poor development of the root system. Maize plants grow differently under different growth conditions. In the greenhouse described in this work, the B104 plants are watered daily with fertilizer solution (Jacks 15-5-15 at 400 ppm, pH 6.0). Every third watering is with RO water. Watering frequency is 1–2 times daily as needed.
9. Female flower (silk) emergence (**Figure 2G**) occurs approximately 60 days after the sowing. To ensure controlled pollination, emerging ears are covered with a wax-treated paper shoot bag prior to silk emergence (**Figure 2H**). To avoid pollen cross-contamination, plants and shoot bags should be closely monitored. Any uncovered or improperly covered female flowers should be discarded.
10. Male flower (tassel) emergence (**Figure 2I**) should occur around the same period, although not always synchronized with the female flowers. The tassel should be covered by a brown pollination bag (**Figure 2J**) once it starts to produce pollen.
11. To produce immature embryos, silks are pollinated using pollen from the same plant or a sibling B104 plant. To encourage silks growth, the ear shoot tip can be cut (**Figure 2K**) one day prior to the pollination. Using a pair of clean scissors, cut the female flower ~2.5 cm (1 inch) from the top of the shoot. The cut ear is immediately covered by a shoot bag and allowed to grow for another day to ensure freshly grown, evenly distributed silks are used for pollinations. Before being used to cut the next ear shoot, scissors should be sanitized with 70% ethanol to prevent fungal or bacteria contamination carryover between ears.
12. Pollination should take place in the mid-morning the next day. Pollen is collected from a B104 plant with a bagged tassel. To release pollen from anthers, the tassel bag, and the tassel should be shaken by hand gently, the bag with the pollen is then removed from the tassel for pollination (**Figure 2L**). The tassel is immediately covered by another new tassel bag if the tassel is to be reused in next day. Otherwise, the tassel should be removed from the plant (detassel) to avoid any unwanted pollen shedding and cross-contamination.
13. Identify a bagged ear shoot that was cut the previous morning. Remove the shoot bag, quickly but carefully sprinkle the pollen evenly onto the freshly grown silks (**Figure 2M**). The pollinated ear is immediately covered with a brown pollination bag that is labeled with the cross information such as plant ID, date, and nature of the cross (**Figure 2F**). Pollen collected from one tassel with 50–70% opened anthers can be used to pollinate multiple ear shoots. Pollen from freshly opened anthers is most desirable, although B104 pollen of up to 4 days post-anther emergence can still be used.
14. Immature embryos of 1.8–2.0 mm (up to 2.5 mm) in size are ideal for maize transformation. To obtain the embryos of the appropriate sizes, ears should be checked for embryo development while they are still on the plant (**Figure 2N**) around 10 days after the pollination. Embryo sizes can be measured by a caliper (**Figure 2O**) or estimated by a small ruler (**Figure 2P**). Typically, ears can be harvested between 10 and 14 days depending on the temperature of



the greenhouse, which may be impacted by exterior weather conditions. In general, embryos reach desired sizes faster in the summer season than in the wintertime.

*Important: Plants should be monitored routinely throughout their life for insect and fungal pathogens and should be appropriately treated when pathogens are present. Plants that have been kept free of pathogens and received the minimum possible pesticide applications to produce the healthiest embryos for transformation.*

## Preparation of *Agrobacterium* Plate Cultures

1. At least three days before the infection or earlier, prepare a “mother” plate (Table 2) of *Agrobacterium* strain KL2013vir/thy from a glycerol stock that was originally prepared from a single colony. Streak *Agrobacterium* on the “mother” plate using a sterile loop.
2. Incubate the mother plate at 28°C in the dark for 36~48 h. The “mother” plate with fully grown *Agrobacterium* colonies (Figure 3A) can be stored at 4°C in the dark for up to 7 days.
3. Day 0: One day before the embryo infection experiment, prepare a “working” plate (Table 2) of KL2013vir/thy. Collect 7–8 colonies (2 mm diameter) from the “mother” plate (Figure 3A) and streak them evenly on the “working” plate surface. The purpose of collecting at least 7–8 colonies from the mother plate is to ensure that sufficient *Agrobacterium* cells are inoculated on the “working” plate. An L-shaped spreader can be used to evenly spread the cells on the plate. To ensure enough *Agrobacterium* culture for infection, prepare one or two additional “working” plates as back-ups.
4. Incubate the “working” plates at 28°C in the dark for 16–20 h (Figure 3B). Avoid using “working” plates that are older than 24 h after the streaking.

## Ear Sterilization and Embryo Dissection (Day 1, Stage 1)

1. Remove the husk leaves and silks from the ears harvested from the greenhouse. Insert an ethanol-sterilized handle into either the top or the base of the ear (Figure 3C). The ear can be cut into two halves horizontally to fit into a large container for sterilization.
2. Place the ear into a large, sterile beaker on a laminar flow bench. Pour sterilization solution [2 L of 20% commercial bleach (8.25% sodium hypochlorite) plus two drops of Tween 20] into the beaker so that the solution will cover the ear completely. Gently swirl the ears and tap them to the beaker bottom 10–20 times to remove bubbles trapped on the surface of the ears. Keep the ear in the sterilization solution for 30 min, stirring lightly every 10 min to ensure all ear surfaces are in contact with the solution.
3. Discard the sterilization solution into a large waste container. Add a large volume of autoclaved Millipore water into the beaker to wash the ears. Stir lightly 2–3 times and leave the ears in the water for 5 min. Repeat the

wash step two more times, for 2 min each to complete the sterilization step.

4. Place the sterilized ear on a large, sterile Petri plate on the laminar flow bench. Using a sharp, clean scalpel, carefully remove the opaque kernel top, 2~3 mm thickness at once until the clear endosperm is exposed (Figure 3G). Cutting too deep into the kernel may accidentally damage the embryos, especially when they are larger than 2 mm.
5. Insert a sterile micro-spatula (Figure 3D) perpendicular to the ear axis at the bottom of the kernel then squeeze gently toward the ear-tip side (Figures 3G,H). The embryo is located at the bottom, ear-tip side of the kernel. The embryo will emerge between the pericarp and endosperm. If the embryo does not pop up from the kernel, gently scoop out the endosperm with the spatula to isolate the embryo from the adhering tissue. Figure 3I demonstrates the use of a dental filling instrument for embryos isolation. The micro-spatula can be used for squeezing or scooping, while the dental filling instrument is more efficient in scooping the immature endosperm.
6. Put the embryo into a 2 mL Eppendorf tube containing 1.6 mL of liquid 700A infection medium without thymidine and acetosyringone (AS, Table 2). Collect up to 100 embryos in one tube (Figure 3G, Step 2). The embryos can be stored in the tube on the bench for 2–3 h.

## *Agrobacterium* Infection and Co-cultivation (Day 1, Stage 2)

1. In a 50 mL conical tube containing 10 mL of 700A infection medium (Table 2), add 20 µL of 25 mg/mL thymidine (final concentration, 50 mg/L) and 10 µL of 100 mM AS (final concentration, 100 µM). Thymidine and AS should be added freshly before each experiment. Divide 700A infection medium into two 50 mL tubes (5 mL each).
2. Harvest *Agrobacterium* cells from the working plate (Figure 3B) using a sterile loop. Inoculate the bacteria in the 5 mL 700A infection medium. Vortex the tube for 4–5 s to fully resuspend the bacteria.
3. Measure optical density (OD) of *Agrobacterium* suspension at 550 nm on a spectrophotometer and adjust the OD<sub>550</sub> of the suspension to 0.50 ± 0.05. This *Agrobacterium* suspension should be used immediately as it can readily form aggregates within 30 min after inoculation.
4. Before infection, wash the isolated embryos once with a freshly prepared 700A infection medium. Carefully remove the 700A infection medium using a pipet, then add 1 mL of freshly made *Agrobacterium* suspension to the embryos in the tube. Cap the tube and gently invert it 3–4 times. Incubate the tube at room temperature (22–24°C) for 5 min, by placing it sideways on the bench.
5. Tap the tube 4–5 times to dislodge the embryos from the sidewalls of the Eppendorf tube. Then pour the bacteria suspension containing the embryos onto a co-cultivation plate (710I, Table 2). Tilt the plate to collect and remove as much bacterial suspension as possible with a pipette.

- Under a dissecting microscope in the laminar flow bench, carefully orient the embryos by placing them scutellum side (smooth and round side) up (**Figure 3G**, Step 3). Use the micro spatula or the dental filling instrument scaler (**Figure 3D**) to gently flip the embryos; avoid damaging the embryos (**Figure 3E**).
- Wrap the plates with a micropore tape or place the unwrapped plates in a clean plastic culture box (**Figure 3F**). Incubate the plates at 20°C in the dark for 16–20 h.

## Resting (Day 2), Maturation and Selection (Day 9)

- Transfer and place the embryos, scutellum side up, to a resting medium (605G, **Table 2**). Place no more than 25–30 embryos per plate. Incubate the plates at 28°C in the dark for 7 days. Transient RFP expression is visible 3 days post-infection.
- Eight days after infection, transfer the embryos to a maturation medium supplemented with 3 mg/L bialaphos (13329B3, **Table 2**). Carefully remove growing hypocotyls with forceps and scalpel. This is to prevent the hypocotyl from lifting or re-orienting the embryo away from the medium. Place no more than 8–10 embryos per plate. Incubate the plates at 28°C in the dark for 10 days. Growing callus tissue emerges in this stage.
- Subculture the callus pieces to a new maturation medium containing 6 mg/L bialaphos (13329B6, **Table 2**). If the calli grow vigorously (over 2 cm<sup>2</sup>), place 4–5 calli per plate. The base of calli with growing shoots may break naturally. If it breaks apart, spread the growing shoots onto the medium. Incubate the plates at 28°C in the dark for 14 days.
- The RFP gene mCherry expression in the callus or developing shoots can be examined by using either a fluorescent microscope (Olympus SZH10 stereo microscope with Texas red filter, excitation wavelength 535–585 nm, emission wavelength 605–690 nm) or using a NIGHTSEA dual fluorescent protein flashlight and filter glasses (NIGHTSEA LLC, Lexington, MA, United States). Tiffen 29 dark red filter can be used for DSLR camera for imaging.

## Rooting (Day 33)

- Transfer callus pieces with fully developed shoots onto a rooting medium containing 2 mg/L bialaphos (13158B2, **Table 2**). Place one or two callus pieces in one plate to ensure enough space for shoot growth. Remove excessive callus materials around the shoots. Incubate the plates at 26°C in a light chamber, with a photoperiod of 16 h light and 8 h dark (80 μmol/m<sup>2</sup>/s) for 14 days.
- Plantlet (>4 cm) with developed roots (>2–3 cm) (**Figures 4A,B**) can be transplanted to soil and moved to the growth chamber for acclimatization. Green mature shoots without roots may be subcultured for an additional 14 days under the same condition. The excessive callus materials associated with the shoots should be removed during the subculture.

- If the T0 plantlets are to be brought to maturity for seeds, pollen donor plants will need to be planted at this time or 60 days prior to the projected date of pollination. This step needs to be taken to ensure access to high-quality pollen. Because female and male flowers of *in vitro* regenerated maize plants are often not synchronized, wild-type B104 plants can be used as pollen donors to pollinate transgenic T0 female flowers. When the root of the T0 plant is visible in the Petri dish, germinate B104 seeds every 5–7 days until all transgenic plantlets are transplanted from Petri dishes to the soil.

## Transplantation and Acclimatization (~Day 50)

- When T0 plantlets have established in tissue culture rooting media, they are ready to be transplanted to soil. Transplant plantlets with healthy roots (longer than 2–3 cm, as shown by red arrows in **Figure 4B**). Smaller plants can be subcultured to fresh medium for continued growth.
- Fill 1801 deep inserts (2/3 of the height) with autoclaved potting mix such as Metromix 360 and place them into STF-1020-OPEN flat with drain holes (**Figure 2A**). Make a hole for the plant in the middle of each cell using a spoon. Autoclaved potting mix is recommended to prevent fungal contamination. The autoclaved moisten potting mix (60~70% saturated) can be stored in a cool place for 2 weeks.
- Using a pair of sterile forceps, first break up the media around the roots on the plate, then hold the base of the plantlet, gently pull it from the gel media without damaging the roots.
- Hold the plantlet with a gloved hand and gently swirl it in sterile water 3–4 times to wash off the plant medium. It is important to remove excess medium associated with the roots as the presence of gel may bring fungal growth, which can kill the young plant. However, it is also important to avoid any physical damage to the plants during the process. If the roots are coated with plant medium, do not scrape it off, but rather gently rinse to remove the remaining media clumps.
- Carefully remove any callus and shoots without roots using a pair of sterile forceps. Non-regenerated tissue will naturally come off from the regenerated plantlets. If the tissue is tightly bound with the plantlet, do not use a scalpel to dislodge them from the plantlet. For bushy plants (**Figure 4C**) or multiple shoot clusters, carefully separate individual plants from the cluster as much as possible but avoid tearing or damaging roots or shoots in the process. The cleaned individual plantlet (**Figure 4D**) can be examined for the red fluorescent protein expression on the root at this stage.
- Place one plantlet per cell. Bury the roots and base of stem 3–5 cm deep in the potting mix (**Figure 4E**). Cover the flat with a plastic humi-dome (**Figure 4F**). Keep the plantlet upright to avoid touching the side of the humi-dome. Place the tray in a growth facility

**TABLE 2 |** Media for B104 transformation (modified from Hoerster et al., 2020).

Name	Chemical	Final conc.	Vendor/Cat info
Mother plate	glucose	5 g/L	Fisher scientific, D16
AB buffer	Bacto agar	15 g/L	BD Biosciences, 214030
	<i>Autoclave, cool to 55°C, then add</i>		
	AB buffer (20X)*	1X	
	AB salts (20X)*	1X	
	FeSO <sub>4</sub> ·7H <sub>2</sub> O (1.25 mg/mL)*	2.5 mg/L	Fisher scientific, I146
	thymidine (25 mg/mL)*	50 mg/L	Millipore Sigma, T1895
	gentamicin (50 mg/mL)*	50 mg/L	Phytotech labs, G570
and/or	kanamycin (50 mg/mL)*	50 mg/L	Millipore Sigma, K1377
and/or	spectinomycin (100 mg/mL)*	100 mg/L	Millipore Sigma, S4014
Working plate	sodium chloride	5 g/L	Fisher scientific, S271
YEP base	yeast extract	5 g/L	Fisher scientific, BP14222
pH 6.8	peptone	10 g/L	BD Biosciences, 211677
	<i>Adjust pH to 6.8 with 1 M NaOH, then add</i>		
	Bacto agar	15 g/L	BD Biosciences, 214030
	<i>Autoclave, cool to 55°C, then add</i>		
	thymidine (25 mg/mL)*	50 mg/L	Millipore Sigma, T1895
	gentamicin (50 mg/mL)*	50 mg/L	Phytotech labs, G810
and/or	kanamycin (50 mg/mL)*	50 mg/L	Millipore Sigma, K1377
and/or	spectinomycin (100 mg/mL)*	100 mg/L	Millipore Sigma, S4014
Infection	MS basal salt mixture	4.33 g/L	MilliporeSigma, M5524
700A	myo-inositol	0.1 g/L	MilliporeSigma, I3011
pH 5.2	nicotinic acid (1 mg/mL)*	0.5 mg/L	MilliporeSigma, N0761
	pyridoxine-HCl (1 mg/mL)*	0.5 mg/L	MilliporeSigma, P8666
	thiamine (1 mg/mL)*	10 mg/L	MP biomedical, 194749
	casamino acids	1 g/L	Fisher scientific, BP1424
	sucrose	68.5 g/L	Fisher scientific, BP220
	glucose	36 g/L	Fisher scientific, D16
	2,4-Dichlorophenoxyacetic acid (2,4-D) (0.5 mg/mL)	1.5 mg/L	MilliporeSigma, D7299
	<i>Adjust pH to 5.6 with 1 M NaOH</i>		
	<i>Filter sterilize (0.22 μM)</i>		
	Add thymidine (25 mg/mL)* freshly before use	50 mg/L	Millipore Sigma, T1895
	Add acetosyringone (AS) (100 mM)* freshly before use	100 μM	Millipore Sigma, D134406
Co-cultivation	MS basal salt mixture	4.33 g/L	MilliporeSigma, M5524
710I	myo-inositol	0.1 g/L	MilliporeSigma, I3011
pH 5.6	nicotinic acid (1 mg/mL)*	0.5 mg/L	MilliporeSigma, N0761
	pyridoxine-HCl (1 mg/mL)*	0.5 mg/L	MilliporeSigma, P8666
	thiamine (1 mg/mL)*	10 mg/L	MP biomedical, 194749
	proline	0.7 g/L	Alfa Aesar, A10199
	sucrose	20 g/L	Fisher scientific, BP220
	glucose	10 g/L	Fisher scientific, D16
	2-(N-morpholino)ethanesulfonic acid (MES)	0.5 g/L	Fisher scientific, BP300
	2,4-D (0.5 mg/mL)*	2 mg/L	MilliporeSigma, D7299
	<i>Adjust pH to 5.6 with 1 M NaOH, then add</i>		
	agar	8 g/L	MilliporeSigma, A7921
	<i>Autoclave, cool to 55°C, then add</i>		
	acetosyringone (AS) (100 mM)*	100 μM	Millipore Sigma, D134406
	thymidine (25 mg/mL)*	50 mg/L	Millipore Sigma, T1895
	silver nitrate (2 mg/mL)*	1 mg/L	Fisher scientific, S181

(Continued)

**TABLE 2 |** (Continued)

Name	Chemical	Final conc.	Vendor/Cat info
Resting	MS basal salt mixture	4.33 g/L	Phytotech labs, M5605 (11 g/L) <sup>#</sup>
605G	N6 macronutrient stock (10X)*	0.6X	Phytotech labs, M5605 (11 g/L) <sup>#</sup>
pH 5.6	B5H Minor salts (1000X)*	0.6X	Phytotech labs, M5605 (11 g/L) <sup>#</sup>
	NaFe EDTA for B5H (100X)*	0.6X	Phytotech labs, M5605 (11 g/L) <sup>#</sup>
	Eriksson's vitamins (1000X)*	0.4X	Phytotech labs, M5605 (11 g/L) <sup>#</sup>
	Schenk and Hildebrandt vitamins (100X)*	0.6X	Phytotech labs, M5605 (11 g/L) <sup>#</sup>
	potassium nitrate	1.68 g/L	Phytotech labs, M5605 (11 g/L) <sup>#</sup>
	thiamine HCl (1 mg/mL)*	0.2 mg/L	Phytotech labs, M5605 (11 g/L) <sup>#</sup>
	proline	2 g/L	Phytotech labs, M5605 (11 g/L) <sup>#</sup>
	sucrose	20 g/L	Fisher scientific, BP220
	glucose	0.6 g/L	Fisher scientific, D16
	casein hydrolysate	0.3 g/L	Thermo fisher scientific, J12855-P2
	2,4-D (0.5 mg/mL)*	0.8 mg/L	MilliporeSigma, D7299
	<i>Adjust pH to 5.6 with 1 M NaOH, then add</i>		
	TC agar	6 g/L	Phytotech labs, A296
	<i>Autoclave, cool to 55°C, then add</i>		
	dicamba (1 mg/mL)*	1.2 mg/L	Phytotech labs, D159
	silver nitrate (2 mg/mL)*	3.4 mg/L	Fisher scientific, S181
	carbenicilline (100 mg/mL)*	100 mg/L	Phytotech labs, C346
Maturation	MS basal salt mixture	4.33 g/L	MilliporeSigma, M5524
13329B	cupric sulfate (1 mg/mL)*	1.25 mg/L	MilliporeSigma, C2857
pH 5.6	myo-inositol	1 g/L	MilliporeSigma, I3011
	proline	0.7 g/L	Alfa Aesar, A10199
	sucrose	60 g/L	Fisher scientific, BP220
	zeatin, <i>trans</i> (0.5 mg/mL)*	0.5 mg/L	Phytotech labs, Z125
	<i>Adjust pH to 5.6 with 1 M NaOH, then add</i>		
	agar	7 g/L	MilliporeSigma, A7921
	<i>Autoclave, cool to 55°C, then add</i>		
	abscisic acid (ABA) (0.1 mg/mL)*	0.1 mg/L	MilliporeSigma, 862169
	6-Benzylaminopurine (BAP) (1 mg/mL)*	1 mg/L	MilliporeSigma, B3408
	thidiazuron (TDZ) (0.1 mg/mL)*	0.1 mg/L	Phytotech labs, T888
	carbenicilline (100 mg/mL)*	100 mg/L	Phytotech labs, C346
11329B3	bialaphos (2 mg/mL)*	3 mg/L	Gold Biotechnology, B0178
11329B6	bialaphos (2 mg/mL)*	6 mg/L	Gold Biotechnology, B0178
Rooting	MS basal salt mixture	4.33 g/L	MilliporeSigma, M5524
13158B2	myo-inositol	0.1 g/L	MilliporeSigma, I3011
pH 5.6	sucrose	40 g/L	Fisher scientific, BP220
	<i>Adjust pH to 5.6 with 1 M NaOH, then add</i>		
	Bacto agar	7 g/L	BD Biosciences, 214030
	<i>Autoclave, cool to 55°C, then add</i>		
	bialaphos (2 mg/mL)*	2 mg/L	Gold Biotechnology, B0178

\*See **Table 1** for stock solution preparation.

<sup>#</sup>Pre-made 605 medium salts is available at Phytotech labs (M5605) or add the ingredients described.

with 14/10 h (day/night) photoperiod, and 28/22°C (day/night) temperature. Plantlets transferred from the tissue culture media to potting mix tend to desiccate quickly due to low humidity. Therefore, the use of a humi-dome is critical to maintaining the moderate humidity level for the optimal acclimation to greenhouse growth conditions.

7. Check the plantlets and soil moisture daily. Water only when the soil becomes dry.

8. Four to six days after transplanting, remove the plastic humi-dome and continue watering as needed.
9. Phenotyping and genotyping of the T0 plantlets can be performed approximately 10–12 days after the transplantation (see below sub-section).
10. After approximately 2 weeks, healthy and robust-looking plantlets can be transplanted into a large pot as described in steps 6–8 in the above section of “Growing donor plants for the production of the immature embryo for





**FIGURE 2 |** Growing maize donor plants for immature embryo production. **(A)** Standard flat with small pots filled with potting mix for planting maize seed. **(B)** Six-day-old germinated seedlings under a humi-dome. **(C)** Two-week-old seedlings ready to be transplanted into large pots. **(D)** A seedling transplanted to a large pot. **(E)** Plants on a 1 m tall bench. **(F)** Pollinated mature B104 plants on the floor. **(G)** An un-pollinated B104 ear (female flower) with emerged silks. **(H)** A shoot bag covering an un-pollinated B104 ear. **(I)** A mature tassel (male flower) ready to be used for pollination. **(J)** A pollination bag covering a mature tassel for the purpose of collecting fresh pollen. **(K)** An un-pollinated B104 ear with cut silks. **(L)** Freshly collected pollen in a tassel bag. **(M)** Freshly pollinated silks, 1 day after silks were cut. **(N)** Extracting an immature embryo for measurement while the ear is still growing on the plant. **(O)** Measurement of an embryo size with a caliper. **(P)** Estimate of an embryo size with a ruler.

transformation.” Both 1 gallon (3.8 L) and 2.5 gallon (9.4 L) pots can be used for growing maize plants to full maturity. It is critical not to overwater the plants, especially when they are young.

## T0 Seed Production

1. When ears start to emerge (50–100 days post-transplant), T0 plants are pollinated to produce seed for subsequent generation testing and analysis. Male and female flower development can occur at separate times on an individual
2. To avoid pollen cross-contamination, transgenic plants should not be grown with any non-transgenic plants in the same growth room. All emerging ears are covered with a wax-treated paper shoot bag to prevent pollen contamination of the silks before pollination.
3. Cover the tassel with a bag. The bag should be folded to secure it around the stem with a paper clip to prevent pollen from escaping (**Figure 2J**).



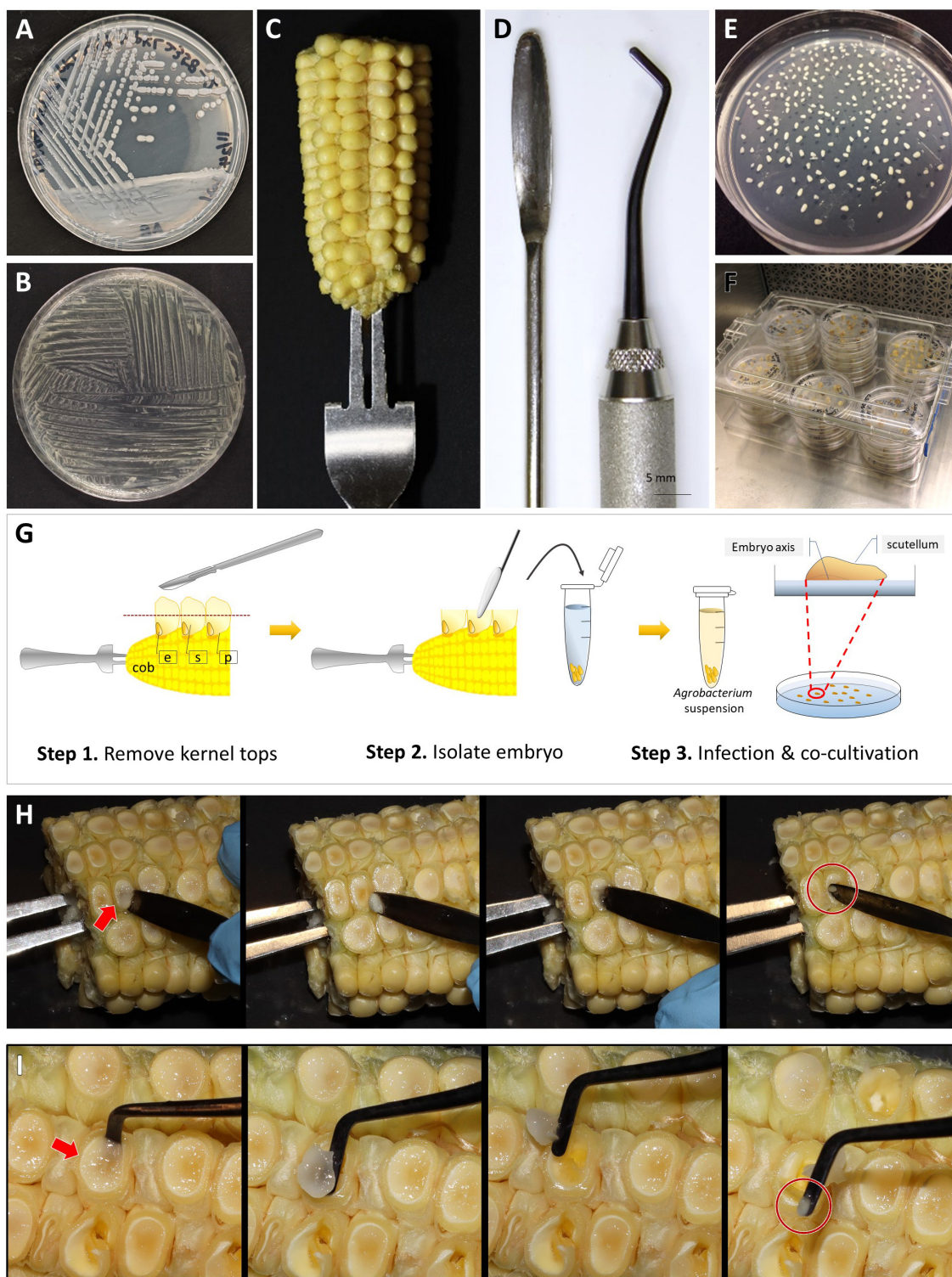


**FIGURE 3 |** Embryo dissection, infection, and co-cultivation. An *Agrobacterium* “mother” plate (A) and “working” plate after 18 h incubation, streaked by a disposable loop (B). (C) A B104 ear halves on a handle made of a fork. (D) Tools for embryo dissection; a micro spatula (left) and a dental filling instrument (right). (E) A co-cultivation plate with dissected immature embryos. All embryos were re-oriented scutellum side up. (F) A plastic culture box filled with plates. (G) Cartoon illustration of the embryo dissection and infection process. Step 1, remove kernel tops using a sterile scalpel; Step 2, isolate embryo from the kernel and transfer it to a tube filled with liquid 700A infection medium; Step 3, after infection, place embryo onto co-cultivation medium and orient the embryos by placing them scutellum side up. e: embryo, s: endosperm, and p: pericarp. Demonstration of embryo dissection using a micro spatula (H) or a dental filler (I). The arrows indicate the embryo side of the kernel. Circles highlight isolated embryos.



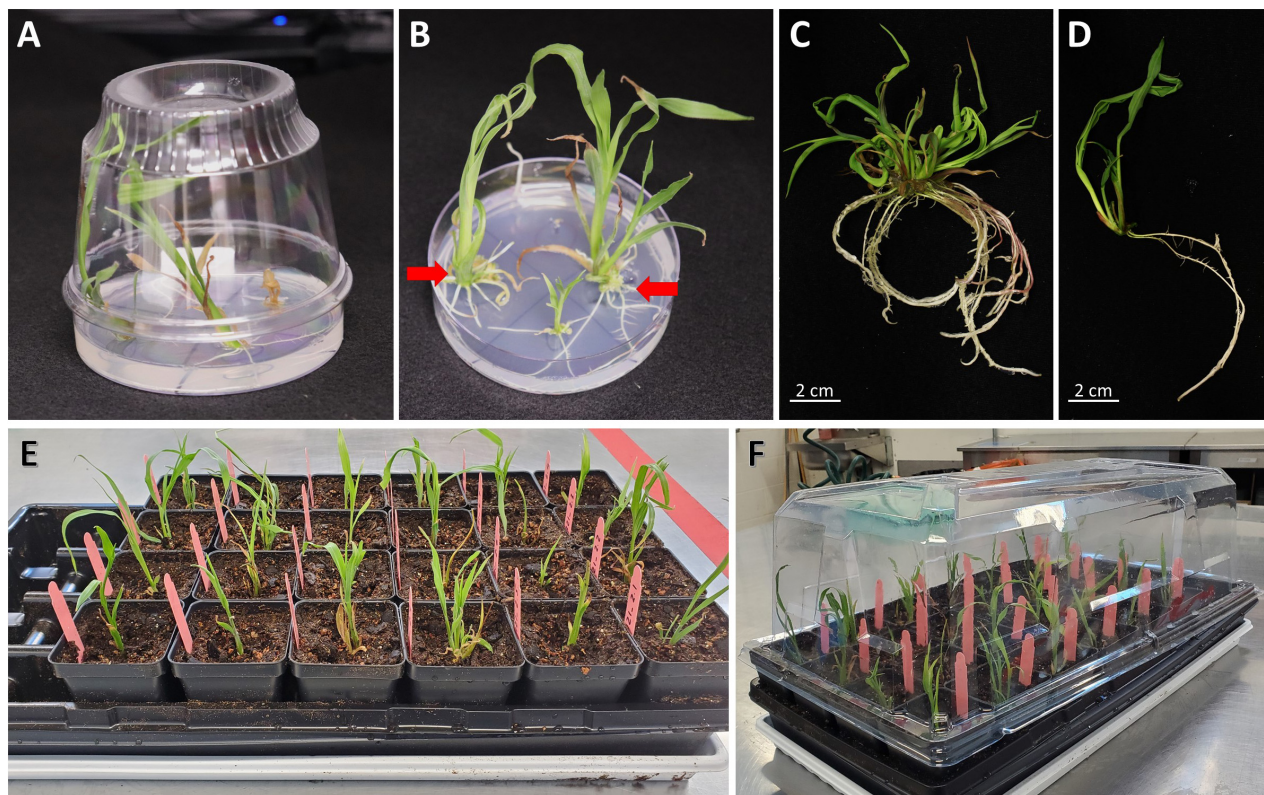


**FIGURE 4 |** Regenerated T0 plantlets from rooting stage to acclimatization in soil. **(A)** Plantlets growing on the rooting medium. Sundae cup is used as a cover to give vertical space to grow. **(B)** Regenerated plantlets ready to be moved to potting mix. Red arrows indicate plantlets with healthy roots. **(C)** Plantlet representing bushy phenotype or multiple shoot cluster. **(D)** Single-shoot plantlet ready to be transplanted to potting mix. **(E)** T0 regenerated plantlets transplanted to potting mix. **(F)** A plant propagation tray covered with a humi-dome to aid in acclimatization.

3. If the greenhouse space is crowded, detasseling the T0 plants will be necessary to prevent transgenic pollen cross-contamination. When the tassel is extended from the whorl, pull it out gently for detasseling. The detasseling may stimulate shoot growth.
4. Follow steps 9–13 described in the section “Growing donor plants for the production of the immature embryo for transformation” for T0 plant pollination.
5. Immediately cover the pollinated ear with the pollination bag. Record the ear donor, pollen donor, silking date, and pollination date on the tassel bag. Staple the back of the tassel bag.
6. Ten days post-pollination, remove the pollination bag and slide it into the node between the ear and the plant's stalk. Peel back the husk to observe the seed set and allow fresh air to the ear to prevent fungal contamination.
7. Thirty days post-pollination, stop watering to allow dry down and senescence of plants with mature ears. Keep the tassel bag on the stalk to keep the record.
8. Forty days post-pollination, harvest mature dried T0 ear and place in pollination bag, record the harvest date on the bag.
9. Dry the ears at room temperature inside the pollination bag on a benchtop for 2–3 weeks.

10. Remove kernels from ear and place in a seed packet, label the packet with appropriate experimental information, harvest date, and seed weight.
11. Seeds can be stored in a cool and dry place (15°C, Relative Humidity < 30%). For long-term storage, seeds can be kept at –20°C with an additional desiccant such as silica gel.

## Evaluating of T0 Plants for *glossy2* Phenotype

1. Knockout mutants of maize *glossy2* (*Gl2*) gene (Bianchi et al., 1975) can be evaluated on T0 plantlets. Although the gene product of *Gl2* is still unknown, it is responsible for the formation of a hydrophobic waxy cuticle layer in juvenile leaf tissues. The loss-of-function mutants can be readily identified by misting water on the young leaf surface (Bianchi et al., 1975). Water will roll off from wild-type leaf, whereas *gl2* null mutations affect the deposition of extracellular cuticular lipids allowing water droplets to adhere to the leaf surface. This is most obvious when working with homozygous or biallelic mutant plants.

*Note that misting on T0 plants can only be used as a preliminary evaluation. It should not be used to make conclusion on whether the plant is a loss-of-function mutant*

*event. Sequencing analysis is necessary to verify and confirm the phenotypes observed on the T0 plants.*

- Plants that have stayed out of the humi-dome at least for 4–6 days (typically 10 days post-acclimatization) can be evaluated for *gl2* phenotype. Use a spray bottle to mist the leaf surface with tap water.
- The *gl2* loss-of-function mutants would show water droplet adherence on both sides of the leaf blades while the surface of wild-type leaf blades would repel water droplets due to the hydrophobic cuticle layer.

## Molecular Analysis of T0 Plants

- Total genomic DNA can be isolated from the transgenic maize plants using a modified version of the protocol described by Edwards et al. (1991). Sample 3~4 cm<sup>2</sup> of fresh leaf tissue in a 1.5 mL tube. Add 500  $\mu$ L DNA extraction buffer containing 100  $\mu$ g/mL RNase A into each tube and grind the leaf tissue using a polypropylene homogenizing pestle attached to an electric drill. Incubate the tubes for 5–10 min at room temperature. If the leaf tissue is smaller than 2 cm<sup>2</sup>, reduce the DNA extraction buffer to 250  $\mu$ L.
- Add 500  $\mu$ L (equal volume to the DNA extraction buffer used in step 1) of chloroform and mix gently by inverting the tubes for 3 min, and centrifuge for 5 min at a maximum speed using a benchtop centrifuge (21,130  $\times$  g).
- Carefully transfer about 300  $\mu$ L of the top aqueous phase to a new tube and add 240  $\mu$ L (80% of aqueous phase, v/v) of isopropanol. If 250  $\mu$ L of extraction buffer was used, then transfer 150  $\mu$ L of the aqueous phase into a new tube and add 120  $\mu$ L of isopropanol. Be careful not to take any interphase or organic phase into the new tube. Mix well by inverting 4–5 times and centrifuge for 5 min at a maximum speed (21,130  $\times$  g).
- Remove the supernatant using a 1 mL pipette and rinse the genomic DNA pellet once with 500  $\mu$ L of ice-cold 80% ethanol.
- Centrifuge for 2 min at a maximum speed on a benchtop centrifuge and carefully remove the ethanol using a 1 mL pipette. Briefly spin down the tubes to collect the remaining ethanol on the tubes and remove it using a 200  $\mu$ L pipette. Air-dry the genomic DNA pellets for 10 min on a flow bench.
- To redissolve the genomic DNA pellet, add 50  $\mu$ L of nuclease-free water and finger tap the tubes 4–5 times. Measure the genomic DNA concentration using a Nanodrop spectrophotometer. Typically, 20–200 ng/ $\mu$ L of genomic DNA is obtained using this method (1–10  $\mu$ g of total genomic DNA), and 1  $\mu$ L of genomic DNA is used for a 20  $\mu$ L PCR reaction.
- Perform PCR screening to identify transgenic plants and to genotype the target gene, *Gl2*. PCR amplifies ~1 kb fragments from the *gl2* locus and the *Cas9* gene using the primer sets and PCR conditions previously reported (Lee et al., 2019).
- Run 1% agarose gel electrophoresis to resolve the PCR products and identify *Cas9*-positive T0 plants.

**TABLE 3** | Summary of transformation frequency (TF) of three experiments.

EXP	Nr. of ears	Nr. of infected Embryos	Nr. of regenerants	% regenerants	Nr. of T0 event	% TF
ALT1-CAS	3	110	38	34.5%	10	9.1%
ALT2-CAS	5	111	11	9.9%	2	1.8%
ALT3-CAS	3	142	23	16.2%	12	8.5%
<b>Total</b>	<b>11</b>	<b>363</b>	<b>72</b>	<b>19.8%</b>	<b>24</b>	<b>6.6%</b>
<b>Average</b>	<b>3.7</b>	<b>121</b>	<b>24</b>	<b>20.2%</b>	<b>8</b>	<b>6.4%</b>

- For the *Cas9*-positive plants, treat the PCR products from the *gl2* locus with the ExoSAP-IT<sup>TM</sup> reagent for Sanger sequencing analysis. Mix 5  $\mu$ L of *gl2* PCR product with 2  $\mu$ L ExoSAP-IT<sup>TM</sup> reagent and incubate 30 min at 37°C followed by incubation for 15 min at 80°C for enzyme inactivation.
- Perform Sanger sequencing using a preferred service provider.
- Analyze the sequence trace files from the transgenic plants and wild-type B104 using publicly available web-based CRISPR editing analysis software; Tracking of Indels by Decomposition (TIDE; Brinkman et al., 2014), Inference of CRISPR Edits (ICE; Hsiao et al., 2019), and Degenerate Sequence Decode (DSDecodeM, Xie et al., 2017). Short indel mutations can be readily identified by these programs and it is recommended to use at least two software to cross-check the outcomes.

*Note: Direct Sanger sequencing of the PCR products and trace file analyses using online decode tools demonstrated here are recommended for rapid screening of mutant events. For precise/final genotyping analysis, cloning of the PCR products into a plasmid vector and then Sanger sequencing of multiple clones are recommended.*

## RESULTS

### Transient and Stable Transformation

In this work, three independent transformation experiments were conducted and a total of 363 embryos collected from 11 ears were infected (Table 3). The binary vector construct pKL2013 (Figure 1A) used in this work carries a red fluorescent protein (RFP) mCherry gene, which is under a constitutive promoter P35S. This visual marker gene was used to monitor the T-DNA delivery and transient gene expression after infection and co-cultivation. Nearly all infected embryos showed transient RFP expression 3 days post-infection (Figures 5A,B). RFP expression patterns can be various; they can be found on the middle of the scutellum (Figure 5A) or the side of the embryos (Figure 5B).

A total of 72 shoots were regenerated from infected embryos that were grown on the bialaphos-containing selection media. The regeneration rates ranged from 9.9 to 34.5% (Table 3) with an average of 20.2%. PCR analysis was performed on all 72 plants and 24 of them (33.3%) were transgenic carrying the *Cas9* gene. The transformation frequency (TF, number of T0 plants



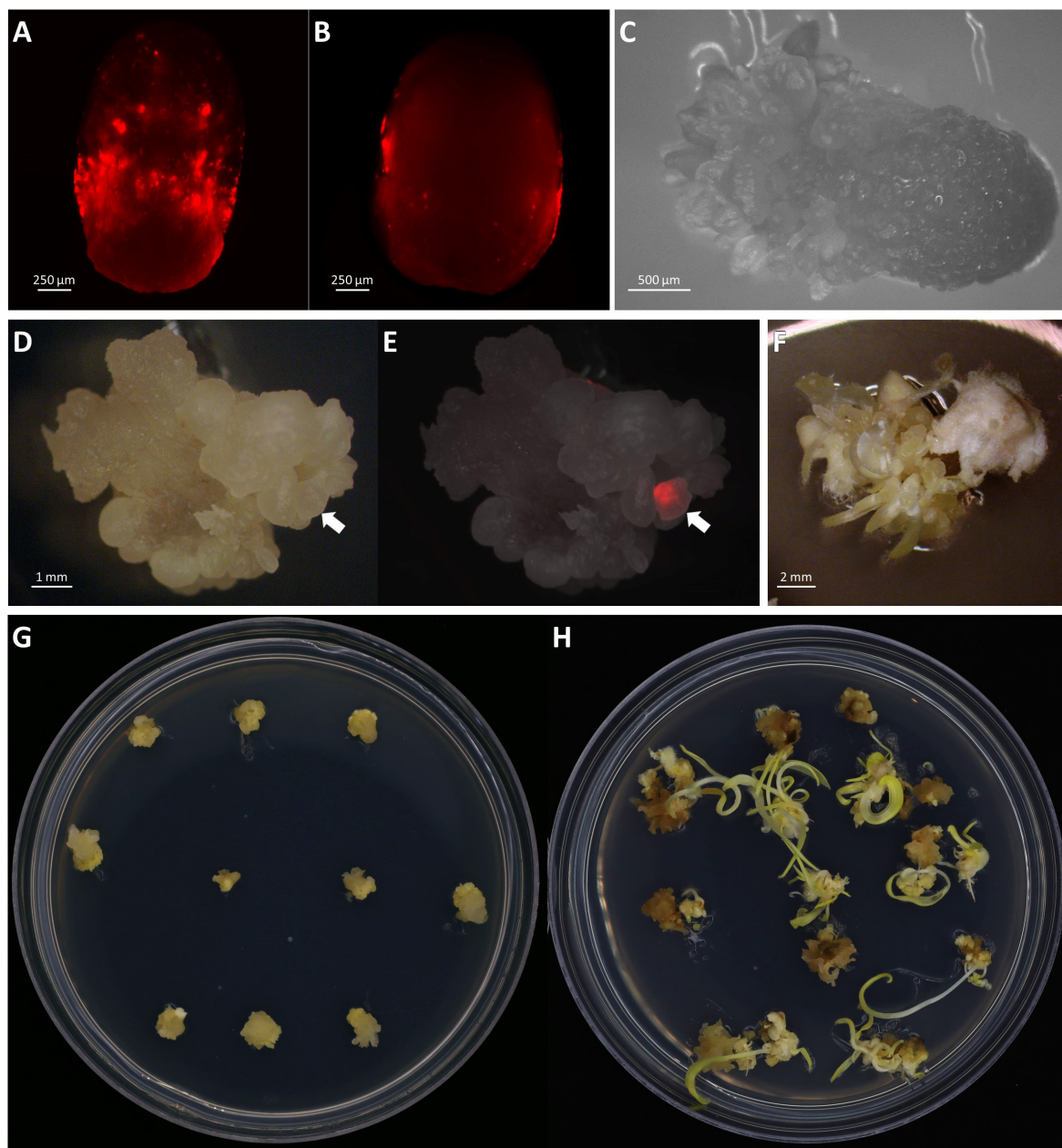


**FIGURE 5 |** Transient and stable transformation. Observation of transient RFP expression 3 days post-infection on the middle of the scutellum (A) or the side of the embryos (B). (C) Somatic embryogenesis on embryo scutellum side, 8 days post-infection in bright field. Observation of stable transformation and callus formation of maize embryo under bright field (D) and RFP field overlayed (E). The arrows indicate callus with the RFP expression. (F) Tentacle-like structure on a callus during the maturation stage, 21 days post-infection. Maize callus on the maturation I medium, 18 days post-infection (G) and the maturation II medium, 31 days post-infection (H).

per 100 infected embryos) of the three infection experiments using this protocol ranged from 1.8 to 9.1% with an average of 6.4% (Table 3), which was comparable to the 4% TF reported previously (Raji et al., 2018).

## Plant Regeneration

A major improvement in this protocol is the significant reduction in the time it takes to produce transgenic plants. In this work,

rooted transgenic T0 plantlets were obtained in as little as 50 days after infection (Table 4). Compared to the conventional B104 protocol (Raji et al., 2018), this method reduces callus selection and the proliferation timeline from 161 to 42 days (Table 4, Steps 4–9). After resting (8 days post-infection), somatic embryos started to emerge on the scutellum of the embryos (Figure 5C). These embryos were transferred to a maturation medium containing 3 mg/L bialaphos (13329B3, Table 2). At

**TABLE 4** | Comparison of conventional and improved B104 transformation methods.

Step	Activities	Day of Action	
		Conventional <sup>1</sup>	Improved <sup>2</sup>
1	Agro strain preparation	Day 0	Day 0
2	Embryo dissection, infection, co-cultivation	Day 1	Day 1
3	Resting	N/A	Day 2
4	Shoot formation and selection I	Day 4	Day 9
5	Shoot formation and selection II	Day 18	Day 19
6	Bulking	Day 60	N/A
7	Regeneration and selection	Day 137	N/A
8	Rooting	Day 151	Day 33
9	Moving to soil	Day 165	Day 51

<sup>1</sup>Based on Raji et al. (2018).<sup>2</sup>This work.

the beginning of the maturation stage, developing tissues form enlarged somatic embryo-like structures which are similar to Type I callus described by Wan et al. (1995) (Figures 5D,E,G). After 10–14 days on the maturation medium (18–22 days post-infection), the callus formed white and opaque tentacle-like tissues (Figure 5F). The tentacle-like tissues further developed to pale-yellow shoots (Figure 5H). To suppress non-transgenic shoot growth, the developing callus tissues were moved to a maturation medium containing 6 mg/L bialaphos (13329B6, Table 2).

Due to high auto-fluorescence from green chlorophyll, RFP expression on the shoot was screened before transferring to the rooting medium and being incubated under the light. RFP expression on pale-yellow developing shoots was observed (Figures 6A,B). Interestingly, not all transgenic plantlets showed RFP expression on the developing shoots. Regardless of the RFP expression, all shoots that were bigger than 2–3 cm with fully developed leaves were transferred to a rooting medium containing 2 mg/L bialaphos (28–32 days post-infection). In the rooting medium, the bialaphos concentration was reduced to 2 mg/L for root development (13158B2, Table 2). After 7 days on the rooting medium (35–39 days post-infection), roots started emerging from the base of the green shoots. Regenerated plantlets with 4–5 cm long mature roots (Figure 4B) were transferred to the growth chamber for acclimatization (48–55 days post-infection). Well-established plants were transferred to the greenhouse for further growth.

After 2–3 months in the greenhouse, transgenic plants started to produce pollen. RFP expression was checked on the collected pollen grains under the fluorescent microscope. Pollen from the T0 plants showed RFP expression indicating the presence of the T-DNA in the gametes (Figures 6E–H). Using this protocol, established transgenic T0 plants were obtained about 50 days after infection (Table 4). It usually takes additional 3–4 months in the greenhouse to produce mature T1 seeds.

## Targeted Mutagenesis in T0

Transformation with the construct pKL2013 carrying a Cas9/gRNA cassette targeting the *Gt2* gene in maize (McCaw

et al., 2021) resulted in the generation of 24 transgenic plants. These plants were characterized by Sanger sequencing to determine the targeted mutagenesis outcomes. The *Gt2* exon2 region was PCR amplified from all Cas9-positive transgenic plants and a wild-type control. The amplified PCR products were subjected to direct Sanger sequencing. Because the T0 plant can have mixed mutation types on the targeted gene, direct sequencing of PCR products containing such mutations often results in superimposed chromatographs. To interpret these data generated from the direct sequencing, the presence of indel mutations at the target site was analyzed by TIDE (Brinkman et al., 2014) and ICE (Hsiao et al., 2019) software using the sequencing trace files and the default parameters. As shown in Table 5, 16 out of 24 (66.6%) Cas9-positive plants carried indel mutations, demonstrating that our improved protocol can be used for targeted mutagenesis applications. Among the mutant plants, seven were biallelic (29.2%), six were mosaic (25%), two were heterozygous (8.3%), and one was homozygous (4.2%) (Table 5). Detected mutations were either 1 bp insertion (A) or short deletions ranging from 1 to 27 bp at the target site (Figure 7). Interestingly, three transgenic plants regenerated from the same embryo were carrying different indel mutations (events 14–16 in Figure 7). All three were biallelic mutants and carried an identical 1 bp insertion on one allele but contained different deletion mutations on the other allele.

The indel mutations on both alleles of the *Gt2* gene target region can lead to the loss-of-function *gt2* phenotype, in which the juvenile leaf surface becomes dull and does not repel water droplets (Figures 6C,D). This phenotype can be observed in both T0 regenerated young plants and T1 seedlings of mutant progenies after misting their leaf surfaces. However, it is much easier to ascertain the phenotype in T1 seedlings than in the T0 plants (McCaw et al., 2021). In this work, although we screened the *gt2* mutant phenotype in the T0 plants after the regenerants were acclimated for 10 days (Figure 7), we consider the water spraying assay as preliminary. As shown in Figure 7, eight out of 16 plants (events 1, 7–9, 11, 12, 14, and 15) that displayed the *gt2* phenotype indeed carried indel mutations at the target site. Two plants (events 2 and 4) showed a mixed phenotype. Six plants, three mosaics (events 3, 5, and 6), one homozygous (event 10), one heterozygous (event 13), and one biallelic (event 16) displayed wild-type phenotype. Further analysis on all these plants should be carried out in T1 progenies.

## DISCUSSION

*Agrobacterium*-mediated genetic transformation is an important tool for both fundamental and applied research for maize. The current *Agrobacterium*-mediated transformation protocol for B104 inbred requires about 16–22 weeks to generate rooted transgenic plants with an average TF of 4% (Raji et al., 2018). Here, we described a rapid *Agrobacterium*-mediated transformation protocol for B104 including detailed media compositions as well as the stepwise procedures of producing transformation starting materials, preparing *Agrobacterium*



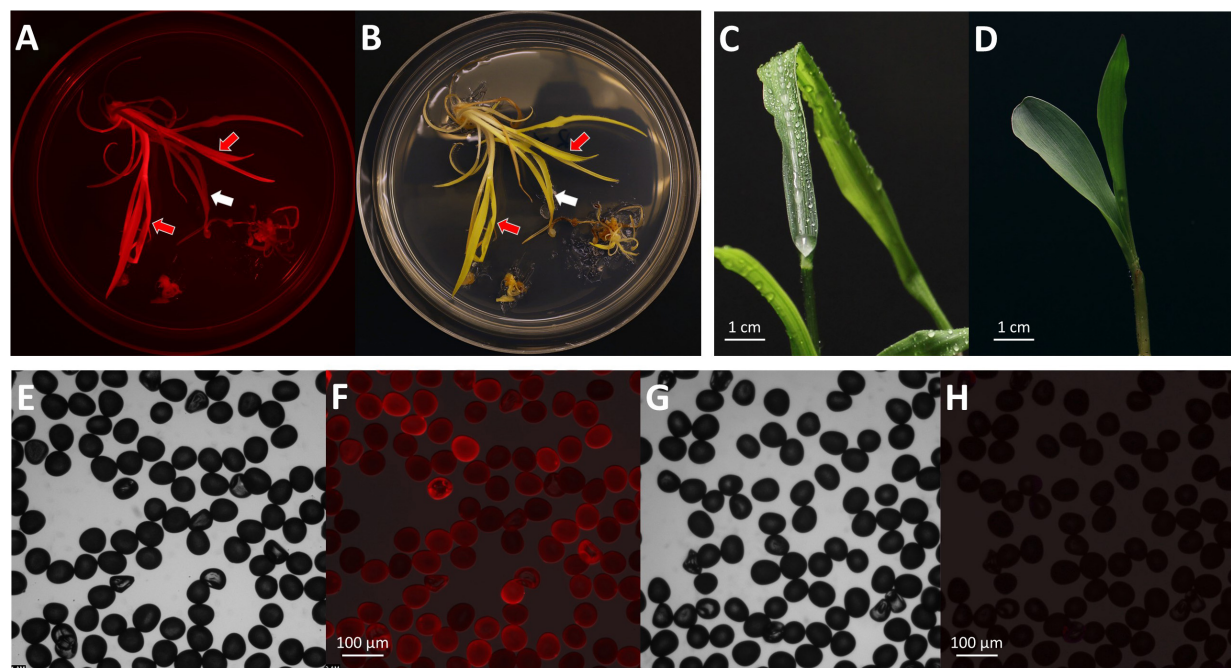


**FIGURE 6 |** Phenotypes of T0 transgenic plants. Observation of mature shoots with roots on the maturation II medium under an RFP channel (A) and a bright field (B). Black arrow indicates a shoot with RFP expression; white arrow indicates a shoot without RFP expression. Observation of the *gl2* knock-out phenotype on a T0 regenerated plant (C) and a wild-type seedling after water spray (D). Observations of pollen grains collected from a T0 plant (E,F) and a wild-type B104 control (G,H). Images of (E,G), bright field; (F,H), RFP field overlay.

**TABLE 5 |** Summary of T0 mutant genotypes.\*

	Number of plants	% T0 mutant
Homozygous	1	4.2%
Biallelic	7	29.2%
Heterozygous	2	8.3%
Mosaic	6	25.0%
Wild type	8	33.3%
<b>Total analyzed</b>	<b>24</b>	<b>100.0%</b>

\*Homozygous, one mutant sequence without wild type allele; Biallelic, two different mutant sequences; Heterozygous, wild type sequence and one mutant sequence; Mosaic, three or more mutant sequences in a single plant.

cultures, conducting infection and regeneration experiments, phenotyping and genotyping of transgenic and mutant plants, and generating T1 seeds. This much-simplified protocol requires only about 7–10 weeks to produce rooted transgenic plants with an average TF of 6.4%.

In this study, CRISPR/Cas9 reagents targeting *Gl2* gene were delivered into maize embryos to further demonstrate the utility of this protocol in genome editing applications. The overall frequency by CRISPR/Cas9-induced indel mutations was 66.6% (16/24 T0 plants) demonstrating that this rapid B104 transformation protocol can be effective for targeted mutagenesis. Compared to McCaw et al. (2021), which used pKL2013 for targeted mutagenesis in a different genotype, Fast-flowering mini maize, the overall targeted mutagenesis frequency is slightly lower (66.6 vs. 79.1%;  $P > 0.05$ , two proportion

z-test). Interestingly, the combined frequency (33.4%) of biallelic (4.2%) and homozygous (29.2%) mutants observed in this study (Table 5) was much lower compared to the 66.3% combined frequency reported in Table 2 of McCaw et al. (2021). This difference is statistically significant (33.3 vs. 66.3%;  $P < 0.01$ , two proportion z-test). This observation may suggest that the reduced callus propagation period in this protocol might have an impact on the efficacy of the CRISPR/Cas9 reagents. The shorter duration of the *in vitro* tissue culture could reduce the chance of targeted mutagenesis by the CRISPR reagents integrated into the genome of the transformed tissues. Nevertheless, loss-of-function mutants were readily obtained in T0 generation with this protocol. A protocol with 50% reduced turnaround time and simplified procedures are clearly advantageous for most genome-editing applications in B104.

The improved transformation protocol could be partially attributable to the ternary helper plasmid, pKL2299, which carries extra copies of essential *Agrobacterium vir* genes used in this study, and adoption of the media used in QuickCorn method (Hoerster et al., 2020; Masters et al., 2020). Various combinations of phytohormones (auxins and cytokinins) in each medium might promote shoot regeneration at the maturation stage reducing the callus selection and proliferation timeline from 161 to 42 days (Table 4, Steps 4–9). For example, selection media used in the previous B104 protocols (Frame et al., 2006; Raji et al., 2018) do not contain cytokinin, while the maturation medium used in this protocol has three cytokinins: zeatin, thidiazuron, and 6-benzylaminopurine.

Event	Plant ID	T0 <i>Gl2</i> phenotype	Wild type	TTTGGTCA <b>CAGAT</b> CACAAACTTCAAA <b>TGCGGT</b> GGGCTG	T0 genotype	Mutant type
1	EXP1 01-01	<i>gl2</i>	Seq1	TTTGGTCA <b>CAGAT</b> CACAAACTTCAANN <b>ATGCGGT</b> GGGCT	+2	Mosaic
			Seq2	TTTGGTCA <b>CAGAT</b> CACAAACTTCAANNNN <b>ATGCGGT</b> GGGCT	+6	
			Seq3	TTTGGTCA <b>CAGAT</b> CAC-----GCT	-24	
2	EXP1 03-02	<i>gl2</i> / wt mixed	Allele 1	TTTGGTCA <b>CAGAT</b> CACAAACT----- <b>GTGGGCTG</b>	-9	Biallelic
			Allele 2	TTTGGTCA <b>CAGAT</b> CACAAACTTCAAA <b>ATGCGGT</b> GGGCTG	1	
3	EXP1 04-02	wt	Seq1	TTTGGTCA <b>CAGAT</b> C-----//-----GCTGGGG	-26	Mosaic
			Seq2	TTTGGTCA <b>CAGAT</b> CACAAACTTCAAN <b>ATGCGGT</b> GGGCT	+1	
			Seq3	TTTGGTCA <b>CAGAT</b> CACAAACTTCA-----TGGGCT	-7	
			Seq4	TTTGGTCA <b>CAGAT</b> CACAAACTTCAAA <b>TGCGGT</b> GGGCT	0	
4	EXP1 05-01	<i>gl2</i> / wt mixed	Seq1	TTTGGTCA <b>CAGAT</b> CACAAACTTCAAA <b>TGCGGT</b> GGGCT	0	Mosaic
			Seq2	TTTGGTCA <b>CAGAT</b> CACAAACTTC-----GTGGGCT	-7	
			Seq3	TTTGGTCA <b>CAGAT</b> CACAAACTTC-----GGTGGGCT	-6	
			Seq4	TTTGGTCA <b>CAGAT</b> CACAAACTT-----//---GCT	-18	
5	EXP1 06-01	wt	Seq1	TTTGGTCA <b>CAGAT</b> CACAAACTT--- <b>ATGCGGT</b> GGGCT	-3	Mosaic
			Seq2	TTTGGTCA <b>CAGAT</b> CACAAACTTCA-----CT	-11	
			Seq3	TTTGGTCA <b>CAGAT</b> CACAAACTTCA-----T	-12	
			Seq4	TTTGGTCA <b>CAGAT</b> CACAAACTTC--- <b>GCGGT</b> GGGCT	-4	
6	EXP1 06-03	wt	Seq1	TTTGGTCA <b>CAGAT</b> CACAAACTTCAAN <b>TGCGGT</b> GGGCT	-1	Mosaic
			Seq2	TTTGGTCA <b>CAGAT</b> CACAAACTTCAAA <b>TGCGGT</b> GGGCT	0	
			Seq3	TTTGGTCA <b>CAGAT</b> CACAAACTTCA-- <b>TGCGGT</b> GGGCT	-2	
			Seq4	TTTGGTCA <b>CAGAT</b> CACAAACTTCAAN <b>ATGCGGT</b> GGGCT	+1	
			Seq5	TTTGGTCA <b>CAGAT</b> CACAAACTT--- <b>ATGCGGT</b> GGGCT	-3	
7	EXP1 10-01	<i>gl2</i>	Allele 1	TTTGGTCA <b>CAGAT</b> CACAAACTTCAA- <b>TGCGGT</b> GGGCTG	-1	Heterozygous
			Allele 2	TTTGGTCA <b>CAGAT</b> CACAAACTTCAAA <b>TGCGGT</b> GGGCTG	0	
8	EXP1 16-01	<i>gl2</i>	Allele 1	TTTGGTCA <b>CAGAT</b> CACAAACT-----G	-16	Biallelic
			Allele 2	TTTGGTCA <b>CAGAT</b> CACAAACTTCAA- <b>TGCGGT</b> GGGCTG	-1	
9	EXP2 02-01	<i>gl2</i>	Allele 1	TTTGGTCA <b>CAGAT</b> CACAAACTTCAAA <b>ATGCGGT</b> GGGCTG	1	Biallelic
			Allele 2	TTTGGTCA <b>CAGAT</b> CACAAACTTCA-----GGGCTG	-8	
10	EXP2 05-04	wt	Allele 1	TTTGGTCA <b>CAGAT</b> CACAAACTTCAAA <b>ATGCGGT</b> GGGCTG	1	Homozygous
			Allele 2	TTTGGTCA <b>CAGAT</b> CACAAACTTCAAA <b>ATGCGGT</b> GGGCTG	1	
11	EXP3 06-01	<i>gl2</i>	Seq1	TTTGGTCA <b>CAGAT</b> C-----//-----TGG	-26	Mosaic
			Seq2	TTTGGTCA <b>CAGAT</b> C-----//-----GCT	-27	
			Seq3	TTTGGTCA <b>CAGAT</b> CAC-----//-----GCT	-24	
			Seq4	TTTGGTCA <b>CAGAT</b> CACAAACTTCA--- <b>GCGGT</b> GGGCTG	-3	
12	EXP3 08-01	<i>gl2</i>	Allele 1	TTTGGTCA <b>CAGAT</b> CACAAAC----- <b>ATGCGGT</b> GGGCTG	-5	Biallelic
			Allele 2	TTTGGTCA <b>CAGAT</b> CACAAACTTCAAA <b>ATGCGGT</b> GGGCTG	1	
13	EXP3 10-02	wt	Allele 1	TTTGGTCA <b>CAGAT</b> CACAAACTTCAAA <b>ATGCGGT</b> GGGCTG	1	Heterozygous
			Allele 2	TTTGGTCA <b>CAGAT</b> CACAAACTTCAAA <b>TGCGGT</b> GGGCTG	0	
14	EXP3 14-01	<i>gl2</i>	Allele 1	TTTGGTCA <b>CAGAT</b> CACAAACTTCAA- <b>TGCGGT</b> GGGCTG	-1	Biallelic
			Allele 2	TTTGGTCA <b>CAGAT</b> CACAAACTTCAAA <b>ATGCGGT</b> GGGCTG	1	
15	EXP3 14-02	<i>gl2</i>	Allele 1	TTTGGTCA <b>CAGAT</b> CACAAACTTCAA-----TGGGCTG	-6	Biallelic
			Allele 2	TTTGGTCA <b>CAGAT</b> CACAAACTTCAAA <b>ATGCGGT</b> GGGCTG	1	
16	EXP3 14-03	wt	Allele 1	TTTGGTCA <b>CAGAT</b> CACAAACTTCA-- <b>TGCGGT</b> GGGCTG	-2	Biallelic
			Allele 2	TTTGGTCA <b>CAGAT</b> CACAAACTTCAAA <b>ATGCGGT</b> GGGCTG	1	

**FIGURE 7 |** Phenotypes and genotypes of sixteen T0 mutant events. Plant ID shows experiment ID, embryo ID, and plantlet ID (EXP-embryo-plantlet). Three *gl2* phenotypes: *gl2*, glossy mutant phenotype; *gl2*/wt mixed, both glossy mutant and wild type phenotype on the same leaf; wt, wild-type phenotype. Red letters, target sequences in *Gl2* exon2; Blue letters, PAM sequences; Black letter, insertion mutations; dashed lines, deletions. T0 *gl2* phenotyping is considered a preliminary screening assay.

Another explanation for the reduced tissue culture period in this protocol is that the QuickCorn media used in this work induce direct somatic embryogenesis. In the direct somatic embryogenesis process, somatic embryos can form from the explant without the formation of an intermediate callus phase (Raghavan, 1986; Zhang et al., 2021). It is likely that this

improved protocol avoids the conventional callus induction and proliferation steps required by the previous B104 transformation protocol (Raji et al., 2018). The major difference of this improved B104 protocol vs. the QuickCorn method is that no morphogenic genes such as *Bbm* and *Wus2* are used in the transformation vectors.



One of the key factors for successful maize transformation is the production of quality immature embryos as starting materials. Here we described the detailed procedure to produce immature embryos for transformation. We recommend using three or more ears for each transformation experiment to reduce the ear-to-ear variation often observed in maize transformation using immature embryos (Frame et al., 2002). The size of immature embryos is another important factor. It is critical to use ears with the right size of embryos (Ishida et al., 2007; McCaw et al., 2021). For *Agrobacterium*-mediated transformation, the typical embryo size is 1.5–1.8 mm for Hi II (Frame et al., 2002) and 1.8–2.0 mm for B104 (Raji et al., 2018). We observed a much lower transformation frequency when small embryos (<1.8 mm) were used in the second experiment. The transformation frequency of the second experiment (EXP2-CAS, Table 3) was significantly lower (1.8%) than the first and the third infection experiments (9.1 and 8.5%, respectively;  $P < 0.05$ , two proportion  $z$ -test). Therefore, immature embryos with 1.8–2.0 mm in size are suitable for B104 transformation using this rapid protocol, consistent with the previous recommendation (Raji et al., 2018).

In this study, we observed a high rate of escapes, that is, only 33.3% (24/72) regenerated shoots were *Cas9*-positive transgenic plants. This might be due to the *bar* gene/bialaphos selection system in the binary vector. This non-selective herbicide acts as a glutamine synthetase inhibitor in plants and causes toxicity by accumulating ammonia in the affected plant cells (Donn and Köcher, 2002). The bialaphos selection in this protocol successfully inhibited plant regeneration from the non-infection controls, however, it was less effective in killing the non-transgenic plants from the infected embryos. This could be due to the shortened callus propagation and selection duration in this protocol or the herbicide bialaphos might not metabolize quickly enough to inhibit the rapidly growing plant tissues. To suppress the non-transgenic plant growth, a higher concentration of bialaphos is recommended for the first maturation medium (13329B3). Alternatively, other fast-acting herbicide resistance genes and selection agents such as *HRA* gene with imazapyr (Lowe et al., 2018; Masters et al., 2020) or antibiotics selection system *NPTII* gene with G418 (Wang et al., 2020) can be adapted to this protocol.

In summary, we presented an improved B104 transformation protocol as an effective and rapid method to generate transgenic

and genome-edited maize plants. This protocol is fast, with a short turnaround time of about 50 days, from the day of infection to obtaining rooted transgenic plants. We expect this method can benefit the maize research community, especially academic laboratories to generate transgenic and CRISPR-edited maize plants for both fundamental and applied research.

## DATA AVAILABILITY STATEMENT

The original contributions presented in the study are included in the article, further inquiries can be directed to the corresponding authors.

## AUTHOR CONTRIBUTIONS

KW, MK, and VV designed the experiments. KL designed and built the constructs and *Agrobacterium* strain. MK and TF performed transformation and regeneration experiments. HC provided corn ears and contributed to the plant care. MK and KL performed phenotyping, genotyping, and data analysis of the plants. KW and VV coordinated the project. MK, KW, KL, TF, and VV prepared the manuscript. All authors contributed to discussion and revision of the manuscript.

## FUNDING

This project was partially supported by National Science Foundation Plant Genome Research Program Grants 1917138 to KW, by the USDA NIFA Hatch project #IOW04714, by State of Iowa funds, by the Crop Bioengineering Center of Iowa State University, and the Plant Transformation Facility at the Donald Danforth Plant Science Center.

## ACKNOWLEDGMENTS

We wish to thank David Wright for providing corn ears, Jacob Zobrist for scientific discussion, and the Plant Growth Facility at the Donald Danforth Plant Science Center for assistance. KW's contribution to this work is partially supported by (while serving at) the National Science Foundation.

## REFERENCES

- Anand, A., Bass, S. H., Wu, E., Wang, N., McBride, K. E., Annaluru, N., et al. (2018). An improved ternary vector system for *Agrobacterium*-mediated rapid maize transformation. *Plant Mol. Biol.* 97, 187–200. doi: 10.1007/s11103-018-0732-y
- Bianchi, G., Avato, P., and Salamini, F. (1975). Glossy mutants of maize. VI. Chemical constituents of glossy-2 epicuticular waxes. *Maydica* 20, 165–173.
- Boutillier, K., Offringa, R., Sharma, V. K., Kieft, H., Ouellet, T., Zhang, L., et al. (2002). Ectopic expression of BABY BOOM triggers a conversion from vegetative to embryonic growth. *Plant Cell* 14, 1737–1749. doi: 10.1105/tpc.001941
- Brinkman, E. K., Chen, T., Amendola, M., and van Steensel, B. (2014). Easy quantitative assessment of genome editing by sequence trace decomposition. *Nucleic Acids Res.* 42:e168. doi: 10.1093/nar/gku936
- Char, S. N., Neelakandan, A. K., Nahampun, H., Frame, B., Main, M., Spalding, M. H., et al. (2017). An *Agrobacterium*-delivered CRISPR/Cas9 system for high-frequency targeted mutagenesis in maize. *Plant Biotechnol. J.* 15, 257–268. doi: 10.1111/pbi.12611
- Donn, G., and Köcher, H. (2002). “Inhibitors of glutamine synthetase,” in *Herbicide Classes in Development: Mode of Action, Targets, Genetic Engineering, Chemistry*, eds P. Boger, K. Wakabayashi, and K. Hirai (Berlin: Springer-Verlag), 87–101. doi: 10.1007/978-3-642-59416-8\_4

- Edwards, K., Johnstone, C., and Thompson, C. (1991). A simple and rapid method for the preparation of plant genomic DNA for PCR analysis. *Nucleic Acids Res.* 19:1349. doi: 10.1093/nar/19.6.139
- Frame, B. R., McMurray, J. M., Fonger, T. M., Main, M. L., Taylor, K. W., Torney, F. J., et al. (2006). Improved *Agrobacterium*-mediated transformation of three maize inbred lines using MS salts. *Plant Cell Rep.* 25, 1024–1034. doi: 10.1007/s00299-006-0145-2
- Frame, B. R., Shou, H., Chikwamba, R. K., Zhang, Z., Xiang, C., Fonger, T. M., et al. (2002). *Agrobacterium tumefaciens*-mediated transformation of maize embryos using a standard binary vector system. *Plant Physiol.* 129, 13–22. doi: 10.1104/pp.000653
- Frame, B., Warnberg, K., Main, M., and Wang, K. (2015). “Maize (*Zea mays* L.),” in *Agrobacterium Protocols*, ed. K. Wang (New York, NY: Springer), 101–117. doi: 10.1007/978-1-4939-1695-5\_8
- Freeling, M., and Walbot, V. (1994). *The Maize Handbook*. New York, NY: Springer. doi: 10.1007/978-1-4612-2694-9
- Gordon-Kamm, W. J., Spencer, T. M., Mangano, M. L., Adams, T. R., Daines, R. J., Start, W. G., et al. (1990). Transformation of maize cells and regeneration of fertile transgenic plants. *Plant Cell* 2, 603–618. doi: 10.2307/3869124
- Hallauer, A. R., Lamkey, K. R., and White, P. R. (1997). Registration of five inbred lines of maize: B102, B103, B104, B105, and B106. *Crop Sci.* 37, 1405–1406. doi: 10.2135/CROPSCI1997.0011183X003700040094X
- Hoerster, G., Wang, N., Ryan, L., Wu, E., Anand, A., McBride, K., et al. (2020). Use of non-integrating *Zm-Wus2* vectors to enhance maize transformation. *In Vitro Cell. Dev. Biol. Plant* 56, 265–279. doi: 10.1007/s11627-019-10042-2
- Hsiau, T., Maures, T., Waite, K., Yang, J., Kelso, R., Holden, K., et al. (2019). Inference of CRISPR edits from Sanger trace data. *bioRxiv* [preprint]. doi: 10.1101/251082
- Ikeuchi, M., Favero, D. S., Sakamoto, Y., Iwase, A., Coleman, D., Rymen, B., et al. (2019). Molecular mechanisms of plant regeneration. *Annu. Rev. Plant Biol.* 70, 377–406. doi: 10.1146/annurev-arplant-050718-100434
- Ishida, Y., Hiei, Y., and Komari, T. (2007). *Agrobacterium*-mediated transformation of maize. *Nat. Protoc.* 2, 1614–1621. doi: 10.1038/nprot.2007.241
- Ishida, Y., Saito, H., Ohta, S., Hiei, Y., Komari, T., and Kumashiro, T. (1996). High efficiency transformation of maize (*Zea mays* L.) mediated by *Agrobacterium tumefaciens*. *Nat. Biotechnol.* 14, 745–750. doi: 10.1038/nbt0696-745
- Kausch, A. P., Wang, K., Kaeppler, H. F., and Gordon-Kamm, W. (2021). Maize transformation: history, progress, and perspectives. *Mol. Breed.* 41:38. doi: 10.1007/s11032-021-01225-0
- Komari, T., Halperin, W., and Nester, E. W. (1986). Physical and functional map of supervirulent *Agrobacterium tumefaciens* tumor-inducing plasmid pTiBo542. *J. Bacteriol.* 166, 88–94. doi: 10.1128/jb.166.1.88-94.1986
- Lardon, R., and Geelen, D. (2020). Natural variation in plant pluripotency and regeneration. *Plants* 9:1261. doi: 10.3390/plants9101261
- Lee, K., Zhang, Y., Kleinstiver, B. P., Guo, J. A., Aryee, M. J., Miller, J., et al. (2019). Activities and specificities of CRISPR/Cas9 and Cas12a nucleases for targeted mutagenesis in maize. *Plant Biotechnol. J.* 17, 362–372. doi: 10.1111/pbi.12982
- Lowe, K., Wu, E., Wang, N., Hoerster, G., Hastings, C., Cho, M.-J., et al. (2016). Morphogenic regulators *Baby Boom* and *Wuschel* improve monocot transformation. *Plant Cell* 28, 1998–2015. doi: 10.1105/tpc.16.00124
- Lowe, K., La Rota, M., Hoerster, G., Hastings, C., Wang, N., Chamberlin, M., et al. (2018). Rapid genotype “independent” *Zea mays* L. (maize) transformation via direct somatic embryogenesis. *In Vitro Cell. Dev. Biol. Plant* 54, 240–252. doi: 10.1007/s11627-018-9905-2
- Manchanda, N., Carson, A., Ye, L., Wimalanathan, K., Rounsley, S., Wang, K., et al. (2016). “Sequencing, assembly, and annotation of maize B104: a maize transformation resource,” in *Proceedings of the 58th Annual Maize Genetics Conference*, March 17–20, 2016, Jacksonville, FL, 92.
- Masters, A., Kang, M., McCaw, M., Zobrist, J. D., Gordon-Kamm, W., Jones, T., et al. (2020). *Agrobacterium*-mediated immature embryo transformation of recalcitrant maize inbred lines using morphogenic genes. *J. Vis. Exp.* 156:e60782. doi: 10.3791/60782
- McCaw, M. E., Lee, K., Kang, M., Zobrist, J. D., Azanu, M. K., Birchler, J. A., et al. (2021). Development of a transformable fast-flowering mini-maize as a tool for maize gene editing. *Front. Genome Ed.* 2:622227. doi: 10.3389/fgeed.2020.622227
- Mookkan, M., Nelson-Vasilchik, K., Hague, J., Zhang, Z. J., and Kausch, A. P. (2017). Selectable marker independent transformation of recalcitrant maize inbred B73 and sorghum P898012 mediated by morphogenic regulators BABY BOOM and WUSCHEL2. *Plant Cell Rep.* 36, 1477–1491. doi: 10.1007/s00299-017-2169-1
- Park, S., Lee, B. M., Salas, M., Srivatanakul, M., and Smith, R. H. (2000). Shorter T-DNA or additional virulence genes improve *Agrobacterium*-mediated transformation. *Theor. Appl. Genet.* 101, 1015–1020. doi: 10.1007/s001220051575
- Que, Q., Elumalai, S., Li, X., Zhong, H., Nalapalli, S., Schweiner, M., et al. (2014). Maize transformation technology development for commercial event generation. *Front. Plant Sci.* 5:379. doi: 10.3389/fpls.2014.00379
- Raghavan, V. (1986). *Embryogenesis in Angiosperms: A Developmental and Experimental Study*. New York, NY: Cambridge University Press.
- Raji, J. A., Frame, B., Little, D., Santoso, T. J., and Wang, K. (2018). “*Agrobacterium*- and biolistic-mediated transformation of maize B104 inbred,” in *Maize: Methods and Protocols*, ed. L. M. Lagrimini (New York, NY: Springer), 15–40. doi: 10.1007/978-1-4939-7315-6\_2
- Ranch, J. P., Liebergesell, M., Garnaat, C. W., and Huffman, G. A. (2012). *Auxotrophic Agrobacterium for Plant Transformation and Methods thereof*. U.S. Patent No. 8,334,429. Washington, DC: U.S. Patent and Trademark Office.
- Romay, M. C., Millard, M. J., Glaubitz, J. C., Peiffer, J. A., Stewarts, K. L., Casstevens, T. M., et al. (2013). Comprehensive genotyping of the USA national maize inbred seed bank. *Genome Biol.* 14:R55. doi: 10.1186/gb-2013-14-6-r55
- Schnable, P. S., Ware, D., Fulton, R. S., Stein, J. C., Wei, F., Pasternak, S., et al. (2009). The B73 maize genome: complexity, diversity, and dynamics. *Science* 326, 1112–1115. doi: 10.1126/science.1178534
- Sun, X., Cahill, J., Van Hautegeem, T., Feys, K., Whipple, C., Novak, O., et al. (2017). Altered expression of maize PLASTOCHRON1 enhances biomass and seed yield by extending cell division duration. *Nat. Commun.* 8:14752. doi: 10.1038/ncomms14752
- Wan, Y., Widholm, J. M., and Lemaux, P. G. (1995). Type I callus as a bombardment target for generating fertile transgenic maize (*Zea mays* L.). *Planta* 196, 7–14. doi: 10.1007/BF00193211
- Wang, N., Arling, M., Hoerster, G., Ryan, L., Wu, E., Lowe, K., et al. (2020). An efficient gene excision system in maize. *Front. Plant Sci.* 11:1298. doi: 10.3389/fpls.2020.01298
- Xie, X., Ma, X., Zhu, Q., Zeng, D., Li, G., and Liu, Y.-G. (2017). CRISPR-GE: a convenient software toolkit for CRISPR-based genome editing. *Mol. Plant* 10, 1246–1249. doi: 10.1016/j.molp.2017.06.004
- Zhang, M., Wang, A., Qin, M., Qin, X., Yang, S., Su, S., et al. (2021). Direct and Indirect Somatic Embryogenesis Induction in *Camellia oleifera* Abel. *Front. Plant Sci.* 12:644389. doi: 10.3389/fpls.2021.644389
- Zhu, H., Li, C., and Gao, C. (2020). Applications of CRISPR–Cas in agriculture and plant biotechnology. *Nat. Rev. Mol. Cell Biol.* 21, 661–677. doi: 10.1038/s41580-020-00288-9
- Zuo, J., Niu, Q. W., Frugis, G., and Chua, N. H. (2002). The WUSCHEL gene promotes vegetative-to-embryonic transition in *Arabidopsis*. *Plant J.* 30, 349–359. doi: 10.1046/j.1365-313x.2002.01289.x

**Conflict of Interest:** The authors declare that the research was conducted in the absence of any commercial or financial relationships that could be construed as a potential conflict of interest.

**Publisher’s Note:** All claims expressed in this article are solely those of the authors and do not necessarily represent those of their affiliated organizations, or those of the publisher, the editors and the reviewers. Any product that may be evaluated in this article, or claim that may be made by its manufacturer, is not guaranteed or endorsed by the publisher.

Copyright © 2022 Kang, Lee, Finley, Chappell, Veena and Wang. This is an open-access article distributed under the terms of the Creative Commons Attribution License (CC BY). The use, distribution or reproduction in other forums is permitted, provided the original author(s) and the copyright owner(s) are credited and that the original publication in this journal is cited, in accordance with accepted academic practice. No use, distribution or reproduction is permitted which does not comply with these terms.



# Low-Input High-Molecular-Weight DNA Extraction for Long-Read Sequencing From Plants of Diverse Families

Alessia Russo<sup>1,2,3\*</sup>, Baptiste Mayjonade<sup>4</sup>, Daniel Frei<sup>5</sup>, Giacomo Potente<sup>3</sup>, Roman T. Kellenberger<sup>6</sup>, Léa Frachon<sup>3</sup>, Dario Copetti<sup>7</sup>, Bruno Studer<sup>7</sup>, Jürg E. Frey<sup>5</sup>, Ueli Grossniklaus<sup>1</sup> and Philipp M. Schlüter<sup>2,3\*</sup>

<sup>1</sup> Department of Plant and Microbial Biology and Zurich-Basel Plant Science Centre, University of Zurich, Zurich, Switzerland, <sup>2</sup> Department of Plant Evolutionary Biology, Institute of Biology, University of Hohenheim, Stuttgart, Germany, <sup>3</sup> Department of Systematic and Evolutionary Botany and Zurich-Basel Plant Science Centre, University of Zurich, Zurich, Switzerland, <sup>4</sup> Laboratoire des Interactions Plantes Microbes Environnement (LIPME), INRAE, Toulouse, France, <sup>5</sup> Department of Method Development and Analytics, Agroscope, Wädenswil, Switzerland, <sup>6</sup> Department of Plant Sciences, University of Cambridge, Cambridge, United Kingdom, <sup>7</sup> Institute of Agricultural Sciences and Zurich-Basel Plant Science Centre, ETH Zürich, Zurich, Switzerland

## OPEN ACCESS

### Edited by:

Ruslan Kalendar,  
University of Helsinki, Finland

### Reviewed by:

Cássio Van Den Berg,  
State University of Feira de Santana,  
Brazil  
Ken Naito,  
National Agriculture and Food  
Research Organization (NARO), Japan

### \*Correspondence:

Alessia Russo  
alessia.russo@systbot.uzh.ch  
Philipp M. Schlüter  
philipp.schluter@uni-hohenheim.de

### Specialty section:

This article was submitted to  
Technical Advances in Plant Science,  
a section of the journal  
Frontiers in Plant Science

**Received:** 25 February 2022

**Accepted:** 21 April 2022

**Published:** 19 May 2022

### Citation:

Russo A, Mayjonade B, Frei D, Potente G, Kellenberger RT, Frachon L, Copetti D, Studer B, Frey JE, Grossniklaus U and Schlüter PM (2022) Low-Input High-Molecular-Weight DNA Extraction for Long-Read Sequencing From Plants of Diverse Families. *Front. Plant Sci.* 13:883897. doi: 10.3389/fpls.2022.883897

Long-read DNA sequencing technologies require high molecular weight (HMW) DNA of adequate purity and integrity, which can be difficult to isolate from plant material. Plant leaves usually contain high levels of carbohydrates and secondary metabolites that can impact DNA purity, affecting downstream applications. Several protocols and kits are available for HMW DNA extraction, but they usually require a high amount of input material and often lead to substantial DNA fragmentation, making sequencing suboptimal in terms of read length and data yield. We here describe a protocol for plant HMW DNA extraction from low input material (0.1 g) which is easy to follow and quick (2.5 h). This method successfully enabled us to extract HMW from four species from different families (Orchidaceae, Poaceae, Brassicaceae, Asteraceae). In the case of recalcitrant species, we show that an additional purification step is sufficient to deliver a clean DNA sample. We demonstrate the suitability of our protocol for long-read sequencing on the Oxford Nanopore Technologies PromethION® platform, with and without the use of a short fragment depletion kit.

**Keywords:** DNA extraction, DNA sequencing, nanopore sequencing, Circulomics, plant genome, ONT long read sequencing, PacBio, genome assembly

## INTRODUCTION

Long-read sequencing technologies have reshaped the research landscape of plant biology over the last few years. With the recent increase in sequencing read length, decrease in sequencing cost, and newly developed bioinformatics tools suitable for these technologies, *de novo* assembly of large and complex plant genomes of non-model species is now feasible (Jiao and Schneeberger, 2017; Kersey, 2019). This offers unprecedented opportunities to investigate genome structure and function, and focus on molecular and evolutionary questions in organisms that were previously inaccessible (Belser et al., 2018). We are now gaining a deeper understanding of genomic diversity,

evolution, and gene function by sequencing more genomes at a higher resolution (Zhang et al., 2017; Chawla et al., 2021). Lately, the possibility to release high quality reference genome assemblies has led to initiatives such as the European Reference Genome Atlas (Formenti et al., 2022) or the Earth BioGenome Project, which “aims to sequence, catalog and characterise the genomes of all of Earth’s eukaryotic biodiversity,” to study evolution and preserve biodiversity (Exposito-Alonso et al., 2020).

Long-read sequencers are able to generate reads of 10 kbp or longer. The recently developed PacBio® HiFi technology from Pacific Biosciences can provide reads up to 25 kbp (the older CLR mode provides longer but less accurate reads)<sup>1</sup>, while Oxford Nanopore Technologies® (ONT®) nanopore sequencing technology provides the longest reads, up to the current record of 4.2 Mbp<sup>2</sup>. Such long reads are able to unambiguously capture complex and repetitive regions in plant genomes, allowing the exploration of genomic regions that were previously inaccessible (Belser et al., 2018; Goerner-Potvin and Bourque, 2018). This, together with their ability to resolve highly heterozygous regions, has enabled the assembly of large plant genomes at the chromosome level (Hu et al., 2019; Hasing et al., 2020; Pu et al., 2020; Niu et al., 2022).

Long reads are also reshaping the way we approach population genetic studies. Structural Variants (SVs) represent a major form of genetic variation, and may contribute to phenotypic variation as much as – or even more so than – single nucleotide polymorphisms (SNPs) (Chawla et al., 2021). However, it is challenging to reliably detect large SVs using short-read sequencing (Saxena et al., 2014). Structural variants can now be captured with long reads, thus enabling the fine-scale characterisation of genomic rearrangements responsible for trait variation in plants (Zhang et al., 2016; Sedlazeck et al., 2018; Heller and Vingron, 2019). Moreover, since PacBio® and ONT® are able to detect chemical modifications on nucleotides, they provide a new method to directly profile patterns of DNA methylation across genomes and allow epigenetic studies (Flusberg et al., 2010; Simpson et al., 2017). However, to fully exploit the potential of long-read sequencing, it is critical to obtain high molecular weight (HMW) DNA of adequate purity and integrity.

Extraction of HMW DNA from plant material can be challenging. First, plant cells have a cell wall composed of polysaccharide polymers, such as cellulose and pectin, as well as glycoproteins and lignin (Zhang et al., 2021), making the cell wall rigid and hard to break. Thus, steps that achieve effective mechanical disruption of the cell wall are necessary. As a chemical defence against herbivores, plants also produce polysaccharides and phenols, which tend to accumulate in leaves and, upon cell lysis, can bind DNA and affect downstream molecular analyses (Katterman and Shattuck, 1983; Varma et al., 2007; Moreira et al., 2011). The presence of polysaccharides has been

shown to inhibit restriction enzyme activity (Pandey et al., 1996). Thus, purification of DNA from plant material requires careful optimisation. Several commercial DNA isolation kits and protocols are available on the market. Many protocols rely on the isolation of nuclei with an osmotic nuclear isolation buffer, and subsequent lysis of nuclear membranes with a detergent to release DNA. These methods are time-consuming, hazardous, and/or require high amounts of input material (Zerpa-Catanho et al., 2021). Furthermore, the resulting genomic DNA (gDNA) is often highly oxidised and, therefore, unsuitable for long-read applications. Kit-based extraction methods are offered by several companies, and are intended to easily remove contaminants; but they are costly and there is a risk of losing DNA during column washes. A previously published protocol (Mayjonade et al., 2016) presented a method to extract plant HMW DNA via a sodium dodecyl sulphate (SDS)-based lysis buffer and magnetic bead-based purification. The described method is easy and quick, taking only 1.5 h to complete DNA isolation from harvested plant material. Moreover, it requires only 0.1 g starting material. Unfortunately, this method did not yield DNA of sufficient quality for long-read sequencing in the plant species used as study organisms by our groups.

Here, we present an improved HMW DNA extraction method based upon the protocol by Mayjonade et al. (2016). We introduced two simple but effective major modifications: the addition of  $\beta$ -mercaptoethanol, which prevents oxidative damage to nucleic acids (Gerstein, 2001) and prevents nuclease activity, and a phenol:chloroform extraction. To demonstrate the robustness of the method, we applied it to plants from diverse families across both monocots and eudicots, including the Mediterranean early spider orchid (*Ophrys sphegodes*, Orchidaceae), Italian ryegrass (*Lolium multiflorum*, Poaceae), wild cabbage (*Brassica incana*, Brassicaceae), and South African beetle daisy (*Gorteria diffusa*, Asteraceae). We successfully extracted HMW DNA of high purity and integrity from all four species, showing that our protocol can be applied to a broad range of angiosperm species. To demonstrate the suitability of our protocol for long-read technology, we sequenced one sample each from *O. sphegodes* and *L. multiflorum* on the ONT® PromethION® platform. Finally, we assessed the use of Circulomics’ Short Read Eliminator Kit and its impact on sequenced read length in these species. We show that short fragment removal can improve the average read length and increase the proportion of ultra-long sequenced fragments [ $>100$  kb (Prall et al., 2021)], thus improving sequencing efficiency. A schematic overview of our protocol is provided in **Figure 1** and a step-by-step version is available at [dx.doi.org/10.17504/protocols.io.5t7g6rn](https://doi.org/10.17504/protocols.io.5t7g6rn) online.

## METHODS

### Species Used for DNA Extraction

We used plants from four families for DNA extraction, specifically *Ophrys sphegodes* Mill. (Orchidaceae), *Lolium multiflorum* Lam. (Poaceae), *Brassica incana* Ten. (Brassicaceae) and *Gorteria diffusa* Thunb. (Asteraceae). Since bee orchids

<sup>1</sup><https://www.pacb.com/literature/application-brief-whole-genome-sequencing-for-de-novo-assembly-best-practices/>

<sup>2</sup><https://nanoporetech.com/about-us/news/ncm-announcements-include-single-read-accuracy-991-new-chemistry-and-sequencing>



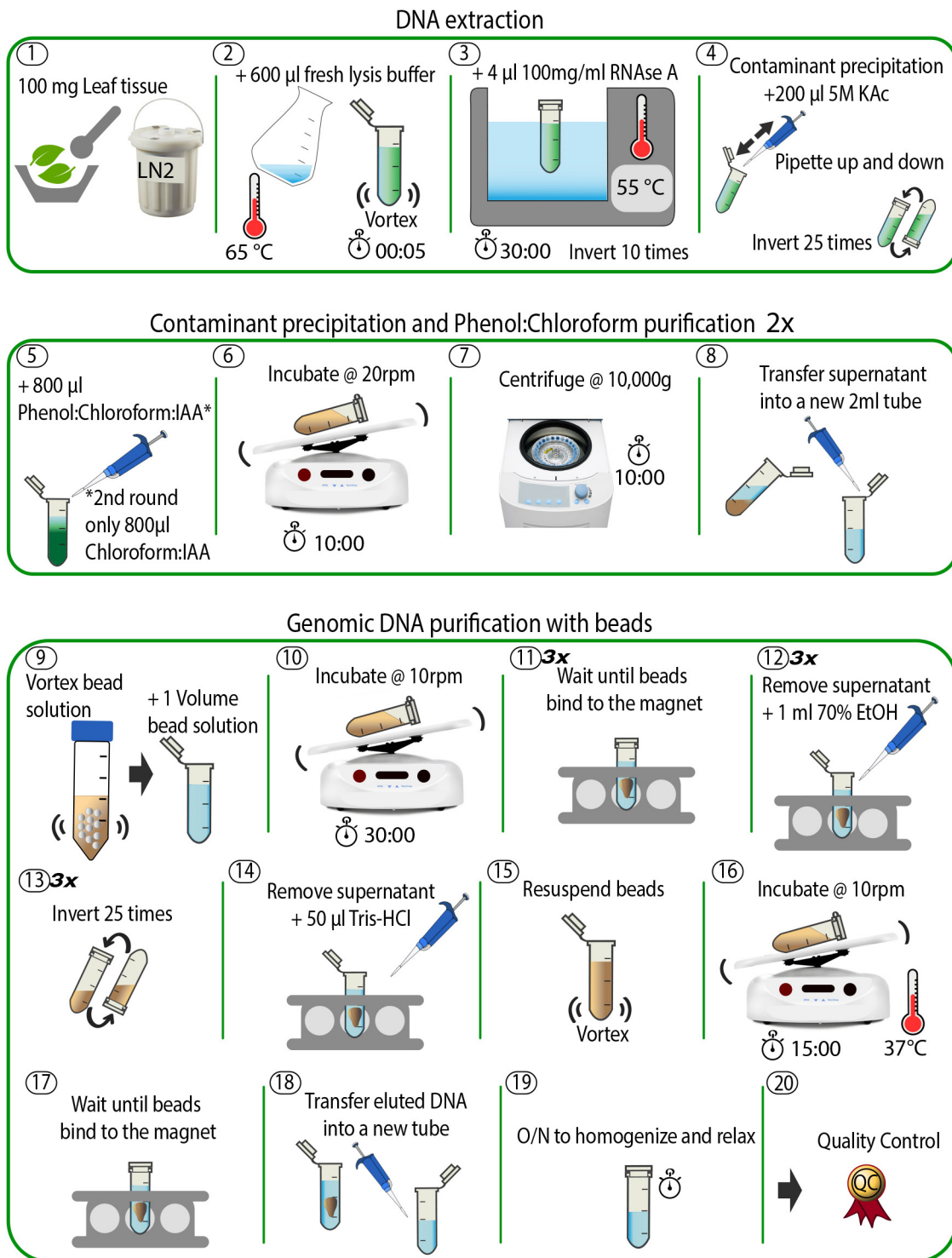


**FIGURE 1** | Schematic overview of the DNA extraction method. The individual steps are described in detail in the see section "Methods" and in the accompanying online protocol.

(*Ophrys*) hardly produce 2 g total leaf mass per individual, common DNA extraction procedures that need  $\geq 1$  g starting material make it difficult to reach a final DNA amount suitable

for long-read sequencing without pooling individuals. This, coupled with the large genome size (ca. 1C = 5 Gbp) and high heterozygosity, would make a genome assembly project

unfeasible. Italian ryegrass is one of the most important forage grasses (Gilliland et al., 2007) and represents a major feed source for livestock farming due to its high digestibility and biomass yield (Wilkins, 1991; Frei et al., 2021). The Brassicaceae family includes diverse plant species widely cultivated for oilseed production and vegetable consumption, including oilseed rape, kale, broccoli and cauliflower. The major challenge of extracting DNA from these plants comes from the high level of secondary metabolites in leaves that interfere with sample purity (Zhao et al., 2020). The leaves of *G. diffusa* are even more challenging and contain milky latex (and other unknown secondary metabolites) in high amounts.

## High Molecular Weight DNA Extraction for *Ophrys sphegodes*

Plant material used for this experiment was collected from a greenhouse-grown *O. sphegodes* individual. Young (2 weeks old) leaves were collected, flash frozen in liquid nitrogen (LN<sub>2</sub>), and stored at  $-80^{\circ}\text{C}$  until DNA extraction. On the day of the experiment, a fresh SDS lysis buffer was prepared as in Mayjonade et al. (2016), supplemented with  $\beta$ -mercaptoethanol ( $\beta$ -ME): 1% polyvinylpyrrolidone 40 (PVP40), 1% sodium metabisulphite, 0.5 M sodium chloride, 100 mM Tris-HCl (pH 8), 50 mM EDTA (pH 8), 2%  $\beta$ -ME, 1.5% sodium dodecyl sulphate (SDS), in ddH<sub>2</sub>O to a final volume of 10 ml of stock solution (see **Supplementary Table 1**). The lysis buffer was incubated at  $65^{\circ}\text{C}$  for 1 h to ensure total dissolution of reagents in the buffer. Meanwhile, 100 mg frozen leaf tissue was ground with mortar and pestle (pre-cooled at  $-80^{\circ}\text{C}$  for  $> 1$  h) in LN<sub>2</sub> until a fine powder was obtained (Step 1, **Figure 1**). Note that it is not advisable to use more than 100 mg starting material, as this decreases DNA purity (as measured by the  $A_{260}/_{230}$  absorbance ratio using a NanoDrop® spectrophotometer). Also, since the grinding step is crucial to ensure optimal outcomes in terms of final DNA yield and integrity, we provide some tips. First, it is critical to keep the sample submerged in LN<sub>2</sub>. If the LN<sub>2</sub> evaporates, plant material will thaw (as indicated by a colour change – it becomes dark green when it thaws) and the DNA will degrade. Second, a fine, flour-like texture of ground plant material is optimal to ensure maximal DNA yield. Hence, the plant material was first crushed in a mortar by gently pounding it with a pestle, until small pieces ( $< 5 \times 5$  mm) were obtained. Then, plant pieces were rubbed against the mortar with circular movements of the pestle to obtain a final powder with a flour-like texture. To avoid thawing, LN<sub>2</sub> was added every half minute (or when LN<sub>2</sub> had almost evaporated). Depending on the plant material and the pressure applied, the grinding can take up to 30 min. After grinding, the powder was immediately transferred to a sterile 2 ml plastic tube with a chilled metal spatula and mixed with 600  $\mu\text{l}$  of the pre-warmed ( $65^{\circ}\text{C}$ ) SDS lysis buffer (Step 2 in **Figure 1**). The sample was vortexed for 3–5 s and incubated on a thermomixer with gentle agitation (400 rpm, 20 min at  $55^{\circ}\text{C}$ ) to inactivate DNases and remove polyphenols that could bind DNA. Afterward, 4  $\mu\text{l}$  of 100 mg/ml DNase-free RNase A (Qiagen, Germantown, MD, United States) were added, and the sample was incubated for 10 additional minutes at  $55^{\circ}\text{C}$  (Step 3, **Figure 1**). To fully

precipitate proteins and polysaccharides that form complexes with SDS (Otzen, 2011), 200  $\mu\text{l}$  of 5 M potassium acetate (KAc) were added, and the solution was mixed by inverting the tube 25 times (Step 4, **Figure 1**). Next, the sample was purified via a phenol/chloroform extraction as follows. Under a fume hood, 800  $\mu\text{l}$  of a phenol:chloroform:isoamyl alcohol mixture (25:24:1 v/v, pH 8) was added, and the sample was incubated for 10 min at room temperature (RT) with gentle agitation on a tube rotator at 20 rpm (Steps 5 and 6, **Figure 1**). The sample was then centrifuged for 10 min at  $10,000 \times g$  at RT (Step 7, **Figure 1**). Afterward, the supernatant was transferred into a new 2 ml tube using a 1,000  $\mu\text{l}$  wide-bore pipette tip, to avoid shearing the DNA (Step 8, **Figure 1**). A second purification step was then undertaken by the addition of 800  $\mu\text{l}$  chloroform:isoamyl alcohol (24:1 v/v), followed by a second incubation (10 min at RT at 20 rpm) and centrifugation (10 min at  $10,000 \times g$  at RT). Finally, the supernatant was transferred to a new 2 ml tube and the final volume was recorded ( $\sim 700$ – $800 \mu\text{l}$ ).

## Carboxyl Magnetic Bead Purification

The supernatant recovered from the previous step was purified with carboxylated magnetic beads (Sera-Mag SpeedBeads™ Carboxyl Magnetic Beads, GE Healthcare 65152105050250, Fisher Scientific). The bead stock solution was prepared as in Schalamun et al. (2019) and added to the sample in a 1:1 ratio (Step 9, **Figure 1**) to remove shorter fragments. Note that a complete resuspension of beads in the stock solution was crucial for optimal DNA yield. The sample tube was incubated for 30 min on a rotator at 10 rpm at RT, spun down for 1 s in a benchtop microcentrifuge, and placed into a magnetic rack until all beads migrated toward the magnet and the solution became clear (Step 10 and 11, **Figure 1**). This step can take several minutes, as the viscosity of the solution may slow down the beads' migration. Afterward, an ethanol (EtOH) washing step was carried out as follows: 1 ml of 70% EtOH was added to the tube; then, the sample tube was removed from the magnetic rack (without extended incubation), mixed by inverting it 25 times to resuspend the bead pellet, spun down for 1 s, and placed back into the magnetic rack. When the solution became clear, the supernatant was discarded, and the washing step repeated for a total of three times (Step 12–14, **Figure 1**). We note that these steps can be quite challenging to perform, as beads tend to aggregate, making it difficult to separate and resuspend them properly. In this case, it helps to gently flick the tube to help the beads separate and to avoid prolonged incubation in EtOH. Thereafter, DNA was eluted by addition of 50  $\mu\text{l}$  of 10 mM Tris-HCl pH 8.5 (using commercial buffer EB from Qiagen) preheated to  $50^{\circ}\text{C}$  to the tube, followed by a last incubation at  $37^{\circ}\text{C}$  for 15 min (Steps 14–16, **Figure 1**). The warm temperature is intended to favour the elution of DNA from the magnetic beads. Finally, to collect the eluted DNA, the tube was placed back into the magnetic rack until the solution became clear (Step 17, **Figure 1**). This step lasted ca. 30 min, as the long fragments migrate slowly in such a small volume. Note that the slow separation speed is an indication of successful HMW DNA extraction. The eluted DNA was gently pipetted into a new 2 ml tube with a wide-bore 1000  $\mu\text{l}$  pipette tip (Step 18, **Figure 1**). The sample was very viscous at this point,

indicating highly concentrated HMW DNA. The tube was left on the bench overnight at RT to allow DNA to homogenise and relax (Step 19, **Figure 1**). The next day, the sample was ready for quality control (Step 20, **Figure 1**). A total of six *O. sphegodes* samples were prepared (named OPH\_1-6). The total amount of time taken for DNA extraction and clean-up was approximately 2.5 h.

## High Molecular Weight DNA Extraction for Other Plant Species

To evaluate the efficacy and reproducibility of the protocol, we applied it to plant material from four different families: Poaceae (Italian ryegrass, *Lolium multiflorum*), Brassicaceae (wild cabbage, *Brassica incana*) and Asteraceae (beetle daisy, *Gorteria diffusa*). When extracting HMW DNA from Italian ryegrass leaf material, we noticed that the ground powder easily clumped when in contact with SDS lysis buffer (Step 2, **Figure 1**), thereby impacting the efficiency of the lysis step. To avoid powder clumping, it was critical to vortex the sample tube immediately after transferring the powder into the pre-warmed SDS lysis buffer. A total of three DNA samples were extracted (named RAB\_1-3).

Wild cabbage leaves contain high amounts of polysaccharides that negatively impact final DNA purity and yield. To reduce the level of polysaccharides in leaf tissues, the plant was placed in the dark for ca. 18 h before harvesting (final sample named BRI\_1).

Milky latex and other unknown secondary metabolites are present in high amounts in *G. diffusa* leaves. Carryover of these substances negatively impacts sample purity, resulting in NanoDrop A<sub>260/230</sub> ratios outside the optimal range for long-read sequencing. We noticed that *G. diffusa* plants perish quickly without light, making a prolonged dark treatment infeasible. To address these issues, we reduced the amount of starting material and included an additional purification step with magnetic beads. Starting with 70–80 mg young leaves, the protocol was performed as described before until the final DNA elution in 50 µl of 10 mM Tris–HCl buffer (pH 8.5) (Steps 1–18, **Figure 1**). A total of eight tubes were prepared. DNA from two tubes each were pooled and carried through an additional bead purification step. Briefly, 1 volume of magnetic bead solution was added to each sample, followed by incubation at RT for 10–15 min (Steps 9 and 10, **Figure 1**). The tubes were placed into the magnetic rack until the solution became clear, and three washing steps were performed with 1 ml of 70% EtOH without removing the tubes from the rack (Step 11–12, **Figure 1**). After the last wash, the tubes were spun down for 1 s and placed back on the magnetic rack. The beads were resuspended in 50 µl 10 mM Tris–HCl buffer (pH 8.5) (Step 14–15, **Figure 1**) and incubated at 37°C for 15 min. Afterward, the tubes were placed on a magnetic rack for final DNA elution (Step 16–19, **Figure 1**) (samples named GOR\_1-4).

## Quality Control Prior to Sequencing

Genomic DNA was evaluated for purity on a NanoDrop® spectrophotometer ND-1000 (Thermo Fisher Scientific, MA, United States). Absorbance at 230, 260, and 280 nm was measured, and A<sub>260/280</sub> and A<sub>260/230</sub> ratios were assessed to determine DNA purity. Genomic DNA concentration was

measured via NanoDrop® and confirmed with a Qubit® 3.0 fluorometer (Invitrogen, CA, United States) using the dsDNA BR Assay Kit (Thermo Fisher Scientific, MA, United States, Q32850). Note that, if the DNA is pure, the measurements of DNA concentrations from NanoDrop® and Qubit® should be identical.

DNA integrity was assessed on a TapeStation 4200 system (Agilent, CA, United States) with a Genomic DNA ScreenTape Assay. Here, DNA quality is assessed using a DNA Integrity Number (DIN) that ranges from 1 (highly degraded DNA) to 10 (intact DNA). Fragment length was measured on a Femto Pulse v-1.0.0.32 system (Agilent, CA, United States, Cat N° M5330AA) using the Genomic DNA 165 kb Ladder Fast Separation assay with a separation time of 70 min (Agilent, CA, United States, Cat N° FP-1002-0275). For *G. diffusa*, DNA integrity was determined on a Pippin Pulse™ electrophoresis system (Sage Science, MA, United States, Cat N° PP10200) with program 5–80 kb and the Bio-Rad CHEF 5 kb DNA Size Standard.

## Size Selection With the Circulomics Kit

We tested the impact of short DNA fragment depletion on final sequencing results by applying the Circulomics Short Read Eliminator Kit (Circulomics, MD, United States, SS-100-101-01) on one of the two samples selected for sequencing (OPH\_3 and RAB\_2). The kit was applied to the *L. multiflorum* sample RAB\_2 before library preparation to remove small DNA fragments. According to supplier information, the kit uses size-selective precipitation to reduce the amount of DNA fragments below 25 kbp in length<sup>3</sup>. Potentially, the kit can thus significantly enhance average read length during sequencing. The kit was used according to the manufacturer's recommendations (handbook v2.0, 07/2019). Briefly, 60 µl of Buffer SRE were added to the sample tube (60 µl volume), gently mixed and the tube centrifuged at 10,000 × g for 30 min at RT. After supernatant removal, two washing steps were performed with 200 µl of 70% EtOH and a centrifugation at 10000 × g for 2 min at RT. Finally, 100 µl Qiagen Buffer EB were added and the tube was incubated at RT overnight to ensure efficient DNA elution (sample named RAB\_2\_Circ). No Circulomics kit was applied to sample OPH\_3.

## ONT® Library Preparation

We tested the suitability of our protocol by sequencing HMW DNA from samples OPH\_3 and RAB\_2\_Circ. Sequencing library preparation was carried out following the general guidelines from Oxford Nanopore Technologies® for 1D Genomic DNA sequencing, with modifications proposed by New England Biolabs® (NEB) to ensure high data yield production and long-fragment sequencing. For library preparation, the following reagents were used: Ligation Sequencing Kit SQK-LSK109 (Oxford Nanopore Technologies®), NEBNext® Companion Module for Oxford Nanopore Technologies® Ligation Sequencing (NEB, MA, United States, Cat N° E7180S), and AMPure XP beads (Beckman Coulter Inc., CA, United States). A DNA amount of 1.5 µg was collected from samples OPH\_3 and RAB\_2\_Circ (since OPH\_3 was highly concentrated, 13 µl of DNA were diluted in 35 µl of 10 mM Tris–HCl buffer to reach

<sup>3</sup><https://www.circulomics.com/store/Short-Read-Eliminator-Kit-p131401036>



a total volume of 48  $\mu$ l) and transferred into a 0.2 ml thin-walled PCR tube. DNA fragments were repaired and end-prepped as follows: 3.5  $\mu$ l NEBNext® FFPE DNA Repair Buffer, 2  $\mu$ l NEBNext® FFPE DNA Repair Mix, 3.5  $\mu$ l NEBNext® Ultra™ II End Prep Reaction Buffer, and 3  $\mu$ l NEBNext® Ultra™ II End Prep Enzyme Mix were added to each tube. After mixing and spinning down, the samples were incubated at 20°C for 30 min, followed by a second incubation at 65°C for 30 min. The original recommendations from NEB were followed, instead of the ONT® guidelines, as preliminary experiments showed better results under NEB supplier conditions: prolonged incubation time allowed recovery of longer fragments. After incubation, the solution from each tube was transferred to a clean 1.5 ml Eppendorf DNA LoBind® tube (Eppendorf AG, Hamburg, Germany) for clean-up. First, a stock solution of AMPure XP Beads was prepared as in Schalamun et al. (2019), and 60  $\mu$ l were added to each tube. The samples were then incubated on a HulaMixer™ sample mixer (Thermo Fisher Scientific, MA, United States, 15920D) for 20 min at RT, until the solution was homogenised. Bead clean-up was performed with two washing steps on a magnetic rack, each time pipetting off the supernatant and adding 200  $\mu$ l of freshly prepared 70% EtOH. The pellet was resuspended in 61  $\mu$ l nuclease-free water (1  $\mu$ l was then taken out for quantification) and incubated for 10 min at RT on a HulaMixer™. Tubes were placed on a magnetic rack to collect the final eluate. For adapter ligation and clean-up, 60  $\mu$ l DNA from the previous step was combined with 25  $\mu$ l Ligation Buffer LNB, 5  $\mu$ l Adapter Mix AMX, and 10  $\mu$ l NEBNext® Quick T4 DNA Ligase (240  $\mu$ l) in a 1.5 ml Eppendorf DNA LoBind tube, and incubated for 20 min at RT. A second AMPure bead clean-up step was carried out by adding 45  $\mu$ l of bead solution to each tube, followed by incubation on a HulaMixer™ for 20 min at RT. After pipetting off the supernatant on a magnet rack, the beads were washed twice with 250  $\mu$ l Long Fragment Buffer LFB. Finally, the supernatant was discarded, the pellet resuspended in 25  $\mu$ l Elution Buffer EB, and incubated for 10 min at RT to collect the final library.

## Long-Read Sequencing

The ONT® PromethION PTC0031 sequencing platform (Alpha-Beta model, OS Ubuntu 16.06, Intel CPU) was used to sequence samples OPH\_3 and RAB\_2\_Circ. For each sample, 0.8–1  $\mu$ g of the prepared library was loaded onto a R9.4.1 chemistry PromethION flow cell. Sequencing ran until the flow cell buffer was exhausted (63.10 h for OPH\_3, 40.14 h for RAB\_2\_Circ). MinKNOW v-2.1 was used for data acquisition, real-time analysis and sample tracking. Basecalling was performed with Guppy v-3.0.4.

## RESULTS

### DNA Purity and Quantity

We compared our DNA extraction protocol with the original version of Mayjonade et al. (2016) and the protocol of Schalamun et al. (2019) which was developed for recalcitrant plant species. We used *O. sphegodes* leaves and compared the results in terms

of purity on a NanoDrop® device. When using the original protocol (Mayjonade et al., 2016), we could recover only small amounts of DNA (1,090 ng DNA total) and failed to recover pure DNA (Figure 2A). The  $A_{260/280} = 1.68$  indicated protein contamination, and the low  $A_{260/230}$  value indicated presence of polysaccharides, polyphenols or other organic compounds. Using the protocol of Schalamun et al. (2019), we were not able to recover any DNA at all (Figure 2B). With our improved extraction protocol, all purity criteria ( $A_{260/280} = 1.80$ – $2.0$  and  $A_{260/230} = 2.0$ – $2.2$ ) were met in all six *O. sphegodes* samples (Figure 2C, OPH\_1-6 in Table 1). Remarkably, we were able to recover an average DNA amount of 5,710 ng per sample (3,950 to 8,450 ng). The NanoDrop® and Qubit® measurements were comparable (NanoDrop®/Qubit® ratio close to 1; Table 1), indicating a clean DNA sample. Since Qubit® measures only double-stranded DNA, a ratio of 1 further indicates that the DNA molecules measured are double stranded and that other molecules with absorption at 260 nm are absent (O'Neill et al., 2011). When the ratio was below 1 (OPH\_2 = 0.87, OPH\_5 = 0.71), we considered the Qubit® values to be more accurate.

To evaluate the efficacy and reproducibility of our method, we applied it to other plant species. All three Italian ryegrass samples met the quality criteria, and the DNA amount recovered was on average 2,400 ng, with a NanoDrop®/Qubit® ratio of  $\sim 1$  (RAB\_1-3, Table 1). When DNA was extracted from *B. incana* leaves,  $A_{260/280}$  was 1.85 and  $A_{260/230}$  was 2.19. Total DNA amount was 7,300 ng, confirmed by a NanoDrop®/Qubit® = 0.97 (Table 1). In *G. diffusa*, we included an additional purification step with magnetic beads after DNA elution. This extra step allowed all samples to meet the purity criteria necessary for sequencing (GOR\_1-4, average DNA amount 5,550 ng per sample,  $A_{260/280} = \sim 1.83$ ,  $A_{260/230} = \sim 2.13$ , Table 1).

### DNA Integrity and Fragment Lengths

Genomic DNA integrity was assessed by determining the degree of fragmentation of the sample. On a TapeStation, all *O. sphegodes* samples had a DIN value of 9.3 or above (with 10 = highly intact DNA, Figure 2D). Fragment lengths of samples OPH\_3, RAB\_2 and BRI\_1 were measured on a Femto Pulse system. Because the fast separation assay was used, it was not possible to distinguish any fragment lengths above 165 kbp, where only a compression band was visible. OPH\_3 showed peaks at 110 and 153 kbp, and RAB\_2 clearly displayed a peak at around 165 kbp (Figures 3A,B). BRI\_1 showed a peak at around 50 kbp and a more heterogeneous distribution of fragment sizes (Figure 3C). DNA of GOR samples showed a clear band above the size of the largest marker of 68 kbp on a Pippin Pulse gel (Figure 3D).

### Size Selection With Circulomics and PromethION Sequencing

We tested our DNA extraction protocol by sequencing samples OPH\_3 and RAB\_2\_Circ. Each library was injected into one flow cell. Flow cell behaviour was comparable, with 2,791 and 2,684 out of 3,000 active channels for OPH\_3 and RAB\_2\_Circ, respectively. Since the sequencing run was longer for OPH\_3, the



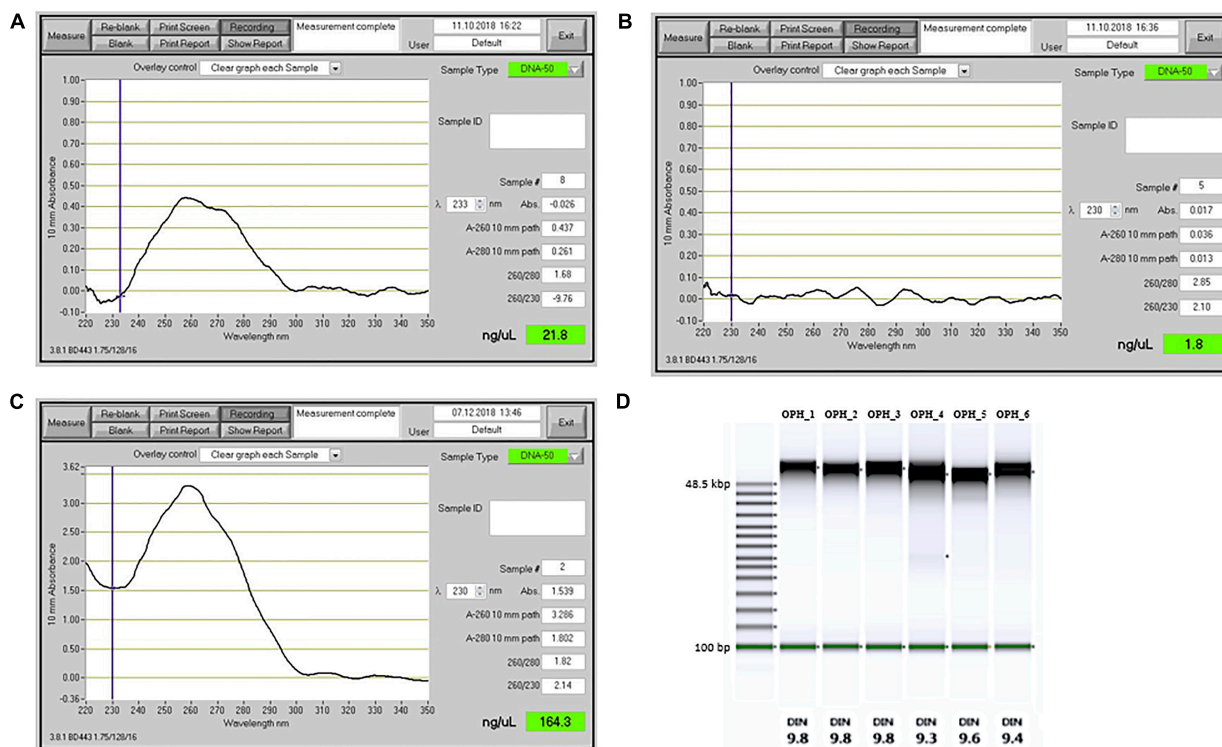


**FIGURE 2 |** Comparison of DNA extraction performance for different extraction methods. **(A–C)** Output from a NanoDrop spectrophotometer. **(A)** DNA extraction results with the Mayjonade et al. (2016) protocol, without  $\beta$ -ME and phenol:chloroform purification step. **(B)** DNA extraction with lysis buffer as described by Schalamun et al. (2019). **(C)** DNA extracted with the protocol described in this study (sample OPH\_3). **(D)** TapeStation results showing the fragment size distribution and the DNA Integrity Number (DIN), for six *O. sphegodes* samples.

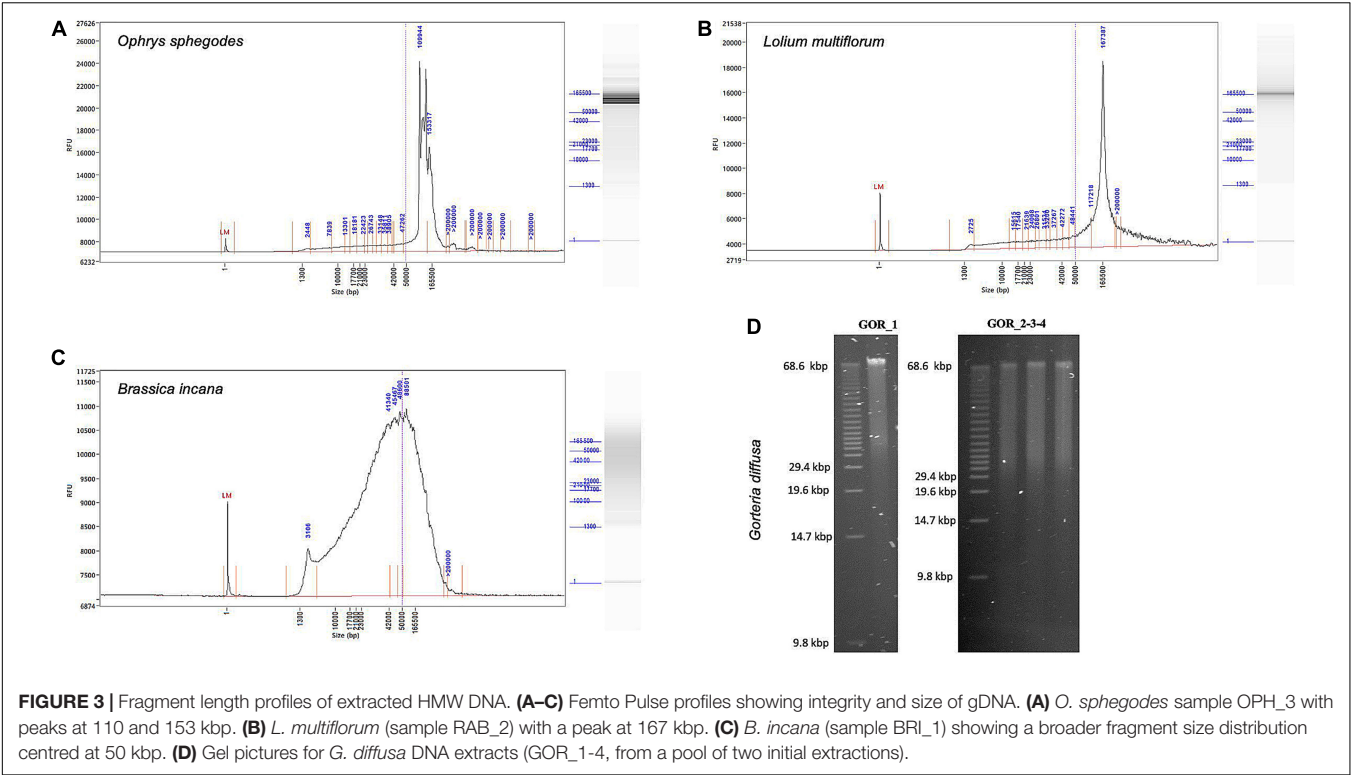
**TABLE 1 |** Summary of DNA quality measurements for all extracted samples.

Species/Sample	Qubit conc. [ng/ $\mu$ l]	NanoDrop conc. [ng/ $\mu$ l]	Output [ $\mu$ g]	A <sub>260/280</sub> ratio	A <sub>260/230</sub> ratio	NanoDrop/Qubit conc. ratio	Qubit conc. after Circulomics [ng/ $\mu$ l]
<i>Ophrys sphegodes</i>							
OPH_1	79.0	114.4	3.95	1.83	1.97	1.45	–
OPH_2	115.0	99.8	5.75	1.83	2.23	0.87	–
OPH_3	169.0	164.3	8.45	1.82	2.14	0.97	–
OPH_4	86.3	85.9	4.32	1.81	2.15	0.99	–
OPH_5	152.0	107.9	7.60	1.79	1.97	0.71	–
OPH_6	83.8	86.4	4.19	1.79	1.79	1.03	–
<i>Lolium multiflorum</i>							
RAB_1	42.0	40.0	2.10	1.95	2.06	0.95	17.0
RAB_2	56.0	53.0	2.80	1.92	2.15	0.95	23.0
RAB_3	46.0	42.0	2.30	1.85	2.30	0.91	18.0
<i>Brassica incana</i>							
BRI_1	150.0	146.0	7.50	1.85	2.19	0.97	–
<i>Gorteria diffusa</i> <sup>1</sup>							
GOR_1	146.0	182.6	7.30	1.84	2.07	1.25	–
GOR_2	93.6	97.0	4.68	1.83	2.18	1.04	–
GOR_3	102.0	108.4	5.10	1.82	2.15	1.06	–
GOR_4	103.0	112.8	5.15	1.82	2.12	1.09	–

<sup>1</sup>For *G. diffusa*, 70–80 mg of input material were used, whereas for the other species, it was ~100 mg.

final sequencing yield in terms of Gbp data produced was higher for OPH\_3 (66 Gbp versus 50 Gbp for RAB\_2\_Circ; Table 2). The effect of the Circulomics Kit in depleting short fragments

is evident when comparing the fragment size distribution of the samples before (Figures 3A,B) and after (Figure 4) sequencing. When DNA molecules from samples OPH\_3 and RAB\_2 were



evaluated on a Femto Pulse system, both showed the presence of smaller fragments (2–10 kbp). After short read depletion in sample RAB\_2\_Circ, the amount of small fragments decreased

**TABLE 2 |** Nanopore (PromethION) sequencing statistics for sequenced samples.

Sample	OPH_3	RAB_2_Circ
Species	<i>O. sphegodes</i>	<i>L. multiflorum</i>
Treatment	No Circulomics	With Circulomics
Run duration (h)	63.10	40.14
Active channels	2,791	2,684
Total reads	9,131,684	2,181,501
Sequencing yield (Gbp)	66.4	50.4
Read length N50 (bp)	27,196	51,861
Mean read length (bp)	7,270.60	23,122.70
Median read length (bp)	2,157.00	11,119.00
# Reads ≥ 10 kbp	1,438,821	1,130,927
# Reads ≥ 25 kbp	635,963	721,668
# Reads ≥ 50 kbp	261,570	331,789
# Reads ≥ 100 kbp	55,592	59,998
# Reads ≥ 200 kbp	2,011	1,204
# Reads ≥ 500 kbp	39	0
% Reads ≥ 10 kbp	15.75%	51.84%
% Reads ≥ 25 kbp	6.96%	33.08%
% Reads ≥ 50 kbp	2.86%	15.21%
% Reads ≥ 100 kbp	0.61%	2.75%
% Reads ≥ 200 kbp	0.02%	0.06%
% Reads ≥ 500 kbp	0.00%	0.00%
Longest read (Mbp)	1.7	0.464

drastically, and as a result, the number of sequenced small reads was appreciably lower than in OPH\_3 (Figure 4A and Table 2). Because short fragments were largely removed in RAB\_2\_Circ, more than half (51.84%) of the total reads were longer than 10 kbp, and one third (33.08%) were longer than 25 kbp. The read length statistics in OPH\_3 were very different, with only 15.75% of the total reads longer than 10 kbp, and a read length N50 roughly half that of RAB\_2\_Circ (27,196 vs. 51,861 bp, Table 2). In both runs, we were able to recover long to ultra-long reads (>100 kbp) (Table 2). The longest reads were 464 kbp for RAB\_2\_Circ, and 1.7 Mbp for OPH\_3.

## DISCUSSION

Long-read sequencing technologies offer a new array of opportunities to study plant genomes in ways that were not feasible before. Our study presents an improved HMW DNA extraction method suitable for a wide variety of plant species and shows how pure high-quality DNA, together with optimised library preparation parameters and size selection, are key for reaching high-throughput ultra-long reads for sequencing projects. Isolated DNA suitable for long-read sequencing has to meet two important criteria: (i) DNA purity and quantity and (ii) DNA integrity.

## DNA Purity and Quantity

Nucleic acid purification from plant tissue can be challenging. In particular, when chemicals such as ethanol or phenol are involved in a DNA extraction procedure, or when proteins or

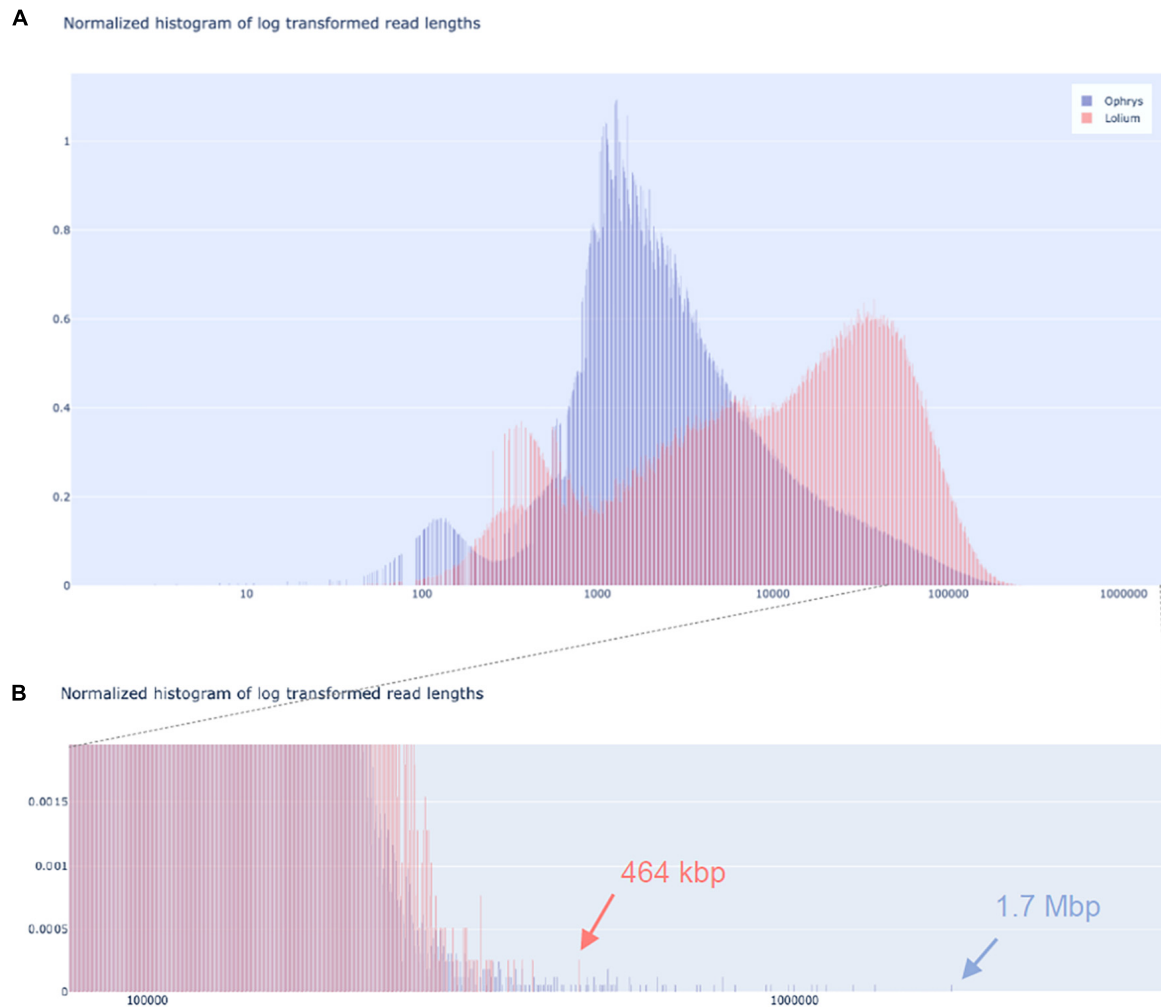


**FIGURE 4 |** Nanopore sequencing read length distributions. Read length distribution for *O. sphegodes* OPH\_3 (blue; without Circulomics kit) and *L. multiflorum* RAB\_2\_Circ (red; after Circulomics kit), showing **(A)** the entire normalised histogram of log-transformed read lengths and **(B)** a zoom-in into the section showing the longest reads (OPH\_3 = 1.7 Mbp; RAB\_2\_Circ = 464 kbp).

other organic components from plant material are present, final nucleic acid purity can be compromised. As a result, the purity of DNA extracts needs to be measured to avoid sequencing samples of inferior quality. The purity of isolated nucleic acids is commonly determined with a spectrophotometer, measuring three UV absorbance (A) values: absorbance at 260, 280, and 230 nm. Nucleic acids absorb UV light at a wavelength with a peak at 260 nm and hence an absorbance spectrum with a 260 nm peak indicates pure DNA. Protein (specifically the aromatic amino acids tryptophan and tyrosine) and phenols absorb UV light at 280 nm. When proteins and phenols contaminate a nucleic acid sample, the absorbance peak at 280 nm decreases by ca. 10-fold (Koetsier and Cantor, 2019). Organic components such as carbohydrates, buffer salts from DNA extraction (like Tris), EtOH, and EDTA strongly absorb at 230 nm. If one or more of these compounds are present in a nucleic acid extract, a lower 230 nm absorbance is detected. Overall, the ratios of the absorbance values  $A_{260/280}$  and  $A_{260/230}$  allow estimation of

the purity of a nucleic acid sample. Pure dsDNA has absorbance ratios of  $A_{260/280} = 1.8 - 2.0$  and  $A_{260/230} = 2.0 - 2.2$ ; lower values indicate the presence of contaminants, while higher  $A_{260/280}$  values can be indicative of RNA contamination (pure RNA has an  $A_{260/280} = 2.0 - 2.2$ ) (Glaser, 1995).

To obtain pure genomic DNA that meets the aforementioned characteristics, we first tried the protocols of both Mayjonade et al. (2016) and Schalamun et al. (2019) on *Ophrys* leaves, and then produced an improved and more robust method. The DNA extraction protocol from Mayjonade et al. (2016) is divided into three main steps: cell membrane disruption with SDS lysis buffer, contaminant precipitation with 5 M KAc, and final purification of gDNA with Sera-Mag SpeedBeads magnetic beads. Schalamun et al. (2019) introduced changes in lysis buffer composition, and used different incubation times at different temperatures. When our *Ophrys* sample was extracted with the protocol of Mayjonade et al. (2016), DNA concentration was low, and the UV absorbance spectrum showed severe contamination.  $A_{260/280}$  and  $A_{260/230}$

are unreliable at DNA concentrations  $< 20 \text{ ng}/\mu\text{l}$  (Koetsier and Cantor, 2019), and in general such weakly concentrated samples are not suitable for long-read sequencing (as per manufacturers' protocols; **Figure 2A**).

To produce a DNA extract of high concentration and purity, we modified the lysis buffer by increasing SDS concentration to 1.5% and adding 2%  $\beta$ -ME. A higher SDS concentration ensures a more effective rupture of cell walls after a first mechanical breakage by grinding under  $\text{LN}_2$ , while  $\beta$ -ME is a reducing agent that denatures proteins by breaking the disulphide bonds between cysteine residues. Together, those two reagents increased the recovery of DNA from cells. Moreover, it has been reported that high levels of  $\beta$ -ME successfully remove polyphenols (Khanuja et al., 1999) and other organic compounds, such as tannins, from plant tissue (John, 1992; Moreira et al., 2011). A second modification was introduced after protein precipitation with 5M KAc. We added a phenol:chloroform:isoamyl alcohol (25:24:1 v/v) purification to remove other carryover contaminants. The separation of the solution in two phases allowed us to extract the isolated DNA in the aqueous phase, while leaving carryover contaminants from the extraction in the organic phase. Residual phenol was then removed during the bead purification step. These changes proved to be effective in delivering highly purified DNA in all our study species (see absorbance ratios in **Table 1**). All samples met the  $A_{260/280}$  and  $A_{260/230}$  criteria suitable for long-read sequencing, regardless of the plant species used. Remarkably, final DNA amounts were on average  $\sim 5,000 \text{ ng}$  per sample (from Qubit® measurement;  $\sim 100 \text{ ng}/\mu\text{l}$ ) and concentrations ranged from 42 to 169  $\text{ng}/\mu\text{l}$ , depending on the species (**Table 1**). Hence, another positive effect of the improvements was the relatively high DNA quantity we were able to recover. ONT® recommends using at least 1  $\mu\text{g}$  DNA per library preparation. Thus, the final DNA amount per sample was enough for several parallel library preparations. Since PacBio® recommends using 5  $\mu\text{g}$  DNA for CLR and CCS sequencing (less if the plant genome of interest is 500 Mbp – 1 Gbp in size), sample pooling would have been necessary for sequencing with this platform.

The same DNA extraction procedure may result in different yields in different plant species, as different plants have different tissue characteristics. If the extracted DNA appears to be suboptimal in terms of purity, we suggest reducing the amount of starting material to 70–80 mg per sample, as we did with *G. diffusa*. In this way, the level of contaminants from plant material that may interfere with SDS during cell lysis is reduced. An additional purification step with magnetic beads can clean the DNA further. As long fragments bind to the magnetic beads and are not washed away, DNA yield is hardly impacted, while residual contaminants are removed. It may often be advisable to use softer and younger rather than older and tougher leaves. In this regard, plant secondary metabolites that negatively impact DNA extraction have been shown to accumulate over time as leaves age (Boege and Marquis, 2005; Moreira et al., 2011), although in other cases higher concentrations of phenolics have been found in young leaves (Barton et al., 2019). It is important to stress that the grinding step is crucial to recover a high DNA yield and that insufficient grinding can reduce final DNA yield.

Finally, heating the elution buffer to 37°C before usage can help to increase the elution efficiency in the final step of the protocol.

## Integrity of DNA Molecules and Effect on Sequencing

In long-read sequencing, the fraction of long reads (10 kbp or longer) depends strongly on the integrity (i.e., degree of fragmentation) of the DNA molecules used for library preparation. Therefore, one of the goals of an HMW DNA extraction method suitable for long-read sequencing is to preserve and maximise long and ultra-long DNA molecules. One critical step is to prevent DNA damage by thawing. When harvesting, plant material should immediately be flash-frozen, stored at  $-80^\circ\text{C}$ , and transferred to a cool mortar only before immediate use. During grinding,  $\text{LN}_2$  should not evaporate completely, as this can thaw plant material and cause DNA damage. Final extracted DNA can be stored at 4°C if actively used. For long-term storage, gDNA is best stored at  $-20^\circ\text{C}$  and only thawed when used, as repeated cycles of freezing and thawing can degrade DNA molecules. Another source of DNA degradation is nuclease activity. During mechanical tissue rupture and chemical cell lysis, enzymes such as DNases are released along with DNA. For this reason,  $\beta$ -ME was added to the lysis buffer, which disrupts disulphide bonds, thus inactivating DNases (Price et al., 1969). For best results, we recommend to quickly homogenise the ground tissue powder immediately after adding lysis buffer by vortexing the sample tube. To prevent DNA fragmentation, it is also advisable to use wide bore pipette tips (or P1000 tips with cut ends). Such tips have a wider opening for aspirating and dispensing viscous solutions, and thus they can decrease DNA shearing due to pipetting. For the same reason, we advise carefully pipetting the DNA with slow, gentle movements of the pipette plunger. Since elution time plays a role in long fragment recovery, we prolonged the elution time during bead purification and library preparation. This helped recovering a higher fraction of long fragments and an overall higher DNA amount. As shown in **Figure 4B** and **Table 2**, these improvements allowed us to obtain long to ultra-long reads in both sequencing runs.

Finally, we recommend to remove short DNA molecules ( $< 10 \text{ kbp}$ ) before sequencing. The presence of these “short” fragments does not result in poorer quality sequence, but it does affect a sequencing run's fragment size distribution (cf. **Figure 4**). Short fragments compete with longer ones for pore occupancy in the flow cell, decreasing the throughput of long reads per sequencing run. Although shorter reads can be discarded bioinformatically, this approach may not be optimal in terms of cost efficiency when the aim of long-read sequencing is to generate data for genome assembly.

## CONCLUSION

Long-read sequencing approaches are starting to dominate as the primary tools for genome sequencing projects. Thanks to continuous improvements in sequencing chemistry and technology, long reads are used in a plethora of applications,



from *de novo* genome assembly to methylome analysis, to field applications. Here, we provide a robust method to extract purified high molecular weight DNA for long-read sequencing. Our DNA extraction method successfully worked on diverse monocot and eudicot plant species, indicating that the method is effective in a wide variety of plant families. For particularly challenging species, we show that adding an extra purification step allows the user to achieve the purity required for long-read sequencing, while maintaining a high integrity of the DNA molecules. A step-by-step version of the protocol is available online at [dx.doi.org/10.17504/protocols.io.5t7g6rn](https://doi.org/10.17504/protocols.io.5t7g6rn).

## DATA AVAILABILITY STATEMENT

The original contributions presented in the study are included in the article/**Supplementary Material**, further inquiries can be directed to the corresponding authors.

## AUTHOR CONTRIBUTIONS

AR and PS: conceptualisation and writing—original draft. AR, BM, GP, and DF: methodology and investigation. RK, LF, and DF: validation. AR: data curation and visualisation. PS and UG:

supervision. DC, BS, JF, UG, and PS: resources. BS, JF, UG, and PS: funding acquisition. All authors: writing, review, and editing.

## FUNDING

This work was supported by the University of Zurich, a Ph.D. project funded by the University Research Priority Programme “Evolution in Action” (to UG and PS) and the Swiss National Science Foundation (mobility grant P400PB\_194374 to RK).

## ACKNOWLEDGMENTS

We are grateful to Salvatore Cozzolino for providing plant material and to Kelsey Byers and Sergio Ramos for comments on the manuscript.

## SUPPLEMENTARY MATERIAL

The Supplementary Material for this article can be found online at: <https://www.frontiersin.org/articles/10.3389/fpls.2022.883897/full#supplementary-material>

## REFERENCES

- Barton, K. E., Edwards, K. F., and Koricheva, J. (2019). Shifts in woody plant defence syndromes during leaf development. *Funct. Ecol.* 33, 2095–2104. doi: 10.1111/1365-2435.13435
- Belser, C., Istace, B., Denis, E., Dubarry, M., Baurens, F. C., Falentin, C., et al. (2018). Chromosome-scale assemblies of plant genomes using nanopore long reads and optical maps. *Nat. Plants* 4, 879–887. doi: 10.1038/s41477-018-0289-4
- Boege, K., and Marquis, R. J. (2005). Facing herbivory as you grow up: the ontogeny of resistance in plants. *Trends Ecol. Evol.* 20, 441–448. doi: 10.1016/j.tree.2005.05.001
- Chawla, H. S., Lee, H. T., Gabur, I., Vollrath, P., Tamilselvan-Nattar-Amutha, S., Obermeier, C., et al. (2021). Long-read sequencing reveals widespread intragenic structural variants in a recent allopolyploid crop plant. *Plant Biotechnol. J.* 19, 240–250. doi: 10.1111/pbi.13456
- Exposito-Alonso, M., Drost, H. G., Burbano, H. A., and Weigel, D. (2020). The earth biogenome project: opportunities and challenges for plant genomics and conservation. *Plant J.* 102, 222–229. doi: 10.1111/tpj.14631
- Flusberg, B. A., Webster, D., Lee, J., Travers, K., Olivares, E., Clark, A., et al. (2010). Direct detection of DNA methylation during single-molecule, real-time sequencing. *Nat. Methods* 7, 461–465. doi: 10.1038/nmeth.1459
- Formenti, G., Theissinger, K., Fernandes, C., Bista, I., Bleidorn, C., Angelica, C., et al. (2022). The era of reference genomes in conservation genomics. *Trends Ecol. Evol.* 37, 197–202. doi: 10.1016/j.tree.2021.11.008
- Frei, D., Veekman, E., Grogg, D., Stoffel-Studer, I., Morishima, A., Shimizu-Inatsugi, R., et al. (2021). Ultralong Oxford Nanopore reads enable the development of a reference-grade perennial ryegrass genome assembly. *Genome Biol. Evol.* 13, 1–6. doi: 10.1093/gbe/evab159
- Gerstein, A. S. (2001). *Molecular Biology Problem Solver: a Laboratory Guide*. Chichester: Wiley-Liss, Inc. doi: 10.1002/0471223905
- Gilliland, T. J., Johnston, J., and Connolly, C. (2007). A review of forage grass and clover seed use in Northern Ireland, UK between 1980 and 2004. *Grass Forage Sci.* 62, 239–254. doi: 10.1111/j.1365-2494.2007.00588.x
- Glasel, J. (1995). Validity of nucleic acid purities monitored by 260/280 absorbance ratios. *BioTechniques* 18, 62–63.
- Goerner-Potvin, P., and Bourque, G. (2018). Computational tools to unmask transposable elements. *Nat. Rev. Genet.* 19, 688–704. doi: 10.1038/s41576-018-0050-x
- Hasing, T., Tang, H., Brym, M., Khazi, F., Huang, T., and Chambers, A. H. (2020). A phased *Vanilla planifolia* genome enables genetic improvement of flavour and production. *Nat. Food* 1, 811–819. doi: 10.1038/s43016-020-00197-2
- Heller, D., and Vingron, M. (2019). SVIM: structural variant identification using mapped long reads. *Bioinformatics* 35, 2907–2915. doi: 10.1093/bioinformatics/btz041
- Hu, L., Xu, Z., Wang, M., Fan, R., Yuan, D., Wu, B., et al. (2019). The chromosome-scale reference genome of black pepper provides insight into piperine biosynthesis. *Nat. Commun.* 10:4702. doi: 10.1038/s41467-019-12607-6
- Jiao, W. B., and Schneeberger, K. (2017). The impact of third generation genomic technologies on plant genome assembly. *Curr. Opin. Plant Biol.* 36, 64–70. doi: 10.1016/j.pbi.2017.02.002
- John, M. E. (1992). An efficient method for isolation of RNA and DNA from plants containing polyphenolics. *Nucleic Acids Res.* 20:2381. doi: 10.1093/nar/20.9.2381
- Katterman, F. R. H., and Shattuck, V. I. (1983). An effective method of dna isolation from the mature leaves of gossypium species that contain large amounts of phenolic terpenoids and tannins. *Prep. Biochem.* 13, 347–359. doi: 10.1080/00327488308068177
- Kersey, P. J. (2019). Plant genome sequences: past, present, future. *Curr. Opin. Plant Biol.* 48, 1–8. doi: 10.1016/j.pbi.2018.11.001
- Khanuja, S., Shasany, A., Darokar, M. P., and Kumar, S. (1999). Rapid isolation of DNA from dry and fresh samples of plants producing large amounts of secondary metabolites and essential oils. *Plant Mol. Biol. Rep.* 17, 74\_1–74\_7. doi: 10.1023/A:1007528101452
- Koetsier, G., and Cantor, E. (2019). *A Practical Guide to Analyzing Nucleic Acid Concentration and Purity with Microvolume Spectrophotometers*. New England Biolabs Tech. Note 7/2019. Available online at: [https://prd-sccd01-international.neb.com/-/media/neb/files/application-notes/technote\\_mv\\_analysis\\_of\\_nucleic\\_acid\\_concentration\\_and\\_purity.pdf?rev=c24cea043416420d84fb6bf7b554dbbb](https://prd-sccd01-international.neb.com/-/media/neb/files/application-notes/technote_mv_analysis_of_nucleic_acid_concentration_and_purity.pdf?rev=c24cea043416420d84fb6bf7b554dbbb) (accessed February 24, 2022).

- Mayjonade, B., Muños, S., Donnadiou, C., Marande, W., Langlade, N., Callot, C., et al. (2016). Extraction of high-molecular-weight genomic DNA for long-read sequencing of single molecules. *Biotechniques* 61, 203–205. doi: 10.2144/000114460
- Moreira, P. A., Oliveira, D. A., Federal, U., Gerais, D. M., Horizonte, B., Estadual, U., et al. (2011). Leaf age affects the quality of DNA extracted from *Dimorphandra Mollis* (Fabaceae), a tropical tree species from the Cerrado region of Brazil. *Genet. Mol. Res.* 10, 353–358. doi: 10.4238/vol10-1gmr1030
- Niu, S., Li, J., Bo, W., Yang, W., Zuccolo, A., Giacomello, S., et al. (2022). The Chinese pine genome and methylome unveil key features of conifer evolution. *Cell* 185, 204.e–217.e. doi: 10.1016/j.cell.2021.12.006
- O'Neill, M., McPartlin, J., Arthure, K., Riedel, S., and McMillan, N. D. (2011). Comparison of the TLDA with the Nanodrop and the reference Qubit system. *J. Phys. Conf. Ser.* 307:012047. doi: 10.1088/1742-6596/307/1/012047
- Otzen, D. (2011). Protein–surfactant interactions: a tale of many states. *Biochim. Biophys. Acta* 1814, 562–591. doi: 10.1016/j.bbapap.2011.03.003
- Pandey, R. N., Adams, R. P., and Flournoy, L. E. (1996). Inhibition of random amplified polymorphic DNAs (RAPDs) by plant polysaccharides. *Plant Mol. Biol. Rep.* 14, 17–22. doi: 10.1007/BF02671898
- Prall, T. M., Neumann, E. K., Karl, J. A., Shortreed, C. G., Baker, D. A., Bussan, H. E., et al. (2021). Consistent ultra-long DNA sequencing with automated slow pipetting. *BMC Genomics* 22:182. doi: 10.1186/S12864-021-07500-W/FIGURES/4
- Price, P. A., Stein, W. H., and Moore, S. (1969). Effect of divalent cations on the reduction and re-formation of the disulfide bonds of deoxyribonuclease. *J. Biol. Chem.* 244, 929–932. doi: 10.1016/s0021-9258(18)91875-2
- Pu, X., Li, Z., Tian, Y., Gao, R., Hao, L., Hu, Y., et al. (2020). The honeysuckle genome provides insight into the molecular mechanism of carotenoid metabolism underlying dynamic flower coloration. *New Phytol.* 227, 930–943. doi: 10.1111/nph.16552
- Saxena, R. K., Edwards, D., and Varshney, R. K. (2014). Structural variations in plant genomes. *Brief. Funct. Genomics* 13, 296–307. doi: 10.1093/BFGP/ELU016
- Schalamun, M., Nagar, R., Kainer, D., Beavan, E., Eccles, D., Rathjen, J. P., et al. (2019). Harnessing the MinION: an example of how to establish long-read sequencing in a laboratory using challenging plant tissue from *Eucalyptus Pauciflora*. *Mol. Ecol. Resour.* 19, 77–89.
- Sedlazeck, F. J., Rescheneder, P., Smolka, M., Fang, H., Nattestad, M., Von Haeseler, A., et al. (2018). Accurate detection of complex structural variations using single-molecule sequencing. *Nat. Methods* 15, 461–468. doi: 10.1038/s41592-018-0001-7
- Simpson, J. T., Workman, R. E., Zuzarte, P. C., David, M., Dursi, L. J., and Timp, W. (2017). Detecting DNA cytosine methylation using nanopore sequencing. *Nat. Methods* 14, 407–410. doi: 10.1038/nmeth.4184
- Varma, A., Padh, H., and Shrivastava, N. (2007). Plant genomic DNA isolation: an art or a science. *Biotechnol. J.* 2, 386–392. doi: 10.1002/biot.200600195
- Wilkins, P. W. (1991). Breeding perennial ryegrass for agriculture. *Euphytica* 52, 201–214.
- Zerpa-Catanho, D., Zhang, X., Song, J., Hernandez, A. G., and Ming, R. (2021). Ultra-long DNA molecule isolation from plant nuclei for ultra-long read genome sequencing. *STAR Protoc.* 2:100343. doi: 10.1016/j.xpro.2021.100343
- Zhang, B., Gao, Y., Zhang, L., and Zhou, Y. (2021). The plant cell wall: biosynthesis, construction, and functions. *J. Integr. Plant Biol.* 63, 251–272. doi: 10.1111/JIPB.13055
- Zhang, G. Q., Liu, K. W., Li, Z., Lohaus, R., Hsiao, Y. Y., Niu, S. C., et al. (2017). The Apostasia genome and the evolution of orchids. *Nature* 549, 379–383. doi: 10.1038/nature23897
- Zhang, J., Chen, L. L., Xing, F., Kudrna, D. A., Yao, W., Copetti, D., et al. (2016). Extensive sequence divergence between the reference genomes of two elite indica rice varieties zhenshan 97 and minghui 63. *Proc. Natl. Acad. Sci. U.S.A.* 113, E5163–E5171. doi: 10.1073/pnas.1611012113
- Zhao, Y., Yue, Z., Zhong, X., Lei, J., Tao, P., and Li, B. (2020). Distribution of primary and secondary metabolites among the leaf layers of headed cabbage (*Brassica oleracea* var. *capitata*). *Food Chem.* 312:126028. doi: 10.1016/j.foodchem.2019.126028

**Conflict of Interest:** The authors declare that the research was conducted in the absence of any commercial or financial relationships that could be construed as a potential conflict of interest.

**Publisher's Note:** All claims expressed in this article are solely those of the authors and do not necessarily represent those of their affiliated organizations, or those of the publisher, the editors and the reviewers. Any product that may be evaluated in this article, or claim that may be made by its manufacturer, is not guaranteed or endorsed by the publisher.

Copyright © 2022 Russo, Mayjonade, Frei, Potente, Kellenberger, Frachon, Copetti, Studer, Frey, Grossniklaus and Schlüter. This is an open-access article distributed under the terms of the Creative Commons Attribution License (CC BY). The use, distribution or reproduction in other forums is permitted, provided the original author(s) and the copyright owner(s) are credited and that the original publication in this journal is cited, in accordance with accepted academic practice. No use, distribution or reproduction is permitted which does not comply with these terms.



# Assessing Grapevine Biophysical Parameters From Unmanned Aerial Vehicles Hyperspectral Imagery

Alessandro Matese<sup>1</sup>, Salvatore Filippo Di Gennaro<sup>1\*</sup>, Giorgia Orlandi<sup>1</sup>, Matteo Gatti<sup>2</sup> and Stefano Poni<sup>2</sup>

<sup>1</sup> Institute of BioEconomy, National Research Council (CNR-IBE), Firenze, Italy, <sup>2</sup> Department of Sustainable Crop Production (DI.PRO.VE.S.), Università Cattolica del Sacro Cuore, Piacenza, Italy

## OPEN ACCESS

### Edited by:

Jose Antonio Jimenez-Berni,  
Institute for Sustainable Agriculture  
(CSIC), Spain

### Reviewed by:

Jingzhe Wang,  
Shenzhen Polytechnic, China  
Shanqin Wang,  
Huazhong Agricultural University,  
China

### \*Correspondence:

Salvatore Filippo Di Gennaro  
salvatorefilippo.digennaro@cnr.it

### Specialty section:

This article was submitted to  
Technical Advances in Plant Science,  
a section of the journal  
Frontiers in Plant Science

**Received:** 17 March 2022

**Accepted:** 12 May 2022

**Published:** 02 June 2022

### Citation:

Matese A, Di Gennaro SF,  
Orlandi G, Gatti M and Poni S (2022)  
Assessing Grapevine Biophysical  
Parameters From Unmanned Aerial  
Vehicles Hyperspectral Imagery.  
Front. Plant Sci. 13:898722.  
doi: 10.3389/fpls.2022.898722

Over the last 50 years, many approaches for extracting plant key parameters from remotely sensed data have been developed, especially in the last decade with the spread of unmanned aerial vehicles (UAVs) in agriculture. Multispectral sensors are very useful for the elaboration of common vegetation indices (VIs), however, the spectral accuracy and range may not be enough. In this scenario, hyperspectral (HS) technologies are gaining particular attention thanks to the highest spectral resolution, which allows deep characterization of vegetative/soil response. Literature presents few papers encompassing UAV-based HS applications in vineyard, a challenging conditions respect to other crops due to high presence of bare soil, grass cover, shadows and high heterogeneity canopy structure with different leaf inclination. The purpose of this paper is to present the first contribution combining traditional and multivariate HS data elaboration techniques, supported by strong ground truthing of vine ecophysiological, vegetative and productive variables. Firstly the research describes the UAV image acquisition and processing workflow to generate a 50 bands HS orthomosaic of a study vineyard. Subsequently, the spectral data extracted from 60 sample vines were elaborated both investigating the relationship between traditional narrowband VIs and grapevine traits. Then, multivariate calibration models were built using a double approach based on Partial Least Square (PLS) regression and interval-PLS (iPLS), to evaluate the correlation performance between the biophysical parameters and HS imagery using the whole spectral range and a selection of more relevant bands applying a variable selection algorithm, respectively. All techniques (VIs, PLS and iPLS) provided satisfactory correlation performances for the ecophysiological ( $R^2 = 0.65$ ), productive ( $R^2 = 0.48$ ), and qualitative ( $R^2 = 0.63$ ) grape parameters. The novelty of this work is represented by the first assessment of a UAV HS dataset with the expression of the entire vine ecosystem, from the physiological and vegetative state to grapes production and quality, using narrowband VIs and multivariate PLS regressions. A correct non-destructive estimation of key parameters in vineyard, above all physiological parameters which must be measured in a short time as they are extremely influenced by the variability of environmental conditions during the day, represents a powerful tool to support the winegrower in vineyard management.

**Keywords:** unmanned aerial vehicles (UAV), precision viticulture, hyperspectral sensing, vegetation indices, image segmentation

## INTRODUCTION

To measure the dynamic response of plants to changing environmental conditions, quantitative vegetation variable extraction is essential. The spatiotemporally explicit retrieval of plant biophysical characteristics is possible using Earth observation sensors in the optical domain. Satellite remote sensing has been widely employed in agriculture during the last few decades (Immitzer et al., 2012; Pastonchi et al., 2020; Squeri et al., 2021). Unmanned aerial vehicles (UAVs) have recently attracted a lot of attention because of their increased mission schedule flexibility, acquiring data with higher spatial resolution in a precision viticulture context (Adão et al., 2017). Over the last 50 years, many approaches for extracting biophysical and biochemical parameters from remotely sensed data have been developed. In this context, UAV based HS sensors (**Figure 1**) are gaining particular attention due to their well-known ability to provide deep spectral characterization of vegetation and soil targets. HS imagery has been applied to quantify leaf area index (Haboudanea et al., 2004; Delegido et al., 2013), plant biomass (Cho et al., 2007; Fu et al., 2014), pigment contents (Yi et al., 2014), plant nitrogen content (Ryu et al., 2011; Inoue et al., 2012), and leaf nitrogen and phosphorus concentrations (Ramoelo et al., 2013; Zhang et al., 2013), soil moisture content (Ge et al., 2021), as well as plant water status and transpiration (Wang and Jin, 2015; Marshall et al., 2016).

Traditionally HS imaging sensors have been manufactured with a push-broom line scanning approach (Suomalainen et al., 2014). Recently, hyperspectral sensing technologies that acquire two-dimensional frame format have entered the market (Aasen et al., 2018). Senop HSC-2 HS camera (Senop Optronics, Finland) is characterized by a global shutter snapshot sensor, a tuneable Fabry-Pérot interferometer, able to record data in the VNIR

(Visible and Near Infrared) spectral range 500–900 nm; Cubert UHD 185-Firefly (Cubert GmbH, Germany) and the IMEC SM5 × 5 (IMEC, Belgium) sensors provide registered bands frames. Photogrammetric experiments using unmanned airborne vehicles (UAVs) may also benefit from scaled-down hyperspectral 2D cameras, making for a more cost-effective mapping process. HS imagery captured by UAVs has mostly been used for agricultural and environmental surveillance (Aasen et al., 2018; Oliveira et al., 2019). As a result, the collection and interpretation of UAV-derived data has become easier, faster, and more accurate.

When operating on a UAV, the Senop camera acquires hypercubes from various spectral ranges and bands, and emits non-registered bands. To prevent band misalignment, co-registration is required. The capacity of various 2D shifts in band registration of time-consecutive camera images was tested by Tommaselli et al. (2015). Honkavaara et al. (2013) found that in flat agricultural scenarios, band registration of such images with feature-based matching and 2D image transformation provided successful registration. MEPHYSTo was introduced by Jakob et al. (2017) as a toolbox for pre-processing UAV HS data, consisting of a pre-processing chain optimized for difficult geometric and radiometric correction. It also includes automated mosaicking and georeferencing algorithms that allow for quick and simple surveying of remote areas where obtaining ground control points (GCP) would be difficult or time-consuming.

The retrieval of biophysical parameters from HS data could be evaluated using parametric regression with discrete band approaches (vegetation indices—VIs) or quasi-continuous spectral bands, or linear/non-linear non-parametric regression with linear (partial least square regression—PLSR) or non-linear non-parametric regression (random forest, support vector machine—SVM, gaussian process regression—GPR) (Matese and Di Gennaro, 2021). Many VIs depend on a combination of near-infrared (NIR) and red reflectance, such as the NIR-to-red ratio. While most structural indices were built using broad-band systems, narrow-band (<10 nm) equivalents can be measured through HS imagery. On the other hand, several biochemical/physiological indices are simply hyperspectral requiring small bands (=10 nm) and non-sample band centers that are not considered by broad-band systems. Several HS-derived VIs (HVIs) based on narrow bands have been proposed for quantifying biophysical parameters since the advent of HS remote sensing, offering additional information and significant advantages over large bands (Thenkabail et al., 2000). Transformed spectrum formats, such as transmittance and derivative spectra, have also been shown to be useful in generating more broadly available VIs for deriving biophysical and biochemical parameters. Derivative techniques, for example, have the advantage of minimizing additive constants and linear functions, allowing for remote sensing of crop parameters (Imanishi et al., 2004).

Traditional methods have been commonly used in post-processing for their ease of manipulation, such as those focused on VIs, stepwise multiple linear regression, partial least-squares regression, and so on (Dorigo et al., 2007). Broadband VIs date back to the 1970s and are primarily focused on multispectral



**FIGURE 1 |** Unmanned Aerial Vehicle used in the study equipped with hyperspectral (HS) imaging sensor.



remotely sensed data. The ratio vegetation index (RVI) (Pearson and Miller, 1972), normalized difference vegetation index (NDVI) (Rouse et al., 1974) and soil-adjusted vegetation index (SAVI) (Huete, 1988) are all common broadband VIs that were designed to eliminate the effects of environment and soil interferences. Many hyperspectral VIs (HVI) based on narrow bands and very high spectral resolution have also been described since the advent of hyperspectral remote sensing. HVIs have long been used to estimate biophysical and biochemical attributes (Rodríguez-Pérez et al., 2007; Marshall et al., 2016). Despite the fact that some HVIs are closely copied or imitated from their broadband equivalents, it has been proposed that narrow bands may offer additional information and have important advantages over large bands in quantifying biophysical parameters (Thenkabail et al., 2000). Indeed, traditionally used VIs have many intrinsic shortcomings despite their ease of understanding and implementation (Baret and Guyot, 1991; Li and Wang, 2011). Such flaws can only be addressed by either increasing the dataset used to calculate VIs or enhancing the accuracy of that data. While the recently developed hybrid method significantly expanded the data volume and hence the likelihood of creating a more broadly usable VI, a variety of transformed spectra formats, such as transmittance and derivative spectra, have also proven to be effective in determining biophysical and biochemical parameters (Rady et al., 2014). Derivative methods, for example, have been shown to be feasible for estimating plant biophysical and biochemical parameters because they minimize additive constants and linear functions (Imanishi et al., 2004). For example, in plant condition detection, the red-edge location (REP), which is the wavelength of the maximum first derivative in the range of 690–750 nm, has been successfully used. As a result, a number of derivative hyperspectral indices (dHVI) have been developed and are now being used to calculate biophysical and biochemical quantities (Demetriades-Shah et al., 1990; Imanishi et al., 2004; Wang and Jin, 2015). Demetriades-Shah et al. (1990) and Zarco-Tejada et al. (2003a,b) found that indices based on derivative spectra are more efficient than reflectance-based indices. However, the advantages of dHVI over reflectance-based VIs, as well as the distinctions between derivatives of different orders, have yet to be thoroughly explored. The significant collinearity in spectral data must be considered when using statistical models for the retrieval of vegetative biophysical characteristics, and full spectrum techniques like PCA and PLS are extensively employed in chemometrics (Wold et al., 1987, 2001). These methods modify the spectral feature space so that the resultant (latent) factors account for the most variation in the feature space (PCA), or in the covariance with the target variables (PLS). State-of-the-art research presents only 7 papers encompassing UAV-based HS applications in a vineyard (Zarco-Tejada et al., 2012, 2013; Vanegas et al., 2018; Horstrand et al., 2019; Maimaitiyiming et al., 2020; Suarez et al., 2021; Di Gennaro et al., 2022), while more than 53 papers focused on HS applications in a vineyard without the use of UAVs. Di Gennaro et al. (2022) suggested a comparison in term of accuracy between broadband multispectral and narrowband HS data by means the calculation of some VIs on canopy and soil targets in

vineyard, assessing in general higher spectral accuracy of HS camera respect to the ground truth provided by reference spectroradiometer (Di Gennaro et al., 2022). Suarez et al. (2021) investigated the links between grape quality parameters such as aroma components vs. image-based spectral indices and photosynthetic plant traits derived by physical model inversion methods. Maimaitiyiming et al. (2020) considered aerial hyperspectral and thermal images acquired by using a visible and near-infrared (VNIR, 400–1,000 nm) push-broom hyperspectral camera (Nano-Hyperspec VNIR model, Headwall Photonics, Fitchburg, MA, United States) installed in tandem with a thermal camera (FLIR Vue Pro R 640, FLIR Systems, Inc., Wilsonville, OR, United States) carried by a hexacopter (Matrice 600 Pro, DJI Technology Co., Ltd., Shenzhen, China). The authors proposed a canopy zone-weighting (CZW) method to estimate physiological indicators, such as stomatal conductance (gs) and steady-state fluorescence (Fs). Horstrand et al. (2019) used a solution based on a commercial DJI Matrice 600 and a Specim FX10 hyperspectral camera to adapt this latter device, mainly conceived for industrial applications, into a flying platform in which weight, power budget, and connectivity are paramount. Vanegas et al. (2018) used an S800 EVO Hexacopter (DJI Ltd., Shenzhen, China) combined with a Headwall Nano-Hyperspec (Headwall Photonics Inc., Bolton, MA, United States) for developing a predictive model aimed at detecting phylloxera infections. Zarco-Tejada et al. (2012, 2013) estimated leaf carotenoid content and water stress in vineyards by considering the same HS camera using narrowband indices. Other interesting studies focused on retrieving biophysical parameters in vineyards even not involving the use of UAVs are reported by Martin et al. (2007) and García-Estévez et al. (2017) who used hyperspectral imagery to map grape quality in “Tempranillo” vineyards, Haboudane et al. (2008) for crop chlorophyll content using derivatives spectral indices, while Pérez-Priego et al. (2015) investigated nutrient uptake. Although several authors focused on the evaluation of hyperspectral reflectance indices to detect grapevine water status (Rodríguez-Pérez et al., 2007; Serrano et al., 2012), only Pôças et al. (2017, 2020) used machine learning methodologies to obtain more detailed results.

Little work has been done about the benefits that might derive from characterizing efficiency parameters pertaining to the vineyard ecosystem from UAV platforms equipped with HS sensors. Moreover, the study has the ambition to move beyond traditional methodologies such as the use of VIs while testing and validating multivariate methods such as PLS, seeking for the significant bands in the characterization of the variables of interest. These objectives are crucial for the technological transfer to winegrowers, either for a better understanding of the vineyard characteristics and as valid tools to achieve winegrowers’ oenological objectives. In detail two main aims were pursued: (i) describe the image acquisition and processing workflow of HS data cubes developed in this work; (ii) test the performance of UAV equipped with an HS camera in grapevine ecophysiological, vegetative, productive and grape composition traits characterization, using narrowband HS-derived VIs and PLS models.

## MATERIALS AND METHODS

### Experimental Site

The study was conducted in 2020 in a 15 rows plot placed within a rainfed Barbera vineyard established in 2003 at Tenuta Pernice (Castelnovo Val Tidone, Italy) (**Figure 2A**). Vines are spaced  $2.4 \times 1$  m (between- and within-row, respectively), long-cane pruned and trained to a vertical-shoot-positioned trellis along NS oriented rows. During the season the canopy was trimmed twice on DOY (day of year) 162 and DOY 204, whilst vineyard management was performed according to organic farming protocols.

### System Description

A Senop HSC-2 HS camera mounted on a DJI Matrice Pro Hexacopter UAV platform (**Figure 2B**) was used for the flight on DOY 223 (10 August). The camera has a global shutter snapshot sensor that records data between the wavelengths of 500 and 900 nm. It has two partly reflecting surfaces that are parallel to each other. The length of the optical path provided between these reflecting surfaces (gap) determines the wavelengths that can be transmitted by the interferometer (Honkavaara et al., 2013). Various wavelengths can be obtained by adjusting this length. If the camera platform changes during the spectral band acquisition process, any spectral band in the same cube exposed to a particular air gap value has a different position and attitude (Honkavaara et al., 2013). The hyperspectral cube bands obtained with the camera can be modified based on individual applications and the camera's spectral range and resolution. The image has a resolution of  $1,024 \times 1,024$  pixels. The Senop camera has a beam splitting system and two CMOS sensors (without the Bayer filter) mounted (Oliveira et al., 2016a): the first is optimized to sense visible bands (500–636 nm), while the second is optimized to record both visible and NIR (650–900 nm). The flights were performed at a speed of 1.8 m/s at a height of 32 m above ground level (AGL) providing spectral images with a ground

sampling distance (GSD) of approximately 2 cm/pixel. Front and side overlapping were 75 and 72%, respectively. The number and spectral sensitivities of the bands and integration time are the key parameters to be set. Time of integration was chosen as 1 ms in order to avoid image overexposure in relation to bright objects. The HSC-2 camera was set with 50 spectral bands (500–900) with a Full Width at Half Maximum (FWHM) of about 8 nm. Two types of reference were assessed; firstly, for reflectance conversion, five Senop targets with 2, 9, 25, 50, and 88% reflectance with sizes  $50 \times 50$  cm. The targets are made of materials with nearly Lambertian reflectance properties and calibrated in laboratory conditions. Secondly, for geometric correction and georeferencing, white plastic targets with size  $15 \times 15$  cm were used as ground control points (GCPs) and placed on the boundary of the test area as well as on the right side of 60 sample vines chosen for ground truth measurements, as described below.

### Ground Measurements

At full bloom (DOY 157) a pool of 60 vines was randomly identified within the 15-row plot and georeferenced by using a GPS. Per each sentinel vine, all clusters were picked, counted and weighed at harvest on DOY 260. In parallel, three representative basal-clusters per vine were collected and immediately taken to the laboratory for subsequent morphological and chemical characterization. Accordingly, from each sample, a 50-berry subsample was randomly collected and weighed to assess the mean berry weight. Grapes were then immediately frozen and stored at  $-18^{\circ}\text{C}$  for subsequent determination of total anthocyanins and phenolics concentration (Ilанд, 1988). The remaining grapes were crushed for assessing total soluble solids (TSS) concentration, must pH and titratable acidity (TA). An aliquot of juice was diluted 1:4 with distilled water and used for quantifying the malic acid concentration as reported in Gatti et al. (2020). At onset of veraison (DOY 213), when full canopy growth was reached, pre-dawn ( $\Psi_{pd}$ ) and mid-day ( $\Psi_{md}$ ) leaf

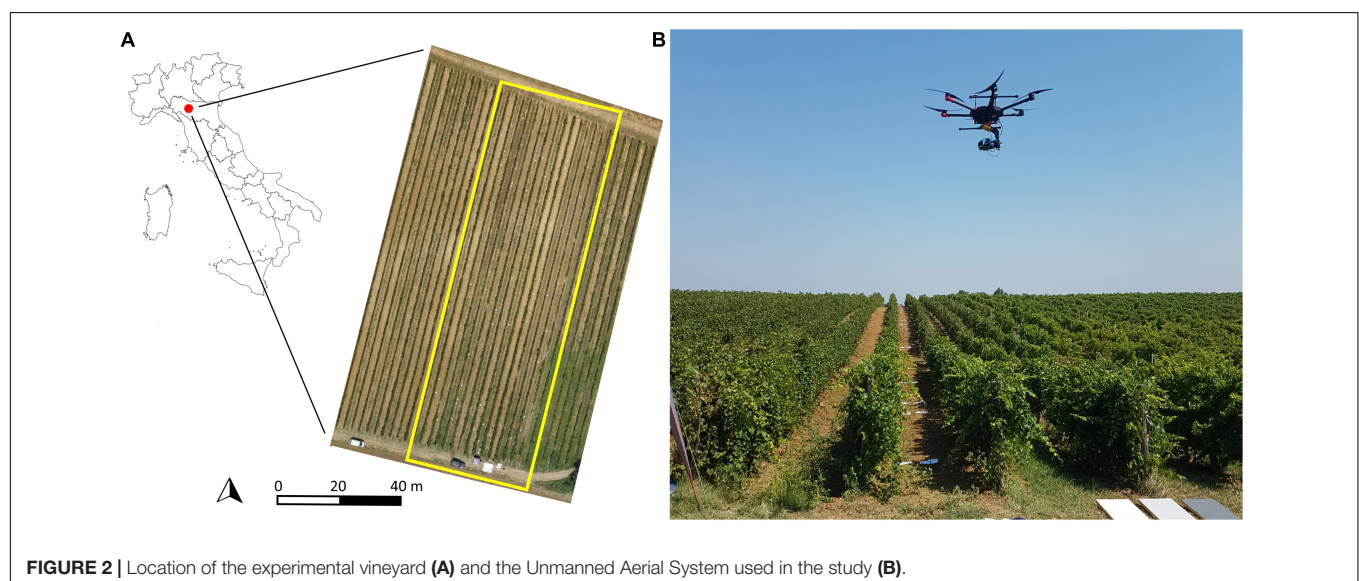


**FIGURE 2 |** Location of the experimental vineyard (A) and the Unmanned Aerial System used in the study (B).

water potential was determined by using a Scholander pressure chamber. Two leaves per plant were collected from a batch of 30 vines out of the 60 sentinel plants. After leaf fall, total nodes per vine on main and lateral dormant shoots was counted. Leaf area (LA) per vine was then calculated by multiplying the node number and corresponding mean values of leaf area for primary and lateral leaves as assessed at harvest (Gatti et al., 2021). In winter, during pruning operations performed on DOY 345, pruning weight for one-year-old canes was quantified by using a portable field-scale.

## Data Processing and Analysis

The initial step was the conversion from DN to radiance, which was done with the use of factory calibration gains of the HS camera. Secondly, noise signals were removed from each image by means of the dark current measurement subtracted from radiance values. Finally, an empirical line method (ELM) was applied for the radiation to reflectance conversion (Matese et al., 2019), using five reference reflectance panels to perform radiometric correction for each band of the HS images. The next step was the HS orthomosaic generation, which is described in **Figure 3**. Agisoft Metashape software (Agisoft LLC., St. Petersburg, Russia) was used for the reconstruction of each single band orthomosaic. After that a supervised procedure of georeferencing using GCPs was performed in QGIS software<sup>1</sup> (2021. QGIS Geographic Information System. QGIS Association).<sup>2</sup> In this work 215 hypercubes were acquired to monitor the whole study site. Once the full orthomosaic had been

processed, Matlab software (MathWorks, Natick, Massachusetts, United States) was used to perform a segmentation procedure applying the DEM (Digital Elevation Model) method described in Cinat et al. (2019) and a further threshold filter was applied to avoid shaded leaves and soil. Finally, a supervised region-of-interest (ROI) procedure based on  $0.8 \times 0.8$  m polygons was used for the HS data extraction from each sample vine, to perform the dataset post-processing in terms of retrieval of ground agronomic variables sampled using HS derived VIs.

Afterward, the following narrowband VIs (**Table 1**) were calculated using 50 bands hypercubes at very high spectral resolution (10 nm intervals) in the visible (VIS), Red Edge (RE), and near infrared (NIR) wavelengths for each polygon. Spectral pre-treatment was done using mean centering. The average of the VIs was calculated within each polygon.

Spectral bands were imported into Matlab and, for the productive, qualitative and vegetative parameters, one dataset was obtained with size  $\{60 \times 50\}$ , composed by the average values corresponding to the 50 wavelengths, for each one of the 60 vine samples. As regards ecophysiological parameters,  $\Psi_{pd}$  and  $\Psi_{md}$  were determined on 30 vines out of the 60 plants, therefore the size of obtained dataset was equal to  $\{30 \times 50\}$ . Partial Least Square regression (PLSr) (Naes et al., 2002) was used to build multivariate calibration models in order to evaluate the correlation performance between the biophysical parameters and hyperspectral imagery using the whole spectral range. The calibration models were calculated on the mean centered dataset and the statistical parameters used to evaluate the PLS performance were the Root Mean Square Error (RMSE) and coefficient of determination ( $R^2$ ); both parameters were calculated in calibration (RMSEC,  $R^2$  Cal) and

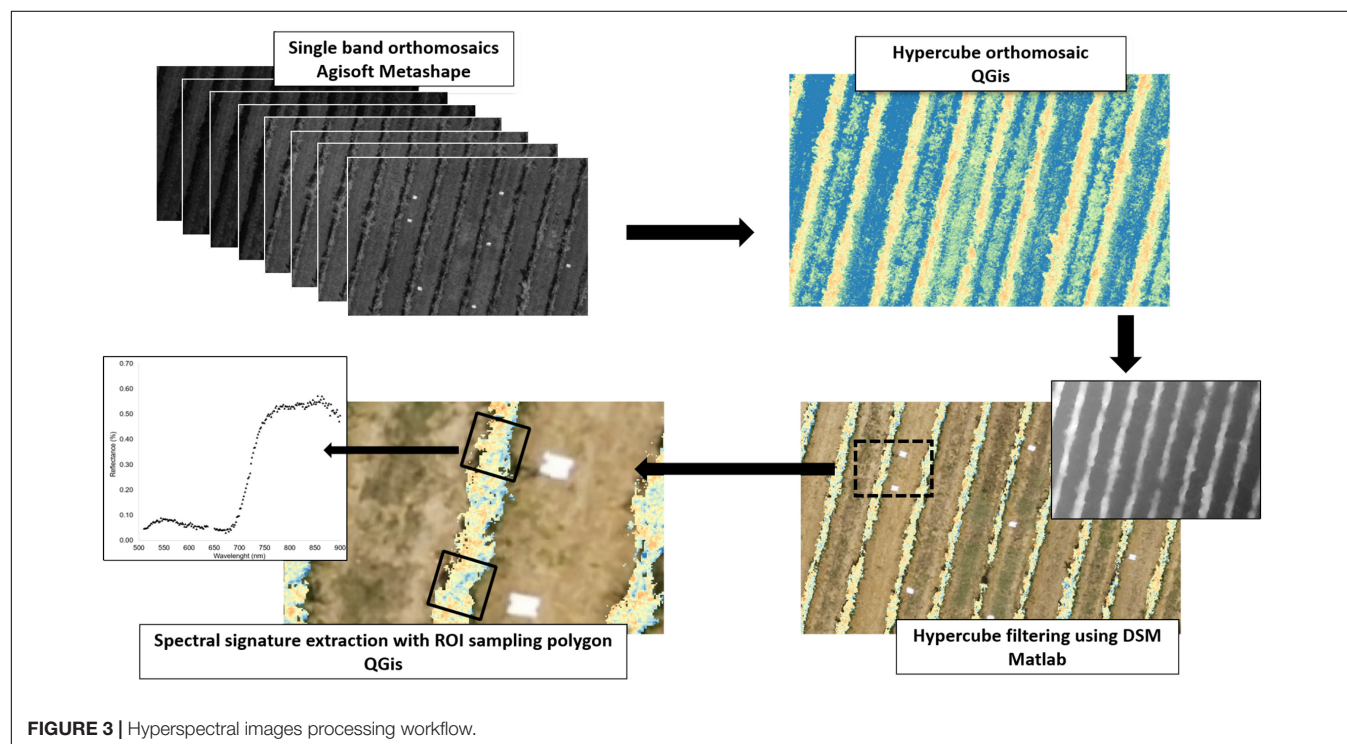




**TABLE 1** | Narrowband vegetation indices calculated from HS dataset.

Vis	Full name	Spectral band group	Equation
NDVI 1	Normalized difference vegetation index	NIR, VIS	$(R_{850} - R_{660}) / (R_{850} + R_{660})$
NDVI 2	Normalized difference vegetation index	NIR, VIS	$(R_{835} - R_{660}) / (R_{835} + R_{660})$
NDVI 3	Normalized difference vegetation index	NIR, VIS	$(R_{850} - R_{660}) / (R_{850} + R_{660})$
GNDVI 1	Green NDVI	NIR, VIS	$(R_{850} - R_{540}) / (R_{850} + R_{540})$
GNDVI 2	Green NDVI	NIR, VIS	$(R_{780} - R_{550}) / (R_{780} + R_{550})$
SAVI	Soil-adjusted vegetation index	NIR, VIS	$(1 + 0.5) \times (R_{802} - R_{660}) / (R_{802} + R_{660} + 0.5)$
RENDVI	Red edge normalized difference vegetation index	NIR, RE	$(R_{850} - R_{680}) / (R_{850} + R_{680})$
NDRE	Normalized difference nir/red edge index	NIR, RE	$(R_{770} - R_{750}) / (R_{770} + R_{750})$
NRER	Nir-re-red normalized difference vegetation index	NIR, RE, VIS	$(R_{850} - R_{695}) / (R_{695} + R_{660})$
TCARI	Transformed chlorophyll absorption ratio	NIR, RE, VIS	$3 \times [(R_{695} - R_{663}) - 0.2(R_{695} - R_{540}) \times (R_{695} / R_{663})]$
MTVI 1	Modified triangular vegetation index	NIR, RE, VIS	$1.2 \times (1.2(R_{800} - R_{540}) - 2.5(R_{660} - R_{540}))$
MTVI 2	Modified triangular vegetation index	NIR, RE, VIS	$1.2 \times (1.2(R_{800} - R_{550}) - 2.5(R_{670} - R_{550}))$
EVI	Enhanced vegetation index	NIR, RE, VIS	$2.5 \times (R_{850} - R_{660}) / (R_{850} + 6 \times R_{660} - 7.5 \times R_{505}) + 1$
NRER	Nir-re-red normalized difference vegetation index	NIR, RE, VIS	$(R_{850} - R_{695}) / (R_{695} + R_{660})$
LCI	Leaf chlorophyll index	NIR, RE, VIS	$(R_{850} - R_{710}) / (R_{850} + R_{680})$
MTCIvar	Meris terrestrial chlorophyll index	NIR, RE	$(R_{850} - R_{680}) / (R_{680} + R_{660})$
NRI	Nitrogen reflectance index	NIR, RE	$(R_{555} - R_{550}) / (R_{555} + R_{550})$
PRI	Photochemical reflectance index	NIR, RE	$(R_{570} - R_{530}) / (R_{570} + R_{530})$
SPVI	Spectral polygon vegetation index	NIR, RE, VIS	$0.4 \times [3.7 \times (R_{800} - R_{670}) - 1.2 (R_{530} - R_{670})]$
SR710	Simple ratio 710	RE	$R_{750} / R_{710}$
SR680	Simple ratio 680	RE	$R_{800} / R_{680}$
RVI	Ratio vegetation index	NIR, VIS	$R_{810} / R_{660}$
VOG1	Vogelmann index	RE	$R_{745} / R_{720}$
GM	Gitelson and Merzlyak index	RE, VIS	$R_{750} / R_{550}$
MNDm	Modified normalized difference	NIR, RE, VIS	$[(R_{750} - R_{705}) / (R_{750} + R_{705} - 2 \times R_{508})]$
NDRE2	Normalized difference nir/red edge index	NIR, RE, VIS	$(R_{795} - R_{720}) / (R_{795} + R_{720})$
MCARI2	Modified chlorophyll absorption in reflectance	NIR, RE, VIS	$[(R_{750} - R_{705}) - 0.2 (R_{750} - R_{550}) \times (R_{750} / R_{705})]$
TVI	Triangular vegetation index	NIR, RE, VIS	$0.5 \times [120 \times (R_{750} - R_{550}) - 200(R_{670} - R_{550})]$
EVI2	Enhanced vegetation indexrep	NIR, RE, VIS	$2.5 \times (R_{800} - R_{670}) / (R_{800} + 6 \times R_{670} - 7.5 \times R_{508}) + 1$
REP	Red Edge position index	NIR, RE, VIS	$700 + (45 \times R_{670} + R_{778}) / 2 - (R_{850}) / (R_{735} - R_{695})$
maxR	1st Derivative Max RED index	dHVI-VIS	Max $[D_{660}, D_{680}]$
sumR	1st Derivative Sum RED index	dHVI-VIS	$\Sigma [D_{660}, D_{680}]$
maxRE	1st Derivative Max RE index	dHVI-RE	Max $[D_{690}, D_{700}]$
sumRE	1st Derivative Sum RE index	dHVI-RE	$\Sigma [D_{690}, D_{700}]$
maxLARE	1st Derivative Max LARE index	dHVI-RE	Max $[D_{690}, D_{710}]$
sumLARE	1st Derivative Sum LARE index	dHVI-RE	$\Sigma [D_{690}, D_{710}]$
maxNIR	1st Derivative Max NIR index	dHVI-NIR	Max $[D_{790}, D_{840}]$
sumNIR	1st Derivative Sum NIR index	dHVI-NIR	$\Sigma [D_{790}, D_{840}]$

in cross-validation (RMSECV,  $R^2$  CV). The optimal number of Latent Variables (LVs) was chosen by minimizing the value of RMSECV. In particular, a random cross-validation method was used, subdividing the samples in 3 deletion groups. In order to evaluate the possibility of reducing the number of wavelengths and selecting the more relevant variables for each parameter, interval-PLS (iPLS) was tested as algorithm for automatically variable selection (Norgaard et al., 2000). Briefly, iPLS consists of subdividing the whole signal into a certain number of intervals of equal length which is defined by the user. Calibration models are calculated by iteratively adding or removing intervals, according to whether the forward or reverse search strategy is considered. The most useful intervals for model calibration are identified by minimizing the RMSECV value (Orlandi et al., 2018). In this

work forward iPLS was applied considering two different interval sizes: 10 and 5 variables. PLS and iPLS calibration models were elaborated and cross-validated by means of PLS-Toolbox ver. 8.9.1 (Eigenvector Research Inc., Manson, WA, United States).

## RESULTS

### Ground Measurements

Data reported in Table 2 identify a significant within-field variability at both physiological and agronomical level. With a CV of 24%,  $\Psi_{pd}$  at veraison varied between  $-0.27$  and  $-0.73$  MPa suggesting a transition from slight to severe water shortage in the soil.  $\Psi_{md}$  showed lower variability (CV = 9.8%) although



**TABLE 2 |** Mean, minimum and maximum values, and coefficient of variation (CV%) for leaf water status, canopy growth, yield components, and fruit composition of Barbera grapevines recorded in 2020.

Variable	Mean	Min	Max	CV (%)
$\Psi_{pd}$ (MPa)	-0.5	-0.27	-0.73	24.2
$\Psi_{md}$ (MPa)	-1.34	-1.08	-1.64	9.8
Total leaf area (m <sup>2</sup> /vine)	1.85	0.65	3.43	33.8
Lateral leaf area (m <sup>2</sup> /vine)	0.17	0.00	0.53	77.6
Pruning weight (kg/vine)	0.48	0.16	1.07	48.7
Yield (kg/vine)	3.37	0.76	8.46	52.2
Cluster weight (g)	178.4	54.3	386.1	41.6
Berry weight (g)	2.0	1.3	2.8	20.2
TSS (°Brix)	24.4	19.0	29.3	11.4
Titrateable acidity (g/L)	9.66	6.58	14.41	15.8
Malate (g/L)	2.13	0.75	5.99	56.8
Total anthocyanins (mg/g)	0.75	0.18	1.43	38.3
Total phenolics (mg/g)	1.78	0.88	2.71	26.0

the calculated mean value (-1.34 MPa) highlights a likely status of relatively severe water stress. Data describing canopy growth and vine capacity depicted a highly variable vineyard condition. Indeed, total leaf area per vine varied between 0.65 and 3.43 m<sup>2</sup> with a coefficient of variation of about 34% that peaked up to 78% in the case of lateral leaf area. This variability was confirmed in winter with pruning weight of 1-year canes varying between 0.16 and 1.07 kg/vine (CV = 49%), identifying the coexistence of very low and high vigor vines within the 15-row plot. Yield in high vigor vines was 11-fold higher as compared to low cropping vines as a result of bigger clusters (386 vs. 54 g) and berries (2.8 vs. 1.3 g). At harvest, a large variability in fruit composition was described for TSS (CV = 11.4%), titrateable acidity (CV = 15.8%) and the variables describing phenolic composition. The highest coefficients of variation were described for malate (56.8%), anthocyanins (38.3%), and total phenolics (26%) concentration.

## Relationship Between Narrowband HVIs and Grapevine Performances

The coefficients of determination ( $R^2$ ) for the linear regressions between narrowband HVIs and ground measurements are reported in **Table 3**.

Generally, the more performing narrowband indices were RVI, EVIm, maxLARE, MTCIvar, and NDVI3. Conversely, poor correlations were achieved between ground measurements and maxNIR, sumNIR, sumR, maxR, NRI, and PRI. As regards the ecophysiological parameters, the majority of narrowband indices showed a good correlation with  $\Psi_{pd}$ . In particular, the closest correlations were obtained with NDVI3 ( $R^2 = 0.65$ ), RVI ( $R^2 = 0.63$ ), and SR680 ( $R^2 = 0.63$ ). Conversely, weaker relationships were found between  $\Psi_{md}$  and the narrowband indices; however, the RVI was confirmed to be the most efficient index ( $R^2 = 0.36$ ). For yield components, best correlations were achieved between berry weight (Bwt) and NDVI2, MTCIva, RVI sharing an  $R^2$  of 0.48. Slightly worse correlations were found for yield and cluster weight (Cwt); for both parameters the more

performing indices were NDVI1, GNDVI and MTCIvar with an  $R^2$  from 0.35 to 0.30. Among the qualitative parameters, satisfactory correlations were achieved between malate and the majority of narrowband indices. In particular, the most fitting was RVI ( $R^2 = 0.63$ ); however, equivalent results were also achieved using SR680 ( $R^2 = 0.62$ ) and EVIm ( $R^2 = 0.61$ ). Conversely, the same narrowband indices showed weaker correlations with titrateable acidity ( $R^2$  from 0.36 to 0.30). Furthermore, quite poor relationships were found between TSS and the narrowband indices. In regard to total anthocyanins and phenols, the most performing indices were RVI and EVIm with an  $R^2$  from 0.48 to 0.40, respectively. Compared with the other ground measurements, the worst performances were obtained for vegetative parameters. Correlation between lateral leaf area (LLA) and maxLARE yielded an  $R^2$  of 0.34, whereas total leaf area (TLA) and pruning weight (Pwt) per vine achieved an  $R^2$  equal to 0.30 and 0.29 when regressed over sumRE and GNDVI2, respectively.

## Relationship Between Partial Least Square Models and Grapevine Performances

For each Y variable, the results of the calibration performance are reported in **Table 4**. Overall, the best correlation performances were obtained for the parameters identifying fruit composition and, among them, malic acid ( $R^2$  CV = 0.59), total phenols ( $R^2$  CV = 0.41), and total anthocyanins ( $R^2$  CV = 0.36). Conversely, the worse correlations were obtained for the vegetative parameters and, among them, pruning weight ( $R^2$  CV = 0.27), and total leaf area ( $R^2$  CV = 0.06). The overall best calibration performance was shown by  $\Psi_{pd}$  ( $R^2$  CV = 0.65-RMSECV = 0.07 MPa). This model was built using only 15 variables (three intervals made of 5 variables) out of 50 original bands. The selected regions include wavelengths belonging to 549–663 nm and 761–794 nm. The measured vs. the predicted values of  $\Psi_{pd}$  are reported in **Figure 4A**. Conversely, it was impossible to obtain a good correlation for  $\Psi_{md}$  ( $R^2$  CV = 0.22-RMSECV = 0.10 MPa).

Concerning the yield and its components (Cwt and Bwt), a satisfactory correlation was obtained for berry weight ( $R^2$  CV = 0.46-RMSECV = 0.30 g). This model was built by means of iPLS using one interval made of 10 bands with the selected wavelengths belonging to 590–704 nm (**Figure 4B**). Among the vegetative parameters, the best correlation performance was achieved for LLA ( $R^2$  CV = 0.31-RMSECV = 0.11 m<sup>2</sup>/vine) by means of iPLS. This result was obtained considering only the wavelengths belonging to 712–753 nm, that were selected using an interval width of 5 variables (**Figure 4D**). When compared with the corresponding PLS model calculated on the whole spectral range, the iPLS model generally resulted in equal values or a slight reduction of the RMSECV value. However, the variable selection also led to reducing the number of wavelengths while selecting the more relevant variables for each Y parameter. The best improvement was achieved for malic acid: the RMSECV value obtained with iPLS is equal to 0.78 g/L instead of an RMSECV value equal to 0.85 g/L obtained with PLS (**Figure 4C**). The variable selection allowed a model to be built using only 10

**TABLE 3** | Coefficients of determination ( $R^2$ ) for linear regressions between narrowband HVIs and ground measurements.

HVIs	$\Psi_{pd}$	$\Psi_{md}$	Yield	Cwt	Bwt	TSS	TA	Malate	Anth	Phenols	TLA	LLA	Pwt
NDVI1	0.6***	0.23**	0.3***	0.34***	0.47***	0.2***	0.29***	0.57***	0.36***	0.43***	0.22***	0.27***	0.23***
NDVI2	0.6***	0.25**	0.28***	0.32***	0.48***	0.19***	0.3***	0.58***	0.37***	0.42***	0.22***	0.27***	0.19***
GNDVI1	0.53***	0.12	0.36***	0.38***	0.41***	0.13**	0.24***	0.48***	0.25***	0.32***	0.17***	0.23***	0.23***
RENDVI	0.52***	0.12	0.29***	0.31***	0.41***	0.12**	0.21***	0.47***	0.28***	0.34***	0.15**	0.25***	0.22***
<b>MTCIvar</b>	0.58***	0.2*	0.32***	0.35***	0.48***	0.18***	0.29***	0.58***	0.36***	0.43***	0.18***	0.26***	0.23***
SAVI	0.6***	0.25**	0.26***	0.29***	0.43***	0.21***	0.3***	0.56***	0.36***	0.39***	0.27***	0.3***	0.16**
TCARI	0.35***	0.35***	0.11*	0.14**	0.26***	0.26***	0.32***	0.44***	0.32***	0.35***	0.23***	0.2***	0.11**
MTVI	0.6***	0.28**	0.23***	0.26***	0.41***	0.22***	0.32***	0.58***	0.38***	0.4***	0.27***	0.31***	0.16**
<b>EVIIm</b>	0.62***	0.28**	0.24***	0.27***	0.41***	0.25***	0.34***	0.61***	0.4***	0.45***	0.24***	0.33***	0.23***
GNDVI2	0.57***	0.23**	0.26***	0.3***	0.32***	0.21***	0.15**	0.41***	0.31***	0.37***	0.16**	0.29***	0.29***
NDRE	0.27**	0.12	0.08*	0.07*	0.07*	0.11**	0.04	0.11**	0.06	0.07*	0.02	0.13**	0.11*
LCI	0.49***	0.09	0.28***	0.28***	0.28***	0.08*	0.21***	0.39***	0.2***	0.25***	0.09*	0.18***	0.21***
MTCI2	0.63***	0.29**	0.23***	0.25***	0.4***	0.22***	0.32***	0.59***	0.38***	0.41***	0.27***	0.31***	0.17**
<b>NDVI3</b>	0.65***	0.26**	0.25***	0.29***	0.44***	0.21***	0.27***	0.58***	0.38***	0.44***	0.23***	0.32***	0.24***
NRI	0.19*	0.04	0.15**	0.17**	0.26***	0.05	0.13**	0.23***	0.09*	0.12**	0.1*	0.04	0.03
PRI	0.13	0.13	0.01	0.01	0.02	0.08*	0.07*	0.15**	0.11**	0.14**	0.01	0.05	0.02
SPVI	0.63***	0.28**	0.23***	0.26***	0.4***	0.21***	0.31***	0.58***	0.37***	0.39***	0.27***	0.32***	0.17**
SR710	0.39***	0.13	0.21***	0.21***	0.21***	0.09*	0.15**	0.29***	0.19***	0.22***	0.07*	0.16**	0.12**
SR680	0.63***	0.24**	0.3***	0.31***	0.47***	0.19***	0.3***	0.62***	0.39***	0.43***	0.22***	0.25***	0.19***
<b>RVI</b>	0.63***	0.36***	0.3***	0.33***	0.48***	0.25***	0.36***	0.63***	0.42***	0.48***	0.21***	0.28***	0.23***
VOG1	0.12	0.03	0.13**	0.08*	0.06	0.09*	0.02	0.08*	0.11*	0.13**	0	0.05	0.17**
GM	0.53***	0.22*	0.28***	0.32***	0.36***	0.19***	0.23***	0.46***	0.3***	0.35***	0.18***	0.28***	0.21***
MNDm	0.23**	0.06	0.12**	0.11*	0.13**	0.12**	0.08*	0.19***	0.14**	0.19***	0.01	0.14**	0.16**
NDRE2	0.3**	0.06	0.19***	0.19***	0.2***	0.08*	0.06	0.15**	0.15**	0.16**	0.04	0.08*	0.13**
MCARI2	0.47***	0.19*	0.1*	0.13**	0.23***	0.24***	0.23***	0.43***	0.3***	0.34***	0.2***	0.31***	0.16**
TVI	0.61***	0.31**	0.19***	0.22***	0.37***	0.26***	0.31***	0.58***	0.39***	0.44***	0.25***	0.33***	0.19***
EVI2	0.63***	0.3**	0.23***	0.25***	0.39***	0.22***	0.31***	0.57***	0.37***	0.4***	0.26***	0.33***	0.17**
REP	0.4***	0.1	0.14**	0.17**	0.28***	0.13**	0.08*	0.3***	0.19***	0.24***	0.18***	0.24***	0.12**
maxR	0.08	0.09	0	0	0.03	0.1*	0.11**	0.08*	0.04	0.04	0.03	0.09*	0.01
sumR	0	0.05	0.04	0.05	0.07*	0.08*	0.1*	0.07	0.05	0.04	0.08*	0.06	0
maxRE	0.49***	0.23**	0.15**	0.19***	0.37***	0.24***	0.24***	0.52***	0.37***	0.41***	0.26***	0.3***	0.16**
sumRE	0.52***	0.28**	0.14**	0.18***	0.36***	0.21***	0.23***	0.53***	0.36***	0.4***	0.3***	0.28***	0.15**
<b>maxLARE</b>	0.59***	0.26**	0.19***	0.2***	0.34***	0.31***	0.34***	0.56***	0.4***	0.43***	0.24***	0.34***	0.2***
sumLARE	0.59***	0.28**	0.16**	0.2***	0.36***	0.25***	0.29***	0.57***	0.38***	0.43***	0.27***	0.32***	0.19***
maxNIR	0.05	0	0.03	0.04	0	0	0.01	0.01	0	0	0.02	0.04	0.01
sumNIR	0	0.04	0.01	0.01	0.01	0.03	0.03	0.01	0	0.01	0.01	0	0.02

Within each column the highest  $R^2$  values are highlighted.

\*\*\*, \*\*, \* and "" indicate  $p < 0.0001$ ,  $< 0.001$ ,  $< 0.01$ , and  $> 0.01$ , respectively.

Narrowband HVIs reported in the first column are described in **Table 1**.  $\Psi_{pd}$ , pre-dawn leaf water potential;  $\Psi_{md}$ , mid-day leaf water potential; Cwt, cluster weight; Bwt, berry weight; TSS, total soluble solids; TA, titratable acidity; Anth, total anthocyanins; TLA, total leaf area; LLA, lateral leaf area; Pwt, pruning weight.

bands (two intervals made of 5 variables) out of 50 original bands. The selected wavelengths belonging to 590–704 nm.

## DISCUSSION

Interpretation of the  $R^2$  data reported in **Table 3** vs. means, range of variation and coefficient of variation (CV) of agronomic and physiological variables is quite puzzling. In general terms, for a given index, closer correlation is expected any time a given variable, primarily due to soil heterogeneity, shows a larger degree of variability (Trought et al., 2008; Baluja et al., 2013; Squeri et al., 2019; Gatti et al., 2021). This concept seems to

hold, for instance, when RVI, NDVI3, SR680, and EVI2 are correlated with  $\Psi_{pd}$  and  $\Psi_{md}$ . In all cases  $R^2$  calculated for  $\Psi_{pd}$  is more or less halved when referred to  $\Psi_{md}$ . The most obvious reason for such a drop seems to be the lower CV (9.8%) calculated for  $\Psi_{md}$  which testifies to a fairly narrow range of variation. As a matter of fact, there is no reason to think that differential sensitivity of the two types of water potential are due to different sampling methodology (both were assessed through the pressure chamber method). This outcome is not encouraging if HS indices are expected to be used as a replacement for the tedious pressure chamber method for total midday or stem water potential measurements; this is not just because  $R^2$  are rather low, but also because given the recorded mean  $\Psi_{md}$  (−1.34 MPa) and

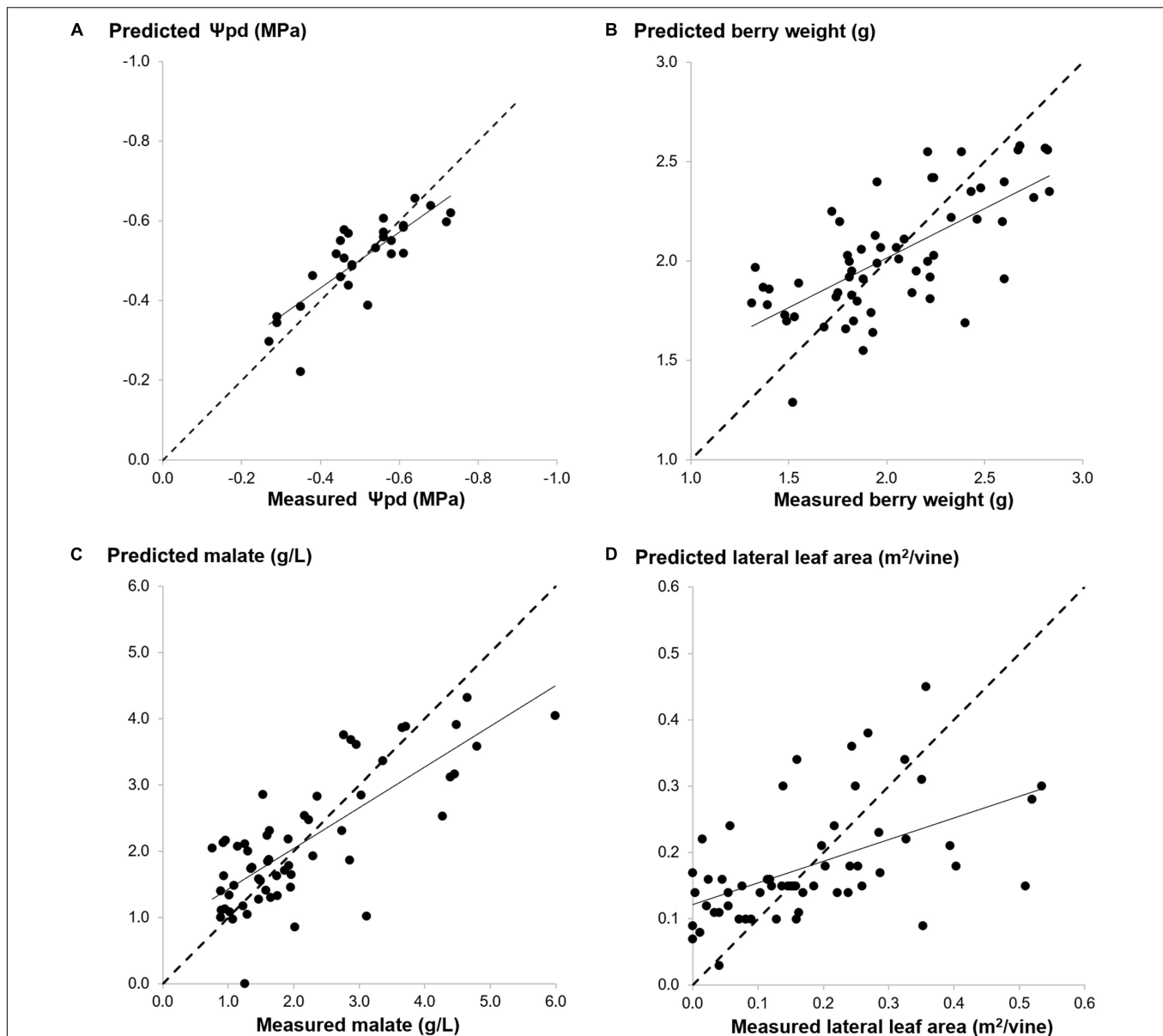


**FIGURE 4 |** Predicted values vs. ground-based measurements of the best calibration performances of multivariate models achieved for each biophysical parameter group:  $\Psi_{pd}$  for ecophysiological Y [(A),  $R^2$  CV = 0.65, RMSECV = 0.07 MPa], Bwt for productive Y [(B),  $R^2$  CV = 0.46, RMSECV = 0.30 g], Malate for qualitative Y [(C),  $R^2$  CV = 0.59, RMSECV = 0.78 g/L], LLA for vegetative Y [(D),  $R^2$  CV = 0.31, RMSECV = 0.11 m<sup>2</sup>/vine]. The dotted line indicates a regression with slope = 1.

calculated RMSECV of about  $-0.1$  MPa the same mean values can represent a condition of either moderate or severe stress depending upon the concurrent evaporative demand (VPD on DOY 213 was 4 kPa). Vice versa, Pearson correlation values found for  $\Psi_{pd}$  vs. NDVI3, SR680 and RVI reveal chances that a quite reliable, yet otherwise slow and laborious reading such as pre-dawn water potential, could be replaced with a fast, non-destructive UAV-hyperspectral protocol resulting in a very high resolution mapping of soil and plant water status. However, when the same concept is applied to yield including two of its main components, the hypothesis basically fails. Results concerning yield per vine and two of its main components (i.e., berry

and cluster weight) showed that berry weight was slightly more responsive to some indices such as NDVI2, MTCIvar, and RVI ( $R^2 = 0.48$ ) although the other components (yield and Cwt) did show higher CVs than berry weight. The hypothesis is that total yield is largely affected by cultural and endogenous factors (e.g., varietal fruitfulness, bud induction, bud load, summer pruning operations) whose description through a spectral signature is more troublesome. For instance, floral bud induction for next season cropping is typically decided in grapevine the season before the image is taken and it is controlled, among several factors, by specific growth and environmental conditions at that time (May, 2004). As per final grape composition, the overall

mild correlations found for all VIs vs. TSS (°Brix) at harvest support recent work by Suarez et al. (2021), who also reported non-significant correlations for data taken on Shiraz. It is quite notable from our study that a few VIs which already provided good correlations with  $\Psi_{pd}$  (EVI<sub>m</sub>, SR680, RVI), were those also having close correlation with malic acid concentration at harvest ( $R^2 = 0.61$ – $0.63$ ) as well as with total anthocyanins and phenols concentration ( $R^2 = 0.40$ – $0.48$ ). This response is quite valuable for at least two main reasons: (i) it is indeed not a case that malate, color and phenolics are well known to be quite responsive to local canopy microclimate conditions and namely those pertaining

to the fruit zone. Such high correlations demonstrate that the proposed indices do have the potential to predict changes in fruit composition at harvest especially for the parameters that are highly dependent on light and thermal conditions around the cluster which have proven to be the main drivers for either synthesis or degradation of the above components (Downey et al., 2004; Pereira et al., 2006; Mori et al., 2007; Sweetman et al., 2009). Such changes might be a function of the inherent vine vigor, type of training system, timing and extent of leaf removal or shoot thinning (Poni et al., 2018); (ii) taking RVI as the best example, it is viticulturally quite relevant and useful to have HS

**TABLE 4 |** Results of PLS and iPLS models.

Y	Calibration method	iPLS interval size	Selected Bands(nm)	LVs	RMSEC	RMSECV	$R^2$ cal	$R^2$ CV
$\Psi_{pd}$	PLS	–	–	1	0.07	0.08	0.65	0.61
	iPLS	10	590:704	3	0.06	0.08	0.76	0.61
	<b>iPLS</b>	<b>5</b>	<b>549:663 761:794</b>	<b>3</b>	<b>0.06</b>	<b>0.08</b>	<b>0.77</b>	<b>0.65</b>
$\Psi_{md}$	<b>PLS</b>	–	–	<b>1</b>	<b>0.10</b>	<b>0.10</b>	<b>0.32</b>	<b>0.27</b>
	iPLS	10	590:794	1	0.10	0.11	0.33	0.18
	iPLS	5	802:835	2	0.09	0.10	0.38	0.22
Yield	PLS	–	–	3	1.25	1.46	0.42	0.21
	iPLS	10	508:704	2	1.34	1.44	0.32	0.23
	<b>iPLS</b>	<b>5</b>	<b>508:541 590:663 712:753</b>	<b>2</b>	<b>1.30</b>	<b>1.40</b>	<b>0.37</b>	<b>0.26</b>
Cwt	PLS	–	–	3	0.06	0.07	0.39	0.24
	<b>iPLS</b>	<b>10</b>	<b>508:704</b>	<b>2</b>	<b>0.06</b>	<b>0.06</b>	<b>0.35</b>	<b>0.27</b>
	iPLS	5	508:541 671:704	3	0.06	0.07	0.39	0.23
Bwt	PLS	–	–	3	0.28	0.32	0.53	0.38
	<b>iPLS</b>	<b>10</b>	<b>590:704</b>	<b>2</b>	<b>0.28</b>	<b>0.30</b>	<b>0.53</b>	<b>0.46</b>
	iPLS	5	549:753	3	0.27	0.31	0.56	0.44
TSS	PLS	–	–	1	2.37	2.47	0.27	0.21
	iPLS	10	590:794	1	2.35	2.41	0.28	0.24
	<b>iPLS</b>	<b>5</b>	<b>549:582 671:794</b>	<b>1</b>	<b>2.35</b>	<b>2.41</b>	<b>0.28</b>	<b>0.24</b>
TA	PLS	–	–	1	1.27	1.36	0.31	0.21
	iPLS	10	508:794	1	1.29	1.35	0.29	0.21
	<b>iPLS</b>	<b>5</b>	<b>508:541 802:835</b>	<b>1</b>	<b>1.27</b>	<b>1.32</b>	<b>0.31</b>	<b>0.25</b>
Malate	PLS	–	–	1	0.78	0.85	0.57	0.51
	iPLS	10	508:704	2	0.73	0.83	0.64	0.53
	<b>iPLS</b>	<b>5</b>	<b>590:704</b>	<b>2</b>	<b>0.74</b>	<b>0.78</b>	<b>0.63</b>	<b>0.59</b>
Anth	PLS	–	–	1	0.23	0.23	0.39	0.36
	iPLS	10	712:794	1	0.23	0.24	0.39	0.32
	<b>iPLS</b>	<b>5</b>	<b>549:582 712:753</b>	<b>1</b>	<b>0.23</b>	<b>0.23</b>	<b>0.38</b>	<b>0.36</b>
Phenols	PLS	–	–	1	0.35	0.36	0.43	0.40
	iPLS	10	712:794	1	0.35	0.36	0.44	0.41
	<b>iPLS</b>	<b>5</b>	<b>16:20 26:30</b>	<b>3</b>	<b>0.33</b>	<b>0.36</b>	<b>0.50</b>	<b>0.41</b>
TLA	PLS	–	–	1	0.55	0.56	0.07	0.04
	<b>iPLS</b>	<b>10</b>	<b>590:704</b>	<b>2</b>	<b>0.52</b>	<b>0.55</b>	<b>0.16</b>	<b>0.06</b>
	iPLS	5	671:704	1	0.52	0.56	0.15	0.05
LLA	PLS	–	–	1	0.11	0.11	0.35	0.27
	iPLS	10	712:794	2	0.11	0.11	0.37	0.29
	<b>iPLS</b>	<b>5</b>	<b>712:753</b>	<b>1</b>	<b>0.11</b>	<b>0.11</b>	<b>0.35</b>	<b>0.31</b>
Pwt	<b>PLS</b>	–	–	<b>2</b>	<b>0.18</b>	<b>0.20</b>	<b>0.38</b>	<b>0.27</b>
	iPLS	10	712:794	2	0.19	0.20	0.36	0.27
	iPLS	5	761:794	2	0.19	0.20	0.35	0.25

Within each Y parameter the best calibration performance is reported in bold.



indices warranting good correlation with a range of variables representing plant water status (e.g.,  $\Psi_{pd}$ ), crop potential (e.g., fresh berry weight), and degree of maturity (e.g., TSS, malate, anthocyanins, and phenols). We also feel that this is the first time this achievement is reported, as in the Suarez et al. (2021) paper the very close correlation that several HS indices show with a few terpene compounds is not reflected in any significant correlation with either color and phenolics.

Many approaches have been proposed to evaluate the biophysical parameters of different plants by means of hyperspectral data (Ismail and Mutanga, 2010; Doktor et al., 2014; Yao et al., 2015). Among them, Atzberger et al. (2010) demonstrated that PLS is better performing than other methods in order to extract the information by the whole spectral range for evaluation of the canopy chlorophyll content in winter wheat. In addition, the current study investigates the possibility of selecting the most relevant feature by means of iPLS. In particular, the results proved that the variable selection allowed the RMSECV values to be slightly reduced or to obtain equal values compared to the results obtained using the whole spectral range.

Pôças et al. (2017) developed an effective approach based on hyperspectral reflectance data aimed at monitoring the grapevine water status. However, the results obtained in this study demonstrated the possibility of assessing other biophysical parameters, such as productive ones. In particular, a good performance was obtained for Bwt with a RMSECV value equal to 0.30 g, using only 10 wavelengths belonging to 590–704 nm.

Furthermore, the results of this study showed better performance than those obtained by Suarez et al. (2021) when using plant traits derived from physical model inversion of hyperspectral imagery for the evaluation of qualitative parameters of grapevine, such as phenolic content. Considering that the grapevine is a complex system characterized by a dynamic balance between vegetative and productive features, another strong point of this work is proving the potential of a hyperspectral imaging sensor on the main key factors of the “vine-ecosystem.” In fact, compared to other cited works, a wide scenario has been explored, both functional aspects related to the eco-physiological state, as well as the vegetative growth and finally the quantitative and qualitative productive response at the end of the cycle. To understand the real effectiveness of a non-destructive optical techniques it is in fact necessary to have a vision of the main traits of the “vine-ecosystem,” not just focusing on single or few aspects. Regarding the high cost of hyperspectral imaging technology, there are very few works in the literature using UAV equipped with these cameras in field conditions, especially with the wide ground truth dataset collected here. Furthermore, another limitation of the research on this topic is the high level of experience necessary to identify and apply correct in-flight data acquisition and management protocols, especially given the lack of ready-to-use software to perform the complete processing workflow of the hypercubes.

Due to their inherent structure, vineyards pose a specific challenge for remote sensing analysis (Singh et al., 2022). This is due not just to a quite typical discontinuous canopy cover which introduces the issue of “mixels” handling, rather to at least three

other peculiar features: (i) vines are extremely sensitive to any factors causing spatial and temporal variation in growth and yield and, on top of them, soil heterogeneity; (ii) large variability in training systems (i.e., vigor, geometry, distance between rows) originates complex interactions in terms of background and shade, including also large diurnal variation, and (iii) more than in any other orchard system, interference exerted by the presence of portions of bare or grassed soil can be of utmost complexity. All of this justifies why remote sensing images of vineyards must be processed to separate canopy pixels from the background. Moreover, considering that viticulture is one of the most profitable agriculture sectors, digital agriculture solutions play a key role in the decision-making processes for grape production respect to other lower valuable crops. Viticulture is a key socioeconomic and cultural sector in many countries and regions worldwide, with a high economic impact in the network of all relevant industry branches of the supply and distribution chains. The latest report of the International Organization of Vine and Wine (OIV, 2019), it is estimated that the world vineyards cover an area of approximately 7.449 million ha (2018). Concerning the winemaking sector, global wine production was 292 million hl in 2018, and wine trade in monetary value has been growing continuously to reach a record-breaking value of approximately EUR 30,000 million in 2018. For these suggestions, however, studies of this type are necessary to guide the technology transfer on solutions that have been adequately tested (Tardaguila et al., 2021; Di Gennaro et al., 2022). Another key issue is the challenge of climate change and the need to describe plant processes at a very detailed level, using a large number of inputs, may currently preclude the applicability of simulation models as decision support tools for farmers. In fact, models coupled with the use of new technologies such as UAV and hyperspectral imagery may represent the most appropriate management practices in the future.

The main limitation in this work is due to the fact that is more reasonable to continuously measure the spectrum and use it to estimate the dynamic changes of various attributes, and finally analyze the yield and quality, but in our case a single flight was used, identified as the best acquisition date in line with our previous studies on vineyard (Matese and Di Gennaro, 2021), to characterize the physiological and biochemical parameters at harvest. Moreover, using this approach the aim was to develop a more prompt predictive model for farmer and thus an operational tool for characterizing quanti-qualitative parameters in the vineyard.

## CONCLUSION

On the agronomic side, the calculation of indices derived from HS data cubes has shown very promising potential for: (i) achieving high correlations with variables that are more closely linked to local canopy microclimate conditions, such as malic acid, total anthocyanins and phenols concentration and (ii) identifying specific indices with the ability to concurrently describe several vine traits including water status, cropping

potential and ripening patterns. The novelty of this work is represented by the first assessment of a hyperspectral UAV dataset with grapevine parameters using several hyperspectral narrowband indices and multivariate PLS regressions. The strength of this research is the study of hyperspectral data acquired by UAV in field conditions by examining the expression of the entire vine ecosystem, from the physiological state, to descriptors of vine vegetative development, and finally on grapes production and quality. The results obtained by applying a wide spectrum of VIs allow alternative solutions to the traditional and time-consuming ground measurements to be identified, which provide the best accuracy, but frequently lead to a limitation for representative sampling in a large vineyard. Above all for the monitoring of physiological parameters, which must be done in a short time as they are extremely influenced by the variability of environmental conditions during the day, such as air temperature and humidity or the intensity and angle of solar radiation. A correct non-destructive estimation of key parameters in the vineyard represents a powerful tool to support the winegrower in optimal vineyard management, both for agronomic input choices and planning the best harvest date. Further work is needed to explore the robustness of this methodology on different phenological stages of grapevines and on the use of innovative Machine Learning algorithms.

## REFERENCES

- Aasen, H., Honkavaara, E., Lucieer, A., and Zarco-Tejada, P. J. (2018). Quantitative remote sensing at ultra-high resolution with UAV spectroscopy: a review of sensor technology, measurement procedures, and data correction workflows. *Remote Sens.* 10:1091. doi: 10.3390/rs10071091
- Adão, T., Hruška, J., Pádua, L., Bessa, J., Peres, E., Morais, R., et al. (2017). Hyperspectral imaging: A review on UAV-based sensors, data processing and applications for agriculture and forestry. *Remote Sens.* 9:1110. doi: 10.3390/rs9111110
- Atzberger, C., Guérif, M., Baret, F., and Werner, W. (2010). Comparative analysis of three chemometric techniques for the spectroradiometric assessment of canopy chlorophyll content in winter wheat. *Comput. Electron. Agric.* 73, 165–173. doi: 10.1016/j.compag.2010.05.006
- Baluja, J., Tardaguila, J., Ayestaran, B., and Diago, M. P. (2013). Spatial variability of grape composition in a Tempranillo (*Vitis vinifera* L.) vineyard over a 3-year survey. *Prec. Agric.* 14, 40–58. doi: 10.1007/s11119-012-9282-5
- Baret, F., and Guyot, G. (1991). Potentials and limits of vegetation indices for LAI and APAR assessment. *Remote Sens. Environ.* 35, 161–173. doi: 10.1016/0034-4257(91)90009-U
- Cho, M., Skidmore, A., Corsi, F., van Wieren, S., and Sobhan, I. (2007). Estimation of green grass/herb biomass from airborne hyperspectral imagery using spectral indices and partial least squares regression. *Int. J. Appl. Earth Observ. Geoinf.* 9, 414–424. doi: 10.1016/j.jag.2007.02.001
- Cinat, P., Di Gennaro, S. F., Berton, A., and Matese, A. (2019). Comparison of unsupervised algorithms for vineyard canopy segmentation from UAV multispectral images. *Remote Sens.* 11, 1023. doi: 10.3390/rs11091023
- Delegido, J., Verrelst, J., Meza, C. M., Rivera, J. P., Alonso, L., and Moreno, J. (2013). A red edge spectral index for remote sensing estimation of green LAI over agroecosystems. *Eur. J. Agron.* 46, 42–52. doi: 10.1016/j.eja.2012.12.001
- Demetriades-Shah, T. H., Steven, M. D., and Clark, J. A. (1990). High resolution derivative spectra in remote sensing. *Remote Sens. Environ.* 33, 55–64. doi: 10.1016/0034-4257(90)90055-Q
- Di Gennaro, S. F., Toscano, P., Gatti, M., Poni, S., Berton, A., and Matese, A. (2022). Spectral Comparison of UAV-Based Hyper and Multispectral Cameras for Precision Viticulture. *Remote Sens.* 14, 449. doi: 10.3390/rs14030449
- Doktor, D., Lausch, A., Spengler, D., and Thurner, M. (2014). Extraction of plant physiological status from hyperspectral signatures using machine learning methods. *Remote Sens.* 6, 12247–12274. doi: 10.3390/rs61212247
- Dorigo, W. A., Zurita-Milla, R., de Wit, A. J. W., Brazile, J., Singh, R., and Schaepman, M. E. (2007). A review on reflective remote sensing and data assimilation techniques for enhanced agroecosystem modeling. *Int. J. Appl. Earth Obs. Geoinf.* 9, 165–193. doi: 10.1016/j.jag.2006.05.003
- Downey, M. O., Harvey, J. S., and Robinson, S. P. (2004). The effect of bunch shading on berry development and flavonoid accumulation in Shiraz grapes. *Aust. J. Grape Wine Res.* 10, 55–73. doi: 10.1111/j.1755-0238.2004.tb00008.x
- Fu, Y., Yang, G., Wang, J., Song, X., and Feng, H. (2014). Winter wheat biomass estimation based on spectral indices, band depth analysis and partial least squares regression using hyperspectral measurements. *Comput. Electron. Agric.* 100, 51–59. doi: 10.1016/j.compag.2013.10.010
- García-Estévez, I., Quijada-Morín, N., Rivas-Gonzalo, J. C., Martínez-Fernández, J., Sánchez, N., Herrero-Jiménez, C. M., et al. (2017). Relationship between hyperspectral indices, agronomic parameters and phenolic composition of Vitis vinifera cv Tempranillo grapes. *J. Sci. Food Agric.* 97, 4066–4074. doi: 10.1002/jsfa.8366
- Gatti, M., Garavani, A., Squeri, C., Diti, I., Demonte, A., Scotti, C., et al. (2021). Effects of intra-vineyard variability and soil heterogeneity on vine performance, dry matter and nutrient partitioning. *Prec. Agric.* 2021:9831. doi: 10.1007/s11119-021-09831-w
- Gatti, M., Schippa, M., Garavani, A., Squeri, C., Frioni, T., Dosso, P., et al. (2020). High potential of variable rate fertilization combined with a controlled released nitrogen form at affecting cv. Barbera vines behavior. *Eur. J. Agron.* 112:125949. doi: 10.1016/j.eja.2019.125949
- Ge, X., Ding, J., Jin, X., Wang, J., Chen, X., Li, X., et al. (2021). Estimating Agricultural Soil Moisture Content through UAV-Based Hyperspectral Images in the Arid Region. *Remote Sens.* 13:1562. doi: 10.3390/rs13081562
- Haboudane, D., Tremblay, N., Miller, J. R., and Vigneault, P. (2008). Remote estimation of crop chlorophyll content using spectral indices derived from hyperspectral data. *IEEE Trans. Geosci. Remote Sens.* 46, 423–437. doi: 10.1109/TGRS.2007.904836
- Haboudane, D., Miller, J. R., Patteyc, E., Zarco-Tejada, P. J., and Strachane, I. B. (2004). Hyperspectral vegetation indices and novel algorithms for predicting

## DATA AVAILABILITY STATEMENT

The datasets presented in this article are not readily available because data are available from the authors upon reasonable request and with permission of the company that hosted the study. Requests to access the datasets should be directed to SD, salvatorefilippo.digennaro@cnr.it.

## AUTHOR CONTRIBUTIONS

AM and SP designed the experiment and coordinated the activity. SD, AM, GO, and MG performed the data acquisition and data processing. SD, AM, MG, and SP wrote and reviewed the manuscript. All authors read and approved the final manuscript.

## ACKNOWLEDGMENTS

We thank Chiara Azzali from Tenuta Pernice srl (Castelnovo Val Tidone, Piacenza, Italy) for hosting the trial. We also thank Andrea Berton (IGG-CNR) for UAV management and data acquisition.

- green LAI of crop canopies: Modeling and validation in the context of precision agriculture. *Remote Sens. Environ.* 90, 337–352. doi: 10.1016/j.rse.2003.12.013
- Honkavaara, E., Saari, H., Kaivosoja, J., Pölonen, I., Hakala, T., Litkey, P., et al. (2013). Processing and assessment of spectrometric, stereoscopic imagery collected using a lightweight UAV spectral camera for precision agriculture. *Remote Sens.* 5, 5006–5039. doi: 10.3390/rs5105006
- Horstrand, P., Guerra, R., Rodríguez, A., Díaz, M., López, S., and López, J. F. (2019). A UAV platform based on a hyperspectral sensor for image capturing and on-board processing. *IEEE Access* 7, 66919–66938. doi: 10.1109/ACCESS.2019.2913957
- Huete, A. R. (1988). A soil-adjusted vegetation index (SAVI). *Remote Sens. Environ.* 25, 295–309. doi: 10.1016/0034-4257(88)90106-X
- Iland, P. G. (1988). “Leaf removal effects on fruit composition,” in *Proceedings of the second international symposium for cool climate viticulture and oenology*, eds R. Smart, R. Thornton, S. Rodriguezand, and J. Young (Auckland: New Zealand Society for Viticulture and Oenology), 137–138.
- Imanishi, J., Sugimoto, K., and Morimoto, Y. (2004). Detecting drought status and LAI of two Quercus species canopies using derivative spectra. *Comput. Electron. Agric.* 43, 109–129. doi: 10.1016/j.compag.2003.12.001
- Immitzer, M., Atzberger, C., and Koukal, T. (2012). Tree species classification with Random forest using very high spatial resolution 8-band WorldView-2 satellite data. *Remote Sens.* 4, 2661–2693. doi: 10.3390/rs4092661
- Inoue, Y., Sakaiya, E., Zhu, Y., and Takahashi, W. (2012). Diagnostic mapping of canopy nitrogen content in rice based on hyperspectral measurements. *Remote Sens. Environ.* 126, 210–221. doi: 10.1016/j.rse.2012.08.026
- Ismail, R., and Mutanga, O. (2010). A comparison of regression tree ensembles: Predicting Sirex noctilio induced water stress in Pinus patula forests of KwaZulu-Natal, South Africa. *Int. J. Appl. Earth. Obs. Geoinf.* 12S, S45–S51. doi: 10.1016/j.jag.2009.09.004
- Jakob, S., Zimmermann, R., and Gloaguen, R. (2017). The need for accurate geometric and radiometric corrections of drone-borne hyperspectral data for mineral exploration: MEPHySTo—A toolbox for pre-processing drone-borne hyperspectral data. *Remote Sens.* 9, 88. doi: 10.3390/rs9010088
- Li, P. H., and Wang, Q. (2011). Retrieval of leaf biochemical parameters using PROSPECT inversion: A new approach for alleviating ill-posed problems. *IEEE Trans. Geosci. Remote Sens.* 49, 2499–2506. doi: 10.1109/tgrs.2011.2109390
- Maimaitiyiming, M., Sagan, V., Sidike, P., Maimaitijiang, M., Miller, A. J., and Kwasiński, M. (2020). Leveraging very-high spatial resolution hyperspectral and thermal UAV imageries for characterizing diurnal indicators of grapevine physiology. *Remote Sens.* 12:3216. doi: 10.3390/rs12193216
- Marshall, M., Thenkabail, P., Biggs, T., and Post, K. (2016). Hyperspectral narrowband and multispectral broadband indices for remote sensing of crop evapotranspiration and its components (transpiration and soil evaporation). *Agric. For. Meteorol.* 218219, 122–134. doi: 10.1016/j.agrformet.2015.12.025
- Martin, P., Zarco-Tejada, P., González, M. R., and Berjon, A. (2007). Using hyperspectral remote sensing to map grape quality in ‘tempranillo’ vineyards affected by iron deficiency chlorosis. *Vitis* 46, 7–14. doi: 10.5073/vitis.2007.46.7-14
- Matese, A., and Di Gennaro, S. F. (2021). Beyond the traditional NDVI index as a key factor to mainstream the use of UAV in Precision viticulture. *Sci. Rep.* 11, 1–13. doi: 10.1038/s41598-021-81652-3
- Matese, A., Di Gennaro, S. F., and Santesteban, L. G. (2019). Methods to compare the spatial variability of UAV-based spectral and geometric information with ground autocorrelated data A case of study for precision viticulture. *Comput. Electron. Agric.* 162, 931–940. doi: 10.3390/rs13112056
- May, P. (2004). *Flowering and fruitset in grapevines*. Adelaide, SA: Lythrum Press.
- Mori, K., Goto-Yamamoto, N., Kitayama, M., and Hashizume, K. (2007). Loss of anthocyanins in red-wine grape under high temperature. *J. Exp. Bot.* 58, 1935–1945. doi: 10.1093/jxb/erm055
- Naes, T., Isaksson, T., Fearn, T., and Davies, T. (2002). *A user-friendly guide to multivariate calibration and classification*. Chichester: NIR Publications, doi: 10.1255/978-1-906715-25-0
- Norgaard, L., Saudland, A., Wagner, J., Nielsen, J. P., Munck, L., and Engelsen, S. B. (2000). Interval partial least-squares regression (iPLS): a comparative chemometric study with an example from near-infrared spectroscopy. *Appl. Spectrosc.* 54, 413–419. doi: 10.1366/0003702001949500
- OIV (2019). *Statistical Report on World Vitiviniculture*. Paris: International Organisation of Vine and Wine, 2019.
- Oliveira, R. A., Tommaselli, A. M., and Honkavaara, E. (2019). Generating a hyperspectral digital surface model using a hyperspectral 2D frame camera. *ISPRS J. Photogramm. Remote Sens.* 147, 345–360. doi: 10.1016/j.isprsjprs.2018.11.025
- Oliveira, R. A., Tommaselli, A. M., and Honkavaara, E. (2016a). Geometric calibration of a hyperspectral frame camera. *Photogram. Record.* 31, 325–347. doi: 10.1111/phor.12153
- Orlandi, G., Calvini, R., Foca, G., and Ulrici, A. (2018). Automated quantification of defective maize kernels by means of Multivariate Image Analysis. *Food Control* 85, 259–268. doi: 10.1016/j.foodcont.2017.10.008
- Pastonchi, L., Di Gennaro, S. F., Toscano, P., and Matese, A. (2020). Comparison between satellite and ground data with UAV-based information to analyse vineyard spatio-temporal variability. *Oeno One* 54, 919–934. doi: 10.20870/oeno-one.2020.54.4.4028
- Pearson, R. L., and Miller, L. D. (1972). “Remote spectral measurements as a method for determining plant cover,” in *Tech. Rept. No. 167, U.S. Internatl. Biological Program*, (Fort Collins, CO: Colorado State University).
- Pereira, G. E., Gaudillere, J. P., Pieri, P., Hilbert, G., Maucourt, M., Deborde, C., et al. (2006). Microclimate influence on mineral and metabolic profiles of grape berries. *J. Agric. Food Chem.* 54, 6765–6775. doi: 10.1021/jf061013k
- Pérez-Priego, O., Guan, J., Rossini, M., Fava, F., Wutzler, T., Moreno, G., et al. (2015). Sun-induced chlorophyll fluorescence and photochemical reflectance index improve remote-sensing gross primary production estimates under varying nutrient availability in a typical Mediterranean savanna ecosystem. *Biogeosciences* 12, 6351–6367. doi: 10.5194/bg-12-6351-2015
- Pôças, I., Gonçalves, J., Costa, P. M., Gonçalves, I., Pereira, L. S., and Cunha, M. (2017). Hyperspectral-based predictive modelling of grapevine water status in the Portuguese Douro wine region. *Int. J. Appl. Earth. Obs. Geoinf.* 58, 177–190. doi: 10.1016/j.jag.2017.02.013
- Pôças, I., Tosin, R., Gonçalves, I., and Cunha, M. (2020). Toward a generalized predictive model of grapevine water status in Douro region from hyperspectral data. *Agric. For. Meteorol.* 280, 107793. doi: 10.1016/j.agrformet.2019.107793
- Poni, S., Gatti, M., Palliotti, A., Dai, Z., Duchêne, E., Truong, T. T., et al. (2018). Grapevine quality: a multiple choice issue. *Sci. Hortic.* 234, 445–462. doi: 10.1016/j.scienta.2017.12.035
- Rady, A. M., Guyer, D. E., Kirk, W., and Donis-Gonzalez, I. R. (2014). The potential use of visible/near infrared spectroscopy and hyperspectral imaging to predict processing-related constituents of potatoes. *J. Food Eng.* 135, 11–25. doi: 10.1016/j.jfoodeng.2014.02.021
- Ramoelo, A., Skidmore, A. K., Cho, M. A., Mathieu, R., Heitkönig, I. M. A., and Dudenli-Thone, N. (2013). Non-linear partial least square regression increases the estimation accuracy of grass nitrogen and phosphorus using in situ hyperspectral and environmental data ISPRS J. Photogramm. Remote Sens. 82, 27–40. doi: 10.1016/j.isprsjprs.2013.04.012Get
- Rodríguez-Pérez, J. R., Riaño, D., Carlisle, E., Ustin, S., and Smart, D. R. (2007). Evaluation of hyperspectral reflectance indices to detect grapevine water status in vineyards. *Am. J. Enol. Viticult.* 58, 302–317.
- Rouse, J. W., Hass, R. H., Schell, J. A., Deering, D. W., and Harlan, J. C. (1974). *Monitoring the vernal advancement and retrogradation (green wave effect) of natural vegetation. Final Report, RSC 1978–4*. Texas: Texas A & M University, College Station.
- Ryu, C., Suguri, M., and Umeda, M. (2011). Multivariate analysis of nitrogen content for rice at the heading stage using reflectance of airborne hyperspectral remote sensing. *Field Crops Res.* 122, 214–241. doi: 10.1016/j.fcr.2011.03.013
- Serrano, L., González-Flor, C., and Gorchs, G. (2012). Assessment of grape yield and composition using the reflectance based Water Index in Mediterranean rainfed vineyards. *Remote Sens. Environ.* 118, 249–258. doi: 10.1016/j.rse.2011.11.021
- Singh, A. P., Yerudkar, A., Mariani, V., Iannelli, L., and Glielmo, L. (2022). A Bibliometric Review of the Use of Unmanned Aerial Vehicles in Precision Agriculture and Precision Viticulture for Sensing Applications. *Remote Sens.* 14:1604.
- Squeri, C., Gatti, M., Garavani, A., Vercesi, A., Buzzi, M., Croci, M., et al. (2019). Ground truthing and physiological validation of VIS-NIR spectral indices for early diagnosis of nitrogen deficiency in cv. Barbera (*Vitis vinifera* L.) grapevines. *Agronomy* 9:864. doi: 10.3390/agronomy9120864
- Squeri, C., Poni, S., Di Gennaro, S. F., Matese, A., and Gatti, M. (2021). Comparison and ground truthing of different remote and proximal sensing platforms

- to characterize variability in a hedgerow-trained vineyard. *Remote Sens.* 13:2056.
- Suarez, L., Zhang, P., Sun, J., Wang, Y., Poblete, T., Hornero, A., et al. (2021). Assessing wine grape quality parameters using plant traits derived from physical model inversion of hyperspectral imagery. *Agric. For. Meteorol.* 306:108445. doi: 10.1016/j.agrformet.2021.108445
- Suomalainen, J., Anders, N., Iqbal, S., Roerink, G., Franke, J., Wenting, P., et al. (2014). A lightweight hyperspectral mapping system and photogrammetric processing chain for unmanned aerial vehicles. *Remote Sens.* 6, 11013–11030. doi: 10.3390/rs6111013
- Sweetman, C., Deluc, L. G., Cramer, G. R., Ford, C. M., and Soole, K. L. (2009). Regulation of malate metabolism in grape berry and other developing fruits. *Phytochemistry* 70, 1329–1344. doi: 10.1016/j.phytochem.2009.08.006
- Tardaguila, J., Stoll, M., Gutiérrez, S., Proffitt, T., and Diago, M. P. (2021). Smart applications and digital technologies in viticulture: a review. *Smart Agric. Technol.* 1:100005.
- Thenkabail, P. S., Smith, R. B., and DePauw, E. (2000). Hyperspectral vegetation indices and their relationships with agricultural crop characteristics. *Remote Sens. Environ.* 71, 158–182. doi: 10.1016/S0034-4257(99)00067-X
- Tommaselli, A. M., Oliveira, R. A., Nagai, L. Y., Imai, N. N., Miyoshi, G. T., Honkavaara, E., et al. (2015). Assessment of bands coregistration of a lightweight spectral frame camera for UAV. *Proc. GeoUAV - ISPRS Geospatial Week* 2015:192.
- Trought, M. C. T., Dixon, R., Mills, T., Greven, M., Agnew, R., Mauk, J. L., et al. (2008). The impact of differences in soil texture within a vineyard on vine vigour, vine earliness and juice composition. *J. Int. Sci. Vigne Vin.* 42, 62–72. doi: 10.20870/oeno-one.2008.42.2.828
- Vanegas, F., Bratanov, D., Powell, K., Weiss, J., and Gonzalez, F. (2018). A novel methodology for improving plant pest surveillance in vineyards and crops using UAV-based hyperspectral and spatial data. *Sensors* 18:260. doi: 10.3390/s18010260
- Wang, Q., and Jin, J. (2015). Leaf transpiration of drought tolerant plant can be captured by hyperspectral reflectance using PLSR analysis. *iForest* 9, 30–37. doi: 10.3832/ifor1634-008
- Wold, S., Esbensen, K., and Geladi, P. (1987). Principal component analysis. *Chemom. Intell. Lab. Syst.* 2, 37–52.
- Wold, S., Sjöström, M., and Eriksson, L. (2001). PLS-regression: a basic tool of chemometrics. *Chemom. Intell. Lab. Syst.* 58, 109–130.
- Yao, X., Huang, Y., Shang, G., Zhou, C., Cheng, T., Tian, Y., et al. (2015). Evaluation of six algorithms to monitor wheat leaf nitrogen concentration. *Remote Sens.* 7, 14939–14966. doi: 10.3390/rs71114939
- Yi, Q., Jiapaer, G., Chen, J., Bao, A., and Wang, F. (2014). Different units of measurement of carotenoids estimation in cotton using hyperspectral indices and partial least square regression. *ISPRS J. Photogramm. Remote Sens.* 91, 72–84. doi: 10.1016/j.isprsjprs.2014.01.004
- Zarco-Tejada, P. J., Pushnik, J. C., Dobrowski, S., and Ustin, S. L. (2003a). Steady-state chlorophyll a fluorescence detection from canopy derivative reflectance and double-peak red-edge effects. *Remote Sens. Environ.* 84, 283–294. doi: 10.1016/S0034-4257(02)00113-X
- Zarco-Tejada, P. J., Miller, J. R., Haboudane, D., Tremblay, N., and Apostol, S. (2003b). “Detection of chlorophyll fluorescence in vegetation from airborne hyperspectral CASI imagery in the red edge spectral region. IGARSS 2003: IEEE Trans. Geosci. Remote Sens. Symposium,” in *Proceedings: Learning from Earth's Shapes and Sizes*, (Manhattan: IEEE International) Vol. I-Vii, 598–600. doi: 10.1109/IGARSS.2003.1293854
- Zarco-Tejada, P. J., González-Dugo, V., and Berni, J. A. (2012). Fluorescence, temperature and narrow-band indices acquired from a UAV platform for water stress detection using a micro-hyperspectral imager and a thermal camera. *Remote Sens. Environ.* 117, 322–337. doi: 10.1016/j.rsenv.2011.10.007
- Zarco-Tejada, P. J., Guillén-Climent, M. L., Hernández-Clemente, R., Catalina, A., González, M. R., and Martín, P. (2013). Estimating leaf carotenoid content in vineyards using high resolution hyperspectral imagery acquired from an unmanned aerial vehicle (UAV). *Agric. For. Meteorol.* 281–294. doi: 10.1016/j.agrformet.2012.12.013
- Zhang, X., Liu, F., He, Y., and Gong, X. (2013). Detecting macronutrients content and distribution in oilseed rape leaves based on hyperspectral imaging. *Biosyst. Eng.* 115, 56–65. doi: 10.1016/j.biosystemseng.2013.02.007

**Conflict of Interest:** The authors declare that the research was conducted in the absence of any commercial or financial relationships that could be construed as a potential conflict of interest.

**Publisher's Note:** All claims expressed in this article are solely those of the authors and do not necessarily represent those of their affiliated organizations, or those of the publisher, the editors and the reviewers. Any product that may be evaluated in this article, or claim that may be made by its manufacturer, is not guaranteed or endorsed by the publisher.

Copyright © 2022 Matese, Di Gennaro, Orlandi, Gatti and Poni. This is an open-access article distributed under the terms of the Creative Commons Attribution License (CC BY). The use, distribution or reproduction in other forums is permitted, provided the original author(s) and the copyright owner(s) are credited and that the original publication in this journal is cited, in accordance with accepted academic practice. No use, distribution or reproduction is permitted which does not comply with these terms.





# Exploration of Alternative Approaches to Phenotyping of Late Leaf Spot and Groundnut Rosette Virus Disease for Groundnut Breeding

Ivan Chapu<sup>1</sup>, David Kalule Okello<sup>2</sup>, Robert C. Ongom Okello<sup>1</sup>, Thomas Lapaka Odong<sup>1</sup>, Sayantan Sarkar<sup>3†</sup> and Maria Balota<sup>4\*</sup>

## OPEN ACCESS

### Edited by:

Shawn Carlisle Kefauver,  
University of Barcelona, Spain

### Reviewed by:

Ronald Kakeeto,  
National Agricultural Research  
Organisation, Uganda  
Santiago Alvarez Prado,  
Consejo Nacional de Investigaciones  
Científicas y Técnicas (CONICET),  
Argentina

### \*Correspondence:

Maria Balota  
mbalota@vt.edu

### †Present address:

Sayantan Sarkar,  
Texas T&M, Texas AgriLife,  
College Station, TX, United States

### Specialty section:

This article was submitted to  
Technical Advances in Plant Science,  
a section of the journal  
Frontiers in Plant Science

Received: 04 April 2022

Accepted: 06 May 2022

Published: 14 June 2022

### Citation:

Chapu I, Okello DK, Okello RCO,  
Odong TL, Sarkar S and Balota M  
(2022) Exploration of Alternative  
Approaches to Phenotyping of Late  
Leaf Spot and Groundnut Rosette  
Virus Disease for Groundnut  
Breeding.  
Front. Plant Sci. 13:912332.  
doi: 10.3389/fpls.2022.912332

<sup>1</sup> College of Agricultural and Environmental Sciences, Makerere University, Kampala, Uganda, <sup>2</sup> National Semi-Arid Resources Research Institute (NaSARRI), Soroti, Uganda, <sup>3</sup> Blackland Research and Extension Center, Texas A&M AgriLife Research, Temple, TX, United States, <sup>4</sup> School of Plant and Environmental Sciences, Tidewater AREC, Virginia Tech, Suffolk, VA, United States

Late leaf spot (LLS), caused by *Nothopassalora personata* (Berk. & M.A. Curt.), and groundnut rosette disease (GRD), [caused by *groundnut rosette virus* (GRV)], represent the most important biotic constraints to groundnut production in Uganda. Application of visual scores in selection for disease resistance presents a challenge especially when breeding experiments are large because it is resource-intensive, subjective, and error-prone. High-throughput phenotyping (HTP) can alleviate these constraints. The objective of this study is to determine if HTP derived indices can replace visual scores in a groundnut breeding program in Uganda. Fifty genotypes were planted under rain-fed conditions at two locations, Nakabango (GRD hotspot) and NaSARRI (LLS hotspot). Three handheld sensors (RGB camera, GreenSeeker, and Thermal camera) were used to collect HTP data on the dates visual scores were taken. Pearson correlation was made between the indices and visual scores, and logistic models for predicting visual scores were developed. Normalized difference vegetation index (NDVI) ( $r = -0.89$ ) and red-green-blue (RGB) color space indices CSI ( $r = 0.76$ ),  $v^*$  ( $r = -0.80$ ), and  $b^*$  ( $r = -0.75$ ) were highly correlated with LLS visual scores. NDVI ( $r = -0.72$ ),  $v^*$  ( $r = -0.71$ ),  $b^*$  ( $r = -0.64$ ), and GA ( $r = -0.67$ ) were best related to the GRD visual symptoms. Heritability estimates indicated NDVI, green area (GA), greener area (GGA),  $a^*$ , and hue angle having the highest heritability ( $H^2 > 0.75$ ). Logistic models developed using these indices were 68% accurate for LLS and 45% accurate for GRD. The accuracy of the models improved to 91 and 84% when the nearest score method was used for LLS and GRD, respectively. Results presented in this study indicated that use of handheld remote sensing tools can improve screening for GRD and LLS resistance, and the best associated indices can be used for indirect selection for resistance and improve genetic gain in groundnut breeding.

**Keywords:** groundnut rosette disease, late leaf spot (LLS), phenotyping, NDVI, RGB indices, logistic models

## INTRODUCTION

Groundnut (*Arachis hypogaea* L.) is the second most important legume in Uganda after the common bean (*Phaseolus vulgaris* L.). It is an important source of protein and vegetable oil and is grown on over 413,000 hectares in Uganda (Deom and Okello, 2018), and over 13 million hectares in Sub-Saharan Africa (SSA; FAOSTAT, 2019). Groundnut productivity in developed countries is higher compared to that in developing countries. For example, the productivity in the USA was 4,072 kg/ha in 2021 (USDA-NASS, 2021), while that in Sub-Saharan Area (SSA) was approximately 950 kg/ha from 2017 to 2019 (FAOSTAT, 2019). The low productivity in SSA is attributed to low agricultural inputs, eroded soil fertility, and extensive biotic stress pressure. Late leaf spot [LLS; caused by *Nothopassalora personata* (Berk. & Curt.) U. Braun, C. Nakash, Videira and Crous] (Giordano et al., 2021) and Groundnut rosette disease (GRD) (caused by *groundnut rosette virus* (GRV)) are the most important biotic constraints to groundnut production in Uganda and SSA (Deom and Okello, 2018). These two diseases often occur simultaneously in farmers' fields causing up to 100% yield loss depending on the variety and management (Mugisa et al., 2016). Several methods can be employed to control these diseases. For example, GRD can be controlled by early planting and use of optimal plant densities (Farrell, 1976) and spraying insecticides to control the aphid vectors (Davies, 1975; Wightman and Amin, 1988). LLS can be controlled by use of biological control agents, such as chitinolytic bacteria (Kishore et al., 2005) and fungicides (Culbreath et al., 2002). These practices are rarely adopted by smallholder farmers in the SSA because of lack of access to information, shortage of resources, and differential priorities of the crops among different households.

The development of disease-resistant varieties is viewed as the most affordable way for smallholder farmers to maintain stable yields and make economic gains. The development of high-yielding varieties with improved resistance to diseases involves phenotyping of large numbers of breeding lines across multiple breeding locations (Araus and Cairns, 2014). In many breeding programs, early selection for the identification of genotypes with improved performance involves the use of breeder scores based on visual assessment of the plant appearance. For LLS, the breeder scores used in groundnut breeding include a 1–9 severity scale (Subrahmanyam et al., 1995), and for the GRD a 1–5 severity scale (Waliyar et al., 2007). These visual scores are subjective (Milberg et al., 2008), and fully dependent upon the expertise of the evaluator. Therefore, to standardize measurements collected by different evaluators or even the same evaluator at different time points is difficult. Furthermore, visual assessment of plant characteristics in breeding programs is labor-intensive, costly, and time-consuming (Araus and Cairns, 2014) because breeding experiments involve a large number of genotypes planted across multiple locations. Although visual assessment is usually performed by well-trained experts, external factors such as size of plot, time of sampling, and changes in weather conditions can lead to variation in the perception even by the same individual (Borra-Serrano et al., 2018). Visual scores allow the capture of a substantial proportion of variation attributed to genotypic

differences, however, methodological inaccuracy usually resulted in low heritability when selection is based on these scores (Visscher et al., 2008). Heritability, along with accuracy and repeatability of the selection method, is important in breeding because traits with high value of heritability are more likely to significantly contribute to the genetic gain (Cobb et al., 2019). A high heritability is indicative of great contribution of genetic factors compared to environmental factors to the expression of a trait (Holland et al., 2003). Several studies have reported high heritability of visual scores of LLS (Anderson et al., 1991) and GRD (Merwe et al., 1999) indicating possibility of attaining genetic gains using these scores. Alternative methods, which involve the use of proxy traits, such as canopy temperature and NDVI, have registered improved heritability, better selection accuracy, and higher genetic gains in various crops, such as sugar cane (*Saccharum officinarum* L.) (Natarajan et al., 2019), cotton (*Gossypium hirsutum* L.) (Andrade-Sanchez et al., 2013), and wheat (*Triticum aestivum* L.) (Wang et al., 2020).

High-throughput phenotyping (HTP) platforms have the potential to ameliorate the challenges associated with visual assessments and, consequently, accelerate genetic gain (Araus and Cairns, 2014; Araus Ortega et al. 2014, 2018). HTP involves the use of advanced technologies for fast data collection and processing, and non-destructive and non-invasive analysis of plant characteristics (Gehan and Kellogg, 2017). HTP platforms offer detailed measurements of plant characteristics of interest (Finkel, 2009). Previous studies have demonstrated the efficacy of the RGB imaging for assessment of yellow rust (*Puccinia striiformis* f. sp. tritici) in wheat (*Triticum aestivum* L.) (Zaman-Allah et al., 2015; Zhou et al., 2015), Verticillium wilt (caused by *Verticillium dahliae* Kleb) in olive (*Olea europaea* L.) (Sancho-Adamson et al., 2019), and lethal necrosis [caused by a combination of *maize chlorotic mottle virus* (MCMV) and *sugar cane mosaic virus* (SCMV)] in maize (*Zea mays* L.) (Kefauver et al., 2015). NDVI has widely been applied in breeding for resistance to yellow rust in wheat and maize, lethal necrosis in maize (Kefauver et al., 2015), and powdery mildew (*Blumeria graminis* f. sp. tritici) in wheat (Franke and Menz, 2007). Canopy temperature has been applied for stripe rust phenotyping in wheat (Cheng et al., 2015), and downy mildew (*Pseudoperonospora cubensis* (Berk & M.A Curtis) Rostovzev) in cucumber (*Cucumis sativus* L.) (Oerke et al., 2006) and tomato (*Solanum lycopersicum* L.) (Raza et al., 2015).

In groundnut breeding, application of HTP methods to complement or replace traditional phenotyping is in incipient stages. Efforts have been put forward to develop HTP methods to assess leaf wilting (Sarkar et al., 2021), plant height (Yuan et al., 2019; Sarkar et al., 2020), and plant population and variety differentiation using RGB and NDVI (Oakes and Balota, 2017). No HTP methods are yet available for phenotyping LLS and GRD resistance in groundnut. The changes in plant physiology and morphology under LLS and GRD pressure can be phenotyped remotely and genotypic differences for resistance to these diseases can be assessed, as in other crops. In this study, handheld tools were used to develop HTP methods to improve phenotyping accuracy within groundnut breeding programs in Uganda and SSA. The overall objective of this study was to evaluate the

effectiveness of several handheld sensors as low-cost phenotyping tools for screening LLS and GRD resistance in groundnut breeding. Specific objectives were as follows: (1) To evaluate the relationship between sensor-derived vegetation indices (VIs) with the LLS and GRD conventional visual scores; (2) determine the heritability of the VIs at different groundnut growth stages; and (3) develop VI-based regression models for selection for LLS and GRD resistance in groundnut breeding programs.

## MATERIALS AND METHODS

### Field Experiment

The experiment was conducted during two planting seasons: 2020A (April–August 2020) and 2020B (September–December 2020), at the National Semi-Arid Recourses Research Institute (NaSARRI), Serere District, Eastern Uganda (1°0′00.0″N, 33°33′00.0″E), and Nakabango Technology Verification Center, Jinja District, Eastern Uganda (0°31′17.6″N, 33°12′49.1″E). These locations receive bimodal rainfall seasons throughout the year; the first between March and May, and the second between August and October. These locations were chosen because they were characterized as hot spots for both GRD (Nakabango) and LLS (Nakabango and NaSARRI) screening in Uganda (Okello et al., 2010). Breeding genotypes were selected for this study; 50 genotypes consisting of commercial varieties and advanced breeding lines from NaSARRI, Uganda, and International Crop Research Institute for the Semi-Arid Tropics (ICRISAT), Malawi. This selected population included three groundnut market types: Virginia (bv. *hypogaea*), Spanish (bv. *vulgaris*), and Valencia (bv. *fastigiata*). The 50 genotypes were selected to represent the different levels of resistance to GRD and LLS as shown in (Table 1). The experiment was laid out in 5 x 10 alpha-lattice design with three replications. The genotypes were planted in two-row plots of 1-m long × 45 m wide. The experimental layout was generated from the Breeding Management Systems (BMS) platform [The IBP Breeding Management System (BMS Pro) Version 13 (2020)].<sup>1</sup> The spacing between the plots within the blocks was 0.6 m, 0.45 m between rows within the plot, and 0.15 m between plants within the row. A distance of 0.9 m was kept between the blocks and 1.5 m between the replicates. The experiment was maintained under rain-fed conditions and standard agronomic practices (Okello et al., 2010).

### Traditional Visual Assessment/Scoring

Visual scores of disease severity were taken by a groundnut breeding technician. Disease data was collected four times across the growing season each data point corresponding with a particular phenological stage of the groundnut. The data was collected at growth stages R2 (beginning of peg formation), R4 (beginning of pod formation), R7 (beginning of maturity), and R8 (harvest maturity) as described by Boote (1982). LLS severity was scored based on a 1–9 visual scale as described in Table 2 (Subrahmanyam et al., 1995). GRD was scored according to Equation 1 based on percentage disease incidence at beginning

**TABLE 1** | A list of genotypes used in the study showing their market type, source, and status.

Entry	Genotype	Market type	Source	Status
1	ICGV-SM 03590	Spanish	ICRISAT	Resistant check LLS
2	DOK 1R	Spanish	NaSARRI	Resistant check; GRD
3	Serenut 14R	Virginia	NaSARRI	Resistant check; LLS & GRD
4	Serenut 7T	Virginia	NaSARRI	Resistant check; LLS & GRD
5	Serenut 11T	Virginia	NaSARRI	Resistant check; LLS & GRD
6	Serenut 8R	Virginia	NaSARRI	Resistant check; LLS & GRD
7	Serenut 9T	Virginia	NaSARRI	Resistant check; LLS & GRD
8	Serenut 4T	Spanish	NaSARRI	Susceptible check; LLS
9	Serenut 6T	Spanish	NaSARRI	Susceptible check; LLS
10	JL 24	Spanish	ICRISAT	Susceptible check; LLS & GRD
11	Acholi white	Valencia	NaSARRI	Susceptible check; LLS & GRD
12	RedBeauty	Valencia	NaSARRI	Susceptible check; LLS & GRD
13	SGV 10010 ER	Spanish	NaSARRI	Test entry
14	DOK 1T	Spanish	NaSARRI	Test entry
15	ICGV 02501	Spanish	ICRISAT	Test entry
16	SGV 0080	Virginia	NaSARRI	Test entry
17	ICGV-SM 16502	Spanish	ICRISAT	Test entry
18	SGV 0060	Virginia	NaSARRI	Test entry
19	SGV 0075	Virginia	NaSARRI	Test entry
20	ICGV 01502	Spanish	ICRISAT	Test entry
21	SGV 07010	Virginia	NaSARRI	Test entry
22	Serenut 5R	Virginia	NaSARRI	Test entry
23	12CS-015	Spanish	USA-UGA	Test entry
24	B7-30-9-3	Spanish	USA-UGA	Test entry
25	ICGV-SM 08556	Spanish	ICRISAT	Test entry
26	ICGV-SM 01709	Virginia	ICRISAT	Test entry
27	ICGV-SM 95526	Valencia	ICRISAT	Test entry
28	ICGV-SM 95355	Virginia	ICRISAT	Test entry
29	ICGV-SM 16520	Spanish	ICRISAT	Test entry
30	ICGV 01504	Spanish	ICRISAT	Test entry
31	SGV 0805	Valencia	NaSARRI	Test entry
32	ICGV-SM 01731	Virginia	ICRISAT	Test entry
33	ICGV-SM 95714	Valencia	ICRISAT	Test entry
34	ICGV-SM 99568	Spanish	ICRISAT	Test entry
35	ICGV-SM 88710	Virginia	ICRISAT	Test entry
36	SGV 0071	Virginia	NaSARRI	Test entry
37	SGV 0084	Virginia	NaSARRI	Test entry
38	ICGV 01514	Spanish	ICRISAT	Test entry
39	ICGV-SM 03702	Virginia	ICRISAT	Test entry
40	SGV 0023	Virginia	NaSARRI	Test entry
41	SGV 990400	Virginia	NaSARRI	Test entry
42	ICGV-SM 16501	Spanish	ICRISAT	Test entry

(Continued)

<sup>1</sup><https://www.bmspro.io>

**TABLE 1 |** (Continued)

Entry	Genotype	Market type	Source	Status
43	ICGV-SM 0205	Spanish	ICRISAT	Test entry
44	ICGV 9555	Spanish	ICRISAT	Test entry
45	SGV 10005	Spanish	NaSARRI	Test entry
46	ICGV 01515	Spanish	ICRISAT	Test entry
47	ICGV 01510	Spanish	ICRISAT	Test entry
48	ICGV-SM 96714	Valencia	ICRISAT	Test entry
49	SGV 0065	Virginia	NaSARRI	Test entry
50	SGV 0047	Virginia	NaSARRI	Test entry

**TABLE 2 |** The 9 point scale used for screening groundnut for resistance for late leaf spot (Subrahmanyam et al., 1995).

Score	Description	Disease severity (%)	Inference
1	No disease	0	Resistant
2	Lesions present on lower leaves; no defoliation	1–5	Resistant
3	Lesions present largely on lower leaves, very few on middle leaves; defoliation of some leaflets on lower leaves	6–10	Resistant
4	Lesions on lower and middle leaves but severe on lower leaves, defoliation of some leaflets evident on lower leaves	11–20	Moderately resistant
5	Lesions present on all lower and middle leaves; over 50% defoliation of lower leaves	21–30	Moderately resistant
6	Severe lesions on lower and middle leaves; lesions present but less severe on top leaves; extensive defoliation of lower leaves; defoliation of some leaflets evident on middle leaves	31–40	Moderately resistant
7	Lesions on all leaves but less severe on top leaves; defoliation of all lower and some middle leaves	4–60	Susceptible
8	Defoliation of all lower and middle leaves; severe lesions on top leaves; some defoliation of top leaves evident	61–80	Susceptible
9	Almost all leaves defoliated, leaving bare stems; some leaflets may remain, but show severe leaf spots	81–100	Susceptible

of peg formation, beginning of pod formation, beginning of maturity and GRD severity at harvest maturity. GRD severity was scored based on a 1–5 scale (Table 3; Waliyar et al., 2007).

$$GRD \text{ Incidence (\%)} = \frac{\text{Number of infected plants}}{\text{Total number of plants}} \times 100\% \quad (1)$$

## High-Throughput Measurements

A Sony α6000 digital camera [model ILCE 6000, 24.3 megapixel (Sony-α, Tokyo, Japan)], GreenSeeker crop sensor (Trimble Inc., Sunnyvale, California, United States), and FLIR C2 Thermal camera (Teledyne FLIR LCC, Wilsonville, Oregon, United States) were used as HTP sensors in this study. HTP measurements were taken on the same dates as traditional visual scoring. The HTP measurements were taken between 10:00 and 16:00 h, on sunny days. To collect the RGB images, the Sony α6000 camera was

**TABLE 3 |** Groundnut rosette severity scale as described by Waliyar et al. (2007).

Score	Genotype reaction	Inference
1	No visible symptoms on the foliage	Highly resistant
2	Rosette symptoms on 1–20% foliage, but no obvious stunting	Resistant
3	Rosette symptoms on 21–50% foliage and stunting	Moderately resistant
4	Severe rosette symptoms on 51–70% foliage and stunting	Susceptible
5	Severe symptoms on 71–100% foliage, stunted or dead plants	Highly susceptible

set to auto so that the lens could adjust to the best sharpness, brightness, and hue based on available light. The camera zoom was set at 0 for all images and a 58 mm camera lens was used. The camera was held at 90 cm above the plant canopy in a zenithal plane and focusing at the center of each plot. The camera had an F-stop of f/8.0, a focal length of 16 mm, and an ISO speed ISO-100 without a flash. The images were saved as Joint Photographic Experts Group (JPEG) files (6,000 × 4,000) with a resolution of 350 dpi. RGB color space indices were extracted from the images using the BreedPix 0.2 option of the CIMMYT maize scanner 1.6 plugin (open software<sup>2</sup>; Copyright 2015 Shawn Carlisle Kefauver, University of Barcelona; produced as part of Image J/Fiji (open source software)<sup>3</sup> (Schindelin et al., 2012; Rueden et al., 2017). Figure 1 illustrates the extraction of the RGB indices using BreedPix, while Table 4 presents the indices and their description.

Canopy NDVI values were determined using a handheld spectroradiometer (GreenSeeker crop sensor, Trimble United States) on the same date the RGB images were taken. The GreenSeeker was held at 60 cm above the plant canopy and average NDVI readings were taken from each row. The trigger of the GreenSeeker was pressed at the beginning of the row and released at the end of the row to obtain the average NDVI of the row. The average of the two rows was taken to determine the plot average NDVI reading. The readings were taken when the sun was overhead to avoid shadows. NDVI was calculated according to Equation 2.

$$NDVI = ((NIR - R)) / ((NIR + R)) \quad (2)$$

Where *R* is the reflectance in the red band (660 nm) and *NIR* is the reflectance in the reflectance in the near-infrared band (760 nm).

Canopy temperature (CT) was measured using a FLIR C2 Thermal camera with a focal length of 2 mm. Images were taken while holding the camera 60–80 cm from the plant at an angle of 45°, and the images were saved as JPEG files with dimensions of 240 × 320 pixels and a resolution of 72 dpi. FLIR Tools software was used to extract the canopy temperature readings from the thermal images in degrees centigrade (Figure 2).

<sup>2</sup><http://github.com/george-haddad/CIMMYT>

<sup>3</sup><http://fiji.sc/Fiji>



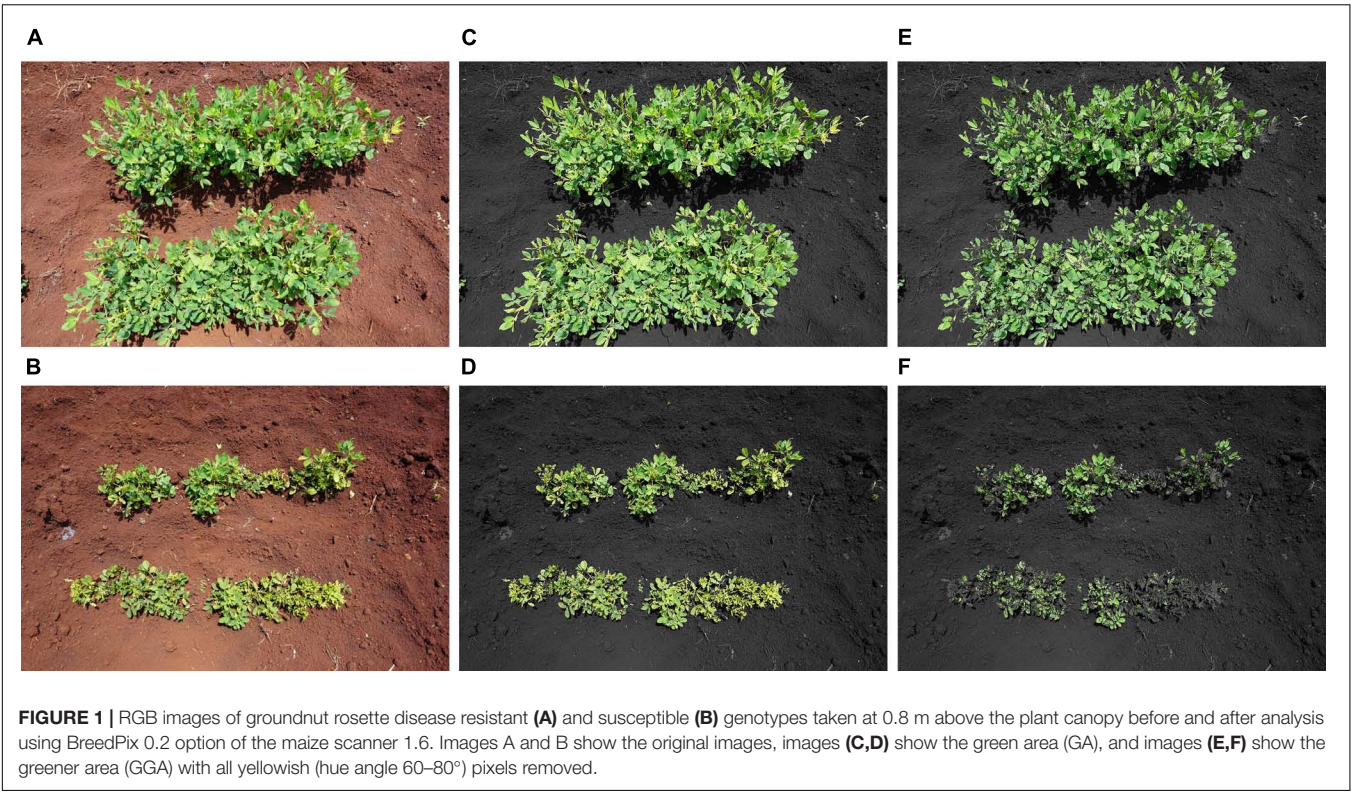


**TABLE 4 |** RGB indices derived from the BreedPix and their description.

RGB Indices	Basis of derivation	Color space	References
Hue	Color description in form of angles [0°–360° (0°-red; 60°-yellow; 120°-green; 240°-blue)]	His	Cheng et al., 2001
Saturation	Measure of dilution of pure hue with white light [0–1]	HSI	
Intensity	Measure of grayness on a 0 (black)–1 (white) scale	HSI	
Lightness	Light reflected by a non-luminous body [0 (black)–100 (white scale)]	CIE-Lab	
a*	Green (a)-Red ( + a) component	CIE-Lab	Cheng et al., 2001
b*	Blue (–b)-Yellow ( + b) component	CIE-Lab	
u*	Green (–u)-Red ( + u) component	CIE-Luv	
v*	Blue (–v)-Yellow ( + v) component	CIE-Luv	
Green area (GA)	Pixels from 60°–120°	HIS	Casadesus et al., 2007; Kefauver et al., 2015; Zhou et al., 2015
Greener area (GGA)	Pixels from 80°–120°	HIS	
Crop senescence index (CSI)	$100 \times (GA - GGA)/GA$	HIS	Zaman-Allah et al., 2015
ab	$a^*b^*$	CIE-Lab	
Normalized difference CIE-lab index (NDLab)	$\frac{1-a^*-b^*}{1-a^++b^*} + 1$	CIE-Lab	Buchailot et al., 2019
uv	$u^*v^*$	CIE-Luv	
Normalized difference CIE-luv index (NDLuv)	$\frac{1-u^*-v^*}{1-u^++v^*} + 1$	CIE-Luv	Buchailot et al., 2019

*\*In this case is associated with the CIE-Lab indices a and b and CIE-Luv indices u and v as derived from the BreedPix.*

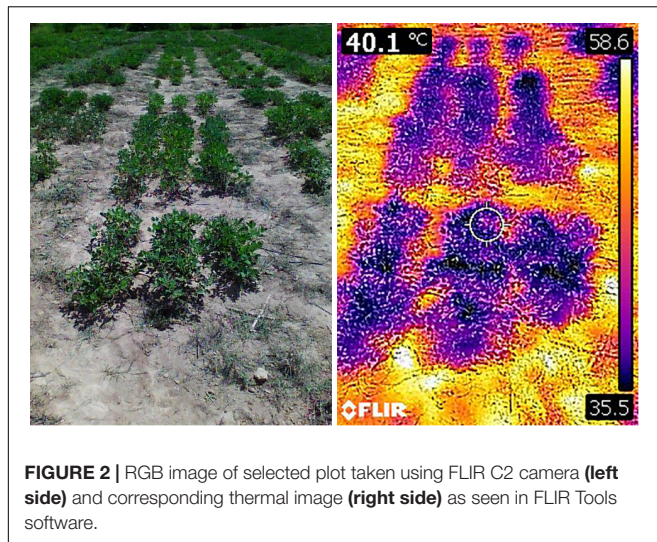


**FIGURE 2 |** RGB image of selected plot taken using FLIR C2 camera (left side) and corresponding thermal image (right side) as seen in FLIR Tools software.

## Statistical Analysis

### Pearson Correlation of Visual Scores and Vegetation Indices

The means of visual measurements and HTP-derived VIs of each genotype were extracted for each day of data collection using the R statistical software (R Core Team, 2021). Pearson correlation was performed between the means of the visual scores and VIs taken at the same time point and for all data points combined, and for individual market types and all the market types combined using the *rcorr* function of the *Hmisc* package of the R software.

### Calculation of Broad Sense Heritability

The broad-sense heritability ( $H^2$ ) was calculated as according to Equation 3

$$H^2 = \frac{\sigma_G^2}{\sigma_G^2 + \frac{\sigma_{GE}^2}{n} + \frac{\sigma_e^2}{nr}} \quad (3)$$

Where  $\sigma_G^2$  is the genotypic variance,  $\sigma_{GE}^2$  is the variance of the genotype by environment (location) interaction,  $\sigma_e^2$  is the residual error variance,  $n$  is the number of environments (locations) and  $r$  is the number of replications within each environment (Piepho and Mohring, 2007). The variance components used were estimated from the analysis of variance (ANOVA) using the *lmer* function of the *lme4* package (Bates et al., 2015) of the R statistical software (R Core Team, 2021).

## Development of Regression Models

### Training of Regression Models

Ordinal logistic regression was used to develop two separate prediction models, one for the LLS and one for GRD, disease severity. The models were developed from data collected at R8 (harvest maturity) because the strongest association between VIs and visual scores was recorded at maturity. Ordinal logistic regression was applied in this case because the GRD and LLS scales used in the study were ordinal variables. The NDVI readings, RGB, and thermal images taken per plot together

with the visual scores allocated to the respective plots were all used in the models. The regression models were developed using stepwise regression using the *caret* (Classification And Regression Training) package (Max et al., 2021) and the *polr* function of the MASS package of R. Data from Nakabango for the 2020A and 2020B seasons was used for training the ordinal logistic regression models and data from NaSARRI was used to validate the models. The backward selection method of stepwise regression was used to select the parameters with the highest contribution to the model. A full model (all predictors) was fitted and the least contributing predictors were removed until all the parameters in the model were statistically significant ( $P < 0.05$ ). K-fold cross-validation was used to evaluate the models. The training data set was randomly split into  $k$ -folds ( $k = 10$ ). The model was trained on nine subsets and one subset was reserved for testing the model. The process was repeated until each of the  $k$ -subsets has served as the testing set. The ten sets of results were then averaged to produce a single model estimation. Akaike's Information Criteria (AIC) and Bayesian Information Criteria (BIC) were used to select the best model. Models with lower AIC and BIC are better predictors than those with higher values. The accuracy of the models was derived from the classification accuracy matrices (Equation 4).

$$\text{Accuracy} = \frac{\text{No. of plots classified correctly}}{\text{Total plots in the set}} \times 100 \quad (4)$$

The nearest score method was also used to improve the classification accuracy of the models. The visually rated scores were matched with the model derived scores, and two of the nearest scores (preceding and succeeding) of the visually rated scores were also matched. If any of the values (actual values, preceding or succeeding) matched with the model derived score, it was assumed as the correct classification (Sarkar et al., 2021).

### Validation of Regression Models

The regression models developed using data from Nakabango were validated using data from NaSARRI. The model was applied to the validation data set to obtain predicted values. A confusion matrix (Sarkar et al., 2021) was developed to determine the accuracy of the model.

## RESULTS

### Distribution of High-Throughput Phenotyping Measurements and Visual Scores

The data presented was collected in Nakabango across the two growing seasons; 2020A and 2020B. The disease pressure was higher in Nakabango across the two seasons. The distribution of the LLS visual scores increased over time peaking at harvest maturity which coincided with the time of harvest. The Spanish and Valencia market types had similar patterns of distribution of LLS scores over time. At all-time points, LLS scores were higher for Valencia and Spanish type compared to Virginia (Virginia appear more resistant). At each data collection time,



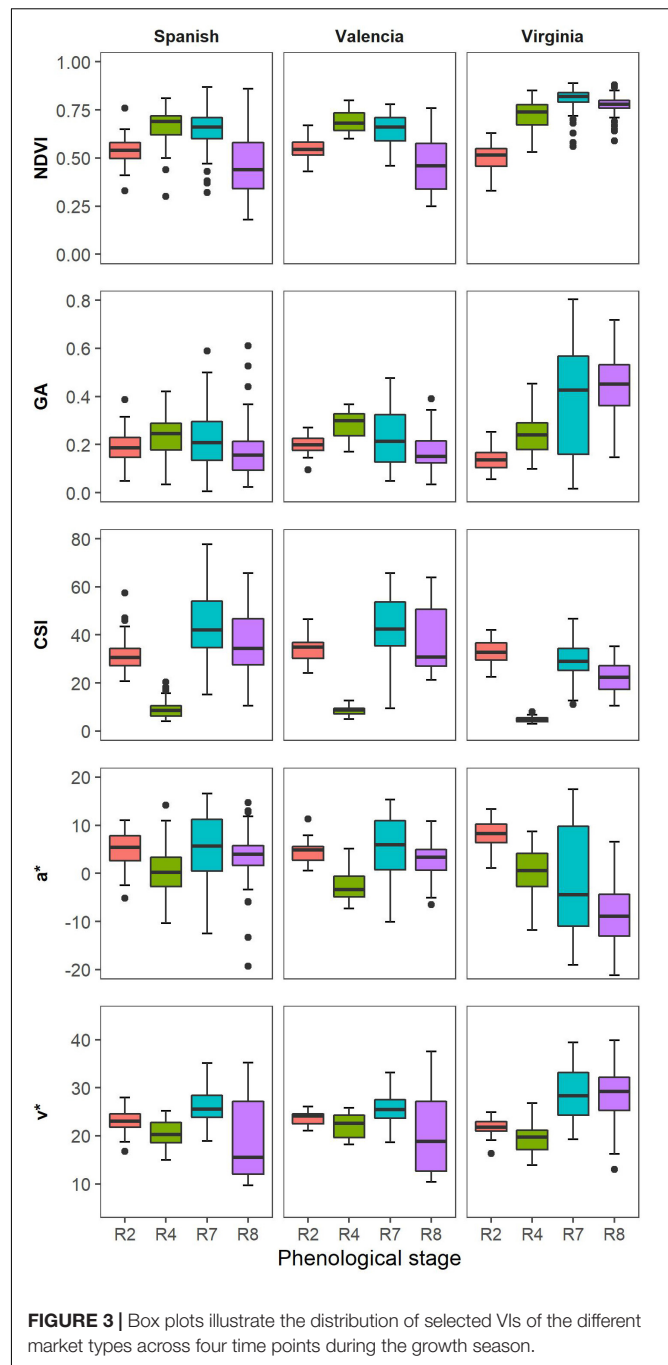
more variability in LLS score was registered in Valencia and Spanish types compared to Virginia. Similarly, for GRD visual scores, the Spanish and Valencia market types showed a similar pattern of distribution over time. The variability in GRD visual symptoms was higher for the Spanish and Valencia, and lower for the Virginia market type at all-time points.

Valencia and Spanish market types showed similarities in the distribution of vegetation indices (VIs) indices with Virginia showing different responses. The NDVI values were similar for all the market types at beginning of peg formation (Figure 3). At full pod formation (R4), all market types had similar medians for the GA, but the variability was greater for Spanish compared to Valencia and Virginia. At beginning of maturity (R7) and harvest maturity (R8), Virginia had higher GA values compared to the other two market types, just like for the NDVI. Within each market type, the CSI medians were lowest at full pod formation (R4) and highest at beginning of maturity, but Virginia market types had lower CSI medians in comparison with Spanish and Valencia at R7. The spread of the CSI values was highest at beginning of maturity for all the market types, but higher for the Spanish and Valencia compared to Virginia. The distributions of the medians of  $a^*$  and  $u^*$  followed similar trends for all market types. The medians were highest at beginning of pegging and lowest at full pod formation. The spread of measurements was highest at beginning of maturity and lowest at beginning of peg formation.

## Pearson Correlation Between Visual Scores and Vegetation Indices

The Pearson correlation between visual scores and the vegetation HTP indices (VIs) was performed using different subsets of the data (each market type, collection dates and for the combined dataset of the three market types). The strongest correlations between LLS visual scores and VIs were recorded at R2 (beginning of pegging) and R8 (harvest maturity). The association between the VIs and NDVI show an increase throughout the season peaking at R8 ( $r = -0.85$ ,  $P < 0.001$ ) (Figure 4). The NDVI was strongly associated with LLS severity of all market types at harvest maturity, with the strongest association recorded in the Spanish type ( $r = -0.89$ ,  $P < 0.001$ ). For Valencia, there was non-significant association between LLS visual score and NDVI until harvest maturity ( $r = -0.83$ ,  $P < 0.001$ ) and for the Virginia type, the association was non-significant as well until harvest maturity ( $r = -0.64$ ,  $P < 0.001$ ).

RGB indices were significantly correlated with the disease symptoms of all the three market types at harvest [Lightness ( $r = -0.74$ ,  $P < 0.001$ ),  $v^*$  ( $r = -0.80$ ,  $P < 0.001$ ), and  $b^*$  ( $r = -0.75$ ,  $P < 0.001$ )]. At R4 (full pod), CSI ( $r = 0.76$ ,  $P < 0.001$ ) was the most sensitive index to the onset of LLS. Some indices, however, performed better only for some market types at particular time points. For example, the RGB indices Hue ( $r = -0.87$ ,  $P < 0.001$ ),  $a^*$  ( $r = 0.84$ ,  $P < 0.001$ ),  $b^*$  ( $r = -0.82$ ,  $P < 0.001$ ), NDLab ( $r = -0.88$ ,  $P < 0.001$ ),  $u^*$  ( $r = 0.84$ ,  $P < 0.001$ ),  $v^*$  ( $r = -0.82$ ,  $P < 0.001$ ), and GA ( $r = -0.83$ ,  $P < 0.001$ ) were highly correlated with disease symptoms of Valencia market type at R7 (beginning of maturity) but moderately correlated with Virginia and Spanish



market type LLS symptoms. At full pod (R4), RGB indices Hue, Saturation,  $b^*$ ,  $v^*$ , and GA were significantly associated with disease symptoms of Virginia ( $r = 0.45, 0.43, 0.53, 0.53, 0.48$ ;  $P < 0.001$ ) and Spanish ( $r = 0.30, 0.59, 0.55, 0.53, 0.26$ ;  $P < 0.001$ ) market types but insignificant for the Valencia type. Canopy temperature ( $r = 0.42$ ,  $P < 0.001$ ) was positively correlated with disease severity, of all the three market types across the different time points. The correlation of the Valencia type ( $r = 0.64$ ,  $P < 0.001$ ) was stronger compared to that of the Spanish ( $r = 0.4$ ,  $P < 0.001$ ) and Virginia ( $r = 0.16$ ,  $P < 0.001$ ) market types.

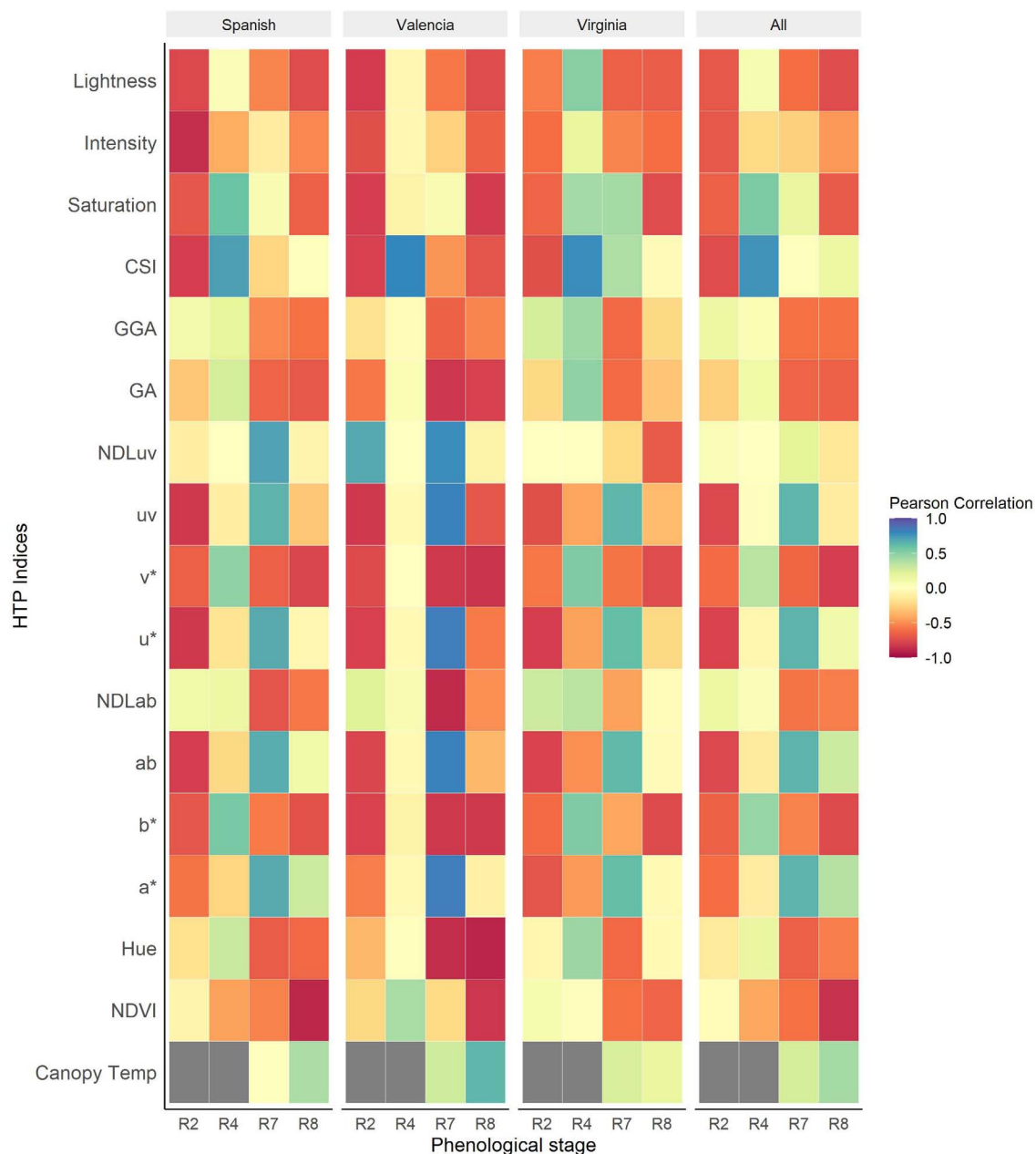


**FIGURE 4 |** Heatmap of Pearson correlations between HTP derived indices and visual scores of Late leaf spot (LLS) severity at different phenological stages of the growth season for the individual market types and all the market types analyzed together. The dark gray boxes represent missing data.

The association between NDVI and the GRD scores show a gradual increase over the season peaking at beginning of maturity. The association between the visual scores and NDVI was strongest at beginning of maturity ( $r = -0.73$ ,  $P < 0.001$ ) and full maturity ( $r = -0.72$ ,  $P < 0.001$ ). The associations among the Spanish and Valencia market types were stronger compared to those among the Virginia type at all data collection points.

The RGB indices were significantly associated with GRD visual scores at beginning of peg formation and at harvest maturity for all the market types. The strongest associations

were recorded at harvest maturity [ $v^*$  ( $r = -0.71$ ,  $P < 0.001$ ), GA ( $r = -0.67$ ,  $P < 0.001$ ), NDLab ( $r = -0.64$ ,  $P < 0.001$ ), GGA ( $r = -0.6$ ,  $P < 0.001$ ), Lightness ( $r = -0.62$ ,  $P < 0.001$ )]. For CSI, the associations gradually increased throughout the season from ( $r = -0.7$ ,  $P < 0.001$ ) beginning of peg formation (R2) and peaking at beginning of maturity (R7) ( $r = 0.6$ ,  $P < 0.001$ ) (Figure 5). The associations were generally higher for the Valencia type compared to the Spanish and Virginia type. Early (R2) detection of disease symptoms was possible among the Valencia market type using RGB indices saturation,



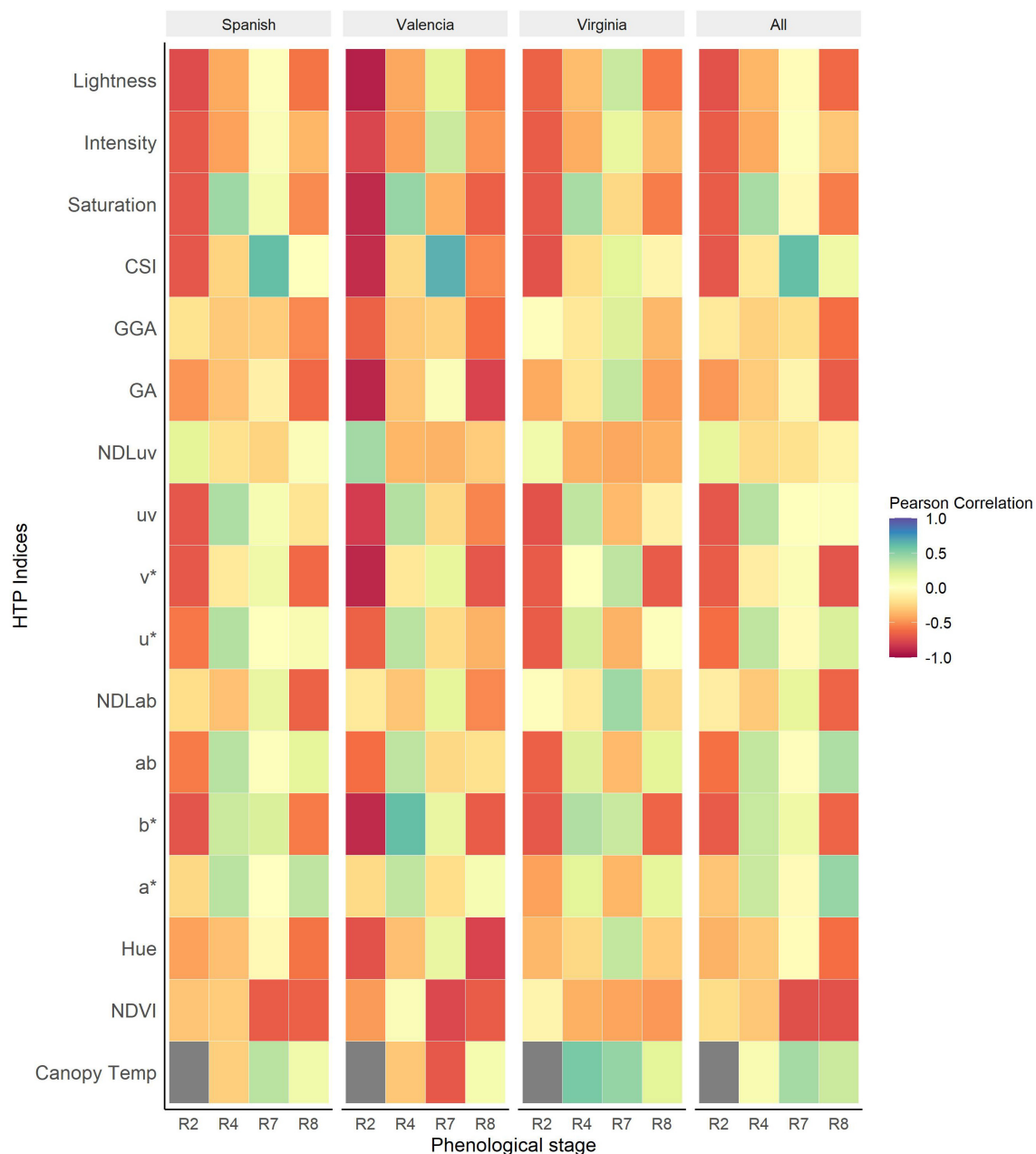


**FIGURE 5 |** Heatmap of Pearson correlations between HTP derived indices and visual scores of Groundnut rosette disease (GRD) at different phenological stages of the growing season for the individual market types and all the market types analyzed together. The dark gray boxes represent missing data.

lightness ( $r = -0.92$ ,  $P < 0.001$ ),  $b^*$  ( $r = -0.88$ ,  $P < 0.001$ ),  $v^*$  ( $r = -0.89$ ,  $P < 0.001$ ), GA ( $r = -0.90$ ,  $P < 0.001$ ), and CSI ( $r = 0.87$ ,  $P < 0.001$ ). Canopy temperature was generally positively correlated with disease symptoms for all market types. The associations were highest at beginning of maturity ( $r = 0.42$ ,  $P < 0.001$ ) and non-significant at full pod formation and harvest maturity. At full pod formation (R4), the Valencia and Spanish had a negative association compared to the Virginia type with positive association. However, at beginning of maturity, the Spanish ( $r = 0.35$ ,  $P < 0.001$ ) and Virginia ( $r = 0.47$ ,

$P < 0.001$ ) had a similar trend with positive correlations compared to Valencia ( $r = -0.69$ ,  $P < 0.001$ ) market type with a negative association.

## Identification of Resistant and Susceptible Genotypes

Identification of the most resistant and susceptible genotypes based on the visual and NDVI rankings is presented in **Table 5**. For LLS, NDVI identified three of the top five most resistant

genotypes based on the visual score ranking. However, both NDVI and visual scores each identified different five, most susceptible, genotypes within the population. For GRD, both NDVI and visual scores identified three common genotypes out of the five most resistant and susceptible genotypes (Table 5).

## Heritability

Table 6 shows the  $H^2$  values calculated for both visually assessed disease traits and the VIs taken at different time points throughout the growing season. The  $H^2$  of the visual scores and VIs show a gradual increase throughout the growing season peaking at R8 (harvest maturity). RGB indices Intensity and NDVI had  $H^2 = 0$  throughout the growing season. The  $H^2$  of the visually assessed LLS scores was higher than that of both GRD incidence and severity throughout the season. The  $H^2$  of the VIs was highest at R8 with exception of CSI which was peaked at R4 (pod formation). The heritability of LLS scores was higher compared to any associated VI at all times of data collection. The strongly associated VIs at R8 [NDVI ( $H^2 = 0.87$ ),  $v^*$  ( $H^2 = 0.72$ ), and  $b^*$  ( $H^2 = 0.60$ )] and R4 (CSI,  $H^2 = 0.75$ ) equally had a high heritability. The  $H^2$  of the GRD visual scores was lower than associated indices; However, all VIs strongly associated with GRD visual scores [NDVI ( $H^2 = 0.87$ ),  $v^*$  ( $H^2 = 0.72$ ), Hue ( $H^2 = 0.81$ ), GA ( $H^2 = 0.77$ ), and GGA ( $H^2 = 0.80$ )] at R8, and CSI ( $H^2 = 0.64$ ) and NDVI ( $H^2 = 0.86$ ) at R7 (beginning of maturity) all had a higher heritability compared to the GRD visual scores.

## Ordinal Logistic Models to Predict Late Leaf Spot and Groundnut Rosette Disease Severity

Late leaf spot severity was scored on a 1–9 scale, however, at R8 (harvest maturity), 6 levels were present and scores were between

**TABLE 5 |** Table genotype ranking for LLS and GRD using visual scores and NDVI. The genotype ranking was done using genotype means.

Rank	Late leaf spot		Groundnut rosette disease	
	Visual score	NDVI	Visual score	NDVI
1	ICGV-SM 03590 <sup>a</sup>	ICGV-SM 03590 <sup>a</sup>	DOK 1R <sup>a</sup>	ICGV-SM 03590 <sup>a</sup>
2	Serenut 14R <sup>a</sup>	Serenut 14R <sup>a</sup>	Serenut 14R <sup>a</sup>	Serenut 14R <sup>a</sup>
3	SGV 990400	Serenut 8R <sup>a</sup>	Serenut 8R <sup>a</sup>	Serenut 8R <sup>a</sup>
4	Serenut 9T <sup>a</sup>	Serenut 9T <sup>a</sup>	Serenut 9T <sup>a</sup>	Serenut 9T <sup>a</sup>
5	SGV 0071	SGV 0060	ICGV-SM 01709	SGV 0060
46	ICGV-SM 08556	Acholi White <sup>b</sup>	JL 24 <sup>b</sup>	Acholi White <sup>b</sup>
47	ICGV-SM16520	ICGV-SM 16501	RedBeauty <sup>b</sup>	ICGV-SM 16501
48	ICGV 01504	ICGV-SM 96714	ICGV-SM 96714	ICGV-SM 96714
49	ICGV-SM 16502	RedBeauty <sup>b</sup>	ICGV-SM 0205	RedBeauty <sup>b</sup>
50	Serenut 4T <sup>a</sup>	SGV 10005	Acholi White <sup>b</sup>	SGV 10005

<sup>a</sup>Resistant check, <sup>b</sup>susceptible check.

\*In this case is associated with the CIE-Lab indices a and b and CIE-Luv indices u and v as derived from the BreedPix.

**TABLE 6 |** Broad-sense heritability of HTP derived indices and visual scores for late leaf spot (LLS) and groundnut rosette virus (GRD) during the 2020A and 2020B growing seasons at different groundnut growth stages.

Trait	Phenological stage			
	R2	R4	R7	R8
NDVI	0.30	0.00	0.86	0.87
Intensity	0.00	0.00	0.00	0.00
Hue	0.54	0.17	0.43	0.81
Saturation	0.58	0.41	0.00	0.20
Lightness	0.00	0.02	0.00	0.54
a*	0.48	0.14	0.53	0.73
b*	0.55	0.32	0.00	0.60
ab	0.41	0.11	0.48	0.68
NDLab	0.29	0.17	0.11	0.34
u*	0.35	0.16	0.51	0.68
v*	0.56	0.27	0.00	0.72
uv	0.00	0.15	0.50	0.64
NDLuv	0.00	0.00	0.00	0.00
GA	0.49	0.09	0.58	0.77
GGA	0.43	0.06	0.64	0.80
CSI	0.39	0.75	0.64	0.66
CT	0.06	0.06	0.00	0.50
<b>Visual score</b>				
LLS	0.87	0.87	0.93	0.95
GRD incidence	0.25	0.25	0.44	0.37
GRD severity			0.43	0.43

\*In this case is associated with the CIE-Lab indices a and b and CIE-Luv indices u and v as derived from the BreedPix.

4 and 9. The probability of predicting the LLS VI-derived score  $P_4 + P_5 + P_6 + P_7 + P_8 + P_9 = 1$ . The model for LLS predicted scores is presented below;

$$P_4 = \frac{1}{1 + e^{(-5.78-\beta)}}$$

$$P_5 = \frac{1}{1 + e^{(-4.17-\beta)}} - P_4$$

$$P_6 = \frac{1}{1 + e^{(-0.36-\beta)}} - P_4 - P_5$$

$$P_7 = \frac{1}{1 + e^{(-1.5-\beta)}} - P_4 - P_5 - P_6$$

$$P_8 = \frac{1}{1 + e^{(-3.72-\beta)}} - P_4 - P_5 - P_6 - P_7$$

$$P_9 = 1 - P_4 - P_5 - P_6 - P_7 - P_8$$

Where  $e = 2.718$  is the Euler's number,

$$\beta = -1.81\text{NDVI} + 0.88\text{CSI} - 2.2b^*.$$

The LLS model with NDVI and RGB indices CSI and  $b^*$  as the best predictors had AIC of 431.94 and BIC of 463.53 compared to the full model (with all the predictors) with AIC of 492.014 and BIC of 520.09. The model had a kappa value of 0.52 and an overall accuracy of 64% (Table 7). The model had the highest predictability for the visual scores 6 and 9, and the lowest prediction accuracy for the visual score 4. The specificity

**TABLE 7** | Classification confusion matrix of LLS visual scores and model predicted scores of the training data set collected at Nakabango.

Breeder score	Plots (n)	Predicted score					
		4	5	6	7	8	9
4	16	<b>3</b>	1	12	0	0	0
5	29	2	<b>7</b>	20	0	0	0
6	82	1	4	<b>69</b>	3	2	3
7	31	0	0	12	<b>12</b>	5	2
8	34	0	0	1	6	<b>17</b>	10
9	55	0	0	1	0	5	<b>49</b>
<b>Total</b>	247						
Accuracy	64%	19%	24%	84%	39%	50%	89%
Nearest score	91%						

The bold figures represent the visual scores which were correctly classified by logistic models.

of the model was high with the lowest value being 0.83 for visual score 6. The highest misclassification of scores was observed at visual score 7 with 9 scores allocated to score 6 by the model. The prediction accuracy of the model increased to 91% when the nearest score method was used.

The Groundnut rosette disease severity was scored on a 1–5 scale. The probability of predicting GRD VI-derived score was  $P_1 + P_2 + P_3 + P_4 + P_5 = 1$ . The model for GRD predicted is presented below;

$$P_1 = \frac{1}{1 + e^{(-0.98-\beta)}}$$

$$P_2 = \frac{1}{1 + e^{(-0.33-\beta)}} - P_1$$

$$P_3 = \frac{1}{1 + e^{(-1.12-\beta)}} - P_1 - P_2$$

$$P_4 = \frac{1}{1 + e^{(-1.77-\beta)}} - P_1 - P_2 - P_3$$

$$P_5 = 1 - P_1 - P_2 - P_3 - P_4$$

Where  $e = 2.718$  is the Euler's number,

$$\beta = 0.044\text{Hue} + 0.42a^* - 0.006uv$$

The GRD model with RGB indices Hue,  $a^*$ , and  $uv$  selected as the best predictors of GRD severity; this model had AIC of 619.2 and BIC of 643.8 compared to the full model (with all predictors) with AIC of 626.5 and BIC of 700.3. The model had a kappa of 0.28 and overall model accuracy of 45%. The model had the highest predictability for the visual scores of 5 followed by 2 and 1. The lowest prediction accuracy was recorded for the class 4. The misclassification between classes was highest between 1 and 2. Twenty-four plots visually scored 1 were given a score of 2 by the model. Similarly, 26 plots which were scored as 2, were predicted by the model as 1 (Table 8). The lowest misclassification was for 4 as indicated by the specificity of 1.00. The prediction accuracy of the model however increased to 84% when the nearest score method was used.

## Validation of the Regression Models

The LLS logistic model was validated using the data collected at NaSARRI 2020B. The model performed with lower accuracy of 40% but performed with a similar accuracy when the nearest score accuracy was used with 88% (Table 9). The Pearson correlation between the model derived score and the breeder score of the validation data was moderate ( $r = 0.58$ ). The GRD logistic model performed with similar accuracy with the validation data set with 38 and 91% (Table 10) when the nearest accuracy was used.

## DISCUSSION

### Association Between Visual Scores and High-Throughput Phenotyping Derived Indices

In this study, the VIs were significantly correlated with the visual scores of groundnut LLS severity among different groundnut genotypes and market groups, and at different growth stages. Overall, NDVI had the strongest relationship with visual

**TABLE 8** | Confusion matrix of GRD visual scores and the model predicted scores of the training dataset of the data collected at Nakabango.

Breeder score	Plots (n)	Predicted score				
		1	2	3	4	5
1	58	<b>31</b>	24	2	0	1
2	80	26	<b>43</b>	6	0	5
3	45	1	20	<b>12</b>	0	12
4	30	1	7	10	<b>0</b>	12
5	35	0	2	8	0	<b>25</b>
<b>Total</b>	248					
Accuracy	45%	53%	54%	24%	0%	71%
Nearest score	84%					

The bold figures represent the visual scores which were correctly classified by logistic models.

**TABLE 9** | Confusion matrix of LLS visual scores of the breeder scores and predicted scores of data collected at NaSARRI 2020B.

Breeder score	Plots (n)	Predicted score					
		4	5	6	7	8	9
4	0	<b>0</b>	0	0	0	0	0
5	3	0	<b>0</b>	3	0	0	0
6	52	0	0	<b>21</b>	24	6	1
7	26	0	0	6	<b>15</b>	3	2
8	30	0	0	0	11	<b>15</b>	4
9	38	0	0	3	6	20	<b>9</b>
<b>Total</b>	149						
Accuracy	40%	0%	0%	40%	58%	50%	24%
Nearest score	88%						

The bold figures represent the visual scores which were correctly classified by logistic models.

**TABLE 10 |** Confusion matrix of GRD severity visual scores and the model predicted scores of data collected at NaSARRI 2020A and 2020B.

Breeder score	Plots scored	Predicted score				
		1	2	3	4	5
1	135	<b>25</b>	97	12	0	1
2	149	23	<b>92</b>	32	0	2
3	46	2	28	<b>15</b>	0	1
4	15	0	11	4	<b>0</b>	0
5	1	0	0	1	0	<b>0</b>
<b>Total</b>	346					
Accuracy	38%	19%	62%	33%	0%	0%
Nearest score	91%					

The bold figures represent the visual scores which were correctly classified by logistic models.

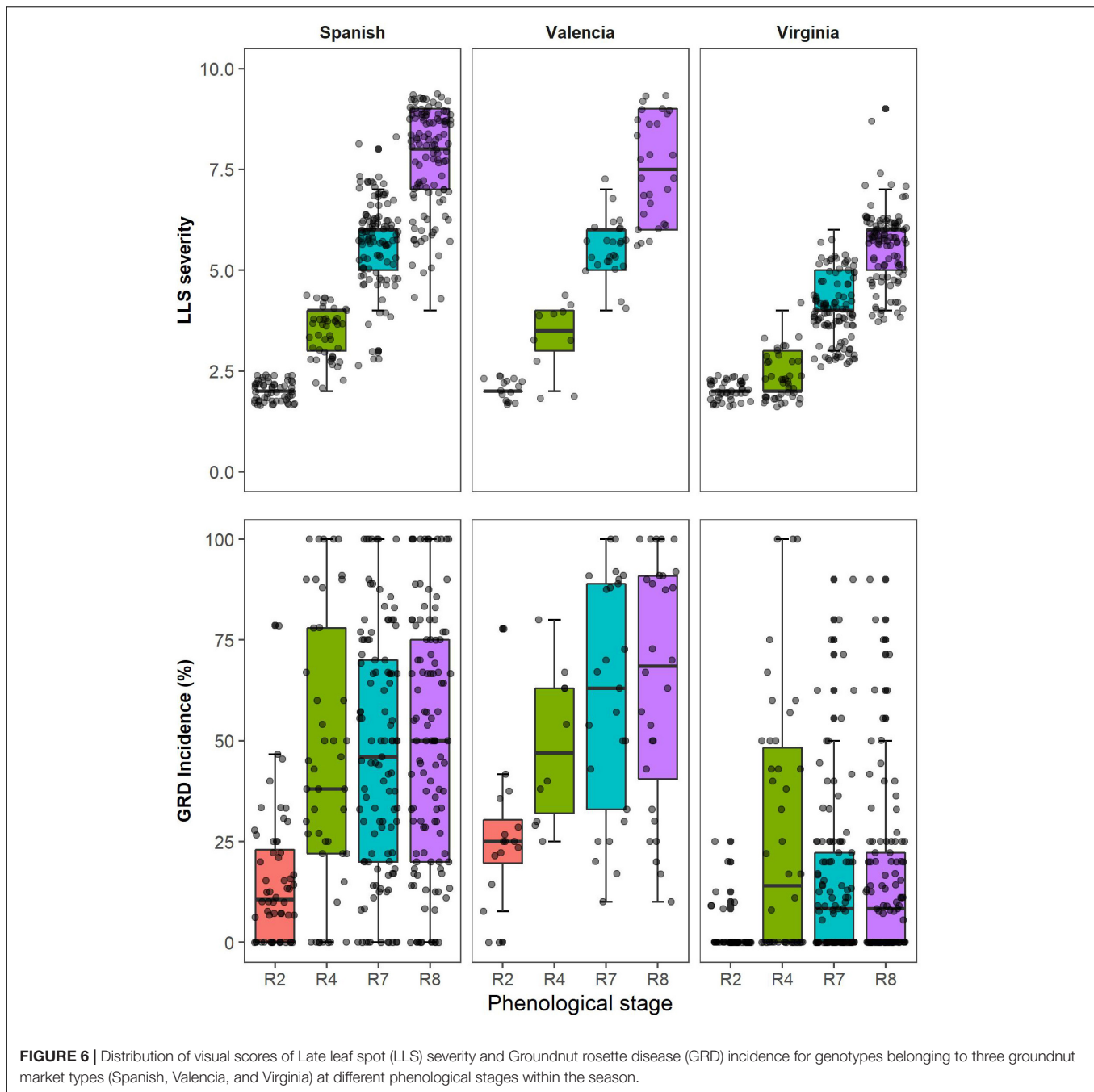
symptoms of the different market types at harvest maturity. NDVI had a negative relationship with LLS severity, i.e., more severe LLS disease less NDVI values, and the effect of the disease was evident at full pod formation (R4) for Spanish. There was a large variation among the Spanish and Valencia groups because the susceptible genotypes were easily affected by the LLS symptoms compared to the Virginia groundnuts which had a low variation of disease symptoms at this stage (Figure 6). The correlations were stronger for all market types ( $r = -0.85$ ) harvest maturity, because there was a higher disease variation and a clear distinction between resistant and susceptible genotypes (Figure 4). Moderate correlations between LLS and NDVI were observed among the Virginia market type ( $r = -0.64$ ) compared to the Spanish ( $r = -0.89$ ) and Valencia ( $r = -0.83$ ) because 75% of the genotypes had scored less than 5 hence belonging to the resistant group (Figure 6). As shown by others, higher NDVI values were associated with healthy canopies (in this case, resistant genotypes) with the ability to absorb red light and effectively reflect NIR (Liu and Huete, 1995; Govaerts and Verhulst, 2010). Increased LLS severity is characterized by increased defoliation (Subrahmanyam et al., 1995) and reduction of leaf chlorophyll content (Singh et al., 2011), thus reducing the light-absorbing capacity of canopies for the susceptible genotypes. Chlorophyll, which is responsible for light absorption, is linearly related to NDVI (Gitelson and Merzlyak, 1996). The reduction in reflectance of the near-infrared radiation is due to the reduction in multiple leaf layers within the canopy, and the increase in background exposure (Knipling, 1970) therefore, reducing NDVI with increase in severity.

Several RGB indices were strongly correlated with visual LLS symptoms (Figure 4). Hue, GA, and Saturation ( $r = -0.55$ ,  $-0.68$ ,  $-0.66$ ) were moderately correlated with visual scores for all groundnut market types at harvest maturity (R8). The effect of LLS on canopy CSI was apparent as early as R4 (at full pod formation) but the effects on hue and GA became visible at R7 (beginning of maturity) when there was clear variation among genotypes. The change of the correlation signs of CSI from negative at beginning of peg formation (R2) to positive at beginning of pod formation indicated the effect of the disease on the canopy color and leaf senescence, i.e. at peg formation

plants were small and, in absence of disease, other factors influenced senescence; at pod formation disease severity doubled and this was the main factor for increased crop senescence. Lower hue and GA values among susceptible genotypes could be attributed to increased yellowing of the canopy due to a decrease in leaf chlorophyll (Sarkar et al., 2021). Defoliation of leaves could also lead to reduced hue and GA since both are associated with presence of green biomass (Casadesús et al., 2007). In highly defoliated canopies (as evident in susceptible genotypes), the soil background is not completely covered. The hue of bare soil is low (Zhou et al., 2015) therefore, the hue of highly defoliated canopies (susceptible) is lower than that in well-developed canopies (resistant genotypes). The correlation among Virginia groundnuts was lower for both GA ( $r = -0.3$ ) and hue ( $r = -0.04$ ) because of the low variation of both, visual scores and VIs (Figure 4).  $b^*$  ( $r = -0.75$ ) and  $v^*$  ( $r = -0.8$ ) were highly correlated with visual scores of LLS among all market types. This is attributed to the yellowing of the canopy (Serret et al., 2020) due to reduced leaf chlorophyll (Singh et al., 2011; Sarkar et al., 2021). Although these indices were able to identify the canopy yellowing later in the season, CSI ( $r = 0.76$ ) identified yellowing of the canopies due to LLS as early as the pod formation. Early detection of LLS would aid early selection of resistant genotypes saving resources in the breeding program. Canopy temperature ( $r = 0.42$ ), was however moderately correlated with the visual scores. Canopy temperature is associated with transpirational cooling of the plant canopy (Pilon et al., 2018). Cool plant canopies are associated with healthy canopies. An increase in canopy temperature is associated with an increase in disease severity (Oerke et al., 2006). This could be attributed to the reduction of evaporative surfaces due to defoliation and damage of leaf surfaces by leaf spot lesions. Results in our study indicated that LLS severity was promoted by warmer canopy temperatures.

Several RGB indices demonstrated moderate to high correlations with GRD visual scores with different market types at different weeks after planting (Figure 5). Generally, the RGB indices Hue, GA, GGA,  $v^*$ , and  $b^*$  were negatively correlated with GRD symptoms. GRD is characterized by shortening of stem internodes, rosetting of the leaves, chlorosis of leaves, and overall stunting of the affected plants (Table 3; Naidu et al., 1998; Waliyar et al., 2007). Indices such as Hue, GA, and GGA which are associated with the presence of green biomass (Casadesús et al., 2007; Casadesús and Villegas, 2014), were, therefore, able to differentiate the resistant and susceptible genotypes based on the size of the plant. Healthy plants have larger canopies compared to the stunted rosette plants, thereby occupying more green area and consequently covering more soil background. Since hue angle is also affected by soil background which has a lower hue value (Zhou et al., 2015), healthy genotypes have a higher hue angle compared to the stunted susceptible genotypes. Increased yellowing of susceptible genotypes was observed. This was evident from the reduction of GA and GGA pixels, and the increase of  $b^*$  and  $v^*$ . Yellowing of leaves has been associated with chlorophyll reduction due to drought in various crops (Serret et al., 2020; Sarkar et al., 2021); in our case, this was due to the high prevalence of chlorotic rosette symptoms (Naidu et al., 1998) also known as yellow rosette symptoms, for which





Nakabango is well known as a hotspot (Okello et al., 2014). The chlorotic symptoms were visible early in the season by during the beginning flowering stage and later in the season, toward harvest. NDVI ( $r = -0.72$ ), which has widely been used for monitoring canopy health status was also negatively correlated with the GRD symptoms. NDVI is indicative of the amount biomass and vigor of vegetation within the plot, and therefore plant biomass (Cabrera-Bosquet et al., 2011). In our case, the reduction of NDVI among susceptible genotypes could be due to reduction of the biomass, vigor, and leaf chlorophyll content. Canopy

temperature increased with an increase in GRD severity although the correlation was weak ( $r = 0.42$ ) at beginning of maturity. GRD is associated with damage of the leaf xylem (Favali, 1977) and this could limit the water transport to the leaves hence causing reduced transpirational cooling. The findings in this study support our hypothesis that there are HTP-derived indices that are correlated with visual scores of LLS and GRD symptoms. Therefore, indices which are highly correlated with LLS and GRD scores can be applied as secondary traits for indirect selection for disease resistance.

## Broad-Sense Heritability

Although the visual scores were highly correlated to several VIs, this alone is not enough to justify replacement of visual scores. Broad sense heritability ( $H^2$ ), also known as repeatability (Piepho and Mohring, 2007) was measured for each of the sensor-derived indices taken at the same time as the visual scores. The measurement of  $H^2$  using different methods (HTP-derived traits and visual scores) could be an estimate of measurement error since the genotypes are constant and environmental effect should be negligible (Piepho and Mohring, 2007; Crain et al., 2016). A high  $H^2$  is indicative of the precision and predictive ability for the secondary traits associated with LLS and GRD resistance (Crain et al., 2016, 2018). Several VIs such as NDVI, GA, GGA, and  $v^*$  which were strongly associated with the disease visual scores had comparable or higher  $H^2$  making them suitable for selection. The high heritability is attributed to high genetic variation which is essential for genetic gain in breeding (Table 6). High NDVI  $H^2$  values have also been reported in other studies in cotton (0.28–0.9) and wheat (Andrade-Sanchez et al., 2013; Crain et al., 2016). The high  $H^2$  could indicate the consistence of the measurements across the different environments (Andrade-Sanchez et al., 2013). The visual scores of LLS had high heritability ( $H^2 = 0.85$ ) as early as peg formation. This can be attributed to the high variation within the population for LLS resistance. Similar results were reported for  $H^2$  for LLS resistance based on leaf defoliation by Anderson et al. (1991). In contrast to LLS, the broad-sense heritability of GRD was lower compared to those in previous studies ( $H^2 = 0.74$ ) (Merwe et al., 1999). This could be attributed to the low variation of VIs at that time of the season (De Swaef et al., 2021). Therefore, NDVI, hue,  $v^*$ , CSI, GA, and GGA which were highly correlated with the visual scores and had high  $H^2$  can be applied for indirect selection for LLS and GRD resistance in groundnut breeding, if timing is toward later part of the season. These findings confirm our hypothesis that HTP derived indices are highly heritable.

## Ordinal Logistic Models

Disease classification models developed in this study were effective in distinguishing disease symptoms. The LLS and GRD models had classification accuracies of 64 and 45% respectively. The LLS select model contained NDVI, CSI, and  $b^*$  indices. The NDVI in the model is associated with canopy biomass (Cabrera-Bosquet et al., 2011) and canopy health (Kefauver et al., 2015) which are both affected by LLS symptoms. The CSI and  $b^*$  represent canopy color changes from green to yellow (Zaman-Allah et al., 2015). This is associated with chlorophyll deterioration among susceptible genotypes (Singh et al., 2011). The GRD model contained RGB indices hue,  $a^*$ , and  $uv$  which represent canopy color. These indices are associated with the presence of green biomass within the plot (Serret et al., 2020). Hue and  $a^*$  represent the greenness of the canopy while  $uv$  represents both the green and yellow part of the canopy (De Swaef et al., 2021), which could include the green and chlorotic symptoms of GRD in our case (Naidu et al., 1998; Waliyar et al., 2007; Okello et al., 2014). The accuracy of the models increased to 91 and 84% for LLS (Table 7) and GRD (Table 8) classification models,

respectively. The nearest score method takes into account that different evaluators, or the same evaluator could rate the same plot differently depending on the time of the day and number of plots scored (Sarkar et al., 2021). For example, on the 1–9 LLS scale, a score of 6 could be under scored as a 5 or over scored as a 7. Similarly, on 1–5 GRD severity scale, a score of 2 could be scored as a 1 or a 3. The method assumes that the model can classify a plot as 1 or 3 instead of a 2 because the reflectance from the plot could be closer to that from a plot scored as a 1 or a 3. This method is the closest to the visual scores by the breeder also gives the because it takes into account that the model is trained based on the visual scores which are not perfect. This misclassification could also be attributed to the differences among the groundnut market types; the three market types have different leaf color, plant height and canopy architecture. These small differences could affect the visual score from one plot to another. The nearest scores method has a higher accuracy and it could be actively applied for selection for LLS and GRD resistance since it increases chances of selecting for genotypes of interest. For example, when selecting for resistance for GRD, a cut off is set at score of 2 (resistant). When the nearest score method is applied, there are higher chances of selecting a score of 1 (highly resistant) or 3 (moderately resistant) (Table 3). The logistic models developed in this study had high accuracy using the nearest score method when applied to independent data sets (Tables 9, 10) indicating the effectiveness of the models and method for selection for resistance in different environments. The findings of this study affirm our hypothesis that VI-derived models can be consistent for routine selection for resistance in breeding programs.

## CONCLUSION

Results from this work present novel methods of screening for LLS and GRD resistance using HTP derived VIs. These results illustrate that HTP derived indices from handheld sensors such as the RGB camera, GreenSeeker, and the thermal camera can complement or even act as alternatives to the visual scores used by breeders. These novel methods have the potential to enhance faster and reduced cost development of new varieties. However, for such methods to be adopted by breeders for active deployment in selection, they have to be highly automated to eliminate drudgery. The application of individual sensors reduced the data collection time by almost half, but the cumulative time spent using the three different sensors was almost the same as that spent when using conventional methods. Therefore, these methods did not meet the desired throughput and might not be feasible in cases where the experiments are very large. Nonetheless, there is potential to improve the methods described in this study. More efficient methods of data collection such as use of unmanned aerial vehicles (UAVs). Recent advances in plant phenotyping involve the use of unmanned aerial vehicles (UAVs) to collect several images generating large amounts of data. Several studies have reported that UAVs are faster and more effective for phenotyping large populations for traits such as height and drought tolerance in groundnut breeding (Sarkar et al., 2020, 2021) hence providing the desired high-throughput.

This study therefore lays the foundation for investment in such more advanced equipment in groundnut breeding for selection for resistance to late leaf spot and groundnut rosette disease which are the most important foliar diseases in Uganda and SSA.

## DATA AVAILABILITY STATEMENT

The original contributions presented in the study are included in the article/**Supplementary Material**, further inquiries can be directed to the corresponding author.

## AUTHOR CONTRIBUTIONS

MB wrote the proposal and won the grant under the PIL. DO selected the study materials. IC and DO designed the experiments. IC took the field measurements, carried out the data analysis with assistance from SS, RO, and TO and wrote the manuscript under the supervision of DO. RO and MB contributed to the editing and reviewing of the manuscript. All authors contributed to the article and approved the submitted version.

## REFERENCES

- Anderson, W. F., Holbrook, C. C., and Wynne, J. C. (1991). Heritability and early-generation selection for resistance to early and late leafspot in peanut. *Crop Sci.* 31, 588–593. doi: 10.2135/cropsci1991.0011183X003100030008x
- Andrade-Sanchez, P., Gore, M. A., Heun, J. T., Thorp, K. R., Carmo-Silva, A. E., French, A. N., et al. (2013). Development and evaluation of a field-based high-throughput phenotyping platform. *Funct. Plant Biol.* 41, 68–79. doi: 10.1071/FP13126
- Araus, J. L., and Cairns, J. E. (2014). Field high-throughput phenotyping: the new crop breeding frontier. *Trends Plant Sci.* 19, 52–61. doi: 10.1016/j.tplants.2013.09.008
- Araus Ortega, J. L., Kefauver, S. C., Zaman Allah, M., Olsen, M. S., and Cairns, J. E. (2018). Translating high throughput phenotyping into genetic gain. *Trends Plant Sci.* 5, 451–466. doi: 10.1016/j.tplants.2018.02.001
- Bates, D., Mächler, M., Bolker, B. M., and Walker, S. C. (2015). Fitting linear mixed-effects models using lme4. *J. Stat. Softw.* 67:1. doi: 10.18637/jss.v067.i01
- Boote, K. J. (1982). Growth Stages of Peanut (*Arachis hypogaea* L.). *Peanut Sci.* 9, 35–40. doi: 10.3146/i0095-3679-9-1-11
- Borra-Serrano, I., De Swaef, T., Aper, J., Ghesquiere, A., Mertens, K., Nuytens, D., et al. (2018). Towards an objective evaluation of persistency of *Lolium perenne* swards using UAV imagery. *Euphytica* 214, 1–18. doi: 10.1007/s10681-018-2208-1
- Buchaillot, M., Gracia-Romero, A., Vergara-Diaz, O., Zaman-Allah, M. A., Tarekne, A., Cairns, J. E., et al. (2019). Evaluating maize genotype performance under low nitrogen conditions using RGB UAV phenotyping techniques. *Sensors* 19:1815. doi: 10.3390/s19081815
- Cabrera-Bosquet, L., Molero, G., Stellacci, A., Bort, J., Nogués, S., and Araus, J. (2011). NDVI as a potential tool for predicting biomass, plant nitrogen content and growth in wheat genotypes subjected to different water and nitrogen conditions. *Cereal Res. Comm.* 39, 147–159. doi: 10.1556/CRC.39.2011.15
- Casadesús, J., Kaya, Y., Bort, J., Nachit, M. M., Araus, J. L., Amor, S., et al. (2007). Using vegetation indices derived from conventional digital cameras as selection criteria for wheat breeding in water-limited environments. *Ann. Appl. Biol.* 150, 227–236. doi: 10.1111/j.1744-7348.2007.00116.x

## FUNDING

This study was made possible by the generous support of the American people through the United States Agency for International Development (USAID) through Cooperative Agreement No. 7200AA 18CA00003 to the University of Georgia as management entity for U.S. Feed the Future Innovation Lab for Peanut (2018–2023).

## ACKNOWLEDGMENTS

We would like to thank the USAID through the Peanut Innovation Lab for funding the study and the staff of NaSARRI-Groundnut improvement program.

## SUPPLEMENTARY MATERIAL

The Supplementary Material for this article can be found online at: <https://www.frontiersin.org/articles/10.3389/fpls.2022.912332/full#supplementary-material>

- Casadesús, J., and Villegas, D. (2014). Conventional digital cameras as a tool for assessing leaf area index and biomass for cereal breeding. *J. Integr. Plant Biol.* 56, 7–14. doi: 10.1111/jipb.12117
- Cheng, H. D., Jiang, X. H., Sun, Y., and Wang, J. (2001). Color image segmentation: advances and prospects. *Pat. Recogn.* 34, 2259–2281. doi: 10.1016/S0031-3203(00)00149-7
- Cheng, J. J., Li, H., Ren, B., Zhou, C. J., Kang, Z. S., and Huang, L. L. (2015). Effect of canopy temperature on the stripe rust resistance of wheat. *New Zeal. J. Crop Hortic. Sci.* 43, 306–315. doi: 10.1080/01140671.2015.1098708
- Cobb, J. N., Juma, R. U., Biswas, P. S., Arbelaez, J. D., Rutkoski, J., Atlin, G., et al. (2019). Enhancing the rate of genetic gain in public-sector plant breeding programs: lessons from the breeder's equation. *Theoret. Appl. Genet.* 132, 627–645. doi: 10.1007/s00122-019-03317-0
- Crain, J. L., Mondal, S., Rutkoski, J., Singh, R. P., and Poland, J. (2018). Combining high-throughput phenotyping and genomic information to increase prediction and selection accuracy in wheat breeding. *Plant Gen.* 11:1. doi: 10.3835/plantgenome2017.05.0043
- Crain, J. L., Wei, Y., Barker, J. III, Thompson, S. M., Alderman, P. D., Reynolds, M., et al. (2016). Development and deployment of a portable field phenotyping platform. *Crop Sci.* 56, 965–975. doi: 10.2135/cropsci2015.05.0290
- Culbreath, A. K., Stevenson, K. L., and Brenneman, T. B. (2002). Management of late leaf spot of peanut with benomyl and chlorothalonil: a study in preserving fungicide utility. *Plant Dis.* 86, 349–355. doi: 10.1094/PDIS.2002.86.4.349
- Davies, J. C. (1975). Insecticides for the control of the spread of groundnut rosette disease in Uganda. *PANS Pest Articles News Summ.* 21, 1–8. doi: 10.1080/09670877509411481
- De Swaef, T., Maes, W. H., Aper, J., Baert, J., Coughnon, M., Reheul, D., et al. (2021). Applying RGB-and thermal-based vegetation indices from UAVs for high-throughput field phenotyping of drought tolerance in forage grasses. *Remote Sens.* 13:147.
- Deom, C. M., and Okello, D. K. (2018). “Developing improved varieties of groundnut,” in *Achieving sustainable cultivation of grain legumes*, ed. S. Sivasankar (Cambridge, MA: Burleigh Dodds Science Publishing), 2. doi: 10.4324/9781351114370-12

- FAOSTAT (2019). *Food and Agriculture Organization of the United Nations*. Rome: FAOSTAT Statistical Database.
- Farrell, J. A. K. (1976). Effects of groundnut sowing date and plant spacing on rosette virus disease in Malawi. *Bull. Entomol. Res.* 66, 159–171. doi: 10.1017/S000748530000657X
- Favali, M. A. (1977). Ultrastructural study of systemic lesions induced by peanut rosette virus in peanut leaves. *J. Phytopathol.* 89, 68–75. doi: 10.1111/J.1439-0434.1977
- Finkel, E. (2009). With ‘Phenomics,’ Plant Scientists Hope to Shift Breeding Into Overdrive Data Integrity Report Sends Journals Back to the Drawing Board. *Science* 325, 380–381. PMID:NOPsMID doi: 10.1126/science.325\_380
- Franke, J., and Menz, G. (2007). Multi-temporal wheat disease detection by multi-spectral remote sensing. *Precis. Agricult.* 8, 161–172. doi: 10.1007/s11119-007-9036-y
- Gehan, M. A., and Kellogg, E. A. (2017). High-throughput phenotyping. *Am. J. Bot.* 104:4. doi: 10.3732/ajb.1700044
- Giordano, D. F., Pastor, N., and Palacios, S. (2021). Peanut leaf spot caused by *Nothopassalora personata*. *Trop. Plant Pathol.* 46, 139–151. doi: 10.1007/s40858-020-00411-3
- Gitelson, A. A., and Merzlyak, M. N. (1996). Signature analysis of leaf reflectance spectra: algorithm development for remote sensing of chlorophyll. *J. Plant Physiol.* 148, 494–500. doi: 10.1080/014311697217558
- Govaerts, B., and Verhulst, N. (2010). *The normalized difference vegetation index (NDVI) GreenSeeker TM handheld sensor: Toward the integrated evaluation of crop management Part A: Concepts and case studies*. Mexico, D.F: CIMMYT.
- Holland, J. B., Nyquist, W. E., and Cervantes-Martínez, C. T. (2003). Estimating and Interpreting Heritability for Plant Breeding: an Update. *Plant Breed. Rev.* 2003, 9–112. doi: 10.1002/9780470650202.ch2
- Kefauver, S. C., El-Haddad, G., Vergara-Díaz, O., and Araus, J. L. (2015). “RGB picture vegetation indexes for high-throughput phenotyping platforms (HTPPs),” in *Remote Sensing for Agriculture, Ecosystems, and Hydrology XVII*, Vol. 9637. (Washington, DC: International Society for Optics and Photonics), 96370J. doi: 10.1117/12.2195235
- Kishore, G. K., Pande, S., and Podile, A. R. (2005). Biological control of late leaf spot of peanut (*Arachis hypogaea*) with chitinolytic bacteria. *Phytopathology* 95, 1157–1165. doi: 10.1094/PHYTO-95-1157
- Knipling, E. B. (1970). Physical and physiological basis for the reflectance of visible and near-infrared radiation from vegetation. *Rem. Sens. Env.* 1, 155–159.
- Liu, H. Q., and Huete, A. (1995). A feedback based modification of the NDVI to minimize canopy background and atmospheric noise. *IEEE Trans. Geosci. Remote Sens.* 33, 457–465. doi: 10.1109/36.377946
- Max, A., Wing, J., Weston, S., Williams, A., Keefer, C., Engelhardt, A., et al. (2021). Package ‘caret’ R topics documented.
- Merwe, P. J. A., van der Reddy, L. J., Subrahmanyam, P., and Naidu, R. A. (1999). Criteria for selecting groundnut varieties in breeding for resistance to rosette disease. *South Afr. J. Plant Soil* 16, 56–58. doi: 10.1080/02571862.1999.10634846
- Milberg, P., Bergstedt, P., Fridman, J., Odell, G., and Westerberg, L. (2008). Observer bias and random variation in vegetation monitoring data. *J. Veget. Sci.* 19, 633–644. doi: 10.3170/2008-8-18423
- Mugisa, I. O., Karungi, J., Akello, B., Ochwo-ssemakula, M. K. N., Biruma, M., Okello, D. K., et al. (2016). Determinants of groundnut rosette virus disease occurrence in Uganda. *Crop Prot.* 79, 117–123. doi: 10.1016/j.cropro.2015.10.019
- Naidu, R. A., Bottenberg, H., Subrahmanyam, P., Kimmins, F. M., Robinson, D. J., and Thresh, J. M. (1998). Epidemiology of groundnut rosette virus disease: current status and future research needs. *Ann. Appl. Biol.* 132, 525–548. doi: 10.1111/j.1744-7348.1998.tb05227.x
- Natarajan, S., Basnayake, J., Wei, X., and Lakshmanan, P. (2019). High-throughput phenotyping of indirect traits for early-stage selection in sugarcane breeding. *Rem. Sens.* 11:2952. doi: 10.3390/rs11242952
- Oakes, J., and Balota, M. (2017). “Distinguishing plant population and variety with UAV-derived vegetation indices,” in *Autonomous Air and Ground Sensing Systems for Agricultural Optimization and Phenotyping II*, Vol. 10218. (Washington, DC: International Society for Optics and Photonics), 102180G. doi: 10.1117/12.2262631
- Oerke, E. C., Steiner, U., Dehne, H. W., and Lindenthal, M. (2006). Thermal imaging of cucumber leaves affected by downy mildew and environmental conditions. *J. Exp. Bot.* 57, 2121–2132. doi: 10.1093/jxb/erj170
- Okello, D. K., Akello, L. B., Tukamuhabwe, P., Odong, T. L., Adriko, J., and Deom, C. M. (2014). Groundnut rosette disease symptoms types distribution and management of the disease in Uganda. *Afr. J. Plant Sci.* 8, 153–163. doi: 10.5897/AJPS2014.1164
- Okello, D. K., Biruma, M., and Deom, C. M. (2010). Overview of groundnuts research in Uganda: past, present and future. *Afr. J. Biotechnol.* 9, 6448–6459.
- Piepho, H. P., and Mohring, J. (2007). Computing heritability and selection response from unbalanced plant breeding trials. *Genetics* 177, 1881–1888. doi: 10.1534/genetics.107.074229
- Pilon, C., Snider, J. L., Sobolev, V., Chastain, D. R., Sorensen, R. B., Meeks, C. D., et al. (2018). Assessing stomatal and non-stomatal limitations to carbon assimilation under progressive drought in groundnut (*Arachis hypogaea* L.). *J. Plant Physiol.* 231, 124–134. doi: 10.1016/j.jplph.2018.09.007
- R Core Team (2021). R: A language and environment for statistical computing. Vienna: R Foundation for Statistical Computing.
- Raza, S.-A., Prince, G., Clarkson, J. P., and Rajpoot, N. M. (2015). Automatic Detection of Diseased Tomato Plants Using Thermal and Stereo Visible Light Images. *PLoS One* 10:e0123262. doi: 10.1371/journal.pone.0123262
- Rueden, C. T., Schindelin, J., Hiner, M. C., DeZonia, B. E., Walter, A. E., Arena, E. T., et al. (2017). ImageJ2: ImageJ for the next generation of scientific image data. *BMC Bioinform.* 18, 1–26. doi: 10.1186/s12859-017-1934-z
- Sancho-Adamson, M., Trillas, M. L., Bort, J., Fernandez-Gallego, J. A., and Romanyà, J. (2019). Use of RGB vegetation indexes in assessing early effects of Verticillium wilt of olive in asymptomatic plants in high and low fertility scenarios. *Remote Sens.* 11:607. doi: 10.3390/rs11060607
- Sarkar, S., Cazenave, A. B., Oakes, J., McCall, D., Thomason, W., Abbot, L., et al. (2020). High-throughput measurement of peanut canopy height using digital surface models. *Phenome J.* 3:e20003. doi: 10.1002/ppj2.20003
- Sarkar, S., Ramsey, A. F., Cazenave, A.-B., and Balota, M. (2021). Groundnut Leaf Wilting Estimation From RGB Color Indices and Logistic Models. *Front. Plant Sci.* 12, 1–16. doi: 10.3389/fpls.2021.658621
- Schindelin, J., Arganda-Carreras, I., Frise, E., Kaynig, V., Longair, M., Pietzsch, T., et al. (2012). Fiji: An open-source platform for biological-image analysis. *Nat. Methods* 9, 676–682. doi: 10.1038/nmeth.2019
- Serret, M. D., Al-Dakheel, A. J., Yousfi, S., Fernández-Gallego, J. A., Elouafi, I. A., and Araus, J. L. (2020). Vegetation indices derived from digital images and stable carbon and nitrogen isotope signatures as indicators of date palm performance under salinity. *Agricult. Water Manag.* 230:105949. doi: 10.1016/j.agwat.2019.105949
- Singh, M. P., Erickson, J. E., Boote, K. J., Tillman, B. L., van Bruggen, A. H., and Jones, J. W. (2011). Photosynthetic consequences of late leaf spot differ between two peanut cultivars with variable levels of resistance. *Crop Sci.* 51, 2741–2748. doi: 10.2135/cropsci2011.03.0144
- Subrahmanyam, P., McDonald, D., Waliyar, F., Reddy, L. J., Nigam, S. N., Gibbons, R. W., et al. (1995). *Screening methods and sources of resistance to rust and late leaf spot of groundnut. Information Bulletin no. 47*. Hyderabad: International Crops Research Institute for the Semi-Arid Tropics.
- USDA-NASS (2021). *U.S. Department of Agriculture. 2020*. Washington, DC: National Agricultural Statistics Service. Agricultural Statistics, U.S. Government Printing Office.
- Visscher, P. M., Hill, W. G., and Wray, N. R. (2008). Heritability in the genomics era—concepts and misconceptions. *Nat. Rev. Genet.* 9, 255–266. doi: 10.1038/nrg2322
- Waliyar, F., Kumar, P. L., Ntare, B. R., Monyo, E., Nigam, S. N., Reddy, A. S., et al. (2007). *A century of research on groundnut rosette disease and its management. Information Bulletin no. 75*. ICRISAT: atancheruvu.
- Wang, X., Silva, P., Bello, N. M., Singh, D., Evers, B., Mondal, S., et al. (2020). Improved Accuracy of High-Throughput Phenotyping From Unmanned Aerial Systems by Extracting Traits Directly From Orthorectified Images. *Front. Plant Sci.* 11, 1–14. doi: 10.3389/fpls.2020.587093
- Wightman, J. A., and Amin, P. W. (1988). Groundnut pests and their control in the semi-arid tropics. *Internat. J. Pest Manag.* 34, 218–226. doi: 10.1080/09670878809371245
- Yuan, H., Bennett, R. S., Wang, N., and Chamberlin, K. D. (2019). Development of a Groundnut Canopy Measurement System Using A Ground-based LiDAR Sensor. *Front. Plant Sci.* 10:203. doi: 10.3389/FPLS.2019.0203



- Zaman-Allah, M., Vergara, O., Araus, J. L., Tarekegne, A., Magorokosho, C., Tejada, P. J. Z., et al. (2015). Unmanned aerial platform - based multi - spectral imaging for field phenotyping of maize. *Plant Methods* 2015, 1–10. doi: 10.1186/s13007-015-0078-2
- Zhou, B., Elazab, A., Bort, J., Vergara, O., Serret, M. D., and Araus, J. L. (2015). Low-cost assessment of wheat resistance to yellow rust through conventional RGB images. *Comp. Electron. Agricul.* 116, 20–29. doi: 10.1016/j.compag.2015.05.017

**Author Disclaimer:** The contents are the responsibility of the authors and do not necessarily reflect the views of USAID or the United States Government.

**Conflict of Interest:** The authors declare that the research was conducted in the absence of any commercial or financial relationships that could be construed as a potential conflict of interest.

**Publisher's Note:** All claims expressed in this article are solely those of the authors and do not necessarily represent those of their affiliated organizations, or those of the publisher, the editors and the reviewers. Any product that may be evaluated in this article, or claim that may be made by its manufacturer, is not guaranteed or endorsed by the publisher.

Copyright © 2022 Chapu, Okello, Okello, Odong, Sarkar and Balota. This is an open-access article distributed under the terms of the Creative Commons Attribution License (CC BY). The use, distribution or reproduction in other forums is permitted, provided the original author(s) and the copyright owner(s) are credited and that the original publication in this journal is cited, in accordance with accepted academic practice. No use, distribution or reproduction is permitted which does not comply with these terms.



# A Substantial Role of Agro-Textiles in Agricultural Applications

Neha Sharma<sup>1,2</sup>, Ben Allardyce<sup>2</sup>, Rangam Rajkhowa<sup>2</sup>, Alok Adholeya<sup>1,2</sup> and Ruchi Agrawal<sup>1,2\*</sup>

<sup>1</sup> TERI-Deakin Nanobiotechnology Centre, The Energy and Resources Institute, TERI Gram, Gual Pahari, Gurugram, India,

<sup>2</sup> Institute for Frontier Materials, Deakin University, Waurn Ponds, VIC, Australia

Agro-textiles have been used in the agriculture sector for thousands of years and are an attractive tool for the protection of crops during their entire lifecycle. Currently, the agro-textile market is dominated by polyolefins or petrochemical-based agro-textiles. However, climate change and an increase in greenhouse gas emissions have raised concern about the future oil-based economy, and petroleum-based agro-textiles have become expensive and less desirable in the modern world. Other products include agro-textiles based on natural fibers which degrade so fast in the environment that their recovery from the field becomes difficult and unattractive even by efficient recycling or combustion, and their lifetime is usually limited to 1 or a maximum of 2 years. Hence, the development of bio-based agro-textiles with a reduced impact on the environment and with extended durability is foreseen to initiate the growth in the bio-based economy. The world is gradually preparing the shift toward a bio-based economy, and research for sustainable bio-based alternatives has already been initiated. This review provides insight into the various agro-textiles used currently in agriculture and the research going on in the area of agro-textiles to offer alternative solutions to the current agro-textile market.

**Keywords:** agro-textile, non-conventional fibers, chemical compositions, retting, application

## OPEN ACCESS

### Edited by:

Miha Humar,  
University of Ljubljana, Slovenia

### Reviewed by:

Mohd Yusuf,  
Glocal University, India  
Sheraz Ahmad,  
National Textile University, Pakistan

### \*Correspondence:

Ruchi Agrawal  
Dr.ruchiagrawal010@gmail.com

### Specialty section:

This article was submitted to  
Technical Advances in Plant Science,  
a section of the journal  
Frontiers in Plant Science

**Received:** 14 March 2022

**Accepted:** 02 May 2022

**Published:** 21 June 2022

### Citation:

Sharma N, Allardyce B, Rajkhowa R,  
Adholeya A and Agrawal R (2022) A  
Substantial Role of Agro-Textiles in  
Agricultural Applications.  
Front. Plant Sci. 13:895740.  
doi: 10.3389/fpls.2022.895740

## INTRODUCTION

Globally, one of the major issues is food security due to the threat of climatic changes caused by the utilization of non-biodegradable petroleum-based agricultural products. A few reports demonstrated that approximately 10–40% losses occurred in crop production because of the drastic increase in climatic temperature. This created a driving force in the agro-textile sectors to improve the yield and quality of the crop every year (Gangopadhyay and Hira, 2010). Current cultivation practices involve the utilization of herbicides and pesticides to prevent crop losses, however, these interventions are expensive and have a long-lasting ecological impact on soil microflora and the environment (Chowdhury et al., 2017). With a significant increase in environmental awareness and development in technology, considerable attention has been diverted to the utilization of textile fibers in agriculture (Kasirajan and Ngouajio, 2012). The textile sector plays a vital role in the development and circulation of the world economy, so it is considered one of the largest industries among numerous sectors around the world. By utilizing biotechnology, the textile sector brings a revolution to textile processing. Textile processing has led to the synthesis of a huge amount of cellulose fibers that can be used in multiple sectors ranging from biomedical to agriculture (Yusuf, 2021). The cellulose-based agricultural products are environmentally friendly with low manufacturing cost. Subsequently, the other concerns associated with petroleum-based products

can be reduced along with greenhouse gas emissions (Janaswamy et al., 2022). Agro-textile products (shade nets, harvest nets, and mulch mats) are capable of supporting agriculture by protecting crops from harsh weather conditions and unwanted pests without impacting the environment as these textile products are biodegradable and non-toxic (Bhavani et al., 2017).

Agro-textiles also help in water conservation, moisture retention, weed suppression, and light reflection (Kumar, 2017). Agro-textiles prevent the soil from drying out and maintain homogeneity thereby increasing the crop yield. Agro-textiles restrict the farmer from the overutilization of harmful pesticides that have a long-lasting impact on the soil as well as the microflora through the utilization of agro-textile covers such as weed control mats, crop covers, and others. The best-known products are shade nets and thermal screens; their usage can save up to 40% on energy in heating greenhouses. The utilization of shades and nets further improves the quality of fruit, prevents staining, and improves the crop by maintaining the overall uniformity in terms of color. Crop covers sustain an optimal micro-climate which protects plants from adverse weather conditions (Bhavani et al., 2017). Various remarkable properties of agro-textile-based products in agriculture are resistant to ultraviolet radiation and micro-organisms and have high tensile strength and biodegradability over petroleum-based products which make them suitable aspirants to overcome numerous conventional problems of agriculture. Textile covers are capable of retaining 15–60 g/m<sup>2</sup> of water and some tend to retain around 100–500 g/m<sup>2</sup> which further facilitates the availability of water under drought conditions (Agarwal, 2013; Kumar, 2017).

## Status of the Global Market

The global market of the agro-textile industry is estimated at US\$9.37 billion in 2021 and is expected to reach US\$13.04 billion by 2028 with a Compound Annual Growth Rate (CAGR) of 4.7%. A report of the global agro-textile market published in

2021 showed that agro-textiles have a US\$ 8.4 billion market that accounts for 6% of the total technical textile market globally. Global demand is directed by developing countries such as China, India, and Brazil (Global Agro Textiles Market Size, Share & Trends Analysis Report by Product by Application by Region, and Segment Forecasts, 2021–2028)<sup>1</sup>. Commercialisation of bio-based agricultural products with increasing global farming standards and technologies is expected to drive the market in the expected period. Asia Pacific is estimated to witness the fastest CAGR from 2021 to 2028. The annual growth rate is credited to the uplifting demand for high-quality agriculture products and increasing awareness of advanced materials by the farmers in the agriculture sector (<https://www.researchandmarkets.com/reports/4479690/global-agro-textiles-market-size-share-and>). The agro-textile market in India is estimated to reach US\$ 14.3 billion in 2025 at a CAGR of 5.5% from 2017 to 2025 (Technavio EMIS Database, 2017). The major vendors manufacturing agro-textiles in the world are given in **Table 1**.

## Stratification of Fibers Utilized in Agriculture

Textile fibers are classified as natural fibers and man-made fibers as depicted in **Figure 1**. Natural agro-textiles are eco-friendly and are obtained from plant-based or animal-based fibrous materials (Swapan et al., 2016; Scarlat et al., 2017; Restrepo et al., 2019). Plant-based fibers are the dominant form of natural fibers and are obtained from various parts of plants such as seeds, stems, leaves, and fruit. Plant fibers are renewable, biodegradable, and have a long history in human civilization (Blackburn, 2005; Mwaikambo, 2006; Mather and Wardman, 2010). Agro-based fibers are composed of cellulose, hemicellulose, and lignin, and also have silica contents as shown in **Table 2**.

<sup>1</sup>Indian Technical Textile Association. Available online at: <http://ittaindia.org/?q=Agro-textile-service-view>.

**TABLE 1** | Agro-textile manufacturing companies around the globe (Indian Technical Textile Association, dataset taken from global agro-textile market).

Company name	Location	Detail of products
Garware Wall Ropes Ltd.	Maharashtra, India	Fisheries, aquaculture, yarn and threads, coated fabrics, agriculture products
Rishi TechTex Ltd.	Daman & Diu, India	Agriculture/ horticulture field, wind breakers, drying of grapes, etc.
Neo Corp Ltd.	Regional offices: New Delhi, Kolkata, Ahmedabad, India	Agro-textiles, geotextiles, textile products for industrial packaging, etc.
CTM Agro Textile Ltd.	Ahmedabad, India	Shade nets, mulching film, greenhouses, anti-insect nets, vermin beds, crop covers
Fibreweb India Ltd.	Daman & Diu, India	Spun-bonded non-woven polypropylene fabrics
B & V Agro Irrigation Co.	Maharashtra, India.	Shade nets, weed mats, insect mesh, anti-hail nets, monofilament
Admire Fibretex Pvt. Ltd.	Gujarat, India	Crop cover, fruit cover, mulching, weed barrier, garden cover
Fortune Agro Net	Gujarat, India	Shading agro nets, anti-hail nets, greenhouse film, sun shade nets mulching sheets, bird protection nets, etc.
Mechanische Netzfabrik Walter Kremmin GmbH & Co. KG	Germany	Nets and ropes
A-BOS limited	United States of America	Ropes and outdoor products
ACE Geosynthetics Enterprise Co., Ltd.	Taiwan	Geotextiles, geogrids

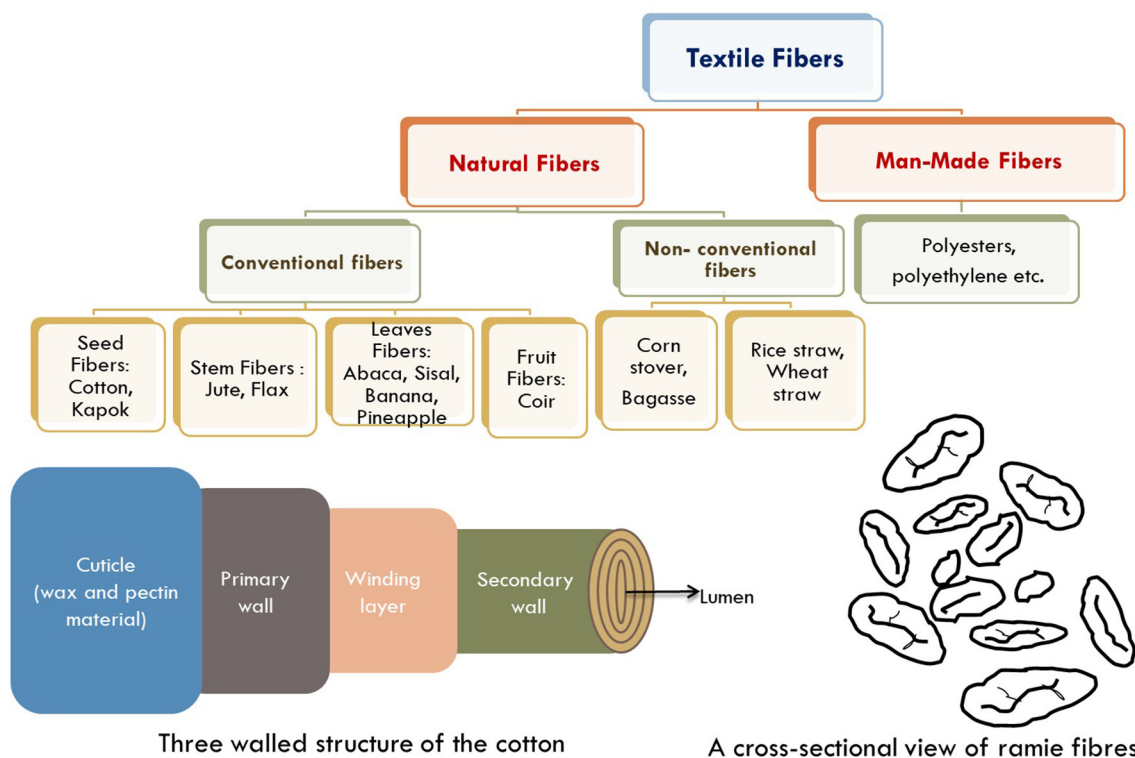


**FIGURE 1 |** Classification of fibers with three-walled structure of cotton and cross-section view of ramie fibers.

**TABLE 2 |** Composition and properties of conventional fibers.

Natural fibers	Source	Cellulose (%)	Lignin (%)	Hemicellulose (%)	Diameter of fiber (μm)	Properties	References
Cotton	Seed	80–90		4–6	12–45	Hydrophilic, stable in water, resistant to alkali	Sfiligoj et al., 2013; Mathangadeera et al., 2020
Kapok	Seed	64	13	10	30–36	Excellent thermal and insulating properties, high buoyancy	Rijavec, 2008; Chen et al., 2013; Liu et al., 2016
Flax	Stem	60–70	2–3	17	40–80	Crystalline structure contributing to strength	Blackburn, 2005; Mohanty et al., 2005; Dai, 2006; Mather and Wardman, 2010; Goudenhooff et al., 2019
Jute	Stem	61–71	12–13	14–20		Antistatic and highly insulating	Lipp-Symonowicz et al., 2011; Salman, 2020
Hemp	Stem	77	1.7		16–50	Excellent moisture resistance	Mohanty et al., 2005; Nykter, 2006; Tara and Jagannatha, 2011; Musio et al., 2018
Ramie	Stem	93	0.65	2.5	34	Excellent mechanical properties, resistant to bacteria, mildew, and insects	Mather and Wardman, 2010; Cheng et al., 2020
Kenaf	Stem	45–57	8–13	21.5	38	Tensile strength	Mohanty et al., 2005; Tara and Jagannatha, 2011; Sreenivas et al., 2020
Sisal	Leaf	70	10–20	10–15	200–400	Durable, resistant to saltwater decomposition	Mohanty et al., 2005; Iniya and Nirmalkumar, 2021
Abaca	Leaf	76.6	8.4	14.6	151	Strong, resistant to saltwater decomposition	Blackburn, 2005; Anthony et al., 2020
Henequen	Leaf	77	13	4.8	170	High tenacity	Blackburn, 2005
Coir	Fruit	43.4	45.8	0.25	150–400	Moisture absorption	Ching et al., 2018



**TABLE 3** | Characteristics of non-conventional fibers derived from agro-waste.

Non-conventional fibers	Length (mm)	Width ( $\mu\text{m}$ )	Crystallinity (%)	Properties	References
Corn stover	0.5–1.5	10–20	48–50	High tensile strength	Reddy and Yang, 2005
Sugarcane bagasse	0.8–2.8	10–34	–	High tensile strength	Reddy and Yang, 2005
Banana leaves	0.9–4.0	80–250	45	Light weight, strong moisture absorption	Subagyo and Chafidz, 2020
Wheat straw	1.32	12.9	55–65	Excellent strength and stiffness	Chen and Liu, 2014
Rice straw	0.92	8.1	40	Significant strength	Chen and Liu, 2014
Pineapple leaves	3–8	7–18	44–60	Higher bending properties	Franck, 2005
Bamboo fibers	2.0	6–12	–	Excellent thermal conductivity, high tenacity	Nayak and Mishra, 2016

## Non-conventional Plant Fibers for Agro-Textiles

Non-conventional plant fibers obtained from corn stover, bagasse, banana, wheat straw, rice straw, pineapple leaves fibers, etc., have potential utilization for crop improvement (Reddy and Yang, 2005). Non-conventional fibers are derived from lignocellulosic agricultural by-products and have potential utilization in textile and paper industries due to their inherent chemical and physical properties. The properties of lignocellulosic-based fiber depend on the chemical composition of the fiber, the source of the fiber, and the extraction procedures (Reddy and Yang, 2005). Generally, the cellulosic waste from crop residues and other agricultural wastes contains 31–60% cellulose, 11–38% pentosans, and 12–28% lignin (Himanish and Sudhir, 2004)<sup>2</sup>.

Due to the orientation of the elevated fibrils, the tensile strength of corn fibers is significantly good but the fibers have low elongation (Li et al., 2012). Various industries are utilizing sugar bagasse as raw material for biofuel production (Sun et al., 2004). The fiber surface of sugarcane bagasse is formed by parallel stripes and is partially covered with residual material whereas, the pith is a more fragile and fragmented structure containing pits, which are small pores connecting neighboring cells on the surface of the walls (Rezende et al., 2011).

Wheat straw is an agricultural residue that is accessible abundantly all over the world and has been used for various applications such as feedstock and energy production (Sain and Panthapulakkal, 2006). According to Liu et al. (2005), wheat straw has a unique physical structure that makes it a suitable candidate for structural composites. Bamboo fibers have the potential for the composite industry and possess numerous excellent properties (Liu and Hu, 2008; Khalil et al., 2012). The crystallinity and structural characteristics of various non-conventional fibers are depicted in **Table 3**.

## Approaches for Extraction of Fibers From Plant Sources

Natural fibers in their native form before any treatment have waxes and other substances on their surfaces that form a thick outer layer to protect the cellulose inside the fibers. The presence of encrusting substances causes the fibers to have an irregular appearance, as shown in **Figure 2**. Natural fibers are extracted through biological, chemical retting, mechanical, and enzymatic

methods. Retting is a process used to extract bast fibers by immersing them in water. Biological retting involves bacteria and fungi to remove lignin, pectin, and other unwanted substances from the fibers and facilitate the accessibility of cellulose (Reddy and Yang, 2005). Water retting is effectively performed using two bacteria (*Bacillus* and *Clostridium species*) whereas dew retting involves fungi (*Rhizomucor pusillus* and *Fusarium lateritium*) for effective removal of a non-cellulosic substance from the fibers (Reddy and Yang, 2005).

The chemical process involves the utilization of alkalis or mild acids for the extraction of fibers. In the case of alkali retting, sodium hydroxide is commonly used while in acid retting, sulfuric acid and oxalic acid are combined with detergent for efficient extraction of specific fibers. Various factors influence the quality of fibers, viz., duration of treatment, temperature, and concentration of chemicals (Reddy and Yang, 2005). Further, the steam explosion method is a greener approach for the extraction of fibers. It involves the disruption of the cell wall with the help of steam which tends to enhance the availability of cellulose (Gollapalli et al., 2002). The extraction process is listed in **Figure 3**.

The enzymatic extraction process involves a combination of enzymes such as pectinases, hemicellulases, and cellulases with pre- or post-chemical treatment. Reddy et al. investigated whether multi-enzyme complexes (10–15 enzymes) efficiently improve the quality of fibers (Reddy and Yang, 2005). Fibers are extracted from the stem through mechanical processing which involves decorticating machines (involving compressive force for stripping the barks, rinds, wood, and plant stalks for further processing). After decortication, fibers are chemically treated to remove lignin, pectin, etc. Another well-known example of cane separation is the Tilby process which separates sugarcane into three materials that are the outer skin, rind, and sugar-containing pith as shown in **Figure 4**. The outer skin of sugarcane is rich in wax that can be separated for pharmaceutical use. The separated rind can be used for the manufacture of paper, panels, and boards. The third part is pith which is used in the manufacturing of fibreboards, absorbents, and fillers (Tilley patent no. 3567511).

## Application of Agro-Textile Products in the Agriculture Sector

Natural and synthetic fibers are used in various applications related to agricultural crop practices (shade net, plant net, mulch net, insect net, bird net, etc.), horticulture, and floriculture (Basu,

<sup>2</sup>[http://www.agrotech.sasmira.org/about\\_coe.html#preamble](http://www.agrotech.sasmira.org/about_coe.html#preamble)

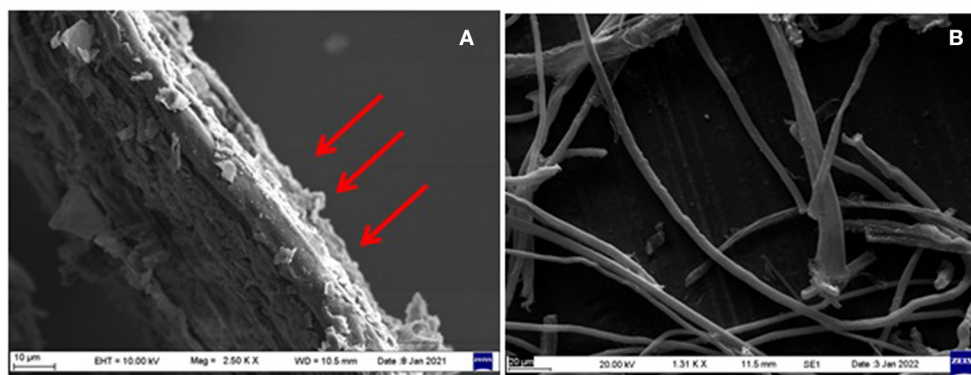


**FIGURE 2** | Scanning electron micrograph of: (A) untreated rice straw fibers, and (B) chemically treated rice straw fibers.

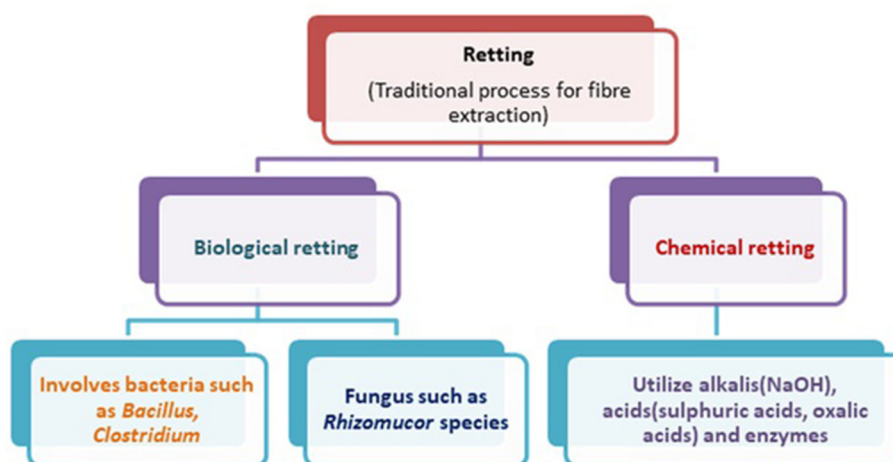


**FIGURE 3** | Schematic representation of retting process.

2011). Different agro-textile products are composed of either natural or synthetic fibers as shown in **Table 4**.

## Agro-Textile-Based Nets and Their Significance

A shade net is mainly made up of polypropylene and polyethylene which are treated with UV-resistant agents during fiber manufacturing to provide enhanced resistance to UV degradation. The polyethylene polymer is a relatively low-melting material (137°C). Bird protection nets are developed from polypropylene or high-density polyethylene (HDPE) monofilament yarn, these yarns are ultraviolet (UV)-stabilized and knitted into a durable mesh fabric (Preston, 2016). Sunscreen, insect meshes, weed control fabric, and greenhouse covers are typically made of UV-resistant polyethylene fibers.

Various agro-textile products are commonly implemented in the agricultural field such as bird protection nets which offer the passive protection of seeds, crops, and fruits from damage caused by birds. The open mesh net fabrics not only prevent

the crop from birds but also provide excellent air circulation which facilitates the optimum growth of the plant; plant nets are composed of polyolefin fibers which are mainly used for tomato crops. The purpose of the plant net is to keep the fruits away from the damp soil which eventually decays the crop. The plant net allows the fruit to grow vertically; monofil nets are designed to protect young branches and flowers against blustery weather and also prevent sand and wind erosion. The nets are set at a right angle to the wind to protect plants against the harmful effects of adverse weather conditions; root ball nets are designed in such a way that when transplanted, roots can protrude through them. They are developed for safe and speedy growth of young plants as the root system remains intact through the net; insect protection nets are made up of polyethylene monofilament meshes to preclude insects from the greenhouses; weed control fabrics halt the growth of unwanted weeds in an environmentally friendly manner and also allow air, water, and fertilizer to sieve through the fabric for plant growth; and fruit covers are made up of non-woven fabric which promotes better growth and enhances the harvest. They tend to protect

vegetables, fruits, and plants against snow, rain, frost, and heat (Preston, 2016).

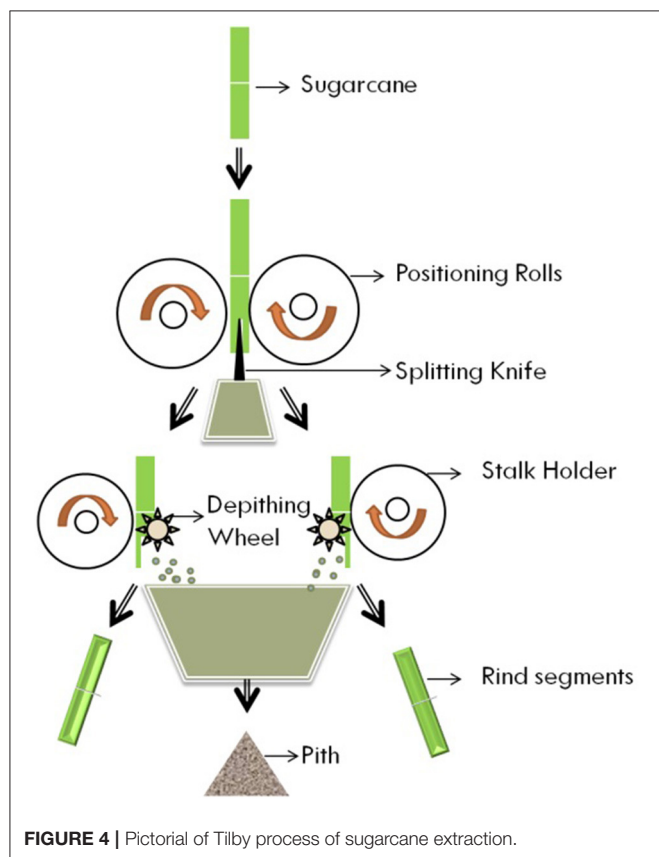


FIGURE 4 | Pictorial of Tilby process of sugarcane extraction.

## Coir-Based Products and Their Effect on Plants

A variety of coir-based products are widely used in agriculture such as erosion control blankets, basket liners, bio-rolls, grow sticks, etc. An erosion control blanket is composed of a woven coir mat that protects seeds or seedlings from wind and rain and further facilitates growth, it also protects soil from erosion and mulching action. The basket liners of the coir provide better aeration for growth as air can flow more effectively through the holes of the coir pad. They also help in the vigorous growth of roots.

Bio-rolls are composed of non-woven coir filled with a coir pith composite which facilitates rapid root growth. A growth stick consists of a wooden pole wrapped with coir fibers which provides support to the plant or a creeper. Other natural fibers such as hemp and sisal are used to develop baler twines which are made up of two or three threads twisted together. Baler twines are used for crop wrapping (tomato, grape yards) (Bhavani et al., 2017).

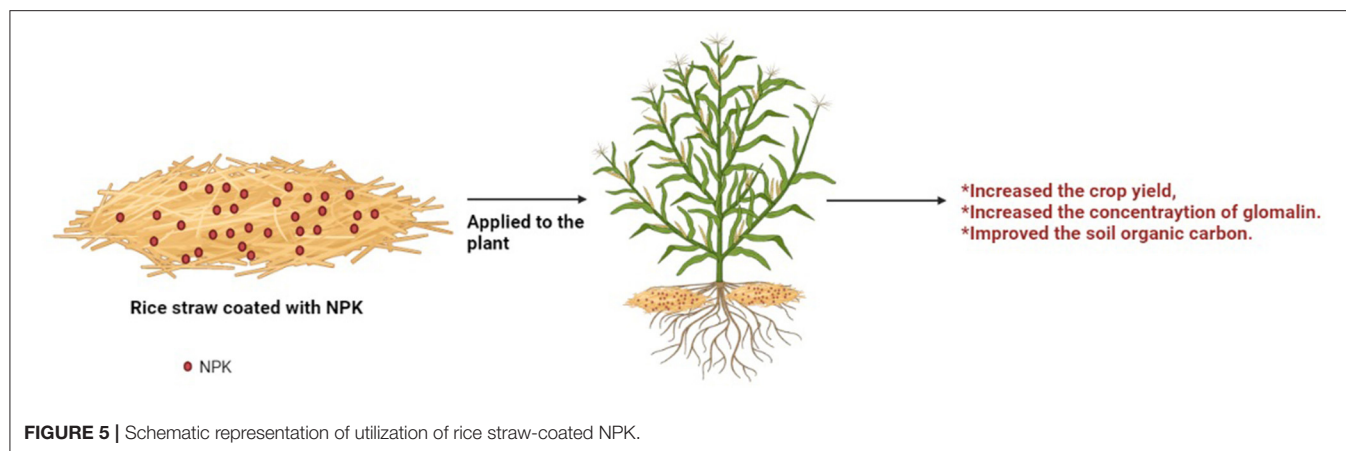
## Agro-Textile-Based Delivery of Fertilizers for Enhancing Plant Yield

Agro-textiles are used as a carrier material where fertilizers are coated through absorption or adsorption onto the non-conventional fibers that further lead to improving crop yield. Nie et al. demonstrated that the combination of fertilizer (nitrogen, phosphorous, potassium) with rice straw tends to elevate the concentration of soil extractable glomalin and total glomalin. The glomalin is the glycoprotein secreted by arbuscular mycorrhizal fungi (AMF) which maintain the stability of soil aggregation. AMF are root symbiotic fungi that play a crucial role in

TABLE 4 | Applications of agro-textile products in agriculture.

Agro-textile product	Fiber type	Textile type	Stability to UV radiation	Use in agriculture	References
Sunscreen	Polyethylene	Woven	Stable	To protect the crop from UV radiation	Subramaniam, 2009; Agarwal, 2013
Anti-bird net	Polypropylene, polyethylene	Knitted	Stable	Protect crop from birds	Chowdhury et al., 2017
Root ball net	Cotton, polyester, cotton-polyester blend	Woven	*NA	Helps to maintain soil on the surface of roots and protect root balls during transportation	Agarwal, 2013
Mulch mat	Wool, polypropylene	Non-woven	Stable	Prevents the growth of unwanted weed, wool mulch mats preserve soil moisture	Agarwal, 2013
Soil protection fabric	Jute, polypropylene	Woven	*NA	Prevent soil erosion	Desai, 2018
Harvesting net	Cotton, nylon	Knitted	Stable	Net helps to protect fruits from mold and make harvesting easier	Subramaniam, 2009
Crop cover	Polypropylene	Plastic sheets	Stable	Protect crop from adverse climatic conditions	Desai, 2018
Anti-hail net	Polyethylene monofilament	Knitted	Stable	Guard vines from hail	Chowdhury et al., 2017
Sleeve/bags for nursery	Jute	Woven		For the growth of seedlings	Ghosh et al., 2016

\*NA means the information was not available.



maintaining the soil environment by extending the root system into the soil. Glomalin was correlated with soil carbon and nitrogen, linked with an oligosaccharide, and sequestered toxic elements in the soil. The total glomalin concentration of NPKs (nitrogen, phosphorous, and potassium) was increased to 5.67% when compared with the control plot. Along with that, it also enhanced soil organic carbon and total nitrogen content as illustrated in **Figure 5** (Nie et al., 2007).

Geng et al. studied whether coated fertilizers (polymer-sulfur-coated urea) can improve crop productivity, soil organic matter, and also nitrogen use efficiency (NUE). Three field implementations of fertilizer (urea coated with sulfur and thin polymer) with the rate of  $180 \text{ kg ha}^{-1}$ ,  $126 \text{ kg ha}^{-1}$ , and  $90 \text{ kg ha}^{-1}$  on rice (*Oryza sativa* L.) and oilseed rape (*Brassica napus* L.). The yield of rice and oilseed rape was improved by 6.1–8.2% and 6.3–15.5%; furthermore, the nitrogen use efficiency was enhanced by 15.4–38.4% (Geng et al., 2015). Environmentally friendly fertilizers have numerous merits as they cause less leaching of nutrients, maintain soil fertility, and further reduce the labor cost as compared to conventional fertilizers (Chen et al., 2018).

## Soil Strengthening Using Agro-Textile Fibers

In a study, the strengthening of cohesive soil was investigated through kerosene-coated coir fiber. Kerosene served as a coating agent that tended to lower the water absorption capacity of coir by up to 170%. The purpose of kerosene coating was to prevent the coir fiber from moisture-induced degradation which further imparts strength and stress-strain response of high-plasticity clay up to 52% (Lestelle et al., 2020). Brahmachary et al. showed the improvement of soil with the utilization of natural bamboo fibers enhanced the strength and stiffness of soil. The quantity of bamboo fiber had a direct relationship with the “California bearing ratio” value of soil (a penetration test that determines the force per unit area), which was considerably increased at 1.2% bamboo fiber dosage (Brahmachary and Rokonzuzaman, 2018).

Kanayama et al. cited that bamboo fibers combined with soil at the ratio of 0, 1, 3, and 5% showed the compression stress of 115, 108, 130, and  $152 \text{ kN/m}^2$  respectively. This suggests that

lower stiffness has a direct correlation with the strength of the soil (Kanayama and Kawamura, 2019).

## Role of Agro-Textiles in Crop Improvement

Several scientists have proved the influence of jute agro-textiles in the improvement of broccoli productivity,  $800 \text{ g/m}^2$  of jute agro-textile showed a significant result with an average weight of broccoli of 1.2 kg and length of 29.5 cm. The yield was around 4.44 tons/ha and the moisture-holding capacity was 49.05%. The jute agro-textile is composed of a natural jute bast fiber product which is eco-friendly and biodegradable and facilitates plant growth by providing essential plant nutrients through lignin decomposition (Sarkar et al., 2018).

Another study investigated the effect of non-woven ramie fiber film on the root zone environment of rice seedlings. The film was used as a pad on the bottom surface of the seedling tray which tended to enhance the oxygen supply that promoted root respiration; therefore, it had a direct impact on the growth of seedlings. The result of the study showed a significantly higher concentration of soil inorganic nitrogen and decreased organic matter in soil which led to enhanced growth and development of rice seedlings (Zhou et al., 2020).

A group of scientists used non-woven agro-textiles of  $10 \text{ g m}^{-2}$  and  $17 \text{ g m}^{-2}$  mass per unit area to protect radish seeds from spit germination and low temperature. Both agro-textile covers enhanced the temperature during the daytime in contrast to the uncovered control plot and tended to improve the germination by around 19% and reduced the germination time (Rekika et al., 2008).

## Other Applications

Jiang et al. (2020) investigated multifunctional TENG (triboelectric nanogenerator) yarn integrated with agro-textiles for various applications. TENG yarn has excellent mechanical and stretchability properties which make it suitable to be woven into a net and incorporated into agro-textiles. TENG is capable of harvesting energy from irregular and low-frequency mechanical energy in the environment that may offer an innovative pattern to take advantage of the rainy phenomenon. Hence, in the meantime, TENG protects crop plantation and the yield of agricultural products; raindrop energy can also be harvested (Jiang et al., 2020).



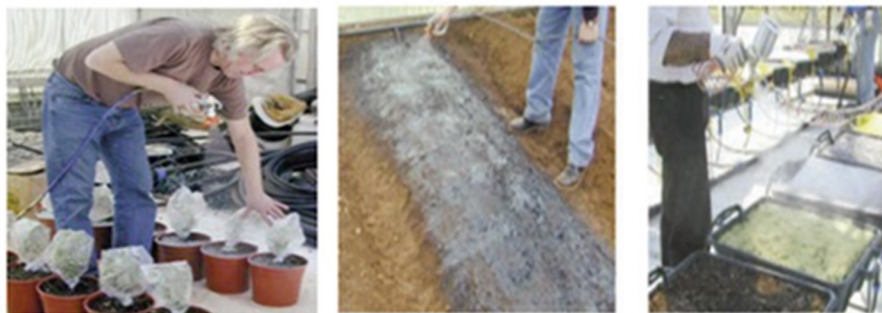


**FIGURE 6** | Representation of mulching of soil with biodegradable material through spraying techniques in a cultivated pot (Source: Vox et al., 2013).

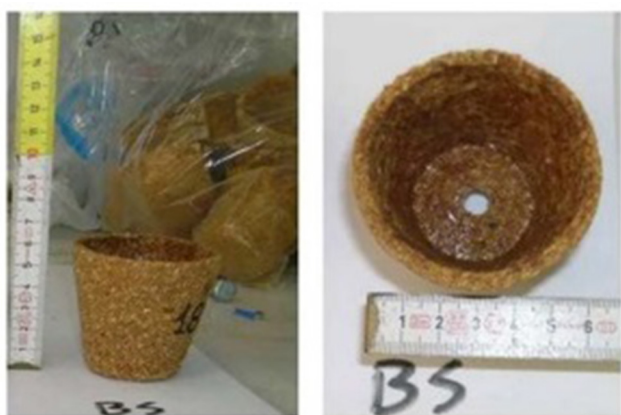


**FIGURE 7** | Representation of the biodegradable pot (Source: Sartore et al., 2016).

## Next-Generation of Agro-Textiles: Innovative Production of Mulches and Biodegradable Pots With a Novel Outlook

Plastic-based mulching film utilization in horticulture extensively caused a serious environmental impact due to non-biodegradability. The plastic film waste causes environmental pollution, so to mitigate such problems, biodegradable and renewable materials were used for soil mulching. Various biodegradable materials are natural polymers including starch, cellulose, and chitosan which were efficiently designed to retain their mechanical and physical properties during their implementation until the end of their life span. These materials were directly introduced into the soil as they have been degraded by soil microflora which converts them into carbon dioxide or methane and water (Santagata et al., 2014).

The biodegradable extruded mulching films were formed through the thermo-plasticising process (polymer was softened when heated and hardened when cooled down). The spray of mulch solution (water-based natural polysaccharide solution) was released on the field, thus covering the cultivated soil with a protective thin geo-membrane (**Figure 6**). Another advantage of spraying technology is to avoid the use of film layer machines,

which are necessary to apply and remove plastic films (Vox et al., 2013; Malinconico, 2019). A report by Malinconico et al. showed the synthesis of mulching film using cellulose fibers, carbon black, fine bran of wheat, and powdered seaweeds that not only improved the mulching function but also enhanced the tensile strength of the coating material (Malinconico, 2016).

Another popular utilized practice in horticulture is transplantation where the seedlings are transferred into the soil or into a large container. Commonly, farmers use pots or cell trays composed of fossil raw materials such as polystyrene, polyethylene, and polypropylene that resist proper root growth as roots tend to circulate over the root ball along during transplanting, but the roots can be damaged. An effective alternative to petroleum-based thermoplastic pots may be biodegradable pots that are engineered in such a way that water, air, and roots will penetrate the walls of the pot that ensure healthy root growth (**Figure 7**). The biodegradable pots can be planted directly into soil, ensuring no pot disposal, reducing cost, labor, and environmental pollution. The mechanism of biodegradation of pots involves the conversion of pots into biomass and inorganic products (e.g., carbon dioxide and water) (Juanga-Labayen and Yuan, 2021).

## Recycling of Agro-Textiles

The current best practice involves the production of value-added products from waste material toward the fulfillment of a sustainable approach which is the part of the circular economy. A circular economy revolves around utilizing textile waste to develop new products. Numerous key elements associated with the circular economy, viz., the utilization of renewable and reusable resources as a raw material, remanufacture resources to enhance the life span of the product, and use the waste resource to recycle or reuse the waste. To achieve this, materials that are meant for landfills or incineration can be recycled into new products/ materials with better quality and higher environmental value (Todor et al., 2019).

A report by Bhatt et al. developed household utility items like lampshades, doormats, wind chimes, coasters, and hanging baskets from defective and damaged textile material used in the university research farms. This fulfills the goal of maintaining the aspect of sustainability with minimal environmental harm and also reduces waste generation. Therefore, waste agro-textiles can

be used to generate value-added products that cut down textile waste that is supposed to be disposed of (Bhatt et al., 2019).

## Major Agro-Textile Projects

The seventh framework program includes the development of new agro-textiles with a tailored biodegradability from renewable resources and BIOAGROTEX, Belgium. The BIOAGROTEX project aims to develop a completely bio-based agro-textile with controlled durability as an alternative to existing PP-based agro-textiles or natural fiber-based agro-textiles with a very short lifespan. Manufacturing of biopolymer formulations using various fiber extrusion techniques include tape or monofilament, staple fiber, and multifilament extrusion on laboratory, pilot, and industrial scales including a range of further industrial processing trials such as knitting, weaving, and needle felt production. Two families of biopolymers are evaluated. The use of biopolyesters as melt-processable polymers, with a focus on PLA, and the use of starch-based formulations. Natural fibers from recycled or from low-value agricultural fractions, and property optimisation by (enzymatic) pre-treatment to optimize yield and properties are developed. Bio-resins (furan-based) for refining NF-based products, extending the self-life without affecting the mechanical properties, processing experimental fibers into non-woven structures and finishing them on a pilot scale, and further scaling to fully integrated industrial processes are developed. Both pathways are supported by laboratory-scale biodegradation tests and detailed chemical analysis of the degradation routes along with the evaluation of the ecological impact and the possible ecotoxicity tests. A set of optimized biopolymer resins or thermoplastics has been defined and can be processed with existing machines to provide excellent processability and properties. Based on these results, different types of agro-textiles can be defined and used directly in the field. The first commercial achievements have already been achieved and hundreds of

thousands of m<sup>2</sup> of specialized agro-textiles are already on sale based on the current development on the market (<https://cordis.europa.eu/project/id/213501/reporting>).

## CONCLUSION AND FUTURE PERSPECTIVES

Agro-textiles provide potential applications in agriculture fields where agro-textile covers help crops to germinate and grow faster. Moreover, it has an overall impact on the plant morphology such as higher plant heights and leaf areas. A variety of fibers from agro-textiles tends to help by improving soil conditions, and also provide organic carbon to the soil when degraded. Next-generation agro-textiles seem to have an inclination toward eco-friendly and biodegradable material drawn from agriculture or farms. Hence, lignocellulosic-based agro-textiles may prove to be an economic and environmentally friendly alternative and may be a boon for agriculture.

## AUTHOR CONTRIBUTIONS

NS contributed to the writing, editing, and revisions of this manuscript. AA and RA are chiefly responsible for executing the idea, managing funding, and article processing for the final submission. RR and BA critically reviewed the article and provided valuable input for multiple sections. All authors contributed to the article and approved the submitted version.

## ACKNOWLEDGMENTS

The authors are thankful to Deakin University, Geelong, Australia for providing all infrastructural, analytical, and financial support as an incubation centre at TERI-Deakin Nanobiotechnology Center (TDNBC), TERI, India.

## REFERENCES

- Agarwal, M. S. (2013). Application of textile in the agriculture. *International journal of advance research in science and engineering*, 2, 9–18.
- Anthony, R., Awasthi, S. Y., Singh, P., and Prasath Kumar, V. R. (2020). An experimental and characteristic study of abaca fiber concrete. *IOP Conf. Ser.* 912. doi: 10.1088/1757-899X/912/3/032077
- Basu, S. K. (2011). Agricultural and horticultural applications of agro textiles. *Indian Textile J.* 121, 141–148.
- Bhatt, P., Rani, A., Gahlot, M., and Bhandari, V. (2019). Recycling and reuse of agrotexiles used in agricultural farms. *Int. J. Curr. Microbiol. App. Sci.* 8, 1566–1576. doi: 10.20546/ijcmas.2019.806.188
- Bhavani, K., Mallikarjun, N., and Sunilkumar, N. M. (2017). Agro textiles - Their applications in agriculture and scope for utilizing natural fibres in agro tech sector. *Int. J. Appl. Home Sci.* 4, 653–662. ISSN: 2394-1413
- Blackburn, R. (2005). *Biodegradable and Sustainable Fibres*. Woodhead Publishing.
- Brahmachary, T. M., and Rokonzaman, M. (2018). Investigation of random inclusion of bamboo fibre on ordinary soil and its effect CBR value. *Int. J. Geoeng.* 9, 10. doi: 10.1186/s40703-018-0079-x
- Chen, H. Z., and Liu, Z. H. (2014). Multilevel composition fractionation process for high-value utilization of wheat straw cellulose. *Biotechnol. Biofuels.* 7, 10.1186/s13068-014-0137-3. doi: 10.1186/s13068-014-0137-3
- Chen, J., Lu, S., Zhang, Z., Zhao, X., Li, X., Ning, P., et al. (2018). Environmentally friendly fertilizers: A review of materials used and their effects on the environment. *Sci. Total Environ.* 613–614, 829–839. doi: 10.1016/j.scitotenv.2017.09.186
- Chen, Q., Zhao, T., Wang, M., and Wang, J. (2013). Studies of the fibre structure and dyeing properties of *Calotropis gigantea*, kapok and cotton fibres. *Colorat. Technol.* 129, 448–453. doi: 10.1111/cote.12051
- Cheng, L., Duan, S., Feng, X., Zheng, K., Yang, Q., Xu, H., et al. (2020). Ramie-degumming methodologies: a short review. *J. Eng. Fibers Fabr.* 15. doi: 10.1177/1558925020940105
- Ching, H. L., Sapuan, S., Hassan, M. R., and Sheltami, R. (2018). Natural fibre reinforced vinyl polymer composites. *Polym. Polym. Compos.* 27–70. doi: 10.1016/B978-0-08-102160-6.00002-0
- Chowdhury, M. J., Nasrin, S., and Faruque, M. A. A. (2017). Significance of agro-textiles and future prospects in Bangladesh. *Eur. Sci. J.* 13. doi: 10.19044/esj.2017.v13n21p139
- Dai, X.-Q. (2006). Fibres biomechanical engineering of textiles and clothing. *Woodhead Pub. Ser. Text.* 163–177. doi: 10.1533/9781845691486.3.161
- Desai, A. (2018). *Textiles Used in Modern Agriculture to Smart Farming*. Available online at: [https://www.academia.edu/35687669/Textiles\\_used\\_in\\_modern\\_agriculture\\_to\\_smart\\_farming#:~:sim:text=root%20ball%20net%2C%20insect%20meshes,agricultural%20is%20not%20new%20invention](https://www.academia.edu/35687669/Textiles_used_in_modern_agriculture_to_smart_farming#:~:sim:text=root%20ball%20net%2C%20insect%20meshes,agricultural%20is%20not%20new%20invention).
- Franck, R.R. (2005). *Bast and Other Plant Fibres*, vol 39. Boca Raton, FL: CRC Press.
- Gangopadhyay, U. K., and Hira, M. (2010). Towards popularizing agro-textiles in India. *Man-Made Text. India.* 53, 41–46.
- Geng, J., Sun, Y., Zhang, M., Li, C., Yang, Y., Liu, Z., et al. (2015). Long-term effects of controlled release urea application on crop yields and soil fertility under rice-oilseed rape rotation system. *Field Crop Res.* 184, 65–73. doi: 10.1016/j.fcr.2015.09.003

- Ghosh, M., Biswas, D., and Sanyal, P. (2016). Development of jute braided sapling bag for nursery use. *J. Nat. Fibres*. 13, 146–157. doi: 10.1080/15440478.2014.1002147
- Global Agro Textiles Market Size, Share & Trends Analysis Report by Product by Application by Region, and Segment Forecasts. (2021–2028). Available online at: <https://www.researchandmarkets.com/reports/4479690/global-agro-textiles-market-size-share-and> <https://www.researchandmarkets.com/content-images/174/174182/2/agro-textiles-market.png>
- Gollapalli, L. E., Dale, B. E., and Rivers, D. M. (2002). Predicting digestibility of ammonia fibre explosion (AFEX)-treated rice straw. *Appl. Biochem. Biotechnol.* 98–100, 23–35. doi: 10.1385/ABAB:98-100:1-9:23
- Goudenhoof, C., Bourmaud, A., and Baley, C. (2019). Flax (*Linum usitatissimum* L.) fibers for composite reinforcement: exploring the link between plant growth, cell walls development, and fiber properties. *Front. Plant Sci.* 10, 1–23. doi: 10.3389/fpls.2019.00411
- Himanish, D., and Sudhir, K. S. (2004). Useful byproducts from cellulosic wastes of agriculture and food industry—a critical appraisal. *Crit. Rev. Food Sci. Nutr.* 44, 2, 77–89. doi: 10.1080/10408690490424630
- Iniya, M., and Nirmalkumar, K. (2021). A review on fiber reinforced concrete using sisal fiber. *IOP Conf. Ser.: Mater. Sci. Eng.* 1055, 012027. doi: 10.1088/1757-899X/1055/1/012027
- Janaswamy, S., Yadav, M. P., Hoque, M., Bhattarai, S., and Ahmed, S. (2022). Cellulosic fraction from agricultural biomass as a viable alternative for plastics and plastic products. *Ind. Crops Prod.* 179, 114692. doi: 10.1016/j.indcrop.2022.114692
- Jiang, C., Li, X., Ying, Y., and Ping, J. (2020). A multifunctional TENG yarn integrated into Agro-textile for building intelligent agriculture. *Nano Energy*. 104863. doi: 10.1016/j.nanoen.2020.104863
- Juanga-Labayen, J. P., and Yuan, Q. (2021). Making biodegradable seedling pots from textile and paper waste-part B: development and evaluation of seedling pots. *Int. J. Environ. Res. Public Health*. 18, 7609. doi: 10.3390/ijerph18147609
- Kanayama, M., and Kawamura, S. (2019). Effect of waste bamboo fibre addition on mechanical properties of soil. *Open J. Civ. Eng.* 09, 173–184. doi: 10.4236/ojce.2019.93012. doi: 10.4236/ojce.2019.93012
- Kasirajan, S., and Ngouajio, M. (2012). Polyethylene and biodegradable mulches for agricultural applications: a review. *Agron. Sustain. Dev.* 32, 501–529. doi: 10.1007/s13593-011-0068-3
- Khalil, H. P. S. A., Bhat, I. U. H., Jawaid, M., Zaidon, A., Hermawan, D., and Hadi, Y. S. (2012). Bamboo fibre reinforced biocomposites: a review. *Mater. Des.* 42, 353–368. doi: 10.1016/j.matdes.2012.06.015
- Kumar, R. S. (2017). Textile is a boon agriculture. *IREJ*. 1, 73–79. ISSN: 2456-8880
- Lestelle, V., Torio, K., Annamaria, M., San, D., and Matthew, T. M. A. (2020). Unconfined compressive strength of clay reinforced with kerosene-treated coir fibre. *Int. J. Geomate*. 18, 97–103. doi: 10.21660/2020.69.9295
- Li, Z., Zhai, H. M., Zhang, Y., and Yu, L. (2012). Cell morphology and chemical characteristics of corn stover fractions. *Ind. Crops Prod.* 37, 130–136. doi: 10.1016/j.indcrop.2011.11.025
- Lipp-Symonowicz, B., Sztajnowski, S., and Wojciechowska, D. (2011). New commercial fibres called 'Bamboo Fibres'- their structure and properties. *Fibres Text. East. Eur.* 19, 18–23.
- Liu, R., Yu, H., and Huang, Y. (2005). Structure and morphology of cellulose in wheat straw. *Cellulose*. 12, 25–34. doi: 10.1007/s10570-004-0955-8
- Liu, Y., and Hu, H. (2008). X-ray diffraction study of bamboo fibers treated with NaOH. *Fibres Polym.* 9, 735–739. doi: 10.1007/s12221-008-0115-0
- Liu, Y., Liu, Y., Zhang, D., Zhang, R., and Li, Z. (2016). Kapok fiber: a natural biomaterial for highly specific and efficient enrichment of sialoglycopeptides. *Anal. Chem.* 88, 1067–1072. doi: 10.1021/acs.analchem.5b04014
- Malinconico, M. (2016). Biodegradable materials for soil mulching based on aqueous mixtures of polysaccharides and plant waste fibres and methods for their application. *Eur. Patent* EP2556284.
- Malinconico, M. (2019). Different applications of biodegradable and compostable materials in agriculture. *Acta Horticulturae*. 39–46. doi: 10.17660/ActaHortic.2019.1252.5
- Mathangadeera, R. W., Hequet, E. F., Kelly, B., Dever, J. K., and Kelly, C. M. (2020). Importance of cotton fiber elongation in fiber processing. *Ind. Crops Prod.* 147, 112217. doi: 10.1016/j.indcrop.2020.112217
- Mather, R. R., and Wardman, R. H. (2010). *Chemistry of Textile Fibres*. Cambridge, UK: RSC Publishing. p. 388.
- Mohanty, A. K., Manjusri, M., and Drzal, L. T. (2005). *Natural Fibres, Biopolymers and Biocomposites*. Boca Raton: CRC Press, Taylor and Francis Group. doi: 10.1201/9780203508206
- Musio, S., Mussig, J., and Amaducci, S. (2018). Optimizing hemp fiber production for high performance composite applications. *Front. Plant Sci.* 9:1702. doi: 10.3389/fpls.2018.01702
- Mwaiambo, L. Y. (2006). Review of the history, properties and application of plant fibres. *Afr. J. Sci. Technol.* 7, 120–133.
- Nayak, L., and Mishra, S. P. (2016). Prospect of bamboo as a renewable textile fibre, historical overview, labeling, controversies and regulation. *Fash Text.* 3, 2. doi: 10.1186/s40691-015-0054-5
- Nie, J., Zhou, J. M., Wang, H. Y., Chen, X. Q., and Du, C. W. (2007). Effect of long-term rice straw return on soil glomalin, carbon and nitrogen. *Pedosphere*. 17, 295–302. doi: 10.1016/S1002-0160(07)60036-8
- Nykter, M. (2006). *Microbial quality of hemp (Cannabis sativa L.) and flax (Linum usitatissimum L.) from plants to thermal insulation* (Academic dissertation). University of Helsinki, Helsinki, Finland.
- Preston, J. (2016). *Man-made fibre, Encyclopaedia Britannica*. Available online at: <https://www.britannica.com/technology/man-made-fibre>
- Reddy, N., and Yang, Y. (2005). Structure and properties of high quality natural cellulose fibres from corn stalks. *Polymer*. 46, 5494–5500. doi: 10.1016/j.polymer.2005.04.073q18
- Rekika, D., Stewart, K. A., Boivin, G., and Jenni, S. (2008). Reduction of insect damage in radish with floating row covers. *Int. J. Plant Soil Sci.* 14, 177–193. doi: 10.1080/19315260801934829
- Restrepo, O. A., Alvarez-Lopez, C., Jaramillo, N., and Fernandez-Morales, P. (2019). "Agrotextiles and crop protection textiles," in *High Performance Technical Textiles*, ed P. Roshan (John Wiley & Sons), 279–318.
- Rezende, C. A., de Lima, M. A., Maziero, P., et al. (2011). Chemical and morphological characterization of sugarcane bagasse submitted to a delignification process for enhanced enzymatic digestibility. *Biotechnol. Biofuels*. 4, 54. doi: 10.1186/1754-6834-4-54
- Rijavec, T. (2008). Kapok in technical textiles. *Tekstilica*. 51, 319–331.
- Sain, M., and Panthapulakkal, S. (2006). Bioprocess preparation of wheat straw fibres and their characterization. *Ind. Crops Prod.* 23, 1–8. doi: 10.1016/j.indcrop.2005.01.006
- Salman, S. D. (2020). Effects of jute fibre content on the mechanical and dynamic mechanical properties of the composites in structural applications. *Defence Technol.* 16, 1098–1105. doi: 10.1016/j.dt.2019.11.013
- Santagata, G., Malinconico, M., Immirzi, B., Schettini, E., Scarascia Mugnozza, G., and Vox, G. (2014). An overview of biodegradable films and spray coatings as sustainable alternative to oil-based mulching films. *Acta Hortic.* 1037, 921–928. doi: 10.17660/ActaHortic.2014.1037.122
- Sarkar, A., Swain, N., Tarafdar, P. K., and De, S. K. (2018). Influence of jute agro textiles on improvement of broccoli productivity in inceptisols. *J. Pharmacogn. Phytochem.* 7, 1451–1454.
- Sartore, L., Schettini, E., Bignotti, F., Pandini, S., and Vox, G. (2016). Biodegradable plant nursery containers from leather industry wastes. *Poly. Compos.* 39, 2743–2750. doi: 10.1002/pc.24265
- Scarlat, R., Pricop, F., and Rusu, L. (2017). Knitted Agro-textiles for a sustainable agriculture. *Industria Textila*. 68, 332–336. doi: 10.35530/IT.068.05.1413
- Sfiligoj, S. M., Hribernik, S., Kleinschek, K. S., and Kreze, T. (2013). Plant fibres for textile and technical applications. *Adv. Agron. Res.* 369–398. doi: 10.5772/52372
- Sreenivas, H. T., Krishnamurthy, N., and Arpitha, G. R. (2020). A comprehensive review on light weight kenaf fiber for automobiles. *Int. J. Lightweight Mater. Manuf.* 3, 328–337. doi: 10.1016/j.ijlmm.2020.05.003
- Subagyo, A., and Chafidz, A. (2020). Banana pseudo-stem fibre: preparation, characteristics, and applications. banana nutrition. *Prog. React. Kinet. Mech.* 10.5772/intechopen.82204. doi: 10.5772/intechopen.82204
- Subramaniam, G. R. (2009). Agro-textiles: production, properties and potential. Nonwoven and technical textiles. *Indian Textile J.*
- Sun, J. X., Sun, X. F., Zhao, H., and Sun, R. C. (2004). Isolation and characterization of cellulose from sugarcane bagasse. *Polym. Degrad. Stab.* 84, 331–339. doi: 10.1016/j.polymdegradstab.2004.02.008
- Swapan, K., Bairagi, G., Bhattacharyya, S., Murari, R., and Mondal, M. (2016). An overview on test standards for evaluation of jute agro-textiles. *Am. J. Engineering Res.* 5, 49–53.

- Tara, S., and Jagannatha, R. (2011). Various industrial applications of hemp, kinaif, flax and ramie natural fibres. *Int. J. Innov. Technol. Manag.* 2, 192–198. Available online at: <http://www.ijimt.org/papers/130-M534.pdf>
- Technavio EMIS Database (2017). Global Technical Textiles Market 2015–2019.
- Todor, M. P., Bulei, C., Kiss, I., and Alexa, V. (2019). Recycling of textile wastes into textile composites based on natural fibres: the valorisation potential. *IOP Conf. Ser.: Mater. Sci. Eng.* 477 012004 doi: 10.1088/1757-899X/477/1/012004
- Vox, G., Santagata, G., Malinconico, M., Immirzi, B., and Scarascia Mugnozza, G., Schettini E (2013). Biodegradable films and spray coatings as eco-friendly alternative to petro-chemical derived mulching films. *J. Agric. Eng. Res.* XLIV, e44. doi: 10.4081/jae.2013.286
- Yusuf, M. (2021). “Chapter 5 – Current and future perspectives of enzyme treatments for cellulosic fibers: a review”, in *Green Chemistry for Sustainable Textiles, Modern Design and Approaches, The Textile Institute Book Series*. 69–76. doi: 10.1016/B978-0-323-85204-3.00020-8
- Zhou, W., Chen, J., Qi, Z., et al. (2020). Effects of applying ramie fibre nonwoven films on root-zone soil nutrient and bacterial community of rice seedlings for mechanical transplanting. *Sci. Rep.* 10, 3440. doi: 10.1038/s41598-020-60434-3

**Conflict of Interest:** The authors declare that the research was conducted in the absence of any commercial or financial relationships that could be construed as a potential conflict of interest.

**Publisher's Note:** All claims expressed in this article are solely those of the authors and do not necessarily represent those of their affiliated organizations, or those of the publisher, the editors and the reviewers. Any product that may be evaluated in this article, or claim that may be made by its manufacturer, is not guaranteed or endorsed by the publisher.

Copyright © 2022 Sharma, Allardycy, Rajkhowa, Adholeya and Agrawal. This is an open-access article distributed under the terms of the Creative Commons Attribution License (CC BY). The use, distribution or reproduction in other forums is permitted, provided the original author(s) and the copyright owner(s) are credited and that the original publication in this journal is cited, in accordance with accepted academic practice. No use, distribution or reproduction is permitted which does not comply with these terms.





# Overexpression of *TwSQS*, *TwSE*, and *TwOSC* Regulates Celastrol Accumulation in Cambial Meristematic Cells and Dedifferentiated Cells

Yadi Song<sup>1,2</sup>, Jiawei Zhou<sup>2</sup>, Yifeng Zhang<sup>1</sup>, Yujun Zhao<sup>3</sup>, Xiujuan Wang<sup>2\*</sup>, Tianyuan Hu<sup>2</sup>, Yuru Tong<sup>4</sup>, Luqi Huang<sup>3</sup> and Wei Gao<sup>1,2\*</sup>

## OPEN ACCESS

### Edited by:

Roger Deal,  
Emory University, United States

### Reviewed by:

Jianing Mi,  
King Abdullah University of Science  
and Technology, Saudi Arabia  
Pan Liao,  
Purdue University, United States

### \*Correspondence:

Xiujuan Wang  
wxj0517@sina.com  
Wei Gao  
weigao@ccmu.edu.cn

### Specialty section:

This article was submitted to  
Technical Advances in Plant Science,  
a section of the journal  
Frontiers in Plant Science

**Received:** 23 April 2022

**Accepted:** 10 June 2022

**Published:** 01 July 2022

### Citation:

Song Y, Zhou J, Zhang Y, Zhao Y,  
Wang X, Hu T, Tong Y, Huang L and  
Gao W (2022) Overexpression of  
*TwSQS*, *TwSE*, and *TwOSC*  
Regulates Celastrol Accumulation  
in Cambial Meristematic Cells  
and Dedifferentiated Cells.  
Front. Plant Sci. 13:926715.  
doi: 10.3389/fpls.2022.926715

<sup>1</sup> Beijing Shijitan Hospital, Capital Medical University, Beijing, China, <sup>2</sup> School of Traditional Chinese Medicine, Capital Medical University, Beijing, China, <sup>3</sup> State Key Laboratory of Dao-di Herbs, National Resource Center for Chinese Materia Medica, China Academy of Chinese Medical Sciences, Beijing, China, <sup>4</sup> School of Pharmaceutical Sciences, Capital Medical University, Beijing, China

Squalene synthase (SQS), squalene epoxidase (SE), and oxidosqualene cyclase (OSC) are encoding enzymes in downstream biosynthetic pathway of triterpenoid in plants, but the relationship between three genes and celastrol accumulation in *Tripterygium wilfordii* still remains unknown. Gene transformation system in plant can be used for studying gene function rapidly. However, there is no report on the application of cambial meristematic cells (CMCs) and dedifferentiated cells (DDCs) in genetic transformation systems. Our aim was to study the effects of individual overexpression of *TwSQS*, *TwSE*, and *TwOSC* on terpenoid accumulation and biosynthetic pathway related gene expression through CMCs and DDCs systems. Overexpression vectors of *TwSQS*, *TwSE*, and *TwOSC* were constructed by Gateway technology and transferred into CMCs and DDCs by gene gun. After overexpression, the content of celastrol was significantly increased in CMCs compared with the control group. However, there was no significant increment of celastrol in DDCs. Meanwhile, the relative expression levels of *TwSQS*, *TwSE*, *TwOSC*, and terpenoid biosynthetic pathway related genes were detected. The relative expression levels of *TwSQS*, *TwSE*, and *TwOSC* were increased compared with the control group in both CMCs and DDCs, while the pathway-related genes displayed different expression trends. Therefore, it was verified in *T. wilfordii* CMCs that overexpression of *TwSQS*, *TwSE*, and *TwOSC* increased celastrol accumulation and had different effects on the expression of related genes in terpenoid biosynthetic pathway, laying a foundation for further elucidating the downstream biosynthetic pathway of celastrol through *T. wilfordii* CMCs system.

**Keywords:** *Tripterygium wilfordii*, squalene synthase, squalene epoxidase, oxidosqualene cyclase, cambial meristematic cells

## INTRODUCTION

*Tripterygium wilfordii* Hook. f. (*T. wilfordii*) is a woody medicinal plant, and its dried root is a well-known traditional Chinese medicine widely used to treat immune dysregulation (Li et al., 2005), inflammation (Xu et al., 1985; Zhang W. et al., 2017), and tumor (Wang et al., 2016). The pharmacologically active constituents of *T. wilfordii* are terpenoids, mainly including diterpenoid and triterpenoid (Liu et al., 2011). Celastrol is a triterpenoid compound and considered to be one of the most likely natural products to develop into modern medicines (Corson and Crews, 2007), which can efficiently treat inflammatory diseases (Guo et al., 2017), tumor (Liu et al., 2019), obesity, and metabolic dysfunction (Ma et al., 2015).

In plants, terpenoids are biosynthesized by the mevalonate (MVA) pathway located in the cytoplasm and the 2-C-methyl-D-erythritol-4-phosphate (MEP) pathway located in the plastid (Vranova et al., 2013). The isopentenyl pyrophosphate (IPP) and its isomer dimethylallyl diphosphate (DMAPP), which are the common precursors of terpenoids, can transfer through the plastid envelope to link the MVA and MEP pathways (Rodríguez-Concepcion and Boronat, 2002). Farnesyl diphosphate synthase (FPS) converts one molecule of DMAPP and two molecules of IPP to form farnesyl pyrophosphate (FPP), and two molecules of FPP can be modified to squalene-by-squalene synthase (SQS), which is the first enzyme to catalyze the MVA pathway in the biosynthesis of the sterols and triterpenoids (Abe et al., 1994). Then, the rate-limiting enzyme squalene epoxidase (SE) (Han et al., 2010) converts squalene into 2,3-oxidosqualene (Zhou et al., 2018). Then, 2,3-oxidosqualene can be subsequently modified by oxidosqualene cyclase (OSC) to friedelin (Zhou et al., 2019), which will be finally transformed to celastrol through a series of biosynthetic reactions. So far, the downstream biosynthetic pathway of celastrol has not been clearly elucidated.

Recently, a stable gene transformation system of *T. wilfordii* suspension cells for studying gene function has been developed, which is fast, convenient, and efficient (Zhao et al., 2017). Cambial meristematic cells (CMCs) are innately undifferentiated cells derived from cambium in plants and they possess characteristics of plant stem cells (Ochoa-Villarreal et al., 2015). CMCs were commonly used as cell culture systems of medical plants, such as *Taxus cuspidata* (Lee et al., 2010), *Catharanthus roseus* (Moon et al., 2015), *Camptotheca acuminata* (Zhang Y. H. et al., 2017), and *Tripterygium wilfordii* (Song et al., 2019), from which CMCs could provide a cost-effective system for producing higher amounts of important natural products than typical dedifferentiated cells (DDCs). However, there is no report on the application of CMCs in genetic transformation system.

Overexpression of genes that encode enzymes in the biosynthetic pathway can directly affect gene expression levels and alter the yields of direct and end products associated with the encoding enzymes, which was extensively researched in plants. In adventitious roots of *Panax ginseng*, overexpressing SQS produced approximately two times more phytosterol than the wild type (Lee et al., 2004). After SE overexpression, the content of ganoderic acid in *Ganoderma lingzhi* was two times

higher than that of the wild type (Zhang D. H. et al., 2017). In *Populus davidiana*, overexpression of OSC increased friedelin accumulation by 233–445% compared with the non-transgenic plants (Han et al., 2019). However, the effects of overexpression of *TwSQS*, *TwSE*, and *TwOSC* on celastrol biosynthesis in *T. wilfordii* CMCs and DDCs still remain unknown.

In this study, we aimed to analyze the effects of individual overexpression of *TwSQS*, *TwSE*, and *TwOSC* on celastrol accumulation and terpenoid biosynthetic pathway related gene expression through *T. wilfordii* CMCs and DDCs, laying a foundation for further research on downstream biosynthetic pathway of celastrol.

## MATERIALS AND METHODS

### Plant Cell Suspension Cultures of *Tripterygium wilfordii* Cambial Meristematic Cells and Dedifferentiated Cells

The plant *Tripterygium wilfordii* Hook. f. was obtained from Yong'an national forest in Fujian Province, China. CMCs and DDCs were isolated from the stem of *T. wilfordii* plant and cultured in Murashige and Skoog (MS) medium (PhytoTechnology Laboratories, Lenexa, KS, United States) as described previously (Song et al., 2019). Briefly, under the sterile condition, cambium, phloem, cortex, and epidermal tissues of the *T. wilfordii* stem were peeled off from the xylem. The epidermal tissue side was laid on MS solid medium that contained 2 mg/L 2,4-dichlorophenoxyacetic acid (2,4-D), 2 mg/L naphthalene-acetic acid (NAA), 30 g/L sucrose, and 8 g/L agar. The pH value of medium was 5.8–6.0. During the culture process, CMCs were formed from the cambium, and DDCs were formed from the phloem, cortex, and epidermis. The characteristic features of CMCs and DDCs were previously identified by our team (Song et al., 2019). Notably, 2.5 g (fresh cell weight) cells from each cell line were cultured in 100 ml Erlenmeyer flasks including 40 ml of MS liquid medium. The composition of the liquid medium is the same as the solid medium except for agar. The flasks were placed at 25°C in dark and agitated at 120 rpm. Subculturing was undertaken at 20-day intervals.

### Construction of Entry Vectors

The full-length cDNA of *TwSQS* (Liu et al., 2016), *TwSE* (Zhou et al., 2018), and *TwOSC* (Zhou et al., 2019) (GenBank accession numbers: *TwSQS* KR401220, *TwSE* MG717396, and *TwOSC* KY885467) was previously cloned. The full open reading frames (ORF) of *TwSQS*, *TwSE*, and *TwOSC* were amplified by PCR using specific overexpression (OE) primers (Supplementary Table 1) and Phusion High-Fidelity Master Mix (New England Biolabs, United States). Their plasmids were used as templates. After detecting that the sequence lengths of the amplified products were the same as their full ORF, the products were purified and then inserted into pENTR<sup>TM</sup>/D-TOPO entry vectors using the Cloning Kit (Thermo Fisher Scientific, United States). The recombinant vectors were transformed into

*Escherichia coli* (*E. coli*). Trans5 $\alpha$  cells (TransGen Biotech, Beijing, China) and then cultured on Luria-Bertani (LB) solid medium with 50 mg/L kanamycin for selection of entry vectors. M13 F/R primers (Supplementary Table 1) were used to verify that entry vectors were successfully constructed.

## Construction of Overexpression Vectors

The overexpressed target fragments of *TwSQS*, *TwSE*, and *TwOSC* were transferred from entry vectors into pH7WG2D vectors using the Gateway LR Clonase TM II Enzyme Mix (Thermo Fisher Scientific), respectively. The promoter of the vector was p35S and the terminator was T35S. The recombinant vectors containing each fragment were transformed into *E. coli* Trans5 $\alpha$  cells individually and selected on LB solid medium with 50 mg/L spectinomycin, followed by pH7 (Supplementary Table 1) sequencing. OE primers (Supplementary Table 1) were used to verify that overexpression vectors were successfully constructed. The plasmids of *TwSQS*, *TwSE*, and *TwOSC* overexpression vectors were extracted using EZNA® Plasmid Maxi Kit (OMEGA, Norcross, GA, United States).

## Transfer of Overexpression Vectors Into *Tripterygium wilfordii* Cambial Meristematic Cells and Dedifferentiated Cells

At the time of subculturing, CMCs and DDCs were cultured on MS solid medium containing 2 mg/L 2,4-D, 2 mg/L NAA, 30 g/L sucrose, and 8 g/L agar. The pH value of medium was 5.8–6.0. Notably, 200 mg (fresh cell weight) cells corresponded to 3 ml medium. Cells grew in dark at 25°C for 7 days before transfer. The plasmids of overexpression vectors were separately transferred into *T. wilfordii* CMCs and DDCs using Gene gun instrument (PDS 100/He, Bio-Rad), and the Gene gun protocol has been described previously in detail (Zhao et al., 2017). Briefly, the plasmids were mixed with 1  $\mu$ m gold microparticles (Bio-Rad), and the mixture was then bombarded into the cells using Gene gun under high-pressure helium. The empty vector pH7WG2D was transferred, respectively, into CMCs and DDCs as a control check. Then, the cells were cultured in the original medium in dark at 25°C for 7 days. After 7 days, the cells were separated from the culture medium, and the cells were stored at –80°C for later use. All samples had five biological replicates.

## Verification of Successful Transfer of Overexpression Vectors in Cells

The cell samples were divided into two parts, i.e., one for terpenoids content measurement and the other for gene expression determination. Total RNAs from all cell samples were extracted using the Total RNA Extraction Kit (Promega, Shanghai, China). Then, all RNAs were reverse-transcribed to first-strand cDNAs using the FastQuant RT kit (with gDNase) (Tiangen Biotech, Beijing, China). The hygromycin (Hyg) fragments were amplified in the cDNAs using Hyg F/R primers (Supplementary Table 1) to verify the successful transfer of overexpression vectors in *T. wilfordii* CMCs and DDCs.

## Extraction and Determination of Terpenoids in *Tripterygium wilfordii* Cambial Meristematic Cells and Dedifferentiated Cells

The remaining cell samples were freeze-dried *in vacuo* for 48 h. Then, 5 mg dried cells were precisely weighed and soaked in 250  $\mu$ l n-hexane for overnight at 4°C. Another 5 mg dried cells were also precisely weighed and soaked in 250  $\mu$ l 80% (v/v) methanol for overnight at 4°C. All cells were ultrasonicated at 25°C and 40 kHz for 1 h the next day. After centrifugation at 10,000  $\times$  g for 10 min, the supernatants were filtered through 0.22  $\mu$ m PTFE microporous membrane. For determining the content of squalene (direct product of *TwSQS* enzyme), 2,3-oxidosqualene (direct product of *TwSE* enzyme), and friedelin (direct product of *TwOSC* enzyme), the n-hexane extracts were detected using GC-MS (Agilent 7000, Agilent) with a DB-5ms capillary column (15 m  $\times$  250  $\mu$ m  $\times$  0.1  $\mu$ m) as described previously (Zhou et al., 2019). The gas chromatography detection conditions were set as follows: the initial column temperature was 50°C, hold for 1 min, increased to 260°C at a rate of 50°C/min, further increased to 272°C at a rate of 1°C/min, and hold for 4 min. The injection temperature was 250°C and the split ratio was 20: 1. The carrier gas was helium, and the flow rate was 1 ml/min. The mass spectrometric detector was operated with ionization energy of 70 eV by electron impact. The ion trap temperature was 230°C, and the spectra were recorded in the range of 10–550 m/z. The sample injection volume was 1  $\mu$ l.

For determining the content of celastrol, the methanol extracts were detected using UPLC (1290 Infinity II, Agilent) with an ACQUITY UPLC® HSS T3 chromatographic column (1.8  $\mu$ m, 2.1 mm  $\times$  100 mm, Waters). Column temperature was 40°C and the flow rate was 0.4 ml/min. Gradient elution with 100% acetonitrile (mobile phase A) and 0.1% (v/v) formic acid in water (mobile phase B) was used: 0 min: 70% B, 5 min: 65% B, 15 min: 30% B, 21 min: 10% B. The UV detector was monitored at 426.0 and 220 nm. The sample injection volume was 5  $\mu$ l.

## Relative Expression Analysis of *TwSQS*, *TwSE*, and *TwOSC*

The determination of gene expression levels was carried out by quantitative real-time reverse transcription-polymerase chain reaction (qRT-PCR). KAPA SYBR® FAST qPCR Master Mix Kit (KAPA Biosystems, Wilmington, MA, United States) was used to perform qRT-PCR experiment on the QuantStudio 5 real-time PCR system (Thermo Fisher Scientific). The cDNA obtained above was used as the templates for qRT-PCR. The qRT-PCR mixture contained 10  $\mu$ l of 2  $\times$  qPCR Master Mix, 1  $\mu$ l of cDNA (10 ng), 0.4  $\mu$ l of 50  $\times$  ROX reference Dye low, 0.4  $\mu$ l of primers (10  $\mu$ M), and 8.2  $\mu$ l of double distilled H<sub>2</sub>O. The qRT-PCR experiment was performed under the following conditions: at 95°C for 3 min, followed by 40 cycles consisted of 95°C for 3 s and 60°C for 30 s, and then a melting curve cycle: 95°C for 1 s and 60°C for 20 s. *Elongation factor 1 $\alpha$*  (*Ef1 $\alpha$* ) was used as the reference gene, and the relative expression was analyzed by the 2<sup>[-Delta Delta C(T)]</sup> method (Livak and Schmittgen, 2001).



with five biological replicates and three technical replicates. The primer sequences employed are listed in **Supplementary Table 1**.

## Relative Expression Analysis of Genes Involved in Terpenoid Biosynthetic Pathway

We also analyzed the expression levels of genes encoding *T. wilfordii* 1-deoxy-D-xylulose-5-phosphate synthase (TwDXS), geranylgeranyl diphosphate synthase (TwGGPPS), hydroxymethylglutaryl-CoA synthase (TwHMGS), hydroxymethylglutaryl-CoA reductase (TwHMGR), isopentenyl diphosphate isomerase (TwIDI), TwFPS, TwSQS, TwSE, and TwOSC enzymes under the conditions of *TwSQS*, *TwSE*, and *TwOSC* overexpression. These enzymes were involved in biosynthetic pathway of terpenoids in *T. wilfordii*. The specific qRT-PCR primers used are listed in **Supplementary Table 1**. The methods of relative gene expression analysis were same as described in the relative expression analysis of *TwSQS*, *TwSE*, and *TwOSC*.

## RESULTS

### Confirmation of *TwSQS*, *TwSE*, and *TwOSC* Overexpression Vectors

The *TwSQS* overexpression fragment of 1,241 bp, the *TwSE* overexpression fragment of 1,584 bp, and the *TwOSC* overexpression fragment of 2,298 bp were obtained. The sequencing results were consistent with the ORF sequence of *TwSQS*, *TwSE*, and *TwOSC*, confirming that overexpression vectors of the three genes were successfully constructed. Agarose gel electrophoresis showed the length of the target fragments in **Figure 1A**. The cDNAs of CMCs and DDCs after transfer were amplified by specific primers and the Hyg fragments with the length of 1,787 bp were found in all cell samples (**Figure 1B**), indicating that the empty vector pH7WG2D and overexpression vectors were successfully transferred into CMCs and DDCs. A schematic diagram of overexpression vector is shown in **Figure 1C**, and the morphology of CMCs and DDCs is shown in **Figure 2**. The texture of CMCs was softer than that of DDCs.

### Accumulation of Squalene, 2,3-Oxidosqualene, and Friedelin in *Tripterygium wilfordii* Cambial Meristematic Cells and Dedifferentiated Cells

To explore the ability of *TwSQS*, *TwSE*, and *TwOSC* enzymes to biosynthesize related terpenoids after overexpression, we determined the content of direct products of the three enzymes in *T. wilfordii* CMCs and DDCs (**Figure 3A**; **Supplementary Figures 1–3**). The contents of squalene and friedelin were detected in CMCs, but not in DDCs. In the pH7WG2D control group, *TwSQS* overexpression group, and *TwOSC* overexpression group, the content of squalene was  $229.5 \pm 42.4$ ,  $283.5 \pm 5.6$ , and  $369.8 \pm 108.7$   $\mu\text{g/g}$ , respectively. The content of friedelin was

$180.8 \pm 4.7$ ,  $226.2 \pm 20.2$ ,  $251.6 \pm 43.7$ , and  $225.9 \pm 19.4$   $\mu\text{g/g}$  in the pH7WG2D control group, *TwSQS* overexpression group, *TwSE* overexpression group, and *TwOSC* overexpression group, respectively. Only the content of squalene determined in the *TwSE* overexpression group had no significant differences compared with the control group. However, we did not detect any 2,3-oxidosqualene in both CMCs and DDCs.

### Accumulation of Celastrol in *Tripterygium wilfordii* Cambial Meristematic Cells and Dedifferentiated Cells

The content of celastrol was determined in *T. wilfordii* CMCs and DDCs after overexpression (**Figure 3B**; **Supplementary Figure 4**). Compared with the control group, the content of celastrol in CMCs overexpression group showed an increase with statistical difference. In the pH7WG2D control group, *TwSQS* overexpression group, *TwSE* overexpression group, and *TwOSC* overexpression group, the content of celastrol in CMCs was  $937.6 \pm 106.9$ ,  $1,209.8 \pm 111.3$ ,  $1,217.6 \pm 95.0$ , and  $1,125.2 \pm 95.7$   $\mu\text{g/g}$ , respectively. In contrast to this, there was no significant difference in the content of celastrol between DDCs overexpression group and the control group.

### Relative Expression Analysis of *TwSQS*, *TwSE*, and *TwOSC* in *Tripterygium wilfordii* Cambial Meristematic Cells and Dedifferentiated Cells

To further investigate the transcription levels of overexpressed genes, the relative expression levels of *TwSQS*, *TwSE*, and *TwOSC* were determined by qRT-PCR (**Figure 4A**). In CMCs, relative expression levels of *TwSQS*, *TwSE*, and *TwOSC* increased by 2.5, 1.8, and 15.8 times compared with the pH7WG2D control group, respectively. As for DDCs, their relative expression levels exhibited 1.3-, 5.1-, and 2.9-fold increase compared with the control group, respectively. In both cell lines, the relative expression levels of the three genes showed statistical significance compared with the control group.

### Relative Expression Analysis of Other Important Genes Involved in Terpenoid Biosynthetic Pathway

Next, we analyzed the relative expression levels of other genes encoding important enzymes involved in terpenoid biosynthetic pathway after overexpression of *TwSQS*, *TwSE*, and *TwOSC*, respectively.

Under the *TwSQS* overexpression condition (**Figure 4B**), in terms of CMCs group, the relative expression levels of *TwSE*, *TwOSC*, *TwHMGR*, *TwIDI*, *TwDXS*, and *TwGGPPS* increased by 1.5, 7.7, 2.8, 3.1, 2.0, and 5.0 times, respectively, compared with the pH7WG2D control groups. The relative expression levels of *TwFPS* and *TwHMGS* were not statistically significant compared with the control group. As for DDCs group, in contrast to the relative expression levels of *TwOSC*, *TwIDI*, and *TwGGPPS* decreasing to 0.3-, 0.6-, and 0.3-fold, respectively,



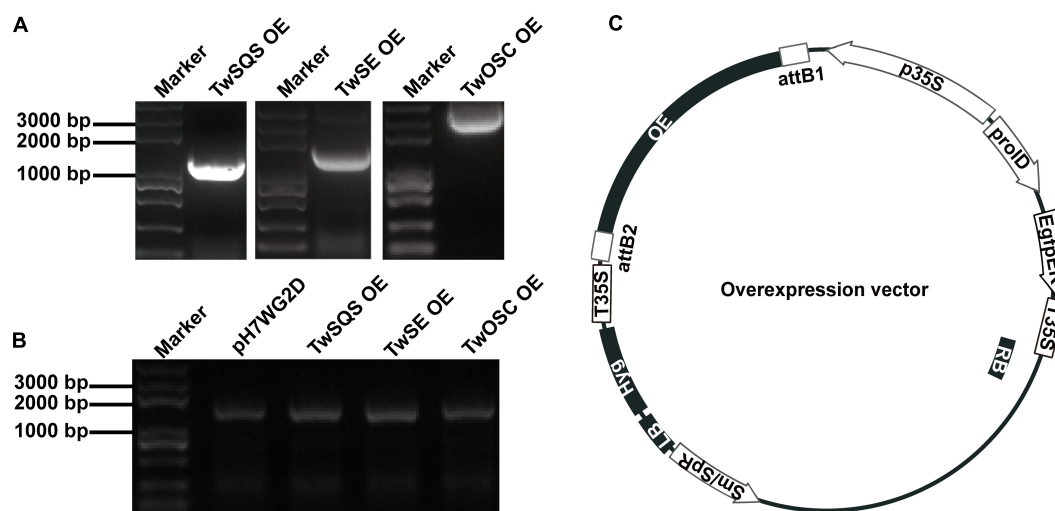


**FIGURE 1** | Construction and transfer verification of *TwSQS*, *TwSE*, and *TwOSC* overexpression vectors. **(A)** *TwSQS*, *TwSE*, and *TwOSC* overexpression fragments. *TwSQS* overexpression fragment of 1,241 bp, *TwSE* overexpression fragment of 1,584 bp, and *TwOSC* overexpression fragment of 2,298 bp. **(B)** Verification of successful transfer of overexpression vectors in *Tripterygium wilfordii* CMCs and DDCs. Agarose gel electrophoresis showed the hygromycin fragment (1,787 bp). **(C)** Schematic diagram of overexpression vectors. OE, overexpression; Hyg, hygromycin.

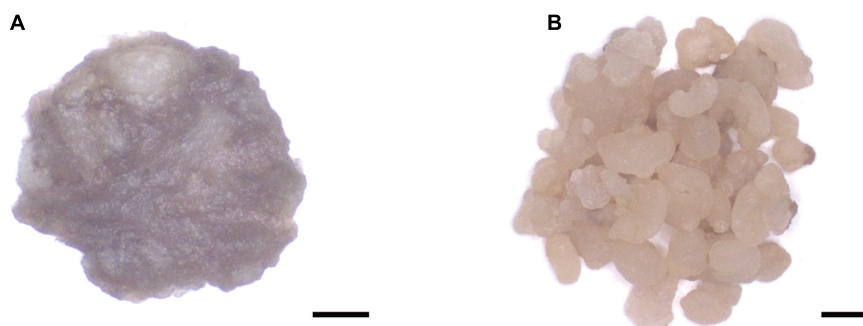


**FIGURE 2** | The morphology of *Tripterygium wilfordii* CMCs and DDCs. **(A)** CMCs were mostly aggregated by small cell groups. Scale bar, 2 mm. **(B)** DDCs were gathered with large cell groups. Scale bar, 2 mm.

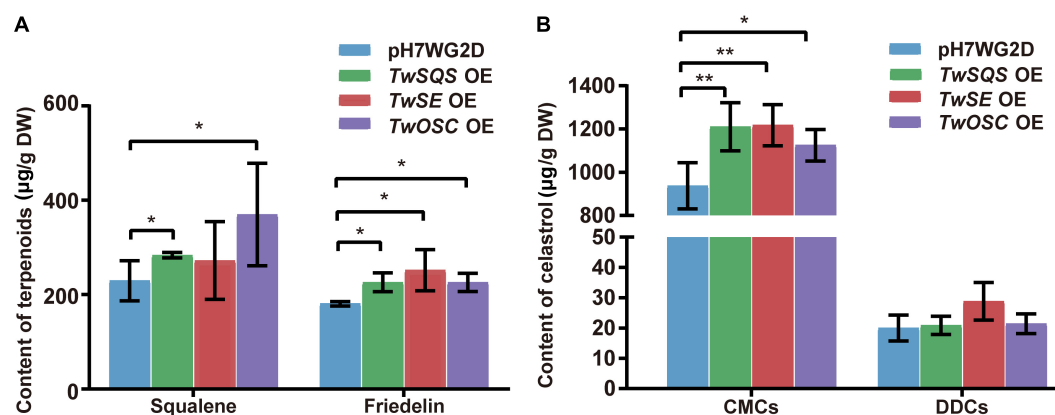


**FIGURE 3** | Accumulation of squalene, friedelin, and celastrol in *Tripterygium wilfordii* CMCs and DDCs after overexpressing *TwSQS*, *TwSE*, and *TwOSC*. **(A)** Accumulation of squalene and friedelin in CMCs. **(B)** Accumulation of celastrol in CMCs and DDCs. OE, overexpression; DW, dry weight. The data are summarized as means  $\pm$  standard deviation. \* $p < 0.05$  and \*\* $p < 0.01$ ,  $n = 5$ . Student's *t*-test.

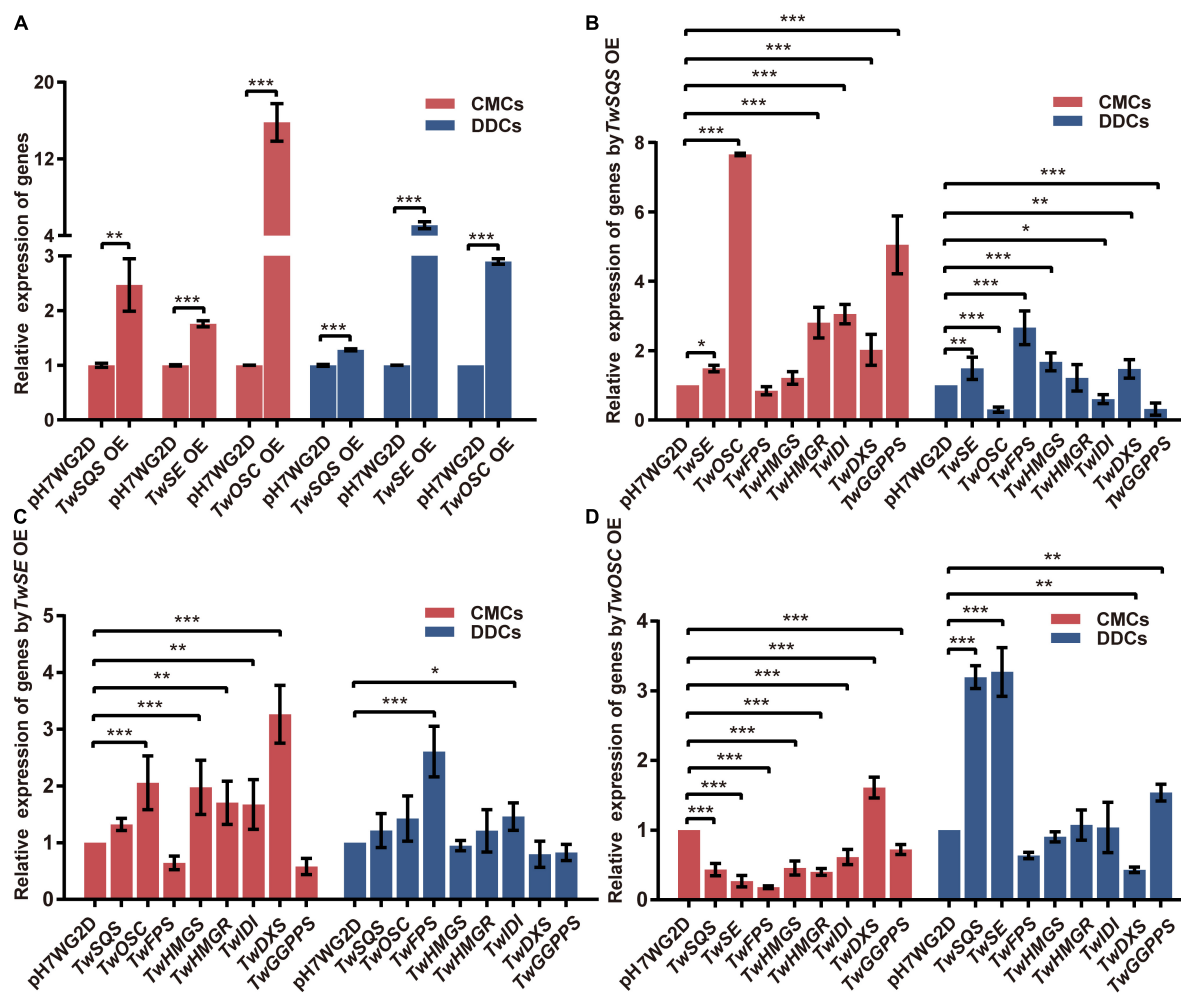


**FIGURE 4 |** Relative expression analysis of related genes involved in terpenoid biosynthetic pathway in *Tripterygium wilfordii* CMCs and DDCs after overexpression of *TwSQS*, *TwSE*, and *TwOSC*. **(A)** Relative expression levels of *TwSQS*, *TwSE*, and *TwOSC*. **(B)** Relative expression levels of related genes in terpenoid biosynthetic pathway after *TwSQS* overexpression. **(C)** Relative expression levels of related genes in terpenoid biosynthetic pathway after *TwSE* overexpression. **(D)** Relative expression levels of related genes in terpenoid biosynthetic pathway after *TwOSC* overexpression. OE, overexpression. The data are summarized as means  $\pm$  standard deviation. \* $p < 0.05$ , \*\* $p < 0.01$ , and \*\*\* $p < 0.001$ ,  $n = 5$ . Student's *t*-test.

the relative expression levels of *TwSE*, *TwFPS*, *TwHMGS*, and *TwDXS* increased by 1.5, 2.7, 1.7, and 1.5 times, respectively, compared with the control group. Only the relative expression level of *TwHMGR* was not statistically significant.

Under the *TwSE* overexpression condition (Figure 4C), in terms of CMCs group, the relative expression levels of *TwOSC*, *TwHMGS*, *TwHMGR*, *TwIDI*, and *TwDXS* increased by 2.1, 2.0, 1.7, 1.7, and 3.3 times, respectively, compared with the control group. The relative expression levels of *TwSQS*, *TwFPS*, and *TwGGPPS* were not statistically significant. As for the DDCs group, only the relative expression levels of *TwFPS* and *TwIDI* were statistically significant, increasing by 2.6 and 1.5 times compared with the control group, respectively.

Under the *TwOSC* overexpression condition (Figure 4D), in terms of CMCs group, apart from an increase in relative expression level of *TwDXS* by 1.61 times, the relative expression levels of *TwSQS*, *TwSE*, *TwFPS*, *TwHMGS*, *TwHMGR*, *TwIDI*,

and *TwGGPPS* reduced by 0.4-, 0.3-, 0.2-, 0.5-, 0.4-, 0.6-, and 0.7-fold compared with the control group, respectively. The relative expression levels of all genes determined were statistically significant. As for the DDCs group, compared with the control group, the relative expression levels of *TwSQS*, *TwSE*, and *TwGGPPS* increased by 3.2, 3.3, and 1.5 times, respectively, but the relative expression level of *TwDXS* decreased to 0.4-fold. The expression levels of *TwFPS*, *TwHMGS*, *TwHMGR*, and *TwIDI* were not statistically significant.

## DISCUSSION

In our study, we obtained the overexpression vectors of *TwSQS*, *TwSE*, and *TwOSC*, and they were transferred into *T. wilfordii* CMCs and DDCs individually. After overexpression of each gene, the content of triterpenoid celastrol increased in CMCs, but not

in DDCs. Meanwhile, the relative expression levels of *TwSQS*, *TwSE*, and *TwOSC* were all enhanced in CMCs. These results indicate that *TwSQS*, *TwSE*, and *TwOSC* were involved in the biosynthesis of celastrol. Furthermore, overexpression of *TwSQS*, *TwSE*, and *TwOSC* had a stronger effect on the biosynthesis of celastrol in CMCs than in DDCs.

In this study, the direct product 2,3-oxidosqualene of *TwSE* enzyme was not detected in both *T. wilfordii* CMCs and DDCs after overexpression of *TwSE*. The reason is probably that 2,3-oxidosqualene contains an epoxy group in the molecule, which is usually unstable and may be easily degraded or converted into other compounds (Araki et al., 2016). Another possibility could be that in other biosynthetic pathways, such as sterol and non-steroidal triterpene biosynthetic pathways, the immediate utilization of the substrate 2,3-oxidosqualene by other downstream enzymes is highly efficient, such as lanosterol synthase and cycloartenol synthase (Babiychuk et al., 2008). Besides, in this study, squalene and friedelin were detected in CMCs, but not in DDCs. The reason for this phenomenon might be that intermediate products in DDCs were likely to transform into other compounds (such as sterol) soon before detection. Furthermore, overexpression of a gene involved in terpenoid biosynthetic pathway might lead to increase the flux toward the steroid biosynthesis pathway (Engels et al., 2008), which could be the reason why no significant increase in celastrol was detected in DDCs. The biosynthetic pathways of *T. wilfordii* terpenoids and steroids are so complex that further research is required to fully elucidate them.

Overexpression of terpenoid biosynthetic enzyme genes may affect the expression of other genes in the pathway (Tong et al., 2019; Zhang et al., 2020). In this study, the relative expression levels of terpenoid biosynthetic pathway related genes showed different trends after overexpression of *TwSQS*, *TwSE*, and *TwOSC* in *T. wilfordii* CMCs and DDCs (Figure 5), resulting in different effects on the biosynthesis of terpenoids. In addition, after overexpression of *TwSQS*, *TwSE*, and *TwOSC* in CMCs, the relative expression of *TwDXS* pathway was increased, leading to an increase in the content of celastrol, which indicates that *TwDXS*, *TwSQS*, *TwSE*, and *TwOSC* seem to have synergistic effects during the biosynthesis of celastrol. Moreover, after *TwOSC* overexpression, though the relative expression levels of terpenoid biosynthetic pathway related genes detected in CMCs were all decreased except *TwDXS*, the content of celastrol was still increased, which could be attributed to the feedback regulation on the expression of genes in the pathway (Zhang et al., 2018).

In this study, the content of celastrol increased in CMCs, but there was no significant increment of celastrol in DDCs after overexpression of each gene. This may be due to the morphological difference between the two cell lines. Studies have shown that vacuoles in plant cells can dynamically store secondary metabolites, including terpenoids, alkaloids, and flavonoids (De Brito Francisco and Martinoia, 2018). In a previous study, we found that the morphology of CMCs and DDCs was quite different. A single CMC had a number of vacuoles, while a single DDC only had one vacuole (Song et al., 2019). Compared with one vacuole in the DDC, the large number of vacuoles could allow celastrol to be stored in the CMC as much

as possible before detection. Moreover, the content of celastrol produced in CMCs was 57.9-, 37.5-, and 53.3-fold higher than that of DDCs after *TwSQS*, *TwSE*, and *TwOSC* overexpression, respectively. In addition to the morphological difference of two cell lines, differences in gene expression may contribute to this result. The relative expression levels of *TwSQS* and *TwOSC* in CMCs were higher than that of DDCs after overexpression. Higher gene expression might contribute to higher celastrol accumulation in CMCs. Our results demonstrate that CMCs could be used as a better system than DDCs to study the function of genes involved in the biosynthetic pathway of celastrol.

After gene overexpression, the content of celastrol produced by the empty vector of CMCs was 46.9 times higher than that of DDCs. It is probably due to the different degrees of stimulation caused by the same empty vector in two different cell lines. As depicted from the results of Figures 3B, 4A, among the three genes, in CMCs, although *TwSE* had the lowest expression level after overexpression alone, it has the most increased celastrol content. While the expression level of *TwOSC* was highest after overexpression alone, the increase in celastrol content was minimal. After overexpression alone, the expression level of *TwOSC* and the increase in celastrol content were moderate. In DDCs, although expression levels of the three genes increased after overexpression, the celastrol content did not increase with a significant difference. As mentioned above, overexpression of *TwSE* was more conducive to the production of celastrol, while overexpression of *TwSQS* had less effect on that among the three genes.

In terms of the effects of downstream genes (Figures 4B–D), when *TwSQS* was overexpressed alone, in CMCs, the expression levels of *TwSE* and *TwOSC* increased; In DDCs, the expression level of *TwSE* increased, but the expression level of *TwOSC* decreased. When *TwSE* was overexpressed alone, in CMCs, the expression levels of *TwSQS* and *TwOSC* increased, but there was no significant difference in *TwSQS*; In DDCs, the expression levels of *TwSQS* and *TwOSC* increased without a significant difference. When *TwOSC* was overexpressed alone, the expression levels of *TwSQS* and *TwSE* decreased in CMCs and increased in DDCs. Moreover, SE is a rate-limiting enzyme in the biosynthetic pathway of terpenoids (Han et al., 2010). In the future, we can further explore the effect of *TwSE* on celastrol biosynthesis in CMCs to fully clarify how *TwSE* increases celastrol content in terms of molecular mechanism. We can also utilize the CMCs system to extract other functional unknown genes in the downstream biosynthetic pathway of celastrol.

In this study, it was the first time that CMCs had been applied to a genetic transformation system. Compared with the stable gene transformation system of suspension cells, CMCs system exhibited unique enchantment. Most CMCs present as a single cell or as clusters of small cells, whereas suspension cells are present as large aggregates (Song et al., 2019). Less aggregation may not form non-productive microenvironments and increase the nutrient and oxygen supply to CMCs (Ochoa-Villarreal et al., 2015), resulting in a more stable growth state of CMCs. Besides, shear stress is a crucial limitation in the scale-up of plant cells, affecting cells by causing death due to fluid motion (Joshi et al., 1996). The reduced aggregation size

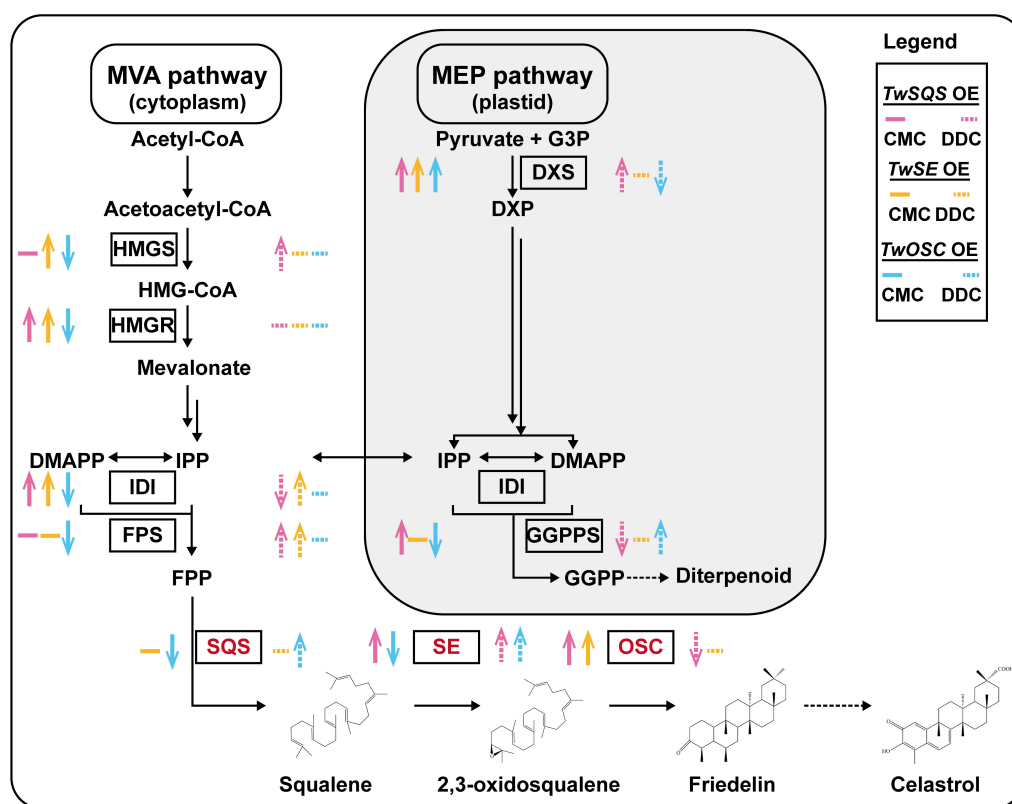


**FIGURE 5 |** The expression trends of genes involved in terpenoid biosynthetic pathway after overexpression of *TwSQS*, *TwSE*, and *TwOSC* based on Figure 4.

A black single arrow represents a one-step reaction, a black double arrow represents a multistep reaction, and a black dotted arrow represents unknown steps. The colored upward or downward arrows indicate corresponding increase and decrease in gene expression. Colored horizontal line represents no statistical significance between the overexpression group and the pH7WG2D control group. The *SQS*, *SE*, and *OSC* enzymes analyzed in this study are highlighted in red. OE, overexpression.

of CMC decreases sensitivity of shear stress. The characteristics of numerous vacuoles and thin cell wall in CMCs are also thought to increase tolerance to shear stress (Lee et al., 2010; Song et al., 2019). When cultured in a 20-L air-lift bioreactor, *Taxus cuspidata* (T. cuspidata) CMCs grew strikingly faster and healthier compared with DDCs, which turned into necrotic cells largely and rapidly (Lee et al., 2010). The production of paclitaxel in T. cuspidata CMCs was considerably higher than that of DDCs. Furthermore, an important factor that negatively impacts production of natural products is the heterogeneous nature of cells. Suspension cells consist of a mixture of different cell types, resulting in a high level of heterogeneity (Lee et al., 2010). As CMCs are innately undifferentiated cells with plant stem cell-like property, CMCs bypass the negative effects of the differentiation step, offering stability in product accumulation. CMCs are also highly responsive to elicitation (Lee et al., 2010; Song et al., 2019). The utilization of CMCs system provides a promising platform for the production of natural products.

Hairy root system can offer high production of natural products. Hairy roots from cocultivation accumulated 1,086 µg/g (fresh weight) of enecalinal, which is more than three times higher than that of suspension cells system

(Hernández-Altamirano et al., 2020). Hairy root system has also gained attention for the production of pharmacologically functional proteins (Parsons et al., 2010). But there is no report on CMCs in these fields. However, an important limitation in the production of natural products from hairy roots is that the target molecule must be biosynthesized within the roots of the original plant. This is significant because relatively few natural products are synthesized in root tissues, with the majority produced in aerial parts (Li and Wang, 2021). Whereas CMCs are obtained from cambium tissue in plants (Lee et al., 2010), they are not limited to the roots of plants. Moreover, a major limitation for the industrial-scale production of natural products using hairy roots is the development of appropriate bioreactors. The complex fibrous structure of the roots makes it difficult for a large-scale culture system. Hairy root growth is not homogeneous, which affects the reactor performance (Wilson et al., 1987), but CMCs are not subjected to the limitations mentioned above, and they could grow stably in 3-ton bioreactor with high performance (Lee et al., 2010). However, there is no report on the comparison of CMCs and hairy root in genetic transformation and accumulation of natural products. These require further studies to comprehensively compare the differences between CMCs and other systems.



In conclusion, it was verified in *T. wilfordii* CMCs that overexpression of *TwSQS*, *TwSE*, and *TwOSC* increased celastrol accumulation and had different effects on the expression of related genes in terpenoid biosynthetic pathway, which laid a foundation for further elucidating the downstream biosynthetic pathway of celastrol through *T. wilfordii* CMCs system. The established CMC system provides a useful tool to analyze other functional unknown genes in *T. wilfordii* in the near future.

## DATA AVAILABILITY STATEMENT

The datasets presented in this study can be found in online repositories. The names of the repository/repositories and accession number(s) can be found in the article/**Supplementary Material**.

## AUTHOR CONTRIBUTIONS

YS, XW, and WG conceived and designed the research. YS conducted the experiments and wrote the manuscript. JZ assisted

the vector construction. YFZ and YJZ assisted the gene gun technology. TH, YT, and LH assisted the data analysis. All authors had given approval to the final version of the manuscript.

## FUNDING

This study was supported by the National Key R&D Program of China (2020YFA0908000), the Key Project at central government level: The ability establishment of sustainable use for valuable Chinese medicine resources (2060302-1806-03), the National Natural Science Foundation of China (81973418), and the Innovation Team and Talents Cultivation Program of National Administration of Traditional Chinese Medicine (ZYYCXTD-D-202005).

## SUPPLEMENTARY MATERIAL

The Supplementary Material for this article can be found online at: <https://www.frontiersin.org/articles/10.3389/fpls.2022.926715/full#supplementary-material>

## REFERENCES

- Abe, I., Rohmer, M., and Prestwich, G. D. (1994). ChemInform abstract: enzymatic cyclization of squalene and oxidosqualene to sterols and triterpenes. *ChemInform* 25, doi: 10.1002/chin.199403295
- Araki, M., Kaku, N., Harada, M., Ando, Y., Yamaguchi, R., and Shindo, K. (2016). Production of auroxanthins from violaxanthin and 9-cis-violaxanthin by acidic treatment and the antioxidant activities of violaxanthin, 9-cis-violaxanthin, and auroxanthins. *J. Agric. Food Chem.* 64, 9352–9355. doi: 10.1021/acs.jafc.6b04506
- Babychuk, E., Bouvier-Navé, P., Compagnon, V., Suzuki, M., Muranaka, T., Van Montagu, M., et al. (2008). Allelic mutant series reveal distinct functions for Arabidopsis cycloartenol synthase 1 in cell viability and plastid biogenesis. *Proc. Natl. Acad. Sci. USA* 105, 3163–3168. doi: 10.1073/pnas.0712190105
- Corson, T. W., and Crews, C. M. (2007). Molecular understanding and modern application of traditional medicines: triumphs and trials. *Cell* 130, 769–774. doi: 10.1016/j.cell.2007.08.021
- De Brito Francisco, R., and Martinoia, E. (2018). The Vacuolar Transportome of Plant Specialized Metabolites. *Plant Cell Physiol.* 59, 1326–1336. doi: 10.1093/pcp/pcy039
- Engels, B., Dahm, P., and Jennewein, S. (2008). Metabolic engineering of taxadiene biosynthesis in yeast as a first step towards Taxol (Paclitaxel) production. *Metab. Eng.* 10, 201–206. doi: 10.1016/j.ymben.2008.03.001
- Guo, L., Luo, S., Du, Z., Zhou, M., Li, P., Fu, Y., et al. (2017). Targeted delivery of celastrol to mesangial cells is effective against mesangioproliferative glomerulonephritis. *Nat. Commun.* 8:878. doi: 10.1038/s41467-017-00834-8
- Han, J. Y., Ahn, C. H., Adhikari, P. B., Kondeti, S., and Choi, Y. E. (2019). Functional characterization of an oxidosqualene cyclase (PdFRS) encoding a monofunctional friedelin synthase in *Populus davidiana*. *Planta* 249, 95–111. doi: 10.1007/s00425-018-2985-8
- Han, J. Y., In, J. G., Kwon, Y. S., and Choi, Y. E. (2010). Regulation of ginsenoside and phytosterol biosynthesis by RNA interferences of squalene epoxidase gene in *Panax ginseng*. *Phytochemistry* 71, 36–46. doi: 10.1016/j.phytochem.2009.09.031
- Hernández-Altamirano, J. M., Ugidos, I. F., Palazón, J., Bonfill, M., García-Angulo, P., Álvarez, J., et al. (2020). Production of Encelalin in Cell Cultures and Hairy Roots of *Helianthella quinquenervis* (Hook.). *Molecules* 25:3231. doi: 10.3390/molecules25143231
- Joshi, J. B., Elias, C. B., and Patole, M. S. (1996). Role of hydrodynamic shear in the cultivation of animal, plant and microbial cells. *Chem. Eng. J. Biochem. Eng. J.* 62, 121–141. doi: 10.1016/0923-0467(95)03062-X
- Lee, E. K., Jin, Y. W., Park, J. H., Yoo, Y. M., Hong, S. M., Amir, R., et al. (2010). Cultured cambial meristematic cells as a source of plant natural products. *Nat. Biotechnol.* 28, 1213–1217. doi: 10.1038/nbt.1693
- Lee, M. H., Jeong, J. H., Seo, J. W., Shin, C. G., Kim, Y. S., In, J. G., et al. (2004). Enhanced triterpene and phytosterol biosynthesis in *Panax ginseng* overexpressing squalene synthase gene. *Plant Cell Physiol.* 45, 976–984. doi: 10.1093/pcp/pch126
- Li, C., and Wang, M. (2021). Application of Hairy Root Culture for Bioactive Compounds Production in Medicinal Plants. *Curr. Pharm. Biotechnol.* 22, 592–608. doi: 10.2174/1389201021666200516155146
- Li, H., Zhang, Y. Y., Huang, X. Y., Sun, Y. N., Jia, Y. F., and Li, D. (2005). Beneficial effect of tripteryne on systemic lupus erythematosus induced by active chromatin in BALB/c mice. *Eur. J. Pharmacol.* 512, 231–237. doi: 10.1016/j.ejphar.2005.02.030
- Liu, X. H., Zhao, P. Y., Wang, X. J., Wang, L., Zhu, Y. J., Song, Y. D., et al. (2019). Celastrol mediates autophagy and apoptosis via the ROS/JNK and Akt/mTOR signaling pathways in glioma cells. *J. Exp. Clin. Cancer Res.* 38:184. doi: 10.1186/s13046-019-1173-4
- Liu, Y. J., Su, P., Wang, X. J., Zhao, Y. J., Tong, Y. R., Hu, T. Y., et al. (2016). [Cloning and expression analysis of squalene synthase gene in *Tripterygium wilfordii*]. *Yao Xue Xue Bao* 51, 657–661.
- Liu, Z., Ma, L., and Zhou, G. B. (2011). The main anticancer bullets of the Chinese medicinal herb, thunder god vine. *Molecules* 16, 5283–5297. doi: 10.3390/molecules16065283
- Livak, K. J., and Schmittgen, T. D. (2001). Analysis of relative gene expression data using real-time quantitative PCR and the 2<sup>(-delta delta c(t))</sup> method. *Methods* 25, 402–408. doi: 10.1006/meth.2001.1262
- Ma, X., Xu, L., Alberobello, A. T., Gavrilova, O., Bagattin, A., Skarulis, M., et al. (2015). Celastrol protects against obesity and metabolic dysfunction through activation of a HSF1-PGC1 alpha transcriptional axis. *Cell Metab.* 22, 695–708. doi: 10.1016/j.cmet.2015.08.005
- Moon, S. H., Venkatesh, J., Yu, J. W., and Park, S. W. (2015). Differential induction of meristematic stem cells of *Catharanthus roseus* and their characterization. *C R Biol.* 338, 745–756. doi: 10.1016/j.crvi.2015.05.005
- Ochoa-Villarreal, M., Howat, S., Jang, M. O., Kim, I. S., Jin, Y. W., Lee, E. K., et al. (2015). Cambial meristematic cells: a platform for the production of plant natural products. *N. Biotechnol.* 32, 581–587. doi: 10.1016/j.nbt.2015.02.003

- Parsons, J., Wirth, S., Dominguez, M., Bravo-Almonacid, F., Giulietti, A. M., and Talou, J. R. (2010). Production of human epidermal growth factor (hEGF) by in vitro cultures of *Nicotiana tabacum* effect of tissue differentiation and sodium nitroprusside addition. *Int. J. Biotechnol. Biochem.* 6, 131–138.
- Rodriguez-Concepcion, M., and Boronat, A. (2002). Elucidation of the methylerythritol phosphate pathway for isoprenoid biosynthesis in bacteria and plastids. A metabolic milestone achieved through genomics. *Plant Physiol.* 130, 1079–1089. doi: 10.1104/pp.007138
- Song, Y. D., Chen, S., Wang, X. J., Zhang, R., Tu, L. C., Hu, T. Y., et al. (2019). A novel strategy to enhance terpenoids production using cambial meristematic cells of *Tripterygium wilfordii* Hook. f. *Plant Methods* 15:129. doi: 10.1186/s13007-019-0513-x
- Tong, Y. R., Zhang, Y. F., Zhao, Y. J., Hu, T. Y., Wang, J. D., Huang, L. Q., et al. (2019). Differential expression of the TwHMGs gene and its effect on triptolide biosynthesis in *Tripterygium wilfordii*. *Chin. J. Nat. Med.* 17, 575–584. doi: 10.1016/s1875-5364(19)30059-7
- Vranova, E., Coman, D., and Grisse, W. (2013). Network analysis of the MVA and MEP pathways for isoprenoid synthesis. *Ann. Rev. Plant Biol.* 64, 665–700. doi: 10.1146/annurev-arplant-050312-120116
- Wang, Z., Ravula, R., Shi, L., Song, Y., Yeung, S., Liu, M., et al. (2016). Overcoming chemoresistance in prostate cancer with Chinese medicine *Tripterygium wilfordii* via multiple mechanisms. *Oncotarget* 7, 61246–61261. doi: 10.18632/oncotarget.10868
- Wilson, P. D. G., Hilton, M. G., Robins, R. J., and Rhodes, M. J. C. (1987). "Fermentation studies of transformed root cultures," in *International Conference on Bioreactors and Biotransformations*, eds G. W. Moody and P. B. Baker (Elsevier), 38–51.
- Xu, W. Y., Zheng, J. R., and Lu, X. Y. (1985). *Tripterygium* in dermatologic therapy. *Int. J. Dermatol.* 24, 152–157. doi: 10.1111/j.1365-4362.1985.tb05746.x
- Zhang, D. H., Jiang, L. X., Li, N., Yu, X., Zhao, P., Li, T., et al. (2017). Overexpression of the squalene epoxidase gene alone and in combination with the 3-hydroxy-3-methylglutaryl coenzyme a gene increases ganoderic acid production in *Ganoderma lingzhi*. *J. Agric. Food Chem.* 65, 4683–4690. doi: 10.1021/acs.jafc.7b00629
- Zhang, W., Li, F., and Gao, W. (2017). *Tripterygium wilfordii* inhibiting angiogenesis for rheumatoid arthritis treatment. *J. Natl. Med. Assoc.* 109, 142–148. doi: 10.1016/j.jnma.2017.02.007
- Zhang, Y. H., Jiang, K. M., Qing, D. G., Huang, B., Jiang, J. Y., Wang, S. M., et al. (2017). Accumulation of camptothecin and 10-hydroxycamptothecin and the transcriptional expression of camptothecin biosynthetic genes in *Camptotheca acuminata* cambial meristematic and dedifferentiated cells. *RSC Adv.* 7, 12185–12193. doi: 10.1039/C7RA00588A
- Zhang, Y. F., Zhao, Y. J., Wang, J. D., Hu, T. Y., Tong, Y. R., Zhou, J. W., et al. (2018). Overexpression and RNA interference of TwDXR regulate the accumulation of terpenoid active ingredients in *Tripterygium wilfordii*. *Biotechnol. Lett.* 40, 419–425. doi: 10.1007/s10529-017-2484-1
- Zhang, Y. F., Zhao, Y. J., Wang, J. D., Hu, T. Y., Tong, Y. R., Zhou, J. W., et al. (2020). The expression of TwDXS in the MEP pathway specifically affects the accumulation of triptolide. *Physiol. Plant* 169, 40–48. doi: 10.1111/ppl.13051
- Zhao, Y. J., Zhang, Y. F., Su, P., Yang, J., Huang, L. Q., and Gao, W. (2017). Genetic transformation system for woody plant *Tripterygium wilfordii* and its application to product natural celastrol. *Front. Plant Sci.* 8:2221. doi: 10.3389/fpls.2017.02221
- Zhou, J. W., Hu, T. Y., Gao, L. H., Su, P., Zhang, Y. F., Zhao, Y. J., et al. (2019). Friedelane-type triterpene cyclase in celastrol biosynthesis from *Tripterygium wilfordii* and its application for triterpenes biosynthesis in yeast. *N. Phytol.* 223, 722–735. doi: 10.1111/nph.15809
- Zhou, J. W., Zhang, Y., Hu, T. Y., Su, P., Zhang, Y. F., Liu, Y. J., et al. (2018). Functional characterization of squalene epoxidase genes in the medicinal plant *Tripterygium wilfordii*. *Int. J. Biol. Macromol.* 120, 203–212. doi: 10.1016/j.ijbiomac.2018.08.073

**Conflict of Interest:** The authors declare that the research was conducted in the absence of any commercial or financial relationships that could be construed as a potential conflict of interest.

**Publisher's Note:** All claims expressed in this article are solely those of the authors and do not necessarily represent those of their affiliated organizations, or those of the publisher, the editors and the reviewers. Any product that may be evaluated in this article, or claim that may be made by its manufacturer, is not guaranteed or endorsed by the publisher.

Copyright © 2022 Song, Zhou, Zhang, Zhao, Wang, Hu, Tong, Huang and Gao. This is an open-access article distributed under the terms of the Creative Commons Attribution License (CC BY). The use, distribution or reproduction in other forums is permitted, provided the original author(s) and the copyright owner(s) are credited and that the original publication in this journal is cited, in accordance with accepted academic practice. No use, distribution or reproduction is permitted which does not comply with these terms.

# Advantages of publishing in Frontiers



## OPEN ACCESS

Articles are free to read  
for greatest visibility  
and readership



## FAST PUBLICATION

Around 90 days  
from submission  
to decision



## HIGH QUALITY PEER-REVIEW

Rigorous, collaborative,  
and constructive  
peer-review



## TRANSPARENT PEER-REVIEW

Editors and reviewers  
acknowledged by name  
on published articles

## Frontiers

Avenue du Tribunal-Fédéral 34  
1005 Lausanne | Switzerland

Visit us: [www.frontiersin.org](http://www.frontiersin.org)

Contact us: [frontiersin.org/about/contact](http://frontiersin.org/about/contact)



## REPRODUCIBILITY OF RESEARCH

Support open data  
and methods to enhance  
research reproducibility



## DIGITAL PUBLISHING

Articles designed  
for optimal readership  
across devices



## FOLLOW US

@frontiersin



## IMPACT METRICS

Advanced article metrics  
track visibility across  
digital media



## EXTENSIVE PROMOTION

Marketing  
and promotion  
of impactful research



## LOOP RESEARCH NETWORK

Our network  
increases your  
article's readership